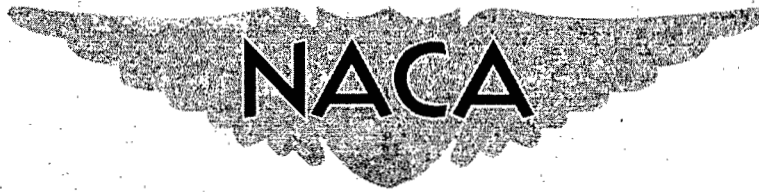


CONFIDENTIAL

C7
Copy 6
RM E56BO3



RESEARCH MEMORANDUM

AERODYNAMIC DESIGN OF AXIAL-FLOW COMPRESSORS

VOLUME I

By Members of the Compressor and Turbine Research Division

Lewis Flight Propulsion Laboratory
Cleveland, Ohio

CLASSIFICATION CHANGED
UNCLASSIFIED

To _____
By authority of *NACA Res also* *effective*
4 RN-130 *Sept 3, 1948*
Am 10-6-54

CLASSIFIED DOCUMENT

This material contains information affecting the National Defense of the United States within the meaning of the espionage laws, Title 18, U.S.C., Secs. 793 and 794, the transmission or revelation of which in any manner to an unauthorized person is prohibited by law.

NATIONAL ADVISORY COMMITTEE
FOR AERONAUTICS

WASHINGTON

August 1, 1956

CONFIDENTIAL

NACA RM E56B03



AERODYNAMIC DESIGN OF AXIAL-FLOW COMPRESSORS

VOLUME I

By Members of the Compressor and Turbine Research Division
Lewis Flight Propulsion Laboratory
Cleveland, Ohio

Edited by
Irving A. Johnsen and Robert O. Bullock

FOREWORD

With the advent of turbojet engines for aircraft propulsion, the necessity for intense research effort on the axial-flow type of compressor became apparent. During succeeding years, stimulated by the demand for improved gas-turbine engines for both military and civil application, compressor research efforts have been accelerated both in this country and abroad.

The pertinent results of these research investigations have been summarized in numerous publications by government, industry, and the universities. Unfortunately, the published material has become so comprehensive that it is difficult for even the compressor specialist to keep abreast of the information in the field. A definite need for a summarization of aerodynamic design information on compressors has, therefore, been recognized. Several excellent texts on this subject have been published, intended primarily for educational use. In addition, the volume on Aerodynamics of Turbines and Compressors, which is to be published in the Princeton series on High-Speed Aerodynamics and Jet Propulsion, represents a valuable addition to the literature. However, since these publications contain only unclassified information, there remains an urgent need for a summary including those recent research results which, because of their significance, have been placed in a classified category.

Recognizing this situation, the staff of the Compressor and Turbine Research Division of the NACA Lewis laboratory has prepared this compendium, intended to form a comprehensive integration of available aerodynamic design information on axial-flow compressors. Of course, detailed treatment of all of the available literature was impossible. Instead, the attempt was made to provide an accurate picture of the state of the art by judicious selection of source material. The references used are considered to be technically pertinent and representative of other literature in the field. In order to summarize the material as clearly and succinctly as possible, it is presented as a series of reports or chapters, each concerning a separate aspect of compressor design.

In the preparation of this compressor design summary, special credit should be given to those members of the Lewis staff who assisted in the editing of the reports. In particular, the efforts of Messrs. Irving A. Johnsen, Robert O. Bullock, William A. Benser, Harold B. Finger, and John F. Klapproth, who comprised the permanent technical editorial board, were invaluable to the authors.

This series of reports, therefore, is dedicated to the summarizing and consolidating of current information on the aerodynamic design of axial-flow compressors. It is hoped that this effort will be of value to those interested in the field.

Oscar W. Schey
Chief, Compressor and Turbine
Research Division

TABLE OF CONTENTS

AERODYNAMIC DESIGN OF AXIAL-FLOW COMPRESSORS

VOLUME I

FOREWORD

CHAPTER

- I - OBJECTIVES AND SCOPE
- II - COMPRESSOR DESIGN REQUIREMENTS
- III - COMPRESSOR DESIGN SYSTEM
- IV - POTENTIAL FLOW IN TWO-DIMENSIONAL CASCADES
- V - VISCOUS FLOW IN TWO-DIMENSIONAL CASCADES

VOLUME II

CHAPTER

- VI - EXPERIMENTAL FLOW IN TWO-DIMENSIONAL CASCADES
- VII - BLADE-ELEMENT FLOW IN ANNULAR CASCADES
- VIII - DESIGN VELOCITY DISTRIBUTION IN MERIDIONAL PLANE
- IX - CHART PROCEDURES FOR DESIGN VELOCITY DISTRIBUTION
- X - PREDICTION OF OFF-DESIGN PERFORMANCE OF MULTISTAGE COMPRESSORS

VOLUME III

CHAPTER

- XI - COMPRESSOR STALL AND BLADE VIBRATION
- XII - COMPRESSOR SURGE
- XIII - COMPRESSOR OPERATION WITH ONE OR MORE BLADE ROWS STALLED
- XIV - THREE-DIMENSIONAL COMPRESSOR FLOW THEORY AND REAL FLOW EFFECTS
- XV - SECONDARY FLOWS AND THREE-DIMENSIONAL BOUNDARY-LAYER EFFECTS
- XVI - EFFECTS OF DESIGN AND MEASUREMENT ERRORS ON COMPRESSOR PERFORMANCE
- XVII - COMPRESSOR AND TURBINE MATCHING

TABLE OF CONTENTS

VOLUME I

Chapter	Page
I - OBJECTIVES AND SCOPE, by Irving A. Johnsen and Robert O. Bullock	1
SUMMARY	1
INTRODUCTION	1
DESCRIPTION OF AXIAL-FLOW COMPRESSOR	2
HISTORICAL BACKGROUND	3
COMPRESSOR DESIGN APPROACH	4
OBJECTIVES OF DESIGN REPORT	6
SCOPE OF DESIGN REPORT	7
CONCLUDING REMARKS	11
REFERENCES	12
FIGURES	14
II - COMPRESSOR DESIGN REQUIREMENTS, by Robert O. Bullock and Ernst I. Prasse	17
SUMMARY	17
INTRODUCTION	17
SYMBOLS	18
EFFECTS OF ENGINE CHARACTERISTICS ON AIRPLANE	
PERFORMANCE	22
Engine Weight	23
Engine Efficiency	29
Thrust per Unit Frontal Area	32
Other Engine Requirements	34
EFFECTS OF COMPRESSOR PRESSURE RATIO, COMPRESSOR EFFICIENCY, AND FLIGHT CONDITIONS ON ENGINE PERFORMANCE . .	34
Assumptions Used in Cycle Analyses	35

Chapter	Page
Effects of Compressor Pressure Ratio and Flight Conditions on Turboprop-Engine Performance	36
Effects of Compressor Pressure Ratio and Flight Conditions on Turbojet-Engine Performance	39
Subsonic flight	40
Supersonic flight	41
Other Engine Cycles	43
Effects of Compressor Efficiency on Engine Performance	43
Turboprop engine	44
Turbojet engine	46
EFFECTS OF COMPRESSOR PRESSURE RATIO, FLOW CAPACITY, AND EFFICIENCY ON FRONTAL AREA OF OTHER ENGINE COMPONENTS .	48
Comparison of Frontal Areas for Subsonic Flight	51
Engine inlet	51
Combustor	52
Turbine	52
Afterburner	54
Nozzle	54
Comparison of Frontal Areas for Supersonic Flight . . .	54
Effects of Compressor Efficiency on Size of Components	
Downstream	56
FACTORS DETERMINING COMPRESSOR FLOW CAPACITY AND WEIGHT .	57
Flow Capacity	57
Layout and Weight	58
COMPRESSOR REQUIREMENTS	62
Design Point	62
Off-Design Considerations	64
One-Spool Turbojet Engine	64
Engine acceleration	65
Varying flight speeds	66
Reynolds number effects	67
Inlet flow distortions	68
Inlet matching problem	69
Two-Spool Turbojet Engine	71
Outer compressor	72
Inner compressor	72
Turboprop Engine	73
CONCLUDING REMARKS AND SUMMARY OF COMPRESSOR DESIGN OBJECTIVES	74
REFERENCES	75
FIGURES	79

Chapter	Page
III - COMPRESSOR DESIGN SYSTEM, by Robert O. Bullock and Irving A. Johnsen	129
SUMMARY	129
INTRODUCTION	129
SYMBOLS	131
FUNDAMENTAL CONCEPTS UNDERLYING DESIGN SYSTEM	134
Equations of Thermodynamics	134
Flow through stators	134
Flow through rotors	135
Analysis of Time-Steady and Inviscid Flow	137
Equations ignoring radial velocity	137
Causes of radial flows	140
Effect of radial flows on stream surface configuration	144
Experimental data required	145
Analysis of Viscosity Problem	145
Two-dimensional-cascade elements	145
Hub and casing boundary layers in compressor blade rows	146
Loading limits	149
Experimental data required	150
Treatment of Time-Unsteady Flows	150
REPRESENTATIVE EXPERIMENTAL DATA SUPPORTING DESIGN	
CONCEPTS	151
Two-Dimensional Cascades	152
Aerodynamic behavior	152
Types of experimental data observed	153
Inlet Guide Vanes	154
Free-vortex flow	155
Non-free-vortex flow	156
Rotors and Single-Stage Compressors	157
Free-vortex rotor blade rows	157
Non-free-vortex rotor blade rows	159
Transonic blade rows	160
Multistage Compressors	161
Performance of fifth stage	161
Performance of tenth rotor	162
Significance of Results	163
Main-flow region	163
Viscous-flow region	164
Accuracy of estimate of state of air	165

Chapter	Page
SYSTEM ADOPTED FOR DESIGN AND RESEARCH	167
Design-Point Solution in Meridional Plane	169
Over-all specifications	169
Velocity diagrams	170
Design equations	170
Average values of energy addition for entire blade row	173
Blade loading	174
Relative Mach number	174
Reynolds number	175
Axial velocity	175
Hub and tip contours	175
Blade Selection	176
Blade profile	176
Blade-element data	177
Chord length and number of blades	178
Off-Design Analysis	178
REQUIRED IMPROVEMENTS IN ANALYSES	179
Radial Distribution of Flow	179
Hub and Casing Boundary Layers	181
Secondary flows of blade boundary layer and wakes	181
Cross-channel flows and passage vortex formation	182
Flow in blade end regions with clearance	182
Mixing of hub and casing boundary layers with main flow	182
Loading Limits	183
CONCLUDING REMARKS	184
REFERENCES	184
FIGURES	189
IV - POTENTIAL FLOW IN TWO-DIMENSIONAL CASCADES, by William H. Roudebush	227
SUMMARY	227
INTRODUCTION	229
SYMBOLS	231
GENERAL CONSIDERATIONS	236

Chapter	Page
LOW-SOLIDITY CASCADES	237
The Direct Problem	237
Isolated airfoils	238
Cascades	239
Solution of low-solidity direct problem	242
The Inverse Problem	248
Isolated airfoils	248
Cascades	248
Solution of low-solidity inverse problem	249
Compressibility Considerations	257
Hodograph method	258
Small-perturbation method	262
HIGH-SOLIDITY CASCADES	265
The Direct Problem	266
Stream-filament method	266
Relaxation and matrix solutions	271
The Inverse Problem	277
Approximate method	278
Exact method	281
ANALOG TECHNIQUES	285
Hydraulic Analog	286
Mechanical Analogs	290
Electrical Analogs	294
CONCLUDING REMARKS	296
APPENDIX A - VELOCITY DISTRIBUTION AT ARBITRARY ANGLE OF INCIDENCE	298
APPENDIX B - CASCADE MAPPING FUNCTION	301
APPENDIX C - RELAXATION CONSIDERATIONS	305
APPENDIX D - MATRIX CONSIDERATIONS	307
REFERENCES	309
FIGURES	316
V - VISCOUS FLOW IN TWO-DIMENSIONAL CASCADES, by William H. Roudebush and Seymour Lieblein	337
SUMMARY	337

Chapter	Page
INTRODUCTION	337
SYMBOLS	338
QUALITATIVE BOUNDARY-LAYER THEORY	341
General Considerations	341
Boundary-Layer Concepts	342
Types of boundary layers	342
Boundary-layer parameters	343
Loss parameters	344
Laminar Boundary Layer	346
Turbulent Boundary Layer	348
Transition	350
Infinitesimal-disturbance theory	351
Finite-disturbance theory	352
Flow about spheres	352
Boundary-layer reattachment	353
Composite Loss Variations	354
Zero loading	355
Low loading	356
Moderate loading	356
High loading	357
Summary	358
QUANTITATIVE BOUNDARY-LAYER THEORY	359
General Considerations	359
Laminar Boundary Layer	361
Thwaites' method	361
Loitsianskii's method	365
Turbulent Boundary Layer	365
Approach	366
Momentum thickness	366
Form factor	368
Initial conditions	369
Evaluation	369
Transition	370
Circulation Defect	370
Calculation of Total-Pressure Loss	373
CONCLUDING REMARKS	375
REFERENCES	376
TABLE I - FUNCTIONS FOR THWAITES SOLUTION OF LAMINAR BOUNDARY LAYER	380
FIGURES	381

AERODYNAMIC DESIGN OF AXIAL-FLOW COMPRESSORS

CHAPTER I

OBJECTIVES AND SCOPE

By Irving A. Johnsen and Robert O. Bullock

SUMMARY

This first chapter of a report on the aerodynamic design of axial-flow compressors presents the general objectives and scope of the overall report. The basic problem of compressor design is outlined, and the approach generally taken to accomplish its solution is pointed out. The sixteen succeeding chapters in the report are summarized.

INTRODUCTION

Currently, the principal type of compressor being used in aircraft gas-turbine powerplants is the axial-flow compressor. Although some of the early turbojet engines incorporated the centrifugal compressor, the recent trend, particularly for high-speed and long-range applications, has been to the axial-flow type. This dominance is a result of the ability of the axial-flow compressor to satisfy the basic requirements of the aircraft gas turbine.

These basic requirements of compressors for aircraft gas-turbine application are well-known. In general, they include high efficiency, high air-flow capacity per unit frontal area, and high pressure ratio per stage. Because of the demand for rapid engine acceleration and for operation over a wide range of flight conditions, this high level of aerodynamic performance must be maintained over a wide range of speeds and flows. Physically, the compressor should have a minimum length and weight. The mechanical design should be simple, so as to reduce manufacturing time and cost. The resulting structure should be mechanically rugged and reliable.

It is the function of the compressor design system to provide compressors that will meet these requirements (in any given aircraft engine application). This design system should be accurate in order to minimize costly and time-consuming development. However, it should also be as straightforward and simple as possible, consistent with completeness and accuracy.

In an effort to provide the basic data for such a design system, and stimulated by the urgent need for improving gas-turbine engines, research on axial-flow compressors has been accelerated both in this country and abroad. The results of this research have been presented in numerous publications. In the majority of instances, each of these reports presents only a fragmentary bit of information which taken by itself may appear to have inconsequential value. Taken altogether and properly correlated, however, this information represents significant advances in that science of fluid mechanics which is pertinent to axial-flow compressors. It was the opinion of the NACA Subcommittee on Compressors and Turbines and others in the field that it would be appropriate to assimilate and correlate this information, and to present the results in a single series of reports. Such a compilation should be of value to both neophytes and experienced designers of axial-flow compressors. Realizing the necessity and importance of a publication of this type, the NACA Lewis laboratory began reviewing and digesting existing data. The chapters in this series represent the current status of this effort.

As the first in the series, this chapter outlines the general objectives and the scope of the design report. The general compressor design problem and the approach usually taken to accomplish its solution are indicated. The various aspects of compressor design to be treated in the over-all compendium are outlined, as well as the specific sequence in which they will be presented. Thus, in addition to presenting the over-all scope of this report on axial-flow-compressor design, it indicates the chapters in which each specific phase of compressor design information is discussed.

Because axial-flow compressors are most extensively used in the field of aircraft propulsion, and because this field requires the highest degree of excellence in compressor design and performance, the attention in this over-all report has been focused primarily on the problems pertinent to the axial-flow compressor of turbojet or turboprop engines. The results presented, however, should be applicable to any class of axial-flow compressors.

DESCRIPTION OF AXIAL-FLOW COMPRESSOR

The basic function of a compressor is to utilize shaft work to increase the total or stagnation pressure of the air. A schematic drawing of an axial-flow compressor as installed in a turbojet engine is shown in figure 1. In the general configuration, the first row of blades (inlet guide vanes) imparts a rotation to the air to establish a specified velocity distribution ahead of the first rotor. The rotation of the air is then changed in the first rotor, and energy is thereby added in accordance with Euler's turbine equation. This energy is manifested as

increases in total temperature and total pressure of air leaving the rotor. Usually accompanying these increases are increases in static pressure and in absolute velocity of the air. A part, or all, of the rotation is then removed in the following stator, thus converting velocity head to static pressure. This stator also sets up the distribution of air flow for the subsequent rotor. The air passes successively through rotors and stators in this manner to increase the total pressure of the air to the degree required in the gas-turbine engine cycle. As the air is compressed, the density of the air is increased and the annular flow area is reduced to correspond to the decreasing volume. This change in area may be accomplished by means of varying tip or hub diameter or both.

In this compression process certain losses are incurred, which result in an increase in the entropy of the air. Thus, in passing through a compressor, the velocity, the pressure, the temperature, the density, the entropy, and the radius of a given particle of air are changed across each of the blade rows. The compressor design system must provide an adequate description of this flow process.

HISTORICAL BACKGROUND

The basic concepts of multistage axial-flow-compressor operation have been known for approximately 100 years, being presented to the French Academie des Sciences in 1853 by Tournaire (ref. 1). One of the earliest experimental axial-flow compressors (1884) was obtained by C. A. Parsons by running a multistage reaction-type turbine in reverse (ref. 2). Efficiencies for this type of unit were very low, primarily because the blading was not designed for the condition of a pressure rise in the direction of flow. Beginning at the turn of the century, a number of axial-flow compressors were built, in some cases with the blade design based on propeller theory. However, the efficiency of these units was still low (50 to 60 percent). Further development of the axial-flow compressor was retarded by the lack of knowledge of the underlying principles of fluid mechanics.

The advances in aviation during the period of World War I and the rapidly developing background in fluid mechanics and aerodynamics gave new impetus to research on compressors. The performance of axial-flow compressors was considerably improved by the use of isolated-airfoil theory. As long as moderate pressure ratios per stage were desired, isolated-airfoil theory was quite capable of producing compressors with high efficiency (ref. 3, e.g.). Compressors of this class were used in such machinery as ventilating fans, air-conditioning units, and steam-generator fans.

Beginning in the middle 1930's, interest in the axial-flow compressor was greatly increased as the result of the quest for air superiority.

Efficient superchargers were necessary for reciprocating engines in order to increase engine power output and obtain improved high-altitude aircraft performance. With the development of efficient compressor and turbine components, turbojet engines for aircraft also began receiving attention. In 1936 the Royal Aircraft Establishment in England began the development of axial-flow compressors for jet propulsion. A series of high-performance compressors was developed, culminating in the F.2 engine in 1941 (ref. 4). In Germany, research such as that reported in reference 5 ultimately resulted in the use of axial-flow compressors in the Jumo 004 and the B.M.W. 003 turbojet engines. In the United States, aerodynamic research results were applied to obtain high-performance axial-flow units such as that reported in reference 6. In the development of all of these units, increased stage pressure ratios were sought by utilizing high blade cambers and closer blade spacings. Under these conditions the flow patterns about the blades began to affect each other, and it became apparent that the isolated-airfoil approach was inadequate. Aerodynamic theory was therefore developed specifically for the case of a lattice or cascade of airfoils. In addition to theoretical studies, systematic experimental investigations of the performance of airfoils in cascade were conducted to provide the required design information.

By 1945, compressors of high efficiency could be attained through the employment of certain principles in design and development (refs. 2 and 7). Since that time, considerable research has been directed at extending aerodynamic limits in an attempt to maximize compressor and gas-turbine performance. One of the major developments in this direction has been the successful extension of allowable relative inlet Mach numbers without accompanying sacrifices in efficiency (ref. 8). The subject of allowable blade loading, or blade surface diffusion, has also been attacked with a degree of success (ref. 9). Accompanying improvements such as these have been an increasing understanding of the physics of flow through axial-flow compressor blading, and corresponding improvements in techniques of aerodynamic design. Therefore, in view of the rapid advances in recent years, it appears appropriate to summarize the present state of the art of compressor design.

COMPRESSOR DESIGN APPROACH

The flow through the blading of an axial-flow compressor is an extremely complicated three-dimensional phenomenon. The flow in the compressor has strong gradients in the three physical dimensions (axial, radial, and circumferential), as well as time. Viscosity effects in compressors are significant and must be accounted for. In general, the design control problem becomes more critical as the level of compressor performance is increased. In order to provide ease of application, the compressor design system must reduce these complications and establish rational and usable procedures.

Because of the complexity of the problem, no complete solution is currently available for the three-dimensional, time-unsteady, viscous flow through an axial-flow compressor. In the main, designers have resolved these difficulties by making approximations that permit the use of two-dimensional techniques. These approximations are usually based on the assumptions of (1) blade-element flow and (2) axial symmetry.

The blade-element approach assumes that flow in the blade-to-blade or circumferential plane can be described by considering the flow about blade profiles formed by the intersection of a flow surface of revolution and the compressor blading (fig. 2).

Axial symmetry assumes that an average value can be utilized to represent the state of the air in the blade-to-blade plane. Equations describing radial variations of these average values may then be written for continuity, energy addition, and equilibrium in the hub-to-tip or meridional plane (fig. 3). In essence, then, a combination of two-dimensional solutions in the two principal planes (circumferential and meridional) is used to approximate the complete three-dimensional flow.

In applying this approach to compressor design, second-order corrections are used to account for three-dimensional variations from this simplified flow picture. Experimentally obtained data are utilized to account for effects such as those arising from viscosity, time-unsteady flow, and blade-row interactions. Empirical limits are established for such aerodynamic factors as maximum permissible Mach number and blade loading.

No rigorous theoretical justification of this simplified design approach can be made. It appears sufficient to state that comparatively excellent compressors can be and have been designed by simplified approaches such as these. In the absence of a more complete three-dimensional solution to the design problem, this quasi-three-dimensional approach has achieved general acceptance in the field.

In practice, the aerodynamic design of a multistage axial-flow compressor may be considered to consist of three principal phases:

- (1) Determination of stage-velocity diagrams for design-point operation
- (2) Selection of stage blading
- (3) Determination of off-design performance

The first part of the design involves the determination of the various air velocities and flow angles from hub to tip at the inlet and outlet of each blade row, to best achieve the design-point requirements of the

compressor (i.e., pressure ratio and weight flow). The annular configuration (variation of hub and tip contours through the compressor) is determined. Next, the blading is selected to satisfy the design-point velocity diagrams and to obtain high efficiency. Basically, this selection requires knowledge of loss and turning characteristics of compressor blade elements. With the compressor geometry established, the final step is the estimation of the performance characteristics of the compressor over a range of speeds and flows. In view of the importance of off-design operation, this procedure may be iterated so as to properly compromise design-point operation and the range requirements of the engine.

A more complete discussion of the compressor design system adopted for this over-all report is given in chapter III. The generalities of the concepts involved have been given merely to clarify the general approach to the problem.

OBJECTIVES OF DESIGN REPORT

The desire to provide a sound compressor design system has formed the basis for most research on axial-flow compressors. As a result, in this country and abroad, design concepts and design techniques have been established that will provide high-performance compressors. In general, these various design systems, although they may differ in the manner of handling details, utilize the same basic approach to the problem. This over-all report is therefore dedicated to summarizing and consolidating this existing design information. This effort may be considered to have three general objectives:

- (1) To provide a single source of compressor design information, within which the major (representative) contributions in the literature are summarized
- (2) To correlate and generalize compressor design data that are presently available only in many different forms and in widely scattered reports
- (3) To indicate the most essential avenues for future research, since, in a summarization of this type, the missing elements (and their importance to the design system) become readily apparent

In this compressor report, an effort is made to present the data in a fundamental form. To illustrate the use of these data, a representative design procedure is utilized. However, since the design information is reduced to basic concepts, it can be fitted into any detailed design procedure.

SCOPE OF DESIGN REPORT

Because of the complexity of the compressor design problem, even the simplest design system necessarily includes many different phases. In order to summarize existing compressor information as clearly and logically as possible, this over-all compendium is divided into a series of chapters, each concerning a separate aspect of compressor design. The degree of completeness of these chapters varies greatly. In some cases, rather complete information is available, and specific data are given that can be fitted into detailed compressor design procedures. In other cases, the information is not yet usable in design. The chapters may give only a qualitative picture of the problem, or they may merely indicate the direction of future research. Those aspects of the compressor problem which are considered pertinent are included, however, regardless of the present applicability of the information.

The following discussion provides an over-all perspective of the material covered in this compressor design compendium. Each chapter is summarized briefly, and the relation of each to the over-all report is indicated.

In order to provide proper emphasis in the design summarization, it is desirable to establish and evaluate the essential characteristics of compressors. Chapter II accomplishes this objective by first evaluating engine requirements with respect to airplane performance. These required engine characteristics are then used to identify essential requirements of the compressor. Characteristics of the compressor that are directly related to engine performance, such as compressor pressure ratio, efficiency, air-flow capacity, diameter, length, and weight, are discussed. Other considerations in compressor design, including off-design requirements and the relation of the compressor to the inlet diffuser, combustor, turbine, and jet nozzle are discussed. Compressor design objectives, based on these considerations, are summarized; these objectives indicate the direction in which compressor designs should proceed.

Chapter III provides a general description of the compressor design system that has been adopted for this report on the aerodynamic design of axial-flow compressors. The basic thermodynamic equations are given, and the simplifications commonly introduced to permit the solution of these equations are summarized. Representative experimental data are presented to justify these simplifications. This chapter thus provides a valid simplified model of the flow, which is the real basis of a design system. The elements of the resulting design system are then individually summarized; basic equations and techniques are given. Finally, the limitations of this adopted system are pointed out, and promising directions for future research are indicated.

The literature on plane potential flow in cascades is next reviewed (ch. IV). Many of the methods are evaluated within the bounds of limited available information on actual use. Some of the methods that have been used successfully are presented in detail to illustrate the mathematical techniques and to indicate the nature of the actual computation. The potential-flow theories discussed include both the design and analysis problems and consider both high-solidity and low-solidity applications. Compressibility is considered, but effects of viscosity are ignored.

A necessary adjunct to this subject of two-dimensional potential flow is the consideration of two-dimensional viscous effects, presented in chapter V. In this chapter, the problem of boundary-layer growth in the calculation of two-dimensional flow about compressor blade profiles is reviewed. A qualitative picture of boundary-layer behavior under various conditions of pressure gradient, Reynolds number, and turbulence normally encountered in two-dimensional blade-element flow is presented. Some typical methods for computing the growth and separation of laminar and turbulent boundary layers are presented. Analyses for determining the total-pressure loss and the defect in circulation are discussed.

Because of recognized limitations of theoretical calculations such as those presented in chapters IV and V, experimental blade-element data are generally required by the designer. The available experimental data obtained in two-dimensional cascade are surveyed and evaluated in chapter VI (ref. 10). These data (for conventional compressor blade sections) are presented in terms of significant parameters and are correlated at a reference incidence angle in the region of minimum loss. Variations of reference incidence angle, total-pressure loss, and deviation angle with cascade geometry, inlet Mach number, and Reynolds number are investigated. From the analysis and the correlations of the available data, rules and relations are evolved for the prediction of blade-profile performance. These relations are developed in simplified form readily applicable to compressor design procedures.

Because of modifying effects (wall boundary layers, three-dimensional flows, etc.), blade-element characteristics in an annular cascade can be expected to differ from those obtained in two-dimensional cascades. Chapter VII (ref. 10) attempts to correlate and summarize available blade-element data as obtained from experimental tests in three-dimensional annular cascades (primarily rotors and stators of single-stage compressors). Data correlations at minimum loss are obtained for blade elements at various radial positions along the blade span. The correlations are compared with those obtained from two-dimensional cascades (ch. VI (ref. 10)). Design rules and procedures are recommended, and sample calculation procedures are included to illustrate their use.

As discussed in the preceding paragraphs, chapters IV to VII deal with the two-dimensional blade-element aspect of design. The design problem in the meridional or hub-to-tip plane is introduced and summarized in chapter VIII (ref. 10). This meridional-plane solution presumes the existence of the required blade-element data to satisfy the velocity diagrams that are established. The general flow equations are presented, together with the simplifying assumptions used to determine the design velocity distribution and flow-passage configuration. Techniques for accounting for effects of viscosity (particularly for wall boundary layers) are described. The application of these design techniques is clarified by a sample stage design calculation.

Since procedures for determining the design velocity distribution and flow-passage configurations in the meridional plane are usually iterative, it is desirable to have approximate techniques available to expedite this process of stage design. The equations for radial equilibrium, continuity, energy addition, efficiency, and diffusion factor, as well as vector relations, are presented in chart form in chapter IX (ref. 10). An example of the application of the chart technique to stage design is included.

In addition to the design-point problem, the compressor designer is vitally concerned with the prediction of compressor performance over a range of flow conditions and speeds. Three techniques for estimating compressor off-design performance are presented in chapter X (ref. 10). The first method establishes the blade-row and over-all performance by means of the integration of blade-element characteristics. The second method utilizes generalized stage performance curves and a stage-by-stage calculation. The third method, which is based on the over-all performance characteristics of existing compressors, may be used to estimate the complete performance map of a new compressor if the compressor design conditions are specified. The advantages and limitations of each of these three off-design analysis techniques are discussed.

Chapter XI (ref. 11) is the first of a group of three concerning the unsteady compressor operation that arises when compressor blade elements stall. The field of compressor stall (rotating stall, individual blade stall, and stall flutter) is reviewed. The phenomenon of rotating stall is particularly emphasized. Rotating-stall theories proposed in the literature are reviewed. Experimental data obtained in both single-stage and multistage compressors are presented. The effects of this stalled operation on both aerodynamic performance and the associated problem of resonant blade vibrations are considered. Methods that might be used to alleviate the adverse blade vibrations due to rotating stall are discussed.

Another unsteady-flow phenomenon resulting from the stalling of compressor blade elements is compressor surge. It may be distinguished from

the condition of rotating stall in that the net flow through the compressor and the compressor torque become time-unsteady. Some theoretical aspects of compressor surge are reviewed in chapter XII (ref. 11). A distinction is made between surge due to abrupt stall and surge due to progressive stall. Experimental observations of surge in compressor test facilities and in jet engines are summarized.

The blade-element approach to the prediction of off-design performance (as presented in ch. X (ref. 10)) is essentially limited to the unstalled range of operation. Because of the complexity of the flow phenomenon when elements stall, no quantitative data are available to permit a precise and accurate synthesis of over-all compressor performance in this range. A prerequisite to the complete solution of this off-design problem, however, is a qualitative understanding of the phenomena involved. An analysis of the part-speed operating problem in high-pressure-ratio multistage axial-flow compressors is presented in chapter XIII (ref. 11). The principal problems considered are poor low-speed efficiency, multiple-valued performance characteristics at intermediate speeds, and poor intermediate-speed surge or stall-limit characteristics. The effects of compromising stage matching to favor part-speed operation are studied. Variable-geometry methods for improving part-speed performance are discussed.

The design approach adopted for this series of reports is based essentially on two-dimensional concepts, assuming axial symmetry and blade-element flow. With the continuing trend toward increasing requirements in compressors, however, a condition may be reached where this simplified approach may no longer be adequate. Therefore, chapter XIV (ref. 11) is devoted to a summarization of those existing design methods and theories that extend beyond the simplified-radial-equilibrium axisymmetric design approach. Design procedures that attempt to remove the two-dimensionalizing restrictions are presented. Various phases of three-dimensional flow behavior that assume importance in design are discussed, including radial flows, the over-all aspects of secondary flows, and time-unsteady effects.

As pointed out in chapter XIV (ref. 11), secondary flows represent one of the most critical aspects of the three-dimensional design problems. In view of the growing importance of this subject, existing literature on secondary flows and three-dimensional boundary-layer behavior is summarized in chapter XV (ref. 11). The material is discussed from two aspects: (1) the principal results obtained from experimental studies, and (2) the theoretical treatment of the problem. The experimental phase is directed at providing a qualitative insight into the origin and nature of the observed secondary-flow phenomena. The theoretical results include a summary and evaluation of both the nonviscous and the boundary-layer approaches.

Errors in blade-element design can seriously affect over-all compressor performance, since these errors not only cause deviations from desired blade-row performance, but also alter the inlet conditions to the next blade row. The effects of errors in the three basic blade-element design parameters (turning angle, total-pressure loss, and local specific mass flow) on compressor performance are analyzed in chapter XVI (ref. 11). The results are presented in the form of formulas and charts. These charts may be used to indicate those design types for which the design control problem is most critical and to estimate the limits in performance that can be anticipated for design data of a given accuracy. Typical design cases are considered, and significant trends are discussed. A second phase of this chapter concerns accuracy of experimental measurements. Proper interpretation and analysis of experimental data require that measurements be precise. This chapter presents a systematic evaluation of the effect of measurement errors on the measured compressor performance. These results, which are also presented in chart form, can be used to estimate the required accuracy of instrumentation.

One of the most important aspects of gas-turbine engine design, particularly for applications where high power output and wide operating range are required, is that of compressor and turbine matching. The existing literature on compressor and turbine matching techniques, which can be used to compromise properly the aerodynamic design of the compressor and turbine to achieve the best over-all engine, is summarized in chapter XVII (ref. 11). Both single-spool and two-spool engines are considered. For equilibrium operation, the basic matching technique, which involves the superposition of compressor and turbine maps, is presented, as well as a simplified and more approximate method. In addition, a simple technique for establishing an engine operating line on a compressor map is reviewed. An available technique for matching during transient operation is also discussed. The use of this method permits engine acceleration characteristics and acceleration time to be approximated for either single-spool or two-spool engines.

CONCLUDING REMARKS

The subsequent chapters in this report summarize available information on the aerodynamic design of axial-flow compressors. It is recognized that many techniques have been proposed for describing the flow in an axial-flow compressor and for accounting for the complex flow phenomena that are encountered. Obviously, consideration of all of these techniques is impossible. However, the available literature in the field is reviewed extensively, and the material presented is considered to be representative and pertinent. In general, the attempt is made to present the information in its most basic form, so that it may be fitted into any generalized design system.

Because of the many difficult and involved problems associated with compressor design, very few of these underlying problems are treated with finality. In some cases, the problem is only partly defined. Nevertheless, many successful designs (by present standards, at least) have been made with the use of this information. The voids in the information clearly indicate the research problems for the future.

REFERENCES

1. Suplee, H. H.: The Gas Turbine. J. B. Lippincott Co., 1910.
2. Howell, A. R.: Fluid Dynamics of Axial Compressors. War Emergency Issue No. 12 pub. by Inst. Mech. Eng. (London), 1945. (Reprinted in U. S. by A.S.M.E., Jan. 1947, pp. 441-452.)
3. Marks, L. S., and Weske, J. R.: The Design and Performance of an Axial-Flow Fan. Trans. A.S.M.E., AER-56-13, vol. 56, no. 11, Nov. 1934, pp. 807-813.
4. Constant, Hayne: The Early History of the Axial Type of Gas Turbine. War Emergency Issue No. 12 pub. by Inst. Mech. Eng. (London), 1945. (Reprinted in U. S. by A.S.M.E., Jan. 1947, pp. 411-426.)
5. Ruden, P.: Investigation of Single Stage Axial Fans. NACA TM 1062, 1944.
6. Sinnette, John T., Jr., Schey, Oscar W., and King, J. Austin: Performance of NACA Eight-Stage Axial-Flow Compressor Designed on the Basis of Airfoil Theory. NACA Rep. 758, 1943. (Supersedes NACA WR E-1.)
7. Howell, A. R.: Design of Axial Compressors. War Emergency Issue No. 12 pub. by Inst. Mech. Eng. (London), 1945. (Reprinted in U. S. by A.S.M.E., Jan. 1947, pp. 452-462.)
8. Lieblein, Seymour, Lewis, George W., Jr., and Sandercock, Donald M.: Experimental Investigation of an Axial-Flow Compressor Inlet Stage Operating at Transonic Relative Inlet Mach Numbers. I - Over-All Performance of Stage with Transonic Rotor and Subsonic Stator up to Rotor Relative Inlet Mach Number of 1.1. NACA RM E52A24, 1952.
9. Lieblein, Seymour, Schwenk, Francis C., and Broderick, Robert L.: Diffusion Factor for Estimating Losses and Limiting Blade Loadings in Axial-Flow-Compressor Blade Elements. NACA RM E53D01, 1953.

10. Compressor and Turbine Research Division: Aerodynamic Design of Axial-Flow Compressors. Vol. II. NACA RM E56B03a, 1956.
11. Compressor and Turbine Research Division: Aerodynamic Design of Axial-Flow Compressors. Vol. III. NACA RM E56B03b, 1956.

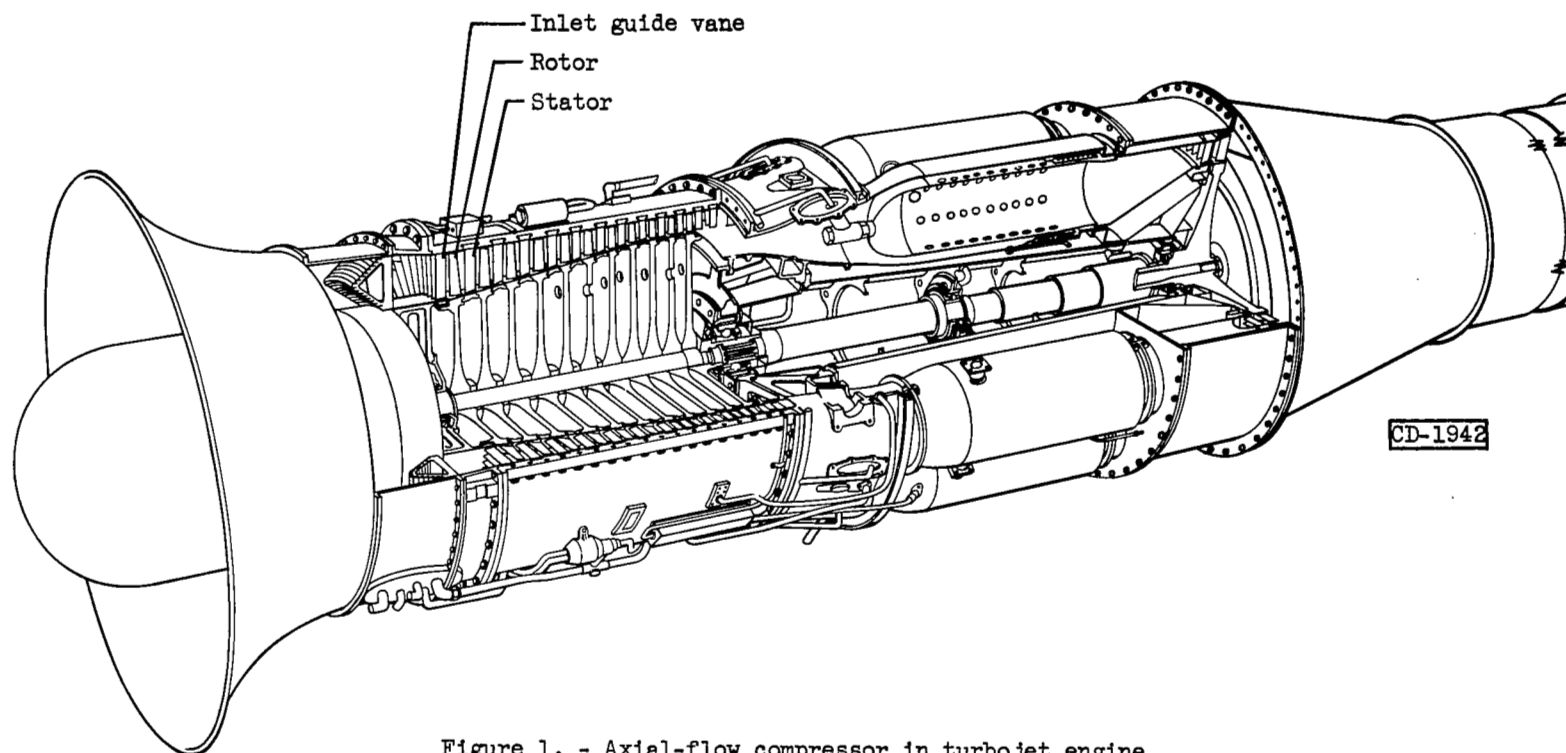


Figure 1. - Axial-flow compressor in turbojet engine.

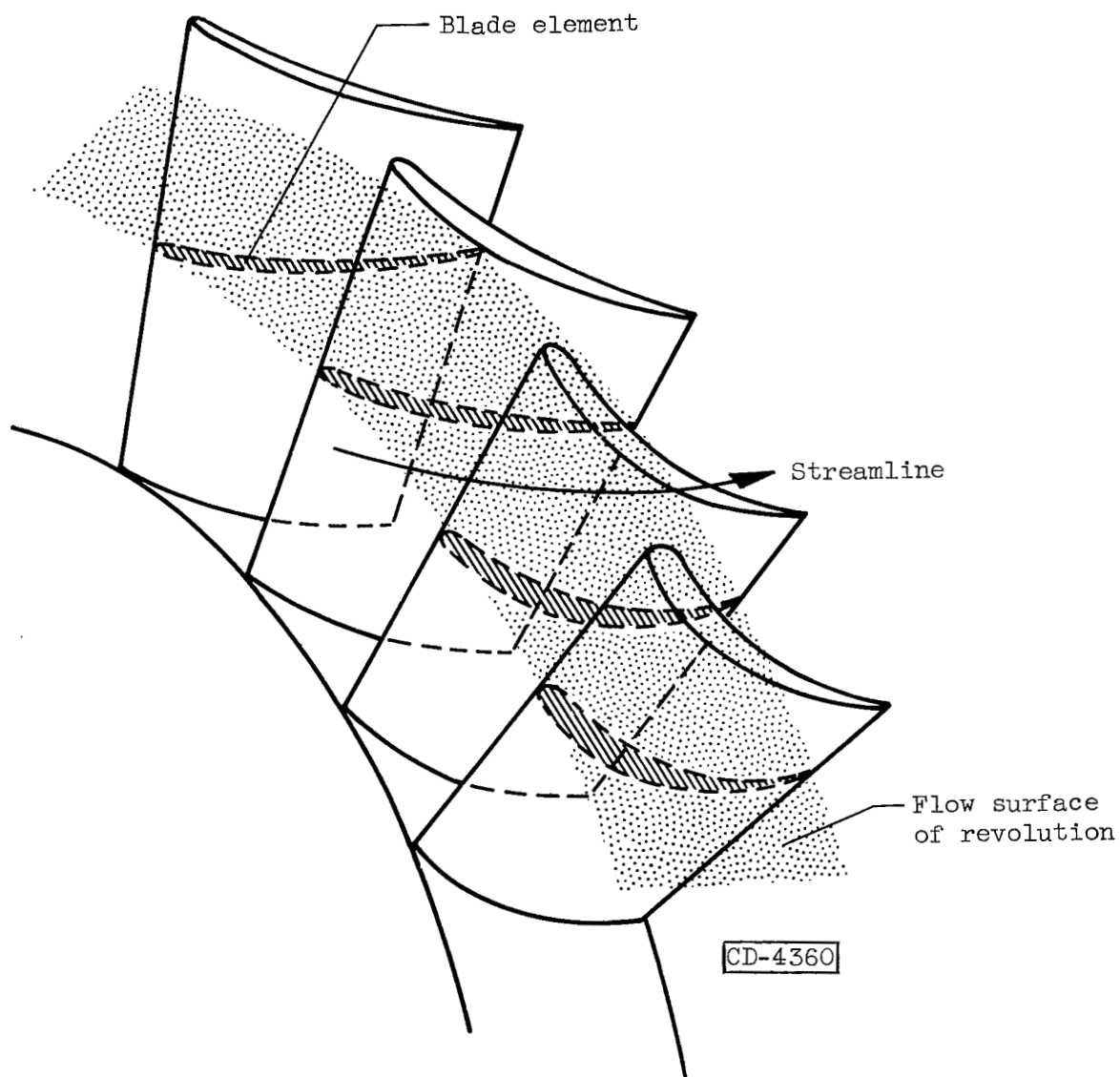


Figure 2. - Flow in circumferential plane.

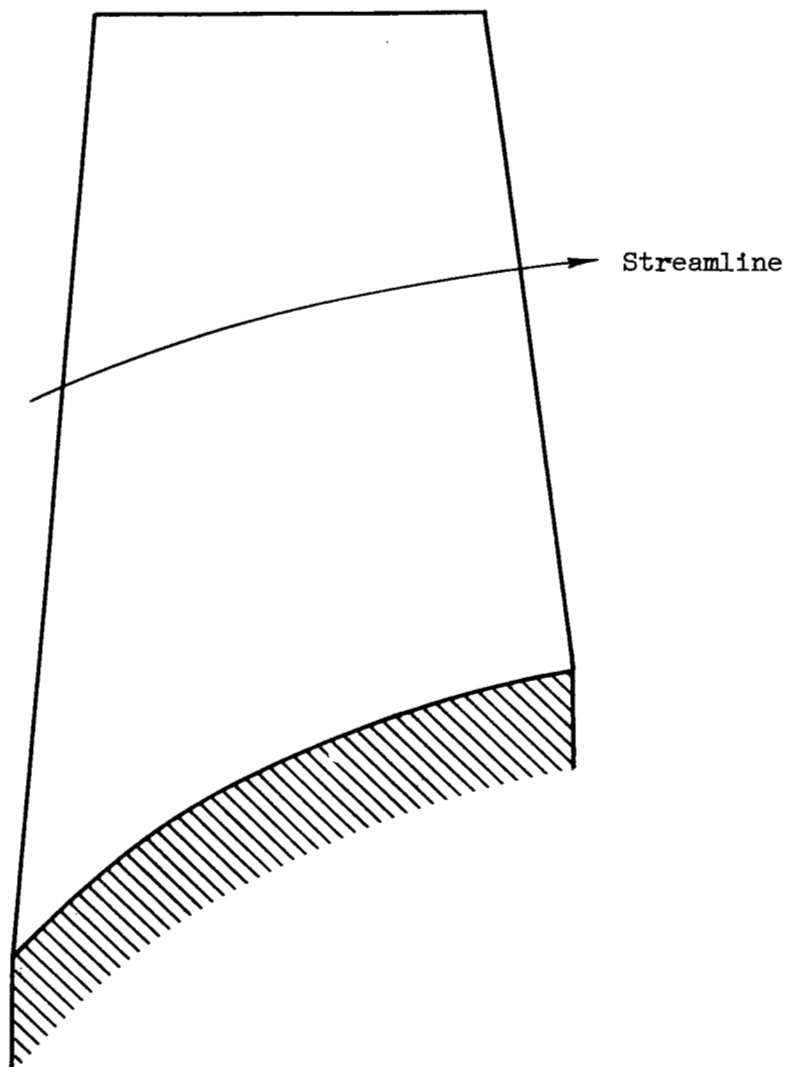


Figure 3. - Flow in meridional plane.

CHAPTER II

COMPRESSOR DESIGN REQUIREMENTS

By Robert O. Bullock and Ernst I. Prasse

SUMMARY

The important requirements of axial-flow compressors for aircraft gas-turbine engines and the reasons for these requirements are reviewed. Attention is first directed to the over-all requirements of the engines themselves; then the desired properties of compressors are examined.

Cycle analyses of the turbojet and turboprop engines are presented to illustrate the effects of compressor pressure ratio and efficiency on engine performance. The significance of high flow capacity in compressors is indicated. The compromises in compressor design dictated by aerodynamic design limitations in the compressor itself as well as aerodynamic and structural design limitations in other components are investigated. The pertinent off-design problems resulting from the necessity of matching the compressor with the inlet and with the turbine over a range of flight conditions are enumerated, and some available methods of coping with these problems are discussed. From these studies, the basic objectives of a compressor design system are evolved.

INTRODUCTION

The information presented in this series of reports is primarily concerned with the problems encountered in designing axial-flow compressors for gas-turbine engines used in aircraft propulsion. In order to enumerate these problems, the important characteristics required of such compressors should be defined. Reviewing these requirements is the object of this chapter.

A compressor, being only one component of an engine, must have characteristics consonant with those required of the engine. The requirements of an engine, in turn, are dictated by the demands of the airplane. Before the desired properties of a compressor can be given, therefore, the interrelations between an airplane and its engines must be examined. Similarly, the important compressor requirements are found from a study

of the interrelations between the engine and its compressor. In the strictest sense, all these interrelations are obtained only after a detailed study of many airplane-engine designs and flight paths. Fortunately, however, broad design objectives may be indicated by a more cursory analysis such as that used in the present report.

What an airplane requires of its engine is viewed from generalized flight situations to obtain the broad objectives for engine design. The important engine variables such as specific weight, specific fuel consumption, and thrust per unit of frontal area are thus defined. The relative importance of these engine performance variables is then examined with regard to the flight conditions to which the airplane will be subjected.

Compressor characteristics having a direct bearing on engine performance are then discussed. Attention is given to compressor efficiency, pressure ratio, and flow capacity and their quantitative effects on specific fuel consumption, size and air-flow capacity of engine components downstream of the compressor, and turbine aerodynamic limits. Other important considerations in compressor design are discussed, including the mutual problems of compressor, turbine, combustor, and inlet diffuser, for both design and off-design conditions. Exact quantitative relations are developed whenever this can readily be done; otherwise, qualitative results are presented and representative examples are used to underline the trends.

Present compressor design objectives, based on the requirements indicated by the analyses of this report, are summarized. These objectives indicate the direction in which compressor designs should proceed.

SYMBOLS

The following symbols are used in this chapter:

- A area, sq ft
- B engine weight parameter (eq. (7b))
- C_{fr} coefficient of skin friction
- C_j jet-nozzle velocity coefficient
- C_m coefficient of maneuver
- c_p specific heat at constant pressure, Btu/(lb)(°R)

D	diffusion factor (eq. (29))
\mathcal{D}	diameter
d	drag, lb
E	pressure-ratio parameter (eq. (20))
eshp	equivalent shaft power, hp
F	thrust, lb
F(sfc)	thrust specific fuel consumption, lb/(hr)(lb)
f	fuel-air ratio
G	pressure-ratio parameter (eq. (16))
g	acceleration due to gravity, 32.17 ft/sec ²
H	total or stagnation enthalpy, Btu/lb
H _f	fuel heating value, Btu/lb
J	mechanical equivalent of heat, 778.2 ft-lb/Btu
k	fraction of gross airplane weight taken by structural weight and useful load, $(W_{st} + W_u)/W_{g,i}$
L	lift, lb
l	length, ft
M	Mach number
N	rotational speed, rpm
P	total or stagnation pressure, lb/sq ft
p	static or stream pressure, lb/sq ft
Q	pressure-ratio parameter (eq. (13))
R	gas constant, 53.35 ft-lb/(lb)(°R)
\mathcal{R}	range of flight, ft
r	radius
sfc	power specific fuel consumption, lb/hp-hr
T	total or stagnation temperature, °R

U	rotor speed, ft/sec
V	air velocity, ft/sec
W	weight
w	weight flow, lb/sec
α	airplane acceleration in direction of flight, ft/sec ²
β	air angle, angle between air velocity and z-axis, deg
Γ	turbine blade metal density, lb/cu ft or lb/cu in.
γ	ratio of specific heats
δ	ratio of total pressure to NACA standard sea-level pressure of 2116 lb/sq ft
ϵ	angle between thrust axis and direction of flight, deg
η	efficiency
θ	ratio of total temperature to NACA standard sea-level temperature of 518.7° R
ρ	density, lb/cu ft
ρV	air weight flow per unit flow area, lb/(sec)(sq ft)
σ	solidity, ratio of chord to spacing
τ	turbine blade centrifugal stress, psf or psi
ψ	turbine blade taper factor
ω	angular velocity of rotor, radians/sec

Subscripts:

ad	adiabatic
B	combustor
C	compressor
d	design value

e	engine
eff	effective
F	frontal
f	fuel
g	gross
h	hub
i	airplane takeoff condition or that after refueling
j	jet nozzle
M	mechanical power
min	minimum
n	nacelle
n-fr	nacelle-friction
PT	power turbine
pr	propulsive
ref	reference
sl	NACA standard sea-level conditions
st	structure
T	turbine
t	tip
u	useful
w	wetted
x	arbitrary engine station
z	axial direction

Stations in engines (fig. 6):

- 0 free stream
- 1 station at compressor inlet
- 2 station at combustor inlet
- 3 station at turbine inlet
- 4 turbine discharge for turbojet engine
- 5 turbine discharge for turboprop engine
- 6 exhaust-nozzle exit

Superscripts:

- ' conditions relative to rotor blade
- denotes average over flight path

EFFECTS OF ENGINE CHARACTERISTICS ON AIRPLANE PERFORMANCE

The suitability of an engine for aircraft propulsion is frequently judged by three quantities - the specific weight, the thrust specific fuel consumption, and the thrust per unit frontal area. While it is patently desirable for engines to have low values of the first two quantities and high values of the third, it frequently happens that the best possible values at all these quantities cannot be obtained simultaneously. Some important requirements for low thrust specific fuel consumption, for example, are incompatible with those for either low specific weight or high thrust per unit of frontal area. Moreover, some of the requirements for low specific weight may be different from those for high thrust per unit frontal area. Thus, the design of an engine and its components is always a compromise in which one feature of engine performance is favored over another. The direction and degree of the compromise depend, among other things, on the design and the intended use of the airplane.

The best compromise is, of course, pinpointed only after detailed studies of a number of definite airplane and engine designs. On the other hand, some basic knowledge of the way the design and mission of an airplane affect these compromises may be obtained from a more general study. Some of the over-all results outlined by such a study are discussed in this section. The significance of specific weight is first examined. The role of thrust specific fuel consumption is then reviewed, and the relative importance of specific weight and thrust specific fuel consumption is noted. Some effects of the drag associated with the engine installation are then indicated. Finally, other engine features that affect the design and performance of an airplane are discussed.

Engine Weight

Specific engine weight is one of the important factors determining how much of the load-carrying capacity of an airplane is consumed by engine weight. Since specific engine weight is defined by W_e/F , the required ratio of engine weight to airplane gross weight for any specific flight condition is

$$\frac{W_e}{W_g} = \left(\frac{W_e}{F} \right) \left(\frac{F}{W_g} \right) \quad (1)$$

where F in W_e/F represents the thrust the engine can produce, and the same symbol in F/W_g stands for the thrust demanded by the airplane. The two thrusts, of course, must always be equal. Both the thrust produced by the engine and the thrust demanded by the airplane vary with flight altitude and speed.

Since the thrust of a given engine varies with altitude and speed, the value of W_e/F must also vary. An example of this variation in a turbojet engine is shown in figure 1, where specific weight is plotted against altitude for flight Mach numbers of 0.8 and 2.0. A point is also shown for corresponding sea-level static conditions. For the purpose of generalization, the specific weights are divided by the specific weight for a flight Mach number of 0.8 at sea level. It may be noted that specific weight is approximately doubled for every 15,000-foot increase in altitude in the stratosphere. This variation is inversely proportional to the change in air density. Increasing the flight Mach number from 0.8 to 2.0 also increases the density of the air in the engine because of the effects of ram. In this example, the specific weight is about halved for this increase in flight Mach numbers.

The curve for the flight Mach number of 0.8 is also more or less applicable to turboprop engines. The sea-level static value of specific

weight for these engines, however, is usually much lower than that for the jet engine; its value depends as much on the selection of the propeller as on the engine itself.

The term F/W_g , which represents the thrust required for a unit gross weight, is a function of a number of variables. The trends may be conveniently studied by the following procedure: At any point in flight, the thrust required of the engines is determined by the relations

$$F \cos \epsilon = d + W_g \frac{\alpha}{g}$$

$$L = C_m W_g - F \sin \epsilon$$

where ϵ is the angle between the thrust axis and the direction of flight, d is the dissipative drag force, $W_g \alpha/g$ is the component of body force in the direction of flight, and $C_m W_g$ is the component of body force perpendicular to the direction of flight. These expressions may be combined to give

$$\frac{C_m + \frac{L}{d} \frac{\alpha}{g}}{\frac{L}{d} \cos \epsilon + \sin \epsilon} = \frac{F}{W_g} \quad (2)$$

where L/d is the ratio of the aerodynamic lifting force to the drag force. When the airplane is in level flight and moving with a constant velocity, then $C_m = 1$ and $\alpha = 0$. Moreover, when the thrust axis is along the direction of flight, then $\epsilon = 0$. Under these conditions, equation (2) becomes

$$\frac{F}{W_g} = \frac{1}{\frac{L}{d}} \quad (2a)$$

For the sake of simplicity, the complete form of equation (2) is expressed by analogy as

$$\frac{F}{W_g} = \frac{1}{\left(\frac{L}{d}\right)_{\text{eff}}} \quad (2b)$$

Because $(L/d)_{\text{eff}}$ is a function of a large number of variables, its trends cannot be generally plotted as a function of altitude and flight Mach number alone without leaving some misleading impressions. The trends described in the following paragraphs may be noted, however.

As the design altitude of the airplane increases, the maximum attainable value of L/d tends to increase. This trend results from increases in the aspect ratio of the wings and from the fact that the fuselage drag becomes a smaller portion of the total drag. High values of L/d may be obtained with subsonic airplanes during level flight. Values in the neighborhood of 20 are not uncommon, and values approaching 30 have been sought. Airplanes designed for high values of L/d with subsonic flight, however, would have very poor values of L/d at supersonic flight. In airplanes designed exclusively for supersonic flight, values of L/d approaching 6 have been observed in some model tests, and reasonably higher values might be obtained in the future. Again, the value of L/d may increase with altitude. In general, an airplane designed exclusively for supersonic flight would have undesirably low values of L/d at subsonic speeds.

When reasonably good performance is desired at both subsonic and supersonic speeds, the attainable values of L/d must be compromised for both regimes. For subsonic speeds, the value of L/d may be expected to be slightly more than 10. The corresponding value of L/d for supersonic flight may be of the order of 3 or lower. The possible increase in L/d with design altitude is again noted for both regimes.

At takeoff conditions, the value of $(L/d)_{\text{eff}}$ can become very low for all types of airplanes. With vertical takeoff, the thrust of the engine must overcome the acceleration of gravity; the value of F/W_g in equation (2b) must then be greater than unity. The magnitude of $(L/d)_{\text{eff}}$ is therefore less than unity. Less stringent takeoff conditions permit the value of $(L/d)_{\text{eff}}$ to be somewhat improved. For an ordinary takeoff, the value of $(L/d)_{\text{eff}}$ may be of the order of 4.

A high-maneuverability requirement also reduces the value of $(L/d)_{\text{eff}}$. A 2g turn, for example, makes the value of C_m equal 2 in equation (2), and $(L/d)_{\text{eff}}$ could be reduced by more than 50 percent.

A study of the combined effects of specific engine weight and $(L/d)_{\text{eff}}$ on W_e/W_g may now be made by combining equations (1) and (2b) to give

$$\frac{W_e}{W_g} = \frac{\frac{W_e}{F}}{\left(\frac{L}{d}\right)_{\text{eff}}} \quad (1a)$$

Since the gross weight at any instant equals the initial weight minus the fuel expended ($W_g = W_{g,i} - \Delta W_f$), equation (1a) may also be written as

$$\frac{W_e}{W_{g,i}} = \frac{\frac{W_e}{F}}{\left(\frac{L}{d}\right)_{\text{eff}}} \left(1 - \frac{\Delta W_f}{W_{f,i}} \frac{W_{f,i}}{W_{g,i}} \right) \quad (1b)$$

The initial gross weight of the airplane is the sum of the structural weight, useful weight or payload, initial fuel weight, and engine weight:

$$W_{g,i} = W_{st} + W_u + W_{f,i} + W_e \quad (3)$$

Using this equation to eliminate $W_{g,i}$ in the right side of equation (1b) (setting $W_{st} + W_u = kW_{g,i}$) gives

$$\frac{W_e}{W_{g,i}} = \frac{\frac{W_e}{F}}{\left(\frac{L}{d}\right)_{\text{eff}}} \left[\frac{1 - \frac{\Delta W_f}{W_{f,i}} (1 - k)}{1 - \frac{\Delta W_f}{W_{f,i}} \frac{\frac{W_e}{F}}{\left(\frac{L}{d}\right)_{\text{eff}}}} \right] \quad (4)$$

Some trends of this relation are shown in figure 2, where $W_e/W_{g,i}$ is plotted against $(W_e/F)/(\frac{L}{d})_{\text{eff}}$. One of the curves of this figure applies to conditions at or shortly after takeoff, where $\Delta W_f/W_{f,i} \approx 0$ and $W_e/W_{g,i} \approx (W_e/F)/(\frac{L}{d})_{\text{eff}}$. The other four curves apply to the case where $\Delta W_f/W_{f,i} = 0.4$; that is, after 40 percent of the fuel weight has been expended. These curves successively represent the condition where $k = (W_{st} + W_u)/W_{g,i} = 0.3, 0.4, 0.5, \text{ and } 0.6$.

For conditions at or shortly after takeoff, the magnitude of $W_e/W_{g,i}$ is independent of k and varies linearly with $(W_e/F)/(\frac{L}{d})_{\text{eff}}$. When $\Delta W_f/W_{f,i} = 0.4$, the assumption that $W_e/W_{g,i}$ is proportional to $(W_e/F)/(\frac{L}{d})_{\text{eff}}$ is again a good approximation as long as $(W_e/F)/(\frac{L}{d})_{\text{eff}}$ is 0.2 or smaller for $k = 0.6$. Compared with the takeoff value of $W_e/W_{g,i}$, however, $W_e/W_{g,i}$ is reduced about 12 percent for $k = 0.6$ and 30 percent for $k = 0.3$. For the same critical flight conditions (a given value of $(W_e/F)/(\frac{L}{d})_{\text{eff}}$), the required engine weight decreases as $\Delta W_f/W_{f,i}$ is increased and as k is decreased. Near the end of the

flight, equation (4) becomes

$$\frac{W_e}{W_{g,i}} = \frac{\frac{W_e}{F}}{\left(\frac{L}{d}\right)_{\text{eff}}} \frac{k}{1 - \frac{\frac{W_e}{F}}{\left(\frac{L}{d}\right)_{\text{eff}}}}$$

For reasonably small values of $(W_e/F)/\left(\frac{L}{d}\right)_{\text{eff}}$, the required value of $W_e/W_{g,i}$ is then approximately k times its required value at takeoff for the same magnitude of $(W_e/F)/\left(\frac{L}{d}\right)_{\text{eff}}$.

The value of $W_e/W_{g,i}$ required in an airplane is determined by the values of W_e/F , $\left(\frac{L}{d}\right)_{\text{eff}}$, and $\Delta W_F/W_{F,i}$ at the critical flight condition. The value of the right side of equation (4) here is the maximum encountered for the flight. At all other flight conditions for the aircraft, the value of $W_e/W_{g,i}$ is of course the same, and the requirements of equation (4) are then satisfied either by reducing F by throttling or by reducing $\left(\frac{L}{d}\right)_{\text{eff}}$ below its attainable value.

Since the attainable value of $\left(\frac{L}{d}\right)_{\text{eff}}$ is relatively low at takeoff, the requirements at takeoff may determine the value of $W_e/W_{g,i}$. For example, if the takeoff value of $\left(\frac{L}{d}\right)_{\text{eff}}$ is 4.0 and the sea-level static value of W_e/F is 0.4, the value of $W_e/W_{g,i}$ is 0.10 (fig. 2). Suppose now that the value of $\left(\frac{L}{d}\right)_{\text{eff}}$ becomes 20 shortly after takeoff. Since $W_e/W_{g,i}$ is unchanged, the required value of W_e/F is 2.0 (fig. 2). The value of F must be reduced either by throttling the engine or by increasing the flight altitude. The value of W_e/F of 2.0 corresponds to a value of $(W_e/F)/(W_e/F)_{\text{ref}}$ of about 5.9 (fig. 1). For the flight Mach number of 0.8, the ordinate of figure 1 is 5.9 at the altitude of about 52,000 feet. As long as the flight is below this altitude, the takeoff condition would govern the selection of engine weight in this particular example. Suppose, however, that the airplane (with $k = 0.5$) must achieve the altitude of 63,000 feet and the Mach number of 0.8 after 40 percent of the fuel is expended. If the takeoff value of W_e/F is still 0.4, the value of W_e/F at the required flight condition is now 3.4. Moreover, if the value of $\left(\frac{L}{d}\right)_{\text{eff}}$ is still 20, the required value of $W_e/W_{g,i}$ is 0.145. Since $W_e/W_{g,i}$ only had to be 0.10 at takeoff, the condition at 63,000 feet would now determine the

required engine weight. Notice that $W_{f,i}/W_{g,i}$ would have to be reduced by 0.045 in order to compensate for the increased engine weight if k remains at 0.5. At the same time, however, the takeoff requirements can be made more stringent; $(L/d)_{\text{eff}}$ can be reduced to 2.76 if the structural strength of the airplane is adequate.

A requirement of supersonic flight may decide the value of $W_e/W_{g,i}$, because the attainable value of $(L/d)_{\text{eff}}$ is comparatively low. Although supersonic flight itself tends to decrease W_e/F (fig. 1), this trend may be offset by the need for making the engines operate at high flight altitudes. (High altitudes may be desired to make $(L/d)_{\text{eff}}$ as high as possible, to obtain a reasonable level of wing loading for takeoff and landing, and to reduce aerodynamic heating.) The low value of $(L/d)_{\text{eff}}$ combined with the high values of W_e/F at high altitudes results in high values of $W_e/W_{g,i}$.

Consider the case where $k = 0.5$ and $(L/d)_{\text{eff}} = 4.0$ for level flight at the Mach number of 2.0. If the value of W_e/F is again 0.4 at static sea-level conditions, it would have the value of 1.2 at the altitude of about 56,000 feet. In order to meet these conditions after 40 percent of the fuel is exhausted, $W_e/W_{g,i}$ must be 0.27 (fig. 2). An additional requirement of high maneuverability ($C_m > 1$) would have to be answered by an added increase in engine weight. Even if the value of C_m is only 1.25, then $(L/d)_{\text{eff}}$ becomes 3.2 and $W_e/W_{g,i}$ is increased to 0.35. Only 15 percent of the gross weight could then be allotted for fuel.

This brief sampling shows how engine weight depends on the conditions of flight. Of particular interest is the increase in $W_e/W_{g,i}$ associated with increases in flight altitude and Mach number. It is under these conditions that reductions in W_e/F are most appreciated. In the first of the preceding examples (subsonic flight at comparatively low altitudes), the value of $W_e/W_{g,i}$ was 0.1 for $W_e/F = 0.4$ at sea-level static conditions. A 50-percent reduction in specific engine weight would reduce $W_e/W_{g,i}$ by 0.05. This saving in weight could be distributed among useful weight, fuel weight, and structural weight. For the last example, on the other hand, such a reduction in specific engine weight would reduce $W_e/W_{g,i}$ by 0.19. A much larger weight movement is available to the other parts of the airplane. The fuel weight, for example, could be more than doubled. To meet the requirements for high altitude or supersonic flight, every effort should be made to make W_e/F as small as possible.

Engine Efficiency

The previous discussion was centered about the size of engines needed to meet certain thrust requirements. Of equal importance is the weight of fuel required to meet the various range requirements demanded of the airplane. The range requirements may be examined with the aid of the familiar Breguet range equation, which can be written as

$$R = -JH_f \left(\frac{\bar{L}}{\bar{d}} \right)_{\text{eff}} \bar{\eta}_e \ln \left(1 - \frac{W_{f,i}}{W_{g,i}} \right) \quad (5)$$

where the bars denote average values over the entire flight path. This expression is modified by using equation (3); it then becomes

$$R = -JH_f \left(\frac{\bar{L}}{\bar{d}} \right)_{\text{eff}} \bar{\eta}_e \ln \left(k + \frac{W_e}{W_{g,i}} \right) \quad (5a)$$

Since $W_e/W_{g,i}$ is determined from equation (4) at the most critical flight condition, equation (5a) may be written as

$$R = -JH_f \left(\frac{\bar{L}}{\bar{d}} \right)_{\text{eff}} \bar{\eta}_e \ln \left\{ 1 - \frac{\left[1 - k - \frac{\frac{W_e}{F}}{\left(\frac{\bar{L}}{\bar{d}} \right)_{\text{eff}}} \right]}{\left[1 - \frac{\frac{W_e}{F}}{\left(\frac{\bar{L}}{\bar{d}} \right)_{\text{eff}}} \frac{\Delta W_f}{W_{f,i}} \right]} \right\} \quad (6)$$

It is immediately noted that the range of flight is proportional to the average efficiency of the engine and the heating value of the fuel used. In other words, the weight of fuel required for a given mission is inversely proportional to both the heating value of the fuel and the engine efficiency. The range is also proportional to the average value of $(\bar{L}/\bar{d})_{\text{eff}}$ over the entire flight path. Finally, the range is proportional to the function in the brackets.

The trends of this function are illustrated in figure 3. The abscissa of this figure is $(W_e/F)/(\bar{L}/\bar{d})_{\text{eff}}$ at the most critical flight condition of the airplane. The ordinate is the calculated range divided by the range when $(W_e/F)/(\bar{L}/\bar{d})_{\text{eff}} = 0.1$, $k = 0.5$, and $\Delta W_f/W_{f,i} = 0$. The curves represent conditions where k is again 0.3, 0.4, 0.5, and 0.6, and where $\Delta W_f/W_{f,i}$ is 0 and 0.4 at the critical flight condition. These

curves show that there is always an incentive for making $(W_e/F)/(L/d)_{\text{eff}}$ as low as possible, but the need for low specific engine weights becomes more imperative as $(W_e/F)/(L/d)_{\text{eff}}$ increases above 0.1. This statement is particularly true for the higher values of k and for situations where the critical flight condition is reached before an appreciable amount of fuel is used.

With respect to range, therefore, light engines are required whenever high-altitude flight is required; when stringent take-off conditions are imposed; when a high degree of maneuverability is demanded; or when high supersonic flight speeds must be attained. Notice in this connection that high design flight altitudes may permit the attainment of relatively high values of $(L/d)_{\text{eff}}$ and range, and that low values of W_e/F are required for this accomplishment.

As previously noted, it frequently happens that some of the design requirements for light weight are incompatible with some of the requirements for high efficiency. As shown by equation (6), the range is directly proportional to the average efficiency during flight. Decreases in engine weight that unduly prejudice the efficiency are therefore unwelcome. At point A of figure 3, a decrease in specific engine weight of 10 percent improves the range about 3 percent, if there is no change in $(L/d)_{\text{eff}}$ or $\bar{\eta}_e$. If, however, the efficiency also decreased 3 percent, there would be no change in range. At this point, then, the efficiency would not be upset in order to obtain trifling improvements in engine weight. At point B, on the other hand, a 10-percent reduction in specific engine weight increases the range by about 23 percent. In this case a 23-percent reduction in engine efficiency is equivalent to a 10-percent reduction in specific engine weight. Significant reductions in efficiency could be tolerated here to obtain moderate reductions in engine weight.

A comparison of the relative effects of a small change in efficiency and a small change in specific engine weight may be directly obtained by differentiating equation (6) with respect to $\bar{\eta}_e$ and W_e/F . The values of k and $(L/d)_{\text{eff}}$ are assumed to be fixed, along with the value of $\Delta W_f/W_{f,i}$, since these are the values at the most critical flight conditions, which determine $W_e/W_{g,i}$:

$$\frac{\frac{\partial(A)}{A}}{\frac{\partial(\bar{\eta}_e)}{\bar{\eta}_e}} = 1 \quad (7a)$$

$$\frac{\frac{\partial(\mathcal{R})}{\mathcal{R}}}{\frac{\partial\left(\frac{W_e}{F}\right)}{\frac{W_e}{F}}} = \frac{\frac{W_e}{F}}{\left(\frac{L}{d}\right)_{\text{eff}}} \frac{1 - \frac{\Delta W_f}{W_{f,i}} (1 - k)}{\left[1 - \frac{\Delta W_f}{W_{f,i}} \frac{\frac{W_e}{F}}{\left(\frac{L}{d}\right)_{\text{eff}}}\right]^2 B \ln B} \quad (7b)$$

where

$$B = 1 - \frac{1 - k - \frac{\frac{W_e}{F}}{\left(\frac{L}{d}\right)_{\text{eff}}}}{1 - \frac{\frac{W_e}{F}}{\left(\frac{L}{d}\right)_{\text{eff}}} \frac{\Delta W_f}{W_{f,i}}}$$

The implications of this equation are shown in figure 4, where the ordinate is

$$-\frac{\frac{\partial(\mathcal{R})}{\mathcal{R}}}{\frac{\partial\left(\frac{W_e}{F}\right)}{\frac{W_e}{F}}} \quad \text{or} \quad -\frac{\frac{\partial(\bar{\eta}_e)}{\bar{\eta}_e}}{\frac{\partial\left(\frac{W_e}{F}\right)}{\frac{W_e}{F}}}$$

and the abscissas and parameters are the same as those in figure 3.

For a long-range airplane, where $(W_e/F)/\left(\frac{L}{d}\right)_{\text{eff}}$ may be of the order of 0.05, a 1-percent increase in efficiency increases the range 1 percent (eq. (7a)); a 7-percent decrease in specific engine weight is necessary to obtain the same range increase if $k = 0.5$ (fig. 4(a)). If high-altitude requirements cause W_e/F to be doubled, the 1-percent increase in efficiency is about equivalent to a 3-percent decrease in specific weight. For supersonic flight, with $(W_e/F)/\left(\frac{L}{d}\right)_{\text{eff}} = 0.33$, $k = 0.5$, and $\Delta W_f/W_{f,i} = 0.4$, a 1-percent increase in efficiency is equivalent to a 1/2-percent decrease in specific engine weight (fig. 4(b)). A maneuverability requirement of $C_m = 1.25$ increases $(W_e/F)/\left(\frac{L}{d}\right)_{\text{eff}}$ to 0.413. Here, 1-percent change in efficiency is equivalent to about

0.2-percent change in specific engine weight. If the required altitude is increased by 15,000 feet, however, specific engine weight must be reduced, regardless of the consequences, because the required engine weight would be so large that there would be no room for fuel.

When engine efficiency must be compromised with specific engine weight, the design and intended use of the airplane determine the direction and the degree of the compromise. When range is the main objective and $(L/d)_{\text{eff}}$ and the required weight of fuel are large, some liberties can be taken with specific engine weight to favor efficiency. There is the provision, of course, that the loss in attainable altitude does not reduce the value of $(L/d)_{\text{eff}}$ by a significant amount. At the other extreme, when the combination of high flight speeds, high altitudes, and maneuverability make $(L/d)_{\text{eff}}$ low and tend to make W_e/F high, the compromise must favor specific engine weight.

Thrust per Unit Frontal Area

Part of the drag d of the airplane results from the drag of the inlet supplying the engine with air and from the drag of the nacelle or that part of the fuselage housing the engine. If this drag is denoted by d_n , then

$$d = d_n + d_0$$

Equation (2) could then be written as

$$\frac{C_m + \frac{L}{d_0} \frac{\alpha}{g}}{\frac{L}{d_0} \left(\cos \epsilon - \frac{d_n}{F} \right) + \sin \epsilon} = \frac{F}{W_g}$$

The term on the left side is again denoted by $1/(L/d)_{\text{eff}}$. For small values of ϵ , the following can be written:

$$\frac{C_m + \frac{L}{d_0} \frac{\alpha}{g}}{\frac{L}{d_0}} = \frac{F}{W_g} \left(1 - \frac{d_n}{F} \right) = \frac{F}{W_g} \left(1 - \frac{d_n}{A_F} \frac{1}{A_F} \right)$$

When d_n/A_F is high, obtaining low values of d_n/F requires high values of F/A_F . Since the highest values of d_n/A_F are usually obtained at supersonic flight conditions, large values of F/A_F are particularly desired for supersonic flight.

The drag of the inlet mainly consists of an "additive drag" (ref. 1), a drag resulting from the pressure forces acting on the outer curved portion of the inlet (fig. 5), and the drag resulting from friction. In some cases, for supersonic flight, it may be desirable to bypass some of the air entering the inlet to the outside. In this case a "bypass" drag is added. The "additive" and "bypass" drags depend on the matching of the inlet with the engine, which is discussed in more detail in a later section.

The drag resulting from pressure forces depends on the difference between the maximum frontal area of the engine housing and the open area of the inlet. It also depends on the slope and curvature of the outer surface of the inlet. The open area of the inlet depends on the mass-flow requirements of the engine and the speed of flight; its order of magnitude is given by

$$A = \frac{w_1}{(\rho_0 V_0)_{\min}}$$

where $(\rho_0 V_0)_{\min}$ is the minimum value of $\rho_0 V_0$ anticipated for steady flight. The maximum frontal area of the engine housing has usually been determined by the frontal area of the engine with its accessories. Small engine diameters and, in particular, small compressor diameters are therefore desired to keep the drag resulting from pressure forces from being greater than it has to be.

It should be noted in passing that the inlet design itself usually requires the frontal area to be greater than the capture area for supersonic flight. The illustration of figure 5 shows such a design. This requirement follows from the necessity of meeting certain area requirements within the inlet and from the necessity of avoiding abrupt changes in flow direction within the inlet. Some requirements of variable inlet geometry aggravate this trend.

Most of the rest of the drag associated with an engine installation is due to friction. An estimate of the magnitude of the friction drag is given by the formula

$$d_{n-fr} = C_{fr} \left(\frac{1}{2} \rho_0 M_0^2 A_w \right) \quad (8)$$

As shown in reference 2, a value of C_{fr} of 0.00168 is in agreement with available data. At a Mach number of 1.0 at 35,000 feet, this formula then becomes

$$d_{n-fr} = 1.84 \mathcal{D}_e l_e$$

In the interest of keeping this drag low, both the diameter \mathcal{D} and the length l of the engine should be small. In particular, small compressor lengths and diameters are desired.

Another component of drag is that resulting from the pressure forces at the rear end of the engine. This drag is much more closely related to other engine components than it is to the compressor, however, and it is therefore dismissed from further consideration.

Other Engine Requirements

Besides affecting airplane drag, the length and diameter of the engine may affect the structural weight of the airplane. In particular, long engines require a long and fairly rigid fuselage, which adds weight to the airplane without noticeably improving the lift-drag ratio.

Engine weight also affects the structural weight and other properties of the airplane, because the concentration of weight in the engine must be supported by the airplane. In fuselage installations, for example, the design of the airplane can be unfavorably compromised to keep the center of gravity of the airplane and its load in the right location. For nacelle or pod installation, the wings must be strong enough to support the engines for landing shocks or other violent maneuvers. Again, light engines tend to lessen structural weight.

The manner in which compressor design influences the length and diameter of the engine is treated in subsequent sections of this chapter. The relations between compressor diameter and the diameters of the other components of the engine are studied and some of the factors involved in engine length are enumerated.

EFFECTS OF COMPRESSOR PRESSURE RATIO, COMPRESSOR EFFICIENCY,

AND FLIGHT CONDITIONS ON ENGINE PERFORMANCE

For a specified performance of its components, the efficiency and specific thrust of an engine are calculated by cycle analyses (refs. 3 and 4). The analysis presented here is similar to that of these references. Sketches of typical turbojet- and turboprop-engine installations with numerical stations are shown in figure 6. (Note that the condition of the engine gases after the work needed to drive the compressor has been extracted from the turbine can be indicated at station 4 of the turboprop engine, and that station 5 is at the discharge of the final turbine. For the turbojet engine, stations 4 and 5 coincide.)

The efficiency of each component is fixed in this analysis. The effect of compressor pressure ratio is examined for a range of flight conditions and turbine-inlet temperatures. The gas charts of reference 5 were used for determining gas properties.

Assumptions Used in Cycle Analyses

The following values were assumed for the several variables involved in the cycle analyses of both the turboprop and the turbojet engine:

Flight Mach number, M_0	Inlet-diffuser total-pressure recovery, P_1/P_0
0	0.87
.8	.98
2.0	.90
3.0	.60

Compressor adiabatic efficiency, $\eta_{ad,C}$	0.88
Combustion efficiency, primary burner, η_B	0.98
Heating value of fuel, H_f , Btu/lb	18,570
Hydrogen-carbon ratio of fuel	0.167
Temperature of fuel injected as a liquid, T_f , $^{\circ}R$	600
Total-pressure ratio across primary burners, P_3/P_2	0.95
Turbine adiabatic efficiency, $\eta_{ad,T}$	0.90
Exhaust-nozzle velocity coefficient, C_j	0.98

No accounting was made for turbine cooling or other cooling that might be necessary at the high temperature levels. For the afterburning turbojet engine, the combustion efficiency of the afterburner was 0.95, the total-pressure ratio across the afterburner was 0.95, and the afterburner-outlet total temperature was 3500 $^{\circ}R$.

For the turboprop engine, the combined propeller and gearbox efficiency was assumed to be 0.86. In addition, the division of power between the propeller and jet was assumed to be such that the pressure ratio P_5/p_0 was 1.087 to obtain a reasonable nozzle area for the sea-level static case. For the other flight conditions considered, P_5/p_0 was assumed equal to P_1/p_0 , a condition approximating that for maximum power.

The selected value of compressor efficiency appears to be attainable up to at least a compressor pressure ratio of 12. The efficiency of the turbine is high compared with the values observed in engine tests. It is comparable, however, to experimental efficiencies observed with uniform inlet conditions on cold-air turbines.

Effects of Compressor Pressure Ratio and Flight Conditions on Turboprop-Engine Performance

Cycle analysis of a turboprop engine yields the power delivered to the propeller, the thrust developed by the jet nozzle, and the fuel burned per pound of engine air. To put the total developed power of the propeller-jet combination on a common basis, it is necessary to use the propeller propulsive efficiency η_{pr} . A power specific fuel consumption sfc may then be determined.

For level flight, thrust F is related to developed power by the equation

$$F = \frac{(\text{Propeller power}) + (\text{Jet power})}{V_0} \quad (9)$$

The propeller power is the power delivered to the propeller multiplied by the efficiency of the propeller and reduction gear. The jet power equals the thrust developed by the jet multiplied by the airplane flight speed V_0 . Hence, the thrust may be related to quantities obtained directly from cycle analysis by writing equation (9) as

$$F = \eta_{pr} \frac{[(\text{Power delivered to propeller}) + (\text{Jet power}/\eta_{pr})]}{V_0} \quad (10)$$

The term in brackets is defined as the equivalent shaft power $eshp$ of the engine, which depends to some extent on the combined propeller-gearbox efficiency η_{pr} . Since the jet power is usually small compared with the propeller power, the equivalent shaft power is essentially unaffected by minor changes in this efficiency; therefore, the results are expressed in terms of equivalent shaft power. Equation (9) is not applicable to the static sea-level case, since $V_0 = 0$. For this condition, the equivalent shaft power is simply the power delivered by the power turbine, and the value of the thrust depends on the propeller selection.

Curves showing specific equivalent shaft power $eshp/w_1$ against power specific fuel consumption sfc and over-all engine efficiency η_e , with

compressor total-pressure ratio P_2/P_1 and turbine-inlet total temperature T_3 as parameters, are presented in figure 7. Specific fuel consumption is used as the main variable for the abscissas because this term is more generally used than engine efficiency. These two quantities are related by the equation

$$\eta_e = \frac{(550)(3600)}{H_f J (\text{sfc})}$$

The efficiency is practically independent of the heating value of the fuel, while the specific fuel consumption is inversely proportional to the fuel heating value. Figures 7(a) and (b) represent sea-level flight at Mach numbers of 0 and 0.8, respectively, while figure 7(c) represents conditions for a flight Mach number of 0.8 in the stratosphere. In figure 8, the curves of figure 7 are repeated, except that compressor pressure ratio is replaced by enthalpy rise in the compressor ΔH_c as one parameter. This parameter is used because the enthalpy rise in a compressor tends to be more constant over a range of flight conditions than pressure ratio when the mechanical speed of the engine is fixed.

The general properties of the turboprop engine can be noted from figures 7 and 8. The turboprop engine is fundamentally capable of developing high shaft efficiency or low specific fuel consumption. The net efficiency of the engine is the product of the shaft efficiency and the efficiency of the reduction gears and the propeller. The shaft efficiency at a given turbine-inlet temperature increases with flight speed, because ram efficiently increases the cycle pressure ratio. Shaft efficiency also increases with altitude up to the tropopause, because the inlet-air temperature is reduced and the engine total-temperature ratio T_3/T_1 is increased. The specific power of the engine follows similar trends.

The actual power developed by the engine at various flying conditions is the product of specific power and the mass flow of air through the engine. The mass flow of air, in turn, depends on the value of $w\sqrt{\theta}/\delta$ of the compressor and the total pressure and temperature at the compressor inlet. The way the value of $w\sqrt{\theta}/\delta$ changes with flight conditions depends on the characteristics of the compressor and the value of the equivalent speed $N/\sqrt{\theta}$. One observed variation of $w\sqrt{\theta}/\delta$ with $N/\sqrt{\theta}$ is shown in figure 9. In this figure the ratio of $w\sqrt{\theta}/\delta$ to its design (sea-level) value is plotted against the ratio of $N/\sqrt{\theta}$ to its design value. This curve represents the general trend, although the specific values change from one compressor design to another.

At a flight Mach number of 0.8 in the stratosphere, the value of $\sqrt{\theta}$ is about 0.92. For a constant value of mechanical speed N , the value of $w\sqrt{\theta}/\delta$ is of the order of 106 percent of its sea-level value. At an altitude of 40,000 feet and a flight Mach number of 0.8, the value

of $\delta/\sqrt{\theta}$ is 0.300. The weight flow through the engine is thus about 32 percent of its sea-level value (including the effects of the assumed diffuser recoveries). For a compressor enthalpy rise of 110 Btu per pound and a turbine-inlet temperature of 2000° R, the power developed by an engine under these conditions is about 55 percent of its value at sea-level static conditions.

Because of the low power at high altitudes, the specific weight of turboprop engines (including the propeller) may vary between 1.5 and 3.0 at 40,000 feet. When flying at sea level, the corresponding specific weights are about half these values. At takeoff, the specific weights depend on propeller design as well as on engine design; values of specific weights under 0.2 are practical, however.

When the takeoff problem is secondary, one of the principal design problems is exploiting the inherently high efficiency of the engine. The selection of the compressor enthalpy rise or pressure ratio is then governed by the requirement of high efficiency. The desired value of either of these quantities depends on the turbine-inlet temperature, the flight speed, and the altitude. However, flight speed and altitude do not greatly affect the desirable value of enthalpy rise; and an enthalpy rise ΔH_c of 170 Btu per pound gives approximately maximum efficiency for 2000° R turbine-inlet temperature for the three flight conditions considered. The corresponding compressor pressure ratios are about 13 for a flight Mach number of 0.8 at sea level, 16 for sea-level static conditions, and 22 for a flight Mach number of 0.8 in the stratosphere.

Engine weight may be adversely affected by these high compressor pressure ratios, but this trend is at least partially overcome by increasing the turbine-inlet temperatures. Although an important fraction of the engine weight is fixed by the weight of the gearbox and propeller (which depend on the maximum output required of the engine), attractive gains are offered by using high turbine-inlet temperature together with the corresponding high pressure ratios. Employing turbine cooling for this purpose may reduce the indicated gains by a small amount but would not alter the general trend of the curves.

On the basis of this discussion, compressor design information must cover the problem of designing compressors for pressure ratios of 16 or higher. Although compressor efficiency has not yet been discussed, it is obvious that high levels of efficiency are required to obtain the highest levels of engine efficiency. While compressor weight may be of relatively minor importance at low design pressure ratios, it can represent a large portion of the engine weight when designs are made for the higher pressure ratios. Minimizing compressor weight for these conditions, without hurting the engine efficiency, is therefore an important design objective.

Effects of Compressor Pressure Ratio and Flight Conditions on Turbojet-Engine Performance

Some results of the cycle analysis of the turbojet engine are given in figures 10 to 12. Figure 10 presents specific thrust F/w_1 plotted against thrust specific fuel consumption $F(\text{sfc})$ or over-all engine efficiency η_e , with compressor total-pressure ratio P_2/P_1 and turbine-inlet total temperature T_3 as parameters, for a nonafterburning engine.

Thrust specific fuel consumption instead of over-all engine efficiency is again used as the main abscissa because it is a more familiar term and because the efficiency of a turbojet engine is always zero for static conditions. The relation between $F(\text{sfc})$ and η_e is given by

$$\eta_e = \frac{3600 V_0}{H_{FJ} F(\text{sfc})}$$

The efficiency is again practically independent of the heating value of the fuel, while $F(\text{sfc})$ is almost inversely proportional to it. Figures 10(a) and (b) represent sea-level altitude for flight Mach numbers of 0 and 0.8, respectively. Figures 10(c), (d), and (e) represent conditions in the stratosphere for flight Mach numbers of 0.8, 2.0, and 3.0, respectively. Figure 11 is identical with figure 10, except that lines of constant compressor total-pressure ratio are replaced by lines of constant enthalpy rise in the compressor ΔH_C . Figure 12, finally, is a carpet plot depicting the same engine variables as figure 10, for an afterburning turbojet engine with an afterburner-outlet total temperature of 3500° R. The carpet plot is used to spread the curves apart. The auxiliary curves show the relation between thrust specific fuel consumption and efficiency.

The thermodynamic efficiency of a turbojet engine (over-all efficiency divided by propulsive efficiency) is just as high as that of a turboprop. It also follows the same trends. The propulsive efficiency of the turbojet engine, which is approximately given by

$$\eta_{pr} = \frac{2V_0}{V_j + V_0} = \frac{1}{\frac{F_g}{w} \left(\frac{1}{2V_0} \right) + 1} \quad (11)$$

cannot be independently controlled, however. At subsonic flight speeds, the propulsive efficiency is of the order of 0.50 or less, and the over-all engine efficiency is therefore low compared with that of the turboprop. At supersonic flight speeds, the propulsive efficiency increases because of the lower values of F/w and the higher values of V_0 . The

thermodynamic efficiency of the engine increases at the same time because of the greater cycle pressure ratios resulting from ram. The net result is an increase in the attainable over-all efficiency with increasing flight Mach number.

By the same token, the specific thrust of a nonafterburning turbojet engine in a subsonic airplane is inherently lower than that of a turboprop. For two otherwise identical engines flying at a given flight speed and altitude, the ratio of the specific thrust of a turboprop engine to that of a turbojet engine is directly proportional to the ratio of their respective propulsive efficiencies. The turbojet engine is unencumbered by a gearbox and propeller, however, so its specific weight in level flight is about half that of the turboprop. This comparison is considerably different at takeoff, where the thrust and power coefficients of the propeller play a dominant role.

Subsonic flight. - As previously noted, the weight flow through the engine at a flight Mach number of 0.8 and an altitude of 40,000 feet may be about 32 percent of the weight flow at sea-level static conditions, for a constant-mechanical-speed engine. The thrust produced by the non-afterburning engine at this altitude flight condition is about 30 percent of its sea-level static value for a turbine-inlet temperature of 2000°R and a compressor enthalpy rise ΔH_C of 110 Btu per pound. A turbojet engine having a specific weight of 0.4 at sea level thus has a specific weight of about 1.3 at this altitude condition.

If a subsonic turbojet engine has about half the efficiency and about half the specific weight of a turboprop engine, it is profitably used when the ordinate of figure 3 is more than doubled by reducing $(W_e/F)/(L/d)_{\text{eff}}$ by 50 percent. For example, reducing $(W_e/F)/(L/d)_{\text{eff}}$ from 0.4 at point B to 0.2 increases the ordinate from 0.44 to 1.0. The same critical flight conditions are met, and the net improvement in range is about 14 percent. At point B, however, a 1-percent decrease in specific engine weight is equivalent to a 2.2-percent increase in efficiency (fig. 4(a)). At the new point (for the turbojet engine) a 1-percent decrease in specific weight is equivalent to only a 0.65-percent increase in efficiency. Even though the lighter and less efficient turbojet engine is more suitable for the flight than the turboprop engine, improvements in its efficiency are now somewhat more desirable than improvements in specific weight. Compressor pressure ratios greater than that for maximum specific thrust are thus desired. For the conditions of figure 10(c), pressure ratios of 16 or higher might be indicated. The rate at which the compressor weight increases with pressure ratio is the governing factor, however, in the selection of pressure ratio. Design information permitting the development of high pressure ratios with lightweight compressors is thus necessary, just as it was for the turboprop engine.

When the high thrust levels are required for only a short time or for a short distance, the use of afterburning is advantageous. Comparison of figure 12(c) with figure 10(c) shows that the specific thrust can be increased 50 to 100 percent by afterburning. At the same time, however, the engine efficiency is reduced by the order of 50 percent. If the use of afterburning is limited to a short period of time, the extra weight of fuel expended is small and the average efficiency is only slightly reduced. The reduction in the critical value of W_e/F is sufficient to more than overcome this loss in efficiency, and an increase in the range results. Referring to figures 3 and 4, the value of $(W_e/F)/(L/d)_{eff}$ is now decided by the afterburning condition. The mean efficiency, however, is practically that at the nonafterburning conditions. Because of the low value of engine specific weight at the critical flight condition, further improvements should favor a small increase in the average efficiency rather than a further decrease in specific engine weight. There is the provision, of course, that the critical condition is the one desired and not compromised to favor range to begin with.

Employing an afterburner may increase the engine weight from 10 to 30 percent. The specific engine weight is consequently not reduced in proportion to the increase in specific thrust. Because it offers resistance to the flow, the afterburner also decreases engine efficiency even when it is not burning fuel. Moreover, its added length increases nacelle drag, moves the center of gravity of the engine rearward, and increases the structural weight of the airplane. The net gains from its use are thus less than those indicated by the simple calculations of specific thrust.

Supersonic flight. - The turbojet engine, by itself, is capable of providing the thrust for takeoff, climb, and acceleration to Mach numbers between 2 and 3. It is therefore being seriously considered for this range of supersonic flight. At the flight Mach number of 2.0 in the stratosphere, the value of $N/\sqrt{\theta}$ is 86 percent of its sea-level value for a constant-speed engine. It is 69 percent of its sea-level value at the flight Mach number of 3.0. The corresponding values of $w\sqrt{\theta}/\delta$ are about 80 and 50 percent of their sea-level values (fig. 9). With the previously assumed inlet recoveries at an altitude of 55,000 feet, the associated values of $\delta/\sqrt{\theta}$ are about 0.5 and 1.4. Under these conditions, the weight flow of air at a flight Mach number of 2.0 is approximately 40 percent of that at sea level; at $M_0 = 3.0$, it is about 70 percent of its sea-level value.

The ratio of the developed thrust for these flight conditions to that at sea level depends on the enthalpy rise or pressure ratio of the compressor as well as the turbine-inlet and afterburner-exit temperatures. If the static sea-level pressure ratio is 8, if the turbine-inlet temperature is $2000^\circ R$, and if the afterburner-outlet temperature is $3500^\circ R$,

then the specific thrust at a flight Mach number of 2 is about the same as that for sea-level static conditions for the afterburning engine. At 55,000 feet and the Mach number of 2, the total thrust would be about 40 percent of its sea-level value. If the specific weight of the afterburning engine were 0.3 at sea level, its specific weight at 55,000 feet and a Mach number of 2 would be about 0.75. For values of $(L/d)_{\text{eff}}$ of the order of 3, $(W_e/F)/(L/d)_{\text{eff}}$ becomes 0.25. At 70,000 feet, $(W_e/F)/(L/d)_{\text{eff}}$ is increased to 0.50. The range of flight is thus drastically curtailed by the combination of high specific engine weights and low values of $(L/d)_{\text{eff}}$ (fig. 3). With lighter engines, higher altitudes are available and larger values of $(L/d)_{\text{eff}}$ might be obtained. Even at the same value of $(W_e/F)/(L/d)_{\text{eff}}$, a greater range would then be obtained if $(L/d)_{\text{eff}}$ is increased (eq. (6)). Emphasis is thus placed on low engine weights for this type of flight condition. As indicated in equation (7a), however, engine efficiency is of equal importance and must not be unduly prejudiced by efforts to reduce specific engine weight.

In order to obtain low specific weights at flight Mach numbers of the order of 2, the use of afterburning engines is attractive. According to figures 12(d) and (e), high pressure ratios and high turbine-inlet temperatures would be desired for afterburning engines, since the highest specific thrust and efficiency are thereby attained. This desire is tempered, however, by the weight problems at the high pressure ratios and the problems associated with the use of high turbine-inlet temperatures. At lower turbine-inlet temperatures, there is a maximum desirable pressure ratio. At higher or lower pressure ratios, both the specific thrust and efficiency decrease. At a flight Mach number of 2, the pressure ratio for the highest specific thrust and efficiency is about 8 for a turbine-inlet temperature between 2000° and 2500° R. The corresponding pressure ratio at sea level for a constant-mechanical-speed engine is about 14.

High turbine-inlet temperatures without afterburning are also attractive at the flight Mach number of 2 (fig. 10(d)). Although the specific thrust is reduced from the afterburning case, the engine efficiency is increased. Moreover, the afterburning engine is penalized by the engine and airframe weight penalties previously discussed. These effects may more than counterbalance the loss in specific thrust. The pressure ratios desired for the nonafterburning engine are of course higher than for the afterburning engine.

At the high flight Mach number of 3, the required compressor pressure ratios are low. With a turbine-inlet temperature of 2000° R, a pressure ratio of the order of 2 is desired for either an afterburning or nonafterburning engine (figs. 10(e) and 12(e)). This value corresponds to a pressure ratio of about 4 at sea level. Since the resulting subsonic

performance is poor, higher turbine-inlet temperatures must be used to realize the advantages of the higher compressor pressure ratios. At the turbine-inlet temperature of 2500°R , the desirable pressure ratio lies between a value of 3 and 4 at the high flight Mach numbers. For constant-mechanical-speed engines, the corresponding sea-level pressure ratios are between 8 and 12. The necessity for lightweight compressors developing this order of pressure ratio at sea level is again apparent.

Other Engine Cycles

There are many thermodynamic cycles suggested for aircraft propulsion. The ducted-fan or bypass engine, for instance, is an intermediate engine between the turboprop and the turbojet engines. The desired characteristics of the main compressor and fan are thus expected to be similar to the ones just outlined. The design data required are consequently the same. Similarly, the design data would be applicable to the design of other low-pressure-ratio compressors such as those used in the turborocket.

Effects of Compressor Efficiency on Engine Performance

The effect of a change in compressor efficiency on the results of the preceding section can be estimated by the following considerations. At a given flight speed and altitude, the enthalpy rise due to ram is fixed, as is the temperature T_1 (fig. 6). With a given inlet recovery, the ram pressure ratio P_1/p_0 is constant. For a given enthalpy rise in the compressor, the combustor-inlet temperature T_2 is fixed. The compressor total-pressure ratio P_2/P_1 is then a function of compressor efficiency only. The turbine-inlet temperature T_3 is given a fixed value as is the combustor pressure ratio P_3/P_2 . Since the work done by the turbine approximately equals the enthalpy rise through the compressor, the turbine-outlet temperature T_4 is fixed. For a given turbine efficiency, the turbine pressure ratio P_4/P_3 is also fixed. Since the output and efficiency of the engine ultimately become functions of T_4 and P_4/p_0 , the effect of compressor efficiency is examined by noting its effect on $P_4/p_0 = P_2/P_1$ times a constant.

Compressor efficiency is defined by the equation

$$\eta_{ad,C} = \frac{\frac{\gamma_C - 1}{\left(\frac{P_2}{P_1}\right)^{\gamma_C} - 1} \Delta H_C}{T_1 c_p} \quad (12)$$

Rearranging this expression and differentiating it, while holding the value of $\Delta H_C / T_1 c_p$ constant, yield the following result:

$$\frac{d\left(\frac{P_2}{P_1}\right)}{\frac{P_2}{P_1}} = Q \frac{d\eta_{ad,C}}{\eta_{ad,C}} \quad (13a)$$

where

$$Q = \frac{\gamma_C}{\gamma_C - 1} \frac{\frac{\gamma_C - 1}{\left(\frac{P_2}{P_1}\right)^{\gamma_C} - 1}}{\left(\frac{P_2}{P_1}\right)^{\gamma_C}} \quad (13b)$$

The effect of a percent change in compressor total-pressure ratio on the total pressure P_x at any point in the engine downstream of the compressor is thus

$$\frac{d\left(\frac{P_x}{P_0}\right)}{\frac{P_x}{P_0}} = \frac{d\left(\frac{P_2}{P_1}\right)}{\frac{P_2}{P_1}} = Q \frac{d\eta_{ad,C}}{\eta_{ad,C}} \quad (14)$$

Turboprop engine. - For a turboprop engine, neglecting the contribution of the jet, the mechanical energy ΔH_M developed in a complete

expansion of the engine gases through the power turbine is given by

$$\Delta H_M = \eta_{ad,PT} T_4 c_p \left[1 - \left(\frac{P_0}{P_4} \right)^{\frac{\gamma_T - 1}{\gamma_T}} \right] \quad (15)$$

and

$$\frac{P_0}{P_4} = \frac{1}{\frac{P_1}{P_0} \frac{P_4}{P_1}}$$

For given values of compressor pressure ratio P_2/P_1 and engine temperature ratio T_3/T_1 , the value of P_4/P_1 may be found from figure 13. (In this figure, the quantity P_4/P_1 is plotted against P_2/P_1 with T_3/T_1 as a parameter. These data are a byproduct of the cycle calculations of the previous section. For a constant value of specific heat and γ , these curves would be independent of the flight condition. Actually, the variations in these quantities cause these curves to vary about ± 6 percent from the values shown over the entire range of flight conditions considered. The important trends of the curves are not affected, however.) Since the ram pressure ratio P_1/P_0 is also known, P_0/P_4 may be determined.

Differentiating equation (15) and utilizing equation (14) while holding $(\eta_{ad,PT} T_4 c_p)$ constant yield

$$\frac{d(\Delta H_M)}{\Delta H_M} = G \frac{d\eta_{ad,C}}{\eta_{ad,C}} \quad (16a)$$

where

$$G = \frac{\gamma_T - 1}{\gamma_T} \frac{\left(\frac{P_0}{P_4} \right)^{\frac{\gamma_T - 1}{\gamma_T}}}{1 - \left(\frac{P_0}{P_4} \right)^{\frac{\gamma_T - 1}{\gamma_T}}} Q \quad (16b)$$

Equation (16a) shows the general effect of a small change in compressor efficiency on the power output of a turboprop engine. Since this equation was derived with the assumption of a constant heat input to the engine, the percent change in power output is the same as the percent change in engine efficiency or specific fuel consumption.

Figure 14 shows the quantity G from equations (16) plotted against compressor total-pressure ratio P_2/P_1 , with the ratio p_0/P_4 as a parameter. In the calculation of this figure, values for γ_C and γ_T of 1.4 and 1.3, respectively, were assumed. Examination of figure 14 reveals that G is large when both P_2/P_1 and p_0/P_4 are large. For these conditions, the power output and efficiency of a turboprop engine are sensitive to small changes in compressor efficiency (eq. (16)).

For a turboprop engine developing a pressure ratio of 16 while flying at a Mach number of 0.8 in the stratosphere, a 1-percent decrease in compressor efficiency reduces the power and engine efficiency by a little less than 1 percent. The results of figures 13 and 14 also show that the effect of compressor efficiency diminishes slightly as turbine-inlet temperature is increased. Since compressor pressure ratio for a given enthalpy rise decreases as the efficiency decreases, a drop in compressor efficiency decreases the pressure ratios for both maximum specific power and maximum engine efficiency.

Turbojet engine. - In the case of a turbojet engine, a small change in compressor efficiency affects the total pressure P_5 in the jet nozzle, which in turn affects the jet velocity and the thrust. The magnitude of these effects may be examined as follows. The jet velocity V_j is expressed in terms of the jet-nozzle pressure ratio p_0/P_5 as

$$V_j = C_j \sqrt{2T_5 c_p g J \left[1 - \left(\frac{p_0}{P_5} \right)^{\frac{\gamma_T - 1}{\gamma_T}} \right]} \quad (17)$$

Differentiating this equation while holding the quantity $C_j \sqrt{2T_5 c_p g J}$ constant provides the relation

$$\frac{dV_j}{V_j} = \frac{\gamma_T - 1}{2\gamma_T} \frac{\left(\frac{p_0}{P_5} \right)^{\frac{\gamma_T - 1}{\gamma_T}}}{1 - \left(\frac{p_0}{P_5} \right)^{\frac{\gamma_T - 1}{\gamma_T}}} Q \frac{d\eta_{ad,C}}{\eta_{ad,C}} \quad (18)$$

using equation (14). The specific thrust F/w_1 is related to the jet velocity V_j by

$$\frac{F}{w_1} = \frac{(1+f)V_j - V_0}{g} \quad (19)$$

Then $d(F/w_1) = (1+f) dV_j/g$, assuming a constant fuel-air ratio f , and hence

$$\frac{d\left(\frac{F}{w_1}\right)}{\frac{F}{w_1}} = \frac{E}{1 - \frac{V_0}{(1+f)V_j}} \frac{d\eta_{ad,C}}{\eta_{ad,C}} \quad (20a)$$

where

$$E = \frac{\gamma_T - 1}{2\gamma_T} \frac{\left(\frac{p_0}{p_5}\right)^{\frac{\gamma_T - 1}{\gamma_T}}}{1 - \left(\frac{p_0}{p_5}\right)^{\frac{\gamma_T - 1}{\gamma_T}}} Q \quad (20b)$$

using equations (18) and (19). The expression for the parameter E is seen to be half the value of G if the power-turbine pressure ratio p_0/p_4 is replaced by the jet-nozzle pressure ratio p_0/p_5 . Figure 14 may therefore be used to evaluate E for given values of P_2/P_1 and p_0/p_5 by taking $E = G/2$. The value of p_0/p_5 is determined from figure 13 in the same way that p_0/p_4 is found for the turboprop engine.

Equation (20a) shows the effect of a percent change in compressor efficiency on the specific thrust of a turbojet engine. As in the case of the turboprop engine, the percent change in specific thrust may be taken as equal to the corresponding percent change in engine efficiency or thrust specific fuel consumption.

For the static case ($V_0 = 0$), the effect of a percent change in compressor efficiency on either specific thrust or efficiency can be determined directly by evaluating E from figure 14. Equations (20) and figure 14 show that for this case specific thrust or engine efficiency is

sensitive to small changes in compressor efficiency when both P_2/P_1 and p_0/P_5 are large. This situation for the turbojet engine, as for the turboprop engine, corresponds to high compressor pressure ratios and low turbine-inlet temperatures. Figure 10(a) shows that these conditions are required for high values of engine efficiency. When engine efficiency is highly important at sea-level static conditions, therefore, high compressor efficiencies are necessary.

When a reasonably high flight speed is involved, the ratio $V_0/(1+f)V_j$ cannot be ignored. Notice, however, that the denominator of the coefficient of $d\eta_{ad,C}/\eta_{ad,C}$ in equation (20a) can be written as

$$1 - \frac{V_0}{(1+f)V_j} = 1 - \frac{1}{\frac{F}{w_1} \frac{g}{V_0} + 1}$$

If F/w_1 is 80 pounds per pound per second at a flight Mach number of 3, the value of this expression is about 0.5, and the coefficient of $d\eta_{ad,C}/\eta_{ad,C}$ in equation (20a) approaches the value of G . If F/w_1 is 60 pounds per pound per second at a flight Mach number of 0.8, this expression has the value of about 0.7.

For the subsonic airplane, in which the compressor pressure ratio is of the order of 16, a percent decrease in compressor efficiency reduces the specific thrust and engine efficiency by a little less than 1 percent for constant enthalpy rise in the compressor. Since the ratio T_3/T_1 is low for supersonic flight, the value of P_4/P_1 is low (fig. 13). On the other hand, the value of P_1/p_0 is high, and a percent decrease in compressor efficiency reduces the thrust and efficiency by the order of only 0.5 percent.

It is again noted that a reduction in compressor pressure ratio accompanies a decrease in efficiency for this analysis. The optimum pressure ratio for either maximum specific thrust or minimum specific fuel consumption, therefore, decreases as compressor efficiency decreases.

EFFECTS OF COMPRESSOR PRESSURE RATIO, FLOW CAPACITY, AND EFFICIENCY ON FRONTAL AREA OF OTHER ENGINE COMPONENTS

Compressor pressure ratio, flow capacity, and efficiency play a prominent role in determining the relative frontal areas of the engine components. The frontal areas of these components are also involved in engine weight. In this discussion, only the internal frontal area is considered. This area is defined by πr_t^2 , where r_t is the radius to

the internal surface of the casing of the component under consideration. Of interest now is the ratio of the internal frontal area of a component to that of the compressor.

The flow area A of any component is determined by stipulating the weight flow and either a maximum velocity V or a Mach number M at the entrance or exit of the component. These maximum values may be either absolute or found from experience; in either case, undesirably high losses result from attempting to exceed these limits. The required flow area may be expressed in terms of the velocity V by the equation

$$A = \frac{w\sqrt{RT}}{\sqrt{\gamma g} \frac{VP}{\sqrt{\gamma g RT}} \left(1 - \frac{\gamma - 1}{2} \frac{V^2}{\gamma g RT}\right)^{\frac{1}{\gamma - 1}}} \quad (21a)$$

or in terms of the Mach number M by

$$A = \frac{w\sqrt{RT} \left(1 + \frac{\gamma - 1}{2} M^2\right)^{\frac{\gamma + 1}{2(\gamma - 1)}}}{MP\sqrt{\gamma g}} \quad (21b)$$

When the values of w and M or V are given, the annular area is determined by the total pressure and temperature at the point considered. The internal frontal area is related to the annular area A by the equation

$$A = A_F \left[1 - \left(\frac{r_h}{r_t}\right)^2\right]$$

Since the weight flow through a conventional engine is essentially constant, the ratio of the frontal area of any component to the frontal area of the compressor is given by

$$\frac{(A_F)_x}{(A_F)_C} = \frac{\left(\frac{w}{A_F}\right)_C}{\left(\frac{w}{A_F}\right)_x}$$

The equivalent weight flow per unit frontal area $w\sqrt{\theta}/A_F\delta$ of the

compressor or of any other engine component may be expressed by substituting

$$A = A_F \left[1 - \left(\frac{r_h}{r_t} \right)^2 \right]$$

$$P = p_{s1} \delta$$

$$T = T_{s1} \theta$$

into equations (21a) and (21b). The results are

$$\frac{w\sqrt{\theta}}{A_F\delta} = \sqrt{\frac{\gamma g}{R}} \frac{V}{\sqrt{\gamma g R T}} \left(1 - \frac{\gamma - 1}{2} \frac{V^2}{\gamma g R T} \right)^{\frac{1}{\gamma - 1}} \left[1 - \left(\frac{r_h}{r_t} \right)^2 \right] \frac{p_{s1}}{\sqrt{T_{s1}}} \quad (22a)$$

$$\frac{w\sqrt{\theta}}{A_F\delta} = \sqrt{\frac{\gamma g}{R}} M \left(1 + \frac{\gamma - 1}{2} M^2 \right)^{-\frac{\gamma + 1}{2(\gamma - 1)}} \left[1 - \left(\frac{r_h}{r_t} \right)^2 \right] \frac{p_{s1}}{\sqrt{T_{s1}}} \quad (22b)$$

Notice that, when $V/\sqrt{\gamma g R T}$ or M is small, these equations are approximated by

$$\frac{w\sqrt{\theta}}{A_F\delta} = \frac{V}{\sqrt{T}} \left[1 - \left(\frac{r_h}{r_t} \right)^2 \right] \frac{p_{s1}}{R\sqrt{T_{s1}}} \quad (22a')$$

$$\frac{w\sqrt{\theta}}{A_F\delta} = M \left[1 - \left(\frac{r_h}{r_t} \right)^2 \right] \sqrt{\frac{\gamma g}{R}} \frac{p_{s1}}{\sqrt{T_{s1}}} \quad (22b')$$

At a value of $V/\sqrt{\gamma g R T}$ of 0.2, the error is about 2 percent. For the same value of M , the error is about 2.4 percent. A quantitative evaluation of equation (22) may be obtained from figures 15 and 16. In figure 15(a), $w\sqrt{\theta}/A_F\delta$ is plotted against $V/\sqrt{\gamma g R T}$, with the hub-tip radius ratio r_h/r_t as a parameter and with $\gamma = 1.4$. Figure 15(b) is the same, except that $\gamma = 1.3$. In figure 16 the flow Mach number M replaces $V/\sqrt{\gamma g R T}$ as the abscissa.

When the given or allowable flow Mach number is known, together with the ratio of the inner to the outer radius, the value of $w\sqrt{\theta}/A_F\delta$ may be determined from figure 16. The ratio of the required frontal area of any component to that of the compressor may be expressed as

$$\frac{(A_F)_x}{(A_F)_C} = \frac{\left(\frac{w}{A_F}\right)_C}{\left(\frac{w}{A_F}\right)_x} = \frac{\left(\frac{w\sqrt{\theta}}{A_F\delta}\right)_C}{\left(\frac{w\sqrt{\theta}}{A_F\delta}\right)_x} \left(\frac{P_1}{P_x} \sqrt{\frac{T_x}{T_1}}\right) \quad (23)$$

The value of the last term in parentheses in equation (23) may be determined from figure 17 for the combustor inlet. For the turbine discharge this term may be evaluated from figure 18. The data for these figures were obtained as a byproduct of the cycle analyses previously presented. While figure 17 exactly represents the condition for the given assumptions, figure 18 is subject to the same error discussed in connection with figure 13. The value of $(P_1/P_x) \sqrt{T_x/T_1}$ at other engine stations can be calculated readily with the aid of these curves. If the flow velocity rather than the flow Mach number is of interest, the total-temperature ratio across the component must be known in order to determine $V/\sqrt{\gamma g R T}$, which is the abscissa of figure 15. These total-temperature ratios may also be evaluated from figure 17 for the combustor inlet and from figures 13 and 18 for the turbine outlet.

Comparison of Frontal Areas for Subsonic Flight

Consider the situation for a flight Mach number of 0.8 in the stratosphere with a compressor pressure ratio of 16. Assume $w\sqrt{\theta}/A_F\delta$ of 30 pounds per second per square foot for the compressor and a turbine-inlet temperature of 2000° R. Component efficiencies are those used in the cycle analyses previously presented.

Engine inlet. - Although it is not affected by compressor pressure ratio, the area of the inlet is also of interest and will be considered first. For reasonably high flight speeds, the internal frontal area of the inlet is equal to or greater than that of the free-stream tube passing the required mass flow. Assuming the internal inlet area to be equal to the free-stream area (the capture area), the value of $w\sqrt{\theta}/A_F\delta$ for the inlet is given by figure 16(a) with M = free-stream Mach number and $r_h/r_t = 0$. With a pressure recovery of 0.98, the ratio of the inlet frontal area to compressor internal frontal area is 0.62. This ratio is directly proportional to both the total-pressure recovery of the inlet diffuser and the flow capacity of the compressor.

Combustor. - In determining the size of the combustor, the average velocity in the annulus is frequently taken as a critical factor, although Mach number is probably just as applicable. The magnitude of the velocity influences combustion efficiency as well as the pressure drop through the combustor. For a limiting velocity of 150 feet per second and r_h/r_t of 0.4, the internal frontal area of the combustor is 43 percent of the compressor internal frontal area. This number is inversely proportional to the limiting velocity (eqs. (22a') and (23)). It increases as compressor pressure ratio decreases; at a pressure ratio of 8, the internal frontal area of the combustor is 70 percent of that of the compressor, other conditions being the same. This ratio is again proportional to the flow capacity of the compressor.

Turbine. - For the turbine, the axial Mach number at the turbine outlet is decisive. This Mach number should be less than about 0.7 to avoid the limiting loading discussed in reference 6. For a leaving Mach number of 0.6 and a hub-tip radius ratio of 0.6, the ratio of the internal frontal area of the turbine to that of the compressor is 0.54. With leaving Mach numbers of 0.5 and 0.4, the respective ratios are 0.61 and 0.72. Decreasing the compressor pressure ratio increases this number. At a compressor pressure ratio of 8 it is 0.70 instead of 0.54. Again, increasing the turbine-inlet temperature to 2200° R ($T_3/T_1 = 5.0$) decreases this number from 0.54 to 0.50. For a fixed turbine-inlet temperature, a reduction in compressor-inlet temperature increases T_3/T_1 with an attendant reduction in this internal-frontal-area ratio.

The flow capacity of the turbine is controlled by the stresses in the turbine blades and the required work output of the turbine, as well as the Mach number at the turbine exit. This effect is outlined in reference 7 and given detailed study in reference 8. Briefly, the permissible annular flow area A is proportional to the allowable centrifugal stress τ at the blade root according to the equation

$$A = \frac{2\pi r g}{\omega^2 \Gamma \psi}$$

where ψ is a taper factor defined as the ratio of the actual root centrifugal stress to the centrifugal stress in a blade having a constant spanwise cross-sectional area. Combining this relation with equation (21b) and noting that $U_t = r_t \omega$ provide the result

$$\frac{w U_t^2}{A_{FG}} \frac{\Gamma}{\tau} = \frac{2P}{\psi \sqrt{T}} \sqrt{\frac{\gamma g}{R}} M \left(1 + \frac{\gamma - 1}{2} M^2 \right)^{-\frac{\gamma + 1}{2(\gamma - 1)}} \quad (24)$$

If reference values of compressor tip speed U_t , τ , and Γ are assigned and attention is focused on the turbine, equation (24) becomes

$$\left(\frac{w_1 \sqrt{\theta}}{A_F \delta_1} \right) \frac{\Gamma}{\Gamma_{\text{ref}}} \frac{\tau_{\text{ref}}}{\tau} \left(\frac{U_t}{U_{t,\text{ref}}} \right)^2$$

$$= \frac{2}{\psi} \frac{P_4}{P_1} \sqrt{\frac{T_1}{T_4}} \sqrt{\frac{\gamma g}{R}} M_4 \left(1 + \frac{\gamma - 1}{2} M_4^2 \right)^{-\frac{\gamma+1}{2(\gamma-1)}} \frac{P_{s1}}{\sqrt{T_{s1}}} \frac{\tau_{\text{ref}}}{\Gamma_{\text{ref}}} \frac{g}{U_{t,\text{ref}}^2} \quad (25)$$

for a constant weight flow throughout the engine. A quantitative study of equation (25) is obtained from figure 19, in which a set of curves showing the left side of this equation as a function of $(P_4/P_1) \sqrt{T_1/T_4}$ and M_4 is adjoined to the curves of figure 18. The following values were assumed in the calculations for this figure, with appropriate units where necessary: $\gamma = 1.3$, $\psi = 0.6$, $U_{t,\text{ref}} = 1000$ feet per second, $\tau_{\text{ref}} = 30,000$ pounds per square inch, and $\Gamma_{\text{ref}} = 0.3$ pound per cubic inch.

When Γ , τ , and U_t assume their reference values, the left side of equation (25) is identically $w_1 \sqrt{\theta_1} / A_F \delta_1$, the flow capacity of the compressor as limited by turbine stress. For the reference condition, the permissible values of $w_1 \sqrt{\theta_1} / A_F \delta_1$ are considerably higher than those assumed in the previous study. The assumed hub-tip radius ratios are thus well within those permitted by the assumed stress limits and compressor flow capacities. Higher compressor speeds or lower turbine stress limits would, of course, reduce the compressor flow capacity permitted.

The relation between the work output of the turbine and the flow capacity of the compressor may be examined in a similar gross way. As a rule of thumb, the maximum output of a turbine stage is determined by the quantity $J\Delta H / (w r_h)^2$, which is inversely proportional to the square of the blade- to jet-speed ratio. An upper limiting value (of about 2) may be assigned to this quantity, and the permissible enthalpy drop in a stage is given when the speed of rotation is known. Only a small enthalpy drop is obtained with the low rotative speeds and at the hub of turbines with low hub-tip radius ratios; accordingly, small enthalpy drops are obtained for the conditions of high flow capacity. High flow capacity is thus associated with a relatively large number of turbine stages.

High rotative speeds and large hub-tip ratios, on the other hand, reduce the flow capacity but tend to decrease the number of turbine stages.

Afterburner. - At the inlet to the afterburner, a limiting velocity is again used for the same reasons that govern its use in the primary combustor. For the present example the limiting velocity is assumed to be 550 feet per second. With this limit, the ratio of the internal frontal area of the afterburner to that of the compressor is 0.58, ($r_h/r_t = 0$). Changing the cycle pressures and temperature will vary this number in about the same proportions as those given for the turbine.

Nozzle. - The area of the jet nozzle depends on the amount of afterburning, the amount of supersonic expansion in the nozzle, and whether or not an ejector is employed. With sonic velocities at the nozzle exit and no afterburning, the area ratio is 0.29. Altering the cycle will change this number somewhat in proportion to the corresponding turbine areas.

It appears that a compressor having a flow capacity of 30 pounds per square foot ($= (w\sqrt{\theta}/A_F\delta)_C$) could have the largest internal frontal area of all the components in an engine for subsonic flight. Since the area ratios are proportional to compressor equivalent flow capacity, there is a strong incentive to make the flow capacity of the compressor as high as possible. The maximum value of compressor flow capacity is 49.4 pounds per second per square foot (fig. 15(a)), however, so that all the other components could presumably have a smaller frontal area than the compressor when the high pressure ratios required for good engine efficiency are used.

Comparison of Frontal Areas for Supersonic Flight

For a given mass flow, the free-stream-tube area increases with Mach number in the supersonic regime. The temperature at the compressor inlet increases and that at the compressor outlet thus also increases with flight Mach number. Both the values of P_2/P_1 and T_3/T_1 are generally lower for supersonic flight than they are for subsonic flight. As a result, the values of P_4/P_1 and $(P_4/P_1)\sqrt{T_1/T_4}$ are reduced (figs. 13 and 18). For a given value of $(w\sqrt{\theta}/A_F\delta)_C$, the value of $(A_F)_x/(A_F)_C$ therefore increases with flight Mach number (eq. (23)). As shown in figure 9, however, the flow capacity of the compressor also decreases with flight Mach number when the mechanical speed of the engine is fixed (since θ increases with flight Mach number). This behavior decreases the value of $(A_F)_x/(A_F)_C$.

In order to examine these trends, consider the situation at flight Mach numbers of 2 and 3 in the stratosphere. Let the respective values

of P_2/P_1 be 8 and 4, and let the turbine-inlet temperature be 2500°R for both cases. Assume, moreover, that $(w\sqrt{\theta}/A_F\delta)_C$ is 30 pounds per second per square foot for the compressor at sea level.

At the flight Mach number of 2, the equivalent flow capacity of the compressor may drop to 24 ((lb/sec)/sq ft) for constant engine speed. With an inlet recovery of 0.90, the ratio $(A_F)_O/(A_F)_C$ becomes 0.74. At the flight Mach number of 3 and a recovery of 0.6, the value of $(w\sqrt{\theta}/A_F\delta)_C$ is 15 pounds per second per square foot and $(A_F)_O/(A_F)_C = 0.77$. Notice that this number applies only to the internal capture area. As indicated in figure 5, the actual frontal area of the inlet may be substantially larger than this.

With a limiting average combustor velocity of 150 feet per second, the ratio of the internal frontal area of the combustor to that of the compressor is 0.70 at the flight Mach number of 2 ($r_h/r_t = 0.4$). It is 0.88 at the flight Mach number of 3. This value is almost inversely proportional to compressor pressure ratio for a given flight condition.

If the hub-tip radius ratio of the turbine is 0.6 and the leaving Mach number is 0.6, the ratio of the internal frontal area of the turbine to that of the compressor is 0.62 at the flight Mach number of 2 and 0.58 at the flight Mach number of 3. Increasing either the compressor pressure ratio or turbine-inlet temperature decreases this ratio in inverse proportionality to the resulting change in $(P_4/P_1)\sqrt{T_1/T_4}$ shown in figure 18. Notice that the assumed flow capacity of the compressor is low enough to satisfy the turbine stress requirements of figure 19 for the reference conditions.

Again using an afterburner-inlet velocity of 550 feet per second, the ratio of the internal frontal area of the afterburner to that of the compressor is found to be 0.77 at the flight Mach number of 2. At the flight Mach number of 3, it is 0.71. These values are again almost inversely proportional to $(P_4/P_1)\sqrt{T_1/T_4}$, and changes in compressor pressure ratio and turbine-inlet temperature will change this ratio following the trends shown in figure 18.

The area of the nozzle again depends on the factors previously mentioned. It is noted, however, that for complete expansion the outlet area of the nozzle is 92 percent of the internal frontal area of the compressor, at the flight Mach number of 2. At the flight Mach number of 3, the area ratio for complete expansion is 1.14. When the nozzle area equals the frontal area of the compressor, the jet velocity V_j is reduced about 2.5 percent, with a resulting loss of thrust of about 1.5 percent compared with the complete-expansion case. Although the developed thrust is decreased

slightly by limiting the expansion, the actual thrust minus drag is probably increased. Internal plugs on an ejector have been frequently recommended when large nozzle pressure ratios are developed. In these cases, the actual flow area is effectively less than the internal frontal area.

For the example chosen, the compressor has a greater frontal area than either the primary combustor or the turbine. The flow through the compressor is much less than its natural capacity, however; and a 20- to 100-percent increase in the flow capacity of the compressor at supersonic flight speeds could easily be obtained by some means or another. Thus, engines could be designed in which the compressor diameter is smaller than that of any other component in the engine. If the increase in flow capacity is obtained by increasing the mechanical speed with flight Mach number, so as to reduce the severity of the drop in $N/\sqrt{\theta}$, then turbine stress problems arise (eq. (25)). On the other hand, if the value of N is sufficiently low to avoid this difficulty, the enthalpy drop per turbine stage is low, and a large number of turbine stages is required. Therefore, the selection of compressor flow capacity is frequently based on a number of considerations other than frontal area. Design information is required, however, to permit designs as close as possible to the natural limit of 49.4 pounds per second per square foot of frontal area. This high value could then be used when it is desired.

Effects of Compressor Efficiency on Size of Components Downstream

Compressor efficiency also affects the size of engine components downstream of the compressor. The magnitude and interrelation of these effects are estimated by the following technique. When the weight flow w and the velocity or Mach number are given, the annular flow area is seen by equations (21) to be determined by the total pressure P and the total temperature T at the point considered.

Presuppose a fixed enthalpy rise in the compressor and a given fuel flow so as to make the total temperature T at any point in the engine independent of the compressor efficiency and pressure ratio. Equation (14) then shows how a small change in compressor efficiency affects the total pressure at any point in the engine downstream of the compressor. Holding w , T , and V or M constant and differentiating either equation (21a) or (21b) with respect to A and P give

$$\frac{dA}{A} = - Q \frac{d\eta_{ad,C}}{\eta_{ad,C}} \quad (26)$$

utilizing equation (14). A curve showing the parameter Q as a function of P_2/P_1 for $\gamma_C = 1.4$ is shown in figure 20. This curve indicates that the sensitivity of the flow area of the components downstream of the

compressor to small changes in compressor efficiency is greatest when the compressor total-pressure ratio P_2/P_1 is high. Under these conditions, the frontal area of the components behind the compressor is usually low. When the components behind the compressor decide the frontal area, however, low compressor efficiency can be costly with respect to size as well as engine efficiency and specific thrust.

FACTORS DETERMINING COMPRESSOR FLOW CAPACITY AND WEIGHT

Flow Capacity

The flow capacity selected for a compressor represents a compromise among several factors that also control engine weight. Some of these factors are discussed in the next main section of this chapter. For the moment it is sufficient to note that, among other things, the flow capacity depends on the rotational speed of the engine. Two causes of this dependency, turbine blade stress and turbine work, were outlined in the previous section. A similar limit involving stress in the compressor blades could also be deduced. The stress in the turbine blades is frequently the governing factor, however, because of the elevated temperatures.

Another factor making the flow capacity depend on the speed of rotation arises from aerodynamic causes in the compressor itself. At the present state of the design art, dictates of efficiency limit the Mach number relative to the compressor blades. This Mach number may be written as

$$M_1^2 = M_1 \cos \beta_1 \sqrt{1 + \left(\frac{U}{V_1 \cos \beta_1} - \tan \beta_1 \right)^2} \quad (27)$$

The equivalent weight flow per unit of flow area at any radius is, however,

$$\frac{w\sqrt{\theta}}{A\delta} = \sqrt{\frac{\gamma g}{R}} M_1 \cos \beta_1 \left(1 + \frac{\gamma - 1}{2} M_1^2 \right)^{-\frac{\gamma+1}{2(\gamma-1)}} \frac{p_{s1}}{\sqrt{T_{s1}}} \quad (28)$$

Because of other considerations, the value of β_1 is usually made as small as possible, and even negative values of β_1 may be desired. With a given value of β_1 and a limiting value of M_1 , the flow capacity is critically dependent on the wheel speed U , decreasing as the wheel speed increases.

If, now, the wheel speed is independently determined, the maximum flow capacity of the compressor is automatically stipulated either by the limitations of blade stress or by the limitations of compressor blade Mach number. At low compressor pressure ratios and low ratios of turbine-inlet to compressor-inlet temperature, turbine blade stress tends to be the deciding factor. At higher levels of these quantities, with cooled turbines, compressor blade Mach number becomes the critical item. In order to overcome this latter limitation, considerable attention must be given to the problem of efficiently coping with high Mach numbers relative to the compressor blades.

The radial distribution of $w\sqrt{\theta}/A\delta$, as well as the hub-tip radius ratio, is required to determine the net equivalent flow capacity of the compressor. The radial-distribution problem is treated in chapter VIII (ref. 9). It will not be discussed here except to note that the flow capacity can be affected by the distribution. The hub-tip radius ratio is affected by two factors: (1) the problem of attaching the blades to the disks, which is chiefly a mechanical problem, and (2) the aerodynamic problem of designing the blades near the hub. The gains in flow capacity are small when the hub-tip radius ratio is reduced below about 0.35 (see figs. 15 and 16), and it is at the lower values of hub-tip radius ratio that the attachment and aerodynamic design problems may become serious. Below some value of hub-tip radius ratio, therefore, the possible gains in weight flow per unit of frontal area could be too small for the effort and expense required to get them.

Layout and Weight

Some of the problems associated with the size and weight of a compressor are illustrated with the aid of a schematic drawing of a representative current compressor and its diffuser (fig. 21). The pressure ratio, turbine-inlet temperature, and weight flow of air of the engine associated with this compressor are presumably determined from preliminary design studies. The speed of rotation is also assumed to have been selected from this study. The flow capacity of the compressor is then fairly well defined, either by stress or aerodynamic considerations.

The number of stages required by the compressor is determined by the pressure ratio or enthalpy rise that each stage can produce. At the present time, the permissible enthalpy rise per stage may be approximately expressed by

$$\Delta H = \frac{2\sigma V_1' U}{J} \left(D + \frac{V_2'}{V_1'} - 1 \right) \quad (29)$$

where D is a measure of the blade loading as presented in reference 10. The enthalpy rise in a stage is thus directly proportional to the blade

speed and to the stage-inlet velocity relative to the rotor. Obtaining high flow capacity by reducing the blade speed increases the number of stages required to obtain a given enthalpy rise. This result is similar to that previously noted for the turbine.

The enthalpy rise in a stage also depends on the relative velocity ratio V_2'/V_1' across the stage. If D has a limiting value of 0.4, changing V_2'/V_1' from 1 to 0.9 reduces the enthalpy rise in the stage by 25 percent. The limitations imposed by this velocity ratio affect the layout and the number of stages required by a compressor. In order to meet the velocity requirements in the combustor, the axial component of air velocity is sometimes reduced by a factor of 5 or more between the compressor inlet and the combustor. Avoiding excessive losses in the diffusing section behind the compressor requires that a considerable part of this deceleration be absorbed in the compressor. Inasmuch as

$$\frac{V_2'}{V_1'} = \frac{V_{z,2}}{V_{z,1}} \frac{\cos \beta_1'}{\cos \beta_2'} = \left(\frac{V_{z,2}}{V_{z,1}} \right) \times \text{a number less than 1.0}$$

the ratio V_2'/V_1' must be appreciably less than 1.0 in the majority of the blade rows. The enthalpy rise per stage is thus restricted, and the number of stages is greater than that required if $V_{z,2}/V_{z,1}$ could be greater.

Continuously decreasing the axial velocity through the compressor also causes V_1' to be continuously reduced. The enthalpy rise per stage is consequently much less in the latter stages of the compressor than it is in the early ones. Obtaining a reasonable enthalpy rise in the latter stages thus requires the use of fairly high blade speeds, even if the inlet flow capacity of the compressor is prejudiced. Moreover, the casing diameter at the rear stages is usually kept large to obtain these high blade speeds. Continuity requirements then dictate the use of small blade heights to the detriment of efficiency.

The number of compressor stages and the compressor layout shown in figure 21 were determined by these principles. As a result of this particular layout, an awkward flow passage is required to connect the compressor to the combustor. Moreover, the bulk and weight of the compressor are large.

The length of each stage is decided by the axial clearance required and the chord length of the blades themselves. The spacing is usually set by mechanical tolerances and the location of the thrust bearing. The chord length of the blades is frequently determined by arbitrarily limiting the bending stress at the blade root. The bending moment normally used to

calculate the stress is that caused by the steady aerodynamic forces on the blade. Because of the dangers of blade vibration, however, a large factor of safety is used, and the calculated steady-state bending force is well below the value that the blade can withstand. The blade chords, and hence the engine length, are thus greater than required by aerodynamics for steady-state stresses. (At high altitudes, however, large blade chords may be required to avoid poor performance at low Reynolds numbers. More information is required on this subject before definite statements can be made.)

Because of the large diameter and high internal pressure at the outlet, the casing is heavy. For the type of mechanical design shown in figure 21, a considerable amount of weight is also associated with the rear disk, which has a large diameter. If the metal in this solid disk had to resist only the stresses created by centrifugal force, the thickness could be considerably less than that actually used. Its weight would then be relatively small. It must, however, be stiff enough to be manufactured readily and handled without danger of warping. The disk must also be stiff enough to withstand the axial force resulting from the pressures acting on the disk face. These forces increase with the diameter of the disk and with compressor pressure ratio.

For a given Mach number limit, increasing the design weight flow through the compressor by reducing the design rotative speed reduces the diameter of the compressor and hence reduces the weight of an individual disk and a unit length of casing. On the other hand, the number of stages is increased. More disks and a longer casing length are needed. It would appear that, for a given limitation between flow capacity and speed, there are optimum values of these quantities that yield the minimum compressor weight. As previously noted, the same reasoning applies to the turbine.

The size and length of the other engine components are fairly independent of the actual design of the compressor after the pressure ratio and flow capacity are given. An exception to this statement might be the diffuser between the compressor and combustor, but this element should be considered to be part of the compressor itself.

Since the Mach number relative to the compressor blades has an important bearing on the flow capacity of the compressor and the number of stages required, the highest permissible Mach number level should be used in design. This statement is particularly true of the inlet stages, where the Mach numbers naturally tend to be the highest. Important improvements of these stages have been made in recent years (see refs. 11 and 12). As a result, higher air-flow capacity can be combined with high stage pressure ratios.

Identifying the true loading limit of a blade has also been given attention. The coarser the definition of the loading limit, the greater

is the aerodynamic factor of safety that must be employed. The design pressure ratio of a stage thus suffers. While reference 10 and equation (29) are definite advancements in this direction, there is still considerable room for improvement.

Although the number of stages is reduced through the use of high Mach numbers and accurately defined loading limits, the over-all length tends to remain the same if the bending-stress limits are unaltered. The higher pressure ratios result partially from larger blade forces, which in turn cause larger bending moments at the blade roots. With a fixed allowable bending-stress limit, the chord length of the blades increases as the stage pressure ratio increases. Recent observations have shown, however, that blade vibrations are primarily the result of rotating stall (ref. 13). Blade wakes and the pressure fields of fixed obstacles may have contributory effects, but these sources can be avoided or otherwise treated by appropriate design. These investigations have also shown that vibration induced by rotating stall can be eliminated or mitigated by such methods as interstage bleed and variable stators. As indicated in reference 14, ramps at the inlet are also useful for evading the blade-vibration problem. Through the use of this type of equipment, the hazards of blade vibration are relieved. The permissible bending stresses can be raised, and marked reductions in chord length are possible. Reducing the chord length and the number of stages reduces compressor length and offers significant reductions in compressor weight.

The necessity of adding stages to a compressor just to reduce the axial velocity is a problem that needs more attention. It is possible that too great a penalty is being paid for the lack of complete information about the pressure loss in diffusers and combustion chambers.

As indicated in reference 15, a basic combustor parameter governing pressure loss may be the velocity in the secondary-air passage. An important variable governing the efficiency of a diffuser is the ratio of the maximum surface velocity before deceleration to the minimum surface velocity after deceleration. If the minimum velocity were that in the secondary-air passage of the combustor and the ratio of maximum to minimum surface velocity were given, the velocity entering the diffuser could not be greater than the product of the allowable secondary-air velocity and the allowable velocity ratio. If the diffuser passage causes local velocity maximums and minimums, however, the inlet velocity must be less than the otherwise allowable value. Potential-flow methods, such as those proposed in reference 15, afford a means of eliminating unnecessary maximums and minimums in the surface velocities.

Figure 22, which is taken from reference 15, illustrates a diffuser designed along these lines. An insert controls the flow area in the passage between the compressor outlet and the secondary-air passage of the combustor. The rate of change of this area has the major effect in

controlling the rate of diffusion. Gentle curvatures are used to minimize the undesirable gradients due to curvature. Deceleration of the primary air is efficiently obtained by the stagnation of the air ahead of the insert. Such a device should permit higher velocities at the compressor outlet and should tend to shorten the diffuser length. These higher velocities could be used to enable the rear compressor stages to develop greater pressure ratios. On the other hand, the diameter of the casing (and hence blade speed) could be reduced between the inlet and outlet of the compressor without increasing the number of stages over those presently required. In the latter case, a lighter casing may result and the diameter and weight of the disks are reduced. The pressure forces on the disks are also reduced, and the disks may be thinner. Because of the greater radial length of the blades in the rear stages, higher efficiencies may be obtained.

A schematic drawing of a compressor in which the compressor design incorporates the ideas suggested is shown in figure 23. The pressure ratio and weight flow are the same as for figure 21. Higher rotative speeds and flow capacities result from raising the permissible blade Mach number. For this layout, the turbine stresses were higher than those normally used, but it was assumed that turbine cooling could be used to obtain the necessary strength in the turbine blades. The diameter of the compressor and the number of compressor stages are reduced. Interstage bleed and a ramp are assumed to eliminate the vibrations caused by rotating stall, and small blade chords are used. The controlled diffusion without reacceleration in the diffuser permits comparatively high velocities at the compressor discharge. These high velocities, together with the high rotative speed, permit the casing diameter to be reduced as shown without any untoward effects on length.

This arrangement is in no sense a recommended one. It merely serves to indicate how several critical aerodynamic factors can greatly influence the shape and weight of a compressor and the weight of the associated engine. The optimum arrangement depends, of course, on the mechanical design and the materials used. Although these factors are not given any other consideration in this series of reports, advances in the field of mechanical design and materials are as important as advances in the aerodynamic field. For example, obtaining the required disk stiffness with lightweight disks is an important mechanical problem. Improving the strength-weight ratio of materials is obviously another.

COMPRESSOR REQUIREMENTS

Design Point

The preceding discussions have indicated many of the over-all design-point requirements of compressors. High efficiency is shown to be

important for several reasons. The thrust and efficiency of the engine increase with compressor efficiency, particularly with high compressor pressure ratios or low ratios of turbine-inlet to compressor-inlet temperature. The diameters of the components downstream of the compressor decrease as compressor efficiency increases. Moreover, the number of compressor and turbine stages required for a given compressor pressure ratio decreases as compressor efficiency increases.

High air-flow capacity is also an important compressor attribute. When the maximum frontal area of the engine is controlled by compressor diameter, high flow capacity is required to reduce nacelle drag. High flow capacity is also a factor in minimizing specific engine weight.

One of the most important requirements of compressors concerns engine weight. The weight of the compressor itself must be small, and its design must not prejudice the weight of the other components. For those flight conditions which are critical to specific engine weight, this requirement is obvious; it is also an important factor when high engine efficiency appears to be the critical item. High engine efficiency is invariably associated with high compressor pressure ratio, particularly for subsonic flight. The full benefits of this high pressure ratio cannot be realized, however, when the increase in engine weight is out of proportion to the increase in engine efficiency.

Obtaining relatively lightweight engines and compressors requires each element to be operated near the limit of its aerodynamic and structural capacity. The dead weight carried must be a minimum. The compressor blades must tolerate large relative Mach numbers so that high flow capacity and high relative speeds can be realized. Provisions must be made for eliminating the sources of blade vibrations so that the thickness and chord length of the blades can be small. The diffuser at the compressor outlet must permit high entering velocities in order to obtain the maximum output from the rear stages of the compressor.

Another important factor in compressor design concerns the mating of flow passages. Aerodynamically clean passages are required for transitions between the inlet diffuser and the compressor inlet, and between the compressor discharge and the combustor. Abrupt increases in the flow area or in the curvature of the passages invite undesirable losses. These losses may immediately result from separation of the flow. The losses, on the other hand, may appear in the downstream components as the result of the thick boundary layers (or distortions) developed in the transition passages. Notice that, by the same token, thick boundary layers from any source entering or leaving the compressor are objectionable because they represent potential sources of loss.

These general requirements are necessary ingredients for efficient lightweight designs. The best design within the limits of these

quantities results from a cut-and-try procedure in which a number of tentative, equivalent aerodynamic designs are made and their estimated weights compared.

Off-Design Considerations

The preceding general comments apply to any operating condition, but they are particularly directed at the design point of the engine and its compressor. The design point refers to a particular flight condition and engine operating condition where the engine components and subcomponents are deliberately matched to achieve certain desired engine characteristics. Besides meeting its obligations at this point, however, the compressor must be able to provide suitable performance at other operating conditions imposed upon it. It must permit the engine to be started readily and accelerated rapidly to its design speed. It must also provide satisfactory performance over a range of engine speeds, pressure ratios, and weight flows when varying flight conditions require them.

The exact nature of these off-design requirements depends on the type of engine and on the design of the components themselves. The general off-design problems are very similar for all engines, however, and the general requirements of the associated compressor can be obtained from the study of the problems of a typical one-spool turbojet engine. The particular problems of other engine types, such as the two-spool turbojet engine and the turboprop engine, are then indicated.

The study of the off-design conditions requires an investigation of the matching of the compressor to the other engine components. The techniques for this investigation are discussed in chapter XVII (ref. 16), and the following results were obtained through the use of these procedures.

One-Spool Turbojet Engine

The off-design requirements of a compressor are conveniently shown on the compressor performance map in figure 24(a). In the usual representation, compressor pressure ratio is plotted against its equivalent weight flow $w\sqrt{\theta}/\delta$. Lines of constant equivalent speed $N/\sqrt{\theta}$ and constant efficiency are parameters. The stall-limit (or surge) line represents the highest pressure ratio attainable at a given equivalent weight flow. The break in this line represents the region where the stall-limit line is not well defined because of multivalued characteristics of the compressors (ch. XIII (ref. 16)). The shaded area of the map represents a region where one or more of the individual blade rows are stalled; here rotating stall and the attendant dangers of blade vibration may be prevalent (ch. XI (ref. 16)).

In the ensuing discussions of off-design performance, the pressure ratio, equivalent speed, and equivalent weight flow are expressed as percentages of their design-point values. Thus, point A of figure 24(a), where the pressure ratio, equivalent speed, and equivalent weight flow are denoted by 100 percent, represents the design point of this particular compressor.

For any operating condition of the engine, the corresponding point on the compressor performance map is given when any two of the following variables are stipulated: the equivalent compressor weight flow, the equivalent compressor speed, and the ratio of turbine-inlet to compressor-inlet temperature. Frequently one of these variables is known directly and the others are functions of the flight Mach number, the recovery of the inlet diffuser, the amount of afterburning, and the jet-nozzle area.

Engine acceleration. - With a fixed jet-nozzle area, the compressor equilibrium operating points may lie along the line BC of figure 24(a) for sea-level static conditions. The principal off-design problems here pertain to blade vibrations and engine acceleration in the low-equivalent-speed regions. Blade vibrations may occur anywhere in the shaded region; and, for the time being at least, this danger appears to be inevitable unless some variable feature is incorporated into the compressor design. Such devices as outlet or interstage bleed, variable inlet guide vanes and stators, or ramps have been used, or suggested, to circumvent the vibration problem.

For the purpose of discussion, the problem of engine acceleration may be conveniently measured by the difference between the pressure ratio of the stall-limit line and that of the equilibrium operating line at a given equivalent weight flow. This difference is called the stall margin. When the stall margin is large, the turbine-inlet temperature, and hence the torque of the turbine, can be appreciably increased without encountering the stall limit. Rapid accelerations are then possible. When the stall margin is small, the acceleration rate is also small unless such devices as an adjustable jet nozzle, interstage bleed (refs. 17 and 18), or variable inlet guide vanes and stators are used. When the operating line intersects the stall-limit line (fig. 24(b)), the stall margin is negative, and such devices are necessary if design-speed operation is to be reached. An alternative to using these variable features is to relocate the design point to A' of figure 24(b). This procedure is equivalent to making the compressor too big and too heavy for the pressure ratio it is required to produce (in particular, the rear stages are too lightly loaded); it is thus an undesirable remedy.

The reason that some compressors have good and others poor stall margins is not completely understood. Irrational design practices have contributed to the problem. Otherwise, the available stall margin usually becomes less as the design pressure ratio increases. Compromising

the design so that the best compressor performance is sought at, say, 90-percent speed (lower design pressure ratio) has been suggested to help the low-speed stall margin. The benefits obtained by this procedure are usually small, however, and this type of design tends to put the compressor in jeopardy at higher speeds. Since some devices are desired anyway to deal with blade vibrations, it is reasonable to extend their use to increase the stall margin and not compromise the design of the compressor too much to combat the acceleration problem.

Varying flight speeds. - As previously indicated, the compressor operating point is a function of a number of variables. The general trend of operation over a range of flight speeds, however, may be indicated by line BC of figure 24(c). Along this line, the mechanical speed of the engine is constant. Point C thus corresponds to small values of θ_1 (low inlet temperatures resulting from low flight Mach numbers in the stratosphere). On the other hand, point B corresponds to large values of θ_1 (high flight Mach numbers). Specifically, values of $(N/\sqrt{\theta_1})/(N/\sqrt{\theta_1})_d$ of 0.7, 0.8, 0.9, 1.0, 1.1, and 1.13 correspond, respectively, to flight Mach numbers of 2.93, 2.30, 1.79, 1.28, 0.71, and 0.45 in the stratosphere for constant mechanical speed.

At flight Mach numbers below 1.28 in the stratosphere, the equivalent speed of the compressor is above its design value. The Mach number of the flow relative to the blades near the compressor inlet is higher than that assumed in design. Moreover, the matching of the compressor stages is upset. These effects combine to reduce the efficiency of the compressor and to reduce the slope of the stall-limit line at the higher equivalent speeds. Besides reducing the efficiency of the engine, this drop in compressor efficiency moves the equilibrium operating line upwards. If the design of the compressor is compromised too much to favor low-speed engine acceleration, the compressor efficiency and slope of the stall-limit line may both drop so rapidly that the operating line intersects the stall line at a slight overspeed (fig. 24(d)). In this event, the rotative speed of the engine may have to be reduced so that the operation is at point D. Instead, the area of the jet nozzle may be increased in order to move the operating point to E. Either procedure causes the performance to decrease, and the latter procedure is ineffective when the turbine is at or beyond the point of limiting loading.

Avoiding these efficiency and stall-limit difficulties requires that considerable attention be given to the high-equivalent-speed operating condition during design. Either the design should be made for the assumed overspeed condition, or the design should be reviewed at this condition. Some approximate methods of making this review are presented in chapter X (ref. 9).

With high flight Mach numbers (above 1.28), the equivalent speed of the compressor is lower than its design value. If the flight Mach number is high enough, the compressor efficiency and stall-limit problems plaguing low-equivalent-speed operation reappear. Again, such devices as interstage bleed and variable inlet guide vanes and stators might be helpful, since they actually improve compressor performance in this regime. Variable inlet guide vanes and stators, however, frequently tend to reduce compressor weight flow at the high Mach numbers, to the detriment of thrust. Interstage bleed, however, might be useful if the problems of handling the bleed air in flight are not too complicated.

An alternative, however, is to increase the rotative speed of the engine, at least to some extent, as the flight Mach number increases. If the compressor is normally required to operate at 70 percent of its design speed, increasing the mechanical speed 14 percent moves the operating point almost to the 80-percent-speed line. If the area of the jet nozzle is increased so that the turbine-inlet temperature is constant, the operating point shifts from B to B' in figure 24(e). Not only is the operating point removed from the stall-limit line, but the compressor handles more weight flow and the engine develops more thrust.

Because of the higher flow rate, the flow capacity of the turbine must be higher for this kind of operation. The higher required flow capacity increases the stresses in the turbine for a given rotative speed (fig. 19). For a given turbine stress limit, therefore, the speed at the compressor design point is lower than it would otherwise be. One or more additional compressor stages may be required to get the original design-point pressure ratios if such is deemed to be necessary. The specific weight of the engine at the original design point is then increased. Whether or not the greater thrust at the high Mach numbers more than compensates for the increase in engine weight depends on the actual design and flight plan. The potential benefits from this kind of operation, however, make it worthy of detailed consideration in the initial design studies.

There may be good reasons, however, for actually reducing the pressure ratio required at design speed for this type of engine. Not only is the number of stages reduced, but the internal pressure forces are lowered and the specific thrust is increased. A lighter engine is then obtained. In this case, the reduced engine speed at the low flight Mach numbers offers a saving in engine weight at the expense of engine efficiency for this flight condition. At the high flight Mach numbers, however, the higher thrust and lighter weight combine to offer significant increases in altitude and flight speed.

Reynolds number effects. - At high flight altitudes and low flight speeds, the Reynolds number of the flow through the inlet stages of a compressor becomes so low that their performance is often impaired. Two-dimensional-cascade data (ch. VI (ref. 9)) indicate that this is a universal trend. The performance of such a cascade invariably deteriorates

when the Reynolds number, based on blade chord, decreases below about 100,000. This behavior is attributed to laminar separation (ch. V). Some concurring evidence is also provided by investigations of multi-stage compressors, either by bench tests or as part of an engine.

In spite of these over-all performance data, the actual effect of Reynolds number on compressor performance is not completely known. The results of the two-dimensional-cascade data are not directly valid, because the behavior of their boundary layers is believed to be different from that of a blade row (ch. XV (ref. 16)). Over the greater part of a blade row the boundary layer may be expelled by centrifugal forces before it separates. Moreover, a much higher level of turbulence is expected in a compressor, which tends to alter the influence of Reynolds number (ch. V). What are the significant characteristic lengths and velocities remain unanswered questions.

Compressor bench tests at low Reynolds numbers have not been completely conclusive, because the results are frequently contaminated by uncontrolled leakage of air from the atmosphere to the low-pressure regions in the compressor, and by heat transfer. The difficulty of obtaining accurate data at low pressures and small pressure differences adds to the confusion. These difficulties are also encountered in engine tests. Moreover, the latter results naturally include the effect of Reynolds number on the other engine components, as well as the effects of changes in the matching of the components.

In order to meet the Reynolds number problem it may be necessary to use one engine, with a big compressor, instead of two. Increasing only the chord lengths of the early stages has been advocated, but there is no guarantee that this remedy will do anything but add weight to the engine. As an alternative, a lower level of performance in the early stages may be anticipated and the matching of the rest of the stages modified accordingly. This procedure would prevent a small decrease in performance of the early stages from being amplified in the rest of the compressor. There is an urgent need for reliable and applicable data in the near future.

Inlet flow distortions. - Uniform flow at the inlet is the usual assumption in compressor design, and extreme precautions are taken to assure uniform flow at the inlet during bench tests of a compressor. Severe inlet flow distortions, however, are encountered in flight. These distortions may result from many sources. They may occur when the airplane is flying at a high angle of attack. They may result from disturbances created by the engine inlet. Distortions may also result from disturbances created by other parts of the airplane or armament fire in the vicinity of the inlet. At high supersonic speeds, current inlets invariably create disturbances resulting from nonuniform shock waves and from shock and boundary-layer interactions. Sharp curvatures in the inlet ducting also contribute to these distortions.

When distortions are present, the performance of the compressor usually deteriorates. As shown in figure 24(f), the stall-limit line drops (dashed line), and the shaded region (rotating stall) moves to the right. Design speed, overspeed, and underspeed performance suffer. In order to avoid compressor-stall difficulties, the operating line must be dropped.

Because of the penalties incurred by inlet flow distortion, a large amount of effort is being devoted to eliminating them. The eventual result of this work is unknown. At the higher equivalent speeds (low flight Mach numbers) the compressor must be designed to produce a greater pressure ratio than that available when distortions are present. The engine is either heavier than it otherwise needs to be, or else the efficiency is low. At the lower equivalent speeds (high flight Mach numbers) the compressor-stall and blade-vibration difficulties may be so severe that constant-mechanical-speed operation is impossible. Increasing the mechanical speed of the engine with flight Mach number, as discussed in connection with figure 24(e), alleviates this problem.

Inlet matching problem. - The characteristics of the inlet over the intended range of flight Mach numbers must be recognized in designing the compressor and selecting the type of engine operation. The matching problem, discussed in reference 19, is briefly reviewed here. At a given supersonic flight Mach number, an ideal matching of the engine and inlet is achieved when a flow pattern similar to that shown in figure 25(a) is produced. The flow ahead of the minimum inlet area is decelerated by one or more oblique shocks. It then passes through the minimum area with reduced supersonic velocities. A normal shock just behind the minimum area causes the Mach numbers to be reduced to high subsonic values. Thereafter, the flow is gradually decelerated to the velocity required by the compressor. This is the flow situation that occurs at critical inlet operation. (Notice that a compressor designed for high axial Mach numbers requires little subsonic diffusion in the inlet.)

If it so happened that the value of $w_1 \sqrt{\theta_1} / \delta_1$ ideally delivered to the compressor with this flow pattern is lower than that required by the compressor, the value of δ_1 must decrease. (The weight flow itself cannot increase, and θ_1 is determined only by the flight Mach number and altitude.) What happens physically is that the normal shock moves downstream as shown in figure 25(b). The Mach number ahead of the shock is thus increased, and the pressure loss through the shock is increased. The shock automatically positions itself so that the loss in pressure through it is exactly that required to make $w_1 \sqrt{\theta_1} / \delta_1$ conform with that required by the compressor. The inlet operation is then supercritical. The thrust and engine efficiency are reduced, and the flow ahead of the compressor becomes disturbed.

On the other hand, if the ideally delivered value of $w_1 \sqrt{\theta_1} / \delta_1$ is too great for the compressor, the value of w_1 must decrease. Either the Mach number immediately ahead of the minimum area, or the total pressure of the flow ahead of the minimum area, or both, must decrease. In this case, the shocks ahead of the minimum area deflect part of the flow around the inlet (fig. 25(c)). The operation of the inlet is then subcritical. The shocks also decelerate the inlet flow, usually with comparatively high recoveries. The over-all recovery of the diffuser is consequently not impaired too drastically. The deflection of the flow, however, does cause an additional drag (ref. 1), which can appreciably reduce airplane performance. This flow condition is also frequently accompanied by an unsteady-flow phenomenon known as "buzz."

Over a range of flight Mach numbers, the inlet flow capacity of a fixed-geometry inlet follows the trend shown in figure 26. The equivalent weight flows are those for critical operation. With a fixed mechanical speed of the engine, the equivalent weight flow demanded by the compressor is also shown. To the left of the intersection of these curves, the inlet wants to supply less air than the compressor requires. It is thus forced to operate supercritically with the attendant loss in total-pressure recovery. To the right of the intersection, the inlet wants to supply more air than the compressor can use. It then operates subcritically with the attendant increase in nacelle drag.

The unhappy alternatives of accepting either large pressure losses or large drags at off-design condition has stimulated research on variable-geometry inlets and on methods of bleeding air from a point between the minimum area of the inlet and the face of the compressor. While considerable improvements in inlet and engine performance have been demonstrated, much work remains to be done to obtain an inlet that is both mechanically and aerodynamically desirable.

In some instances, the severity of this problem can be reduced by modifications in compressor design and engine operation. In theory, the engine curve of figure 26 can be made to coincide with any desired inlet curve by appropriately adjusting compressor equivalent speed with the flight Mach number. Essentially constant equivalent speed is required over the flight Mach number range where the inlet curve is flat. Beyond the break in the curve, the equivalent speed would decrease with Mach number. The change in equivalent speed with Mach number depends on the characteristics of the inlet and compressor. (In this connection, it is noted that the rate of change in compressor air flow with speed appears to decrease as the inlet axial Mach number increases.) This type of engine operation is not inconsistent with that described in connection with figure 24(e).

The degree to which compressor design and engine operation can accommodate the inlet depends on the attendant changes in specific engine weights, engine efficiency, and engine frontal area that can be tolerated. Again, the decision must be based on the intended design and use of the airplane. The engine and airplane must be an integrated unit rather than separate entities.

Two-Spool Turbojet Engine

In the two-spool turbojet engine, the pressure ratio is developed in two separate and independently driven compressors. The upstream compressor is called the outer compressor; the downstream compressor, the inner compressor. Since the design pressure ratio of each compressor is less than that of the equivalent one-spool compressor, fewer difficulties might be expected with the slope and the discontinuities of the stall-limit line.

Because of the higher pressure of the air entering the inner-spool compressor, the value of $w\sqrt{\theta/\delta}$ there is less than that at the outer compressor; the diameter of the inner-spool compressor may thus be decreased. The higher air temperature permits the use of higher blade speeds for a given limit in the relative blade Mach number. Notice that the value of P/\sqrt{T} downstream of the inner turbine is higher than that for the other turbine. According to equation (24), the tip speed of the inner turbine, or compressor, can be increased if the other design factors are fixed. The higher compressor blade speeds thus are also consistent with the turbine blade stress limitations. With uncooled blades, the allowable stress limits are lower for the inner turbine because of the higher temperature; less marked increases in wheel speed are then offered. The smaller diameters and higher blade speeds of the inner spools in any event offer possible reductions in engine size and weight.

Because of the complicated interrelations between the two compressors, the two turbines, and the other engine components, the trends of the operating lines are not as readily exposed as they are for one-spool engines. The important trends are indicated, however, in references 20 to 22, and the following discussion and the associated figures are taken from these reports.

Representative performance maps and operating lines for the outer and inner compressors, respectively, are shown in figures 27(a) and (b). In this example, the ratio of the design pressure ratio of the outer compressor to that of the inner compressor is 0.75. The trends described, however, are fairly independent of this ratio. The operating line represents the conditions where the inner-turbine-inlet temperature is constant, the mechanical speed of the outer-spool compressor is constant (at its design value), and the flight Mach number is varying. At any

flight Mach number, therefore, the equivalent speed of the outer compressor and the engine temperature ratio (ratio of inner-turbine-inlet to outer-compressor-inlet temperature) are defined. These two variables are sufficient to completely define the operating point of each component of the over-all compressor-turbine unit, as for the one-spool engine. The points A, B, and C on the map, respectively, represent the conditions for sea-level takeoff and for flight Mach numbers of 0.9 and 2.8 in the stratosphere.

Outer compressor. - The performance map and operating line of the outer compressor are shown in figure 27(a). At low flight Mach numbers or high engine temperature ratios, a large stall margin appears. The operating line tends to move towards the stall-limit line at low engine speeds. For the example illustrated, the slope of the stall-limit line increases with the equivalent speed. With a more critical compressor design, however, this trend may be reversed. At the high flight Mach numbers or low engine temperature ratios, the operating line approaches the stall-limit line. This behavior is similar to that of one-spool compressors. The equilibrium operating line at sea-level static conditions describes a similar trend.

With the possible exception of the overspeed problems, the outer spool experiences the same sort of difficulties that a one-spool engine encounters under off-design conditions. This statement includes the difficulties associated with Reynolds number and inlet distortions. The possible remedies are also similar, except that bleeding air between the two compressors might be substituted for interstage bleed. These remedies could, however, result in a greater reduction in thrust for the two-spool engine than they do for a single-spool engine.

Inner compressor. - The operating line of the inner compressor differs from that of the outer compressor in two respects: The slope of the operating line is greater, and the change in equivalent speed for a given change in flight conditions is less. For equilibrium operation, the principal stall-limit problem arises at the high equivalent speeds of the inner spool (low flight Mach numbers or high engine temperature ratios). This problem responds to the same treatment indicated for the similar problem of the one-spool compressor, but, again, the thrust penalties may make the solution an undesirable one.

An important point to note is that higher-than-equilibrium engine temperature ratios momentarily move the operating point of the inner compressor towards the stall-limit line, even though the surge margin is increased when equilibrium is finally attained. This higher-than-equilibrium temperature is required for engine acceleration. Bleeding air between the two compressors to assist the outer spool may also narrow the stall margin of the inner spool. For transient conditions, therefore, the benign indications of the equilibrium operating line may be deceiving.

As the inner compressor is started from rest, its front stages are inevitably stalled. The attendant rotating stall may induce vibrations in the blades. Similarly, rotating stalls developed by the outer compressor may induce vibrations in the inner compressor. In addition, the rotating stalls originating in the outer compressor may impair the performance of the inner compressor and lower the stall-limit line. The published data are too meager to settle this point definitely, but the apparent wide stall margin of the inner compressor may disappear during engine acceleration as a result of the above-mentioned phenomena.

The inner compressor itself may not be subject to any Reynolds number problems, as both the density and the turbulence are relatively high. It can, however, amplify any deterioration in performance encountered by the outer compressor. The solution to this problem is again subject to speculation, but it should yield to the same treatments that may be found for the one-spool compressor.

Inlet distortions may affect the performance of the inner compressor because the inner compressor amplifies changes in the performance of the outer spool. A wide margin between the operating line and the stall-limit line is therefore desired. This requirement may be particularly needed at the high equivalent speeds where the stall margin is the smallest.

Turboprop Engine

In general, the design and off-design requirements of compressors for turboprop engines are similar to those of the turbojet engine. Since high compressor pressure ratios are desired for the turboprop engine, the stall margin and vibration problems at low speeds cannot be overlooked. Variable stator blades, interstage bleed, or some similar device may be absolutely necessary to obtain satisfactory engine acceleration at the low speeds and still use the pressure-ratio capacity of the compressor at high speeds.

At the design point, the efficiency of the engine should be the maximum obtainable for continuous operation. Practically speaking, this point then represents the maximum power that the engine can develop under continuous operation. Higher power can be obtained for brief periods by increasing the pressure ratio and speed of the compressor. When the compressor is coupled to the propeller, the compressor speed can be controlled independently by adjusting the pitch of the propeller blades. When the propeller is independently driven by its own turbine, the speed of the compressor depends on the turbine-inlet temperature and the power delivered to the propeller. The best location of the compressor operating point at the high-power condition depends on the characteristics of the propeller, the stress margin of the engine components, and the characteristics of the airplane. The stall margin required at design or higher speeds thus depends on individual studies of the engine and its intended service. As a

rule, however, the required margin is no greater than that required of subsonic jet-engine compressors (see ref. 23).

Except for starting and acceleration, operating the compressor below the design pressure ratio has been thought to be undesirable because of the incurred loss in engine efficiency. An exception to this principle has been made for takeoff and low-altitude flight. The pressures and power developed are so high that engine weight is decided by the low-altitude operating conditions. While high sea-level power is desired for rapid takeoff and climb, the sea-level output and compressor pressure ratio of a turboprop engine can be kept considerably below their maximum values without seriously hurting airplane performance. The resulting decrease in specific engine weight at altitude improves the altitude performance and range of the airplane. Although compressor speed is reduced at sea level for this type of operation, the reduction in most cases is small enough to avoid the stall and blade-vibration difficulties associated with low-speed operation.

Because of its high specific power, the air flow required by the engine is small. The diameter and blade chords of the compressor are also small. The compressor is therefore more susceptible to Reynolds number problems at high flight altitudes. As before, this problem can only be pointed out. Its definition and cure require much research.

CONCLUDING REMARKS AND SUMMARY OF COMPRESSOR DESIGN OBJECTIVES

The final specifications for a compressor gradually emerge from a detailed study of a number of engine and airplane layouts. The design-point pressure ratio, flow capacity, and rotative speed of the compressor represent a compromise that is established only after extensive preliminary studies have been made of various engine and airplane designs for a given mission or missions. These tentative values may be subsequently modified for selecting the best method of meeting the various off-design conditions encountered. The weight, complexity, and efficiency or drag penalties associated with the available techniques for varying the geometry or performance of components are involved in this decision.

Regardless of the final specifications, the compressor should produce the required pressure ratio with high efficiency. It should, moreover, be subjected to the highest aerodynamic loading and Mach number allowed by available knowledge.

The resulting design should not require extensive development. The performance estimates at the design and off-design points must therefore be reasonably accurate. Moreover, mechanical problems arising from aerodynamic sources, such as blade vibrations, must be anticipated and the design made so that these problems can be either overcome or successfully evaded. Finally, with respect to manufacturing, the component parts should be as few in number as possible, and their shape should be simple.

The material presented in the subsequent chapters is the result of research specifically aimed at realizing the objectives set forth in the previous paragraphs. Because of the importance of light and compact designs for aircraft, attention is paid to many problems that may not be so important in other fields of application. This point of view does not limit the usefulness of the information. Many successful designs, by present standards at least, have been made in a wide variety of commercial fields with this information.

REFERENCES

1. Sibulkin, Merwin: Theoretical and Experimental Investigation of Additive Drag. NACA Rep. 1187, 1954. (Supersedes NACA RM E51B13.)
2. Esenwein, Fred T., and Valerino, Alfred S.: Force and Pressure Characteristics for a Series of Nose Inlets at Mach Numbers from 1.59 to 1.99. I - Conical Spike All-External Compression Inlet with Subsonic Cowl Lip. NACA RM E50J26, 1951.
3. Pinkel, Benjamin, and Karp, Irving M.: A Thermodynamic Study of the Turbojet Engine. NACA Rep. 891, 1947. (Supersedes NACA WR E-241.)
4. Pinkel, Benjamin, and Karp, Irving M.: A Thermodynamic Study of the Turbine-Propeller Engine. NACA Rep. 1114, 1953. (Supersedes NACA TN 2653.)
5. English, Robert E., and Wachtl, William W.: Charts of Thermodynamic Properties of Air and Combustion Products from 300° to 3500° R. NACA TN 2071, 1950.
6. Hauser, Cavour H., and Plohr, Henry W.: Two-Dimensional Cascade Investigation of the Maximum Exit Tangential Velocity Component and Other Flow Conditions at the Exit of Several Turbine-Blade Designs at Supercritical Pressure Ratios. NACA RM E51F12, 1951.
7. Alpert, Sumner, and Litrenta, Rose M.: Construction and Use of Charts in Design Studies of Gas Turbines. NACA TN 2402, 1951.
8. Cavicchi, Richard H., and English, Robert E.: Analysis of Limitations Imposed on One-Spool Turbojet-Engine Designs by Compressors and Turbines at Flight Mach Numbers of 0, 2.0, and 2.8. NACA RM E54F21a, 1954.
9. Compressor and Turbine Research Division: Aerodynamic Design of Axial-Flow Compressors. Vol. II. NACA RM E56B03a, 1956.

10. Lieblein, Seymour, Schwenk, Francis C., and Broderick, Robert L.: Diffusion Factor for Estimating Losses and Limiting Blade Loadings in Axial-Flow-Compressor Blade Elements. NACA RM E53D01, 1953.
11. Lieblein, Seymour, Lewis, George W., Jr., and Sandercock, Donald M.: Experimental Investigation of an Axial-Flow Compressor Inlet Stage Operating at Transonic Relative Inlet Mach Numbers. I - Over-All Performance of Stage with Transonic Rotor and Subsonic Stators Up to Rotor Relative Inlet Mach Number of 1.1. NACA RM E52A24, 1952.
12. Klapproth, John F., Jacklitch, John J., Jr., and Tysl, Edward R.: Design and Performance of a 1400-Foot-Per-Second-Tip-Speed Supersonic Compressor Rotor. NACA RM E55A27, 1955.
13. Huppert, Merle C., Calvert, Howard F., and Meyer, André J.: Experimental Investigation of Rotating Stall and Blade Vibration in the Axial-Flow Compressor of a Turbojet Engine. NACA RM E54A08, 1954.
14. Lucas, James G., Finger, Harold B., and Filippi, Richard E.: Effect of Inlet-Annulus Area Blockage on Over-All Performance and Stall Characteristics of an Experimental 15-Stage Axial-Flow Compressor. NACA RM E53L28, 1954.
15. Stockman, Norbert O.: Application of Stream-Filament Techniques to Design of Diffuser between Compressor and Combustor in a Gas-Turbine Engine. NACA RM E55F06, 1955.
16. Compressor and Turbine Research Division: Aerodynamic Design of Axial-Flow Compressors. Vol. III. NACA RM E56B03b, 1956.
17. Rebeske, John J., Jr., and Rohlik, Harold E.: Acceleration of High-Pressure-Ratio Single-Spool Turbojet Engine As Determined from Component Performance Characteristics. I - Effect of Air Bleed at Compressor Outlet. NACA RM E53A09, 1953.
18. Rebeske, John J., Jr., and Dugan, James F., Jr.: Acceleration of High-Pressure-Ratio Single-Spool Turbojet Engine As Determined from Component Performance Characteristics. II - Effect of Compressor Interstage Air Bleed. NACA RM E53E06, 1953.
19. Wyatt, DeMarquis D.: An Analysis of Turbojet-Engine-Inlet Matching. NACA TN 3012, 1953.
20. Dugan, James F., Jr.: Two-Spool Matching Procedures and Equilibrium Characteristics of a Two-Spool Turbojet Engine. NACA RM E54F09, 1954.

21. Dugan, James F., Jr.: Effect of Design Over-All Compressor Pressure Ratio Division on Two-Spool Turbojet-Engine Performance and Geometry. NACA RM E54F24a, 1954.
22. Dugan, James F., Jr.: Component Operating Trends during Acceleration and Deceleration of Two Hypothetical Two-Spool Turbojet Engines. NACA RM E54L28, 1955.
23. Davison, Elmer H.: Compressor and Turbine Matching Considerations in Turboprop Engines. Preprint No. 695, SAE, 1956.

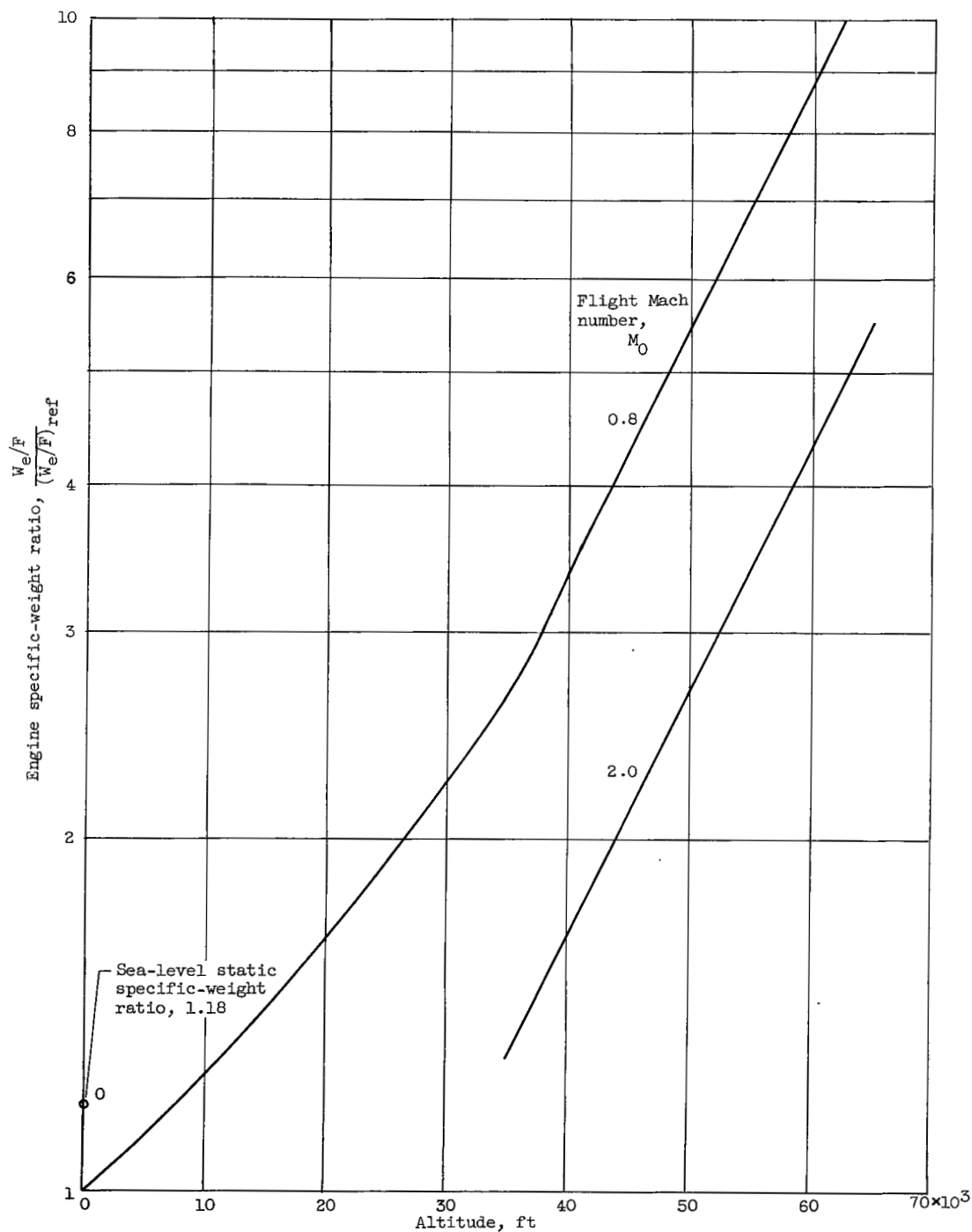


Figure 1. - Typical variation of turbojet-engine specific weight with altitude at constant engine mechanical speed. Reference condition: altitude, sea level; flight Mach number, 0.8.

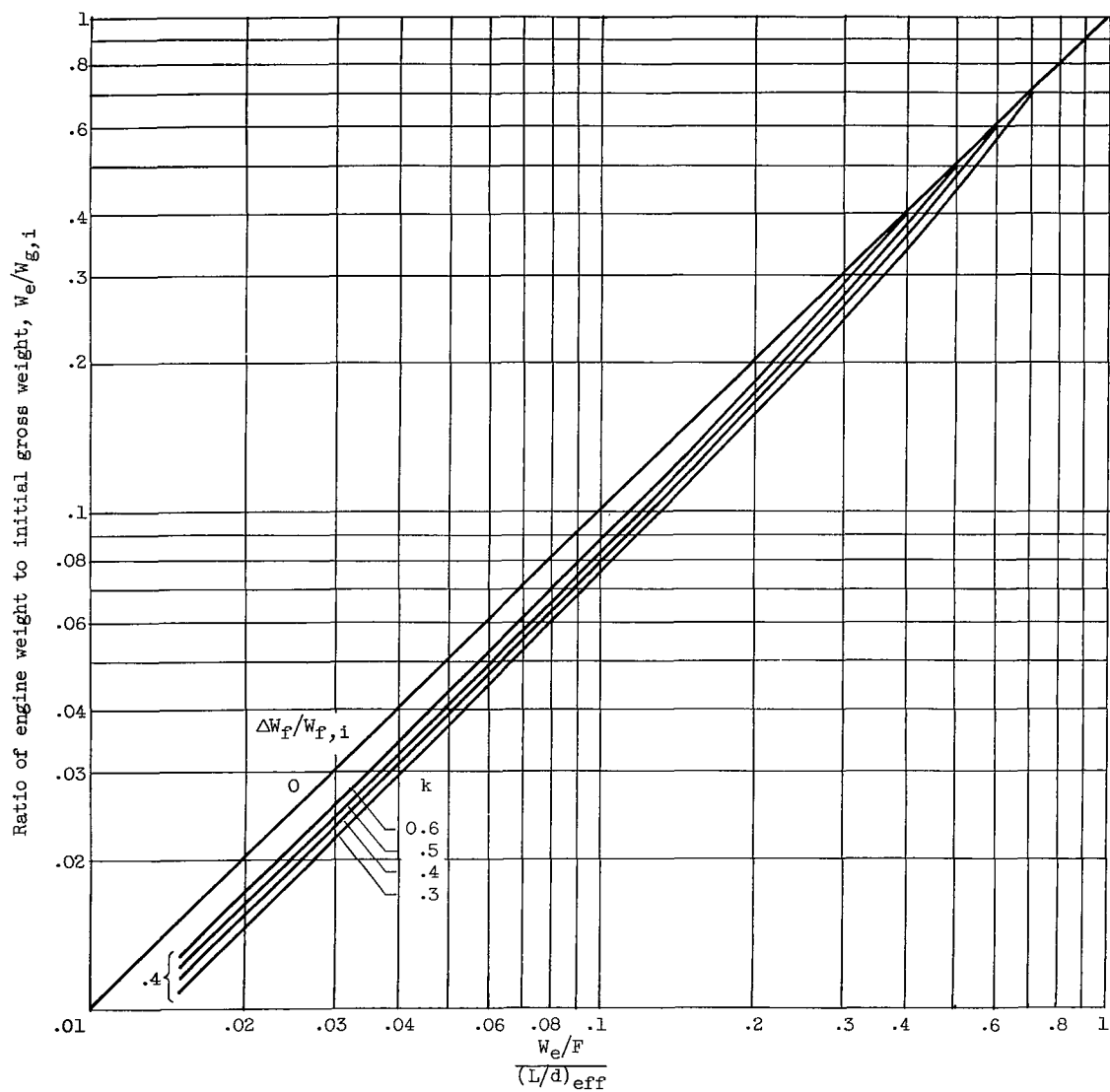


Figure 2. - Graphical representation of equation (4).

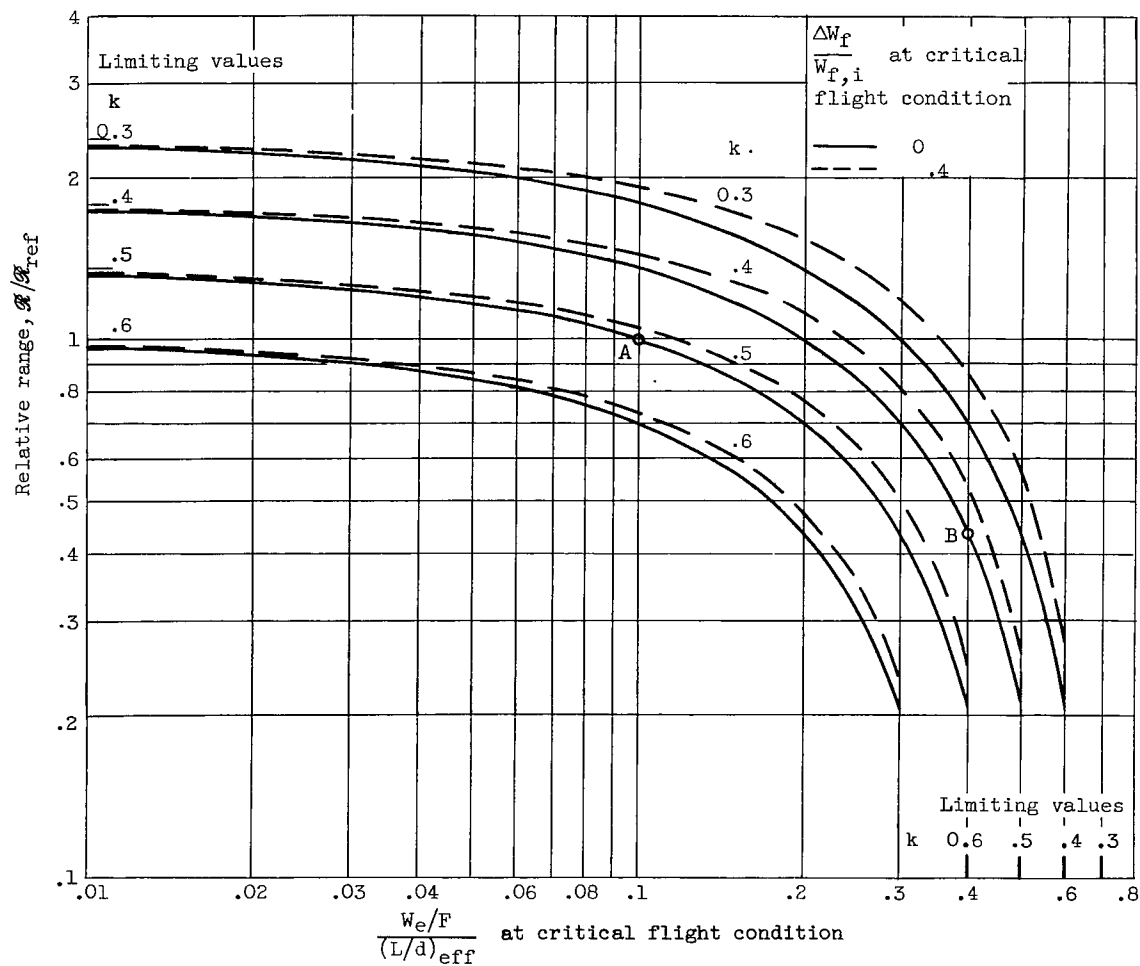
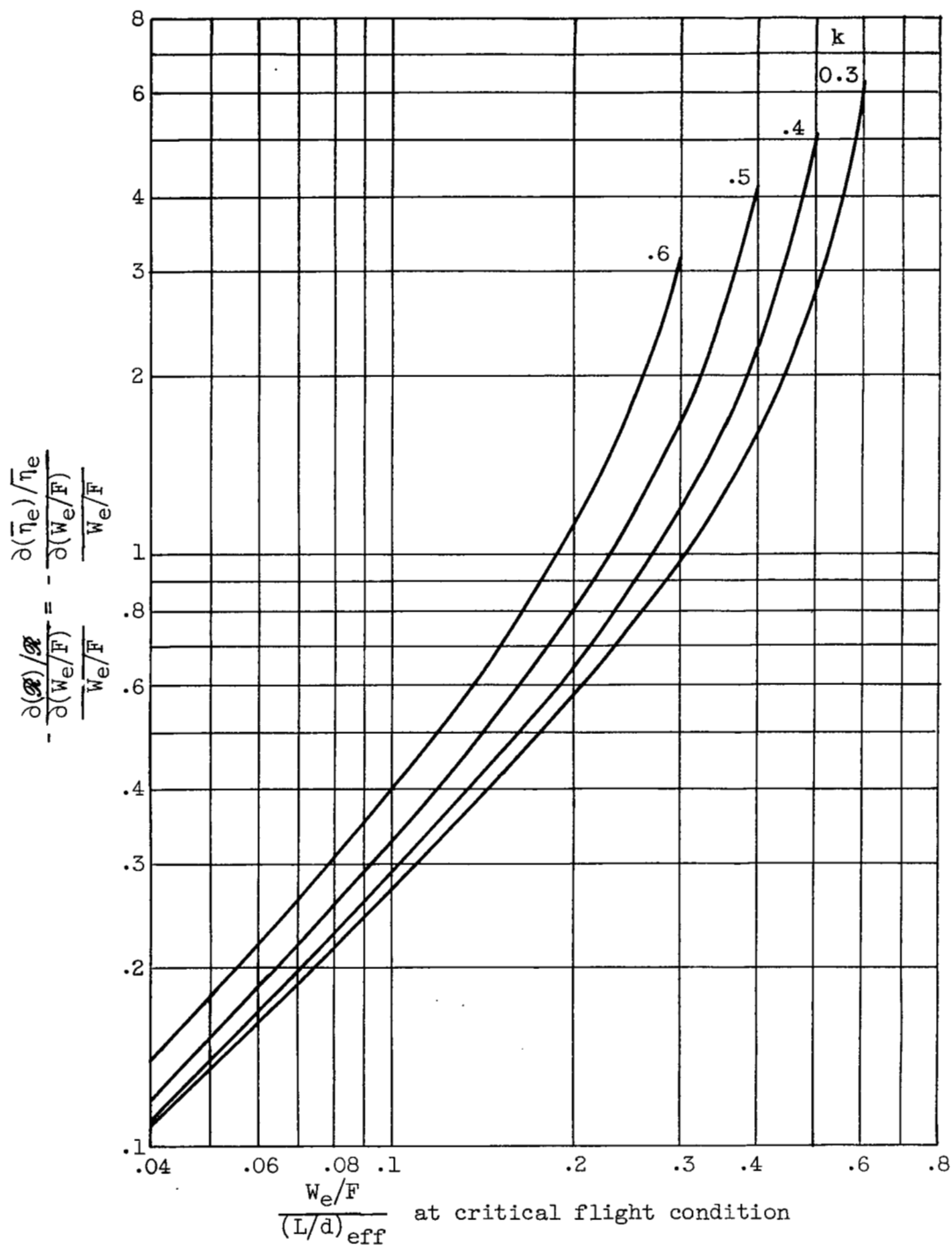
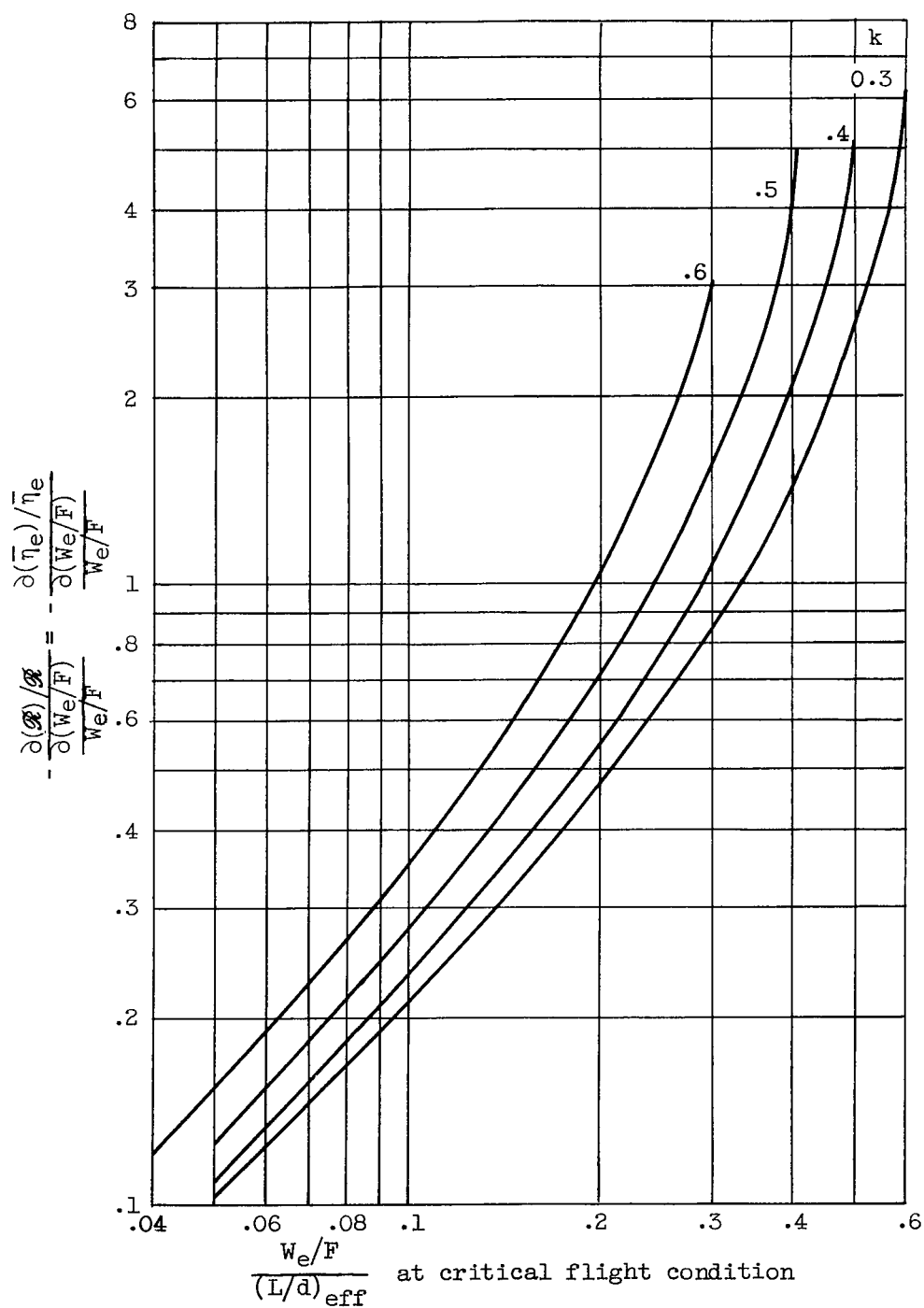


Figure 3. - Graphical representation of equation (6).



(a) $\Delta W_f/W_{f,i}$ at critical flight condition, 0.

Figure 4. - Graphical representation of equation (7b).



(b) $\Delta W_f/W_{f,i}$ at critical flight condition, 0.4.

Figure 4. - Concluded. Graphical representation of equation (7b).

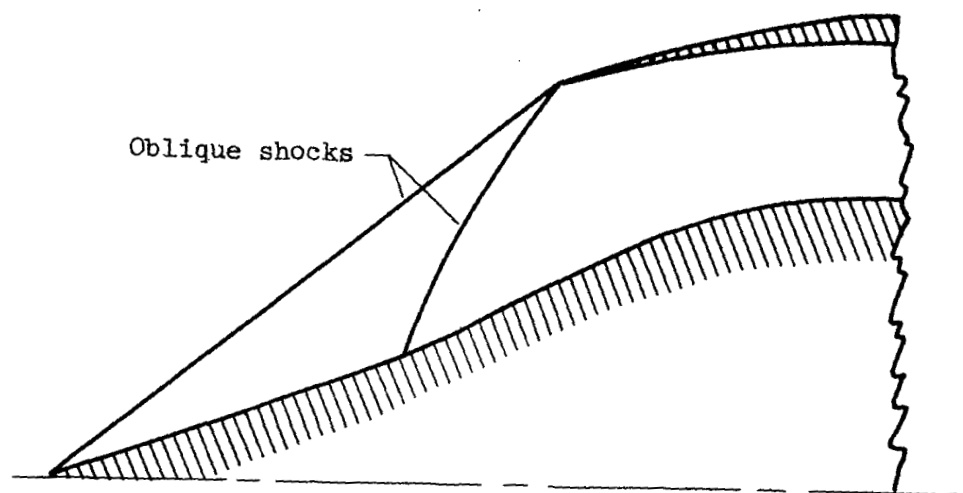
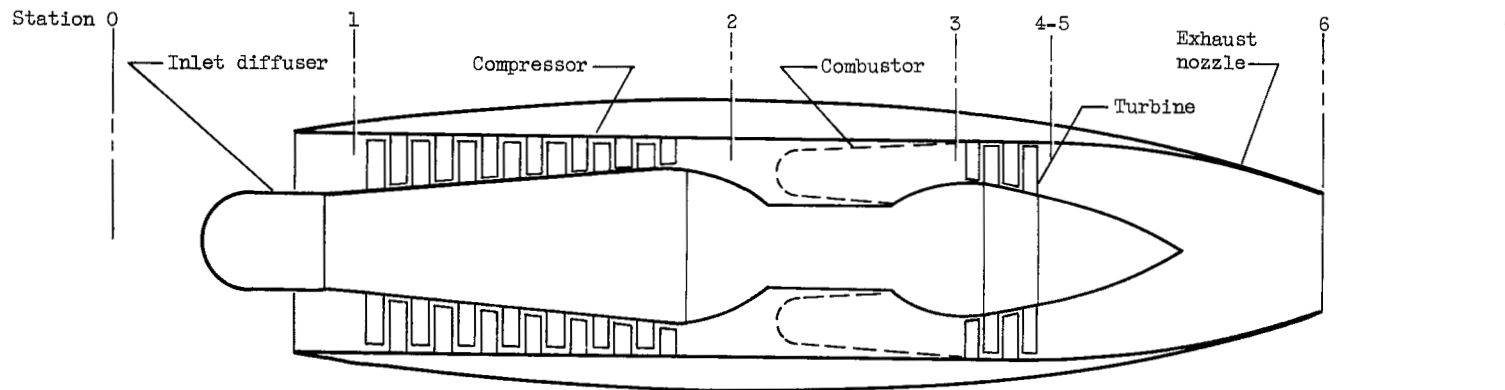
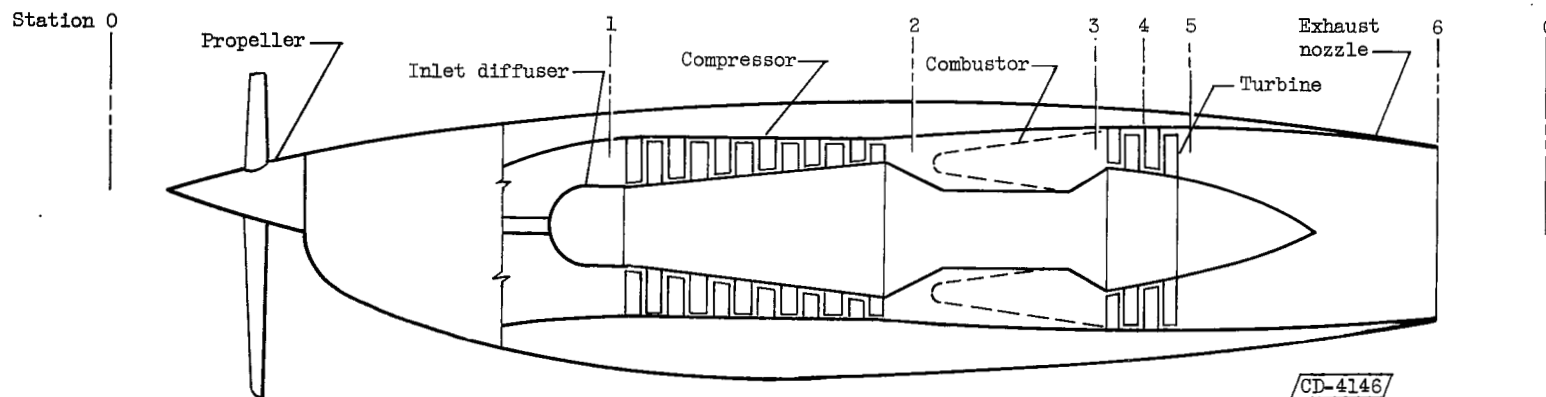


Figure 5. - A representative supersonic inlet.



(a) Turbojet engine.



(b) Turboprop engine.

Figure 6. - Sketches of turbojet- and turboprop-engine configurations showing stations used in analysis.

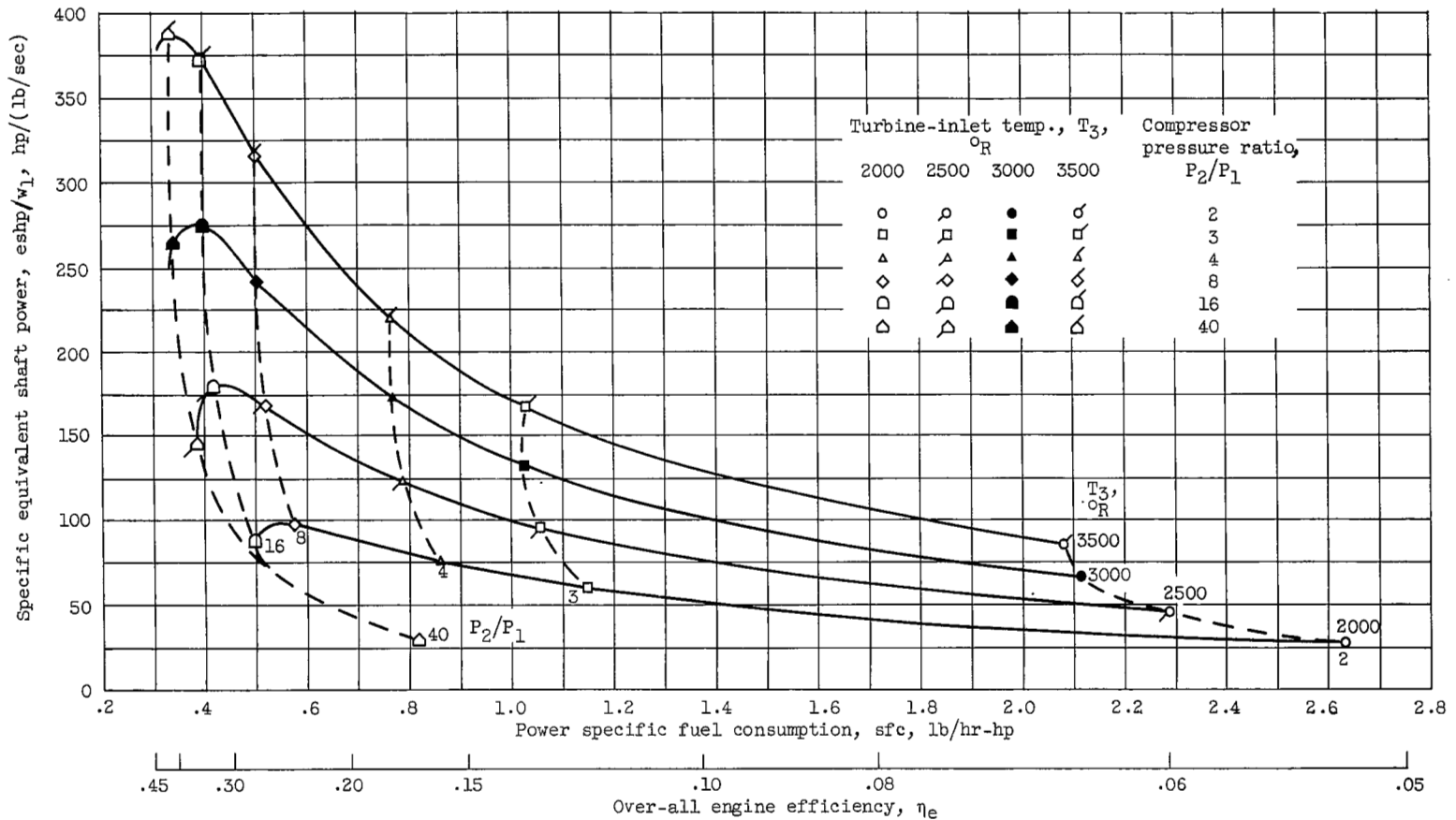
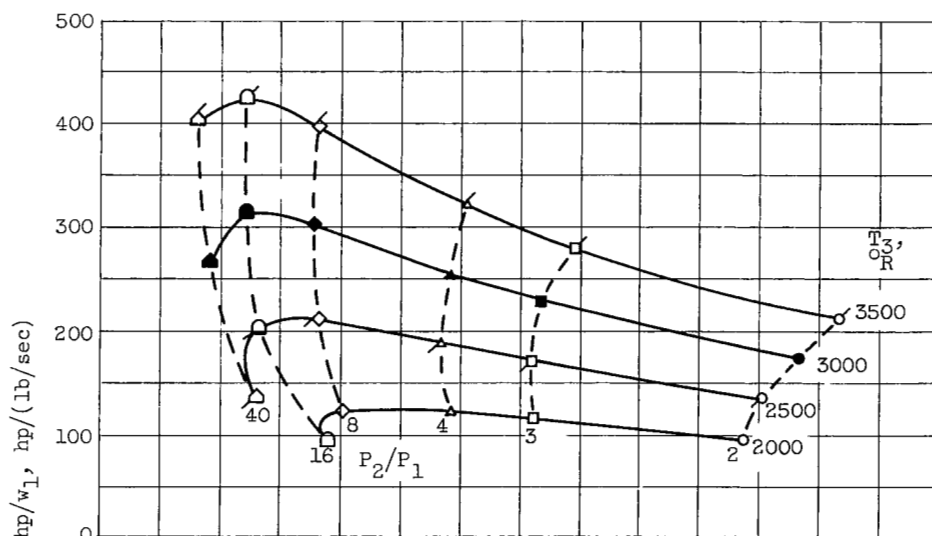
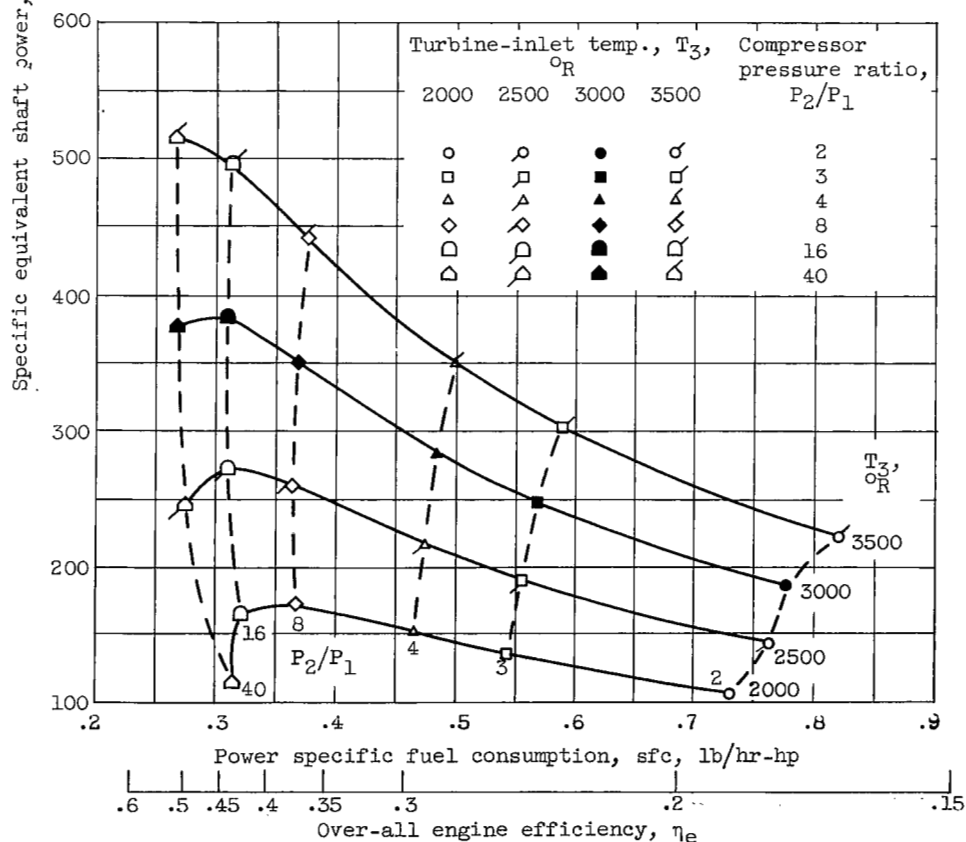


Figure 7. - Thermodynamic performance of turboprop engines (compressor pressure ratio as a parameter).

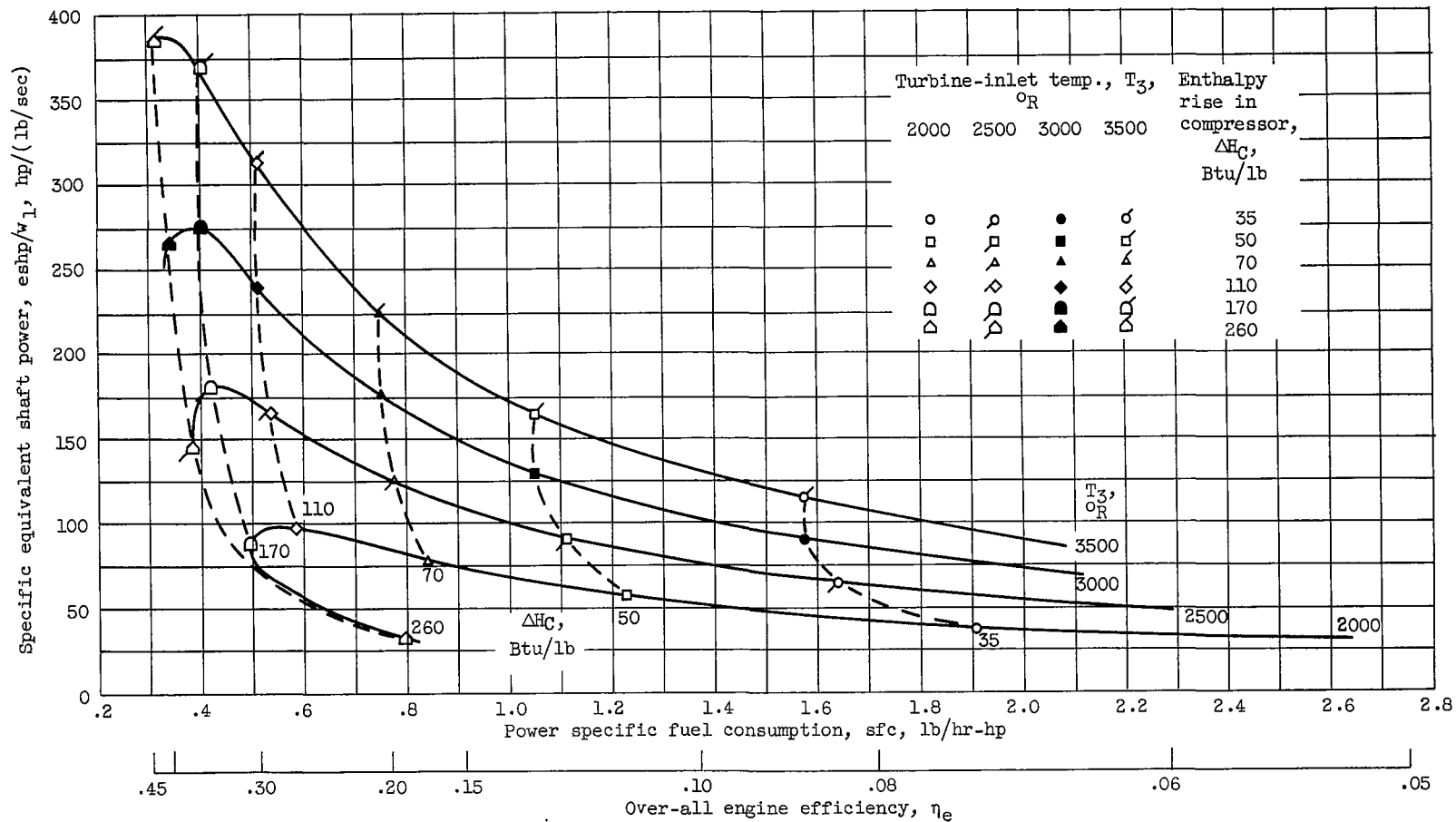


(b) Altitude, sea level; flight Mach number, 0.8.



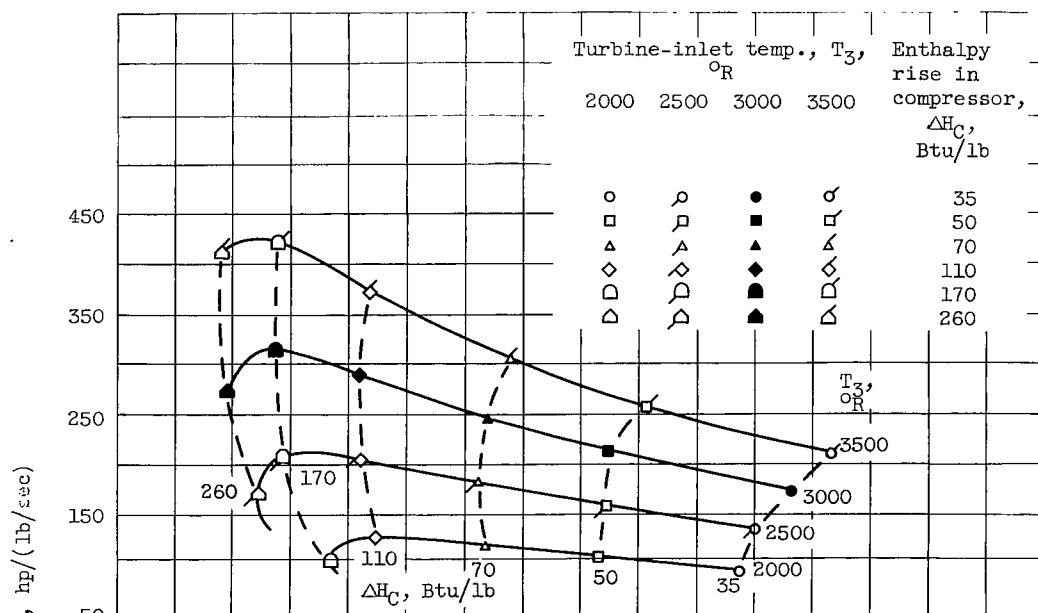
(c) Altitude, stratosphere; flight Mach number, 0.8.

Figure 7. - Concluded. Thermodynamic performance of turboprop engines (compressor pressure ratio as a parameter).

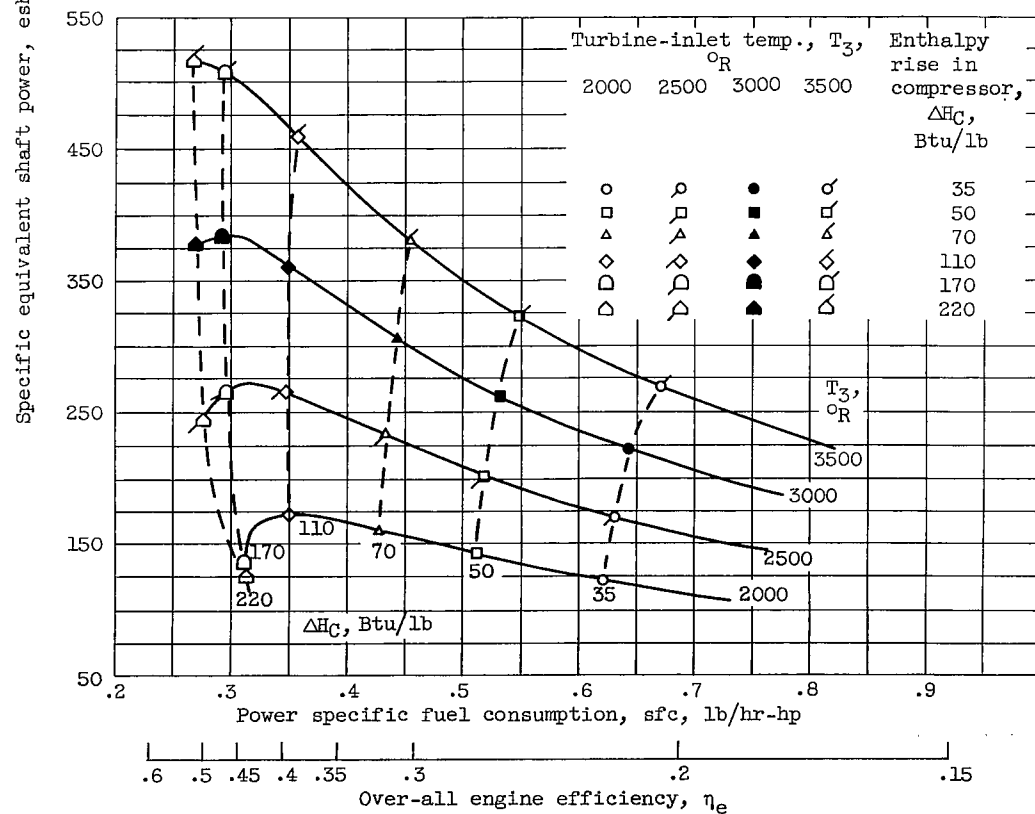


(a) Altitude, sea level; flight Mach number, 0.

Figure 8. - Thermodynamic performance of turboprop engines (enthalpy rise in compressor as a parameter).



(b) Altitude, sea level; flight Mach number, 0.8.



(c) Altitude, stratosphere; flight Mach number, 0.8.

Figure 8. - Concluded. Thermodynamic performance of turboprop engines (enthalpy rise in compressor as a parameter).

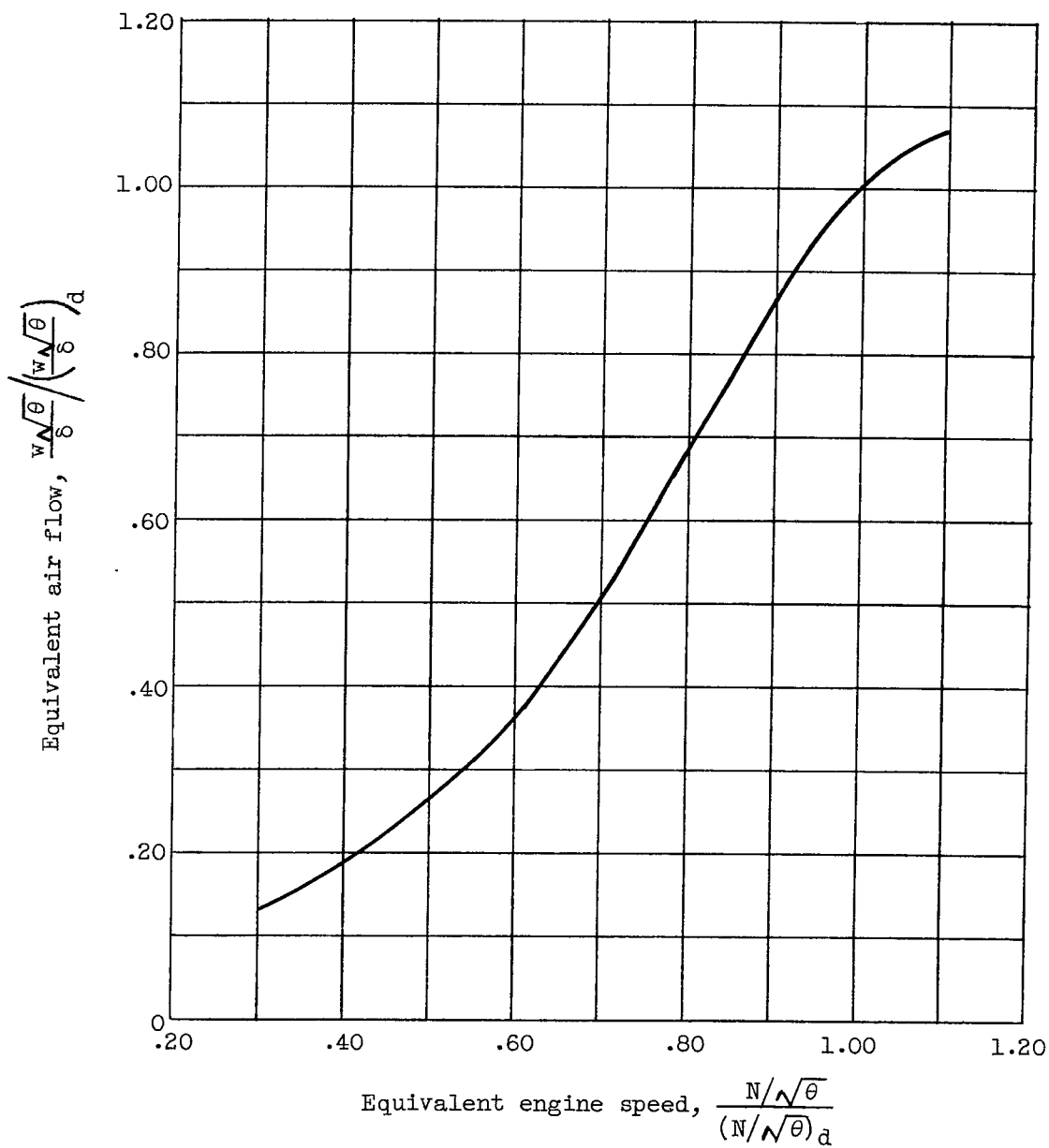
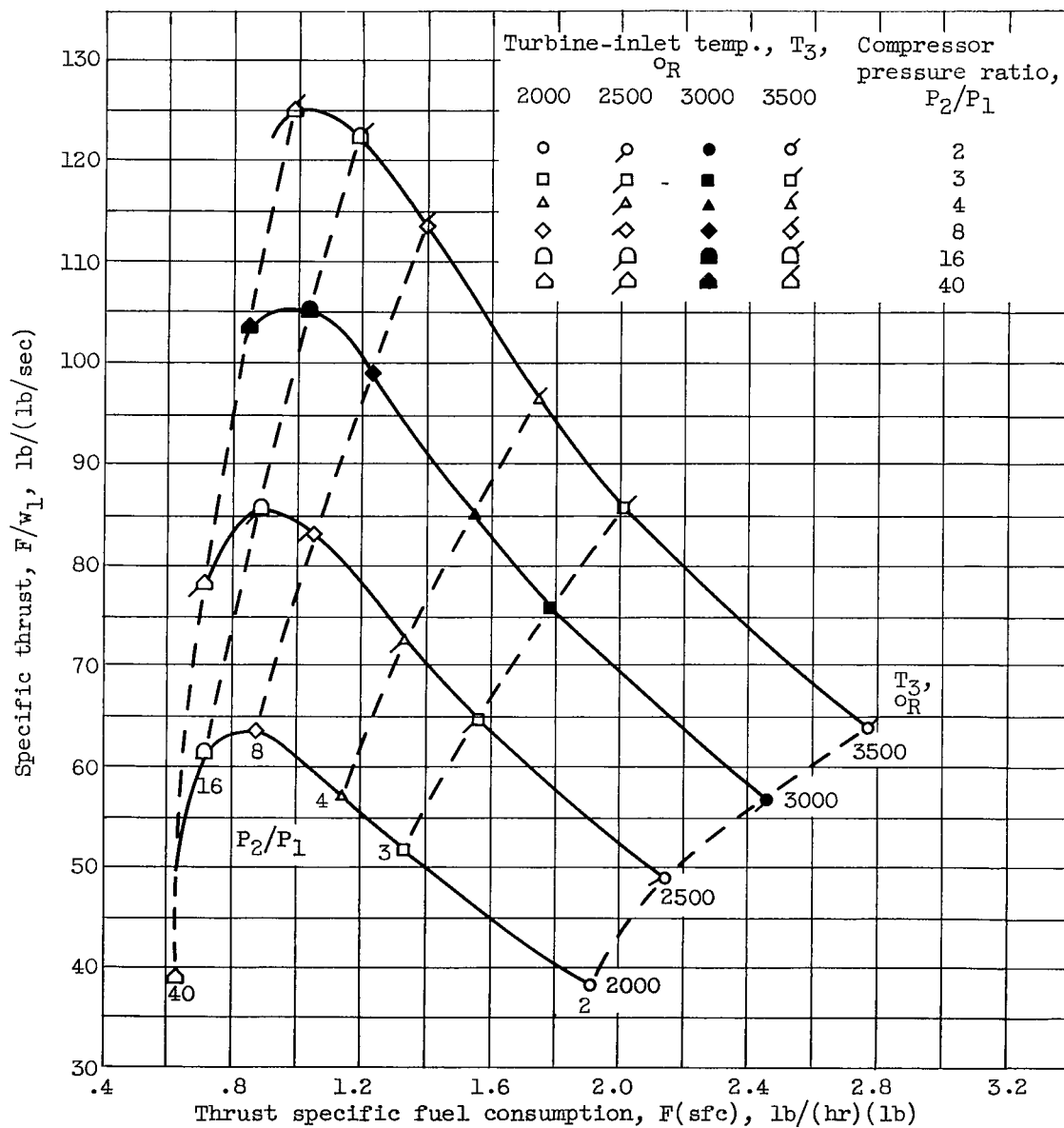
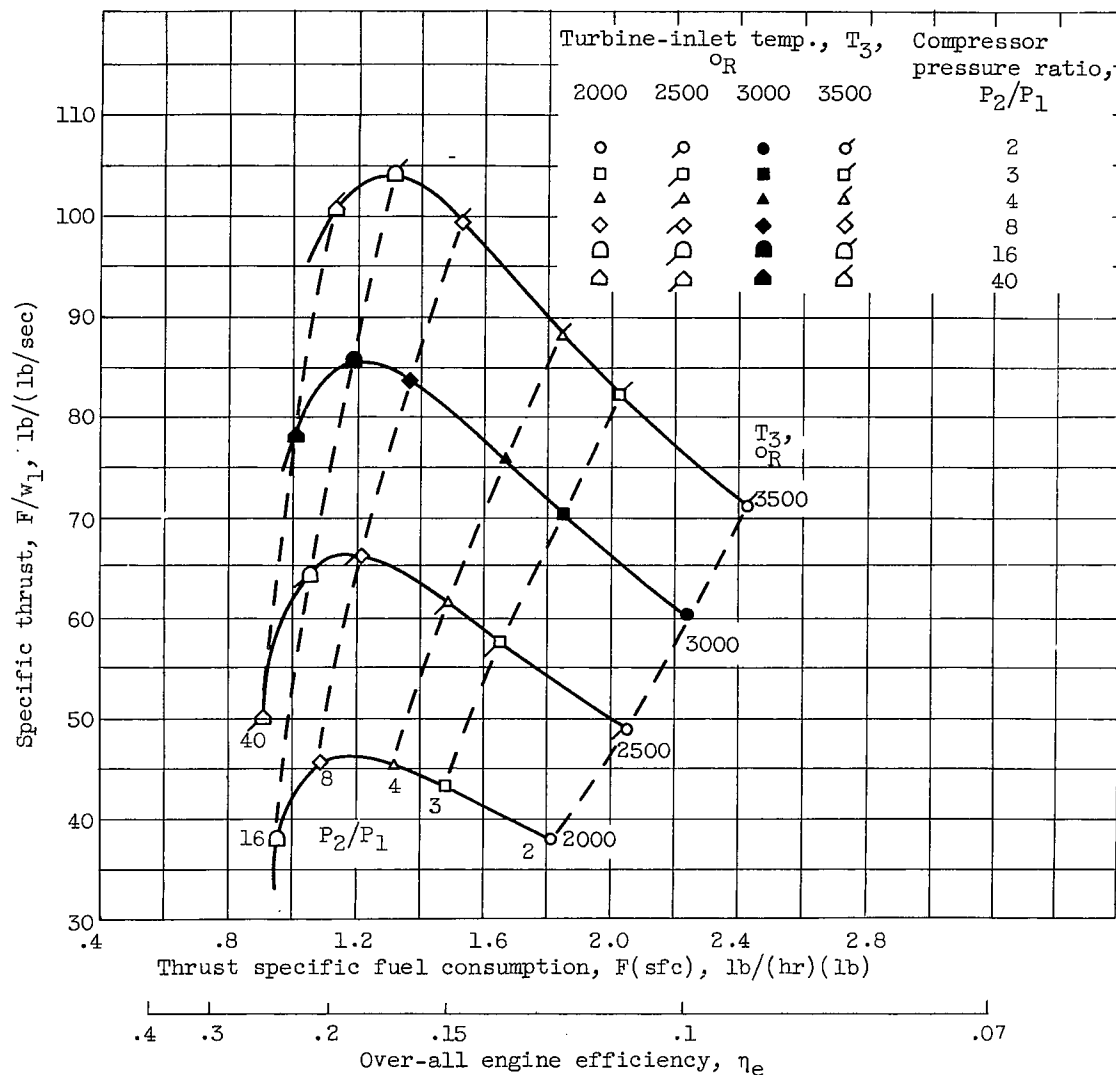


Figure 9. - Representative variation of equivalent air flow with equivalent speed.



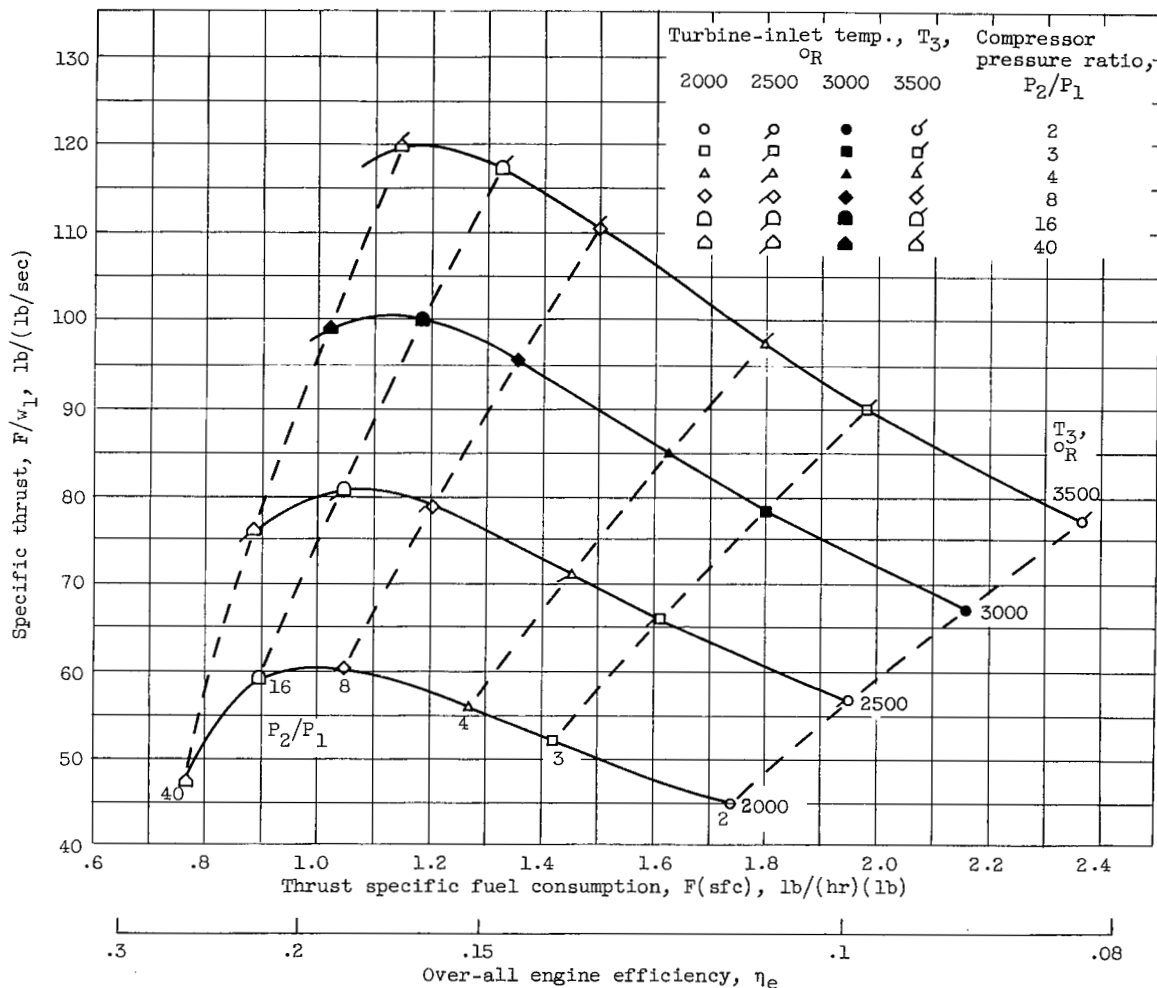
(a) Altitude, sea level; flight Mach number, 0.

Figure 10. - Thermodynamic performance of nonafterburning turbojet engines (compressor pressure ratio as a parameter).



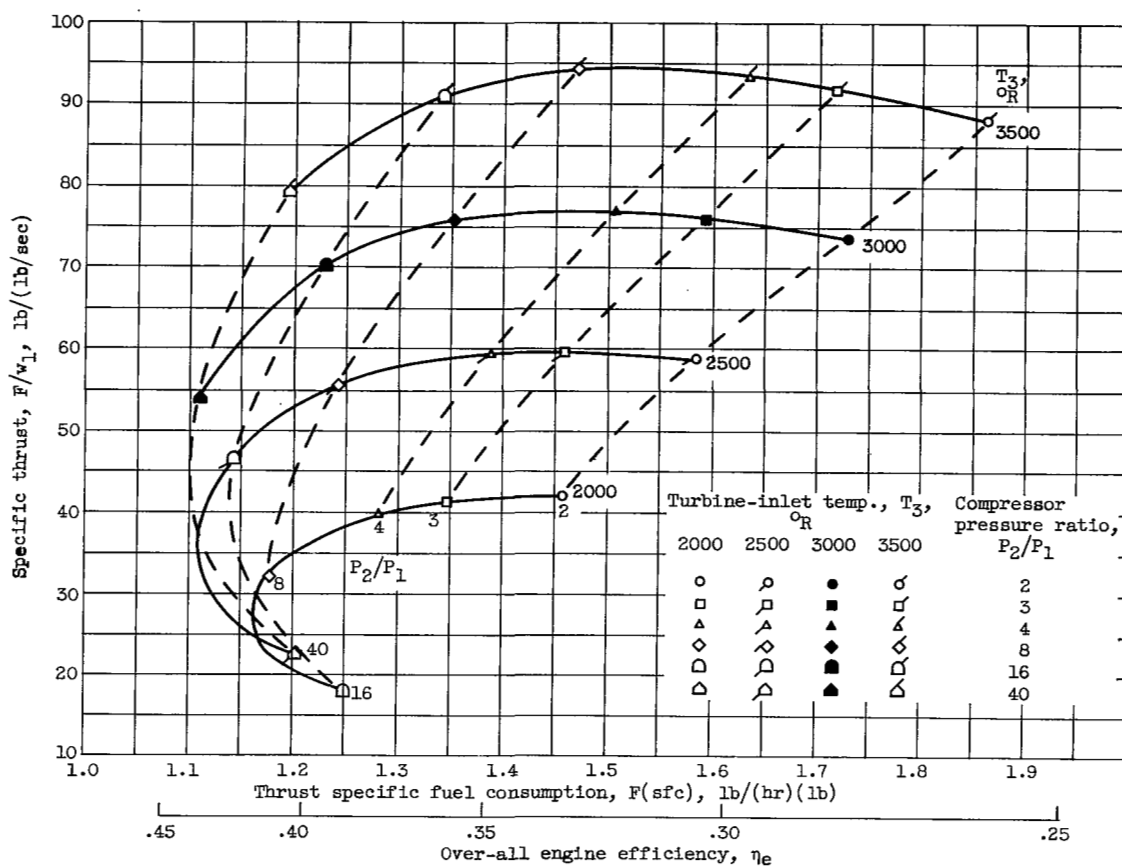
(b) Altitude, sea level; flight Mach number, 0.8.

Figure 10. - Continued. Thermodynamic performance of nonafterburning turbojet engines (compressor pressure ratio as a parameter).



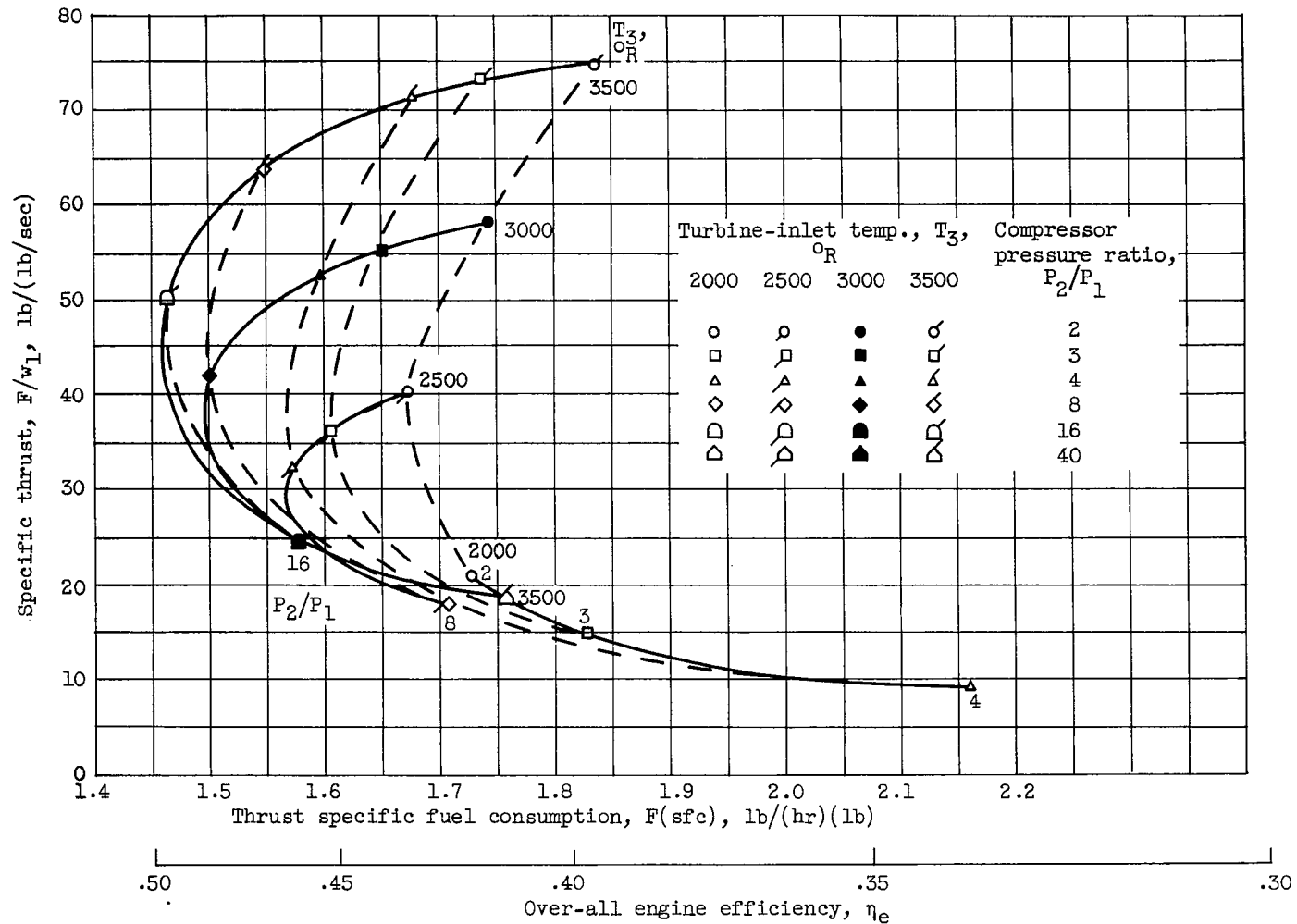
(c) Altitude, stratosphere; flight Mach number, 0.8.

Figure 10. - Continued. Thermodynamic performance of nonafterburning turbojet engines (compressor pressure ratio as a parameter).



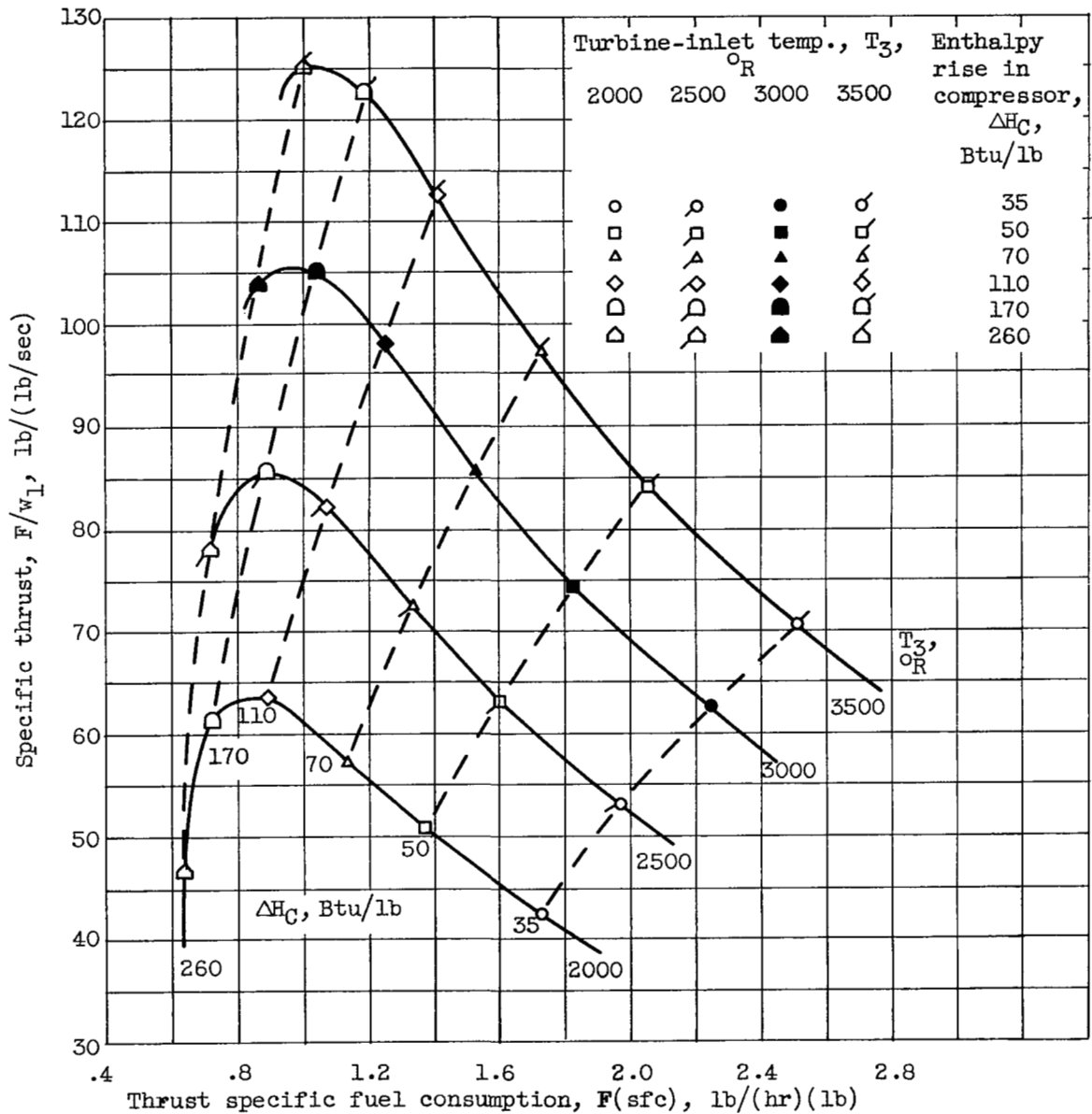
(d) Altitude, stratosphere; flight Mach number, 2.0.

Figure 10. - Continued. Thermodynamic performance of nonafterburning turbojet engines (compressor pressure ratio as a parameter).



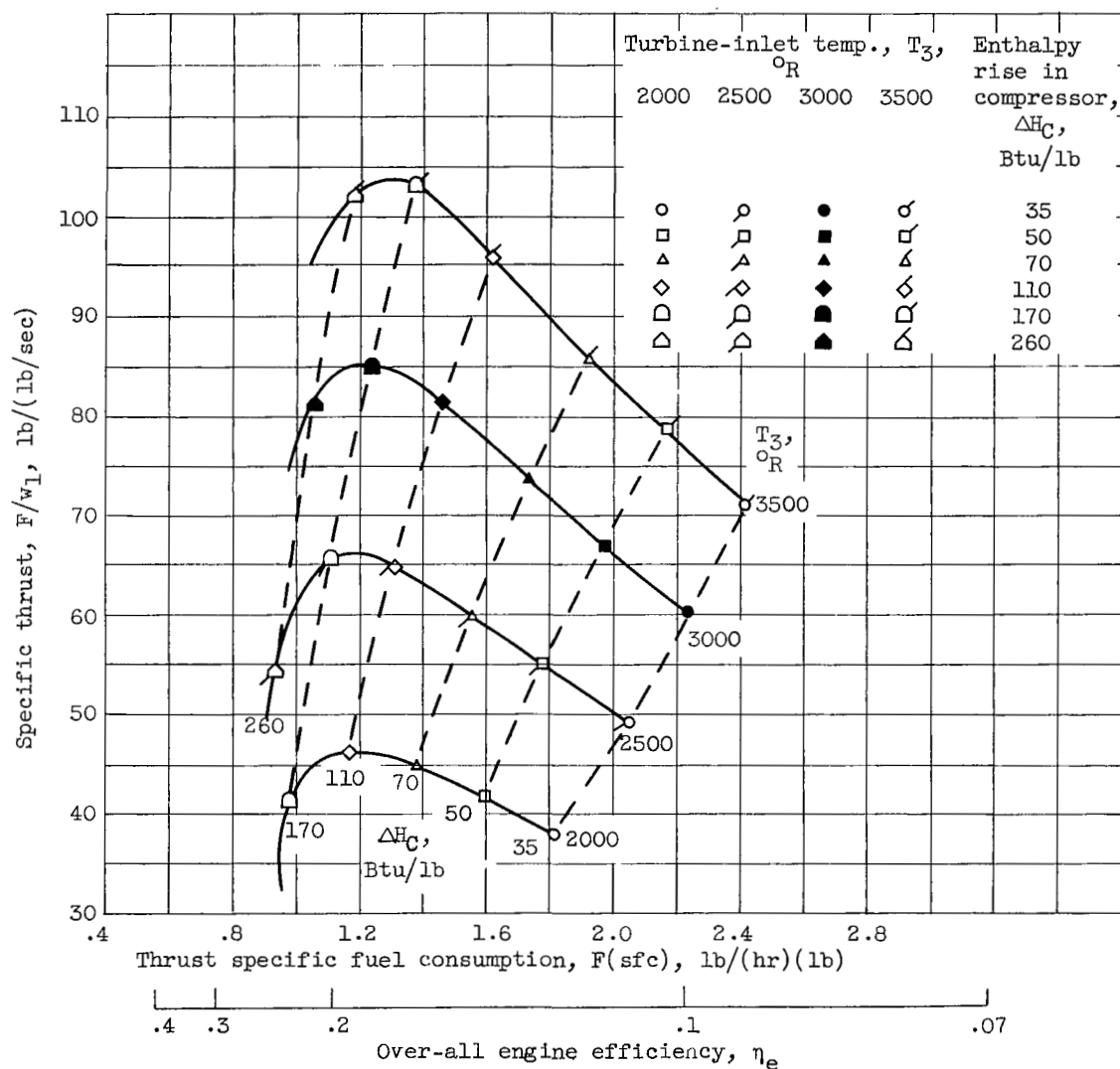
(e) Altitude, stratosphere; flight Mach number, 3.0.

Figure 10. - Concluded. Thermodynamic performance of nonafterburning turbojet engines (compressor pressure ratio as a parameter).



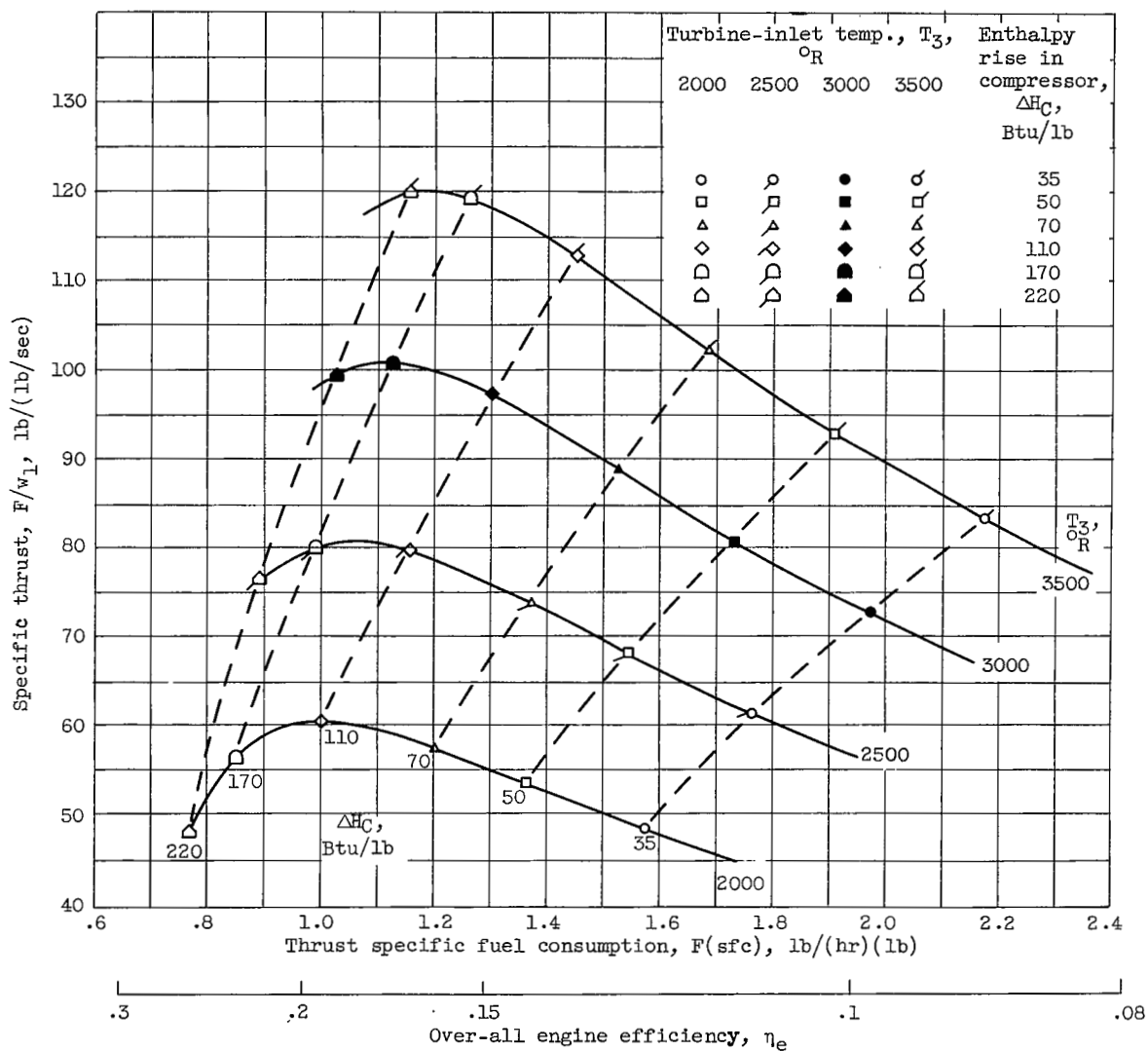
(a) Altitude, sea level; flight Mach number, 0.

Figure 11. - Thermodynamic performance of nonafterburning turbojet engines (enthalpy rise in compressor as a parameter).



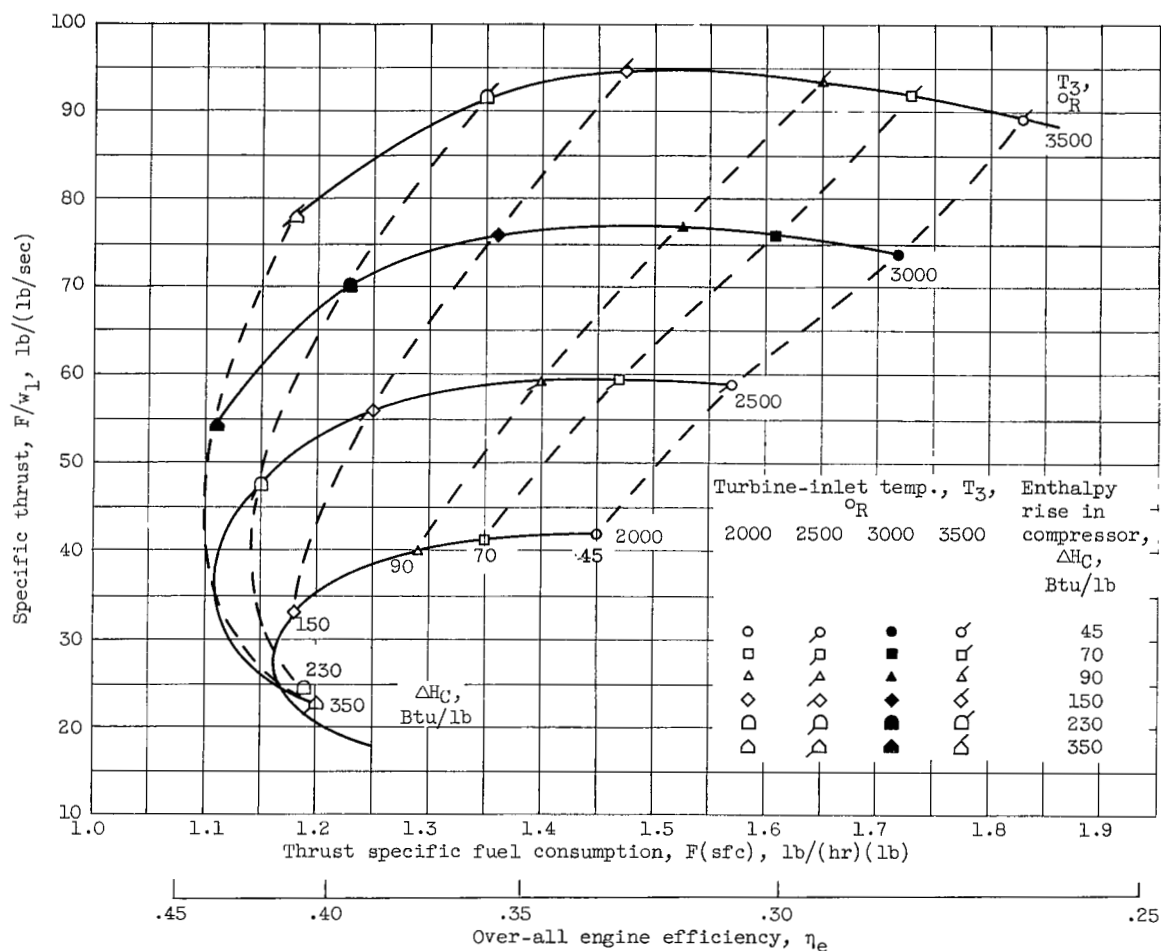
(b) Altitude, sea level; flight Mach number, 0.8.

Figure 11. - Continued. Thermodynamic performance of nonafterburning turbojet engines (enthalpy rise in compressor as a parameter).



(c) Altitude, stratosphere; flight Mach number, 0.8.

Figure 11. - Continued. Thermodynamic performance of nonafterburning turbojet engines (enthalpy rise in compressor as a parameter).



(d) Altitude, stratosphere; flight Mach number, 2.0.

Figure 11. - Continued. Thermodynamic performance of nonafterburning turbojet engines (enthalpy rise in compressor as a parameter).

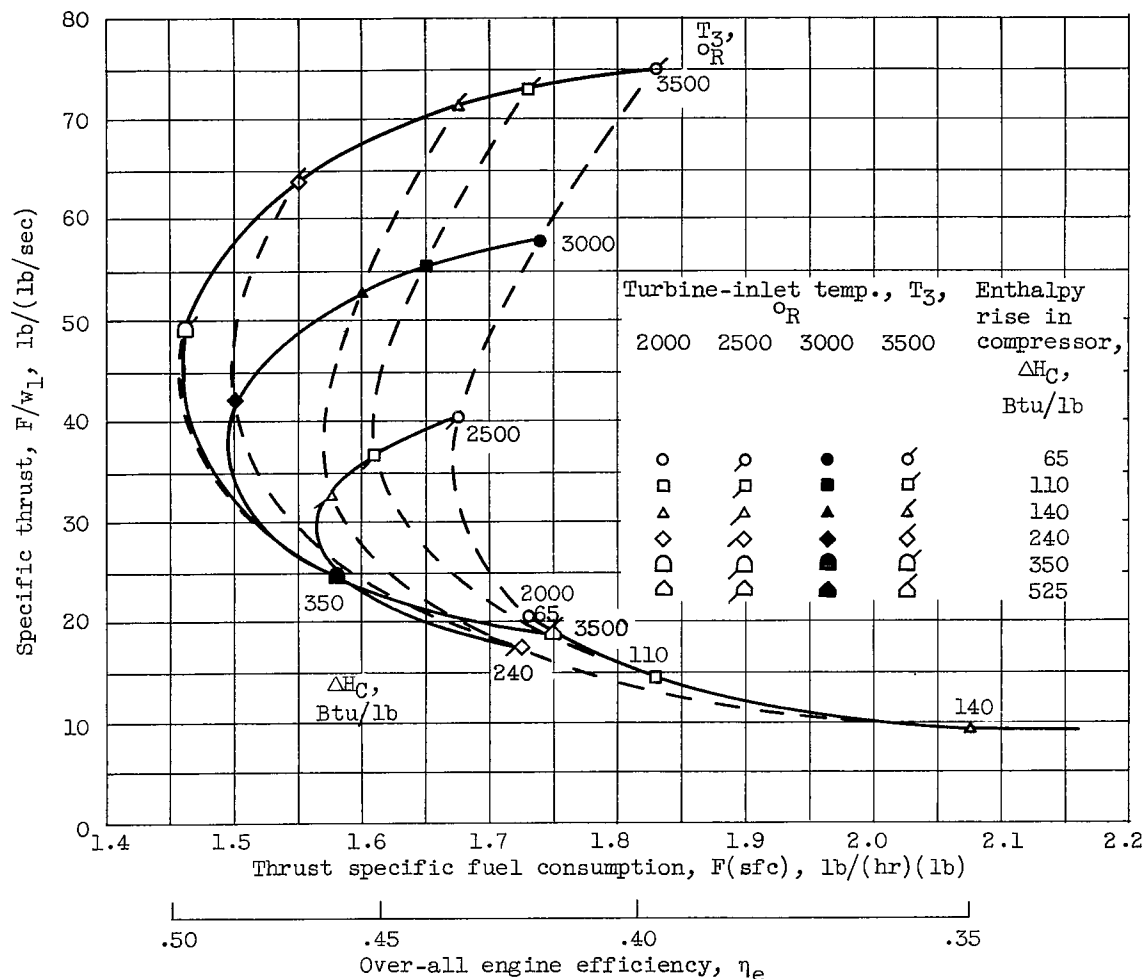
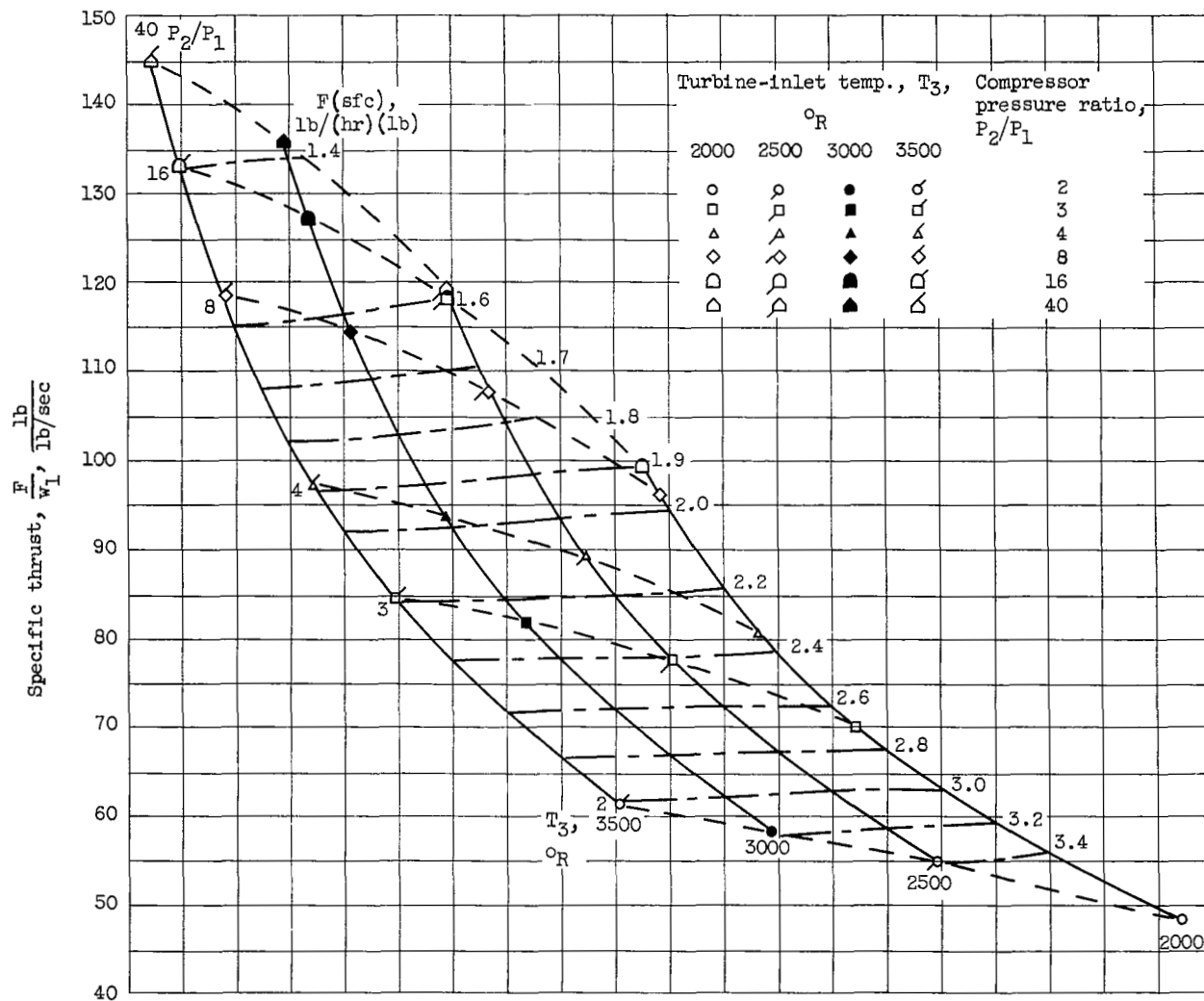
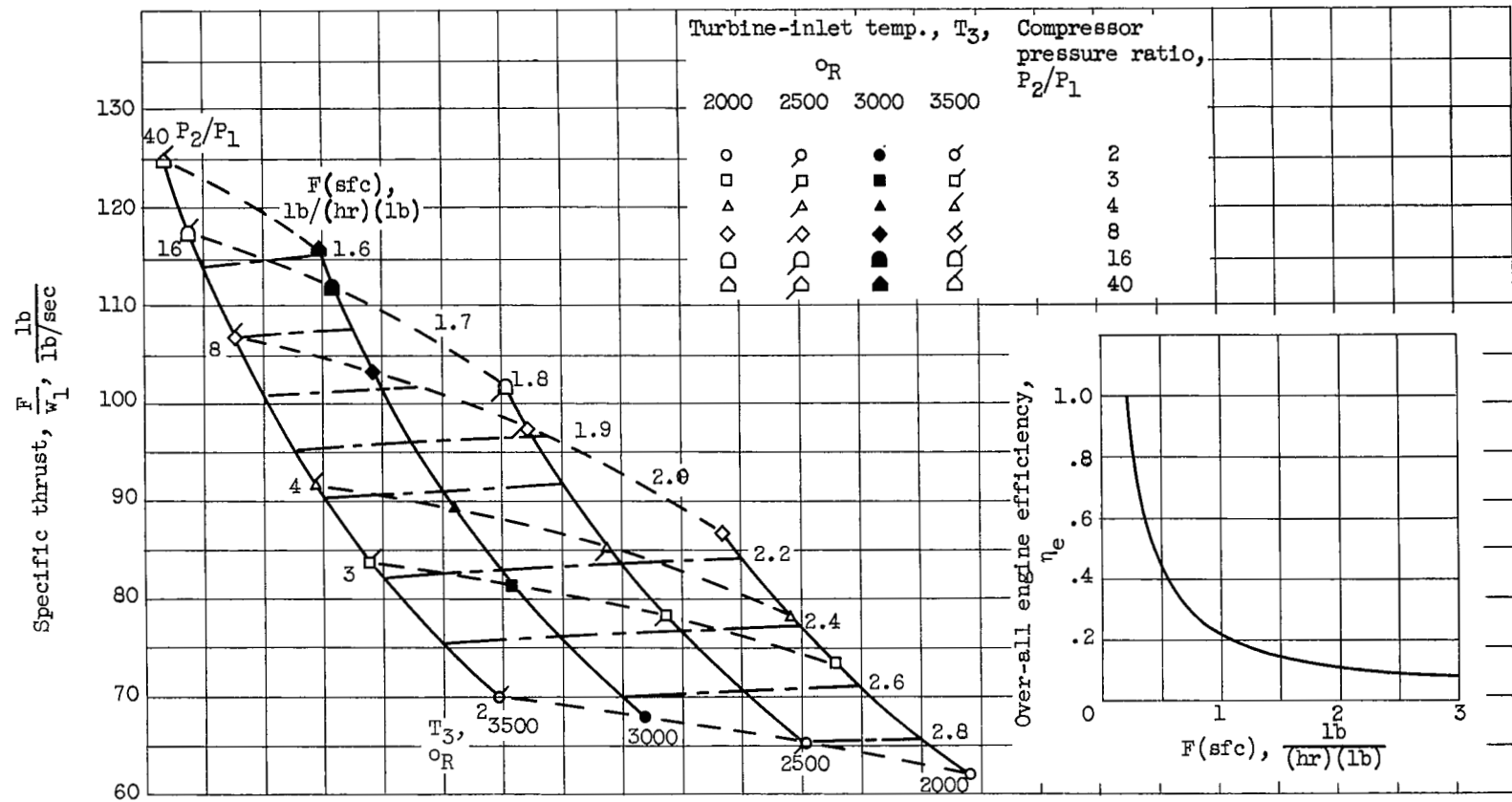


Figure 11. - Concluded. Thermodynamic performance of nonafterburning turbojet engines (enthalpy rise in compressor as a parameter).



(a) Altitude, sea level; flight Mach number, 0.

Figure 12. - Thermodynamic performance of afterburning turbojet engines.



(b) Altitude, sea level; flight Mach number, 0.8.

Figure 12. - Continued. Thermodynamic performance of afterburning turbojet engines.

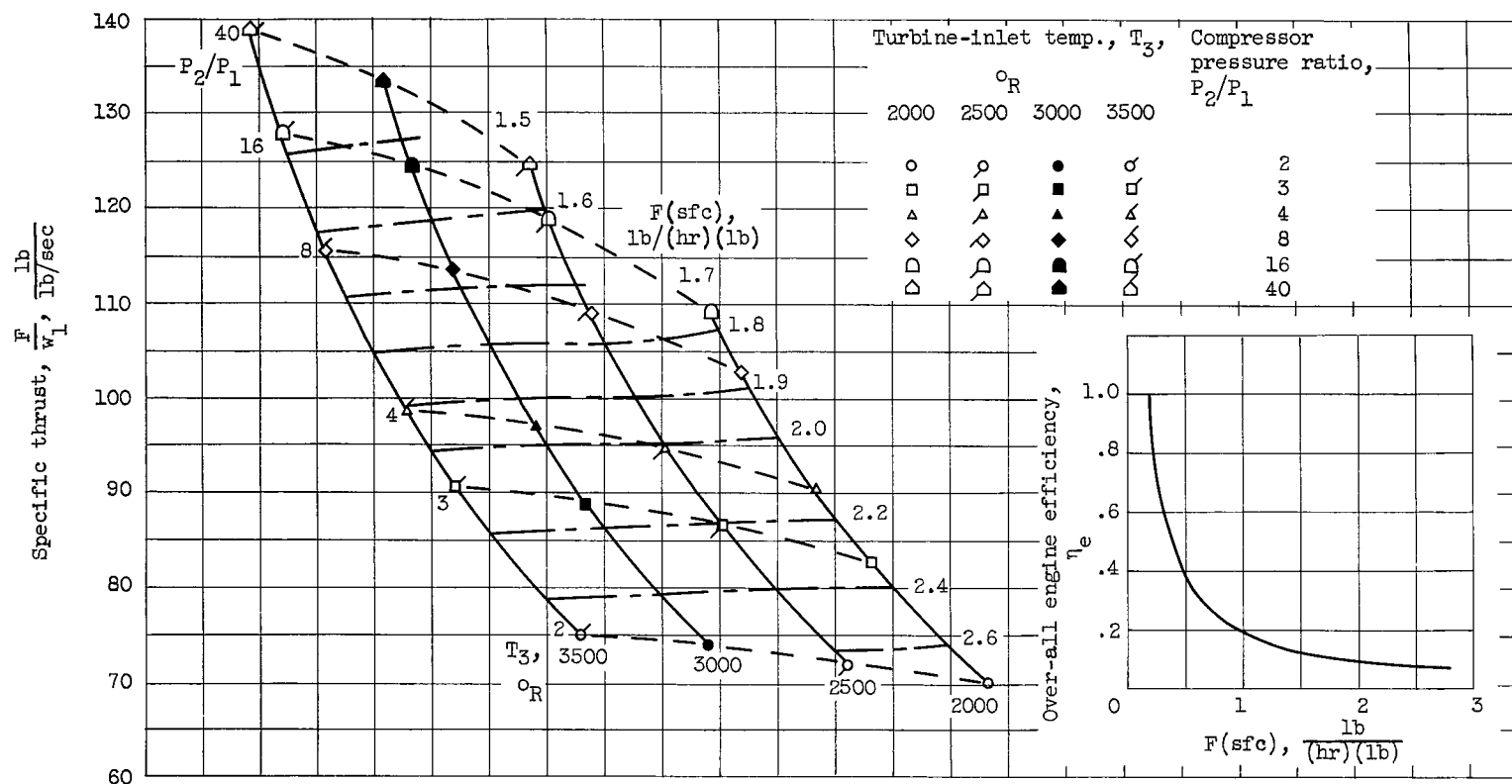
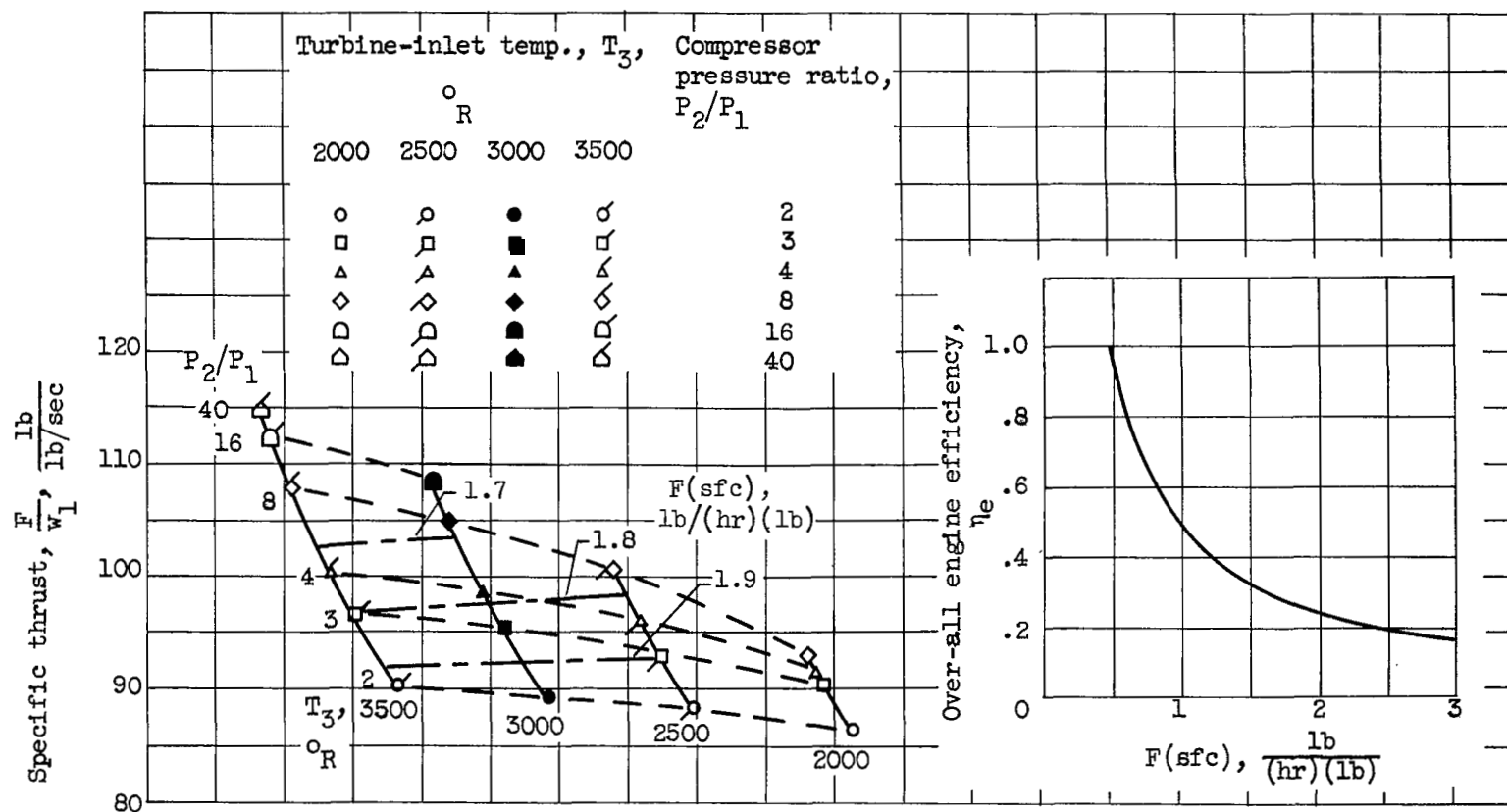
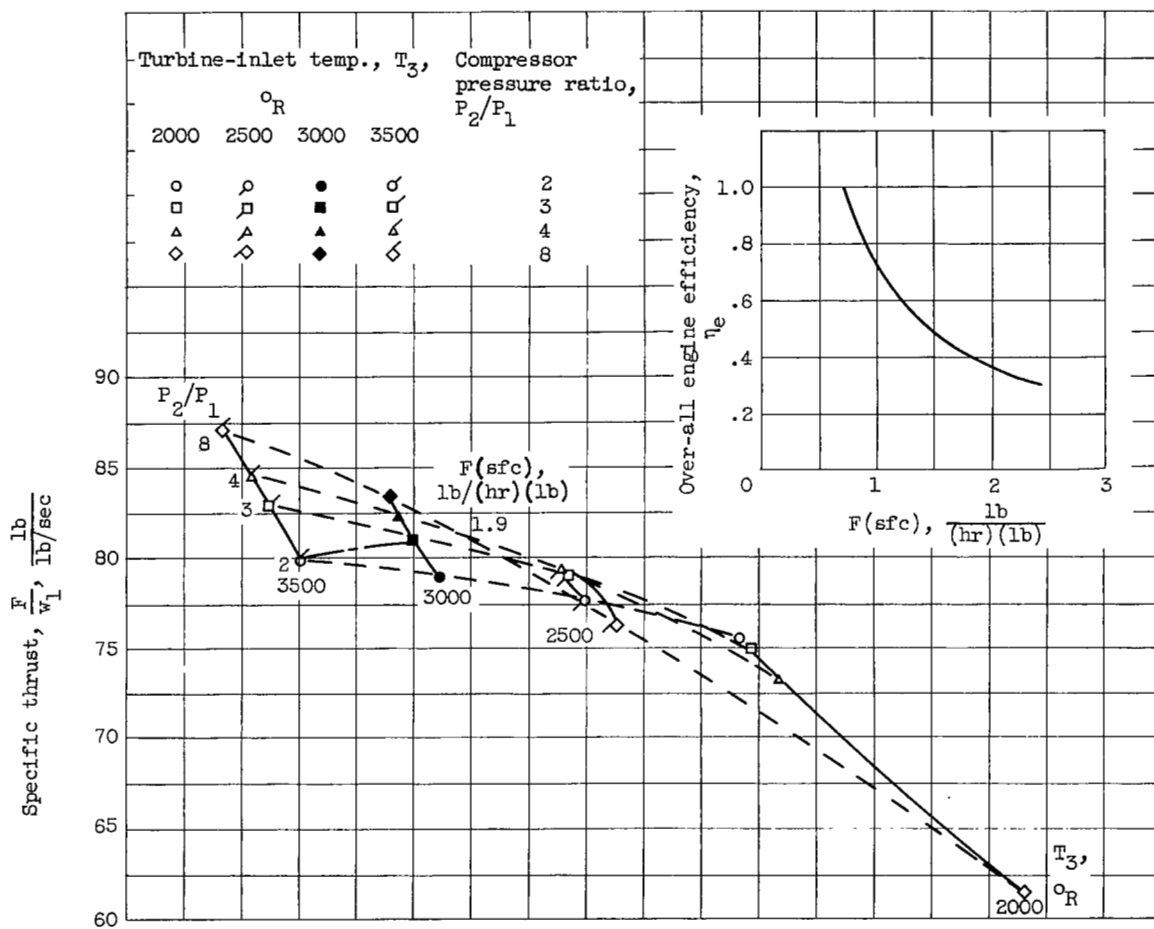


Figure 12. - Continued. Thermodynamic performance of afterburning turbojet engines.



(d) Altitude, stratosphere; flight Mach number, 2.0.

Figure 12. - Continued. Thermodynamic performance of afterburning turbojet engines.



(e) Altitude, stratosphere; flight Mach number, 3.0.

Figure 12. - Concluded. Thermodynamic performance of afterburning turbojet engines.

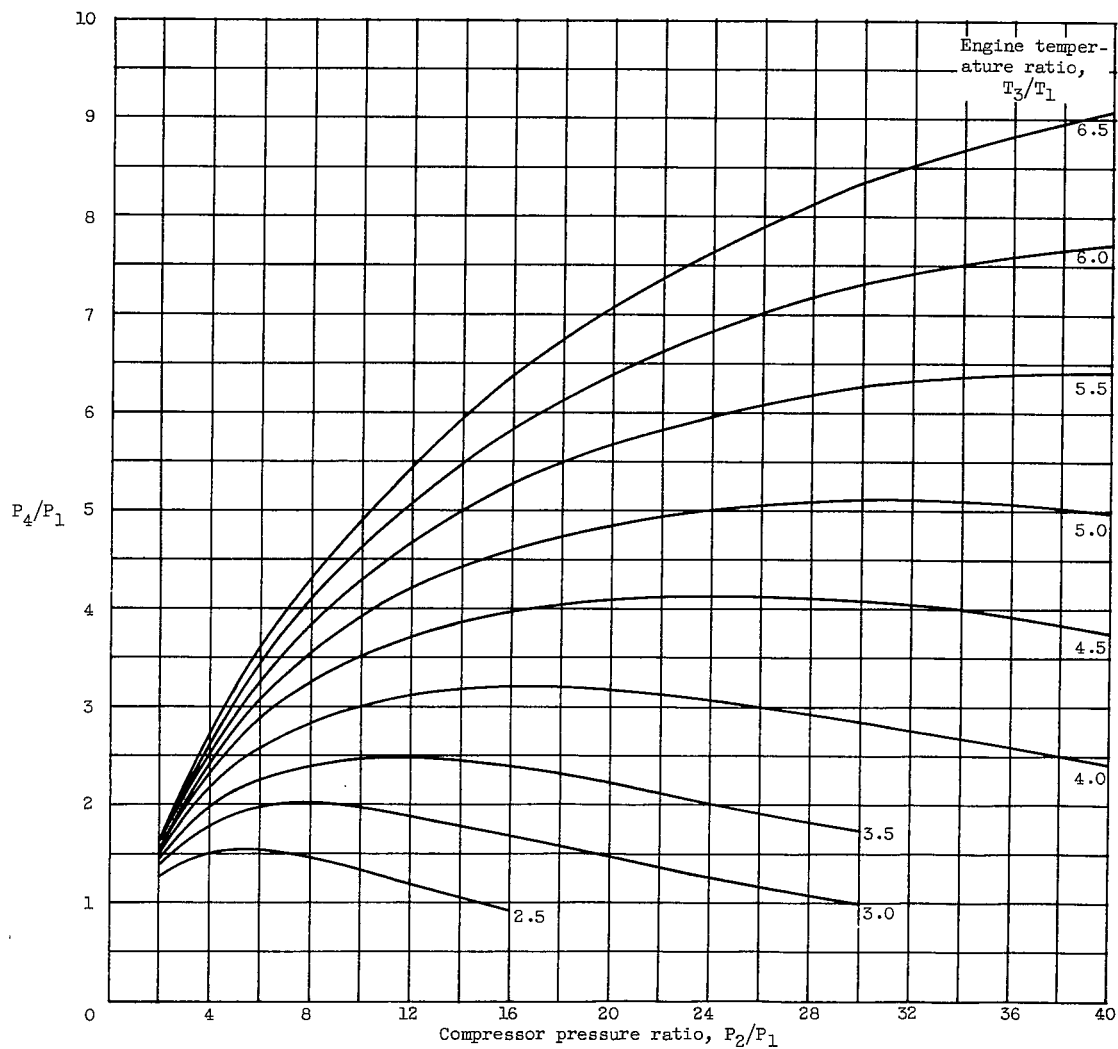


Figure 13. - Chart for estimating total pressure behind turbines driving compressors.

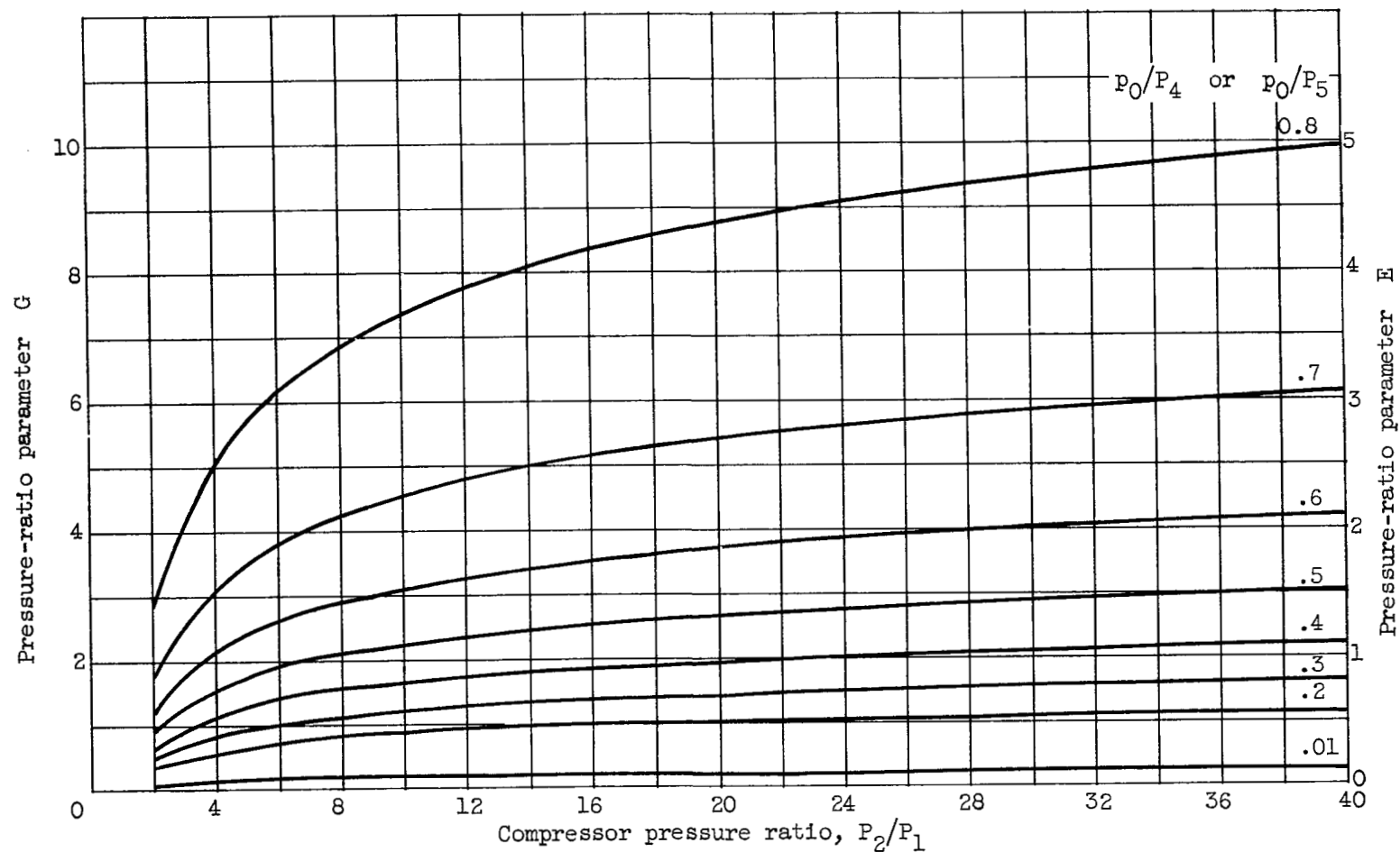
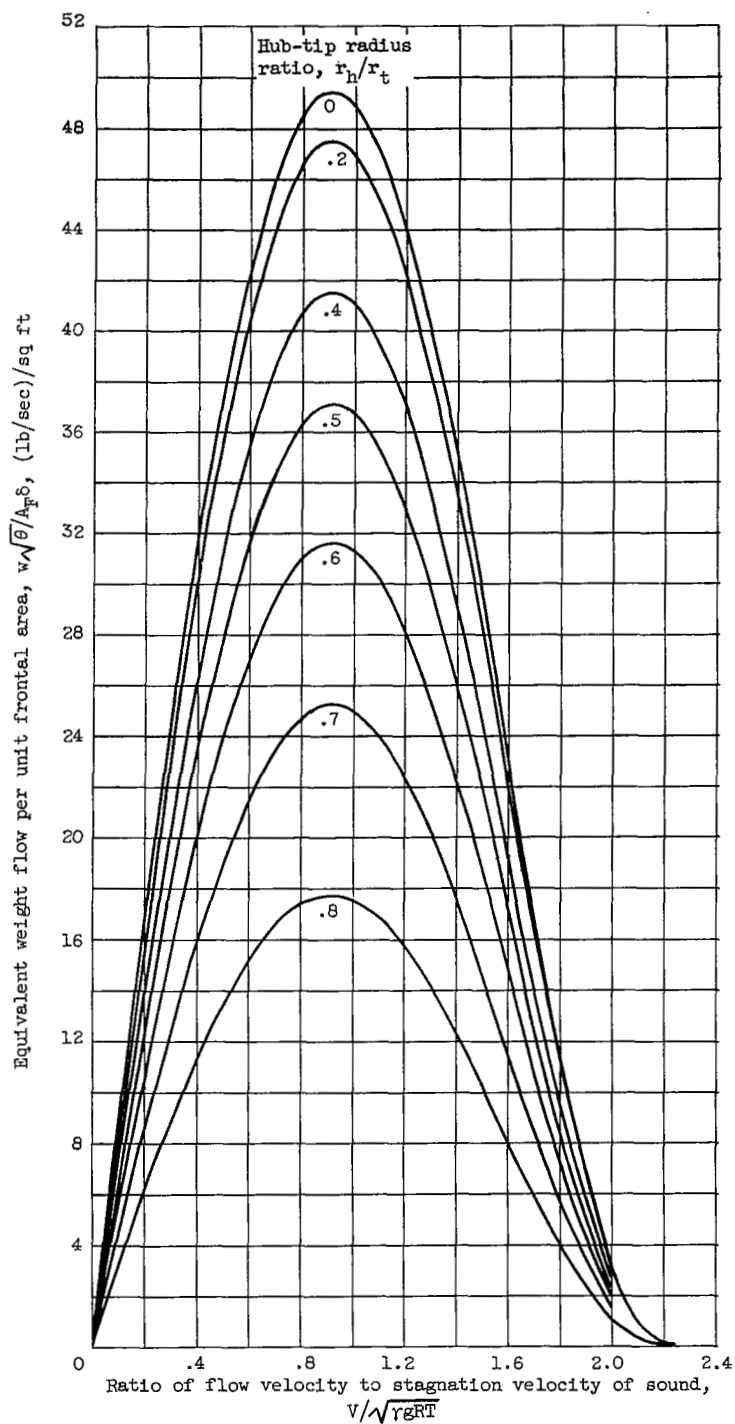
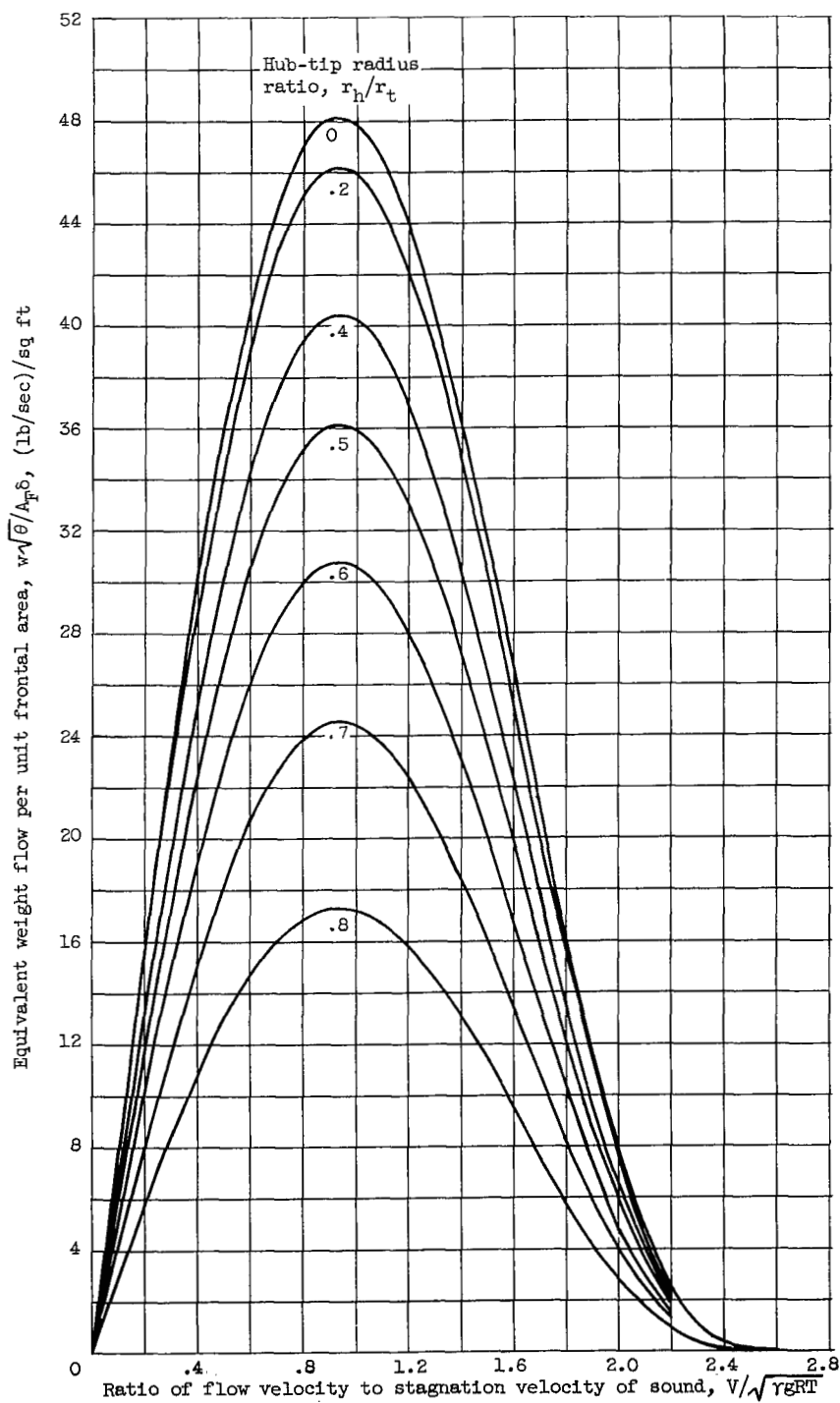


Figure 14. - Variation of parameters G and E with compressor pressure ratio (eqs. (16) and (20)).



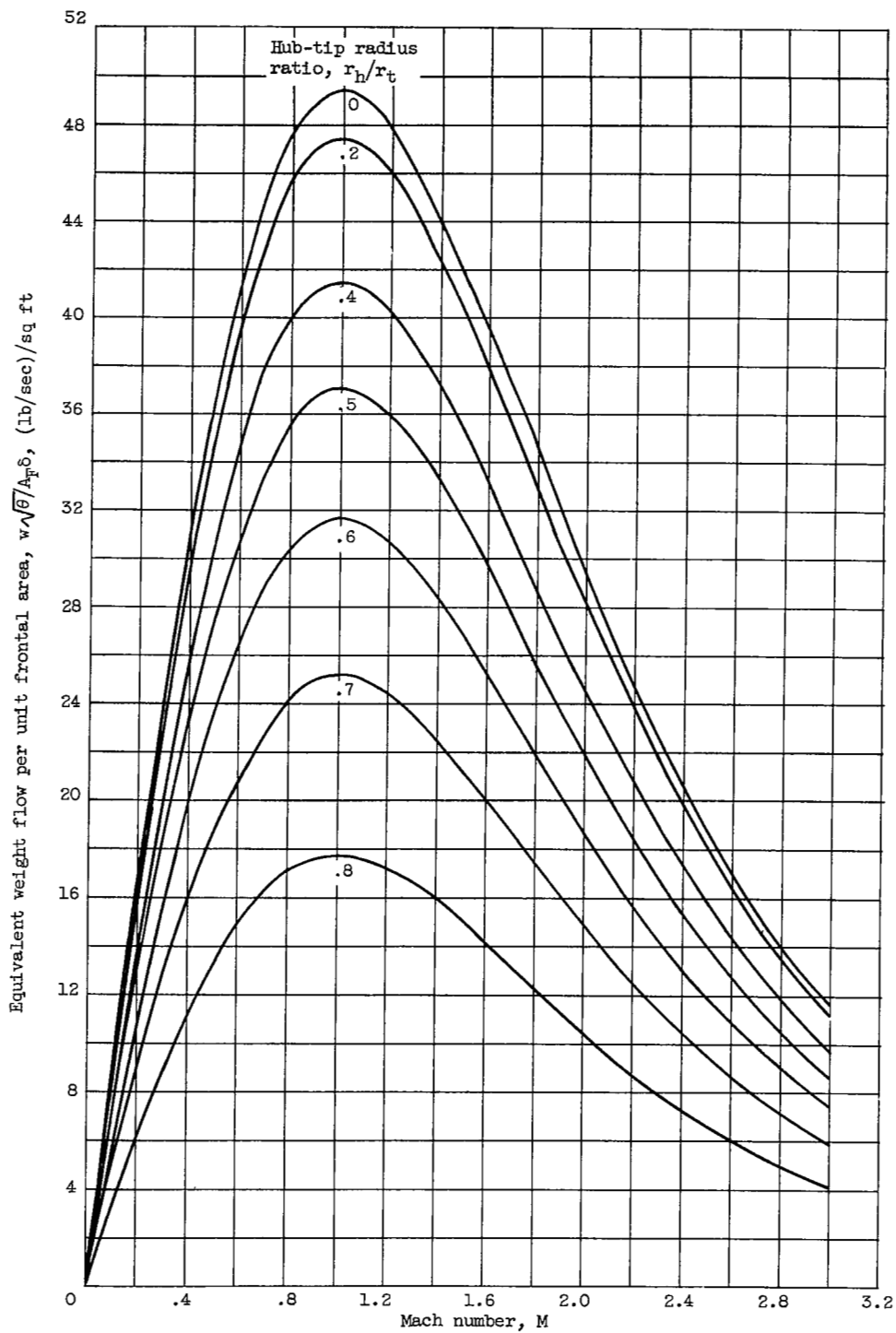
(a) Ratio of specific heats, 1.4.

Figure 15. - Variation of equivalent weight flow per unit frontal area with $V/\sqrt{\gamma gRT}$ for several values of hub-tip radius ratio.



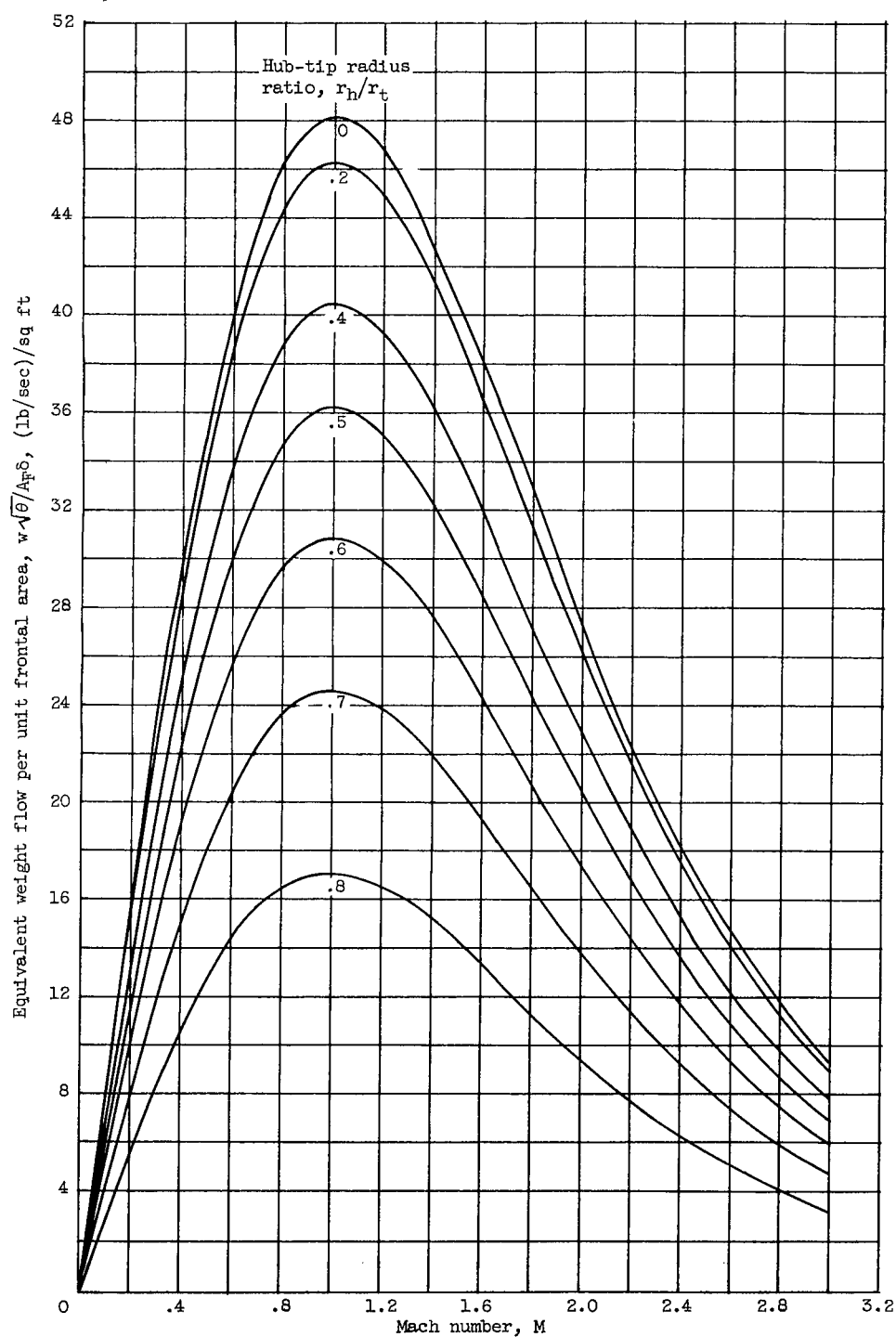
(b) Ratio of specific heats, 1.3.

Figure 15. - Concluded. Variation of equivalent weight flow per unit frontal area with $V/\sqrt{\gamma gRT}$ for several values of hub-tip radius ratio.



(a) Ratio of specific heats, 1.4.

Figure 16. - Variation of equivalent weight flow per unit frontal area with Mach number for several values of hub-tip radius ratio.



(b) Ratio of specific heats, 1.3.

Figure 16. - Concluded. Variation of equivalent weight flow per unit frontal area with Mach number for several values of hub-tip radius ratio.

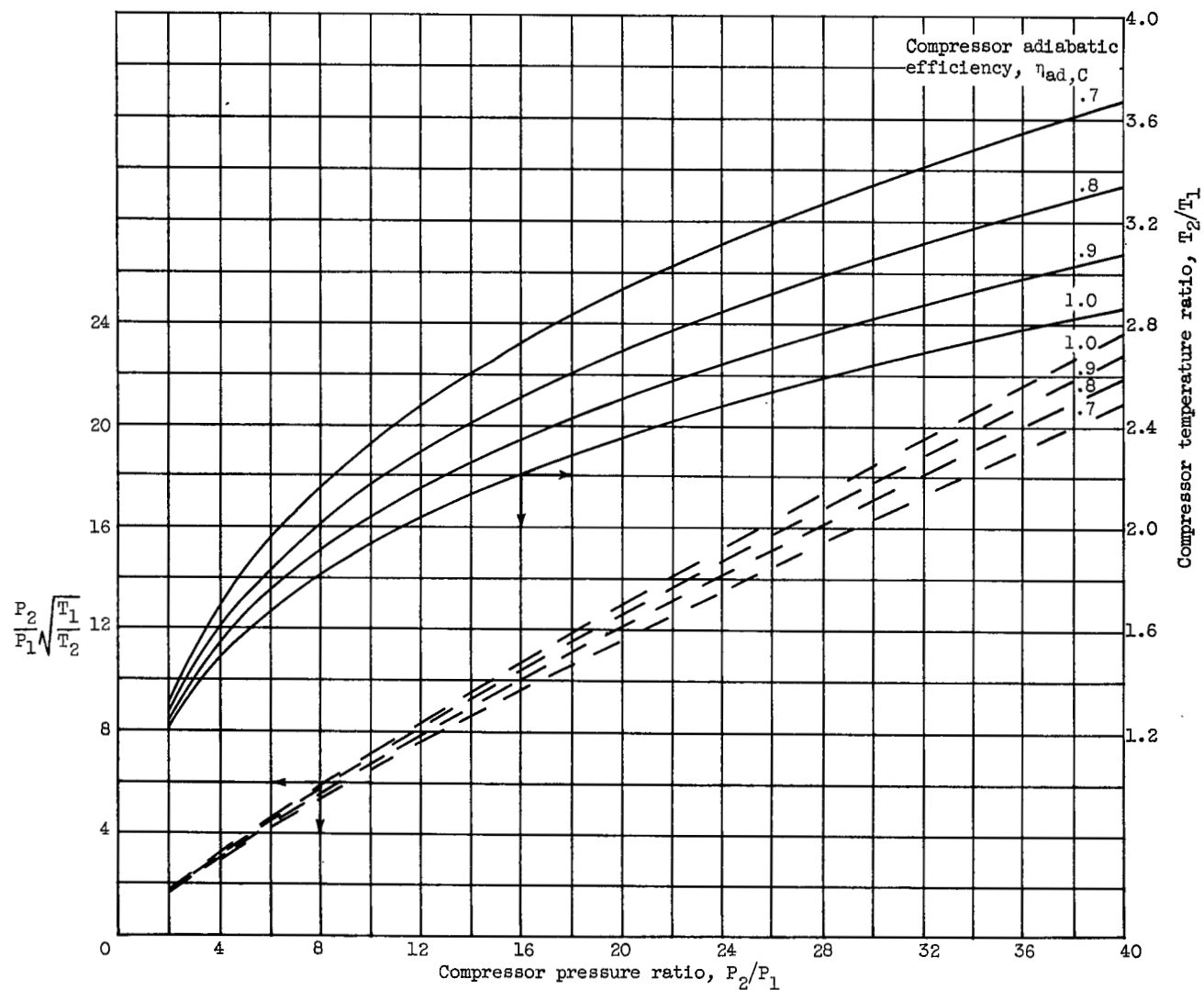


Figure 17. - Chart for estimating total pressure and temperature behind compressor; $\gamma_c = 1.4$.

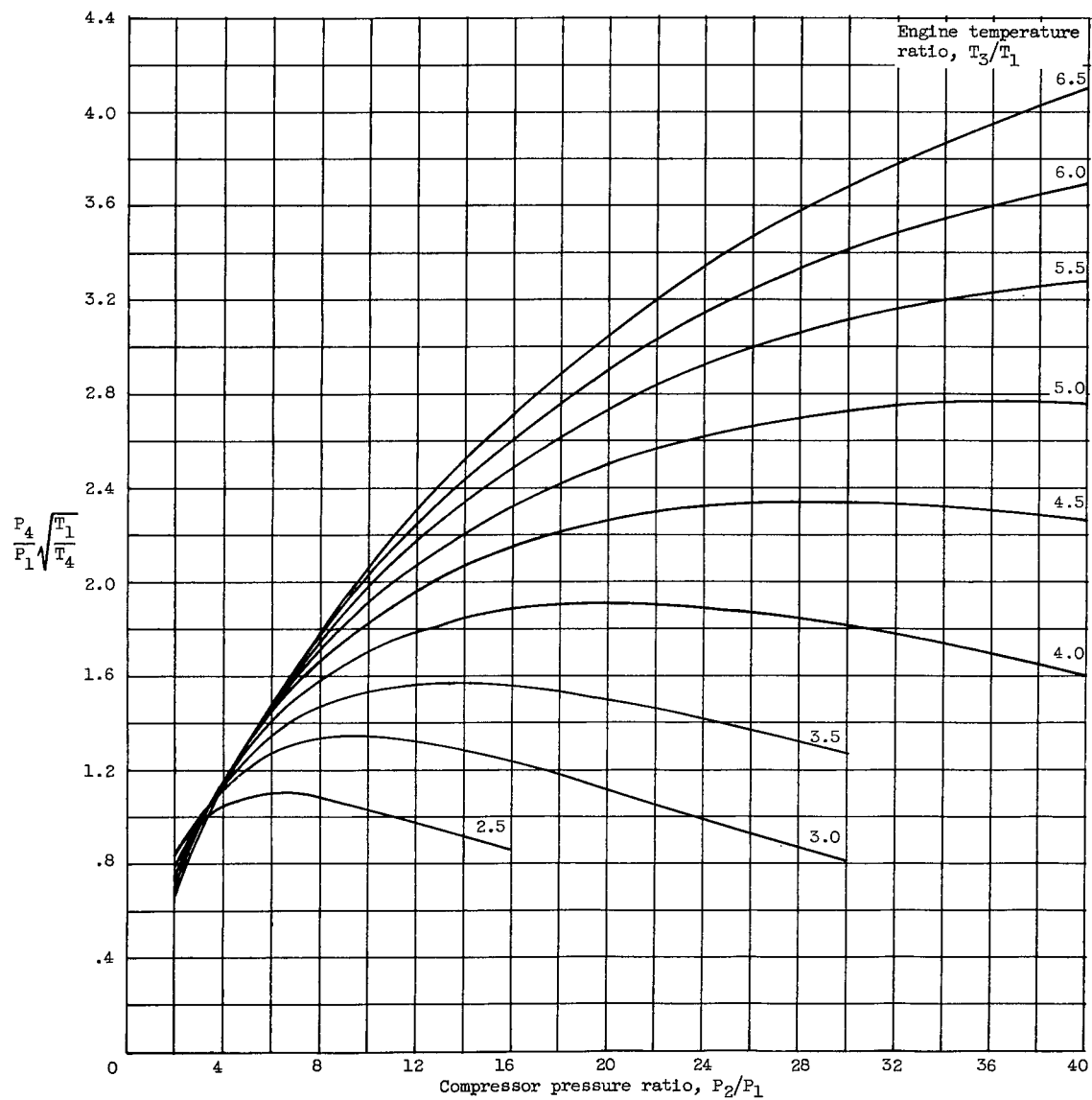


Figure 18. - Chart for estimating equivalent weight flow behind turbines driving compressors.

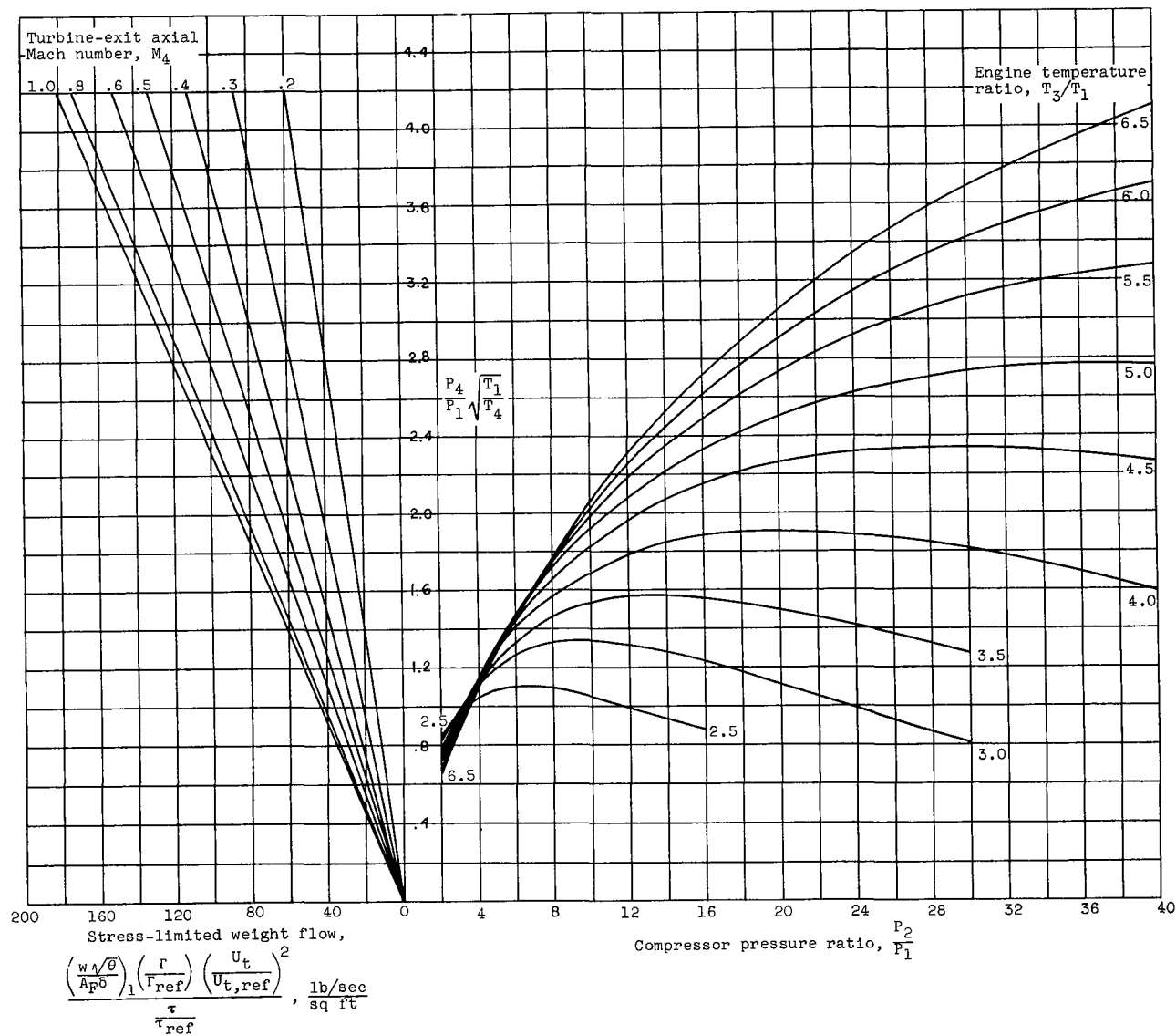


Figure 19. - Stress-limited air flow and tip speed for compressor or turbine (eq. (25)).

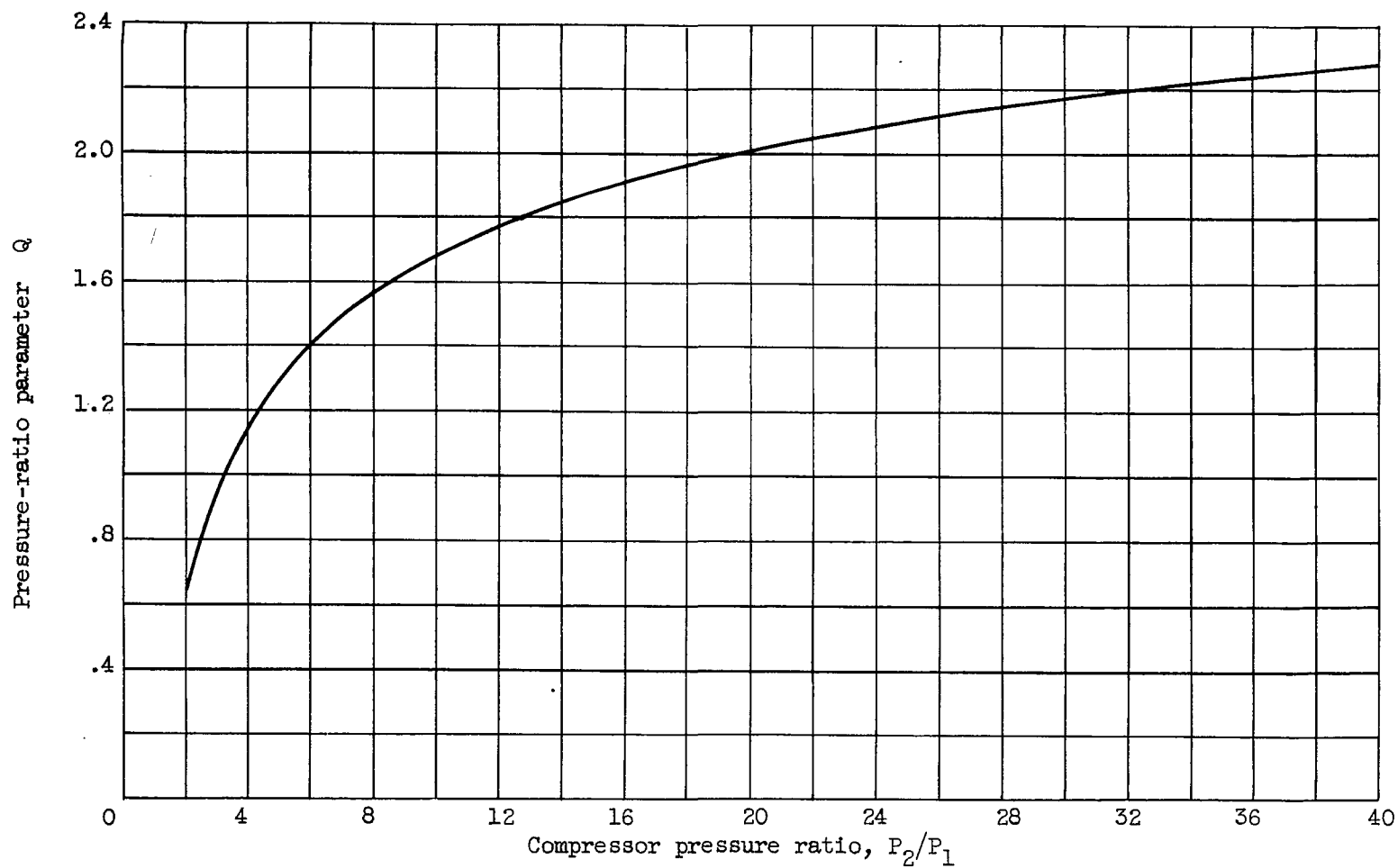


Figure 20. - Variation of parameter Q with compressor pressure ratio (eqs. (13) and (26));
 $\gamma_c = 1.4$.

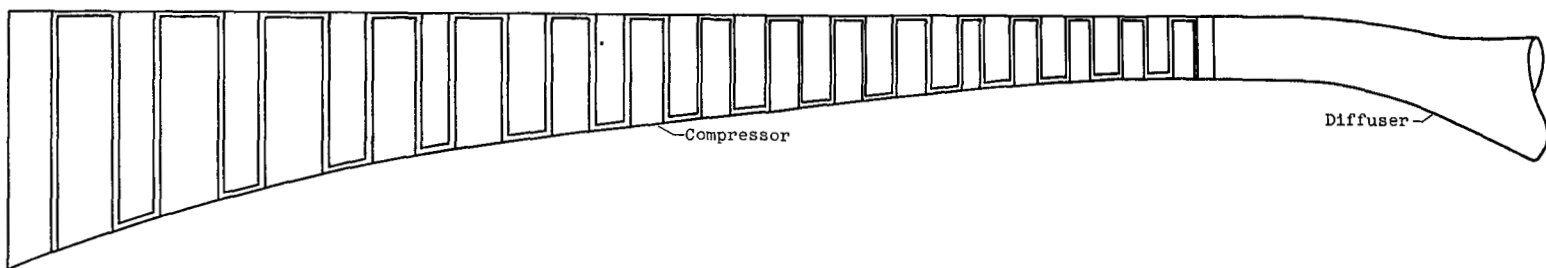


Figure 21. - Typical current layout of axial-flow compressor and exit diffuser.

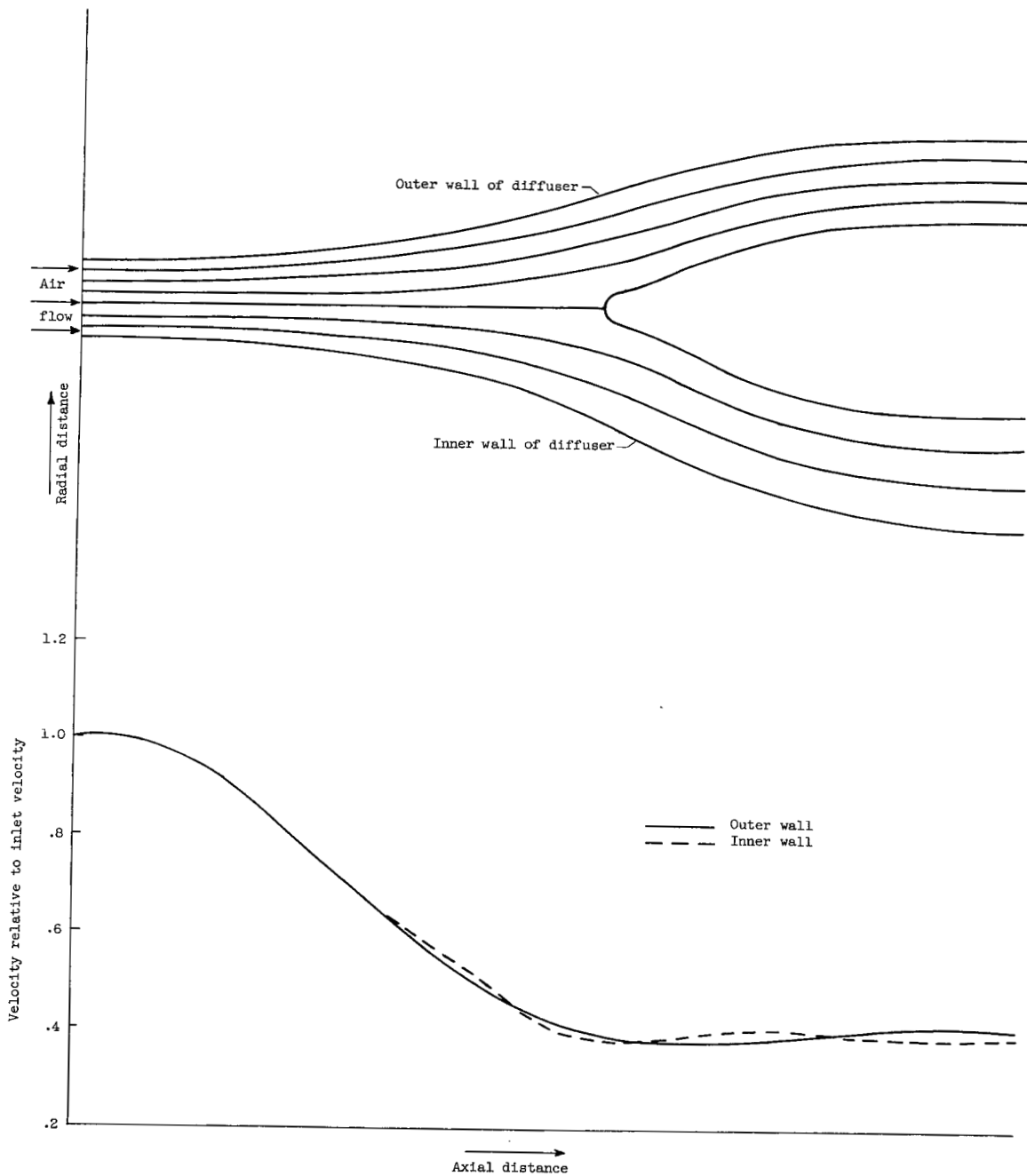


Figure 22. - Streamlines and velocity distributions in symmetric diffuser with continuous diffusion between compressor and combustor (ref. 15).

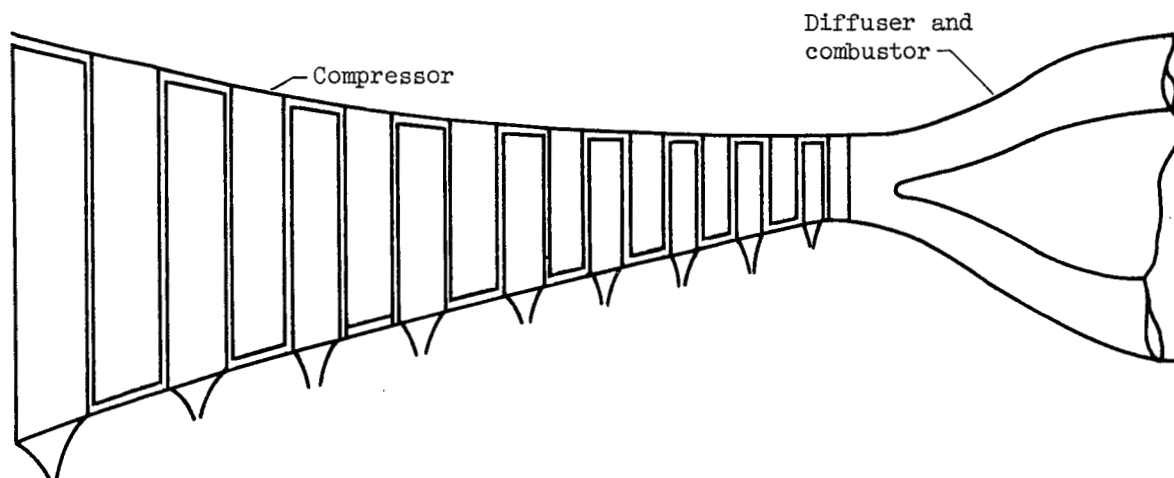
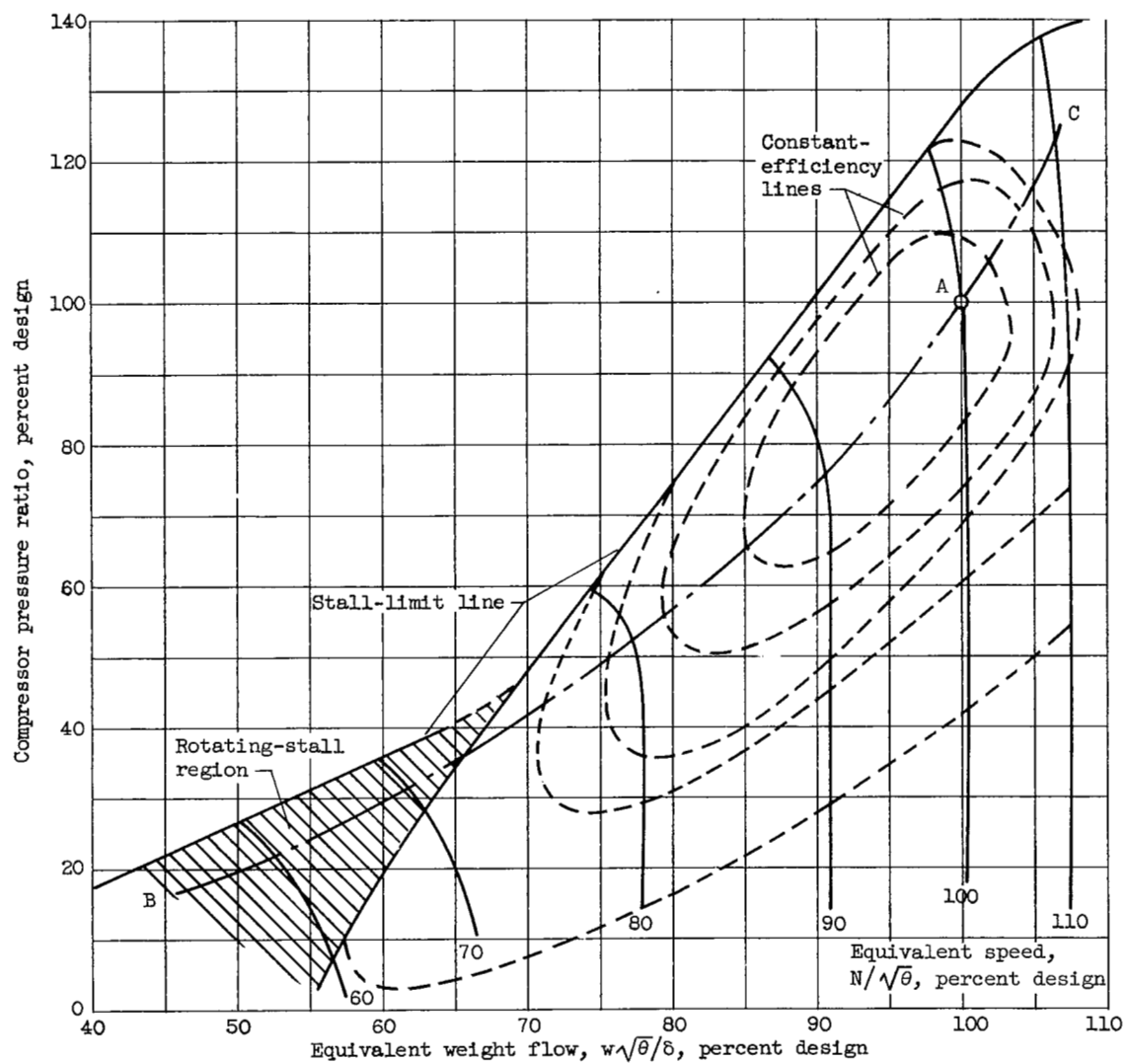
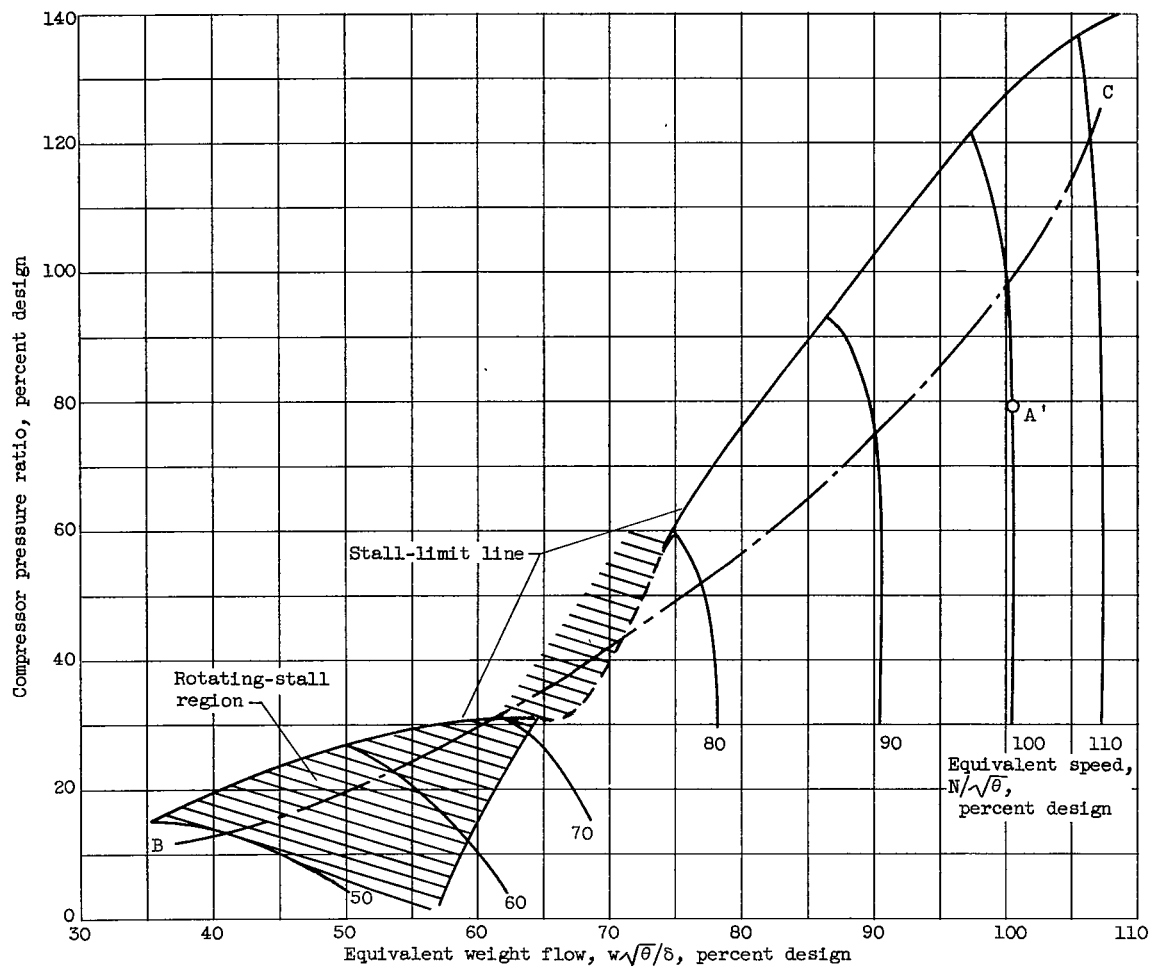


Figure 23. - Possible layout of axial-flow compressor and exit diffuser.



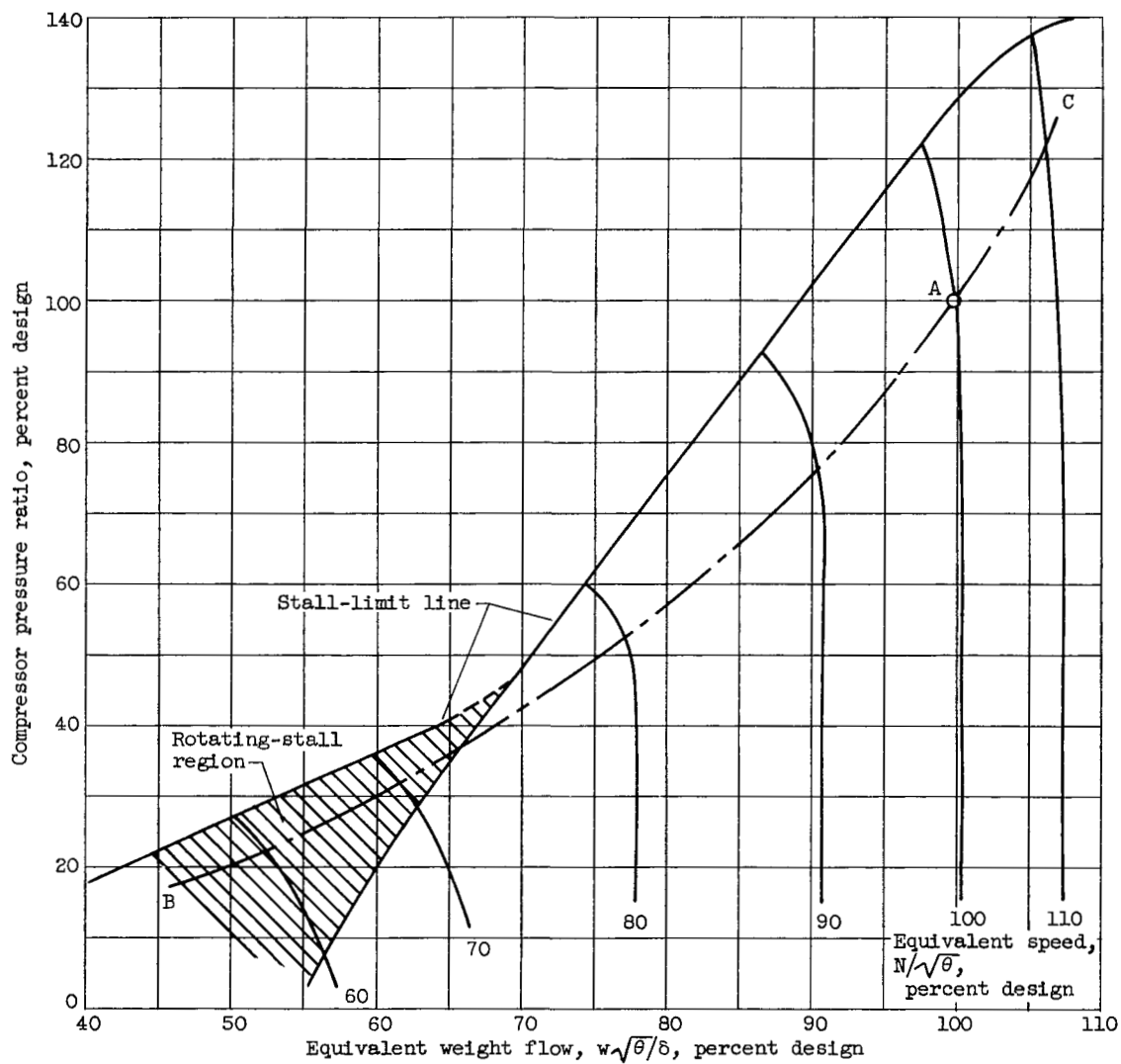
(a) Operating line for sea-level static conditions.

Figure 24. - Compressor maps for various operating conditions.



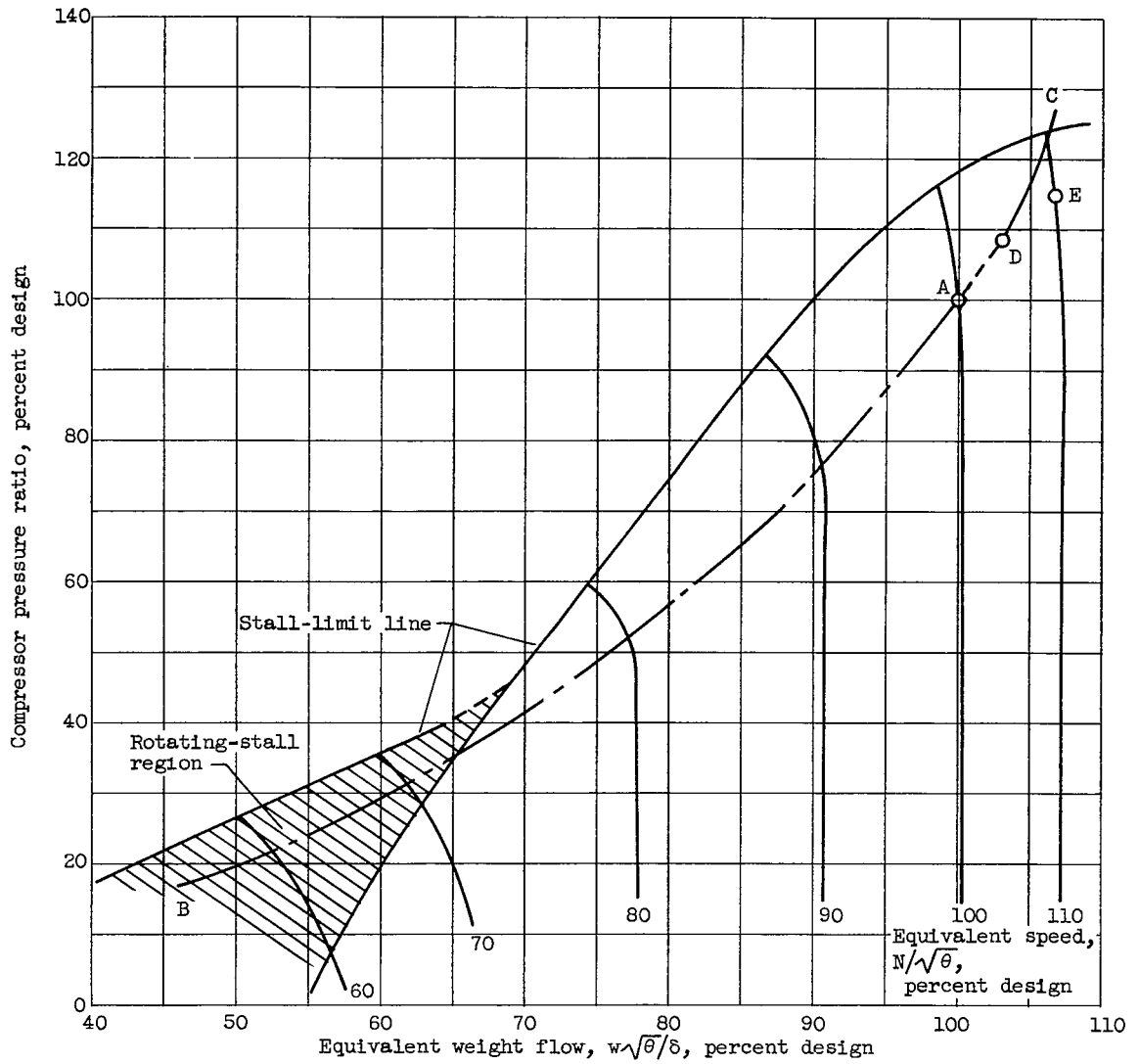
(b) Sea-level static operating line intersecting stall-limit line.

Figure 24. - Continued. Compressor maps for various operating conditions.



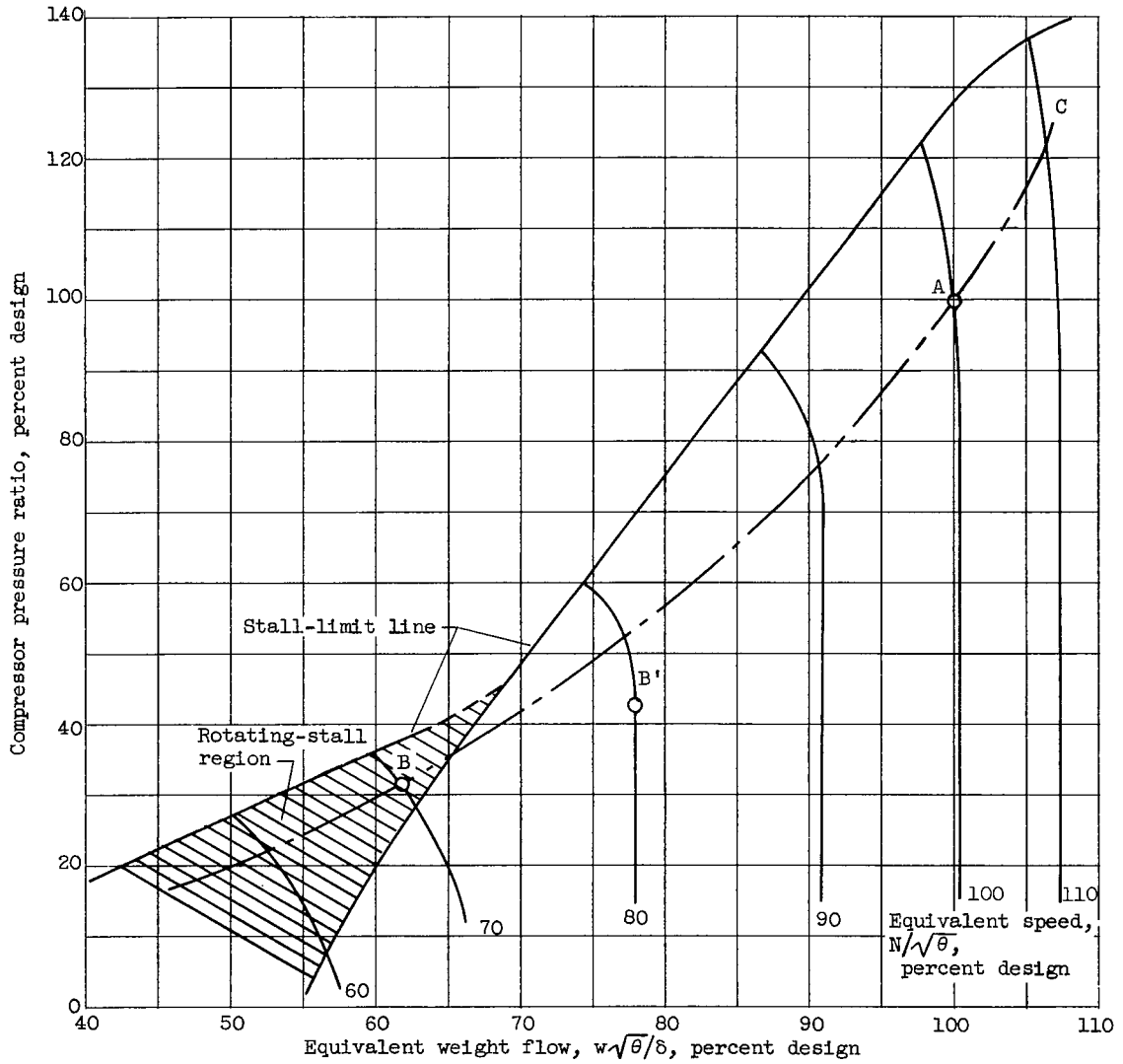
(c) Operating line for fixed engine mechanical speed over range of flight Mach numbers.

Figure 24. - Continued. Compressor maps for various operating conditions.



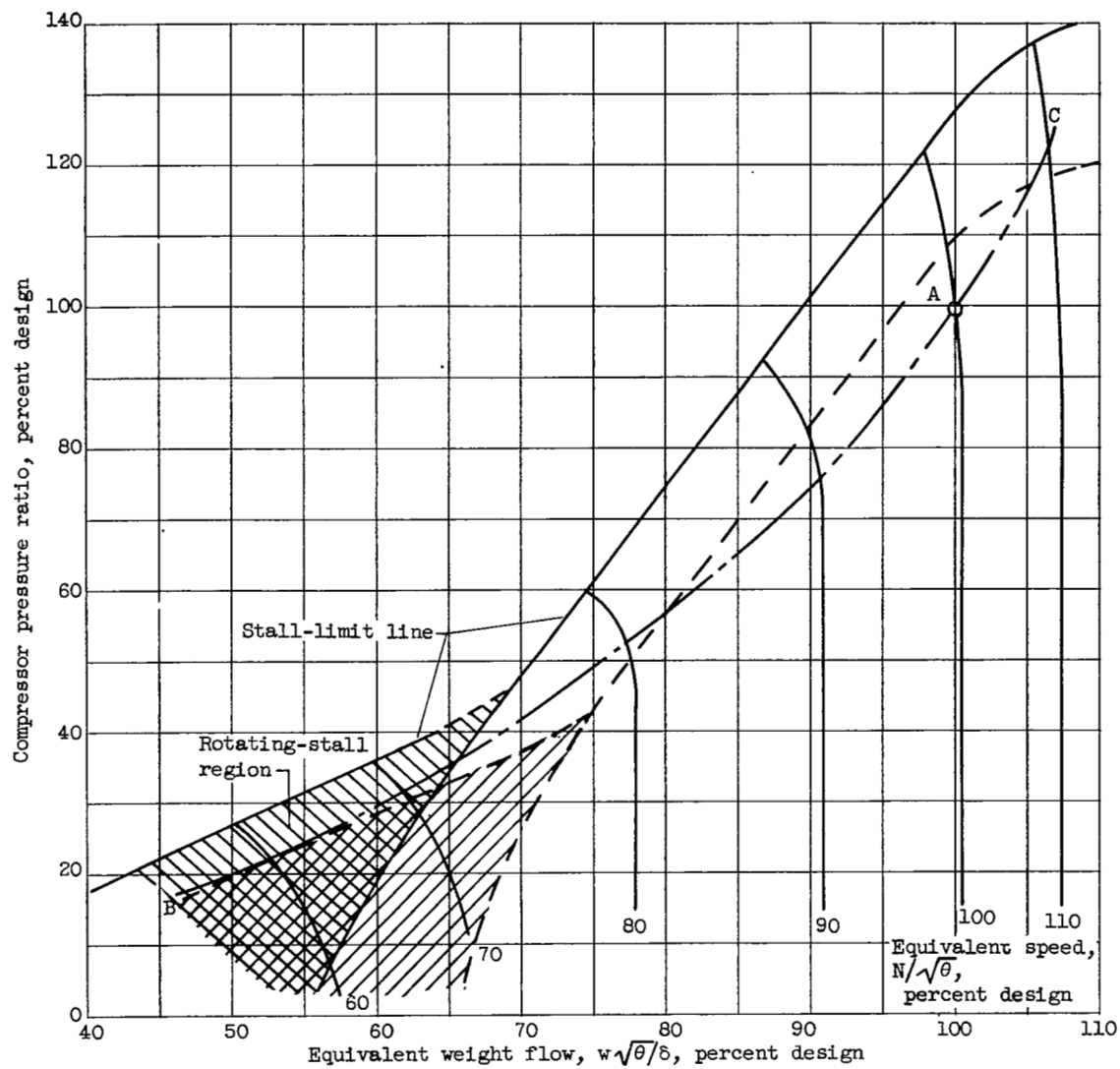
(d) Operating line intersecting stall-limit line at low flight speeds in stratosphere.

Figure 24. - Continued. Compressor maps for various operating conditions.



(e) Change in operating point resulting from increasing engine speed and opening exhaust nozzle.

Figure 24. - Continued. Compressor maps for various operating conditions.



(f) Effect of inlet flow distortions.

Figure 24. - Concluded. Compressor maps for various operating conditions.



(a) Critical operation.



(b) Supercritical operation.



(c) Subcritical operation.

Figure 25. - Shock-wave configurations on engine inlets.

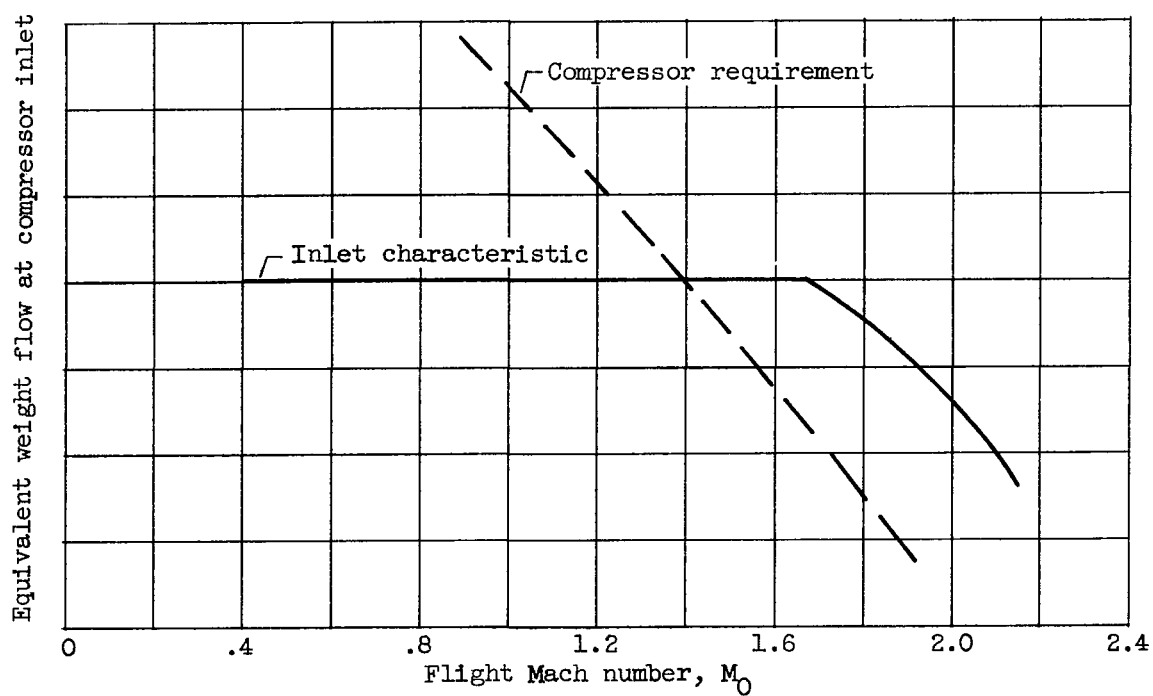
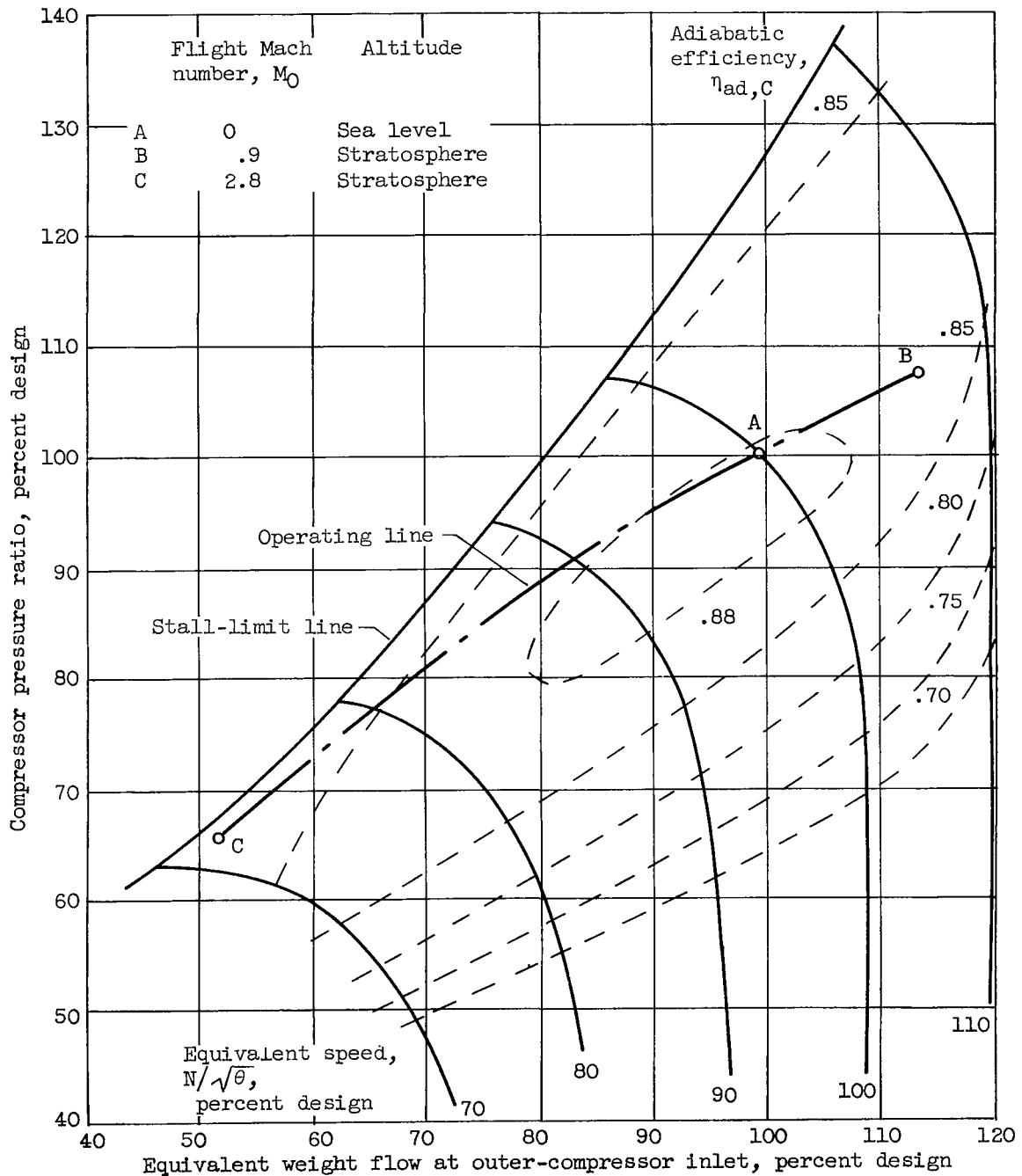
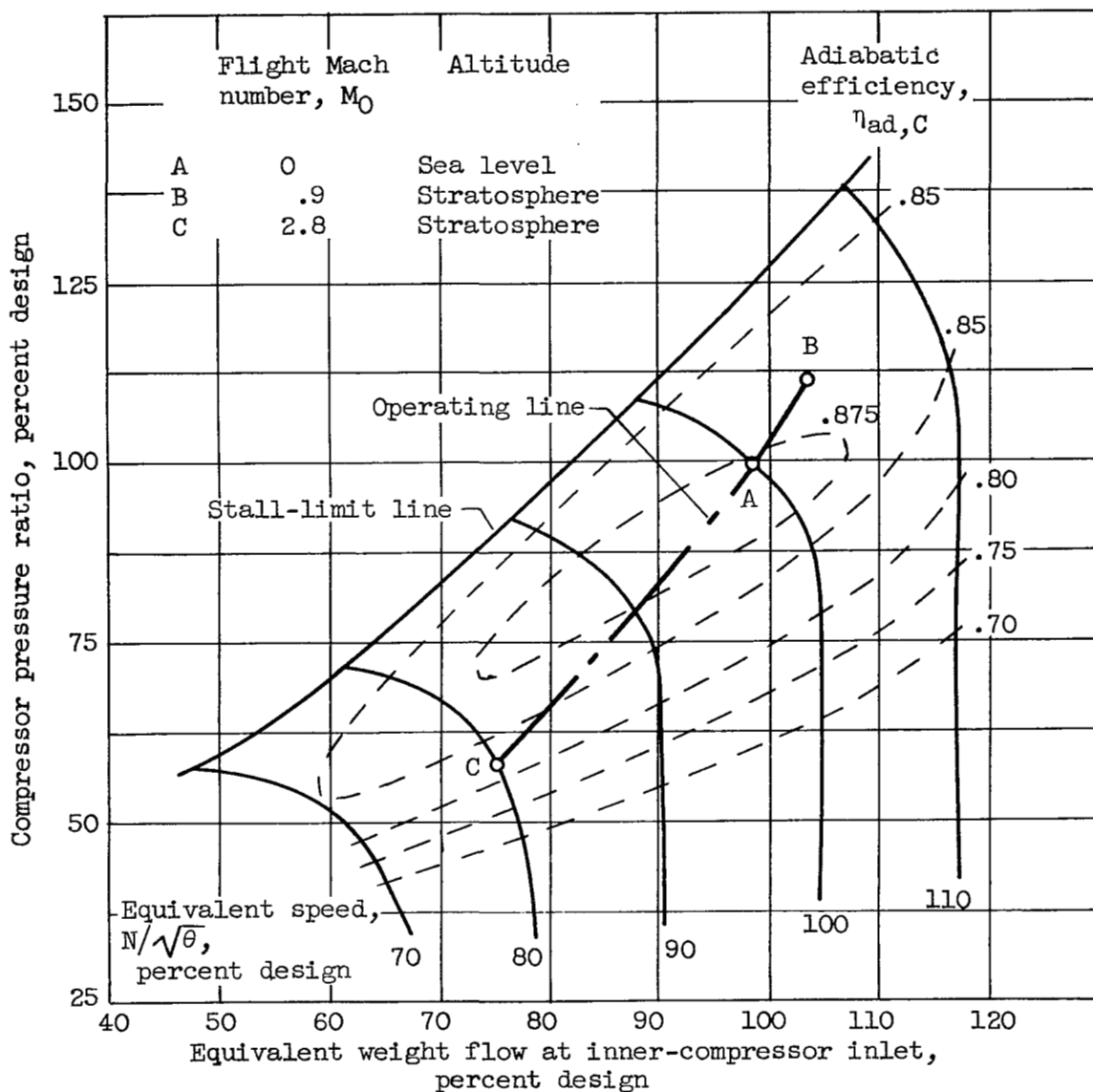


Figure 26. - Engine and inlet matching requirements.



(a) Outer-compressor performance map.

Figure 27. - Off-design compressor performance in two-spool turbojet engine (ref. 21).



(b) Inner-compressor performance map.

Figure 27. - Concluded. Off-design compressor performance in two-spool turbojet engine (ref. 21).

CHAPTER III

COMPRESSOR DESIGN SYSTEM

By Robert O. Bullock and Irving A. Johnsen

SUMMARY

A general description is presented for the compressor design system that has been adopted for this report on the aerodynamic design of axial-flow compressors. The basic thermodynamic equations are given, and the simplifications commonly introduced to permit the solution of these equations are summarized. Representative experimental data are presented to justify these simplifications. Thus, a valid simplified flow model (which is the real basis of a design system) is provided. The individual elements of the design system and the basic calculations required to execute the aerodynamic design of a compressor are summarized. The improvements in knowledge required to make compressor design a truer science and promising directions of future research are indicated.

INTRODUCTION

The problem of designing axial-flow compressors ultimately becomes the problem of accurately calculating the flow through compressor blade rows. In order to be accurate and have the greatest range of applicability, these calculations should be based on the fundamental laws of motion as much as possible. At the same time, they should be of such a nature that they can be made readily with available computing techniques and equipment.

To be strictly accurate, the fundamental theory should account for the fact that the motion of the air has components in the three physical dimensions. It must also account for the effects of viscosity as well as time-unsteady motion. By assessing each particle of air with these requirements, the differential equations of motion may be derived. The Navier-Stokes equations are, for example, obtained from this procedure. Although they are of great theoretical interest, these equations themselves are of little use in compressor design. They cannot yet be solved to express the flow through the complicated flow passages formed by the blades, the hub, and the casing.

In order to obtain more tractable methods of analysis, various techniques have been devised which combine simplified theories with empirical data. The simplifications made to the equations of motion are essentially the same as the simplifications that have been developed for airfoil analyses. The foundations of the simplified theories are thus the time-steady equations of the motion of an inviscid gas. In this attack, it is tacitly assumed that any important effects of viscosity and time-unsteady flow can be treated as correction factors and that the effects of viscosity are confined to thin boundary layers. The important flow properties not directly given by the simplified equations of motion must be obtained empirically.

The simplified equations, together with the empirical data required to calculate the flow with a reasonable degree of accuracy, constitute a framework for analysis or a design system. The techniques presented in references 1 to 5 are representative of such a system. It is the purpose of the present series of reports to derive an up-to-date design framework and to review the extensive published analytical and experimental results that are the building blocks for this framework. The function of this particular chapter is to coordinate the subsequent chapters by summarizing the important ideas presented in them. Therefore, the following are reviewed: (1) the important ideas underlying the design system, (2) some experimental investigations directed at examining these ideas, (3) the design system and the basic calculations required to execute the aerodynamic design of a compressor, and (4) the improvements in knowledge required to make compressor design a truer science.

The basic thermodynamic equations are first presented, and the general goals of aerodynamic flow analyses outlined. The equations of motion for an inviscid time-steady flow are introduced. The problem of solving these equations is then discussed. Some of the commonly used simplifications are presented and the experimental data necessary to justify these simplifications are noted. Some rather obvious ways of treating the important viscous effects are indicated, and the experiments required both to evaluate these methods and to supply the necessary empirical data are enumerated. Some causes of time-unsteady flows and the approach used to account for them are then presented.

Representative experiments which answer the questions raised in the foregoing analyses are then reviewed. These results provide a valid simplified model of the flow, which is the real basis of a design system. In developing this model, the results of experiments with the simplest conceivable flows are first considered. The effects of complicating flows are then discussed one by one whenever possible. The scope of the investigations is the range over which data are available.

The elements of the resulting design system are then individually summarized. The basic equations and techniques are given. The interrelations among the various elements are pointed out, but no attempt

is made to prescribe an actual sequence for their use. In this manner, the structure of a compressor design system is provided, within which the individual designer may work with considerable freedom.

Finally, the shortcomings of the previously outlined approaches are enumerated, and the direction of future research is discussed. Some promising though unproved techniques of analysis are mentioned.

SYMBOLS

The following symbols are used in this chapter:

a_a	stagnation velocity of sound
\mathcal{C}	curvature of meridional streamlines, see fig. 34
c	chord length, see fig. 2
D	diffusion factor, defined by eq. (25)
\mathcal{F}_c	centrifugal force due to curvature of meridional streamline, see fig. 34
$\mathcal{F}_{fr,r}$	radial component of frictional force
\mathcal{F}_R	centrifugal force due to rotation of air about axis of compressor
g	acceleration due to gravity, 32.17 ft/sec ²
H	total or stagnation enthalpy per unit mass
I	modified total enthalpy, $H - \omega(rV_\theta)$, see eqs. (10) and (19b)
i	incidence angle, angle between inlet-air direction and tangent to blade mean camber line at leading edge (see fig. 2), deg
J	mechanical equivalent of heat, 778.2 ft-lb/Btu
K_{bk}	weight-flow blockage factor, implicitly defined in eq. (24a)
M	Mach number
P	total or stagnation pressure
p	static or stream pressure
R	gas constant, 53.35 ft-lb/(lb)(°R)

r	radius
S	entropy per unit mass
ΔS	entropy increase in stream tube between inlet and outlet of a blade row
s	blade spacing, see fig. 2
T	total or stagnation temperature
t	static or stream temperature
V	air velocity
w	weight flow
z	distance along compressor axis
α	angle of attack, angle between inlet-air direction and blade chord ($\alpha = \beta_1 - \gamma^0$, see fig. 2), deg
β	air angle, angle between air velocity and axial direction (see fig. 2), deg
$\Delta\beta$	turning angle, $\beta_2 - \beta_1$ (see fig. 2), deg
Γ	circulation, rV_θ
γ	ratio of specific heats
γ^0	blade-chord angle, angle between blade chord and axial direction (see fig. 2), deg
δ	boundary-layer thickness, see fig. 12
δ^0	deviation angle, angle between outlet-air direction and tangent to blade mean camber line at trailing edge (see fig. 2), deg
ϵ	angle between tangent to streamline projected on meridional plane and axial direction (fig. 34), deg
ζ	vorticity
η	efficiency
θ	angular distance

μ	viscosity
ρ	mass density
σ	solidity, ratio of chord to spacing
ϕ	blade camber angle, difference between angles of tangents to mean camber line at leading and trailing edges, deg
ω	angular velocity of rotor
ω_{air}	angular velocity of air for solid-body rotation
$\bar{\omega}$	total-pressure-loss coefficient, see eq. (29)

Subscripts:

ad	adiabatic
h	hub
i	initial or reference position
id	ideal
m	arithmetic mean
p	polytropic
r	radial direction
t	tip
z	axial direction
θ	tangential direction
1	station at inlet to blade row
2	station at blade-row exit

Superscript:

'	relative to rotor
---	-------------------

FUNDAMENTAL CONCEPTS UNDERLYING DESIGN SYSTEM

Equations of Thermodynamics

The design or analysis problem may be stated as the problem of determining how the shape of a blade row alters the thermodynamic flow properties and velocities of each particle of gas flowing through it. The changes in the total (or stagnation) state as well as the changes in the static state of the gas are of interest.

In order to avoid unnecessary complications in the thermodynamic equations, it has usually been the custom to assume that the entire flow may be subdivided into individual tubes of flow that maintain their identity. Another assumption is that there are no important effects of heat transfer into or out of these tubes of flow. (In the discussion of experimental data, it will be shown that these assumptions usually do not cause serious errors.) By virtue of these assumptions, the change in the total enthalpy or total temperature in the stream tube of the gas is equated to the mechanical energy transferred to it by the compressor rotors. The changes in both the total and static states of a gas can then be expressed in terms of the component velocities.

Flow through stators. - Since no energy is added to the flow by the stators, the total enthalpy and total temperature of a stream tube of the flow through stators are constant:

$$H_1 = \frac{\gamma}{\gamma-1} gRT_1 = \frac{\gamma}{\gamma-1} gRT_2 = H_2 \quad (1)$$

From the definition of total and static states, this equation may be written as

$$\begin{aligned} H_1 &= \frac{\gamma}{\gamma-1} gRt_1 + \frac{1}{2} V_{r,1}^2 + \frac{1}{2} V_{z,1}^2 + \frac{1}{2} V_{\theta,1}^2 \\ &= \frac{\gamma}{\gamma-1} gRt_2 + \frac{1}{2} V_{r,2}^2 + \frac{1}{2} V_{z,2}^2 + \frac{1}{2} V_{\theta,2}^2 = H_2 \end{aligned} \quad (2)$$

This equation relates the change in static temperature to the changes in the individual components of velocity.

If there is an increase in entropy through a stream tube (e.g., from friction or an interchange of heat within the stream tube itself), the total pressure changes according to the equation

$$\frac{P_2}{P_1} = e^{-\frac{\gamma}{R} \Delta S} \quad (3)$$

When the change in entropy, or total pressure, is known, the changes in static pressure and density corresponding to the changes in static temperature may be determined. Static pressures are related by the equation

$$\frac{p_2}{p_1} = \left(\frac{t_2}{t_1} \right)^{\frac{\gamma}{\gamma-1}} \frac{p_2}{p_1} \quad (4)$$

The densities are then related to the pressures and temperatures by the gas law

$$p = \rho g R t \quad (5)$$

or

$$\frac{\rho_2}{\rho_1} = \frac{p_2}{p_1} \frac{t_1}{t_2} \quad (6)$$

Equations (5) and (6) may, of course, also be used to relate the total conditions of state.

If the changes in the velocity components and the entropy in a stream tube are known, the resulting changes in static temperature, total and static pressure, and total and static density can be determined.

Flow through rotors. - Since the rotors do work on the gas, the enthalpy of a tube of flow changes through the rotor according to Euler's turbine equation:

$$H_2 - H_1 = \omega(r_2 V_{\theta,2} - r_1 V_{\theta,1}) \quad (7)$$

or

$$\begin{aligned} \frac{\gamma}{\gamma-1} g R t_1 + \frac{1}{2} V_{r,1}^2 + \frac{1}{2} V_{z,1}^2 + \frac{1}{2} V_{\theta,1}^2 - \omega r_1 V_{\theta,1} &= \frac{\gamma}{\gamma-1} g R t_2 + \frac{1}{2} V_{r,2}^2 + \\ \frac{1}{2} V_{z,2}^2 + \frac{1}{2} V_{\theta,2}^2 - \omega r_2 V_{\theta,2} & \end{aligned} \quad (8)$$

Notice that the changes in V_{θ} due to casing friction are ignored in these equations.

Since a stationary observer could not observe continuous tubes of flow through a rotor, recourse is frequently made to relative flow conditions, where the observations are theoretically made from the rotor itself. Continuous stream tubes can then be distinguished. The relative velocities are related to the absolute velocities by the equations

$$\left. \begin{aligned} V'_r &= V_r \\ V'_z &= V_z \\ V'_\theta &= V_\theta - \omega r \end{aligned} \right\} \quad (9)$$

(V'_θ is usually negative in the compressor case in the sense that ωr is positive.) Equation (7) then becomes

$$I_1 = H'_1 - \frac{1}{2} \omega^2 r_1^2 = H'_2 - \frac{1}{2} \omega^2 r_2^2 = I_2 \quad (10)$$

where

$$H' = \frac{\gamma}{\gamma-1} gRT' = \frac{\gamma}{\gamma-1} gRt + \frac{1}{2} (V'_r)^2 + \frac{1}{2} (V'_z)^2 + \frac{1}{2} (V'_\theta)^2 \quad (11)$$

When only the flow ahead of and behind the rotor is of interest, the use of relative quantities is not necessary; in this case equation (8) may also be applied to relate the changes in total and static temperatures with the changes in the individual components of velocity.

The corresponding changes in total pressure are given by

$$\frac{P_2}{P_1} = \left(\frac{T_2}{T_1} \right)^{\frac{\gamma}{\gamma-1}} e^{-\frac{J}{R} \Delta S} = \left(\frac{T_2}{T_1} \right)^{\frac{\gamma}{\gamma-1}} \eta_p = \left[1 + \left(\frac{T_2}{T_1} - 1 \right) \eta_{ad} \right]^{\frac{\gamma}{\gamma-1}} \quad (12)$$

$$\frac{P'_2}{P'_1} = \left(\frac{T'_2}{T'_1} \right)^{\frac{\gamma}{\gamma-1}} e^{-\frac{J}{R} \Delta S} \quad (13)$$

(The magnitude of ΔS for absolute quantities is the same as for relative quantities.) The resulting change in static pressure is given by

$$\frac{p_2}{p_1} = \left(\frac{t_2}{t_1} \right)^{\frac{\gamma}{\gamma-1}} \frac{\frac{P_2}{P_1}}{\left(\frac{T_2}{T_1} \right)^{\frac{\gamma}{\gamma-1}}} = \left(\frac{t_2}{t_1} \right)^{\frac{\gamma}{\gamma-1}} \frac{\frac{P'_2}{P'_1}}{\left(\frac{T'_2}{T'_1} \right)^{\frac{\gamma}{\gamma-1}}} \quad (14)$$

The corresponding density changes may be determined by equations (5) and (6).

With these relations, the changes in total and static states of a gas can be determined when the changes in the velocity components, the entropy, and the radius of the stream tube (measured from the axis) can be estimated. The concepts discussed in the rest of this section were developed with the idea of making these estimates.

Analysis of Time-Steady and Inviscid Flow

As will be shown in chapter XIV (ref. 6), the three-dimensional equations of motion of even time-steady and inviscid flow are much too complicated for general use at the present time. Coping with all the three-dimensional gradients in the motion and properties of the gas is too big a problem for routine analysis. An inviting simplification appears, however, when the radial components of velocity in a blade row are small enough to be ignored.

Equations ignoring radial velocity. - Stationary blade row: Ignoring the radial components of velocity is tantamount to assuming that a streamline of the flow lies on the surface of a right circular cylinder (fig. 1). If this surface and its streamlines are developed into a plane, the streamlines through a two-dimensional cascade of airfoils are obtained (fig. 2).

When the radial velocity is ignored, the equation of continuity (reviewed in ch. XIV (ref. 6)) becomes

$$\frac{\partial(\rho v_\theta)}{r \partial \theta} + \frac{\partial(\rho v_z)}{\partial z} = 0 \quad (15)$$

The basic equations for the radial, axial, and tangential components of vorticity are, respectively,

$$\frac{\partial v_z}{r \partial \theta} - \frac{\partial v_\theta}{\partial z} = \zeta_r \quad (16)$$

$$\frac{1}{r} \frac{\partial(r v_\theta)}{\partial r} - \frac{\partial v_r}{r \partial \theta} = \zeta_z \quad (17)$$

$$\frac{\partial v_r}{\partial z} - \frac{\partial v_z}{\partial r} = \zeta_\theta \quad (18)$$

If the inviscid flow is originally without vorticity, it will remain this way; ζ_r is then zero. Inasmuch as r is assumed to be constant along a streamline, equations (15) and (16) then represent the flow through a two-dimensional cascade of airfoils. Figure 2 is thus again shown to represent the flow at a given radius for the assumed conditions of figure 1.

If V_r as well as ζ_z is zero, equation (17) becomes

$$\frac{1}{r} \frac{\partial(rV_\theta)}{\partial r} = 0$$

and $rV_\theta = \Gamma = \text{constant}$ along a radial line. This distribution of tangential velocity is known as free-vortex flow. Similarly, equation (18) becomes

$$\frac{\partial V_z}{\partial r} = 0$$

and $V_z = \text{constant}$ along a radial line.

Besides these relations, equation (7b) of chapter XIV (ref. 6) must also be satisfied. This equation may be written as, neglecting any radial forces exerted by the blades,

$$\frac{\partial H}{\partial r} - t \frac{\partial S}{\partial r} = V_\theta \zeta_z - V_z \zeta_\theta \quad (19)$$

If radial flows are neglected, this equation becomes

$$\frac{\partial H}{\partial r} - t \frac{\partial S}{\partial r} = \frac{V_\theta}{r} \frac{\partial(rV_\theta)}{\partial r} + V_z \frac{\partial V_z}{\partial r} \quad (19a)$$

When ζ_z and ζ_θ are zero, then the right side of this equation must be zero. The left side of this equation must also be zero - a condition which is realized when there are no radial gradients in enthalpy or entropy.

It may be noted that equation (19) is also applicable when the axial and tangential components of vorticity are not zero. For the condition of no radial flow, one component of vorticity (say ζ_z) may be stipulated by the radial variation of V_θ (eq. (17)). If the radial variations in enthalpy and entropy are also given, then the radial variations in V_z are determined by equations (18) and (19).

Rotating blade rows: In order to utilize steady-flow equations in rotors, the flow in rotors is referred to a coordinate system that rotates at rotor speed. The velocities in the rotating coordinate system (the relative velocities) are related to the absolute velocities by equations (9), which are rewritten here as

$$\left. \begin{aligned} V_r &= V_r' \\ V_z &= V_z' \\ V_\theta &= V_\theta' + \omega r \end{aligned} \right\} \quad (9)$$

Again $V_r' = 0$; the relative velocities are then directly substituted for the absolute velocities in equation (15), and

$$\frac{\partial(\rho V_\theta')}{r \partial \theta'} + \frac{\partial(\rho V_z')}{\partial z} = 0 \quad (15a)$$

The corresponding equations for the radial, axial, and tangential components of vorticity are

$$\frac{\partial V_z'}{r \partial \theta'} - \frac{\partial V_\theta'}{\partial z} = \zeta_r' = \zeta_r \quad (16a)$$

$$\frac{1}{r} \frac{\partial(r V_\theta')}{\partial r} - \frac{\partial V_r'}{\partial \theta'} = \zeta_z' = \frac{1}{r} \frac{\partial(r V_\theta')}{\partial r} - \frac{\partial V_r}{\partial \theta} - 2\omega = \zeta_z - 2\omega \quad (17a)$$

$$\frac{\partial V_r'}{\partial z} - \frac{\partial V_z'}{\partial r} = \zeta_\theta' = \zeta_\theta \quad (18a)$$

If the radial flows and absolute vorticity are again assumed to be zero, equations (15a) and (16a) become the equations of a two-dimensional cascade. This simplification of flow equations is thus applicable to rotors as well as stators.

Equation (17a) may then be integrated along a radial line to become

$$r V_\theta' = \Gamma - \omega r^2 = r(V_\theta - \omega r)$$

In order to meet the requirements of no tangential gradients in the radial flow through a rotor, the absolute flow along a radial line must be defined by

$$r V_\theta = \Gamma$$

This is the same requirement previously derived for stators. The tangential velocity distributions for rotors and stators are thus compatible. Similarly, the integration of equation (18a) shows the compatibility of axial velocity, namely,

$$V_z = \text{constant}$$

As shown in chapter XIV (ref. 6, eq. (7c)), the equation analogous to equation (19a) is

$$\frac{\partial I}{\partial r} - t \frac{\partial S}{\partial r} = \frac{V_\theta'}{r} \frac{\partial(r V_\theta')}{\partial r} + V_z \frac{\partial V_z}{\partial r} \quad (19b)$$

where, according to equation (10),

$$I = H' - \frac{1}{2} \omega^2 r^2 = H - \omega r V_\theta = H - \omega^2 r^2 - \omega r V_\theta'$$

If H and rV_θ are constant along a radial line, then I is also constant along a radial line. If the entropy is also constant along a radial line, equation (19b) is satisfied for free-vortex flows. Equation (19b), like equation (19), may be used when the vorticity components are not zero. The procedure involved is similar to that previously outlined.

When radial flows do not have important effects, the analysis of flow in a blade row is relatively simple. The three-dimensional problem for both stators and rotors is broken down into the two-dimensional-cascade problem and the separate problem of determining the radial distribution of the flow. It is, of course, practically impossible to eliminate radial flows completely. Because of the simplification offered by this type of approach, however, it has been deemed advisable to seek and study those designs in which the radial flows are small. Attention is therefore directed to the study of the causes of radial flows in a blade row. The question concerning admissible radial flows is temporarily deferred to the review of experimental data.

Causes of radial flows. - Changes in radial density gradients: One cause of radial flows is the change in the radial density gradient between the inlet and the outlet. If the radial velocities are zero, the hydrodynamic equation of equilibrium (eq. (4) of ch. XIV (ref. 6)) becomes

$$\frac{1}{\rho} \frac{\partial p}{\partial r} = \frac{V_\theta^2}{r}$$

If $V_\theta = \Gamma/r$ and there are no radial gradients in entropy (i.e., $p = C_p \Gamma$), this equation may be solved to read

$$\frac{r}{r-1} C_p \Gamma^{-1} = \left(\text{constant} - \frac{\Gamma^2}{2r^2} \right)$$

A change in Γ through a blade row therefore makes the radial distribution of density behind the blade row different from that in front of it. Figure 3 shows a representative change in the radial distribution of density for a blade row through which Γ is increased from 150 to 300 feet squared per second. Also shown in this figure is the change in rpV_z .

Continuity of mass flow requires the following equation to be satisfied in a stream tube:

$$\int_{r_{i,1}}^{r_{t,1}} \rho_1 V_{z,1} r \, dr = \int_{r_{i,2}}^{r_{t,2}} \rho_2 V_{z,2} r \, dr \quad (20)$$

where the subscripts 1 and 2 refer to conditions far enough upstream and downstream of the blade row that V_r is practically zero and any circumferential gradients have disappeared; and r_i and r_t refer to the radius of a given streamline and that of the tip (or casing), respectively (see fig. 4). Notice, however, that equation (20) is valid even when V_r is finite.

In the vicinity of the tip, rpV_z has a greater value behind the blade row than in front of it (fig. 3). The distance ($r_t - r_i$) between two adjacent streamlines near the tip is therefore expected to decrease as rpV_z increases if r_t is constant. As shown by streamline A of figure 4, this trend does occur and the streamline moves radially outward. (This drawing actually represents the projection of the flow on a plane through the axis. This representation is conventionally called the flow lines in the meridional plane.) A radial component of velocity, as indicated by the slope of the dashed streamline, must therefore exist within the blade row. Near the hub, on the other hand, the value of rpV_z decreases through the blade row and the distance between streamline B and the hub is greater behind the blade row than in front of it. In this case, the motion of the streamline is again radially outward, and radial components of velocity must again exist within the blade row.

Even for ideal conditions, therefore, where the tangential and axial components of velocity upstream and downstream of the blade row satisfy the requirements for no radial velocities, some radial flow must take place within the blade row. The magnitudes of the radial flows increase with the change in Γ through the blade row and with the corresponding change in rpV_z .

Blade thickness distribution: Another source of radial flow is the radial distribution of blade thickness. Some aspects of this problem are discussed in reference 7. Ahead of the blade row, a cross section of the stream surface in a plane normal to the axis would look like that shown in figure 5(a). A streamline of the flow between two adjacent blades lies within the area of the sector bounded by A-A and B-B. Because of blade thickness, these lateral boundaries are changed to C-C and D-D within the blade row (figs. 5(b) and (c)). If C-C and D-D are also radial lines (fig. 5(b)), the area of each of the original stream tubes is reduced uniformly along the radius. The radial position of the streamlines then tends to remain unchanged. In the more usual case, the lines C-C and D-D are not radial lines; then, as indicated in figure 5(c), the flow would be deflected outwards with respect to that of figure 5(a). The areas of the original stream tubes are not uniformly reduced, and some radial adjustment of the streamlines is required to

compensate for this. Some notion of the resulting flows is given in reference 7. As shown in figure 6, this reference indicates that radial flow starts ahead of the blade row. A maximum radial displacement occurs within the blade row, and thereafter a radially inward flow begins and continues downstream of the blade row.

Radial component of blade force: Still another source of radial flow is the radial component of blade force. This concept is reviewed in chapter XIV (ref. 6). The turning of the air at any point in a blade row is the result of tangential forces originating on the surface of a blade. The direction of these forces, however, must be perpendicular to the corresponding blade surfaces. If the surfaces are inclined to the radius, a radial component of force is imposed on the flow, and radial flows may thereby be induced. Since the forces on the high-pressure surface of the blade are dominant, the radial movements of the flow depend on the angle between this surface and a radial line. Depending upon how the blade elements are radially aligned, inward or outward radial velocities could be generated. In the blade of figure 7(a), the predominant force is radially outward; so is the radial component of the flow. For figure 7(b), in which the shape of the individual cascade elements at each radius is the same as that of figure 7(a), the flow would be first inward, then outward.

Non-free-vortex flow: In order to alleviate some problems arising from Mach number limits, such as those described in reference 8, tangential velocity distributions differing from the free-vortex type are frequently used. One type of tangential velocity distribution that tends to overcome these difficulties is given by the equation

$$V_{\theta} = \omega_{\text{air}} r + \frac{\Gamma}{r} \quad (21)$$

where both ω_{air} and Γ are constant. Other distributions could also be used, but this type permits a simple discussion of nonvortex distributions. Suppose now that uniform flow entered a row of blades designed to produce this distribution at the outlet. Since the flow is originally without vorticity, equation (17) becomes

$$2\omega_{\text{air}} - \frac{\partial V_r}{r \partial \theta} = 0$$

and tangential variations in radial velocity are thus introduced.

The resulting flows can be visualized by dividing V_{θ} into three parts,

$$V_{\theta} = V_{\theta,a} + V_{\theta,b} + V_{\theta,c}$$

where

$$\frac{1}{r} \frac{\partial(rV_{\theta,a})}{\partial r} = 0$$

$$\frac{1}{r} \frac{\partial(rV_{\theta,b})}{\partial r} = 2\omega_{\text{air}}$$

$$\frac{1}{r} \frac{\partial(rV_{\theta,c})}{\partial r} - \frac{\partial V_r}{r \partial \theta} = -2\omega_{\text{air}}$$

The velocity $V_{\theta,a}$ is that required for free-vortex flow. The circumferential-plane streamlines for the condition of no through-flow are shown in figure 8(a). The velocity $V_{\theta,b}$ represents the rotation of a solid body, and the corresponding streamlines are shown in figure 8(b). The flow determined by $V_{\theta,c}$ is more complex. No general solution to this flow has been found, but solutions for several particular conditions are presented in reference 9. The streamlines for two of these solutions are shown in figures 8(c). In general, both $V_{\theta,c}$ and V_r must vary in the tangential direction. This trend is suggested by figure 8(c). It is evident that the velocity defined by equation (21) really cannot exist at every circumferential position. Equation (21), however, is approximated at every circumferential position when the blades are close enough together that the actual circumferential changes in V_{θ} and V_r are very small. The velocity $V_{\theta,c}$ might then be ignored. The change in V_r along the circumference could also be ignored. In this event, one could write

$$V_{\theta} = V_{\theta,a} + V_{\theta,b} = \omega_{\text{air}} r + \frac{\Gamma}{r}$$

The resulting streamlines are those of figure 8(a) combined with figure 8(b).

The vorticity represented by this flow, however, is $2\omega_{\text{air}}$. This result means that vorticity must be added to the flow by the blade row. Such a thing cannot be done in an ideal fluid, because the vortex lines would extend downstream of the blades and they would be confined to infinitesimally thin sheets. Between them, the flow would be irrotational. Inasmuch as these vortex sheets actually enclose the wakes in a real fluid, they eventually do permeate the entire flow field by the mixing of the wakes with the rest of the flow. Accordingly, for a reasonably close spacing between the blades, the entire flow could be assumed to have an axial component of vorticity of $2\omega_{\text{air}}$ downstream of a blade row, even though the upstream vorticity is zero. (For a further discussion of this point, see ref. 10.)

In this event, equation (17) may be used, and

$$\frac{1}{r} \frac{\partial(rV_\theta)}{\partial r} = 2\omega_{\text{air}} = \zeta_z$$

Equation (19) can then be written as

$$\frac{\partial H}{\partial r} - t \frac{\partial S}{\partial r} = 2\omega_{\text{air}} V_\theta - V_z \zeta_\theta \quad (19c)$$

With uniform enthalpy and entropy, equation (19c) is written

$$V_z \zeta_\theta = 2\omega_{\text{air}} V_\theta$$

By using equation (18), this equation becomes

$$2\omega_{\text{air}} V_\theta + V_z \frac{\partial V_z}{\partial r} = V_z \frac{\partial V_r}{\partial z}$$

Here again, radial flows are required, since $\partial V_r / \partial z$ cannot, in general, be zero. In many designs, these radial flows are far from negligible within a blade row and may be considerably more severe than those previously discussed. Far enough downstream of the blade row, the radial flow must disappear. Some studies of these flows are reviewed in chapter XIV (ref. 6).

For other radial distributions of tangential components of velocity, other equations must be used to describe the flow. The important point to note, however, is that additional radial flows tend to be introduced whenever the distribution is not that of a free vortex. These radial flows not only exist within the blade row but also may be found upstream and downstream of it.

Shape of hub and casing: Some radial flows must exist in the vicinity of the hub and casing when the slope is not zero (fig. 9). Such configurations usually cannot be avoided because of the exigencies of other considerations (blade surface velocity diffusion, attainable total-pressure ratio, etc.), which are discussed later in this chapter. The magnitude of the radial flows within and without the blade rows naturally increases as the slope of the boundaries increases.

Effect of radial flows on stream surface configuration. - As previously shown, the simplifying assumption of no radial flow presumes the streamlines of the flow to lie on the surfaces of right circular cylinders (fig. 1). The radial flows resulting from the changes in radial density gradients, the blade thickness distribution, and the radial component of blade force make these streamline surfaces undulate and twist as shown by comparing the upper surface of figure 10(a) with the lower surface. The additional disturbances encountered when rV_θ is not constant along

a radial line and when annulus walls converge are indicated in figure 10(b). The increased twisting of the surfaces results from the flows shown in figure 8(c)(left side).

Experimental data required. - Although the magnitudes of these radial flows can sometimes be estimated by mathematical analyses, their actual effects on the performance of a blade row must eventually be measured by experiment. The deflections of the air at a given radius of a blade row and those of a two-dimensional cascade having identical geometry and inlet conditions may be compared; the agreement between the two sets of results is a measure of the usefulness of the simple concepts obtained by ignoring radial flows. Similarly, a comparison of the measured radial distributions of flow with those given by equations (17) to (19) (with $V_r = 0$) provides another test of these concepts. The representative experimental data subsequently presented are examined from these points of view to show that, in many cases, the simple equations just derived provide an accurate estimate of the main flow.

Analysis of Viscosity Problem

Two-dimensional-cascade elements. - Following the procedures used in other fields of aerodynamics, compressor design and analysis techniques assume that the important effects of viscosity are confined to thin boundary layers and to blade wakes. For the cascade elements (defined in fig. 2), the boundary layers are indicated by the shaded areas immediately in contact with the blades in figure 11(a). Beyond the trailing edge of the blade, the boundary layers are shed as wakes. Within the shaded areas of the figure, the retarded flow of the wakes is mixed with the rest of the flow. The shaded areas, therefore, become wider in the direction of the flow. Far enough downstream, complete mixing would occur and the flow would be homogeneous.

A representative example of the velocity variation within a boundary layer is shown in figure 11(b), which presents the velocity distribution along a line A-A in figure 11(a). Between points a and b of figure 11(b), the effects of viscosity are small, because the velocity gradients are relatively small. Between the blade surfaces and points a or b, however, the velocity gradients are severe and viscous effects are dominant. Besides the indicated change in velocity, the total pressure, the entropy, and even the total temperature also vary. The static pressure, however, is likely to be approximately constant through the boundary layer.

One of the most important effects of viscosity is that it retards the relative flow in the boundary layers. (In making this statement, it is implied that the flow is viewed from the coordinate system attached to the blades. For stators, such a coordinate system is stationary, as

previously noted; for rotors, it moves at blade speed.) Because of the low relative flow, the boundary layer may be almost replaced by a region of no flow for inviscid-flow analyses. Effectively, then, the boundary layer changes the aerodynamic shape of the blades, a phenomenon which must be recognized in interpreting inviscid-flow analyses. Although some methods of partially correcting inviscid-flow analyses for these changes in boundary conditions have been developed, it has usually been more practicable to use experimental results as a source of two-dimensional-cascade data (ch. VI (ref. 11)). Two-dimensional-cascade inviscid-flow theory (ch. IV) may then be used to correlate these data.

Important data derived from two-dimensional-cascade experiments are the deflections or turning angles as functions of blade shape and inlet flow conditions. The turning angles are given by

$$\Delta\beta = (\beta_1 - \beta_2) = \left[\tan^{-1} \frac{V_{\theta,1}}{V_{z,1}} - \tan^{-1} \frac{V_{\theta,2}}{V_{z,2}} \right]$$

When the turning angle is known, the change in V_{θ} is a function of the change in V_z . Also of importance are the losses in the relative total pressure suffered in the boundary layer, because these represent part of the over-all change in entropy.

It is noted that all changes in flow properties occurring in the boundary layer are passed on to the wakes, which are eventually mixed with the rest of the flow. The distribution of losses as indicated by total pressure behind a two-dimensional cascade thus varies in two dimensions. Along the line B-B of figure 11(a), the distribution of total pressure resembles that shown in figure 11(c). Farther downstream, along C-C, the total-pressure distribution is more uniform (see fig. 11(d)). Rigorously coping with the loss distributions is not practical at the present time. An average flow condition behind the blade row is therefore sought. Such an average is also required when unsteady flows are prevalent, as discussed in the section on Treatment of Time-Unsteady Flows (p. 150).

The best way of averaging the flow conditions behind a two-dimensional cascade is not established at the present time. Discussions on this point in reference 12 indicate that one method of averaging is probably as good as another as long as the trailing-edge boundary layers are thin and the flow Mach numbers are subsonic. Inasmuch as these conditions are satisfied at the design point of many compressors, no case has yet been made for a particular method of averaging.

Hub and casing boundary layers in compressor blade rows. - The hub and casing boundary layers are indicated by the shaded areas of figure 12(a). The corresponding radial distributions of the circumferentially

averaged total pressure ahead of and behind a blade row are shown in figure 12(b). Between a_1 and b_1 of this figure the total pressure at the inlet is practically constant. Beyond these lines, it drops rapidly. The distance from the hub to a_1 (fig. 12(b)) is indicative of the boundary-layer thickness at the hub of the inlet. The distance from the casing to b_1 (fig. 12(b)) indicates the boundary-layer thickness at the casing. Similarly, the lines a_2 and b_2 represent the extent of the boundary layer at the outlet. The boundary layer is also indicated by the distribution of circumferentially averaged axial velocity at the inlet and outlet of a row of blades (fig. 12(c)).

Reference to figure 12(b) shows that the circumferentially averaged losses between a_1 - b_1 and a_2 - b_2 can be small. (The difference between inlet and outlet total pressure is a measure of the loss.) Within this area the flow properties might be considered to be a function of the two-dimensional cascade, where the circumferentially averaged losses are usually quite small. In these cases, little error in the state of this main flow is introduced even by assuming the flow to be isentropic. Beyond these lines, at the blade ends, the circumferentially averaged losses are more severe. Since the flows causing these end losses have no counterpart in a truly two-dimensional cascade, loss data and flow-angle data from such cascades are expected to be useless in the vicinity of the hub and casing. Therefore, pertinent data must preferably come from the blade row itself.

This retarded flow in the hub and casing boundary layers poses an important problem in design. The nature of this problem may be studied from the following considerations.

The requirements of continuity may be expressed by the following equations:

$$w = 2\pi \int_{r_{h,1}}^{r_{t,1}} \rho_1 V_{z,1} r_1 dr_1 = 2\pi \int_{r_{h,2}}^{r_{t,2}} \rho_2 V_{z,2} r_2 dr_2 \quad (22)$$

where

$$\rho = \frac{P}{gRT} \left(1 - \frac{r-1}{2r} \frac{V_z^2 + V_r^2 + V_\theta^2}{gRT} \right)^{\frac{1}{r-1}} \quad (23)$$

This expression is derived from equations (2), (4), and (5). The various flow quantities here must be the circumferentially averaged values ahead of and behind a blade row. For the flow behind a blade row, equations (22) and (23) may be combined to read

$$w = 2\pi \int_{r_{h,2}}^{r_{t,2}} \frac{P_2 V_{z,2}}{gRT_2} \left(1 - \frac{\gamma-1}{2\gamma} \frac{V_{z,2}^2 + V_{r,2}^2 + V_{\theta,2}^2}{gRT_2} \right)^{\frac{1}{\gamma-1}} r_2 dr_2 \quad (24)$$

If the circumferentially averaged flow properties were known as a function of radius between the hub and casing, it would be a simple matter to use equation (24) to relate the hub and tip radii to the mass flow. Unfortunately, computing the extent of the boundary layer and the distribution of flow within it remains an unsolved problem except for extremely simple flow situations. Therefore, methods of making reasonable allowances for it have been sought.

When the circumferentially averaged flow between a-a and b-b of figure 12 is known, equation (24) may be written as

$$w = 2\pi \int_{(r_{h,2} + \delta_{h,2})}^{(r_{t,2} - \delta_{t,2})} \frac{P_2 V_{z,2}}{gRT_2} \left(1 - \frac{\gamma-1}{2\gamma} \frac{V_{z,2}^2 + V_{r,2}^2 + V_{\theta,2}^2}{gRT_2} \right)^{\frac{1}{\gamma-1}} r_2 dr_2 +$$

$$\left[\int_{r_{h,2}}^{(r_{h,2} + \delta_{h,2})} \frac{P_2 V_{z,2}}{gRT_2} \left(1 - \frac{\gamma-1}{2\gamma} \frac{V_{z,2}^2 + V_{r,2}^2 + V_{\theta,2}^2}{gRT_2} \right)^{\frac{1}{\gamma-1}} r_2 dr_2 + \right.$$

$$\left. \int_{(r_{t,2} - \delta_{t,2})}^{r_{t,2}} \frac{P_2 V_{z,2}}{gRT_2} \left(1 - \frac{\gamma-1}{2\gamma} \frac{V_{z,2}^2 + V_{r,2}^2 + V_{\theta,2}^2}{gRT_2} \right)^{\frac{1}{\gamma-1}} r_2 dr_2 \right]$$

The first integral is readily evaluated from data. The last two integrals, within the brackets, represent the relatively small mass flow through the space-consuming boundary layers. For lack of a better way of coping with these two integrals, they have usually been assumed to be adequately handled by the factor K_{bk} in the equation

$$w = 2\pi K_{bk} \int_{r_{h,2}}^{r_{t,2}} \frac{P_2 V_{z,2}}{gRT_2} \left(1 - \frac{\gamma-1}{2\gamma} \frac{V_{z,2}^2 + V_{r,2}^2 + V_{\theta,2}^2}{gRT_2} \right)^{\frac{1}{\gamma-1}} r_2 dr_2 \quad (24a)$$

where the blockage factor K_{bk} is a function of the design of the blade row, the inlet flow, and the position of the blade row in the compressor. The quantities P_2 , $V_{z,2}$, $V_{r,2}$, and $V_{\theta,2}$ are taken as those in the main flow. However, an estimated average value of total pressure over the entire flow passage (including the boundary layer) might also be used; in this case a different value of K_{bk} would be necessary.

As long as the boundary layers are really thin, one technique is probably as good as another. If the boundary-layer correction itself amounts to 1 or 2 percent, a 20-percent error in the correction amounts to only 0.2 or 0.4 percent in the estimate for a single blade row. Notice, however, that the compounding effects in a multistage compressor might make even this error excessive. When the boundary layers become thick, greater accuracy is needed. When the flow resembles fully developed pipe flow, this method of accounting for viscous effects may leave something to be desired. It should also be noted, moreover, that, when the boundary layers are relatively thick, a consistent system of handling the boundary layers is especially imperative. Serious errors can result, for example, if one system is used to estimate P_2 and another to select the correction factor K_{bk} .

In addition to complicating the continuity relation, the existence of wall boundary layers could make the determination of average total pressure and total temperature difficult. It may be noted that the total pressures and total temperatures of the boundary layers may appreciably differ from those in the main stream. The problem of correctly averaging the total pressure and total temperature thus arises. A technique similar to that just discussed for continuity suggests itself. Correction factors, when they are required, could be applied to the main flow to estimate the mass-averaged quantities. These correction factors are again functions of the blade design, the inlet flow, and the position of the blade row in the compressor.

Loading limits. - Any flow device using a diffusion process will have a limiting diffusion at which the flow breaks down. This flow breakdown, or separation, can be directly attributed to the boundary layers; they do not have enough momentum to overcome the adverse static-pressure gradient accompanying the diffusion. In the usual compressor design, the velocity diffusion required on the blade surface increases as the ideal turning in a blade row increases. The intensity of this diffusion is frequently taken as a measure of the blade loading. The condition at which serious flow separation begins to occur is therefore called the loading limit.

The details determining the loading limit are still imperfectly understood. This statement is true even for relatively simple flow devices, and this situation is therefore not uniquely familiar to compressors. One of the important variables involved seems to be the ratio of

the required static-pressure rise to an appropriate velocity pressure (refs. 13 and 14). The shape of the blades, the inlet flow conditions, and the required downstream flow conditions are thus expected to be involved in the loading limit. It should be noted that the previously discussed radial shifts in the streamlines also influence the diffusion; this effect is particularly noteworthy for non-free-vortex distributions and at Mach numbers in the neighborhood of 1.00, where slight changes in stream-tube distribution can cause large changes in velocity distribution. Some important differences between the loading limits of blade rows and those of corresponding two-dimensional cascades may therefore be anticipated. Since the demands of aircraft encourage the use of compressors with highly loaded blades (ch. II), at least some loading-limit information is a vital necessity. Experiments on actual blade rows are again the only positive source of data.

Experimental data required. - There are a number of questions relating to viscosity that can only be answered by experiment. The losses and loading limits of two-dimensional cascades over a range of blade shapes and inlet flow conditions are of interest. Data for various blade rows and inlet flow conditions in the actual compressor are required to evaluate the usefulness of the loss and loading-limit data obtained from two-dimensional cascades. Data are also required to establish the effect of staging on the losses suffered and the loading limits.

Data are required for the performance of the hub and tip sections of the blades as well as for those in the main flow regions. Because of the increased viscous effects in the wall regions, the turning-angle data, loss data, and loading-limit data can be quite different from those obtained under ideal two-dimensional-flow conditions.

Some examples of the studies required are given in the section of this chapter devoted to experimental data. Representative turning-angle, loss, and loading-limit data are first presented for two-dimensional cascades. The trends of these variables in various compressor blade rows and under various conditions are then noted. The relative thicknesses of the hub and tip boundary layers are discussed.

Treatment of Time-Unsteady Flows

Time-unsteady flows must exist in a compressor, because both stationary and rotating blade rows are used. Even for ideal flow conditions, as previously noted, the flow in a stator can be steady only when the motion is referred to a coordinate system that is also stationary. Similarly, a coordinate system moving at rotor speed must be used for the rotor. From a purely theoretical point of view, then, the flow through a rotor is therefore always unsteady with respect to uniform flow in a stator, and vice versa.

Moreover, time-steady circumferential variations in the flow ahead of or behind a rotor cause the flow in the preceding or following stator to be time-unsteady irrespective of the coordinate system used. Similarly, time-steady circumferential variations with respect to the rotor induce inevitable time-unsteady flows in the preceding and succeeding stators. It may also be noted that time-unsteady flows are also inevitable when either rotating stall (ch. XI (ref. 6)) or surge (ch. XII (ref. 6)) occurs.

Circumferential variations in the flow behind a blade row, and thus unsteady flows in the following blade row, are encountered even when the flow is completely inviscid. Some circumferential gradients in the flow persist for some distance upstream and downstream of even an ideal two-dimensional cascade. Similar circumferential gradients are associated with the types of flow presented in figure 8(c).

Additional circumferential gradients are brought about by the blade wakes (fig. 11). These gradients are made even more complicated by the fact that a fluctuating pressure field ahead of a blade row periodically changes the character of the wakes leaving the previous blade row. As a result of all these phenomena, both the rotor and stator are beset by complex unsteady flows. Notice that any two adjacent blade rows, one rotating and the other stationary, experience the same sort of disturbances.

Because of these time-unsteady components of the flow, average values of flow properties leaving one blade row have been used to represent the inlet flow to the next blade row. In this way, the unsteady-flow problem is rather arbitrarily reduced to a steady-flow problem. As discussed in chapter XIV (ref. 6), some theoretical considerations indicate that additional time-unsteady effects may be of importance. How vital these effects are must eventually be determined by experimental data.

The validity of this treatment of unsteady flow can also be judged by experimental data. Comparing the performance of isolated blade rows with those subjected to unsteady flows provides the basis for this evaluation. Notice of this problem is taken during the discussion of experimental data presented in the following section.

REPRESENTATIVE EXPERIMENTAL DATA SUPPORTING DESIGN CONCEPTS

Many of the questions that have been raised about the simplified flow concepts in the previous section have been answered by the published results of a large number of experiments and analyses. Some representative examples of these experiments and the indicated conclusions are presented in this section. Through this review, a qualitative picture of the flow is established that becomes the basis of a design system. Moreover, the results presented indicate the classes of assumptions and

calculation techniques that may be used with a reasonable degree of confidence. The areas where design information must be tempered by intuition and judgment are also spotlighted.

Before presenting the data on actual compressor blade rows, attention is first focused on the aerodynamic properties of the two-dimensional cascade, since this type of reference data is the basis for many of the developed procedures. Typical data from inlet guide vanes are then reviewed. For inlet guide vanes with free-vortex flow distribution, the assumption of no radial flow is examined under conditions where the radial flows and viscous effects may be reduced as much as possible and the unsteady-flow effects are completely eliminated. The effects of changes in radial density gradients, of blade thickness distribution, of blade force, and of the hub slopes are noted. Radial flows resulting from non-free-vortex flow distributions are then examined.

Representative data obtained from rotating blades are also reviewed. The effects of blade rotation, over and above the effects considered for inlet guide vanes, are thus evaluated. Some effects of unsteady flows and the mixing of wakes are noted from the results of tests of both stationary and rotating blades.

Several significant results obtained from experiments on multistage compressors are next reviewed. These data indicate the validity of the simplified flow concepts under adverse, but typical, conditions. They also provide a basis for indicating important missing gaps in available knowledge.

For each experiment, the turning-angle data are presented and the loss or efficiency data are noted. Flow conditions in the main flow are discussed. The influence of the hub and tip boundary layers are also noted. Comments are made about the indicated effects of radial flows and unsteady flows. The significant knowledge derived from these classes of experiments is then summarized by outlining a model of the flow that can be used for design.

Two-Dimensional Cascades

Aerodynamic behavior. - Five quantities determine the aerodynamic behavior of a cascade with ideal flow. One of these is the shape of the blades, which is usually expressed in terms of the distribution of thickness and camber. Another quantity is the orientation of the blades with respect to the cascade axis; this orientation may be defined by the blade-chord angle γ^0 (fig. 2). The third quantity is the solidity ($\sigma = c/s$), although the pitch-chord ratio, the reciprocal of this number, is sometimes used. With these three quantities, the geometry of the cascade of blades is defined. The fourth quantity identifies the direction of the

flow ahead of the cascade. The relative inlet-air angle β_1' is frequently used for this purpose. Finally, the relative Mach number of the flow at some point must be known. This quantity is also usually referred to the relative inlet flow. Theoretically speaking, all details of the flow of an ideal inviscid fluid can be determined from these data.

For real flows, the factors involving friction are also pertinent. The Reynolds number of the relative flow thus becomes an important item. The Reynolds number is usually based on the properties of the inlet flow, using the chord length as the characteristic dimension. The factors involved are the turbulence of the incoming flow and the condition of the airfoil surfaces (see ch. V in this volume and VI (ref. 11)). Because of the complicating effects of friction, the most reliable cascade data are derived from experiment rather than analysis.

Types of experimental data observed. - One of the most important pieces of cascade data required is the deflection of the flow ($\beta_1 - \beta_2$), since deflecting the flow is the main purpose of the cascade. Although analytical techniques have been developed and are occasionally used for determining this deflection (ch. IV), the greatest amount of data is obtained by experiment. A typical sample of the experimental data is shown in figure 13, which was obtained from reference 15. These data were obtained for fixed values of blade shape, solidity, and inlet-air angle. The blade angle was varied, the magnitude of the variation being described by the angle of attack $\alpha = \beta_1 - \gamma^0$. The deflection, or turning angle, is measured by the angle $\Delta\beta = \beta_1 - \beta_2$.

The losses incurred by the cascade may be described in a variety of ways. In reference 15 the loss is measured by a drag coefficient; an average total-pressure loss or an average entropy increase could also have been used. (Notice that the drag coefficient is independent of the position of the downstream measurement and that no averaging techniques are required. The total-pressure loss and the increase in entropy, however, depend on the axial position of the measurements, the Mach number of the flow, and the method of averaging.) Of particular importance are the regions where the loss rises rapidly; the rapid rise in loss and the accompanying droop in the turning-angle curve indicate the point of flow separation or the loading limit of the cascade. For the particular family of blade shapes discussed in reference 15, it has been possible to correlate the loading limit by the following equation, developed in reference 13:

$$D = \left(1 - \frac{V_2}{V_1}\right) + \frac{\Delta V_\theta}{2\sigma V_1} \quad (25)$$

All the blades reached their loading limit at a value of D of approximately 0.6. This equation is simply an empirical means of estimating

$$\frac{\text{Downstream static pressure} - \text{minimum static pressure on blade surfaces}}{\text{Maximum velocity pressure on blade surface}} \quad (26)$$

Since it was derived for one family of blades, it is not expected to be universally applicable. It does, nevertheless, provide an indication of the loading limit as good as or better than many other recommended empirical rules. A more fundamental approach would utilize equation (26) with the actual velocity and pressure data (see ref. 14).

Other details of the flow within a blade row may also be partially examined by studying the velocity distribution about a cascade element. The results of a typical experimental measurement in a two-dimensional cascade are shown in figure 14. The velocity distribution presented corresponds to the operating condition indicated by point A in figure 13. These data are valuable for interpreting over-all results, since comparing these data with similar measurements in a compressor blade row provides a means of comparing the internal flows.

The data described thus far were obtained at low inlet Mach numbers, the operating condition for most published cascade data. Increasing the inlet Mach number in two-dimensional-cascade rigs has the effect shown in figure 15, which was obtained from data of reference 16. As the Mach number increases, the range of angle of attack decreases. When the Mach number becomes high enough, the cascade is choked and the flow deteriorates to such an extent that the cascade is completely ineffective. The behavior of the flow at high Mach numbers is shown by the schlieren photographs of figure 16, which is taken from reference 17. The strong shocks that have developed cause the boundary layer to separate at all angles of attack. This type of data indicates an interrelation between loading limit and flow Mach number.

These results represent the principal knowledge obtained from numerous tests of two-dimensional cascades. As previously noted, the turning-angle data obtained are of primary interest. When the observed turning angle in an actual blade row agrees with that observed in two-dimensional cascades, credence may be given to the simple equations obtained by ignoring radial flows in that type of blade row. The relatively inexpensive two-dimensional cascade can then be used as an important source of design turning-angle data.

Inlet Guide Vanes

Tests of inlet guide vanes alone have been invaluable for studying and developing flow concepts and theory. In the laboratory setup, the flow ahead of inlet guide vanes has no tangential component of velocity, so the inlet guide vanes have the function of creating a preconceived

distribution of tangential velocity. When tested alone, the inlet guide vanes are exposed to essentially time-steady flow; therefore, time-unsteady-flow effects are eliminated. Moreover, the flow velocity behind the guide vanes is usually greater than that in front; thus, many adverse effects of viscosity arising from unfavorable pressure gradients are avoided. Inlet guide vanes, therefore, provide an excellent vehicle for studying the effects of radial flows brought about by the changes in radial density gradients through a blade row, by the radial distributions of blade thickness, by the radial components of blade force, by the slope of the hub or casing, and by nonvortex distributions of tangential velocity.

A typical setup used to conduct flow investigations is schematically shown in figure 17. Measurements are made ahead of and behind the blade row to determine the velocities and state properties of the air at these two stations. Sufficient data are taken behind the blade row to determine the radial gradients of the circumferentially averaged properties of the main flow. Ahead of the blade row, precautions are taken to ensure a uniform distribution of the flow. Complete uniformity cannot, of course, be achieved in the hub and casing boundary layers, where the radial variation of entropy and the tangential component of vorticity are not zero. Care is taken, however, to make these boundary layers as thin as possible.

Free-vortex flow. - A representative result of an investigation with free-vortex blades is shown in figure 18, which was obtained from reference 18. (The experimental setup was essentially the same as that shown in fig. 17.) In figure 18, the observed turning angle of the cascade elements of the blade row is compared with the turning angle that the same cascade elements would have in a two-dimensional cascade. As indicated in this figure, the observed turning was substantially the same as that of the corresponding two-dimensional cascade. The order of magnitude of the radial flows in this blade row is just about the same as that in many conventional compressors having free-vortex subsonic blade rows. There are strong indications, therefore, that the radial flows themselves have relatively minor effects, if any, on the turning angle at subsonic Mach numbers. Some discrepancies are noted in the vicinity of the blade ends. Those differences within the boundary layers are not unexpected, but the observed boundary layers were thin enough for these variations to be disregarded. The circulation gradients, or vorticity, within the boundary layer do, however, induce some deviations in the main flow. As shown in reference 19, these deviations are sometimes significant; they can, however, be accurately treated by the technique reported therein.

The radial distribution of circumferentially averaged flow was also studied in reference 18. In general, the flow was fairly accurately described by equation (19a). An important point to note, however, is that the flow Mach numbers were not very close to 1.0, and the value of

the local Mach numbers were therefore not extremely sensitive to small changes in the area of the stream tubes. At Mach numbers nearer 1.0, a small change in stream-tube area accompanying radial flows may give different results.

The loss data reported in reference 18 show that the average losses in total pressure were small. This trend agrees with two-dimensional-cascade data. In the hub and casing boundary layers, the losses increase; and eventually, of course, all the dynamic pressure is lost at the hub and casing surfaces. The main thing to notice with respect to losses is that radial flows themselves do not necessarily create large additional losses. The important losses, when the blades are operated within their loading limits, appear near the hub or casing. Probably the most important effect of these losses is the fact that they occupy space without transporting much mass. The correction K_{bk} in equation (24a) is thus an important quantity that depends on loss data. Therefore, two-dimensional-cascade loss data do not tell the whole story; data from actual blade rows are required to complete the loss picture.

Non-free-vortex flow. - Several investigations have been made with inlet guide vanes designed to establish the type of flow described by equation (21). Except for the type of velocity distribution created, these blade rows are physically similar to many of the free-vortex blades that have been tested. Studies of the non-free-vortex blade rows, therefore, provide a means of studying the effects of radial flows resulting from the radial gradients in circulation.

In figure 19 are shown representative data from a test of inlet guide vanes designed for wheel-type rotation ($\Gamma = 0$ in eq. (21)). These data are taken from reference 20. The average flow angles at the exit of the inlet guide vanes agree fairly well with those obtained from two-dimensional-cascade considerations. The effect of radial flows themselves is again quite small, if there is any effect at all. The other effect of circulation gradients, as reported in reference 19, cannot be completely ignored, however; and the correction techniques developed in this reference are frequently necessary for refining the analysis. But, when the radial gradient of tangential velocity is correctly established, the radial distribution of through-flow usually agrees with the distribution expressed by equation (19a) (with radial flows ignored). The finite values of both ζ_z and ζ_θ required for axisymmetric flow are apparently suitable; the complicating flows shown in figure 8(c) seem to have little effect on the radial distribution of the circumferentially averaged flow.

The loss data available are similar to those obtained with free-vortex blade rows. Almost negligibly small losses are impressed on the main flow. The important losses again appear at the blade ends. Even here, the losses themselves are not as serious as their blockage effects are. The important loss information to be obtained is that required to evaluate K_{bk} in equation (24a) (or some similar function).

Rotors and Single-Stage Compressors

A large number of investigations have been made with rotors alone, rotors with inlet guide vanes, and complete stages formed from inlet guide vanes, rotors, and downstream stators. Tests of rotors alone have many of the same aims as the tests of inlet guide vanes - to study the net effects of radial flows. In addition, the effects of rotation that are not accounted for in simplified theories are investigated. Tests of inlet guide vanes and rotors examine the effects of unsteady flow and other phenomena for interferences between rotating and stationary blade rows that are otherwise neglected. Tests of a complete stage add the effects of another blade row.

A representative schematic layout for testing a complete stage is shown in figure 20. As with the inlet-guide-vane investigations, care is exercised to have thin hub and casing boundary layers at the inlet. Circumferentially uniform flow without distortion at the inlet of the first blade row is also sought. Enough measurements are taken upstream and downstream of each blade row to obtain an accurate picture of the behavior of the cascade elements at several radii. These data also enable the radial distribution of flow to be compared with that indicated by simple theory.

Free-vortex rotor blade rows. - A representative investigation of a free-vortex rotor with axial inflow is presented in reference 21. The observed turning-angle data are compared with those of the corresponding two-dimensional cascades in figure 21 for three radial positions: (a) near the tip, (b) at the center of the span, and (c) near the hub. As shown in figure 21(a), the observed turning at the tip is slightly higher than that of the corresponding two-dimensional cascade. The rate of change of turning with angle of attack is about the same for both, however. At midspan (fig. 21(b)), the agreement in turning angle is good at low angles of attack. With high angles of attack, the turning through the rotor is greater than that indicated by two-dimensional-cascade data. The faired turning-angle curve for the data at the rotor hub (fig. 21(c)) has a steeper slope than the corresponding cascade curve. In this respect, the flow about the blade near the hub is comparable to ideal two-dimensional flow. Apparently this section can operate at much higher angles of attack than cascade data would indicate. In the vicinity of the design angle of attack of the cascade, the difference in turning is small.

In this particular investigation, the pressure distribution about the blades was also measured at the same time. These data are compared with those of the corresponding cascade in figure 22. At the hub and midspan, the agreement is excellent, except for some irregularity of the cascade curves between the 40- and 80-percent-chord points on the upper surface. The irregularities, however, are attributed to laminar

separation (see ch. V), which may have occurred during the cascade tests but which did not occur during the rotor blade tests. The agreement near the tip is not quite so good, but there apparently are no pronounced effects of radial flows in the main stream.

These and other similar data indicate that the flow around the blade elements of a rotating row is reasonably the same as that in the two-dimensional-cascade counterpart, except at the blade ends. In the main flow, the anticipated enthalpy rise is realized as long as flow separation is avoided.

In the boundary layer at the tip, however, the energy added by the rotor is usually higher than that anticipated from two-dimensional-cascade data. The total-temperature distribution indicated in figure 23 is fairly representative. There is always some scattering in the rotor data, which might be attributed to radial and time-unsteady flows as well as to instrument errors. The higher energy addition at the blade ends may be expressed in terms of a higher turning angle; however, a gross correction for the higher temperature rise is probably just as good as any other at the present time.

As was the case with inlet guide vanes, the rotor loss or efficiency is not always comparable to that of the corresponding two-dimensional cascade. A typical radial distribution of compressor rotor blade-element efficiency is shown in figure 23. Losses increase rapidly near the casing, and the loading limit frequently appears at lower values of D (eq. (25)) than suggested by two-dimensional-cascade data. It must be emphasized, however, that the changes in the absolute total pressure do not follow a simple trend. They depend on the relative magnitudes of the temperature rise as well as the loss in relative total pressure (see eqs. (12) and (13)).

The problem of accurately correlating the net effects of the flows in the hub and casing boundary layers is still somewhat confused. As proposed in the section on Analysis of Viscosity Problem (p. 145), the space-consuming properties of the boundary layer can frequently be correlated by factor K_{bk} in equation (24a). In using this factor, a fictitious mass flow for ideal flow conditions is computed or assumed and the result is multiplied by K_{bk} to obtain the true mass flow. Similarly, the ideal temperature rise and total pressure could be estimated by analyzing the ideal flow and then multiplying the result by an empirical correction factor. Satisfactory answers to these problems are still to be found. Except for their effects on blockage, the variations in total temperature and pressure at the blade tips are usually either ignored or are treated together as part of the over-all efficiency.

Investigations of the type just described have been extended to rotors with inlet guide vanes and to complete single stages. The results of these investigations are comparable with those indicated previously. As far as could be determined, the unsteady flows introduced by the alternate stationary and rotating blade rows had little effect on the turning angle of the blade row; the turning over a large part of the annulus was primarily decided by the corresponding two-dimensional-cascade variables. Moreover, the losses were not drastically increased by unsteady flows in the normal operating conditions.

Non-free-vortex blade rows. - An investigation was conducted on a setup consisting of inlet guide vanes and a rotor to study the effect of circulation gradients on the performance of a rotor and stator. The inlet guide vanes, the performance of which is presented in reference 20 and in figure 19, were designed to establish a solid-body type of rotation ($\omega_{air} \neq 0$, $\Gamma = 0$ in eq. (21)). No change in ω_{air} was then required of the rotor; instead, the value of Γ was increased through the rotor. The arrangement of the inlet guide vanes and rotor reported in reference 20 is shown in figure 24. The large pitch of the inlet guide vanes suggests that the warping of the flow surfaces (fig. 10(b)) must be more than negligible. Notice also that the gap between the inlet guide vanes and the rotor is small. It is doubtful whether complete readjustment of the flow (that ideally occurring at an infinite distance downstream of the vanes) could have taken place at the rotor inlet. The radial distribution of flow at the rotor inlet might be in question, and severe time-unsteady flows might be anticipated.

As previously noted, the average flow angle at the exit of the inlet guide vanes alone agreed fairly well with that anticipated from two-dimensional blade-element considerations (fig. 25). The presence of the rotor may have had some additional influence on the flow angle, and some of this discrepancy might be attributed to time-unsteady flow. The major cause of the differences, however, is believed to be minor changes in the average radial distribution of flow due to the presence of the rotor. Even this effect is not excessive, however. Therefore, it has generally been ignored in practice, and equation (19a), obtained by ignoring radial flows, is usually quite accurate for this type of design.

The average turning through the rotor (fig. 26) was observed at the five radial positions indicated in figure 24. At radial position a, the observed turning was slightly higher than that of the corresponding two-dimensional cascade. At the low angles of attack, the trends of the two curves are similar. The flow at the tip section of the blade apparently separated at a slightly lower angle of attack than cascade data would indicate.

In this particular type of flow distribution, the static-pressure rise near the casing is higher than that for the corresponding two-dimensional cascade. If equation (26) is a criterion for the loading limit, this premature separation is expected. The rise in turning following the dip in the curve is not related at all to normal two-dimensional-cascade performance.

At the other radial positions, the agreement is surprisingly good. Moreover, the trends observed are the same as those observed with free-vortex flow. The hub regions appear to be capable of operating at much higher angles of attack than the corresponding two-dimensional cascades. At those angles of attack where the data may be compared, the turning of the rotor is somewhat lower than that of the two-dimensional cascade. The similarity of these trends to those of rotors alone suggests that the effect of unsteady flows is relatively trivial.

The loss problem appears not to differ from that of the free-vortex designs. Only small losses are imposed on the active flow. The problem introduced by the boundary layers is principally that of boundary-layer blockage, although the different total temperatures and pressures in the boundary layers introduce complications that confuse the theory if not the flow. Losses cannot be predicted from two-dimensional-cascade data with sufficient accuracy to correlate actual blade-row data.

Transonic blade rows. - Recent investigations on free-vortex rotors (see refs. 22 and 23, e.g.) demonstrate the feasibility of obtaining high efficiency from rotors in which the Mach numbers at the tips are as high as 1.35. The turning angle of the blade elements at these higher Mach numbers cannot be compared with similar two-dimensional-cascade data, because usable two-dimensional cascades for transonic flows are yet to be developed. The compressor blade-element data that have been obtained, however, seem to lend themselves to the same correlation techniques that have been developed for two-dimensional-cascade data (ch. VI (ref. 11)). It may be inferred from these data, for the time being at least, that radial flows themselves do not seriously affect the turning angle in the main-flow regions of the blade row.

Studies of the radial distribution of the circumferentially averaged flow properties indicate that equation (19a) or (19b) is not entirely adequate for the types of blade rows investigated. Reliable solutions to this problem have not yet been found, but the treatment discussed in the last section of this chapter offers some promise.

The loss picture is not different from that in subsonic blade rows, except that low losses are obtained only over a very narrow range of inlet flow angles at high Mach numbers. The viscous-flow regions near the hub and tip frequently have different total-pressure and total-temperature changes from those of the main flow. Their principal effect is again that of blocking part of the flow area. Whether the flow is subsonic or transonic is immaterial with regard to the factor K_{bk} in equation (24a), if

the loading limits are not exceeded. The loading limit of the blade row, as indicated by the value of D , is about the same as that for conventional subsonic blade rows. The allowable values of D near the casing of the rotor appear to be lower than those elsewhere on the blade row.

Multistage Compressors

A representative example of the performance of the blade rows of a multistage compressor is shown in references 24 to 26. A schematic layout of this unit is shown in figure 27. This compressor was designed (see ref. 24) for finite values of both ω_{air} and Γ (eq. (21)). Strong radial flows and time-unsteady flows are thus expected to be prevalent, particularly in the latter stages.

In reference 26 data for the performance of the first, fifth, and tenth stages are presented. Only the fifth and tenth stages are discussed here, however, since the flow entering the first stage is similar to that in single stages, and the results are similar to those previously presented.

Performance of fifth stage. - In spite of the fact that the hub and casing boundary layers seem to have ample opportunity to thicken, the flow distribution entering the fifth rotor at design speed (see fig. 28) was almost that expected for ideal flow, which was the basis for design computations. The observed turning angles through the rotor are shown for several radial positions in figure 29. Near the tip, the turning-angle data suggest that the blade is stalled; the loading limit is apparently exceeded even though the angle of attack and the value of D are within the limits of good two-dimensional-cascade performance. At the next two radial positions, good agreement with cascade data is found. At the two lowest radii (closest to the hub), the turning angle is somewhat below that obtained in two-dimensional cascades. These trends are similar to those presented in figures 21 and 26.

The turning-angle data for the following stator is presented in figure 30. The agreement with cascade data is fairly satisfactory, particularly near the design angle of attack. The tip (outer radius) of the stator appears to have a greater range of useful operation than is indicated by two-dimensional-cascade data. This trend, which is opposite to that of rotors, is fairly common for stators.

These results suggest that the turning angle of the main flow is not significantly affected by the wakes introduced by the upstream blade rows. The effect of the unsteady flows created in this compressor is apparently within the accuracy of instrumentation.

Qualitative observations of the losses in the main flow indicate that no unexpected developments have occurred. The main point of concern is the apparent premature stalling at the rotor blade tip. As previously indicated, this phenomenon is frequently observed, and the loading limits near the extremities of a blade row are frequently much different from those in the corresponding two-dimensional cascades. An important point to notice, however, is shown in figure 31. Because of the poor flow created by the rotor, significant entropy gradients were found in the entire flow field behind the fifth stage. In other words, thick hub and casing boundary layers appeared. When the observed entropy gradients were used in equation (19a), reasonably good correlation between the observed and computed axial velocity distribution was found. If the entropy gradients were ignored, however, the correlation was not only poor but misleading. This experience shows the importance of recognizing entropy gradients when the boundary layers are thick. This point is elaborated in reference 27.

Performance of tenth rotor. - In contrast to the flow conditions at the entrance to the fifth rotor, the flow ahead of the tenth rotor was quite different from design (fig. 32). The axial velocity is lower than the design value at all radii. Instead of being fairly uniform, as designed, the velocity distribution is parabolic. The boundary layers at the hub and casing resemble those of fully developed pipe flow. The design values of absolute flow angles β_1 are realized near the center of the passages; at the hub and casing they tend to be high. The resulting relative angles of attack on the rotor blades are higher than the design values at all radii, the greatest angles occurring at the hub.

In spite of the difference between the design and observed inlet conditions, the observed turning angle at a given angle of attack (fig. 33) is surprisingly similar to the corresponding turning angle of the two-dimensional cascade. The trend is the same as that observed in investigations of single blade rows and single stages. This result is consistent over a wide range of compressor tip speeds and operating points at a given speed. These and similar tests indicate that the turning angle of a cascade element in a blade row is just about completely determined by the corresponding two-dimensional-flow conditions. The one important qualification is that the cascade element must not be stalled. Two-dimensional-cascade data are not always a reliable source of stalling data, however.

The poor flow distribution at the rotor inlet caused the over-all losses to be rather high. How this flow can be estimated properly in design remains an unanswered problem. Both intuition and judgment are still required to estimate the appropriate values of K_{bk} and P in equation (24a).

The radial distribution of the flow is adequately described by equation (19a). All the terms must be used in this equation, because the enthalpy and entropy gradients permeate the entire flow instead of being confined to thin boundary layers. Accurate estimates of the radial gradients in enthalpy and entropy would thus be necessary to make accurate designs, if this type of flow cannot otherwise be avoided.

Significance of Results

The results of experiments like those presented show that many features of the flow can be correlated with the aid of a few simple concepts. As long as the loading limits are not exceeded, the flow through a blade row may be divided into two regions. One of these regions is the main flow, where the viscous effects are comparatively small. In the other region, the velocity gradients are steep and the viscous effects are large.

Main-flow region. - In the main-flow region, the deflection of the flow at a given radius obeys about the same laws that govern the deflection in a two-dimensional cascade having the same geometry and inlet flow conditions. Two consistent differences are noted, however: (1) At a given angle of attack the turning angle is usually slightly higher near the casing of a rotor than that of the corresponding two-dimensional cascade. (2) Near the hub of a rotor the rate of change of turning with angle of attack is greater than that of the two-dimensional cascade.

In the previous discussion, the governing flow has been assumed to be parallel to the axis of the blade row. These and other data may also be used to show that no accuracy is sacrificed when the cascade element and the governing flow are assumed to lie along a conical surface (fig. 34). This device is frequently useful when there is a pronounced radial shift in the streamlines through a blade row.

The radial distribution of flow ahead of and behind subsonic blade rows is quite accurately described by equation (19a), the form obtained by neglecting radial flows. As long as the boundary layers are rather thin, the entropy-gradient term is ignored. When thicker boundary layers are encountered, the entropy gradients must be recognized. For some transonic blade rows, this technique leaves something to be desired. In these cases, it is believed that techniques similar to those used in turbines and mixed-flow compressors may be useful. In these more erudite analyses, only axial symmetry is assumed, and the radial-distribution problem is treated as part of a two-dimensional-flow problem involving axial and radial gradients. This point is discussed in more detail in the last section of this chapter.

To a first approximation, the losses encountered by the main flow may be ignored if the design is not too critical. Recognition of the losses in the main flow, however, may be made by using two-dimensional-cascade loss data. In order to obtain greater accuracy, the losses measured from similar blade rows in similar flow environments should be used. The losses would then also be a function of the radial positions of the cascade element.

Of vital importance is the question of loading limits and Mach number limits. Although the D factor of equation (25) is far from the perfect criterion of blade loading, it does offer some guide for selecting the deflection required of a blade row. When the static-pressure rise near the casing of a rotor is of the order of that of the corresponding two-dimensional cascade, the limiting value of D for the rotor tip seems to be about 0.35. When the static-pressure rise is higher than that for the corresponding two-dimensional flow, lower values of D seem to be necessary. The selection, for the time being, must be left to the judgment of the designer. If development time is to be minimized, low values of D are to be favored, even though the number of blade rows may be increased.

Up to Mach numbers at least as high as 1.35 there appears to be no fundamental reason for prescribing a Mach number limit. As the design Mach number is increased, however, more and more attention must be paid to the details of the flow. Defining and accounting for the important details is not yet a science, however; there have been too few successful designs above the Mach number of 1.2 to clarify the problem. Up to the Mach number of 1.2, however, the design problem does not appear to be much more complicated than the problem of executing a subsonic design.

For design, then, the main flow at the inlet of a blade row may be known or assumed. The main flow downstream of the blade row may be stipulated, if it can be prescribed within known loading limits, and if the distribution meets the requirements of equation (19) or its equivalent. Two-dimensional-cascade data or the equivalent may then be used to select blades to obtain the required deflection of the main flow.

Viscous-flow region. - Between the main flow and the hub and between the main flow and the casing is the second flow region, where viscous forces dominate the motion. The laws governing the movement of flow in this region are very imperfectly understood. Since the actual mass flow in these regions is often small, the areas usually contribute little to the mass-averaged enthalpy. Therefore, this effect is usually either ignored or given partial recognition by the use of gross correction factors. By the same token, the losses at the blade ends offer only a small contribution to the local mass-averaged loss. Significant additional losses may result from subsequent mixing, however. One important factor that cannot be ignored is the space-consuming property of these viscous-flow regions. This problem is discussed in the section on Analysis of

Viscosity Problem, where the use of the correction factor K_{bk} is suggested. Methods of accurately estimating K_{bk} have not yet been developed, however, and frequently an educated guess is the best technique available. It is the lack of information on this problem that has led to serious errors in estimating the flow in the latter stages of many compressors. This point is developed more fully in the following paragraphs.

Accuracy of estimate of state of air. - Many of the difficulties encountered in development have resulted from the fact that the flow towards the rear of the compressor is different from that anticipated in design. A common experience has already been mentioned in connection with figure 32. In this particular instance, the magnitude of the velocity is lower than the design value at all radii. In other compressors, however, the opposite behavior has been observed, the average velocity being higher than its design value. The high angles of attack shown in figure 32 increase the turning through the rotor; the enthalpy rise through the rotor is then increased, and the performance of the following rotor blade row deteriorates. The difference between the design and observed values of the average axial velocity is one of the principal reasons for this result. The error in turning angle owing to different radial gradients in flow properties may have contributed to the problem, but these effects are usually small (fig. 33) and in any event are masked by differences in the average velocity.

Errors in estimating the axial velocity can frequently be attributed to small errors in estimating the various terms in equation (24a). Suppose, for example, that the effective thicknesses of the hub and casing boundary layers after the first stage of a compressor are smaller than those anticipated; that is, K_{bk} is actually greater than the value used in design. If the estimated enthalpy and total-pressure increases in the main flow are otherwise accurately predicted, the axial velocity actually obtained after the stage is lower than that anticipated (eq. (24a)). (Notice that the same result would occur if K_{bk} were correctly predicted but the efficiency of the blade row or the turning angle of the cascade elements were underestimated in design.)

The angle of attack on the blade elements of the next rotor row is too high as a result of the low axial velocity. The turning angle is increased, and the energy addition is higher than its design value. (This trend of energy addition with turning angle is required by the relations expressed in eqs. (9) to (11)). If the efficiency and the value of K_{bk} for this stage were correctly estimated, the total pressure of the leaving flow would be too high and the axial velocity further reduced from its design value. Repeating this trend of error from stage to stage eventually causes an important error in the estimated axial velocity to result from only a small error in estimating the blockage effects of the hub and casing boundary layers. Of course, the same kind of result is obtained if the efficiency happens to be higher than the design value.

A qualitative indication of these trends is shown in figure 35. The dashed lines of figure 35(a) represent a design distribution of axial velocity and efficiency through the blade rows. A typical trend of the observed values of these quantities is shown by the solid lines. Because of the lower than estimated boundary-layer thicknesses or the higher than estimated efficiencies obtained in the front stages of the compressor, the annular area for these stages is greater than it should have been. If the flow ahead of the compressor were that designed, the axial velocity leaving the front stages would be too low. Towards the middle of the compressor, the observed axial velocity would be so much less than its design value that the angle of attack on the blade rows would be such that the stage efficiency would suffer and the boundary-layer blockage increase. Flow separation might even occur. The axial velocity thereafter would not decrease as rapidly as before. It might still stay lower than the design value, however; and in any event the efficiency of the compressor always becomes low enough or the flow distribution distorted enough for the air to fill the passage made for it.

The opposite trend in axial velocity distribution occurs when the efficiency is lower or the boundary-layer thickness is greater than the design value. As indicated in figure 35(b), if the design mass flow were obtained, the axial velocity leaving the first stage would then be too high. The subsequent energy rise and pressure ratio would be too low, and the axial velocity would increase with respect to its design value. The axial velocity would eventually become so high that the angle of attack on the blade rows would be too low for efficient performance, and the efficiency would drop still further. In the extreme case, the velocity would become so high that the rear stages would be choked. In this case the mass flow is limited, so that the axial velocity in the front stages may be reduced below that shown.

As a matter of fact, experience indicates that, while the trends of figure 35 are observed, the flow usually adjusts itself so that the middle stages operate at about the optimum angles of attack; the front stages deviate in one direction about as far as the rear stages do in the other. In this way the excessive losses due to high angles of attack at one end of the compressor are about equal to those resulting from low angles of attack at the other end.

It should be noted that an overestimated value of K_{bk} in equation (24a) is just as bad as an underestimated value. The same thing may be said of the estimated blade-row turning and the total-pressure loss or efficiency.

The inability to estimate K_{bk} correctly is the principal reason that most successful compressors have required at least some development. There is an urgent need for better design information on these problems. The present difficulty is not due to the fact that the problems have not been recognized. Instead, the difficulty lies in obtaining the required

data. Multistage data are required because efficiency and boundary-layer thickness are, among other things, functions of the axial position, which, in turn, partially determines the distribution of flow ahead of a blade row. Actual measurement of the blockage in numerous compressors is of little value, since the blockage adjusts itself to the design anyway. The blockage that is required for maximum efficiency, which is really the blockage desired, remains undetermined. Systematic readjustments in the annular area or the blade setting of a number of compressors will probably be required before correct estimates of the minimum required blockage area (that for highest blade-row efficiency) can be made. In the meantime, some development effort must be expended to fully exploit the merits of a given design.

SYSTEM ADOPTED FOR DESIGN AND RESEARCH

The preceding discussions have presented the techniques that have been useful for describing the important features of the three-dimensional time-unsteady motion of the viscous fluid through an axial-flow compressor. They have also indicated the general approaches that have been utilized in compressor design. These design procedures simplify the three-dimensional aspect of the problem by considering the main flow to be described essentially by two-dimensional solutions in two principal planes, thus making the problem mathematically tractable.

First, the blade-element approach is used. That is, the flow in the blade-to-blade or circumferential plane is treated by considering flow about the developed blade profiles formed by the intersection of flow surfaces of revolution and the compressor blading (fig. 2). The performance of such a blade element in the main flow is then described by a circumferentially averaged value of (1) turning and (2) loss; these data are obtained experimentally, preferably under conditions similar to those existing in the compressor. Thus, effects such as those arising from viscosity, time-unsteady flow, and blade-row interactions are accounted for in a gross manner. Losses may be treated as functions of cascade geometry of the blade element, inlet Mach number, diffusion factor, radial position of the blade element, and axial position of the blade row. Turning may be treated as a function of cascade geometry, loss, Mach number, and radial position of the blade element. On the basis of available experimental data, limits are suggested for certain critical design parameters such as Mach number and blade loading.

Secondly, under the assumption of axial symmetry, the average quantities in the blade-to-blade plane are used to describe the distribution of the flow in the hub-to-casing or meridional plane (fig. 34). Equations representing the radial variation of this average state of the air are written for continuity, energy addition, and radial equilibrium. In this system, certain difficulties are created by the hub and casing boundary layers. It is eventually hoped that reliable estimates of the

state of the air can be made at all radial positions, even within the wall boundary layers. For the present, however, the meridional-plane analysis is based on the main-flow region (a_1 - b_1 of fig. 12), and the effects of wall boundary layers are accounted for by applying gross corrections.

In essence, then, a combination of two-dimensional solutions in the two principal planes (circumferential and meridional) is used to approximate the complete three-dimensional flow. Comparatively excellent compressors have been and can be designed by this approach, if the essence of the derived technique is used in its entirety and if the data are not extrapolated too far.

It is recognized that this quasi-three-dimensional design procedure can be an oversimplification of the problem, particularly as performance is extended to higher levels. However, this simplified flow model has been adopted for this series of reports on the basis that (1) it correlates experimental data as well as the more complicated systems that have been tested; (2) it provides adequate compressor designs, at least up to current levels of performance; (3) it has received general acceptance in the field; and (4) no practical and tested three-dimensional design procedure is yet available.

In practice, the design system can be considered to consist of three principal phases:

(1) Design-point solution in the meridional plane: As previously indicated, this phase of the problem is based on the assumption of axial symmetry. The problem is reduced to a two-dimensional system, in which only radial and axial variations are considered, by assuming circumferential averages to represent the flow at all points along the meridional-plane streamline. In many cases, the problem may be further reduced by ignoring the axial gradients as well. Equations describing radial variations of these average values are written to account for equilibrium, continuity, and energy addition. For a given flow distribution ahead of a blade row, a quantity like the radial distribution of tangential velocity may be selected. Another quantity such as the axial velocity at the casing (required for a certain loading limit) may also be selected. The radial distribution of the axial component of velocity may then be calculated. Velocity diagrams (fig. 36) may be then constructed at each of several radii to depict the air velocities and flow angles at the entrance and discharge of each blade row. The functions of the blade elements are thus given.

(2) Blade selection: This phase of the problem is based currently on the concept of blade-element flow, with the flow limited to the surfaces of a cone which approximates the surface of revolution generated by rotating the meridional-plane streamline (for the circumferentially

averaged flow) about the axis (fig. 34). Blade elements must then be selected which are consistent with the average conditions established in the meridional-plane analysis. This requires a knowledge of loss and turning characteristics of compressor blade elements. This information is usually provided by correlated empirical data, which are obtained from both two-dimensional cascades and from actual blade rows.

(3) Off-design performance: With the compressor blading and geometry established, the final phase of design is the estimation of the performance characteristics of the compressor over a range of speeds and flows. A rigorous solution to this "analysis" problem involves the use of the relations previously established in the meridional and blade-to-blade planes.

As might be inferred from the preceding brief description, such a design system is not direct in the sense that a single step-by-step procedure will result in the desired compressor. For example, because of the large number of factors involved in design (including matching with other engine components), the optimum compressor for any application is obtained only after a series of compromises among these various factors. Obtaining the required off-design characteristics usually necessitates a trial-and-error screening of a number of alternate designs. Therefore, this chapter does not attempt to outline a complete systematic step-by-step design procedure. Instead, the various elements entering into the design system that must be considered in the design process are summarized and interrelations are pointed out. The actual sequence in which these elements are then utilized is left to the individual designer. In the following discussion, the design concepts are grouped under the three principal phases previously listed.

Design-Point Solution in Meridional Plane

Over-all specifications. - As indicated in chapter II, the specifications for an axial-flow compressor in an aircraft gas-turbine engine cannot be stipulated in an arbitrary fashion. Preliminary design studies and combined engine and airplane analyses are usually needed before the requirements are sufficiently explicit to define the design. Based on these preliminary studies, the following data may be given:

- (1) Design weight flow
- (2) Design over-all pressure ratio
- (3) Design equivalent speed
- (4) Desired level of efficiency

- (5) Range of operation for which a high level of efficiency must be obtained
- (6) Inlet and outlet diameters
- (7) Maximum velocity of air at compressor outlet
- (8) Desired length and weight
- (9) Some idea of velocity distortions likely to be encountered at inlet

In the process of design, adjustments in some of these initial specifications are necessary when they are not completely compatible.

Velocity diagrams. - Initially, the meridional-plane solution is directed at determining the velocity diagrams throughout the compressor for the design operating conditions. In the past, analyses have been made in the attempt to establish the most desirable radial distribution of velocity diagrams for aircraft gas-turbine application. For example, reference 8 showed that, for given Mach number and lift-coefficient limitations, the use of a symmetrical velocity diagram at all radii would produce higher mass-flow and pressure ratios than the free-vortex type of diagram. With the use of blade-element theory based on incompressible airfoil concepts and with the assumption of constant axial velocity across the blade row, it was also shown that the symmetrical velocity diagram at all radii was also optimum with respect to profile efficiency.

With advances in the field, such as the raising of Mach number limits (ref. 17) and the establishment of more significant parameters for blade loading (ref. 13), specific velocity-diagram types begin to lose their significance. Research results have shown that satisfactory performance can be achieved for a wide range of velocity diagrams. Although specific velocity-diagram types may still be used because of the resulting convenience in design calculations, the present trend in compressor design is toward a greater freedom in their choice.

For example, raising the Mach number limitations has made free-vortex velocity diagrams attractive because of their simplicity. The design can be further simplified by specifying zero inlet and exit whirl in each compressor stage. With constant work input from hub to tip, as is frequently specified in compressor designs, calculating the radial distribution of the velocity diagram becomes a rather simple process. High-performance compressors have been obtained through the use of this design approach (refs. 28 and 29).

Design equations. - In order to satisfy the aerodynamic and thermodynamic requirements for the circumferentially averaged flow in the

meridional plane, a number of the previously given equations are used. The enthalpy change brought about by a blade row in a tube of flow is given by the energy equation:

$$H_2 - H_1 = \frac{\gamma}{\gamma-1} gR(T_2 - T_1) = \omega(r_2 V_{\theta,2} - r_1 V_{\theta,1}) \quad (7)$$

or

$$\frac{T_2}{T_1} = 1 + \frac{(\gamma-1)\omega r_1}{a_{a,1}^2} \left(\frac{r_2}{r_1} V_{\theta,2} - V_{\theta,1} \right) \quad (7a)$$

If the inlet flow conditions are known, for example, and the outlet tangential velocity is assumed, the temperature ratio T_2/T_1 may be computed. An assumed radial distribution of tangential velocity at the outlet thus determines the outlet radial distribution of enthalpy. The associated radial distribution of axial velocity between blade rows must satisfy equation (19), which is frequently called the equilibrium equation since it may be derived from the consideration of the radial equilibrium of forces:

$$\frac{\partial H}{\partial r} - t \frac{\partial S}{\partial r} = V_{\theta} \zeta_z - V_z \zeta_{\theta} \quad (19)$$

where

$$\zeta_z = \frac{1}{r} \frac{\partial(rV_{\theta})}{\partial r} - \frac{\partial V_r}{r \partial \theta} \quad (17)$$

and

$$\zeta_{\theta} = \frac{\partial V_r}{\partial z} - \frac{\partial V_z}{\partial r} \quad (18)$$

For axial symmetry with no radial flows, equation (19) assumes the following form:

$$\frac{dH}{dr} - t \frac{dS}{dr} = \frac{V_{\theta}}{r} \frac{d(rV_{\theta})}{dr} + V_z \frac{dV_z}{dr} \quad (19a)$$

By integration, this equation becomes

$$V_z^2 - V_{z,1}^2 = 2(H - H_1) - (V_{\theta}^2 - V_{\theta,1}^2) - 2 \int_{r_1}^r \frac{V_{\theta}^2}{r} dr - 2 \int_{r_1}^r t \frac{dS}{dr} dr \quad (27)$$

The velocity V_z at any radius is then expressed in terms of $V_{z,i}$, the velocity at any reference point (e.g., the hub). By interchanging the limits of integration, the casing radius could be used as a reference point.

Another relation between V_z and V_θ is given by the continuity equation:

$$w = 2\pi K_{bk} \int_{r_h}^{r_t} \frac{PV_z}{gRT} \left(1 - \frac{r-1}{2r} \frac{V_z^2 + V_r^2 + V_\theta^2}{gRT} \right)^{\frac{1}{r-1}} r dr \quad (24b)$$

Notice that $V_z^2 + V_r^2 = V_z^2 \sec^2 \epsilon$ (fig. 34). With a known value of ϵ , the value of V_z may now be determined at any radius. For example: A value of $V_{z,i}$ may be tentatively assumed; equation (27) then enables the corresponding values of V_z to be found at various radii; substituting the known values of V_θ and the tentative values of V_z into equation (24b) determines the resulting mass flow w as a function of r_h and r_t . If r_t is given, r_h is then found. If the values of r_h and r_t are independently given, the mass flow calculated may differ from the known value; another trial value of V_i is then assumed, and the procedure is repeated. In making this calculation a value of K_{bk} must be selected. For this and other details in these calculations, see chapter VIII (ref. 11).

The static temperature at various radii at the outlet may now be determined by

$$\frac{r}{r-1} gRT = \frac{r}{r-1} gRt + \frac{1}{2} V_r^2 + \frac{1}{2} V_z^2 + \frac{1}{2} V_\theta^2 \quad (8a)$$

If V_z is known, V_r may be estimated to be $V_z \tan \epsilon$ (see fig. 34).

The change in the total pressure of a stream tube through a blade row may be estimated by one or another form of the following equation:

$$\frac{P_2}{P_1} = \left(\frac{T_2}{T_1} \right)^{\frac{r}{r-1}} e^{-\frac{J}{R} \Delta S} = \left(\frac{T_2}{T_1} \right)^{\frac{r}{r-1} \eta_p} = \left[1 + \left(\frac{T_2}{T_1} - 1 \right) \eta_{ad} \right]^{\frac{r}{r-1}} \quad (12)$$

Estimates may be made of η_p or η_{ad} to determine P_2/P_1 . Or, the change in the relative total pressure may be estimated and the entropy change determined from

$$\frac{P_2'}{P_1'} = \left(\frac{T_2'}{T_1'} \right)^{\frac{\gamma}{\gamma-1}} e^{-\frac{J}{R} \Delta S} \quad (13)$$

where

$$\frac{\gamma}{\gamma-1} gRT' = \frac{\gamma}{\gamma-1} gRt + \frac{1}{2} V_r^2 + \frac{1}{2} V_z^2 + \frac{1}{2} (V_\theta - \omega r)^2 \quad (11a)$$

Notice that V_r may frequently be used in the thermodynamic equations even though it is effectively ignored in other correlations and equations. By using the entropy change in equation (12), the change in total pressure of a stream tube through a blade row is estimated. Notice that different efficiencies and entropy rises are required when the average change in total pressure over the entire blade row is desired.

The change in the static pressure of each stream tube may now be determined by the equation

$$\frac{P_2}{P_1} = \left(\frac{t_2}{t_1} \right)^{\frac{\gamma}{\gamma-1}} \frac{\frac{P_2}{P_1}}{\left(\frac{T_2}{T_1} \right)^{\frac{\gamma}{\gamma-1}}} \quad (14)$$

The total pressures in this equation must be those in the given stream tube ahead of and behind the blade row. The associated change in density is finally given by

$$p = \rho gRt \quad (5)$$

or

$$\frac{\rho_2}{\rho_1} = \frac{P_2}{P_1} \frac{t_1}{t_2} \quad (6)$$

Average values of energy addition for entire blade row. - In order to determine mass-flow-averaged values of pressure and temperature (or efficiency) at the discharge of a compressor blade row, the contributions of the boundary layer must be accounted for. As previously discussed, a precise integration from wall to wall is not possible, because of a lack of knowledge of the conditions within the boundary layer. In the main-flow region, however, all the conditions of state may be presumed to be known. A possible technique for accounting for the effects of wall boundary layers is to write the equations as if the main-flow conditions

prevailed across the entire annular height, and to utilize modifying coefficients (based on the experimental data) to correct for the defects in the boundary layer. As previously noted, this technique is similar to that used for satisfying continuity. A detailed discussion of techniques available for establishing mass-averaged values of pressure, temperature, or efficiency is given in chapter VIII (ref. 11).

Blade loading. - In the preceding sections, relations have been presented that permit the designer to determine velocity diagrams. In general, designers establish these velocity diagrams on the basis of optimizing such performance characteristics as specific mass flow, stage pressure ratio, and efficiency. Unfortunately, the conditions for obtaining maximum values of all three factors are not usually compatible. Therefore, the designer must consider the selected values of the design parameters on the basis of their effect on each of the several factors describing compressor performance. Blade loading is one of the primary aerodynamic factors influencing this performance that must be selected in the process of determining compressor velocity diagrams. It is apparent that large values of ΔV_θ are desirable with respect to obtaining a large pressure ratio per stage (eqs. (7) and (12)). In the past, the concept of maximum lift coefficient as used in isolated-airfoil design has been also applied to compression to estimate the maximum blade turning angle, or loading limit, for which high efficiency may be obtained (e.g., the $C_{L\sigma}$ limit of ref. 8). It has been recognized, however, that the lift coefficient is not completely adequate as a measure of loss variation and of loading limits in a compressor.

An improved approach to the problem is one previously outlined. It considers the pressure distribution about a two-dimensional blade element in cascade and its influence on boundary-layer growth and separation. References 13 and 14 show that loading parameters based on the diffusion on the suction surface provide improved criteria for loss and for limiting loading. The diffusion factor as proposed in reference 13 is given for the case of a rotor with no radius change as

$$D = \left(1 - \frac{V_2'}{V_1'}\right) + \frac{\Delta V_\theta'}{2\sigma V_1'} \quad (25)$$

A discussion of diffusion limits, as well as empirical loss correlations based on available experimental data, is given in chapters VI and VII (ref. 11). Notice that, for a given value of $\Delta V_\theta'$ and a given value of D , the corresponding value of V_2' is automatically determined. This value could be used as a guide for selecting $V_{z,i}$ in equation (27), or, instead, $V_{z,i}$ could be independently scheduled and $V_{\theta,i}$ determined.

Relative Mach number. - Another important aerodynamic factor that has been discussed previously is the Mach number relative to rotor blade elements. As a result of the demand for high stage pressure ratios and

high mass-flow capacity, the trend in compressor design has been toward higher compressor relative Mach numbers. The earliest attempts (ref. 30) to utilize these high relative Mach numbers led to large sacrifices in efficiency. However, with an improved understanding of the physics of flow over compressor blading (ref. 17), the gains associated with high Mach numbers have been achieved without corresponding reductions in efficiency. High performance has been demonstrated in multistage axial-flow compressors utilizing local relative entrance Mach numbers above 1.0 (refs. 29 and 31). Mach numbers up to 1.35 have been successfully utilized in single-stage units (ref. 23). It is generally accepted that this high level of relative Mach number can be maintained in compressors if proper consideration is given to the accompanying value of diffusion factor and to the form and thickness of the blade profiles. For routine design purposes, Mach numbers up to 1.2 may be contemplated. For higher Mach numbers, more refined techniques must be used.

Reynolds number. - Compared with the effects of loading and Mach number, the effect of Reynolds number on compressor performance is of secondary importance for the current types of aircraft. Reynolds number in a compressor is usually expressed in terms of blade chord $\rho Vc/\mu$, and the effect of a reduction in Reynolds number is to reduce the pressure ratio, weight flow, and efficiency of the compressor. This reduction in performance depends basically on the development of the boundary layer over the airfoil surfaces, the magnitude of the effect depending on the magnitude of Reynolds number, the turbulence level, and the pressure gradients in the flow. Discussions of Reynolds number effects are included in chapters V, VI, and VII (see ref. 11). Although Reynolds number has been largely ignored in the past, it may play an important role in establishing the size of the compressors in high-altitude aircraft.

Axial velocity. - In a multistage axial-flow compressor, the axial velocity at the inlet is usually fixed by the mass flow per unit frontal area and the compressor hub-tip ratio. The axial velocity at the compressor exit is usually fixed by the diffuser and combustor requirements. The exact scheduling of axial velocity between these points is largely a function of blade-row design. Large reductions of axial velocity across any one blade element should be avoided whenever possible, since, for a given value of ΔV_θ , the diffusion factor is thereby increased.

Hub and tip contours. - In a multistage axial-flow compressor, configurations are possible in which the tip diameter, the hub diameter, or both, vary from stage to stage through the compressor. As pointed out in reference 8, a progressive increase in tip diameter is desirable with regard to maintaining high pressure ratios per stage and keeping the relative Mach number below a given value. However, the weight flow per unit frontal area is reduced. Furthermore, an increase in tip diameter results in reduced annular heights (for a given flow area) and reduced aspect ratios (for a given blade chord). Consequently, tip-clearance

and annulus losses are probably larger for the increased tip diameter than for a comparable constant-tip-diameter design. Moreover, the high relative Mach numbers that may now be used tend to reduce many of the advantages cited in reference 9.

Constant-hub- or constant-tip-diameter designs offer some advantage with respect to fabrication and therefore are frequently used. However, there is increasing evidence that a configuration with a decreasing tip diameter may provide the best compressor layout, even though it may require one or two more stages for a given over-all pressure ratio. From the aerodynamic point of view, the increased annular heights near the exit may also offer higher efficiencies.

Thus, the final selection of the configuration in the meridional plane is seen to depend to a large degree on the application being considered. Again, this is a phase of design in which the designer has considerable freedom; at least, several designs should be evaluated to establish an optimum for a given application.

Blade Selection

The basic principle of compressor blade selection is that, if the blade element turns the air through the required angle with the predicted loss, the desired blade-row velocity diagrams will be closely achieved. The selection of blade sections and settings for a given turning may be obtained from two-dimensional-cascade testing (ch. VI (ref. 11) and refs. 15 and 32) or from blade-element measurements made in rotating or stationary annular cascades (ch. VII (ref. 11)). Loss data are usually based on measurements made in the actual compressor environment (ch. VII). By using data such as these, elements are selected to obtain the desired turning with a minimum loss and to provide a maximum range of operation. The complete blade is built up from the blade-element profiles determined at several selected stations along the radial height of the passage.

Blade profile. - Basic blade shapes for compressor application are usually obtained by (1) establishing a mean line and (2) imposing a thickness distribution on this mean line. This method of designation is a carryover from isolated-airfoil experiences. It should be noted that the mean line and thickness distribution do not have the same significance in cascades as they did in isolated airfoils. Mean lines may be based on geometric shapes (e.g., circular- or parabolic-arc) or on prescribed loading distributions (NACA A₁₀). The mean-line shape is then scaled to give any desired camber. Thickness distributions are similarly determined; two popular thickness distributions are the NACA 65-series and the British C.4. Variations in absolute blade thicknesses are obtained by proportionally scaling the basic thickness distribution.

In the past, only a limited number of basic blade shapes have been used in compressor design, primarily because of the lack of adequate cascade data. In the United States, the NACA 65-series blade section has found the greatest application. In England, the blades with circular and parabolic mean lines have been used extensively. With the recent trend toward high Mach number applications, however, blade sections such as the double circular arc (ref. 33) and the modified 65-series blades (ref. 34) have received the most attention. All these common denominators for developing blade families are rather synthetic. The aerodynamic significance of geometric blade shapes changes so much with solidity and blade angle that some implied correlations are misleading.

Blade-element data. - The basic parameters selected in this report for the description of flow about compressor blade elements are:

- (1) Incidence angle i (angle between inlet air-flow direction and tangent to mean line at leading edge, fig. 2)
- (2) Deviation angle δ^o (angle between outlet air-flow direction and tangent to mean line at trailing edge, fig. 2)
- (3) Total-pressure-loss coefficient $\bar{\omega}'$

Incidence angle has been selected as the basic directional approach parameter rather than angle of attack, since incidence angle is independent of blade camber and therefore provides a more significant description of flow around the blade leading edge. Deviation angle is selected as a measure of the blade guidance capacity; turning angle can then be determined by the relation

$$\Delta\beta = \varphi + i - \delta^o \quad (28)$$

The loss coefficient is defined as

$$\bar{\omega}' = \frac{(P_2')_{id} - P_2'}{P_1' - P_1} = \left(\frac{P_2'}{P_1'} \right)_{id} \left\{ \frac{1 - \frac{P_2'}{P_1'}}{\left(\frac{P_2'}{P_1'} \right)_{id}} \right. \quad (29)$$

$$\left. 1 - \left[\frac{1}{1 + \frac{\gamma-1}{2}(M_1')^2} \right]^{\frac{\gamma}{\gamma-1}} \right\}$$

where $(P_2'/P_1')_{id}$ is

$$\left(\frac{P_2'}{P_1'}\right)_{id} = \left\{ 1 + \frac{r-1}{2} \frac{(\omega r_2)^2}{rgRT_1} \left[1 - \left(\frac{r_1}{r_2}\right)^2 \right] \right\}^{\frac{r}{r-1}} \quad (30)$$

Blade-element characteristics are presented in terms of these turning and loss parameters in chapters VI and VII (ref. 11). In chapter VI, the data are correlated for blades in a two-dimensional low-speed cascade; in chapter VII, the data are given for blade elements of single-stage rotors and stators.

In the latter case, data are presented as functions of the radial position of the element. Through the use of this type of experimental data, obtained in the actual compressor environment, it is hoped that the important effects of three-dimensional flows will be accounted for. This concept is probably valid if the design under consideration does not deviate too greatly from the conditions under which the data were obtained.

Chord length and number of blades. - The aerodynamic design normally establishes the desired value of the cascade solidity. The actual selection of the chord length and number of blades then involves a consideration of a large number of factors, including blade-chord Reynolds number, weight, available length, blade root choking, blade root fastening, steady-state stresses, vibratory stresses, and manufacturing problems. Over and above many of these factors is the fact that the curvature of the hub and casing changes with chord length. This factor is discussed in the section REQUIRED IMPROVEMENTS IN ANALYSES.

Off-Design Analysis

With the compressor flow channel and the blading established, the final phase of compressor design is the estimation of the performance of the compressor over a range of speeds and flows. Basically, the same relations and data are required for a thorough treatment of this problem. This blade-element type of solution, however, necessitates a rather complete knowledge of the blade-element flow, radial equilibrium, boundary-layer growth, blade-row interactions, radial mixing, and so forth. Unfortunately, this type of information is limited, and the prediction of compressor performance on the basis of the integration of blade-element characteristics is probably limited to operating points close to design. In particular, this technique always breaks down when a stalled condition occurs in the blade rows and may break down sooner owing to the lack of appropriate data concerning the behavior of K_{bk} and loading limits in the latter stages of a compressor.

Other simpler and more approximate approaches to the prediction of off-design performance have been developed. In particular, a stacking technique that utilizes certain generalized stage performance curves has been used effectively in the qualitative study of off-design operating problems. A discussion of those techniques which are available for prediction of off-design performance of multistage compressors is given in chapter X (ref. 11).

REQUIRED IMPROVEMENTS IN ANALYSES

As previously noted, there are three areas in which a better understanding of the flow is required in order to improve design techniques. One area encompasses the problem of estimating the radial distribution of flow in compressors of advanced design. The second area concerns the problem of treating the boundary layers at the hub and casing. The third area deals with the problem of estimating loading limits. Some of the work that has been done to clarify these problems is discussed in this section. While none of the work is far enough advanced to be included in a recommended design system, some phases can be useful for refining the design calculations. In other cases, the work has progressed only far enough to partially identify the real underlying problems.

Radial Distribution of Flow

The problem of accurately estimating the radial distribution of the flow in compressors of advanced design may be appreciated from the following considerations: In order to obtain high flow capacity and short length, the first rotor of advanced multistage compressors may look more like those shown in figures 37(a) and (b) than that shown in figure 37(c), which represents current practice. The higher pressure ratios in the new designs require a greater change in the annular area through the blade row, and the chord length will be as small as possible. In order to obtain high air-flow capacity, the new designs will have lower hub-tip ratios and higher axial velocities.

Because of these differences in geometry, the curvature of the streamlines of figure 34 will be greater for the new designs. In flowing through the stream tubes, the air exerts a centrifugal force:

$$\mathcal{F}_c = \rho v_z^2$$

The large curvatures and high axial velocities make \mathcal{F}_c have the same order of magnitude as

$$\mathcal{F}_R = \frac{v_\theta^2}{r}$$

which is the centrifugal force resulting from the rotation of the air about the compressor axis. (Eqs. (19a) and (19b) are essentially based on the premise that \mathcal{F}_C is low enough in comparison to \mathcal{F}_R to be ignored.) Since \mathcal{F}_R has been found to be quite important (it is a dominant term in eq. (19a)), it follows that \mathcal{F}_C must also be taken into account in the new designs.

An indication of the problems encountered by neglecting curvature is obtained from reference 35. An investigation was made of a single-stage compressor with an inlet hub-tip ratio of 0.4 and an inlet axial velocity that was intended to be constant along the radius. Tests showed, however, that the inlet axial velocity actually had the variation shown in figure 38. The ordinate in this figure is the ratio of the measured axial velocity to that at the mean radius. While the difference between the design and observed velocities did not seriously affect the average performance of this particular rotor, it did upset the flow in the neighborhood of the casing. Both the angle of attack and the blade loading can be critically upset by this order of error, and the multistaging effects become undesirable.

Some methods of including the effects of streamline curvature in the flow analysis have been developed for mixed-flow compressors (ref. 36). These methods are similar to those attributed to Flügel in reference 37. Substantial improvements in the design performance of these compressors immediately resulted from the use of this technique (refs. 38 and 39). It enabled the designer to eliminate adverse or impossible flow situations that would otherwise be unknown. The method has also been extended to turbines (ref. 40). As shown in references 41 to 43, techniques such as this had to be used when the curvature of the hub and the axial velocities were high. Otherwise, the measured velocity distribution differed so much from that designed that poor performance was inevitable. In other instances, premature choking within the blade row could be recognized and avoided in design only by using such an analysis.

The extent to which these methods can be used in axial-flow compressors is unknown. The small chord length compared with the blade spacing and the span makes some of the necessary assumptions rather tenuous. Perhaps some of the techniques reviewed in chapter XIV (ref. 6) may have to be used. One critical problem is that of estimating the circumferentially averaged flow distribution through the blade row for flows at high Mach numbers. Some hope is offered by the approximate methods of reference 23. In particular, the method used for designing the Mach 1.35 rotor in reference 23 may be of value, crude though it is. More work along these lines is necessary.

Hub and Casing Boundary Layers

One of the greatest limitations of current design techniques is the fact that the flows in the hub and casing boundary layers cannot be correlated against anything definite. The importance of this problem has been the impetus for a considerable amount of research, both in the field of compressors and in the allied field of turbines. The results of preliminary studies suggest that the key to the problem may be an understanding of secondary flows. Some noteworthy advances in this understanding are described in the following paragraphs.

Secondary flows of blade boundary layer and wakes. - Detailed studies of the flow distribution in annular stators (ch. XV (ref. 6)) reveal that some of the losses at the blade ends may be created or transported there by secondary flows. One type of secondary flow arises from the requirements of radial equilibrium (eq. (4) of ch. XIV (ref. 6)):

$$-\frac{1}{\rho} \frac{\partial p}{\partial r} = V_r \frac{\partial V_r}{\partial r} + V_\theta \frac{\partial V_r}{r \partial \theta} + V_z \frac{\partial V_r}{\partial z} - \frac{V_\theta^2}{r} - \mathcal{F}_{fr,r}$$

Within the boundary layers and wakes of a blade row, the pressures and pressure gradients are approximately the same as those in the adjacent potential-flow streams. In the type of stators normally used, the value of V_r is small in the main stream, and the values of V_θ and V_z are lower in the boundary layer and wakes than they are in the main stream. Unless $\mathcal{F}_{fr,r}$ is also large, the derivatives of V_r must increase (in the absolute sense), and V_r may thus assume moderately high values. When the boundary layers are thin, the value of $\mathcal{F}_{fr,r}$ throughout the entire boundary layer may be high enough to prevent large radial movements of the flow. When the boundary layers are thick, however, the frictional forces are relatively low. The boundary layer on the stator blades then flows from a region of high pressure to one of low pressure - that is, toward the hub. Since the value of $\mathcal{F}_{fr,r}$ is small in the wakes, the fluid in the wakes also moves toward the hub. Physical evidence of this flow is presented in chapter XV (ref. 6).

In rotors, on the other hand, the boundary layers and wakes travel radially outward. Since the tangential velocity of the blades is greater than that of the main stream, the value of V_θ in the boundary layer exceeds that of the main stream. The sign of the derivatives of V_r is thus reversed.

Existing evidence, such as that reviewed in chapter XV, suggests that a considerable portion of the losses near the casing of a rotor and near the hub of a stator may be attributed to losses created at some other point of the blade and transported to these regions. Besides just being there, the boundary layers at the blade ends may disturb the flow

enough to induce flow separation and thereby create additional losses. Conversely, the movement of boundary layers away from the rotor hubs and stator tips may permit these regions to operate at conditions that would be impossible for their two-dimensional counterparts. This reasoning could partially explain why the cascade elements of rotor hubs and stator tips can sometimes operate at higher angles of attack than their two-dimensional counterparts.

Cross-channel flows and passage vortex formation. - Secondary flow also describes a movement of the boundary layer on the hub or casing. The flow is from the high-pressure side of one blade to the low-pressure side of the adjacent blade (fig. 39(a)). The phenomenon is fundamentally the same as that for the radial flows just described. The transverse pressure gradients in the main flow are again greater than those which the slowly moving boundary layers can support. Part of these gradients are resisted by friction and the rest tend to accelerate the flow to the low-pressure region. The experiments reviewed in chapter XV show that the boundary layers move across the passage and then roll up into a vortex (fig. 39(b)). It is conceivable that this movement of boundary layer may cause the flow near the suction surface of the blade ends to be more easily separated than the corresponding flow in ideal two-dimensional cascades.

Flow in blade end regions with clearance. - Other secondary flows result from the clearance between the blades and the adjacent wall. If the blades and the wall are stationary, air flows through the clearance space from the high- to the low-pressure side. It then rolls up as a vortex (fig. 40(a)). If the wall is moving with respect to the blades (such as an unshrouded rotor tip or stator hub), the blades may also scrape the boundary layer from the walls; a vortex similar to that of figure 40(b) is then formed near the pressure side of the blades.

Mixing of hub and casing boundary layers with main flow. - After the boundary-layer distributions are established behind a blade row (e.g., a rotor), the following blade row (in this case a stator) tends to mix them with the main flow. This behavior is clearly shown in reference 44. Figure 41(a), taken from this reference, shows the measuring stations and radial positions of measurements taken to determine the radial distribution of the efficiency of the rotor and the corresponding radial distribution of efficiency of rotor and stator. An example of the efficiency distribution is shown in figure 41(b). Because the rotor was severely loaded (large D factor), the rotor efficiency dropped rapidly in the vicinity of the outer radius. Measurements after the stator, however, indicated that the over-all efficiency at the outer radius was higher than that measured after the rotor. At the inner radii, the efficiency was much lower. The increase in efficiency at the outer radius can only be explained by a radially inward movement of the thick boundary layer as the flow passes through the stator. This movement also helps to

explain the low efficiency of the air leaving the stator at the inner radii. Because of the different boundary-layer motions in a rotor and stator, a stator tends to mix up the boundary-layer distributions set up by a rotor, and vice versa. Although the energy added to the main flow by the hub and casing boundary layers usually does not noticeably increase the enthalpy of the main flow, these wayward movements of the boundary layer make the correlation of losses a difficult problem. Among other things, the losses transported by the boundary layer to a given radius must be separated from those created at that radius. The losses created must, in turn, be divided into those which are inherent at the radius in question, and those which are induced or allayed by the inward or outward flux of the boundary layer. To date, no satisfactory technique has been found for separating these losses. At present, perhaps the best alternative is to continue to report the observed losses as a function of four quantities: the aerodynamic loading of the blade element, which involves relative Mach number and something akin to the diffusion factor; the geometry of the cascade element; the radial position of the element with respect to the hub and tip; and the distribution of flow ahead of the blade row.

Loading Limits

The analyses presented in references 13 and 14 suggest that the loading limits of a two-dimensional cascade can be quite ably described. Experience in actual blade rows, however, indicates that the loading limit of a cascade element depends upon the location of the element. Cascade elements near the casing of a rotor seem to stall at lower loadings than those near the center of the span or near the hub. There are also some indications that the hub regions of a stator are critical. Moreover, the condition of the hub and casing boundary layers is suspected to play an important role in determining the loading limit of the nearby cascade elements.

Because of the importance of the problem of loading limits, a large amount of work is being devoted to it. One of the questions to be answered is whether or not the ideas expressed by equation (26) are the important ones. Another important question is concerned with estimating the various terms of this equation. Still a third problem is the determination of the way the inlet flow conditions influence the loading parameter.

Improving the understanding of these loading limits is another incentive for continued effort in the study of ideal flows and the study of boundary layers. Reasonably simple yet accurate methods of estimating the critical velocities about various cascade elements are required. The interrelation between boundary-layer behavior and the pressure gradients created by the main flow must be better understood. Intensive efforts, both theoretical and experimental, will probably be required to pinpoint the answers within a tolerable range.

CONCLUDING REMARKS

A general picture of the flow characteristics of axial-flow compressors has been developed, indicating those features that must be considered in the design process. On the basis of this qualitative description of flow, the structure of a design system is outlined. The individual elements of the design system, including basic techniques and equations, are summarized. Also noted are some of the important gaps in knowledge, where art must be substituted for science. This information provides a design system and summarizes much of the work presented in the succeeding chapters. This general treatment is expanded in these chapters to provide specific design data that describe the techniques of application in detail.

REFERENCES

1. Sorensen, Harry A.: Gas Turbines. Ronald Press Co., 1951.
2. Wislicenus, George F.: Fluid Mechanics of Turbomachinery. McGraw-Hill Book Co., Inc., 1947.
3. Howell, A. R.: The Present Basis of Axial Flow Compressor Design. Pt. II - Compressor Theory and Performance. Rep. No. E.3961, British R.A.E., Dec. 1942.
4. Bowen, John T., Sabersky, Rolf H., and Rannie, W. Duncan: Theoretical and Experimental Investigations of Axial Flow Compressors. Mech. Eng. Lab., C.I.T., Jan. 1949. (Navy Contract N6-ORI-102, Task Order IV.)
5. Zucrow, Maurice Joseph: Principles of Jet Propulsion and Gas Turbines. John Wiley & Sons, Inc., 1948.
6. Compressor and Turbine Research Division: Aerodynamic Design of Axial-Flow Compressors. Vol. III. NACA RM E56B03b, 1956.
7. Stanitz, John D.: Effect of Blade-Thickness Taper on Axial-Velocity Distribution at the Leading Edge of an Entrance Rotor-Blade Row with Axial Inlet, and the Influence of This Distribution on Alinement of the Rotor Blade for Zero Angle of Attack. NACA TN 2986, 1953.
8. Sinnette, John T., Jr.: Analysis of Effect of Basic Design Variables on Subsonic Axial-Flow-Compressor Performance. NACA Rep. 901, 1948. (Supersedes NACA RM E7D28.)
9. Stanitz, John D., and Ellis, Gaylord O.: Flow Surfaces in Rotating Axial-Flow Passages. NACA TN 2834, 1952.

10. Ruden, P.: Investigation of Single Stage Axial Fans. NACA TM 1062, 1944.
11. Compressor and Turbine Research Division: Aerodynamic Design of Axial-Flow Compressors. Vol. II. NACA RM E56B03a, 1956.
12. Stewart, Warner L.: Investigation of Compressible Flow Mixing Losses Obtained Downstream of a Blade Row. NACA RM E54I20, 1954.
13. Lieblein, Seymour, Schwenk, Francis C., and Broderick, Robert L.: Diffusion Factor for Estimating Losses and Limiting Blade Loadings in Axial-Flow-Compressor Blade Elements. NACA RM E53D01, 1953.
14. Savage, Melvyn: Analysis of Aerodynamic Blade-Loading-Limit Parameters for NACA 65-(C₇O A₁₀)10 Compressor-Blade Sections at Low Speeds. NACA RM L54L02a, 1955.
15. Herrig, L. Joseph, Emery, James C., and Erwin, John R.: Systematic Two-Dimensional Cascade Tests of NACA 65-Series Compressor Blades at Low Speeds. NACA RM L51G31, 1951.
16. Andrews, S. J.: Tests Related to the Effect of Profile Shape and Camber Line on Compressor Cascade Performance. Rep. No. R.60, British N.G.T.E., Oct. 1949.
17. Klapproth, John F.: General Considerations of Mach Number Effects on Compressor-Blade Design. NACA RM E53L23a, 1954.
18. Beatty, Loren A., Savage, Melvyn, and Emery, James C.: Experimental Investigation of Flow through Three Highly Loaded Inlet Guide Vanes Having Different Spanwise Circulation Gradients. NACA RM L52D25a, 1952.
19. Lieblein, Seymour, and Ackley, Richard H.: Secondary Flows in Annular Cascades and Effects on Flow in Inlet Guide Vanes. NACA RM E51G27, 1951.
20. Mahoney, John J., Dugan, Paul D., Budinger, Raymond E., and Goelzer, H. Fred: Investigation of Blade-Row Flow Distributions in Axial-Flow-Compressor Stage Consisting of Guide Vanes and Rotor-Blade Row. NACA RM E50G12, 1950.
21. Westphal, Willard R., and Godwin, William R.: Comparison of NACA 65-Series Compressor-Blade Pressure Distributions and Performance in a Rotor and in Cascade. NACA RM L51H20, 1951.

22. Lieblein, Seymour, Lewis, George W., Jr., and Sandercock, Donald M.: Experimental Investigation of an Axial-Flow Compressor Inlet Stage Operating at Transonic Relative Inlet Mach Numbers. I - Over-All Performance of Stage with Transonic Rotor and Subsonic Stators Up to Rotor Relative Inlet Mach Number of 1.1. NACA RM E52A24, 1952.
23. Klapproth, John F., Jacklitch, John J., Jr., and Tysl, Edward R.: Design and Performance of a 1400-Foot-Per-Second-Tip-Speed Supersonic Compressor Rotor. NACA RM E55A27, 1955.
24. Johnsen, Irving A.: Investigation of a 10-Stage Subsonic Axial-Flow Research Compressor. I - Aerodynamic Design. NACA RM E52B18, 1952.
25. Budinger, Ray E., and Thomson, Arthur R.: Investigation of a 10-Stage Subsonic Axial-Flow Research Compressor. II - Preliminary Analysis of Over-All Performance. NACA RM E52C04, 1952.
26. Budinger, Ray E.: Investigation of a 10-Stage Subsonic Axial-Flow Research Compressor. VI - Performance Evaluation and Flow Distributions in the First, Fifth, and Tenth Stages. NACA RM E54F28, 1954.
27. Hatch, James E., Giamati, Charles C., and Jackson, Robert J.: Application of Radial-Equilibrium Condition to Axial-Flow Turbomachine Design Including Consideration of Change of Entropy with Radius Downstream of Blade Row. NACA RM E54A20, 1954.
28. Sandercock, Donald M., Kovach, Karl, and Lieblein, Seymour: Experimental Investigation of a Five-Stage Axial-Flow Research Compressor with Transonic Rotors in All Stages. I - Compressor Design. NACA RM E54F24, 1954.
29. Kovach, Karl, and Sandercock, Donald M.: Experimental Investigation of a Five-Stage Axial-Flow Research Compressor with Transonic Rotors in All Stages. II - Compressor Over-All Performance. NACA RM E54G01, 1954.
30. Dugan, Paul D., Mahoney, John J., and Benser, William A.: Effect of Mach Number on Performance of an Axial-Flow Compressor Rotor-Blade Row. NACA RM E8D29, 1948.
31. Geye, Richard P., Budinger, Ray E., and Voit, Charles H.: Investigation of a High-Pressure-Ratio Eight-Stage Axial-Flow Research Compressor with Two Transonic Inlet Stages. II - Preliminary Analysis of Over-All Performance. NACA RM E53J06, 1953.

32. Felix, Richard A.: Summary of 65-Series Compressor-Blade Low-Speed Cascade Data by Use of the Carpet-Plotting Technique. NACA RM L54H18a, 1954.
33. Lewis, George W., Jr., Schwenk, Francis C., and Serovy, George K.: Experimental Investigation of a Transonic Axial-Flow-Compressor Rotor with Double-Circular-Arc Airfoil Blade Sections. I - Design, Over-All Performance, and Stall Characteristics. NACA RM E53L21a, 1954.
34. Savage, Melvyn, Erwin, John R., and Whitley, Robert P.: Investigation of an Axial-Flow Compressor Rotor Having NACA High-Speed Blade Sections (A_2I_{8b} Series) at Mean Radius Relative Inlet Mach Numbers Up to 1.13. NACA RM L53G02, 1953.
35. Montgomery, John C., and Glaser, Frederick W.: Experimental Investigation of a 0.4 Hub-Tip Diameter Ratio Axial-Flow Compressor Inlet Stage at Transonic Inlet Relative Mach Numbers. II - Stage and Blade-Element Performance. NACA RM E54I29, 1955.
36. Hamrick, Joseph T., Ginsburg, Ambrose, and Osborn, Walter M.: Method of Analysis for Compressible Flow through Mixed-Flow Centrifugal Impellers of Arbitrary Design. NACA Rep. 1082, 1952. (Supersedes NACA TN 2165.)
37. Stodola, A.: Steam and Gas Turbines. Vol. I. McGraw-Hill Book Co., Inc., 1927. (Reprinted, Peter Smith (New York), 1945.)
38. Withee, Joseph R., Jr., and Beede, William L.: Design and Test of Mixed-Flow Impellers. II - Experimental Results, Impeller Model MFI-1A. NACA RM E52E22, 1952.
39. Smith, Kenneth J., and Osborn, Walter M.: Design and Test of Mixed-Flow Impellers. VI - Performance of Parabolic-Bladed Impeller with Shroud Redesigned by Rapid Approximate Method. NACA RM E55F23, 1955.
40. Stewart, Warner L.: Analytical Investigation of Flow through High-Speed Mixed-Flow Turbine. NACA RM E51H06, 1951.
41. Stewart, Warner L., Whitney, Warren J., and Monroe, Daniel E.: Investigation of Turbines for Driving Supersonic Compressors. III - First Configuration with Four Nozzle Settings and One Nozzle Modification. NACA RM E53A20, 1953.

42. Stewart, Warner L., Whitney, Warren J., and Heaton, Thomas R.: Effect of Certain Combinations of Wall Contouring and Design Exit Velocity Distribution on Prediction of Turbine-Nozzle Mass Flow. NACA RM E53E14, 1953.
43. Stewart, Warner L., Wong, Robert Y., and Evans, David G.: Design and Experimental Investigation of Transonic Turbine with Slight Negative Reaction Across Rotor Hub. NACA RM E53L29a, 1954.
44. Standahar, Raymond M.: Investigation of Three Highly Loaded Subsonic-Inlet-Stage Axial-Flow Compressors Employing Varying Radial Gradients of Energy Addition. NACA RM E54G20, 1954.

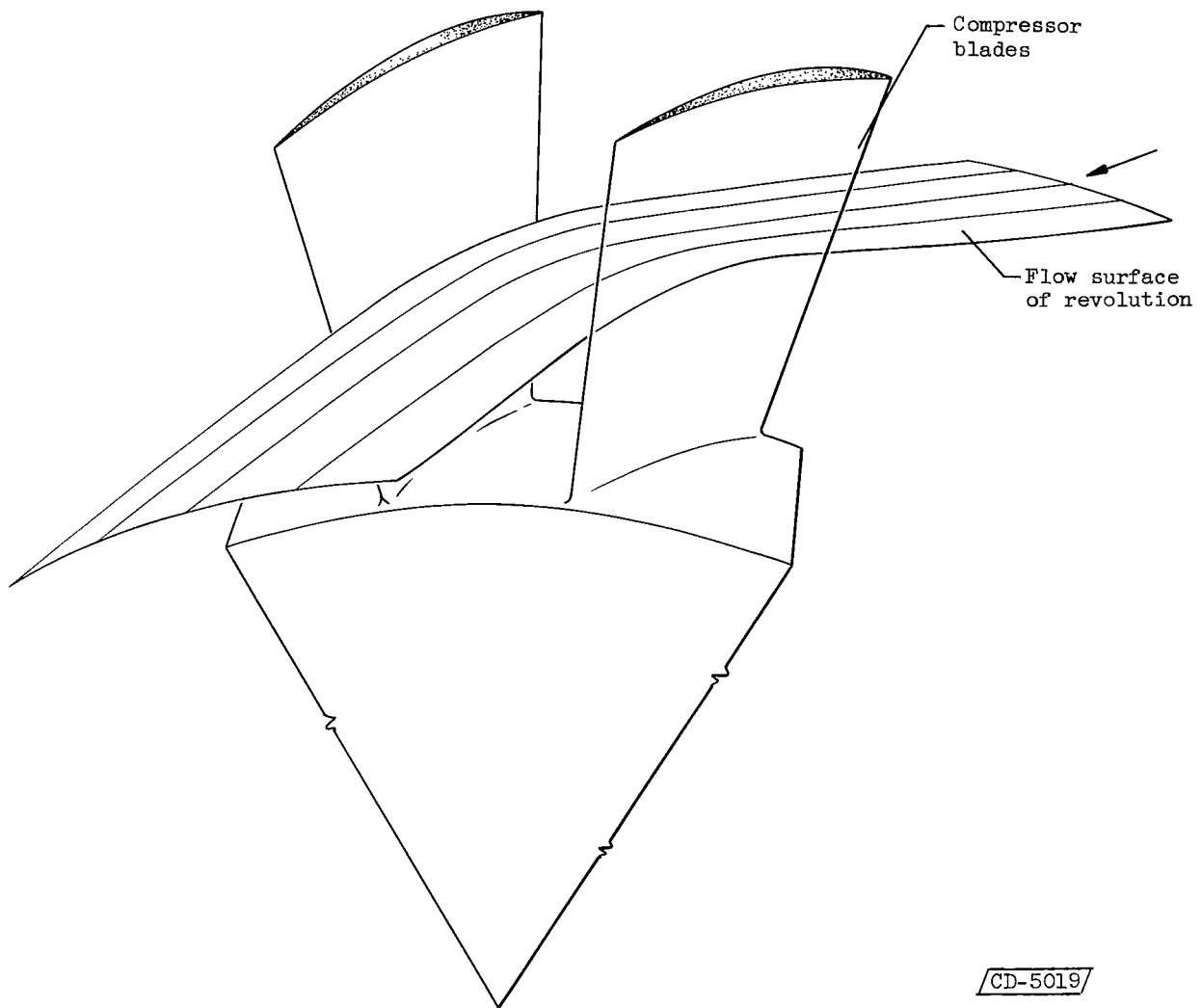


Figure 1. - Sketch of flow surface and streamlines when assumed flow lies on the surface of a right circular cylinder.

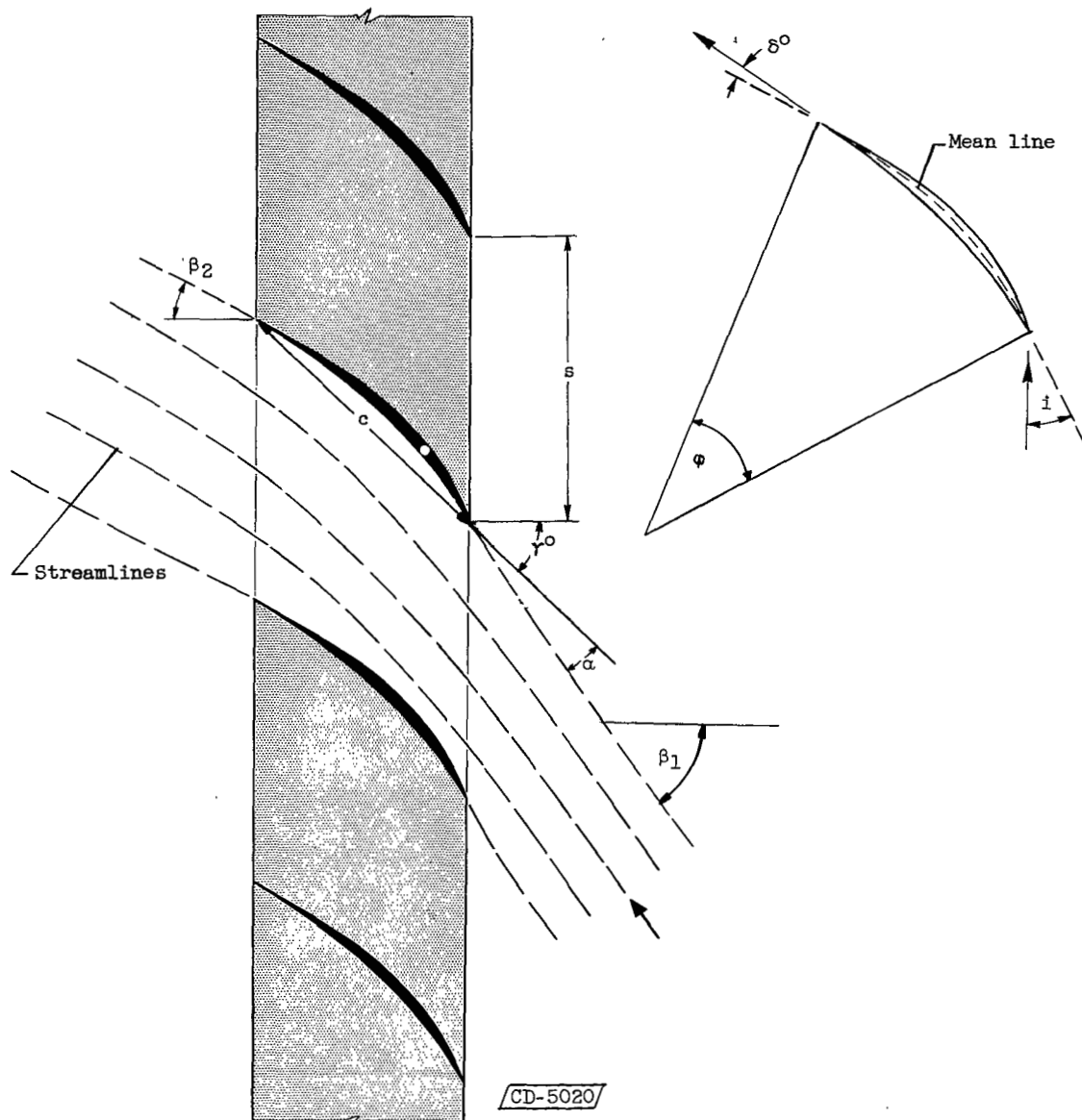


Figure 2. - Sketch of two-dimensional cascade showing streamlines and nomenclature.

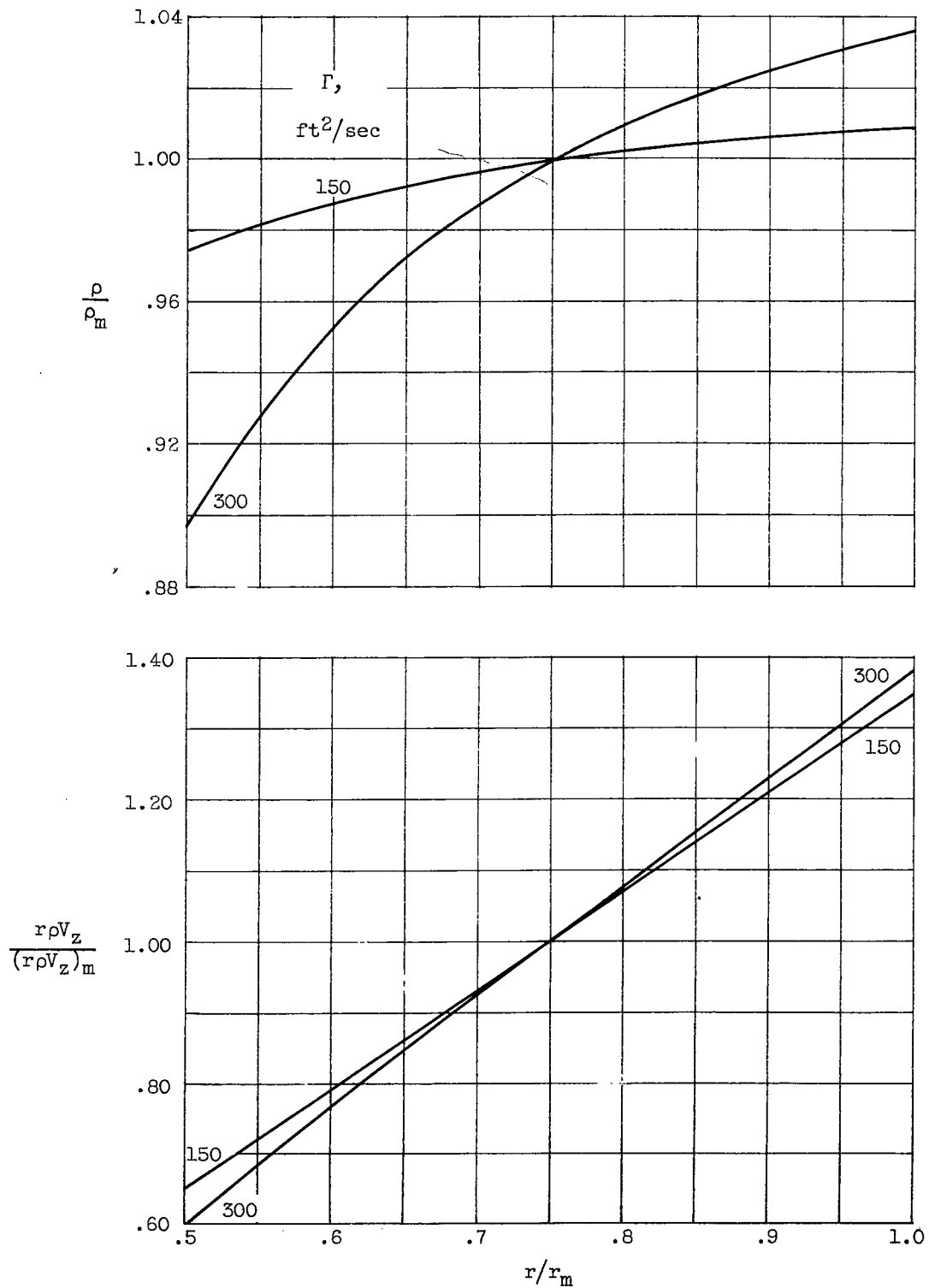


Figure 3. - Changes in distributions of ρ and $r\rho V_z$ due to change in Γ through blade row.

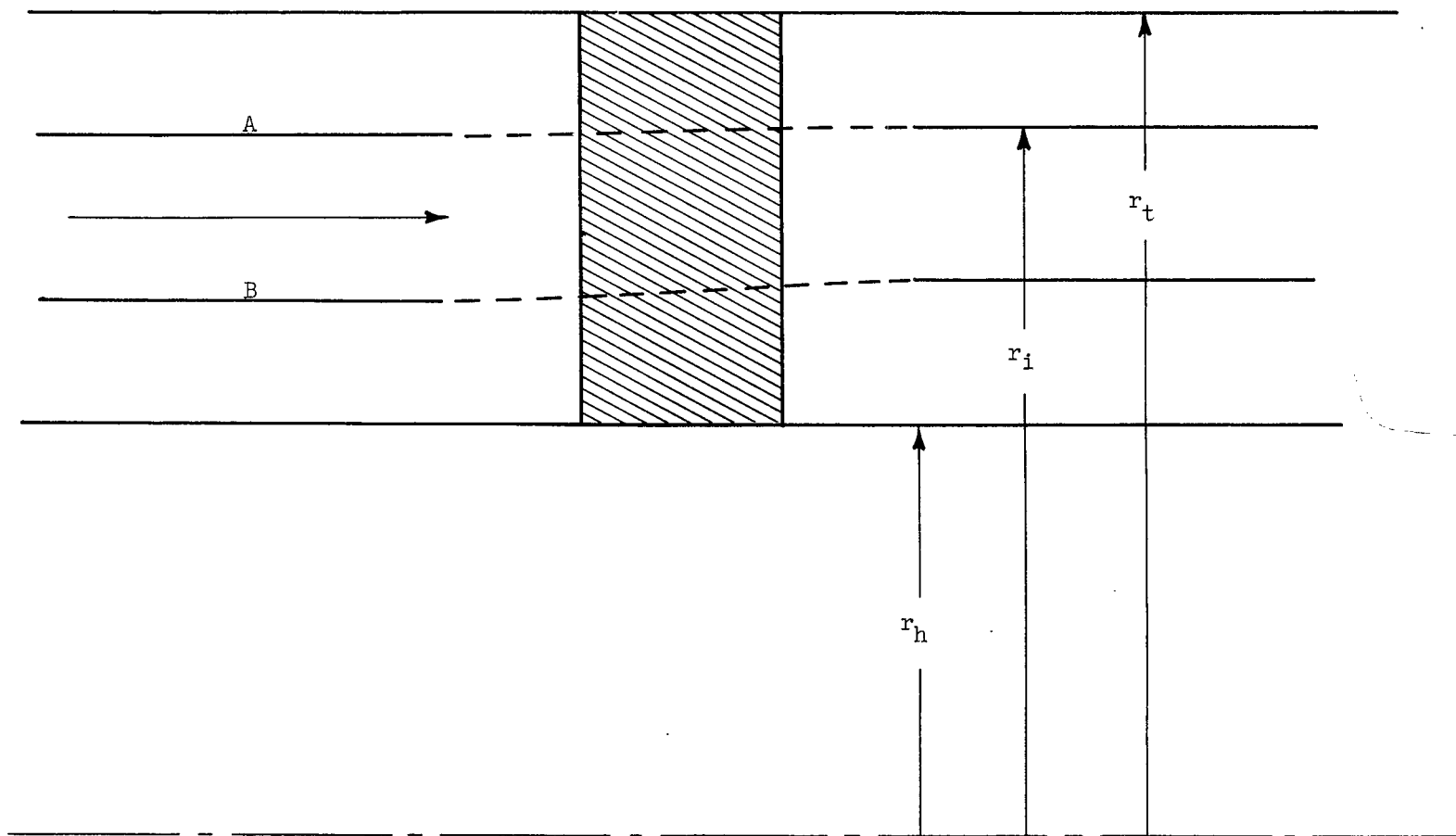


Figure 4. - Radial shift of streamlines due to change in radial density gradient through a blade row.

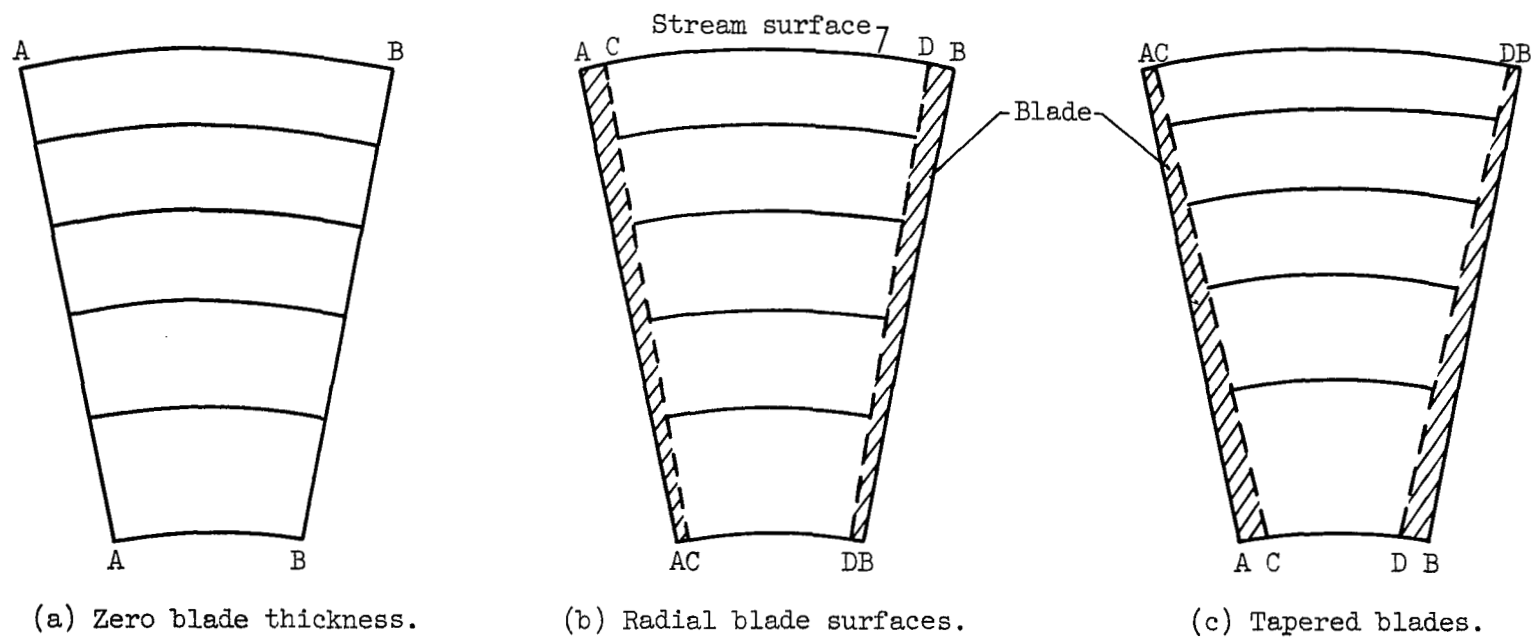


Figure 5. - Effect of blade thickness on radial location of stream surfaces.

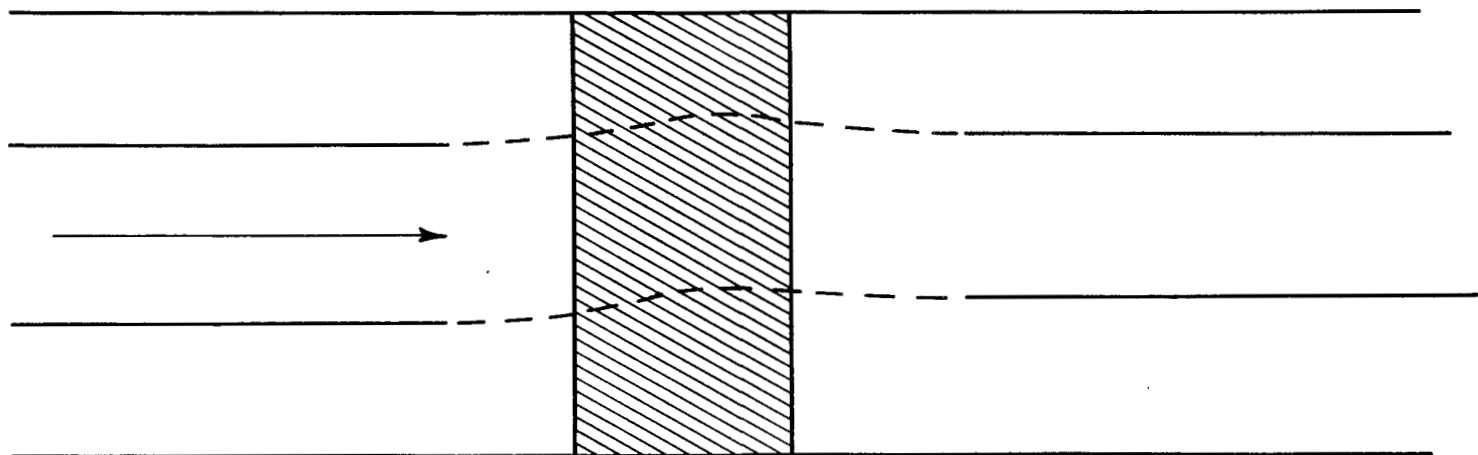
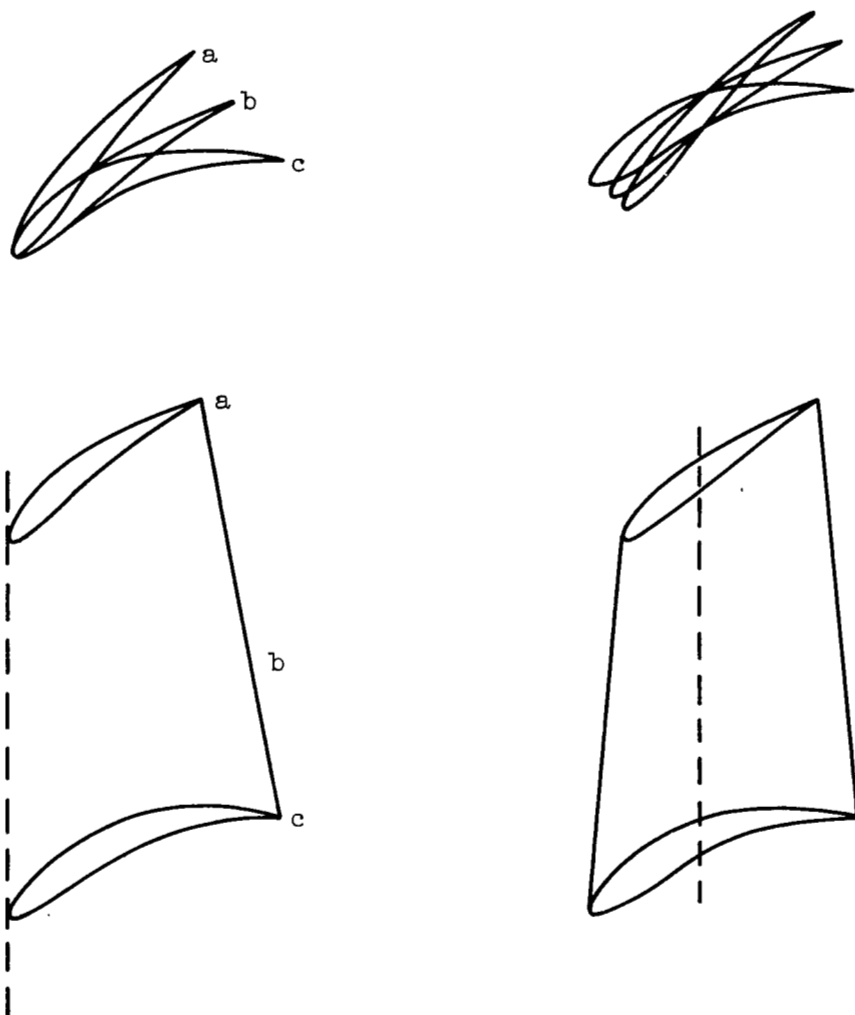


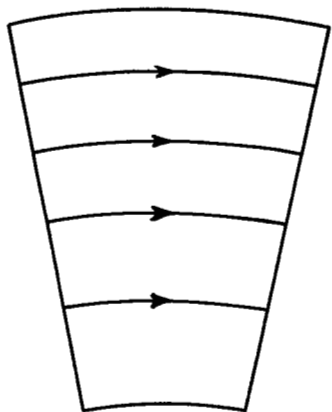
Figure 6. - Radial shift of streamlines due to blade thickness.



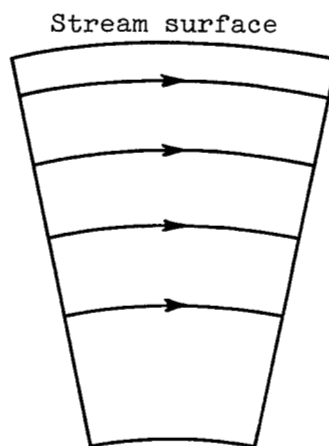
(a) Radial line through leading edge.

(b) Radial line through center of gravity.

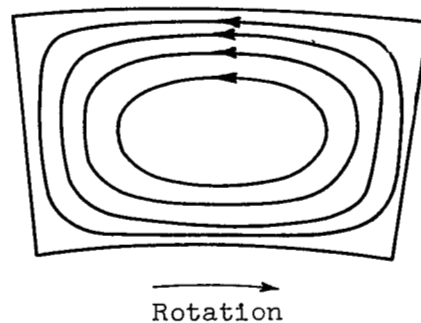
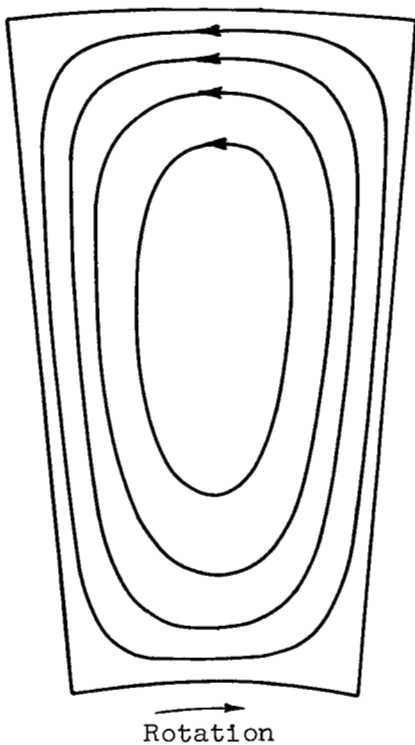
Figure 7. - Various radial alignments of compressor blade elements having the same radial distribution of cascade elements.



(a) Free-vortex rotation.



(b) Solid-body rotation.



(c) Eddy flow (ref. 9).

Figure 8. - Circumferential-plane streamlines for no through-flow.

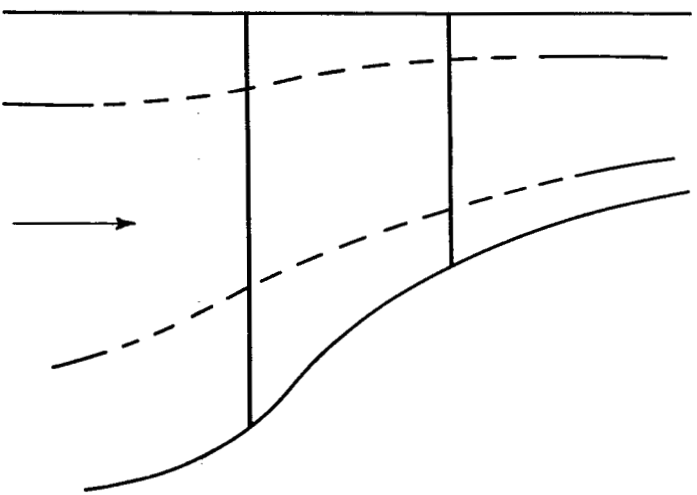
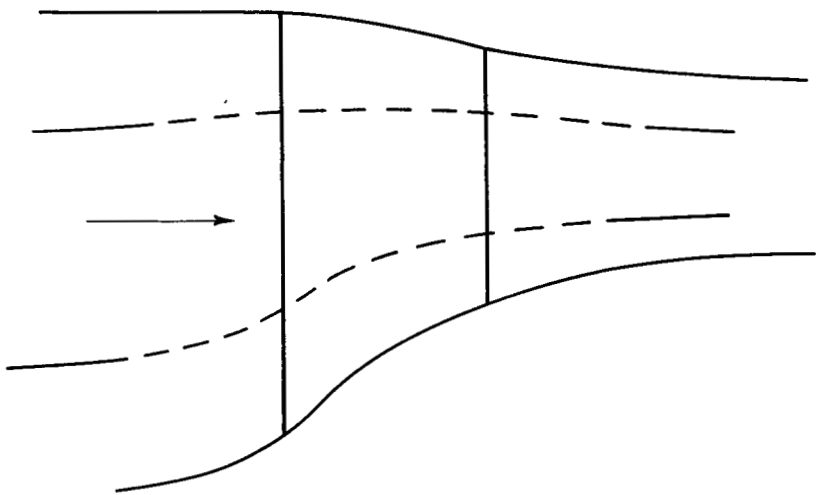
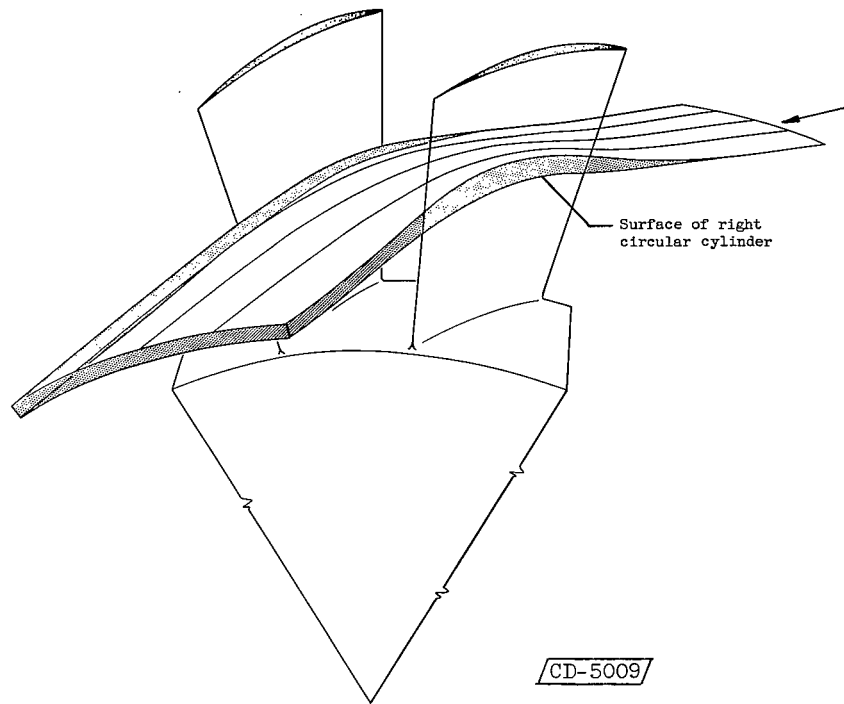
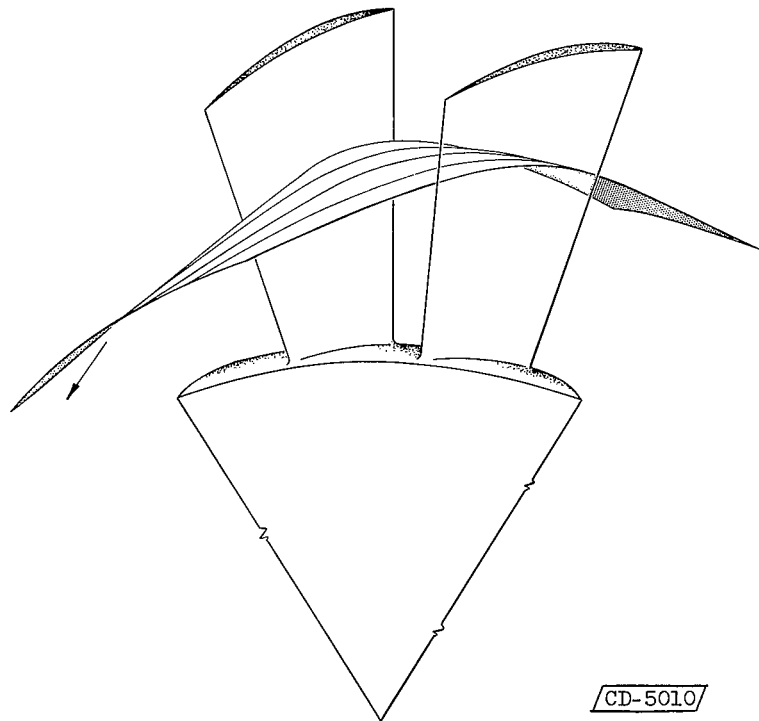


Figure 9. - Radial shift of streamlines due to hub and casing curvature.

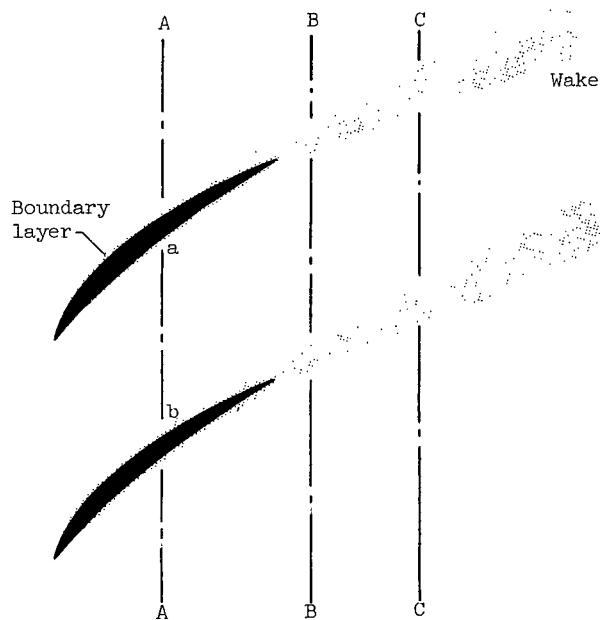


(a) Free-vortex design.



(b) Non-free-vortex design with converging annulus area.

Figure 10. - Warping of stream surfaces through a blade row.



(a) Sketch of boundary layers and wakes.

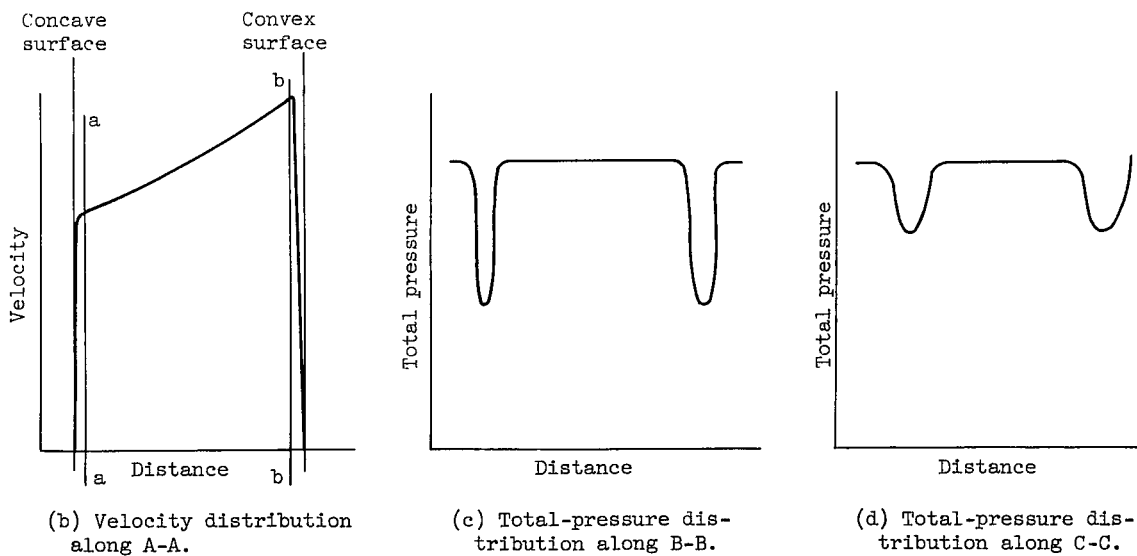
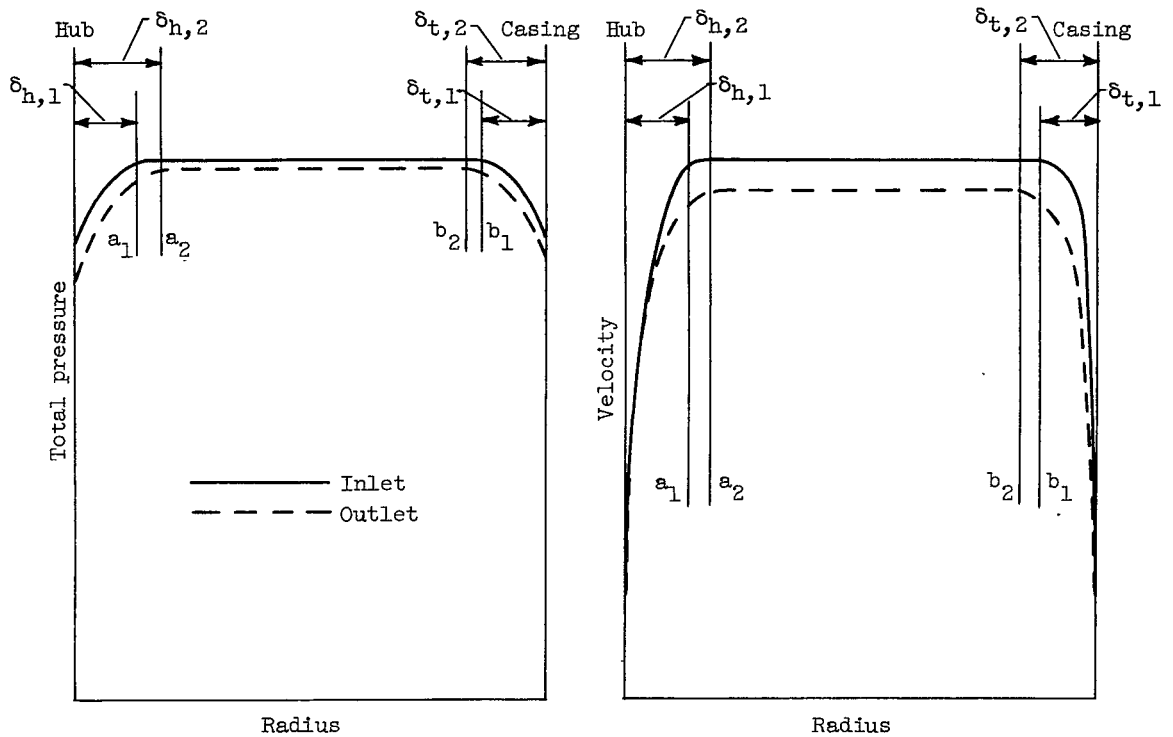
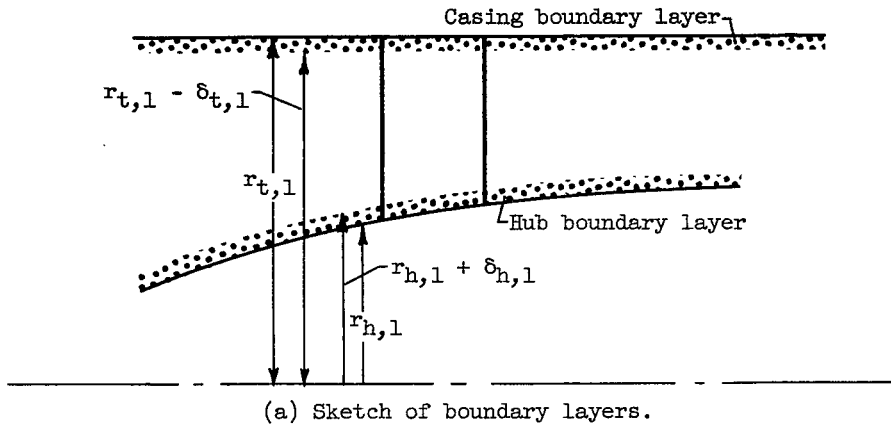


Figure 11. - Boundary layers and wakes formed by cascade elements.



(b) Total-pressure distribution.

(c) Velocity distribution.

Figure 12. - Boundary layers at hub and casing.

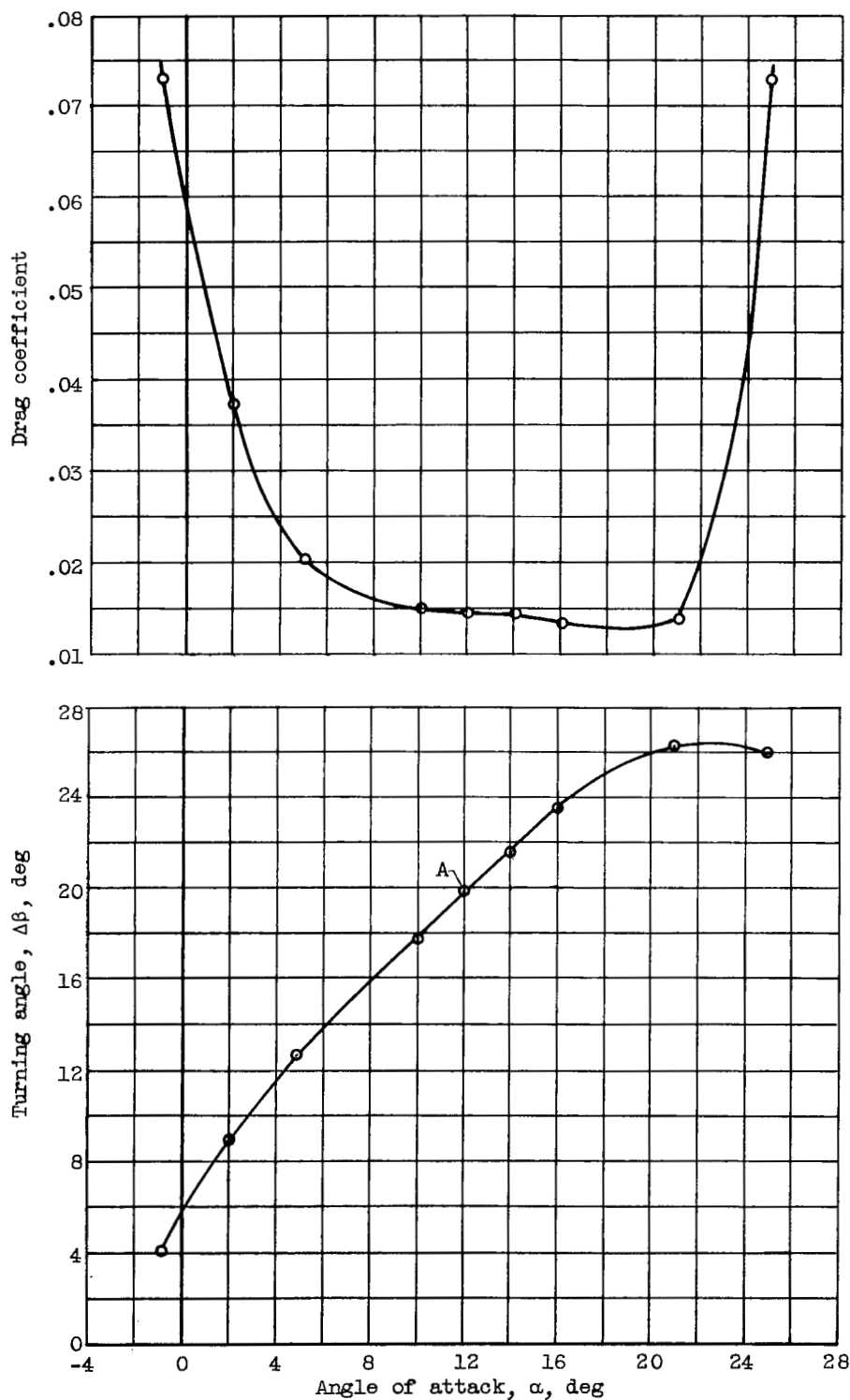


Figure 13. - Drag and turning-angle distribution for cascade combination. Blade section, NACA 65-(12)10; inlet-air angle, 45° ; solidity, 1.0 (ref. 15).

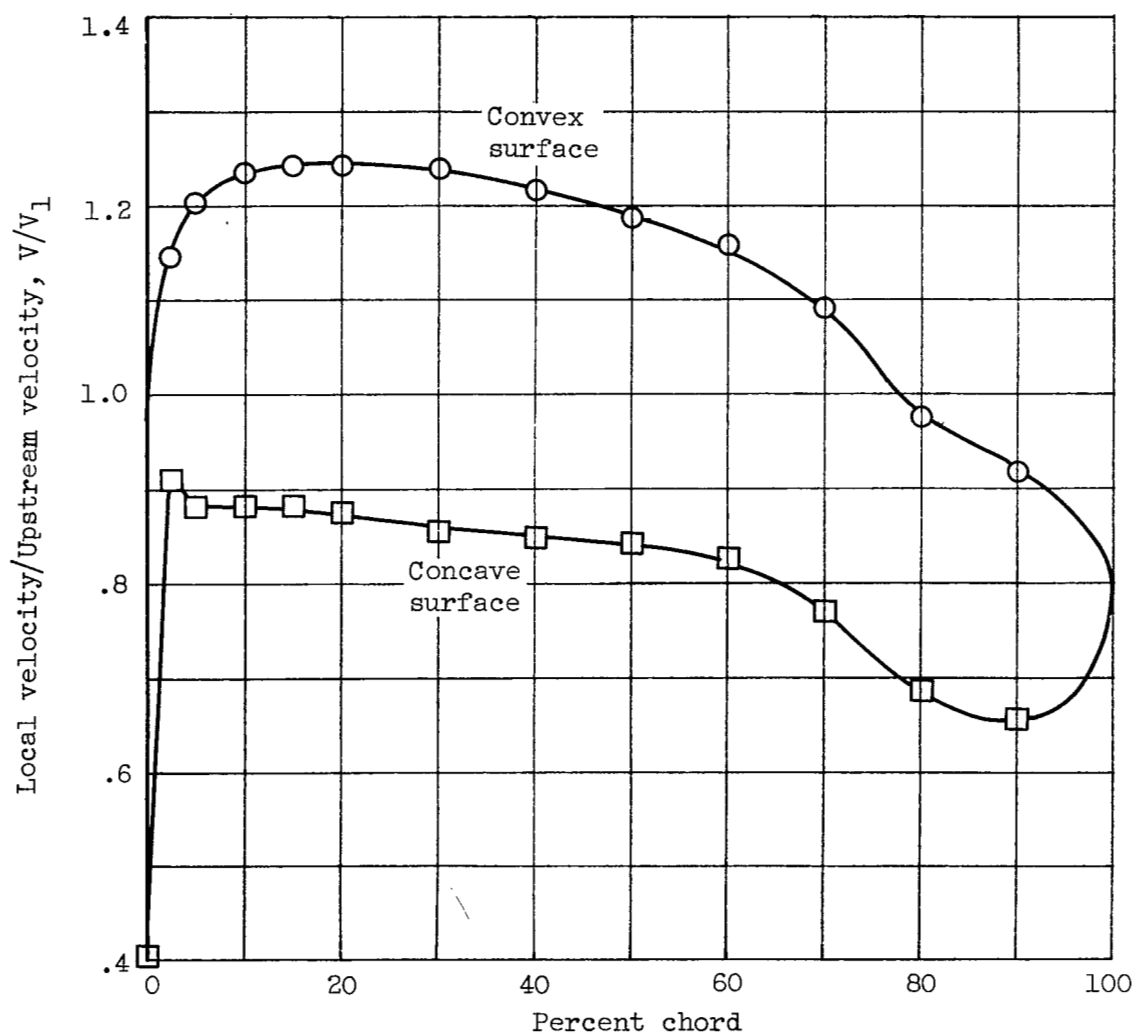


Figure 14. - Blade surface velocity distribution for cascade combination. Blade section, NACA 65-(12)10; inlet-air angle, 45° ; solidity, 1.0 (ref. 15).

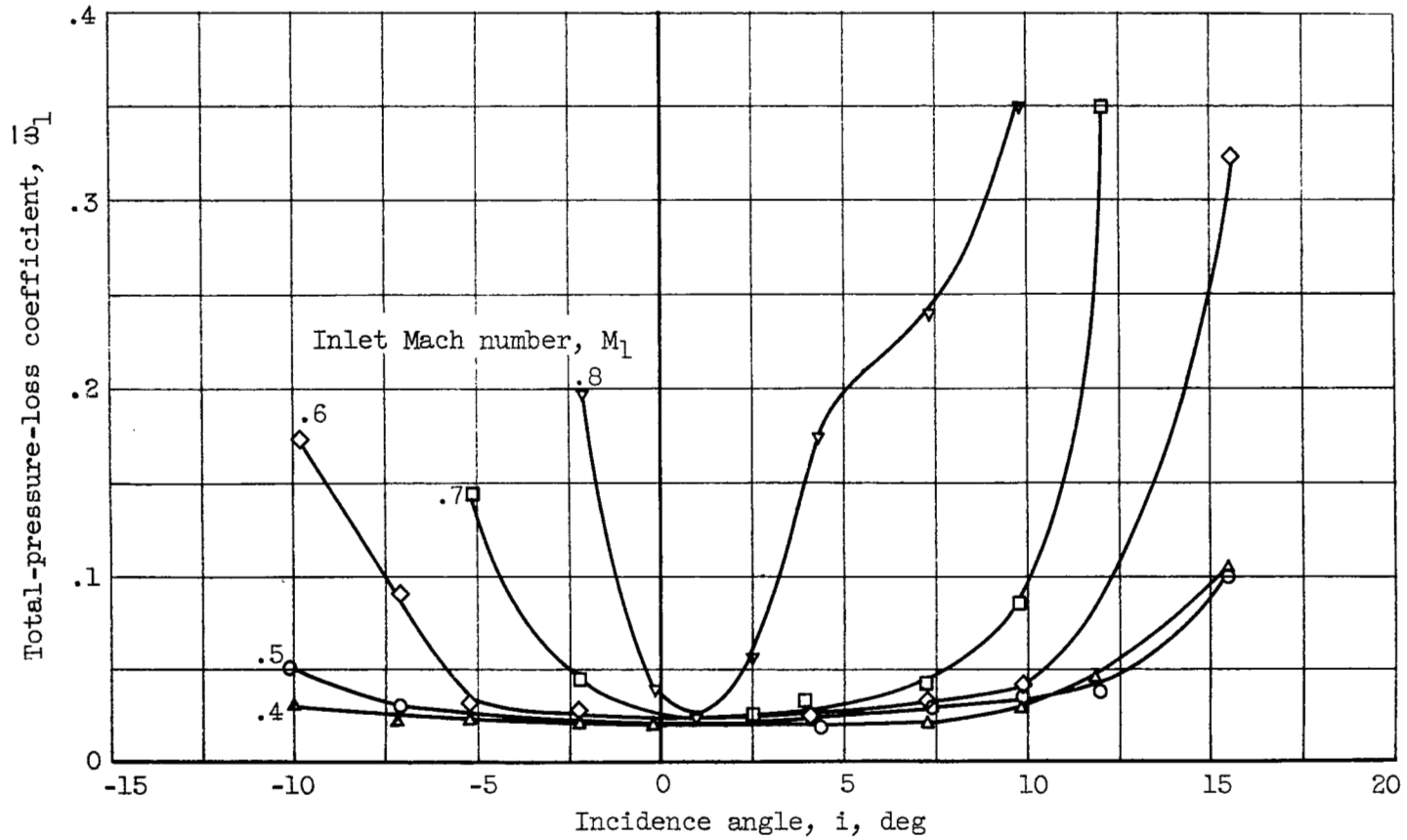


Figure 15. - Effect of inlet Mach number on loss characteristics of cascade blade sections (ref. 16).



Mach number, 0.70



Mach number, 0.75



Mach number, 0.82



Mach number, 0.88



Mach number, 0.93



Mach number, 0.95

C-34417

Figure 16. - Schlieren photographs for a range of Mach number.

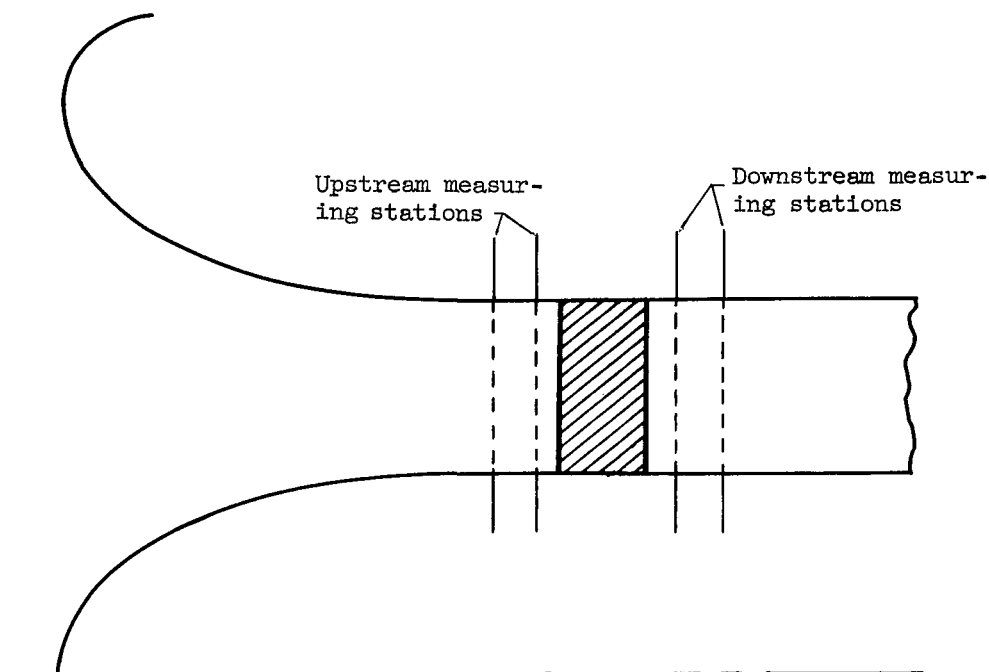


Figure 17. - Schematic diagram of an inlet-guide-vane test rig.

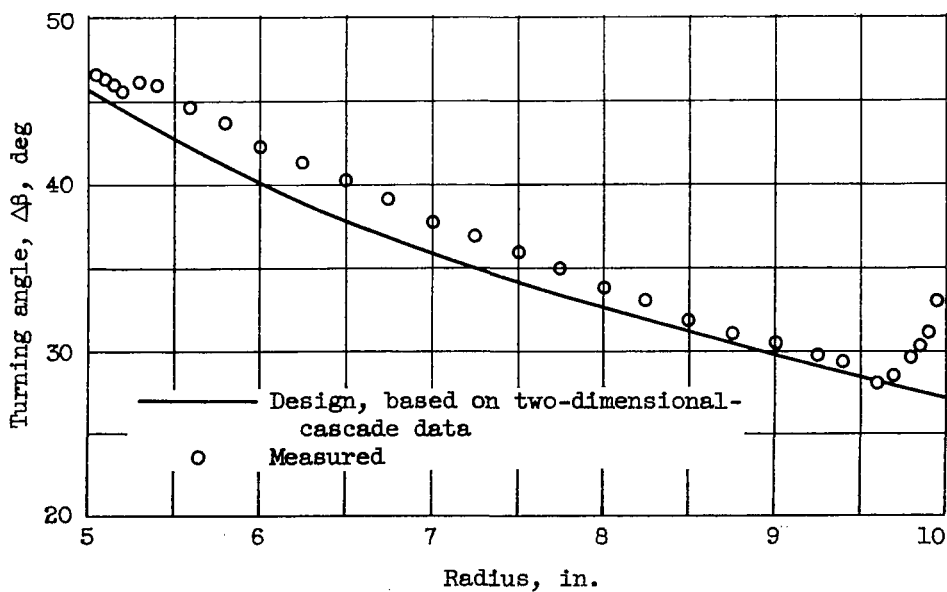


Figure 18. - Comparison of measured and design turning angles for free-vortex guide vanes (ref. 18).

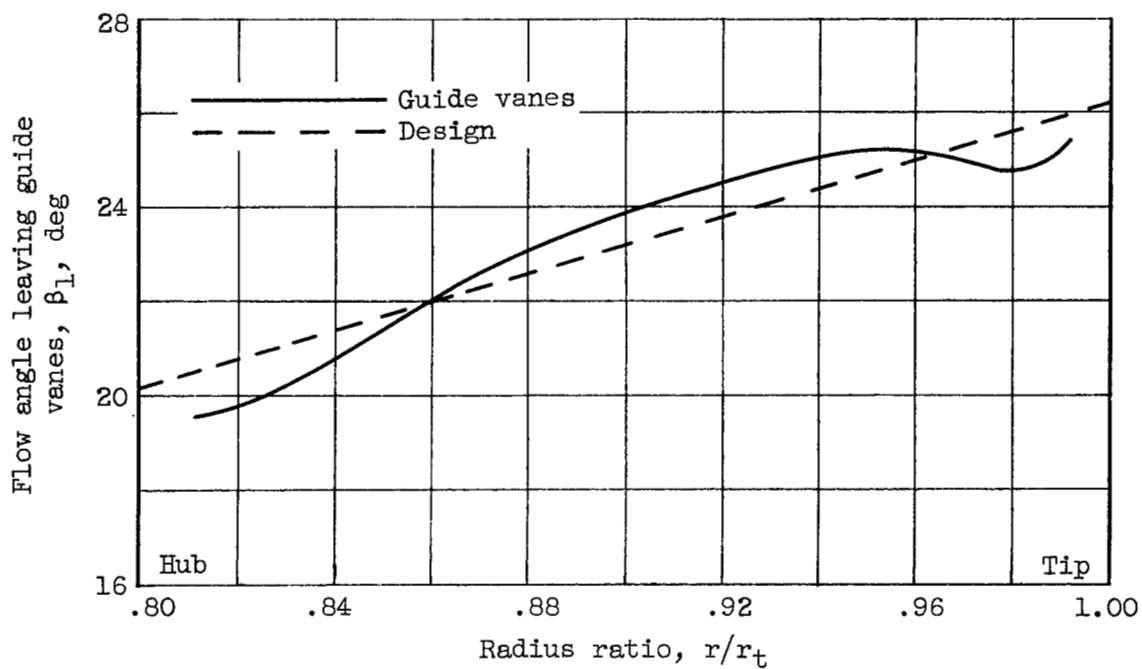


Figure 19. - Comparison of measured and design turning angles for non-free-vortex guide vanes.

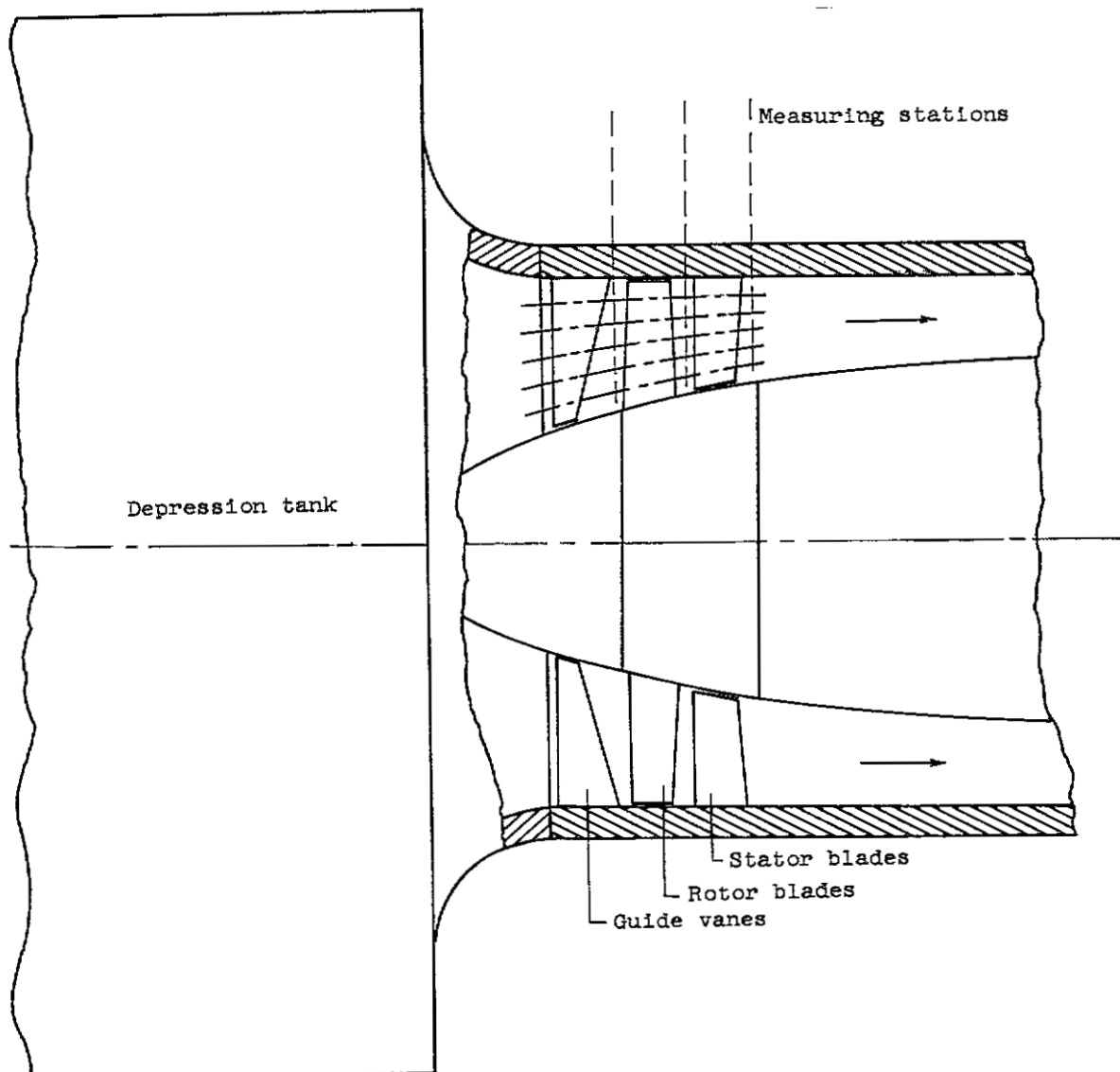


Figure 20. - Schematic layout of compressor stage.

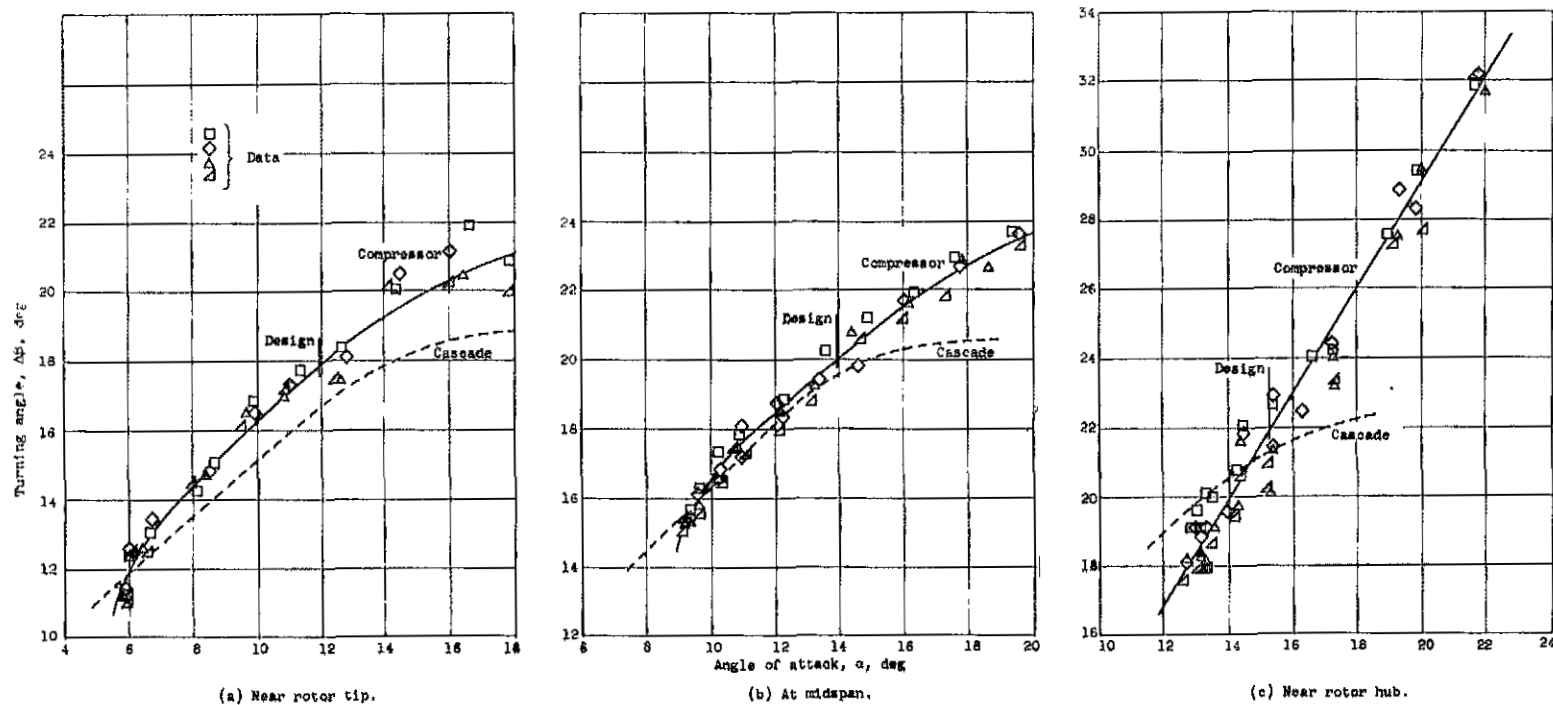


Figure 21. - Compressor rotor and cascade turning angles (ref. 21).

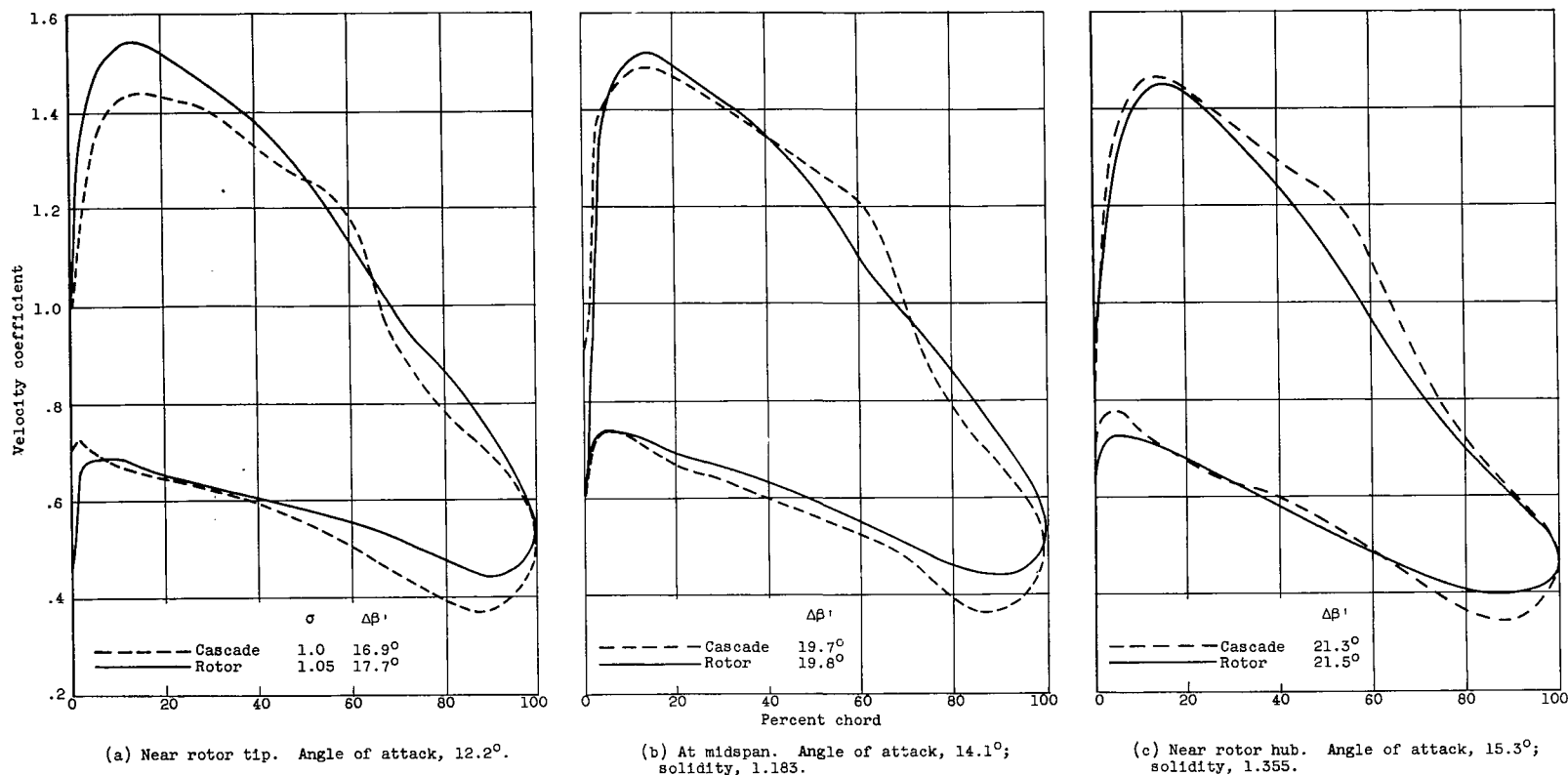


Figure 22. - Compressor rotor and cascade pressure distributions. Relative inlet-air angle, 60° .

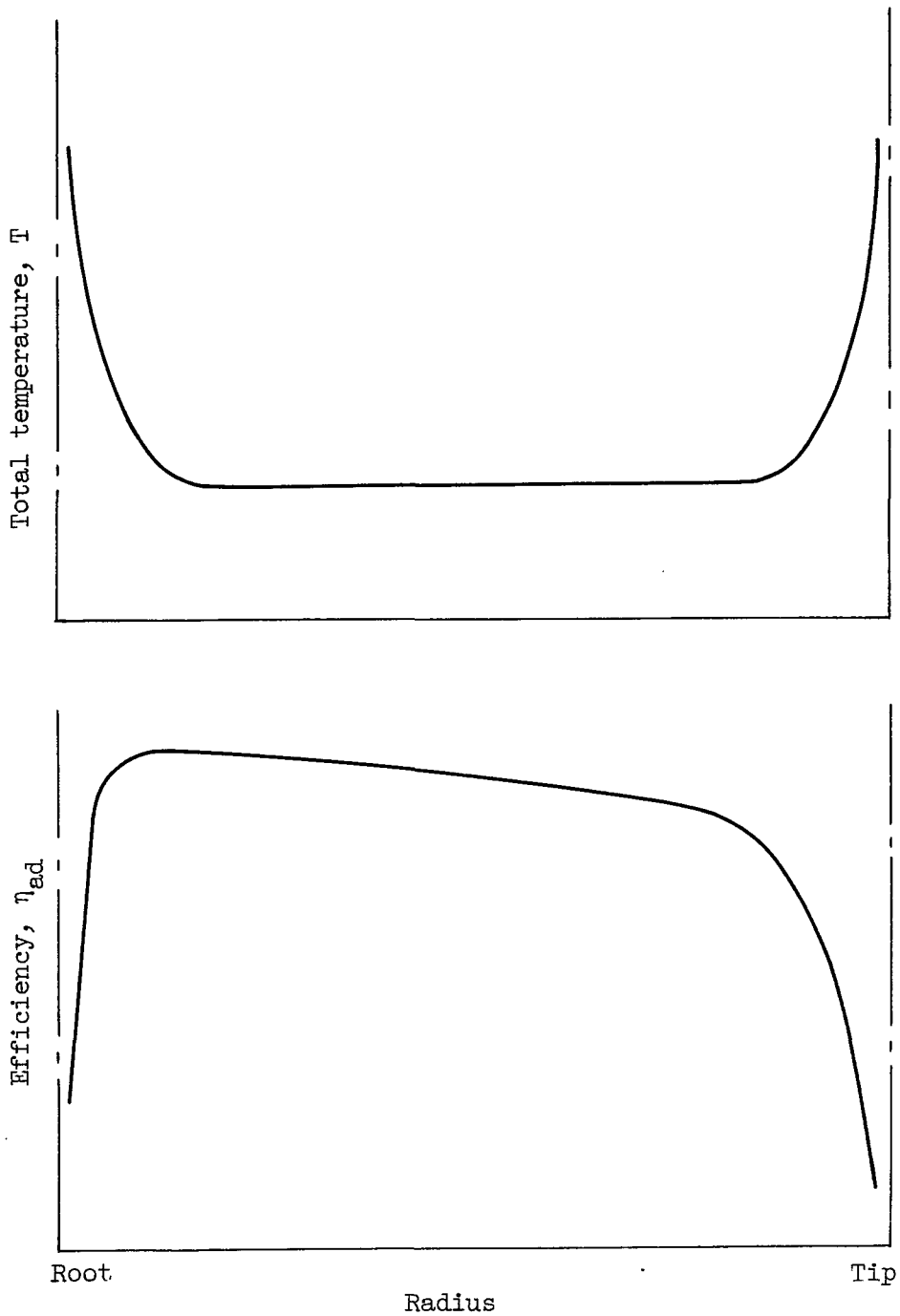


Figure 23. - Radial distribution of total temperature and efficiency through compressor rotor.

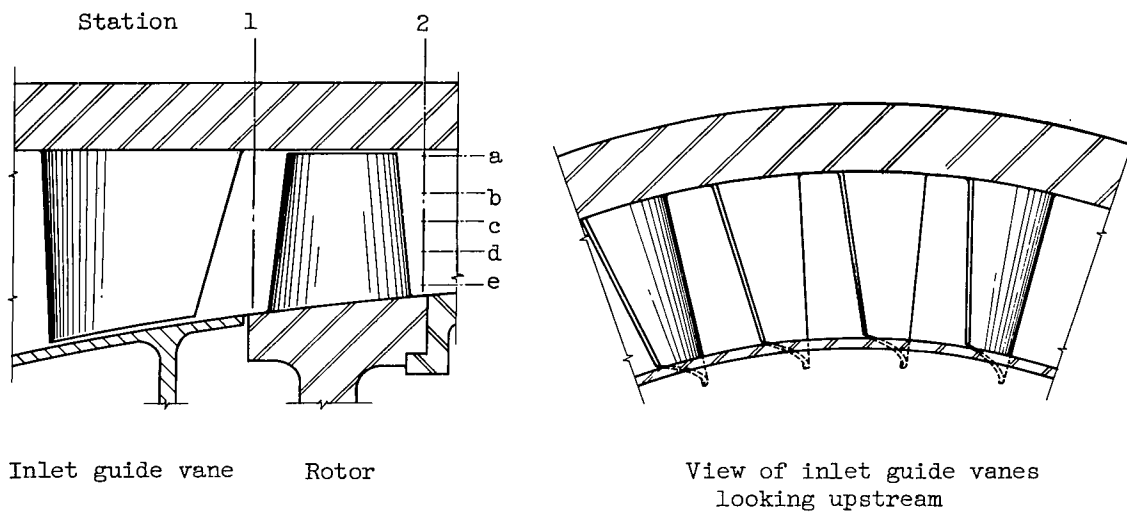


Figure 24. - Schematic layout for tests of inlet guide vanes and rotor (ref. 20).

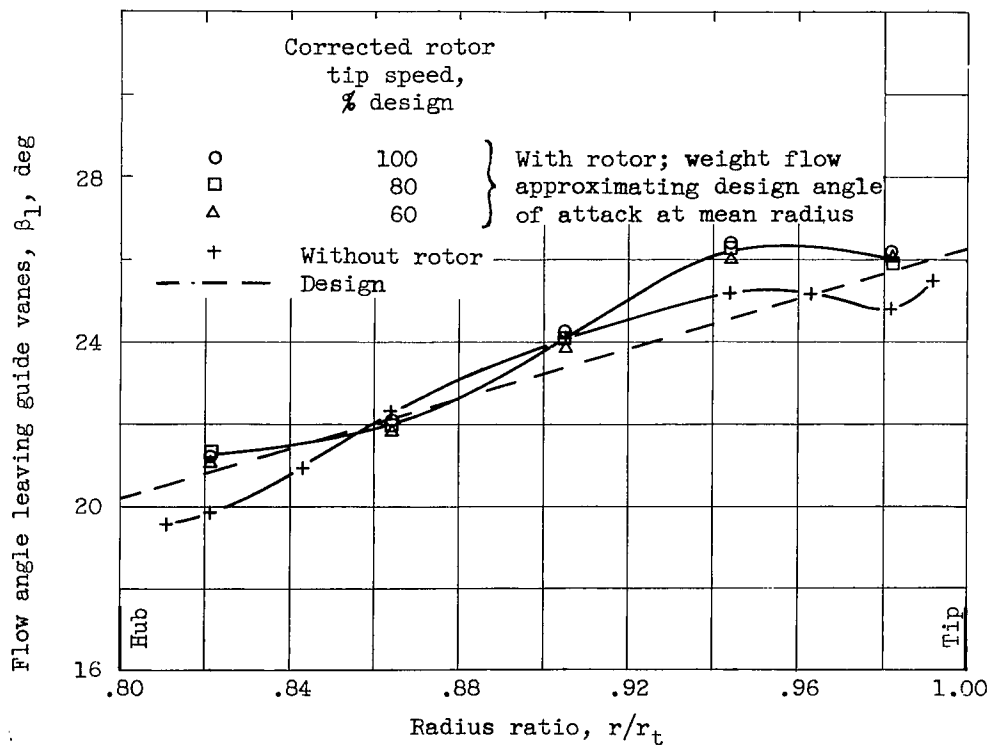


Figure 25. - Radial variation of flow angle leaving inlet guide vanes with and without rotor (ref. 20).

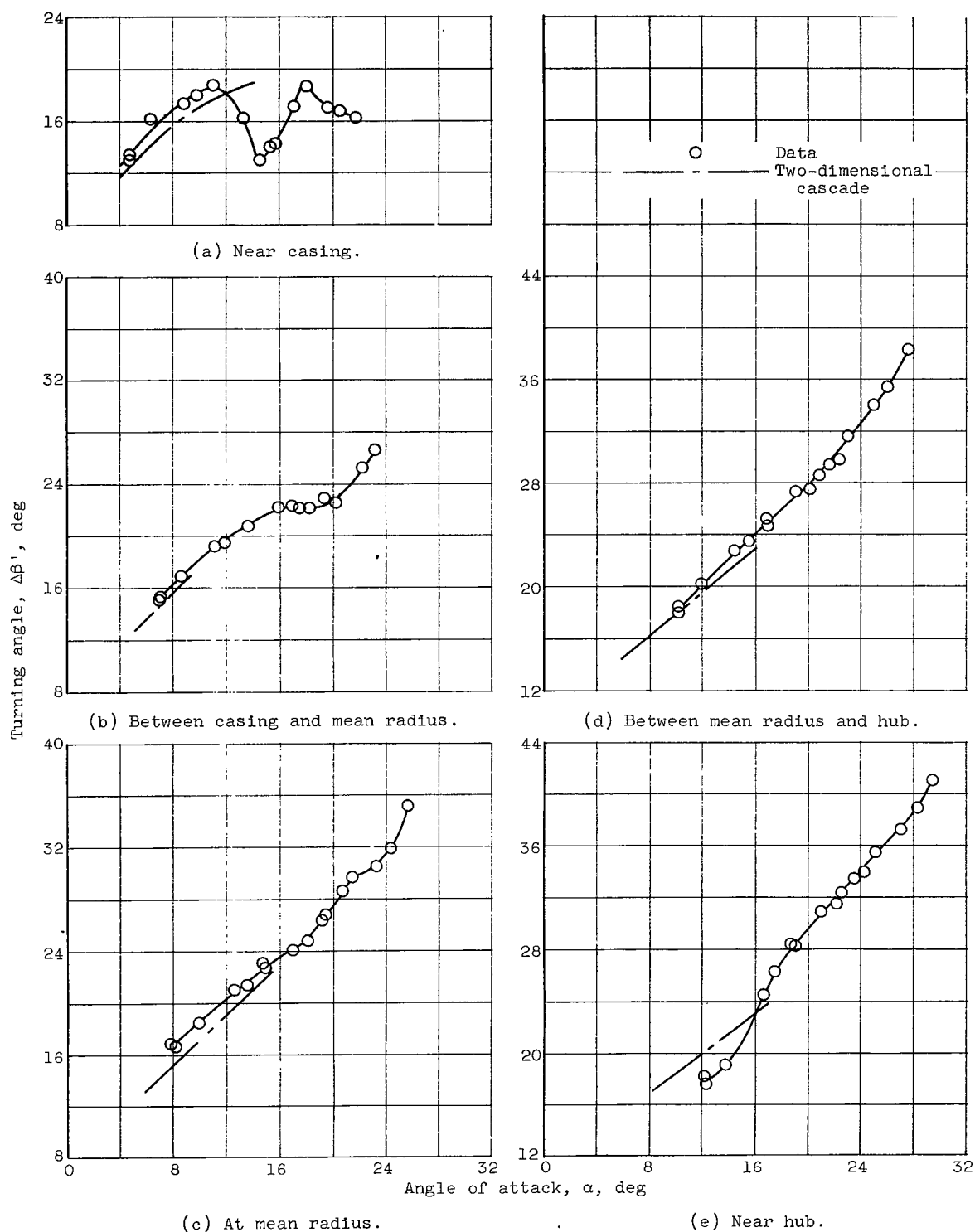


Figure 26. - Variation of turning angle across rotor blades with angle of attack at design speed (ref. 20).

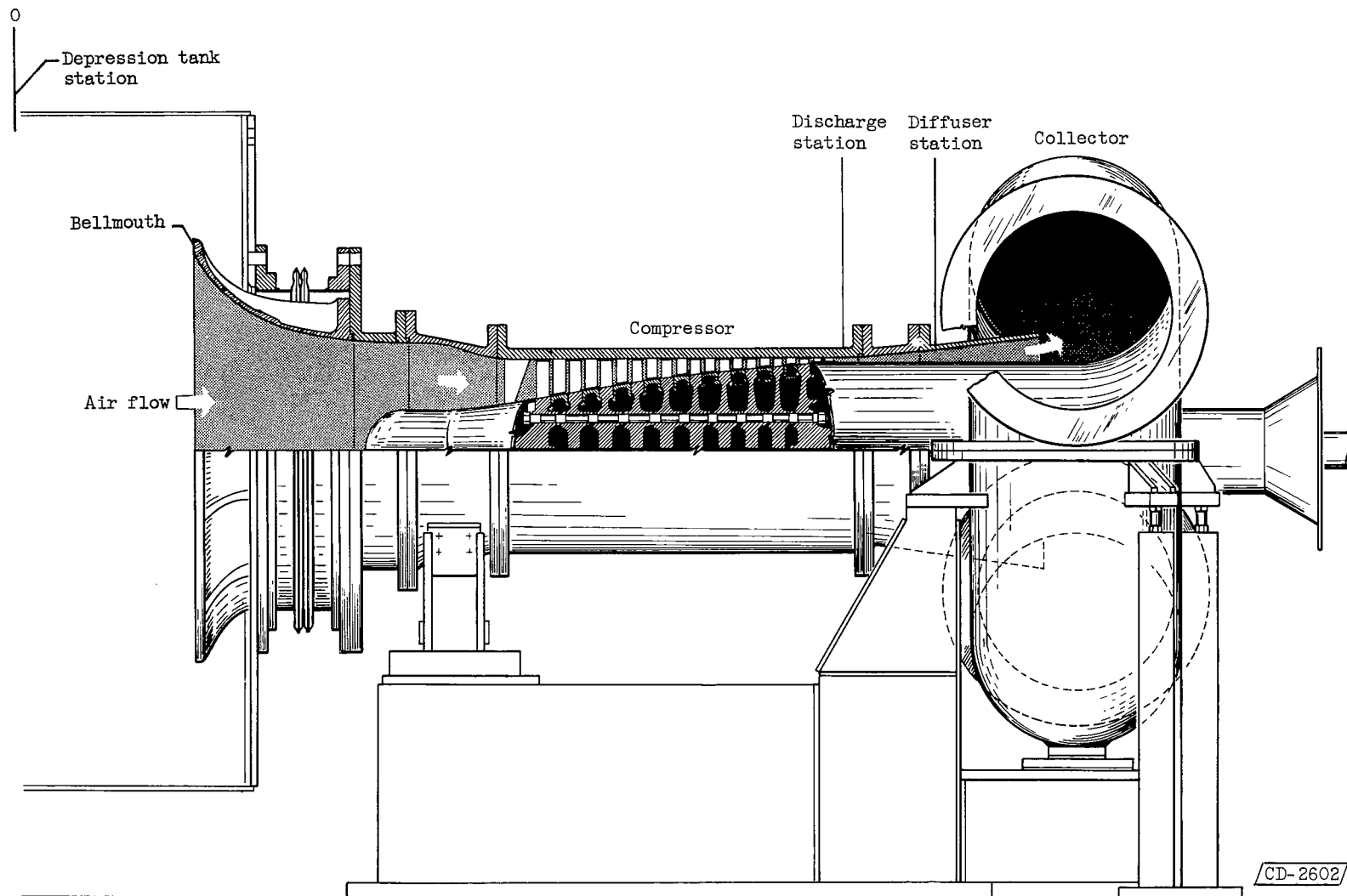


Figure 27. - Cross section of 10-stage axial-flow compressor, inlet bellmouth, and discharge collector (ref. 25).

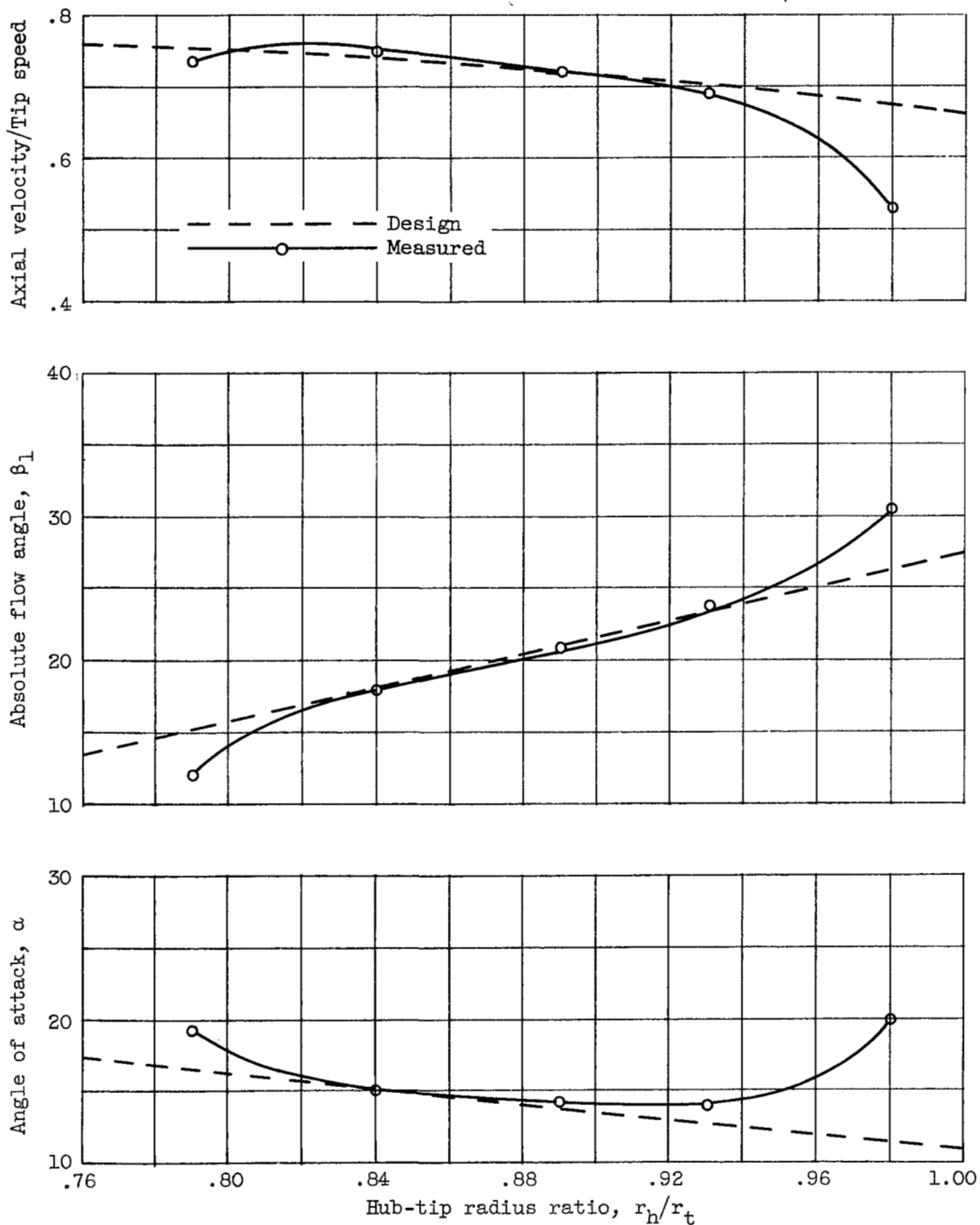


Figure 28. - Radial distribution of flow properties entering fifth rotor row of 10-stage compressor (ref. 26).

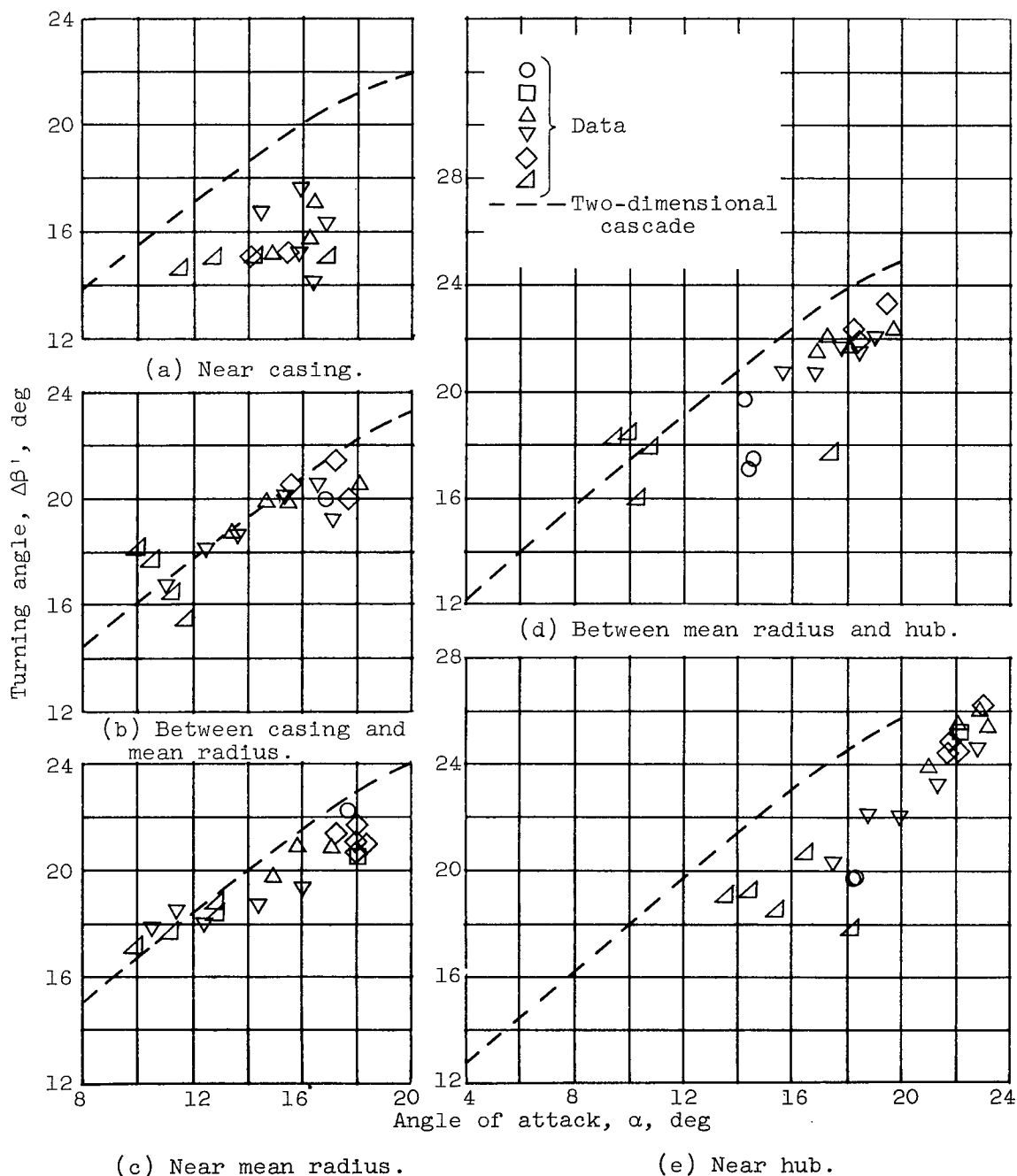


Figure 29. - Variation of fifth-rotor turning angle with angle of attack at five radial positions (ref. 26).

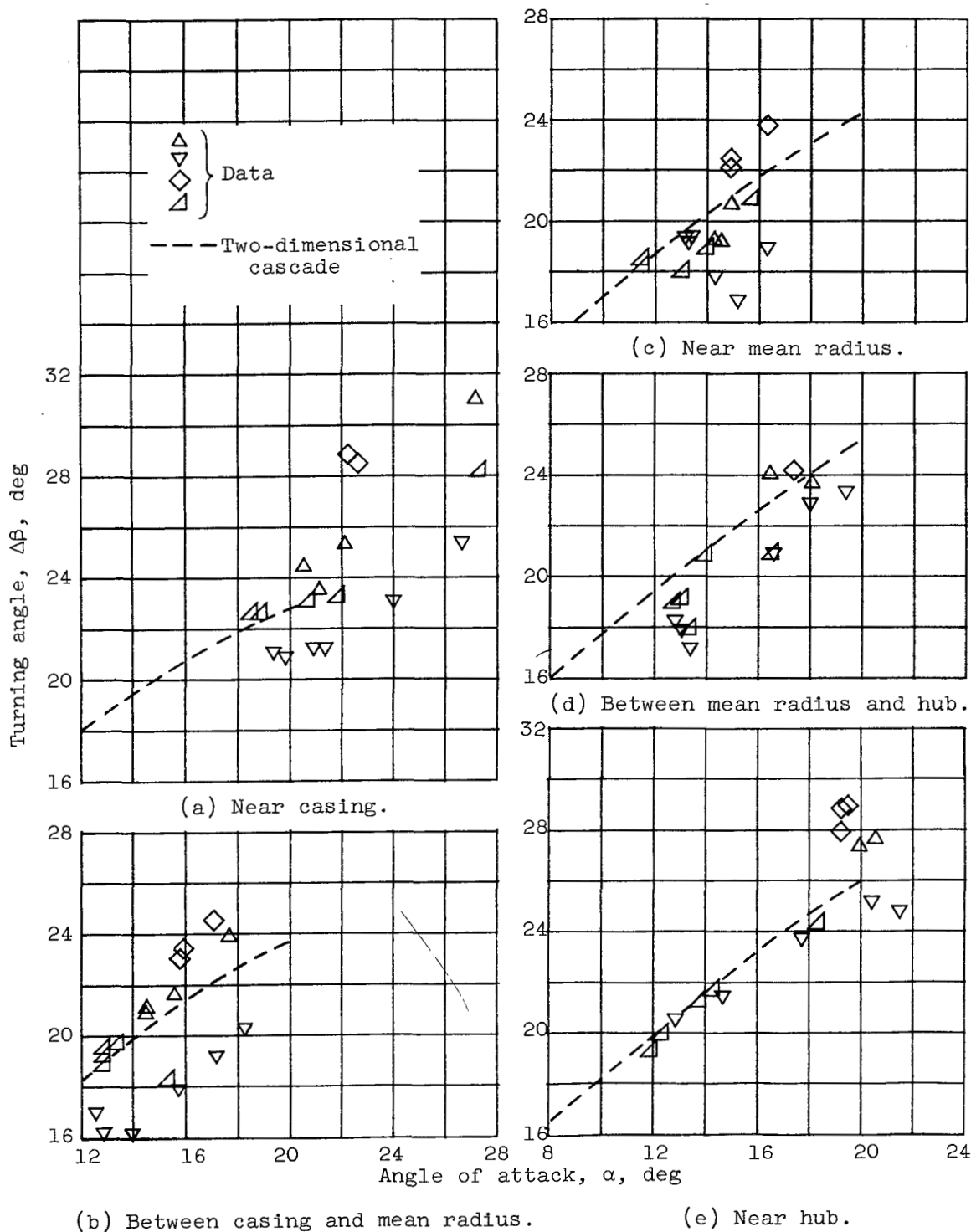


Figure 30. - Variation of fifth-stator turning angles with angle of attack at five radial positions (ref. 26).

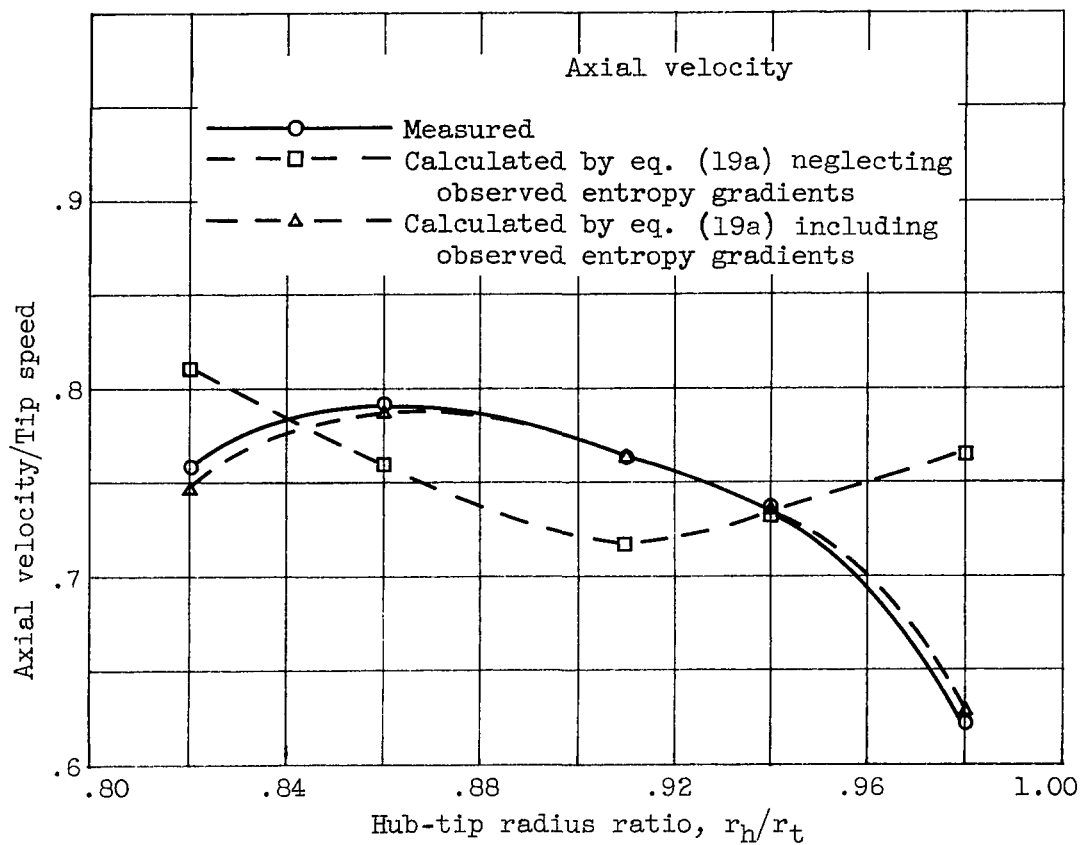


Figure 31. - Axial velocity distribution after fifth stage of 10-stage compressor (from ref. 26).

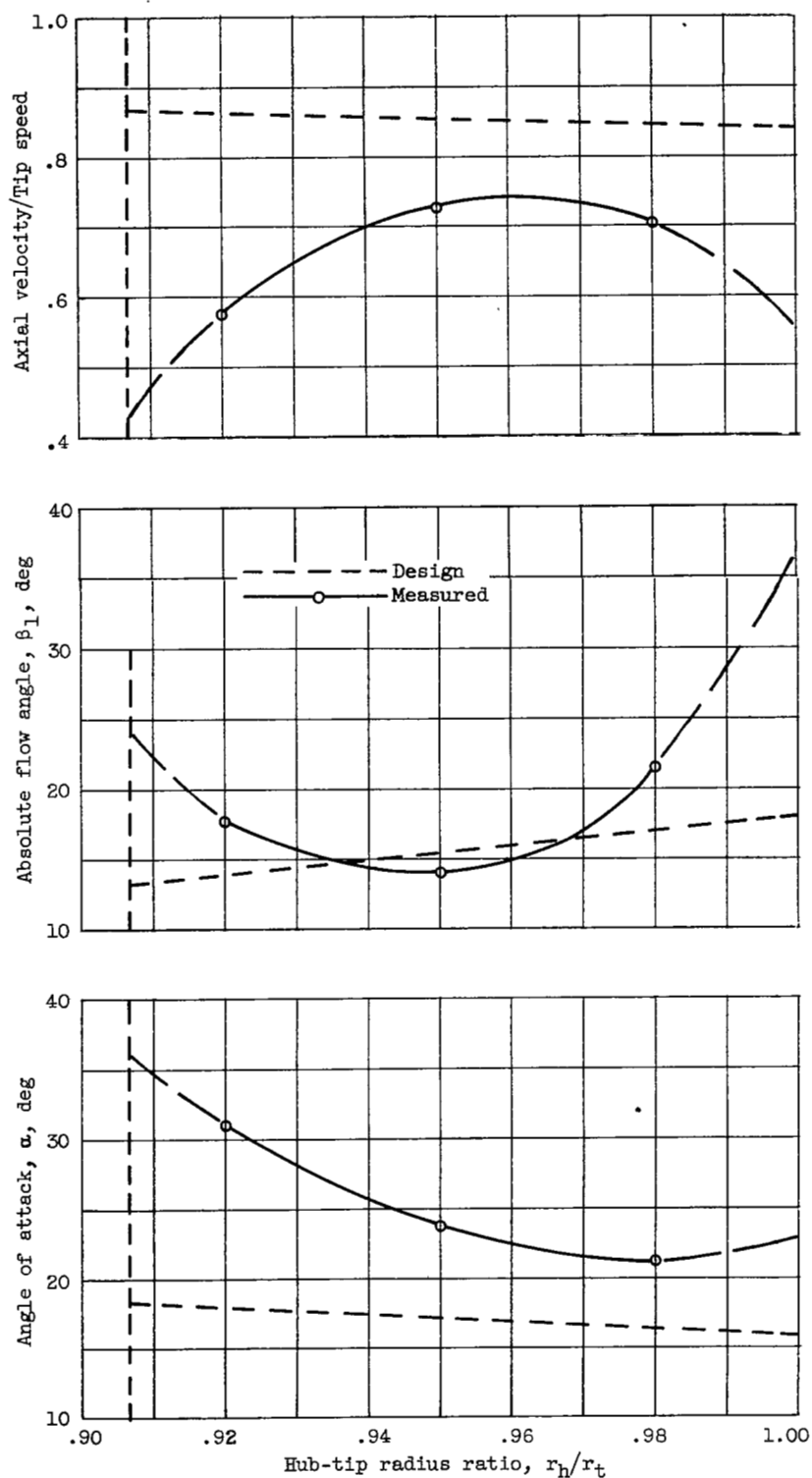


Figure 32. - Radial distribution of flow properties entering tenth rotor row of 10-stage compressor (ref. 26).

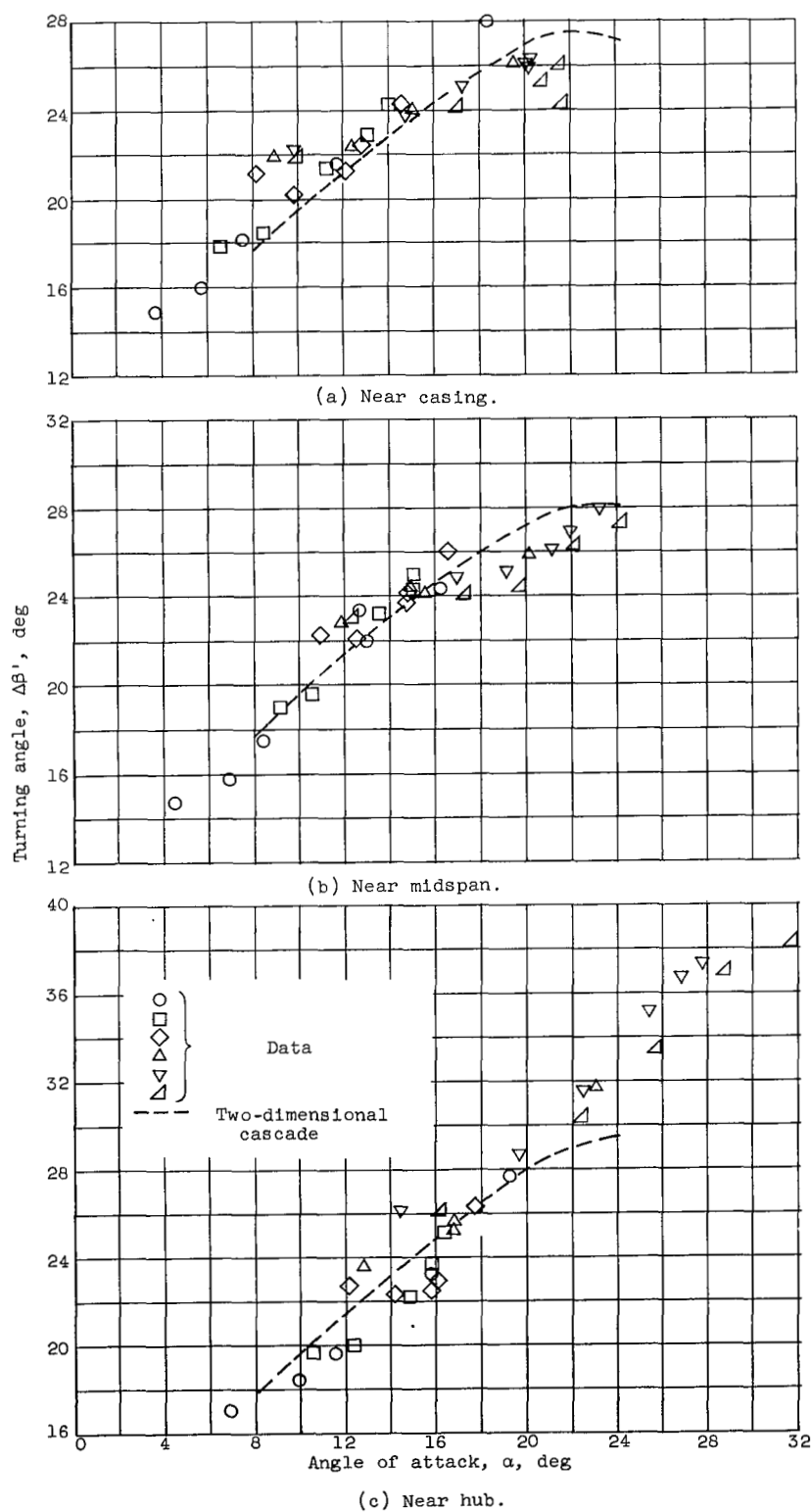


Figure 33. - Variation of tenth-rotor turning angle with angle of attack at three radial positions (ref. 26).

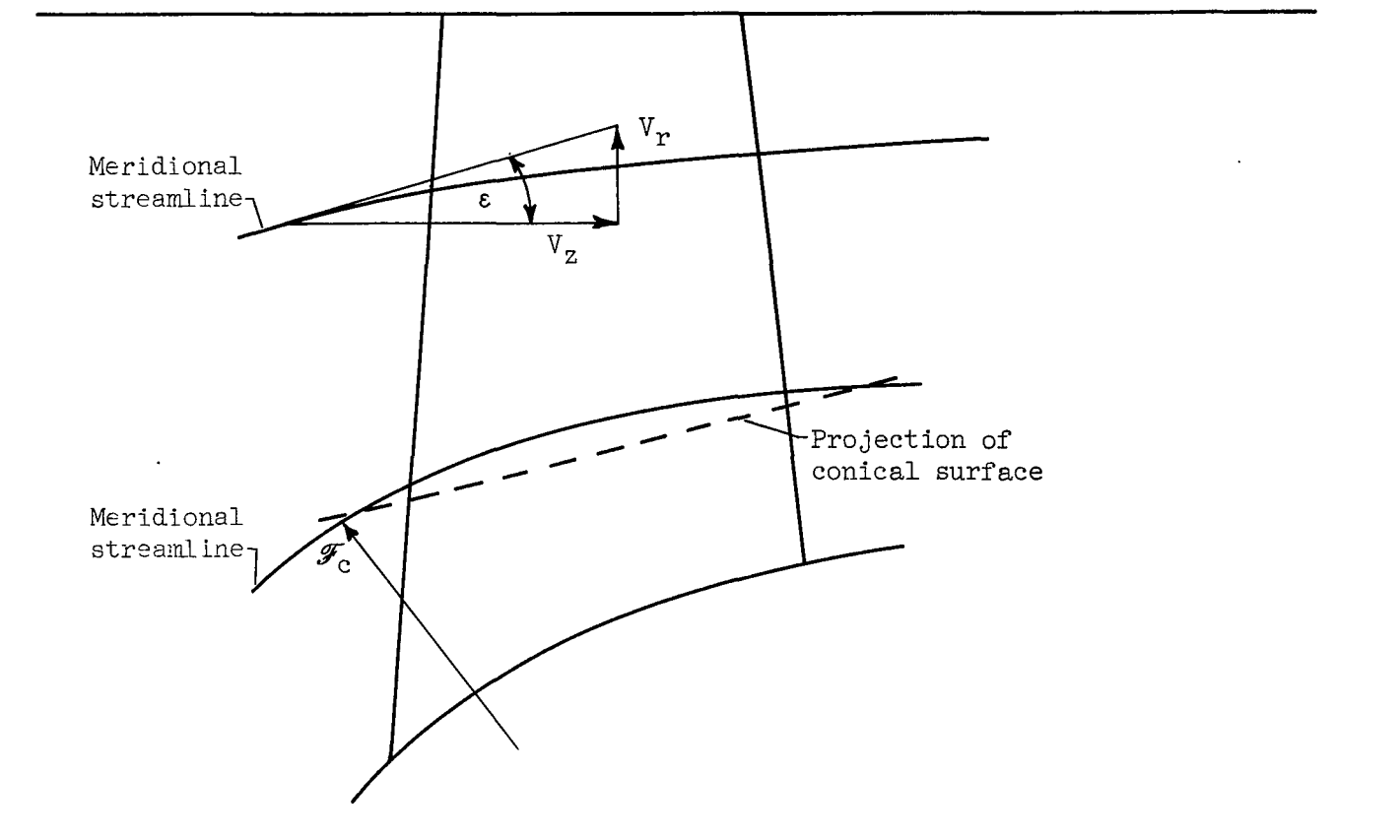
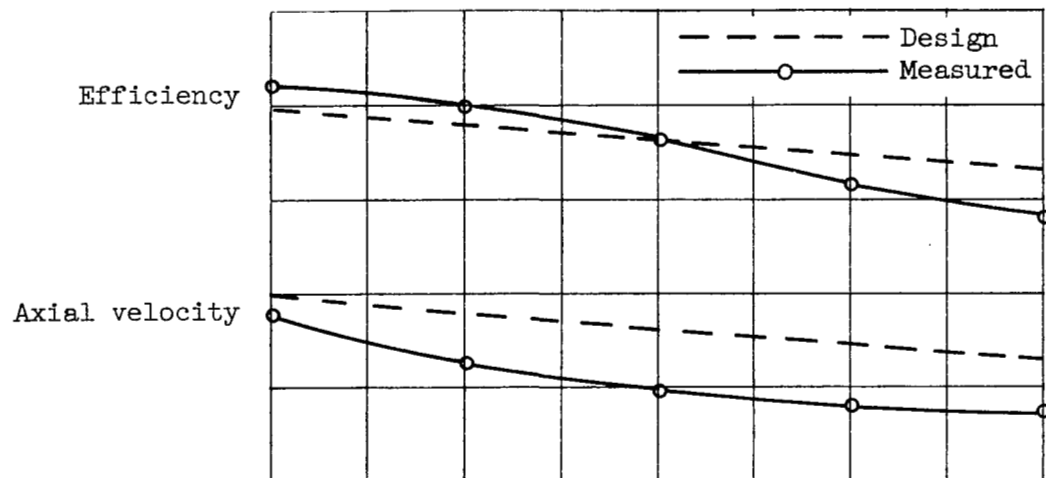
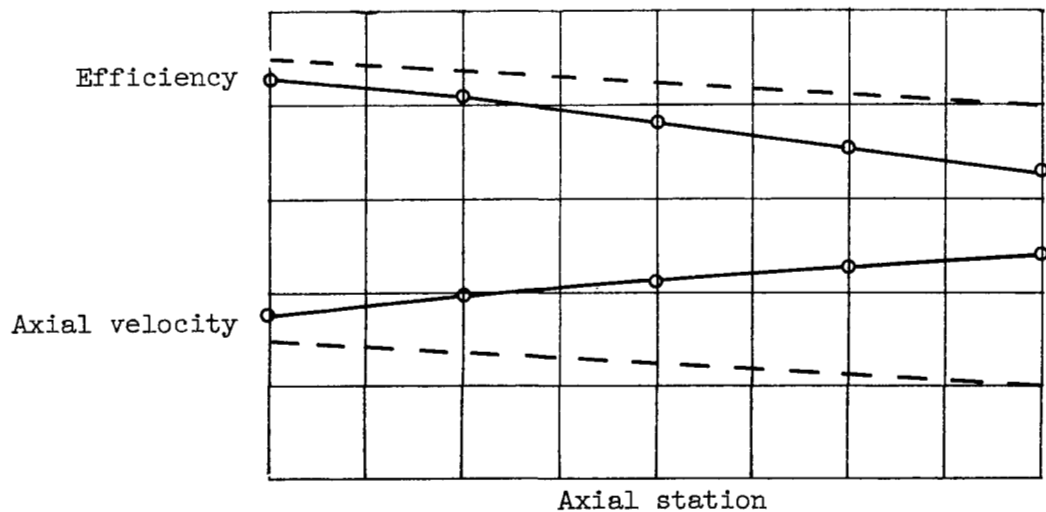


Figure 34. - Sketch showing typical projection of streamlines on meridional plane.



(a) Case I.



(b) Case II.

Figure 35. - Axial distribution of efficiency and axial velocity in multistage axial-flow compressors.

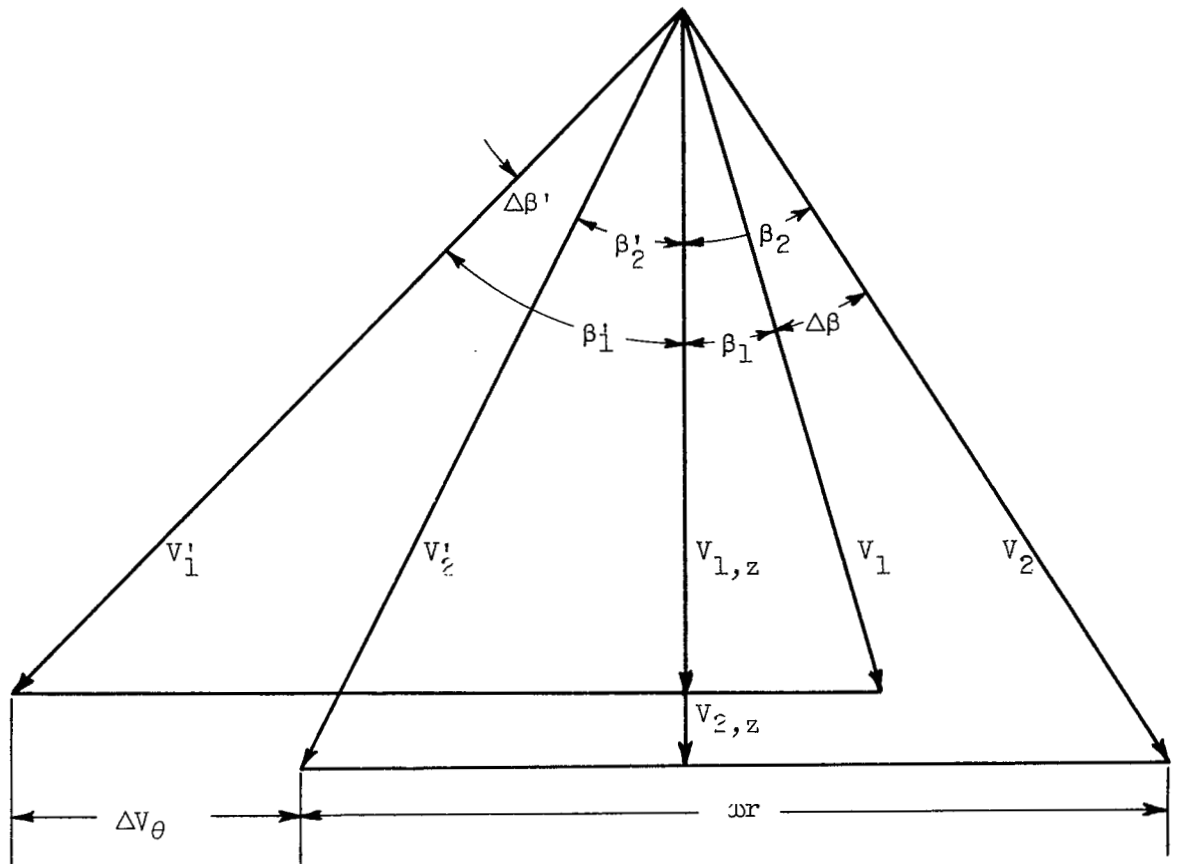


Figure 36. - Typical rotor velocity diagram for a cascade element.

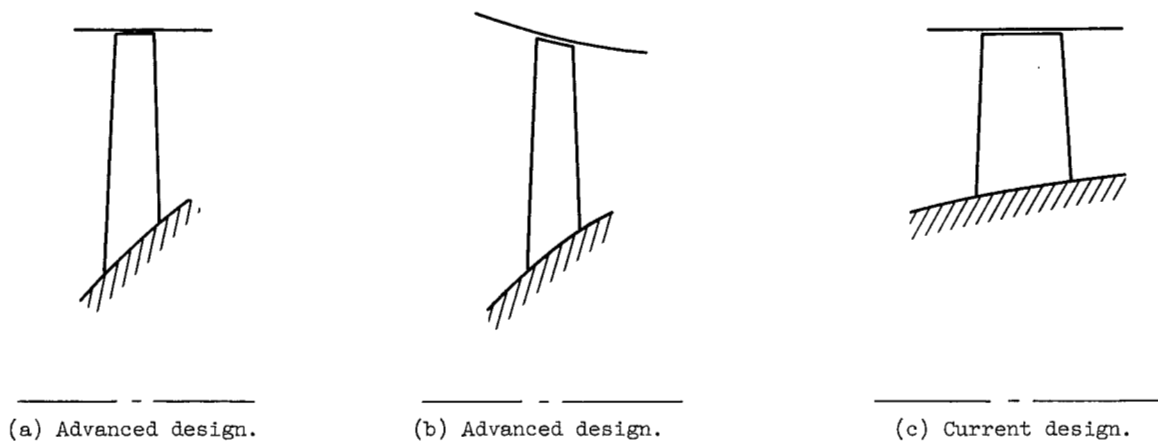


Figure 37. - Schematic drawing of several compressor-inlet stages.

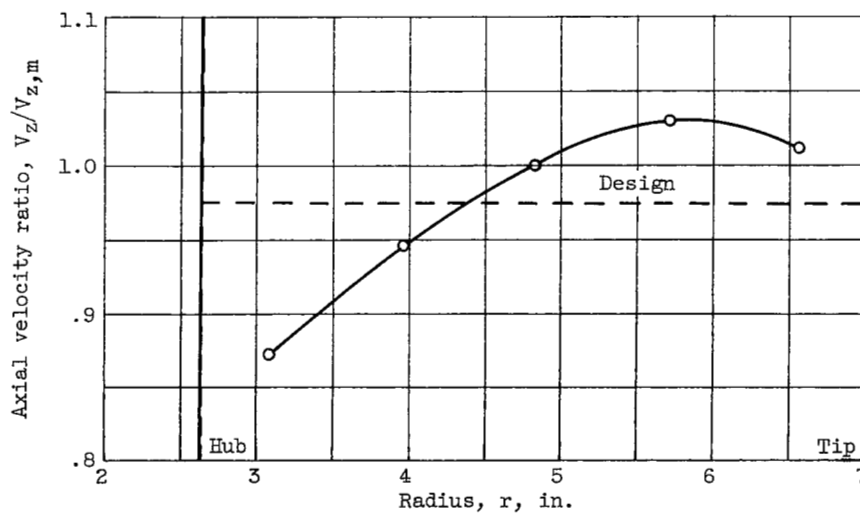
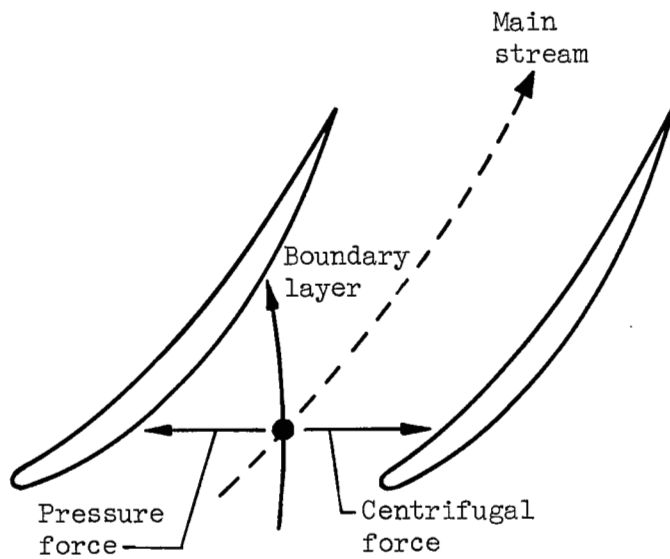
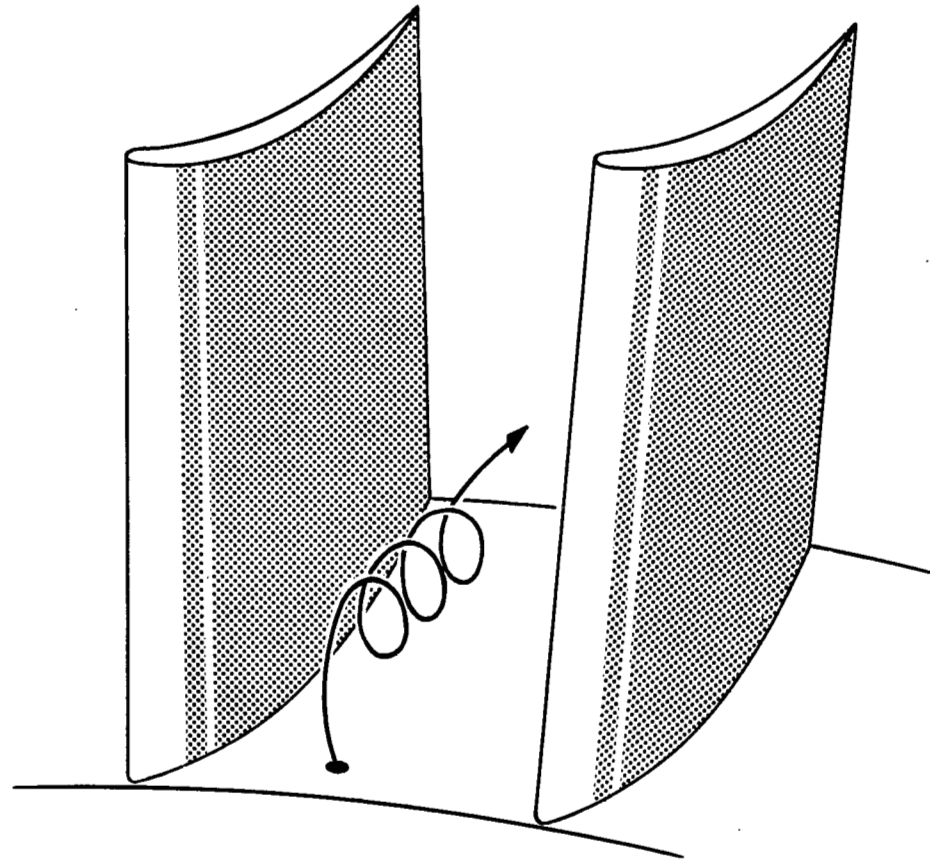


Figure 38. - Inlet axial velocity distribution for compressor of reference 35.



(a) Cross-channel flow.



(b) Corner vortex.

CD-3741

Figure 39. - Secondary flow resulting from boundary layer on annulus walls.

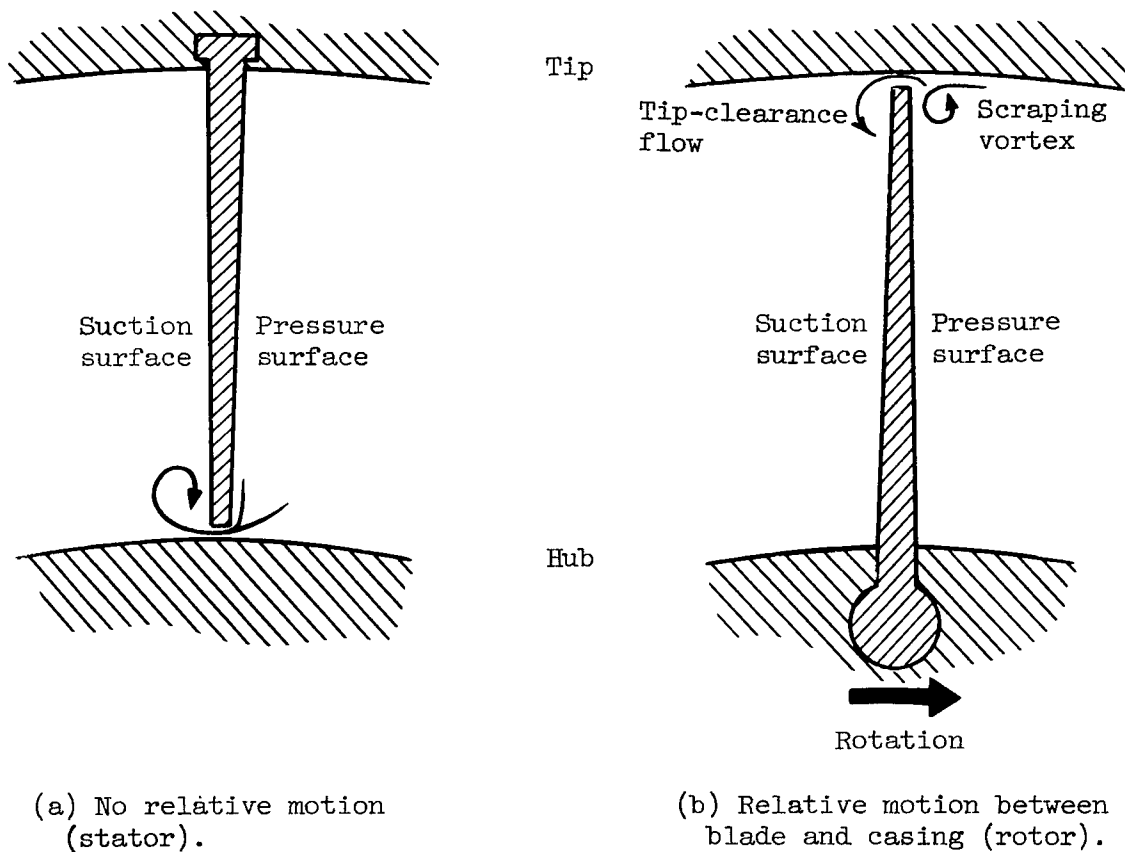
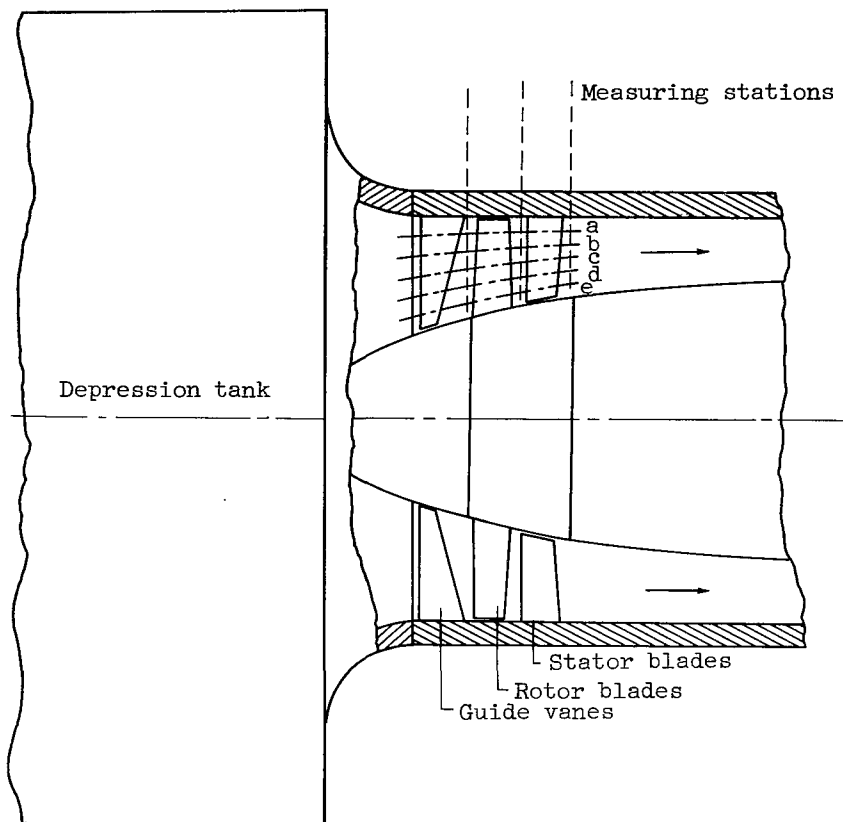
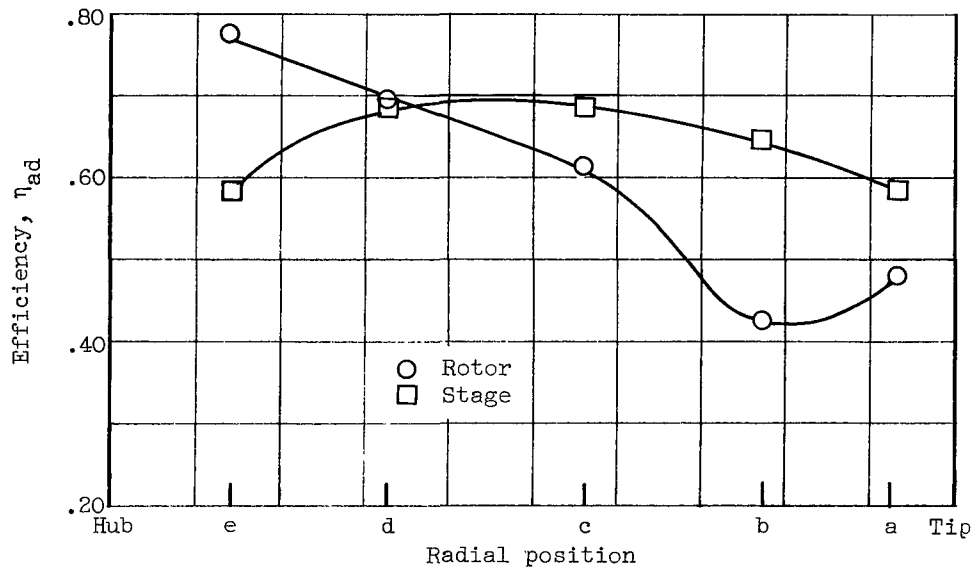


Figure 40. - Secondary flow in blade end-clearance region.



(a) Measuring stations.



(b) Efficiency variation.

Figure 41. - Measuring stations and radial variation of efficiency for compressor A of reference 44.

CHAPTER IV

POTENTIAL FLOW IN TWO-DIMENSIONAL CASCADES

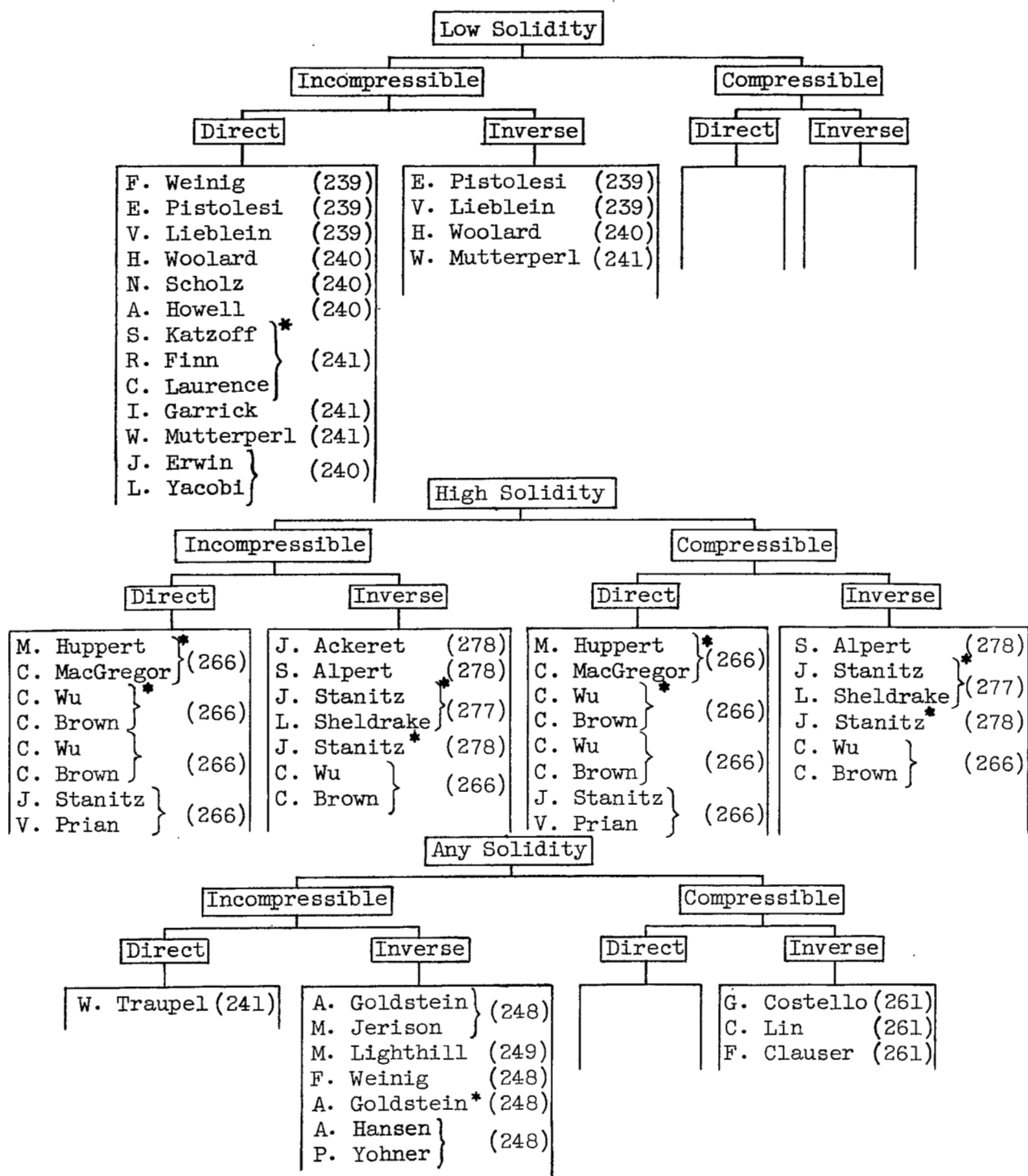
By William H. Roudebush

SUMMARY

The complexity of the flow of a fluid through a rotating blade row makes a direct theoretical attack on the general problem very difficult. However, the flow through axial-flow compressors, at least near the mean radius, is often sufficiently close to a mathematically two-dimensional flow that valuable results can be achieved by using two-dimensional theory.

An extensive review is presented of the literature concerning plane potential flow in cascades. No method of determining the flow is preferable under all conditions. The nature of the individual problem and the computing equipment available will dictate the method to be used. Some of the available techniques for solving the two basic problems, design and analysis, are evaluated; and several of the methods that have been used satisfactorily are presented in considerable detail.

The potential-flow cascade theories to be discussed are indicated by author in the following chart, arranged with regard to general regions of applicability. The divisions are not absolute and can serve only as a general guide. The numbers in parentheses indicate the page where the reference is first cited, and the asterisks denote those authors whose methods are presented in detail in this chapter.



INTRODUCTION

Compressor design techniques should always reflect the current basic knowledge of air flow. Time limitations may prevent a designer from using refined theoretical methods in individual design problems, but the simplifying assumptions made should be based on a sound theory. Unfortunately, the flow through a rotating blade row is very complex. The three-dimensional potential-flow equations, representing a highly idealized flow and a substantial simplification of the true problem, still cannot be solved satisfactorily. The added difficulties of boundary-layer buildup and displacement, separation, tip-clearance effects, compressibility effects, unsteady flow, and local regions of supersonic flow make compressor design one of the very difficult practical engineering problems.

Since a complete solution is not currently obtainable, another approach must be used. Historically, a problem of this nature is treated by making simplifying assumptions. Chapter III indicates that flow through an axial-flow compressor can be represented in many important instances by a combination of essentially two-dimensional solutions. Generally speaking, one of these solutions is from hub to shroud and the other is from blade to blade.

Within the limitations discussed in chapter III, the change in radius of a particle passing through a compressor blade row can be assumed small, and the two-dimensional blade-to-blade flow surface is taken as cylindrical. This cylindrical surface can be developed into an infinite plane cascade. The theoretical determination of the potential flow about such a cascade is treated in the present paper. Some of the methods considered are not restricted to plane flows, as will be indicated in the discussion.

The exact theoretical treatment of two-dimensional-cascade flow is not a simple problem, and past investigators have relied heavily on experimental cascades to obtain basic flow information. Early experimental cascades, however, did not successfully achieve two-dimensional flow. The data obtained in different cascades exhibited a considerable lack of uniformity, primarily as a result of using blades of small aspect ratio in different tunnel geometries without adequate boundary-layer bleed. It was difficult to separate the essential characteristics of the two-dimensional flow about a given blade system from the characteristics introduced into the flow by the individuality of the particular cascade operation. As a result, comparison of early experimental and theoretical results was not always practicable.

~~CONFIDENTIAL~~

This situation has been corrected in recent cascades by the development of successful boundary-layer controls. A close approximation of two-dimensionality has been obtained, and accurate data are now available (see ch. VI (ref. 1)). Therefore, it has become possible and highly desirable to interpret experimental cascade results in the light of theoretical analyses. In the future development of axial-flow compressors, more accurate predictions of turning angles and loss characteristics will probably be required over a wider range of operating conditions. A careful coordination of theory and experimental data may make possible accurate extrapolation of present data and should also provide a guide to future experimentation. Research on the off-design problems, in particular, can profitably employ this coordinated approach.

The flow of a viscous fluid through a cascade cannot yet be determined in its general form. However, since the effects of the viscosity are concentrated, in many cases, at the blade surfaces, the problem can be treated by boundary-layer theory. In this event the flow outside a narrow region at the boundaries is practically irrotational. Potential-flow calculations often provide reasonable pressure distributions, although they completely ignore viscosity. At times when thick boundary layers or separation exist or when knowledge of loss is desired, the potential-flow solution does not alone suffice. Even then, however, the pressure distribution obtained from the potential-flow calculation is indispensable for boundary-layer computation by existing methods. For these reasons the two-dimensional potential-flow solutions provide what is probably the most important single theoretical tool for analyzing the flow through an axial-flow compressor.

A survey of the large body of existing plane potential-flow theory may help to increase its present application. Although the theory has attained a high degree of completeness, the time involved in obtaining exact solutions is considerable. A reduction in time may be anticipated if the methods are used and understood and if attempts are made to adapt them to modern computing equipment in the most practical manner. There are also simplified approximate solutions that save time and may be quite worthwhile. Often the range of application of such methods is quite restricted; and accurate results in certain regions, such as the leading edge, are sometimes unobtainable. Subsequent examination may reveal, however, that some of these approximations are substantially valid in the region of interest to designers of axial-flow compressors.

An extensive review of the literature on the potential flow about cascades is presented herein. Many of the methods are evaluated within the bounds of limited available information on actual use. No method is universally applicable. The individual nature of a particular problem and the computing equipment available are large factors in determining the method of solution to be used. Some of the methods that have been

used successfully are presented in detail to illustrate the mathematical techniques and to indicate the nature of the actual computation.

SYMBOLS

The following symbols are used in this chapter:

a	speed of sound
\hat{b}	dimensionless blade thickness
C_p	pressure coefficient
\mathcal{C}	curvature
c	chord length
c_p	specific heat at constant pressure
c^*	characteristic length of thin blade for small-perturbation theory
D	height of water surface
E	electric-field strength
$\pm e^K$	locations of singularities in circle plane
g	acceleration due to gravity, 32.17 ft/sec ²
h	mapping function defined by eqs. (13) to (16)
h_1	real part of h
h_2	imaginary part of h
h^*	mapping function corrected to satisfy closure conditions
I	electric-current density
l	distance along streamline
l_{le}	leading-edge stagnation point

$l_{te,P}$	trailing edge approached from pressure surface
$l_{te,S}$	trailing edge approached from suction surface
l^*	function relating corrected distance about blade perimeter to circle central angle
M	Mach number
m	plate thickness
P	total or stagnation pressure
p	static or stream pressure
q	velocity in compressible medium
\bar{q}	vector velocity in compressible medium
\tilde{q}	disturbance velocity in small-perturbation theory
R	electrical resistance
r	radius
s	blade spacing
\hat{s}	dimensionless blade spacing
T	total or stagnation temperature
t	static or stream temperature
v	velocity in incompressible medium
\bar{v}	vector velocity in incompressible medium
\hat{v}	velocity in cascade plane expressed as function of circle plane coordinates
\hat{v}^*	velocity in cascade plane expressed as function of circle plane coordinates corrected for closure condition
\tilde{v}	disturbance velocity in small-perturbation theory
W	complex potential function

w	complex velocity
Δw	rate of mass flow
\hat{w}	complex velocity in cascade plane expressed as function of circle plane coordinates
x	abscissa in cascade plane
\bar{x}	axial length of region of validity of solutions by ref. 72
\hat{x}	dimensionless distance along x-axis
y	ordinate in cascade plane
\hat{y}	dimensionless distance along y-axis
z	complex variable in cascade plane
β	angle between air velocity and x-axis
Γ	circulation
γ	ratio of specific heats
γ^0	blade-chord angle, angle between blade chord and x-axis (fig. 1)
δ_x	increment in x-direction
δ_y	increment in y-direction
ζ	complex variable in plane of mapping circle
η	imaginary part of ζ
Λ	constant in affine transformation (58)
μ	angle made by tangent to blade profile and x-axis
\hat{v}	thickness ratio, \hat{b}/\hat{s}
ξ	real part of ζ
ρ	density
σ	solidity, ratio of chord to spacing

Φ	potential function
$\tilde{\Phi}$	disturbance potential function
$\hat{\Phi}$	electric potential function
ϕ	central angle in mapping circle plane
ϕ_{le}	angle corresponding to leading-edge stagnation point
$\phi_{te,P}$	angle corresponding to trailing edge approached from pressure surface
$\phi_{te,s}$	angle corresponding to trailing edge approached from suction surface
Ψ	stream function
$\hat{\Psi}$	electric-current function
Ω	specific resistance

Subscripts:

a	stagnation conditions
add	additional
add _s	additional due to sources
add _v	additional due to vortices
av	arithmetic average of values at suction and pressure surfaces
C	compressible
\mathcal{C}	curvature
c	compensating
c _s	compensating due to sources
c _v	compensating due to vortices
cr	critical

d	disturbance
d_s	disturbance due to sources
d_v	disturbance due to vortices
inc	incompressible
l	arbitrary position along potential line
le	leading edge
m	mean of upstream and downstream conditions
max	maximum
o	isolated airfoil
P	pressure surface
r	radial direction
s	suction surface
te	trailing edge
x	direction of x-axis
y	direction of y-axis
z	in cascade plane
Γ	circulatory
ζ	in mapping circle plane
θ	tangential direction
Σ	total
1	upstream at infinity
2	downstream at infinity

GENERAL CONSIDERATIONS

Potential-flow theory, as it pertains to two-dimensional cascades of blades, is concerned with two basic problems, referred to as "direct" and "inverse." In the direct (or analysis) problem, the geometry of a cascade and a characteristic velocity (usually \bar{v}_1 , the velocity vector far upstream, or \bar{v}_m , the mean free-stream velocity vector; see fig. 1) are given. A solution yields the velocity distribution in the region of the cascade. For the inverse (or design) problem, the velocity distribution on the surface of a cascade blade is given along with the vector velocities far upstream and far downstream. A solution, if one exists, gives the geometry (blade shape, chord angle, spacing) of the cascade.

In solving either the direct or inverse problem, an important distinction exists in the underlying approach. From figure 1 it can be seen that the flow about the cascade is given from a knowledge of the flow between streamlines bb and dd as a result of the periodicity of the flow pattern in the direction of the y-axis. Similarly, a knowledge of the flow field between streamlines aa and cc constitutes a complete solution. When the cascade flow field is considered to be made up of sections of the type bbdd, the cascade is pictured as an infinite array of isolated bodies. On the other hand, when sections of the type aacc are considered, the cascade appears as an infinite array of adjacent channels.

As a result of these two basic points of view, different mathematical techniques are employed in the two cases. Either point of view is theoretically applicable for a given cascade. However, the mathematical techniques employed in the "isolated-body" approach become clumsy and tedious as the effects of the neighboring blades on each other become large. Similarly, the "channel-flow" approach works well only when the neighboring cascade blades exert an appreciable guidance on the fluid. Hence, the cascade solidity σ (ratio of chord length to spacing) determines the point of view that should be adopted for a given cascade. The solutions considered are divided into "low-solidity" and "high-solidity" methods, where each of these distinctions is subdivided into its relation to the direct and inverse problems. It must be noted that the classification by solidity is not rigid, but may depend on such factors as cascade stagger angle, experience with the technique, and the computational equipment available.

Although few of the methods of solution have been widely used, in most instances some solutions have been obtained by the author of the method. In some cases, experimental cascades have been investigated and compared with the theoretical results. Some authors have compared their solutions with other theoretically obtained solutions.

While the ultimate objective of any theoretical method is to design or analyze an actual cascade, there exists a practical difficulty in appraising a theoretical method by comparison with an actual cascade. Such an evaluation is indecisive, since the fluid has been divested of at least some of its natural properties by the mathematician. Therefore, the most reasonable test of a given theoretical method is comparison with an exact known theoretical solution. Such exact solutions do exist comparable to the Joukowski airfoils of isolated-airfoil theory. If this comparison is good, the new method is satisfying its function by predicting the flow of an idealized fluid. Determining the flow relations that actually exist about the experimental counterpart of a theoretically determined cascade is an entirely different problem, which has not been adequately investigated.

In this paper an attempt is made to discuss and, to some extent, to evaluate many of the theoretical methods available to the designer. Experimental data are not used for purposes of evaluation, for the reasons given in the preceding paragraph. Three design methods (two for high solidity and one for low solidity) and three analysis methods (two for high and one for low solidity) are presented in detail.

LOW-SOLIDITY CASCADES

Almost all the available work on low-solidity cascades has been done on incompressible flow because of the intractability of the nonlinear equations involved in the compressible-flow problem. The assumption of constant density is justifiable for a considerable range of low Mach number flows. When sonic speeds are approached in regions of the flow field, the effects of density variation are, of course, pronounced. If shock waves occur, qualitative as well as quantitative errors may be introduced. Therefore, some methods of treating compressible flows and correcting incompressible-flow solutions for the effects of compressibility are discussed following the sections concerning the direct and inverse problems.

The Direct Problem

The pattern for solution of the direct problem has developed along two distinct lines. The first approach is to find a conformal mapping of the cascade onto a simple geometric shape, such as a straight line or a circle. The flow about the simple shape is readily determined, and the mapping function is applied to yield the desired flow about the original body. This method of solution has been of considerable mathematical interest for many years.

The second approach to the problem is based on the following fact: The effect of a solid body on the fluid surrounding it can be closely approximated by replacing the body with a carefully chosen system of flow singularities (sources, sinks, vortices). The characteristics of these singularities are well-known, and their effect on the uniform flow can be obtained.

By way of introduction to the cascade problem, the history of the application of these two approaches to the isolated-airfoil problem is discussed briefly in the following section.

Isolated airfoils. - Early significant results concerning the flow of fluid about an isolated airfoil were achieved by Kutta and Joukowski. The theory was extended and improved by von Kármán, Trefftz, von Mises, and many others (see ref. 2). This is an exact theory of special airfoil shapes that are obtained from a circle by simple conformal transformations. The airfoils thus obtained are not superior aerodynamically to many others, and a method to analyze the flow about arbitrary wing profiles was considered necessary.

A significant contribution to the problem was made by Munk (ref. 3), who presented a technique for determining the over-all characteristics of the flow about a thin, slightly cambered airfoil of otherwise arbitrary shape. The mapping $z = \xi + 1/\xi$ is used to transform the thin airfoil (actually the camber line) into a near-circle in the ξ -plane. The near-circle is transformed into an exact circle resulting in a simple integral equation for determining the stagnation point of the flow about the exact circle. When the location of the stagnation point is known, the circulation (and consequently the lift) can be determined about the circle and hence about the airfoil. The technique is improved and utilized by Glauert in reference 4, where several comparisons are made with experimental data.

In 1923, Birnbaum (ref. 5) applied a method of singularities to the same problem. The thin airfoil is replaced by a continuous distribution of vortices along the mean camber line. This method, which is applicable to the inverse as well as the direct problem, is set forth in detail by Glauert in his text on airfoil theory (ref. 6). Glauert uses the trigonometric series

$$2v \left(A_0 \cot \frac{\theta}{2} + \sum_{n=1}^{\infty} A_n \sin n\theta \right)$$

for the distribution of vorticity. The abscissa x of the airfoil is related to θ by

$$x = \frac{R}{2} (1 - \cos \theta)$$

The constants A_n are determined by the shape of the camber line. The first term of the expression for the vorticity distribution represents the distribution on a straight-line airfoil, and the sine terms compensate for the curvature of the thin airfoil. This expression has been used in cascade work as well as in isolated-airfoil theory.

In later work along these lines, source and sink distributions were added by Allen (ref. 7) to approximate the effect of airfoil thickness. However, since the solution still applied only to thin airfoils of small camber, a more general solution was desired.

In 1931, Theodorsen (ref. 8) and Theodorsen and Garrick (ref. 9) produced an exact solution to the direct problem of two-dimensional, incompressible flow about an airfoil of arbitrary shape. A Joukowski transformation is used to map the airfoil into a near-circle. The mapping of the near-circle into an exact circle then leads to an integral equation, solved by an iteration process. (The numerical evaluation of the cotangent integral in the Theodorsen method is considered in refs. 10 and 11.) This general solution had considerable significance both in the impetus it gave to the work on the airfoil problem and in its direct application to later work on cascades of airfoils. A consideration of conditions sufficient to assure convergence of the iteration process of Theodorsen appears in reference 12.

Cascades. - The development of the theory of flow about cascades of blades is similar to the development of the isolated-airfoil theory. Particular cascades, corresponding to the so-called "theoretical airfoils" of the isolated-airfoil theory, were developed (refs. 13 and 14). Solutions were also found for cascades of thin, slightly cambered, but otherwise arbitrary, blades. Finally, solutions for general blade shapes were obtained of a more or less exact nature.

In 1935, a comprehensive text on the theory of turbomachines was presented by Weinig (ref. 15), in which was introduced and demonstrated the concept that every cascade has a corresponding straight-line cascade that is equivalent insofar as it produces the same turning and has the same circulation. Methods for approximately determining the equivalent-line cascade are given, and the foundations are laid for exact solutions to the general cascade problem. The theory of equivalent-line cascades will not be discussed herein, since it does not give information about local conditions on the blade surfaces. The more general theory will be mentioned later in its connection with other methods that have been developed from it.

In 1937, Pistolesi (ref. 16) extended the work of Birnbaum and Glauert to cascades of thin blades. This work is significant theoretically, but the complexity in the case of a staggered cascade makes computation difficult. In addition, the inherent limitation to thin, lightly loaded blades is an undesirable restriction in present-day design. This technique has been extended by V. Lieblein (ref. 17) to include the effect of thickness distribution. The approximations made in

this analysis become increasingly inexact with higher camber and greater thickness. A closer examination of such approximate methods may indicate that they are reasonably valid in the ordinary range of compressor blade shapes. If this should be the case, such methods will become important because of the savings in time realized over the more exact methods.

An approximate theory of practical interest has been developed by Erwin and Yacobi (ref. 18), utilizing the principle of superposition common in isolated-airfoil theories. The local velocity on the cascade blade surface is taken to be the sum of the average velocity in the passage and incremental velocities due to thickness, camber, and angle of attack. The average velocity is determined from area change through the cascade, and the incremental velocities are related to corresponding incremental velocities on an isolated airfoil of the same shape. The relation is determined empirically in the report, but could probably be determined theoretically as well. This method provides solutions to the direct cascade problem quite rapidly when the characteristics of the corresponding isolated airfoil are known.

Other approximate methods, using a technique employing singularities, have been presented by Woolard (ref. 19) and Scholz (ref. 20). Results obtained in reference 19 show fair agreement with results obtained by the more exact method of reference 21 for NACA 4412 airfoils in a cascade of nearly unit solidity over a range of angle of attack.

In 1941, Howell (ref. 22) produced an exact solution to the general problem, employing the method of conformal mapping. A cascade, located in the z -plane, is transformed into a distorted airfoil in the z_1 -plane by the equation $z_1 = \tanh z$. The distorted airfoil is then transformed into a near-circle by two successive Joukowski transformations. Finally, the near-circle is transformed into an exact circle by using conjugate Fourier series. Since four transformations are involved, the work is necessarily lengthy. However, a detailed computational layout and some suggestions for decreasing the labor involved are available in reference 23, and a number of theoretical solutions are obtained for a cascade with a solidity slightly greater than 1.0. In reference 22 theoretical results are compared with experimental data for a cascade with a solidity of 0.85.

Howell's method appears to give reasonable and consistent results for solidities as high as 1.0. Higher solidities could be used, but the shape obtained in the first transformation would be distorted and the amount of labor would be increased. It is estimated in reference 23 that a complete solution for several angles of attack can be made in 3 weeks. If only the deviation angle is required, the time is reduced. Some further simplifications of the method are given in reference 24.

In 1944, Garrick (ref. 25) presented a solution using the well-known mapping (refs. 26 and 27) of a straight-line cascade into a circle. By means of this transformation, a cascade is mapped into a near-circle, and finally the near-circle is mapped into an exact circle. A computational procedure is given, and an example is worked out. As in the case of Howell's solution, the computations are lengthy.

A different approach was presented by Traupel (ref. 28), who mapped the flow field of the cascade onto the interior of an internally concave closed curve. A minimum of four transformations is generally required, and the computer must exercise a certain amount of skill and judgment in the selection of some of the transformations. Using Green's second formula, the author arrived at an integral equation which he solved by an iterative procedure. No comparison with other results is made in the report, although an example is computed. The method is mentioned also in connection with an experimental investigation on internal-combustion prime movers in reference 29.

Mutterperl (refs. 30 and 31) mapped the arbitrary cascade directly onto a straight-line cascade. Although the method does reduce computational time, some difficulty has been encountered at the Lewis laboratory in obtaining accurate numerical results. It is difficult to determine when the results have converged to a valid solution. This method was used in an investigation by Resnick and Green (ref. 32), but the validity of the pressure distributions obtained cannot be determined.

An exact solution, using a continuous distribution of vortices on the perimeter of a cascade of blades, was developed by Katzoff, Finn, and Laurence (ref. 21). With the velocity distribution of an arbitrary isolated blade known, the velocity distribution about the blade in cascade can be accurately determined with reasonably little computation, and can be approximated in even less time. Experience enables the user to compare the greater accuracy obtainable at any step of the solution with the attendant cost in computational time. Comparison of a solution by this method with one for a cascade about which the ideal flow is known exactly shows good agreement (fig. 2).

In reference 33 a comparison is made of experimental results and theoretical results obtained by the Katzoff, Finn, and Laurence method. As an example of the magnitude of agreement between experiment and theory when good two-dimensional-cascade data are available, a typical figure from reference 33 is presented (see fig. 3). The disagreement is due largely to the use of the Kutta condition for establishing the branch point of the flow, as indicated in the figure by the results obtained

when the experimental lift coefficient is used instead to determine circulation. Finally, very good agreement is obtained by reducing the angle of attack slightly. Although this reduction in angle was made arbitrarily to obtain good agreement, it can be justified qualitatively on the basis of boundary-layer formation on the blade surface.

The method of Katzoff, Finn, and Laurence (ref. 21) is developed in the following section in greater detail as an illustration of an adequate method for solving the direct problem for a low- or medium-solidity cascade. (Solutions are presented in the literature for solidities up to 1.5.) The mathematics involved is not complicated. This method is advantageous in that it can be used as an approximate method with any desired degree of accuracy.

Solution of low-solidity direct problem. - In the direct problem, the geometry of the cascade (blade shape, cascade chord angle γ^0 , and solidity $\sigma = c/s$) and the mean free-stream velocity \bar{v}_m (i.e., vector average of the velocities far upstream and far downstream of the cascade) are given (see fig. 1). The problem is to find a flow with mean free-stream velocity \bar{v}_m , having the blade profiles as partial streamlines, and leaving the blades at a fixed point. In the case of a sharp trailing edge, the Kutta condition places this point at the trailing edge. If the trailing edge is rounded, the position of the trailing-edge stagnation point must be prescribed from an empirical knowledge of this type of flow.

The cascade will be considered to consist of a central blade (the one containing the origin) and a lattice of external, or interference, blades. The solution obtained will be a superposition of flows, derived by first treating the central blade as an isolated body in the mean free stream of the cascade and then finding the interference flow due to the presence of the external blades. Such a superposition of solutions is possible because of the linear and homogeneous character of the equations governing a two-dimensional, irrotational, and incompressible flow.

The total complex potential function $W_\Sigma = \Phi_\Sigma + i\Psi_\Sigma$ will be composed of the following parts:

- (1) The function $W_0 = \Phi_0 + i\Psi_0$ of the flow about the isolated central blade oriented as in the cascade with respect to the mean free-stream velocity. Since the blade profile forms part of a streamline, Ψ_0 will be zero on the blade.
- (2) The interference flow function $W_d = \Phi_d + i\Psi_d$ representing a distribution of isolated singularities along the mean camber lines (or a continuous distribution of vortices along the profiles) of the infinitely many external blades. The central-blade profile will not be a streamline in this flow.

(3) The function $W_c = \Phi_c + i\Psi_c$ of the compensating flow necessary to make the central-blade profile a streamline in the disturbance flow; $\Psi_c = -\Psi_d$ on the blade. This flow function is analytic exterior to the central blade.

(4) The function $W_\Gamma = \Phi_\Gamma + i\Psi_\Gamma$ of the circulatory flow, which causes the compensating flow to leave the blade at the trailing edge. Since the blade profile forms part of a streamline, $\Psi_\Gamma = 0$ on the blade in this flow.

The problem of finding the flow about an isolated profile in a free stream is well-known and will be considered as already having been solved for this application. An extensive treatment can be found in references 8 and 9. The potential distribution, as well as the mapping function of the central blade onto a circle (derived from the isolated-profile computation), is assumed in what follows. The presentation given herein of the cascade solution is concerned only with finding the disturbance effects of the external blades on the central blade.

For purposes of demonstrating the technique, the assumption is made that the final velocity distribution about the cascade is already known. The applicability of an iteration process will be indicated later. Using the known velocity distribution and blade shape, the first step is to represent the external blades by singularities arranged on the mean camber lines at intervals measured along the chords. A good approximation can usually be obtained with two sources, three sinks, and five vortices. A guide to the location of these singularities is given later. To evaluate the effect on the central blade of these infinite rows of singularities, the chart (first appearing in ref. 34) shown in figure 4 is used. This chart represents an infinite row of vortices (or sources) of unit strength placed a unit distance apart with the central vortex omitted. A drawing of the cascade blade is now prepared, with chord length chosen to give the proper solidity when used with the graph. To find the effect on the central blade of an infinite row of vortices, located at a point x on each exterior blade, the drawing of the central blade is placed with the point x on the origin of the graph and with the blade properly oriented with respect to the y -axis. The values of the stream function and potential function can be read from the graph at selected points on the central-blade profile. The values indicated on the graph must be multiplied by the vortex strength at the position being considered. If the singularity involved is a source, the lines marked Ψ become $-\Phi$ and those marked Φ become Ψ . A sink is regarded as a negative source. In this manner, the effect of each infinite row of singularities is found at certain prescribed points on the central blade. Adding all these contributions gives Φ_d and Ψ_d .

Although the use of isolated singularities distributed along the mean camber line is clearly an approximation, the results obtained in this manner are usually so accurate that no other technique is required. In instances where some doubt may exist concerning the accuracy of

results thus obtained, a somewhat different approach is available for finding the disturbance flow. It has been shown (ref. 35) that a cascade of blades in a uniform stream can be represented exactly by a continuous distribution of vortices on the perimeter of each blade, where the vortex strength per unit length at each point is equal to the velocity of the flow about the blade at that point. With this result in view, the blade model is placed with a point of its contour on the origin, and the effects are computed as in the preceding discussion. At each point the vortex strength is $v \, dl$, where dl is an increment of the airfoil arc length. The velocity is taken as positive on the suction surface and negative on the pressure surface; that is, the velocity is taken as positive in the positively oriented arc-length direction (see fig. 5).

The disturbance flow function is then given at a point $z_0 = x_0 + iy_0$ on the central blade by

$$\left. \begin{aligned} \Phi_d(z_0) &= \oint \Phi \cdot v(z) \, dl \\ \Psi_d(z_0) &= \oint \Psi \cdot v(z) \, dl \end{aligned} \right\} \quad (1)$$

where Φ and Ψ are the values read at z_0 from the chart (note that these values are for vortices of unit strength and unit spacing) when the origin is at z on the central blade. The integration is performed over the blade profile. It is convenient to rewrite equations (1) as

$$\left. \begin{aligned} \Phi_d(z_0) &= \oint \Phi \cdot d\Phi_\Sigma(z) \\ \Psi_d(z_0) &= \oint \Psi \cdot d\Phi_\Sigma(z) \end{aligned} \right\} \quad (2)$$

From equations (2), Φ_d and Ψ_d are readily evaluated by plotting Φ and Ψ against Φ_Σ and integrating numerically or with a planimeter.

A disturbance flow has now been calculated yielding a Ψ_d and Φ_d distribution on the central-blade profile. To make this profile a streamline in the disturbance flow, a compensating flow W_c is now added such that $\Psi_c = -\Psi_d$ on the blade profile. It is necessary to compute the potential distribution Φ_c of which Ψ_c is the harmonic conjugate. This problem is greatly simplified, since the mapping of the central blade onto a circle is known from the initial computation of the flow about the isolated profile. The actual procedure is given in detail in reference 11 and will not be considered herein.

The flow $W_c = \Phi_c + i\Psi_c$ thus generated will have, in general, a value of $d\Phi_c/d\phi$ unequal to zero at the trailing edge (ϕ is the central

angle in the circle plane). In order to satisfy the Kutta condition, a vortex is added at the center of the circle with a strength

$$\Gamma_{\text{add}} = -2\pi \, d\Phi_c / d\phi$$

The corresponding contribution to the potential function is $\Phi_\Gamma = (\Gamma_{\text{add}}/2\pi)\phi$.

The complete potential function Φ_Σ is now obtained by summing the contributions Φ_o , Φ_d , Φ_c , and Φ_Γ obtained in the various stages of the solution. The final velocity distribution is obtained by differentiating Φ_Σ with respect to arc length on the blade profile.

The foregoing discussion was advanced on the assumption that the final velocity distribution was known initially. In the actual case, the velocity distribution about the isolated central blade may be taken as a convenient starting value. Adding the disturbance velocities calculated from this initial velocity distribution yields a distribution nearer the correct one. The disturbance effects are then recalculated on the basis of the corrected velocity, and so on. The rapidity of convergence will depend on the accuracy of the initial approximation. It is clear that for high-solidity cascades the initial approximation will be poor and slower convergence can be expected.

In the course of actual application, the authors of the method developed a technique for the iteration process that results in much faster convergence. As the iteration process is carried out, each change in the exterior singularities necessitates a change in the singularities within the central airfoil, that is, a change in W_c . In turn, this results in a change in W_Γ and a change in total circulation. In this sense, the change in circulation about the central blade can be attributed to changes made in the location and strength of the exterior sources and vortices. Then, if Γ_Σ is the total circulation and Γ_o the circulation about the isolated blade, the following equation is obtained:

$$\Gamma_\Sigma = \Gamma_o + \Gamma_{\text{add}_s} + \Gamma_{\text{add}_v} \quad (3)$$

where Γ_{add_s} and Γ_{add_v} are the additional circulations about the central blade attributable to the presence of the exterior sources and vortices, respectively. In actual practice, the value of Γ_{add_s} changes very little from one iteration to the next, and Γ_{add_v} is nearly proportional to the total circulation. Therefore, the following equation may be written instead of equation (3):

$$\Gamma_\Sigma \approx \Gamma_o + \Gamma_{\text{add}_s} + (\Gamma_\Sigma / \Gamma_o) \Gamma_{\text{add}_v}$$

or

$$\Gamma_{\Sigma} = \frac{\Gamma_o + \Gamma_{add_s}}{1 - \frac{\Gamma_{add_v}}{\Gamma_o}} \quad (4a)$$

Values of Γ_{Σ} calculated from equation (4a) have proven to be considerably closer to the final correct value than those calculated from equation (3). Correspondingly, the potential function can be written

$$\Phi_{\Sigma} = \Phi_o + \Phi_{add_s} + \frac{\Gamma_{\Sigma}}{\Gamma_o} \Phi_{add_v} \quad (4b)$$

where Φ_{Σ} is now considered as the sum of Φ_o and Φ_{add} , where

$$\Phi_{add} = \Phi_d + \Phi_c + \Phi_r$$

The second iteration can be similarly adjusted:

$$\Gamma_{\Sigma_2} = \frac{\Gamma_o + \Gamma_{add_s}}{1 - \frac{\Gamma_{add_v}}{\Gamma_{\Sigma_1}}} \quad (4c)$$

where the subscripts 1 and 2 refer to the first and second approximations, respectively. This modification is highly effective in obtaining rapid convergence. The additional complication of separating the effects of the vortices and sources is not great.

When an arrangement of isolated singularities is used (this is recommended by the author of the method almost without reservation), the proper number and location are largely a matter of experience. For solidities near 1.0, five vortices spaced at 0.1, 0.3, 0.5, 0.7, and 0.9 of chord length will probably give an adequate representation of the velocity distribution effects. The vortex strength at a given chord position is determined from the difference in potential on the upper and lower surfaces. For example, the difference in these potentials at 0.2 chord is approximately the vortex strength from the leading edge to the 0.2-chord position. This vorticity is assumed to be concentrated at the 0.1-chord position. The sum of the isolated vortex strengths must equal the total circulation about the blade.

In the example of reference 21, a source was placed at 0.025 chord and another midway between the leading edge and the position of maximum

thickness. Sinks were placed at 0.5, 0.7, and 0.9 of the chord length. To determine the source strength, the average velocity v_{av} is defined as $(v_s + v_p)/2$, where v_s and v_p are the local velocities on the suction and pressure surfaces, respectively. The internal flow at each axial position is defined to be the product of the blade thickness at that position and the corresponding average velocity. The strength of a source or sink is then taken as the difference between the internal flow at a station midway between the location of the source in question and the preceding source and at a station midway between the location of the source in question and the following source. The total source strength must equal the total sink strength. The optimum arrangement of these singularities will differ with blade shapes, but a suitable arrangement should be evident.

The velocity distributions at other angles of incidence can be easily obtained by the method of conformal mapping. No knowledge of the actual mapping function is required; therefore, the off-design conditions can be readily obtained from the exact solution. The procedure for this computation is given in appendix A and is applicable in any case of plane incompressible irrotational flow where a solution at one angle of attack is available. This characteristic of the incompressible-flow solution offers an advantage over the compressible-flow solutions for the same problem.

An outline of the general procedure to be used in applying the Katzoff, Finn, and Laurence method follows:

(1) Solve the problem of the isolated geometrically similar blade profile, oriented properly with respect to the mean free-stream velocity. The method of reference 9 or some related method yielding the blade mapping on a circle is used.

(2) Determine the location and strength of the singularities from considerations of cascade geometry and the isolated-blade solution, respectively.

(3) Determine ϕ_{d_s} , ψ_{d_s} , ϕ_{d_v} , and ψ_{d_v} from the chart in figure 4.

(4) Let $\psi_{c_s} = -\psi_{d_s}$ and $\psi_{c_v} = -\psi_{d_v}$ on the blade surface. Then determine ϕ_{c_s} and ϕ_{c_v} by the method of reference 11.

(5) Find Γ_{add_s} and Γ_{add_v} from the trailing-edge criterion. Find Γ_Σ from equation (4a) and ϕ_Σ from equation (4b).

(6) Compute the final velocity distribution as the derivative of ϕ_Σ with respect to arc length.

(7) Reevaluate the strength of the singularities in step (2) on the basis of the new velocity and potential distribution.

(8) Carry through all steps of the process again. If there exists a doubt concerning the accuracy of results obtained by using isolated singularities, replace these singularities by a continuous distribution in step (2) and carry out the remainder of the procedure.

(9) Continue the iteration until convergence is obtained. A second or third trial should be sufficient.

The Inverse Problem

In the inverse problem for low solidities, as in the direct problem, the methods of conformal mapping and representation by singularities are used. Contrary to the direct problem, however, the solidity often is not significant in the methods for solving the inverse problem. In particular, the method presented in detail in this section can be used for any solidity. This generality, where it exists, is indicated in the table contained in the SUMMARY.

Either the direct or inverse problem can generally be solved by the method of singularities applied to thin blades, either isolated or in cascade. Therefore, the techniques developed by Birnbaum, Glauert, and Allen, mentioned previously in connection with the direct problem for isolated airfoils, and the solutions of the cascade problem by Pistolesi, Lieblein, and Woolard are applicable to the inverse problem as well.

The current use of higher cambered blades in compressors somewhat restricts the value of the approximate methods. Hence, this section is concerned chiefly with the more exact solutions, which have achieved a complete and convenient form in recent years.

Isolated airfoils. - In 1935, Betz (ref. 36) presented an approximate method for modifying the shape of an existing isolated airfoil to assure a predetermined change in the velocity distribution. Theodorsen also presented a method of modification based on his exact solution of the direct problem (ref. 37). More general methods have been given by Gebelein (ref. 38) and Peebles (ref. 39) using conformal mapping and by Goldstein and Jerison (ref. 35) using singularities. Other solutions of the isolated-airfoil design problem exist, but the foregoing illustrate the essential characteristics of a solution to the problem.

Cascades. - An approach to an exact solution of the cascade problem was given by Weinig (ref. 15). A complete solution by conformal mapping was developed and presented in a series of unpublished lectures by Arthur Goldstein. The computational procedure was given in considerable detail by Hansen and Yohner (ref. 40), and a theoretical solution was obtained.

This method, considered to represent an accurate and reasonably fast solution to the problem, will be outlined later in some detail. There is no restriction on solidity.

A similar approach was given in 1945 by Lighthill (ref. 41), in which the velocities are not prescribed directly as a function of airfoil arc length but rather as a function of the central angle of the mapping circle. Hence, a certain amount of experience is required to obtain a desired velocity distribution on the cascade itself.

The method of Mutterperl (ref. 31), mentioned in connection with the direct problem, is applicable also to the inverse problem. As mentioned before, some results have indicated that the numerical answers might not always be reliable. If the accuracy can be improved, the method may find practical application.

All the inverse cascade methods considered so far have made use of conformal-mapping theory. A method of singularities was developed by Goldstein and Jerison (ref. 35), but they encountered some practical difficulty in the application of their technique in regions where the curvature of the blade surface is large, particularly in the leading-edge region of a thick blade. However, the solidity is not an important factor, and the method is considered to be quite useful for the design of thin blades.

Of the methods discussed above, the conformal-mapping method of Goldstein has been selected for a detailed presentation. A report (ref. 40) is available on the computational procedure.

Solution of low-solidity inverse problem. - The low-solidity inverse problem is twofold: (1) to determine the flow about a unit circle that will have the desired characteristics when mapped into the cascade plane, and (2) to determine the mapping function and hence the blade coordinates. The problem is simpler than the corresponding direct problem in that no iteration is required. Furthermore, the solution is known to be exact, since no convergence is involved. A difficulty is introduced, however, by the fact that an arbitrarily selected velocity distribution may fail to result in a closed profile. In this event, the method to be described indicates the necessary change in the prescribed velocity distribution that will yield a closed profile. The suction-surface velocity distribution, usually the most critical, can be maintained as originally specified.

The following information must be given to obtain a solution: (1) the vector velocities infinitely far upstream and downstream of the cascade, and (2) the velocity distribution as a function of arc length on the contour of a blade. Velocities are considered positive in the positively oriented arc-length direction (fig. 5). Note that the arc length is increasing ($dl > 0$) as the blade is traversed in a counterclockwise direction.

The following information is obtained in the solution: (1) the blade profile, and (2) the blade-chord angle γ^0 and solidity σ .

In the following discussion the complex plane containing the cascade will be referred to as the $z = x + iy$ plane (or cascade plane). The complex plane containing the circle (fig. 6) will be referred to as the $\zeta = \xi + i\eta$ plane (or circle plane).

The most convenient mapping for this problem is one which takes the cascade into a unit circle with center at the origin. The points at $\pm\infty$ on a line normal to the y -axis are transformed into points $\pm e^K$, symmetrically located about the origin on the real axis (fig. 6). Such a mapping is discussed in considerable detail in references 15 and 26. Under a mapping of this kind, the complex potential function in the circle plane can be written (see ref. 15)

$$W_\zeta(\zeta) = \frac{v_m s}{2\pi} \left[e^{i\beta_m} \log_e \left(\frac{\zeta - e^K}{\zeta + e^K} \right) + e^{-i\beta_m} \log_e \left(\frac{\zeta - e^{-K}}{\zeta + e^{-K}} \right) \right] + \frac{\Gamma}{4\pi i} \log_e \left(\frac{\zeta^2 - e^{-2K}}{\zeta^2 - e^{2K}} \right) + \text{constant} \quad (5)$$

This equation is quite general and holds for an arbitrary cascade in the z -plane. The quantities v_m , β_m , s , Γ , and K are functions of the particular cascade to be mapped into the circle. When these quantities have been chosen properly for a given cascade, the flow about the circle will map back into the desired flow about the cascade. The symbols v_m , β_m , s , and Γ are the mean free-stream velocity, mean free-stream velocity angle, spacing, and circulation of the cascade, respectively; K is a measure of the location $\pm e^K$ of the singularities in the flow about the circle. All five of these quantities can be determined from the prescribed conditions in the inverse problem.

From the velocity diagram (fig. 1) it can be seen that

$$\beta_m = \tan^{-1} \left(\frac{\tan \beta_1 + \tan \beta_2}{2} \right), \quad -\frac{\pi}{2} < \beta_m < \frac{\pi}{2} \quad (6)$$

and

$$v_m = \frac{v_1 \cos \beta_1}{\cos \beta_m} \quad (7)$$

The circulation is given by

$$\Gamma = \int_{l_{te,P}}^{l_{te,S}} v(l) dl \quad (8)$$

where $v(l)$ is the signed velocity on the cascade blade prescribed as a function of arc length (fig. 5). The blade spacing is given by

$$s = \frac{\Gamma}{v_1 \sin \beta_1 - v_2 \sin \beta_2} \quad (9)$$

Determination of the constant K is somewhat more difficult and depends upon certain considerations of the potential functions. The range of the velocity potential (the difference between maximum and minimum values of the potential) on a cascade blade must equal the corresponding potential range on the circle. On the blade this range is computed as

$$\Delta\Phi_Z = \Phi_Z(l_{te,S}) - \Phi_Z(l_{le}) \quad (10)$$

where $l_{te,S}$ and l_{le} are identified in figure 5. From the simple relation connecting the potential distribution to the velocity distribution, Φ_Z can be calculated as

$$\Phi_Z(l) = \int_{l_{te,S}}^l v(l) dl$$

The velocity potential on the circle is given by

$$\Phi_\zeta = \text{Real} \left[W_\zeta(e^{i\varphi}) \right] \quad (11)$$

where Real designates the real part, and φ is the central angle of the circle. Then,

$$\Delta\Phi_\zeta = \Phi_\zeta(e^{i\varphi_{te,S}}) - \Phi_\zeta(e^{i\varphi_{le}}) \quad (12)$$

where $\varphi_{te,S}$ and φ_{le} are the values of φ (as yet unknown) corresponding to the trailing-edge and leading-edge stagnation points on the circle (see fig. 6). By the process of trial and error outlined in appendix A (described in detail in ref. 40), $\varphi_{te,S}$, φ_{le} , and K can be determined such that $\Delta\Phi_\zeta = \Delta\Phi_Z$.

In this manner, the flow in the circle plane is determined uniquely for a prescribed set of conditions in the plane of the cascade (step (1) in the solution of the inverse problem). The function that conformally maps the cascade into the circle must yet be determined from the knowledge of velocities about the circle and about the cascade.

In appendix B the following form of a general mapping function is developed:

$$\frac{dz}{d\xi} = \frac{se^{-K}}{\pi} F(\xi) e^{\frac{h(\xi)}{F(\xi)}} \quad (13)$$

where

$$F(\xi) = \frac{\xi^2 (e^{2K} - e^{-2K})}{(e^{2K} - \xi^2)(\xi^2 - e^{-2K})} \quad (14)$$

and

$$h(\xi) = h_1(\xi, \eta) + ih_2(\xi, \eta) \quad (15)$$

The function $h(\xi)$ is regular outside the unit circle, and

$$\lim_{\xi \rightarrow \infty} \xi h(\xi) = 0 \quad (16)$$

The function $z = z(\xi)$, defined by equations (13) to (16), will map an arbitrary cascade into the unit circle such that the points far upstream and far downstream of the cascade are transformed into the points $\pm e^K$ in the circle plane. The function $h(\xi)$ will determine the shape of the cascade. The problem is to determine $h(\xi)$, and hence the blade shape, from the available information.

Let W_ξ and W_z represent the complex potential functions in the circle plane and cascade plane, respectively. Then, if $z = z(\xi)$ is the desired mapping between the two planes,

$$W_z(z) = W_z(z(\xi)) = W_\xi(\xi) \quad (17)$$

Differentiating equation (17) gives a relation between the complex velocity conjugates w_z and w_ξ as follows:

$$w_\xi(\xi) = \frac{dW_\xi}{d\xi} = \frac{dW_z}{dz} \frac{dz}{d\xi} = w_z(z) \frac{dz}{d\xi} \quad (18)$$

If only the unit circle is considered, then $\xi = e^{i\phi}$, and it can be determined from equation (14) that $F(e^{i\phi})$ is real. As a matter of convenience, all functions of $e^{i\phi}$ are written simply as functions of ϕ in the following expressions. Combining equations (13) and (18) gives

$$\frac{w_\zeta(\varphi)}{w_z(l)} = \left(\frac{dz}{d\zeta} \right)_{\zeta=e^{i\varphi}} = \frac{se^{-K}}{\pi} F(\varphi) e^{\frac{h_1(\varphi)+ih_2(\varphi)}{F(\varphi)}} \quad (19)$$

where $w_z(l)$ indicates that w_z has now been expressed as a function of distance along the blade perimeter.

The value of the potential at any point on the blade is given by

$$\Phi_z(l) = \int_{l_{te,P}}^l v(l) dl \quad (20)$$

The values of $\Phi_\zeta(\varphi)$ are known to an additive constant from the real part of equation (5). The additive constant should now be chosen so that $\Phi_z(l_{te,P}) = \Phi_\zeta(\varphi_{te,P})$. Then, equating the values of potential in the two planes gives a functional relation of l with φ , say $l = l(\varphi)$.

Now, by means of the function $l = l(\varphi)$, $w_z(l)$ can be written as a function of the central circle angle φ as follows:

$$w_z(l) = w_z(l(\varphi)) = \hat{w}_z(\varphi) \quad (21)$$

where \hat{w} denotes the velocity in the cascade plane expressed as a function of the circle plane coordinates. Then the ratio of the velocities in the two planes can be written

$$\frac{w_\zeta(\varphi)}{\hat{w}_z(\varphi)} = \frac{v_\zeta(\varphi) e^{-i(\varphi+\pi/2)}}{\hat{v}_z(\varphi) e^{-i\mu}} \quad (22)$$

where v_ζ and v_z are signed velocities, and μ is the angle made by a tangent to the blade profile and the x-axis. Substituting equation (22) into equation (19) and taking the logarithms of both sides yield:

$$\log_e \left[\frac{v_\zeta(\varphi)}{\hat{v}_z(\varphi)} \right] + i(\mu - \varphi - \pi/2) = \log_e \left[\frac{se^{-K}}{\pi} F(\varphi) \right] + \frac{h_1(\varphi)}{F(\varphi)} + i \frac{h_2(\varphi)}{F(\varphi)} \quad (23)$$

Since $F(\varphi)$ is real, equating real and imaginary parts of equation (23) gives

$$h_1(\varphi) = F(\varphi) \log_e \left[\frac{\pi e^K}{sF(\varphi)} \frac{v_\zeta(\varphi)}{\hat{v}_z(\varphi)} \right] \quad (24)$$

$$h_2(\varphi) = F(\varphi)(\mu - \varphi - \pi/2) \quad (25)$$

Equations (24) and (25) are the essential relations of the inverse solution. If h_1 and h_2 are determined, then h is known and the complete mapping of the cascade profile into the circle is known. Equation (24) gives h_1 as a function of the circle central angle φ . Since $h = h_1 + ih_2$, it follows that h_2 is the harmonic conjugate of h_1 . Therefore, h_2 can be found by one of the methods of harmonic synthesis, such as the one given in reference 11. When h_2 has been found as a function of φ , then μ is known as a function of φ from equation (25), and hence as a function of l .

Since $dx/dl = \cos \mu$ and $dy/dl = \sin \mu$ on the perimeter of the blade,

$$\left. \begin{aligned} x - x_{te,P} &= \int_{l_{te,P}}^l \cos \mu \, dl \\ y - y_{te,P} &= \int_{l_{te,P}}^l \sin \mu \, dl \end{aligned} \right\} \quad (26a)$$

or, more conveniently,

$$\left. \begin{aligned} x - x_{te,P} &= \int_{\varphi_{te,P}}^{\varphi} \frac{v_{\xi}(\varphi)}{\hat{v}_z(\varphi)} \cos \mu \, d\varphi \\ y - y_{te,P} &= \int_{\varphi_{te,P}}^{\varphi} \frac{v_{\xi}(\varphi)}{\hat{v}_z(\varphi)} \sin \mu \, d\varphi \end{aligned} \right\} \quad (26b)$$

Equation (26a) or (26b) gives the coordinates of the cascade blade and completes the solution, except for the case in which the cascade blades fail to close.

Equation (16) leads to the following conditions, necessary and sufficient for closure of the blades:

$$\int_{\varphi_{te,P}}^{\varphi_{te,S}} h_1(\varphi) d\varphi = \int_{\varphi_{te,P}}^{\varphi_{te,S}} h_1(\varphi) \sin \varphi \, d\varphi = \int_{\varphi_{te,P}}^{\varphi_{te,S}} h_1(\varphi) \cos \varphi \, d\varphi = 0 \quad (27)$$

For an arbitrary velocity distribution this condition will not, in general, be satisfied. Suppose

$$\left. \begin{aligned} \int_{\varphi_{te,P}}^{\varphi_{te,s}} h_1(\varphi) d\varphi &= C_1 \\ \int_{\varphi_{te,P}}^{\varphi_{te,s}} h_1(\varphi) \cos \varphi d\varphi &= C_2 \\ \int_{\varphi_{te,P}}^{\varphi_{te,s}} h_1(\varphi) \sin \varphi d\varphi &= C_3 \end{aligned} \right\} \quad (28)$$

Form a function $f(\varphi)$ such that

$$\left. \begin{aligned} \int_{\varphi_{te,P}}^{\varphi_{te,s}} f(\varphi) d\varphi &= -C_1 \\ \int_{\varphi_{te,P}}^{\varphi_{te,s}} f(\varphi) \cos \varphi d\varphi &= -C_2 \\ \int_{\varphi_{te,P}}^{\varphi_{te,s}} f(\varphi) \sin \varphi d\varphi &= -C_3 \end{aligned} \right\} \quad (29)$$

From equations (28) and (29), it is seen that $h_1^*(\varphi) = h_1(\varphi) + f(\varphi)$ will satisfy the closure conditions. It should be noted that the conditions on $f(\varphi)$ are not severe and that the designer has considerable freedom in the selection. In particular, the velocity distribution on the suction surface can generally be maintained by a proper choice of $f(\varphi)$.

The changes caused by a change in $h_1(\varphi)$ require some consideration. From equation (24) it is seen that a change in $h_1(\varphi)$ causes a change in $\hat{v}_z(\varphi)$. That is, when considered as a function of the central circle angle, the cascade velocity has changed from $\hat{v}_z(\varphi)$ to some function $\hat{v}_z^*(\varphi)$. The function $\hat{v}_z^*(\varphi)$ is given by equation (24) as follows:

$$h_1^*(\varphi) = F(\varphi) \log_e \left[\frac{\pi e^K}{sF(\varphi)} \frac{v_\zeta(\varphi)}{\hat{v}_z^*(\varphi)} \right] \quad (30)$$

Subtracting equation (30) from equation (24) and solving for $\hat{v}_z^*(\varphi)$ gives

$$\hat{v}_z^*(\varphi) = \hat{v}_z(\varphi) e^{-f(\varphi)/F(\varphi)} \quad (31)$$

In the case of the blades that failed to close, $l(\varphi)$ was a function of φ such that

$$v_z(l) = v_z(l(\varphi)) = \hat{v}_z(\varphi) \quad (32)$$

Similarly, a new relation $l^*(\varphi)$ must be found such that

$$v_z^*(l^*) = v_z^*(l^*(\varphi)) = \hat{v}_z^*(\varphi) \quad (33)$$

Combining equations (32) and (33) and substituting from equation (31) yield

$$\frac{v_z(l)}{v_z^*(l^*)} = \frac{\hat{v}_z(\varphi)}{\hat{v}_z^*(\varphi)} = e^{f(\varphi)/F(\varphi)} \quad (34)$$

It follows from equation (18) that

$$v_z(l) = v_\xi(\varphi) \frac{d\varphi}{dl} \quad (35)$$

Therefore, $l^*(\varphi)$ must be a function which satisfies the relation

$$v_z^*(l^*) = v_\xi(\varphi) \frac{d\varphi}{dl^*} \quad (36)$$

if the flow in the circle plane is to remain unaltered. Combining equations (35) and (36) and substituting from equation (34) give

$$dl^* = \frac{v_z(l)}{v_z^*(l^*)} \frac{dl}{d\varphi} d\varphi = e^{f(\varphi)/F(\varphi)} \frac{dl}{d\varphi} d\varphi$$

or

$$l^* - l_{te,P}^* = \int_{\varphi_{te,P}}^{\varphi} e^{f(\varphi)/F(\varphi)} \frac{dl}{d\varphi} d\varphi \quad (37)$$

These equations show the changes arising in the cascade velocity distribution as a result of changing $h_1(\varphi)$ to satisfy closure.

An outline for the general procedure to be used in applying the method follows:

- (1) Prescribe a velocity distribution as a function of arc length about a cascade blade.
- (2) Prescribe v_1 , v_2 , β_1 , and β_2 .
- (3) Determine v_m , β_m , s , Γ , and K from equations (6) to (12) and appendix A.
- (4) Determine $\Phi_Z(l)$ from equation (20).
- (5) Determine $\Phi_\zeta(\varphi)$ as the real part of equation (5) plus an additive constant.
- (6) Choose the arbitrary constant in equation (5) such that $\Phi_Z(l_{te,P}) = \Phi_\zeta(\varphi_{te,P})$, and equate the potential functions yielding a relation $l = l(\varphi)$.
- (7) Find $\hat{v}_Z(\varphi)$ and, with $v_\zeta(\varphi)$, solve equation (24) for $h_1(\varphi)$. Check for closure and make the necessary changes.
- (8) By the method of reference 11, or some related method, find $h_2(\varphi)$ as the harmonic conjugate of $h_1(\varphi)$.
- (9) Solve equation (25) for μ as a function of φ .
- (10) Find the blade coordinates from equation (26b).

Appendix A can be used to analyze the resulting blade shape at all angles of incidence. A prescribed velocity distribution, the velocity distribution corrected to ensure closure, and the resulting blade shape are shown in figure 7 (from ref. 40).

Compressibility Considerations

Both the direct and inverse problems for low-solidity cascades have been discussed only for an incompressible fluid. The equations governing an incompressible two-dimensional flow are simple in form and, as has been shown, can be solved by complex-function theory. When the fluid density is permitted to vary, the ordinary formulations of the flow equations become nonlinear and very much more difficult to solve.

In high-solidity cascades, where a channel treatment is possible, the finite-difference techniques can be used. The relaxation method of Southwell (refs. 42 to 44) has been used to solve many difficult differential equations. Since the advent of high-speed digital computing machinery, the direct solution of a large number of simultaneous linear equations in a reasonable period of time has become feasible. Thus, a complicated differential equation can be represented over the flow domain by a set of linear finite-difference equations, which can be solved either by the relaxation method (usually done on a desk computing machine) or by a direct matrix solution on high-speed computing equipment.

In high-solidity cascades the physical boundaries of the flow favor a solution of the compressible-flow equations by finite-difference techniques. In the low-solidity cascades, however, the guidance exerted by the blades is less pronounced, and the proper satisfaction of boundary conditions is more difficult. Hence, for low-solidity cascades the problem of obtaining compressible-flow solutions still exists, at least for the direct problem. (A solution for compressible flow with a linear pressure-volume relation has been obtained for the inverse problem and is discussed later in this section.) In general engineering practice, two methods of attacking this problem are currently being used, the hodograph method and the small-perturbation method. These two important theories will be discussed in this section, where the following notation is used: v is the magnitude of velocity in an incompressible-flow field, and q is the magnitude of velocity in a compressible-flow field.

Hodograph method. - Although the equations relating the stream and potential functions of a two-dimensional compressible flow of an ideal fluid are, in general, nonlinear, they can be rewritten in terms of a new set of independent variables such that the equations become linear. This result was discussed extensively by Chaplygin (ref. 45) in 1902. For many years thereafter very little was done in this direction, probably because of the adequacy of the incompressible-flow solutions for interpreting low-speed flows. However, in more recent years it has become necessary to consider the effects of density variation in many applications. Under this impetus, the hodograph theory (investigation of flow in the velocity plane) has been advanced considerably and is still expanding. The essential advantage of the hodograph method is the linearization of the equations relating the stream and potential functions by a proper choice of independent variables. An important disadvantage is the difficulty in establishing boundary conditions in the hodograph plane to represent a given problem in the physical plane. In spite of this major handicap, however, important use has been made of the theory.

For incompressible flow, the following relations hold:

$$\left. \begin{aligned} \frac{\partial \Phi}{\partial x} &= \frac{\partial \Psi}{\partial y} \\ \frac{\partial \Phi}{\partial y} &= - \frac{\partial \Psi}{\partial x} \end{aligned} \right\} \quad (38a)$$

Equations (38a) can be rewritten with v and β replacing x and y as the independent variables (see e.g., ref. 46), where β is the inclination of the velocity vector to the x -axis:

$$\left. \begin{aligned} \frac{\partial \Phi}{\partial \beta} &= v \frac{\partial \Psi}{\partial v} \\ \frac{\partial \Phi}{\partial v} &= - \frac{1}{v} \frac{\partial \Psi}{\partial \beta} \end{aligned} \right\} \quad (39a)$$

For compressible flow the relations corresponding to equations (38a) can be written

$$\left. \begin{aligned} \frac{\partial \Phi}{\partial x} &= \frac{\rho_a}{\rho} \frac{\partial \Psi}{\partial y} \\ \frac{\partial \Phi}{\partial y} &= - \frac{\rho_a}{\rho} \frac{\partial \Psi}{\partial x} \end{aligned} \right\} \quad (38b)$$

As in the incompressible case, equations (38b) can be written in terms of the independent variables q and β , with M as the local Mach number:

$$\left. \begin{aligned} \frac{\partial \Phi}{\partial \beta} &= \frac{\rho_a}{\rho} q \frac{\partial \Psi}{\partial q} \\ \frac{\partial \Phi}{\partial q} &= - \frac{\rho_a}{\rho} \frac{1 - M^2}{q} \frac{\partial \Psi}{\partial \beta} \end{aligned} \right\} \quad (39b)$$

Introducing the variables V and Q , defined by

$$\left. \begin{aligned} dV &= \frac{dv}{v} \\ dQ &= \sqrt{1 - M^2} \frac{dq}{q} \end{aligned} \right\} \quad (40)$$

into (39a) and (39b), respectively, yields

$$\left. \begin{aligned} \frac{\partial \Phi}{\partial \beta} &= \frac{\partial \Psi}{\partial v} \\ \frac{\partial \Phi}{\partial v} &= - \frac{\partial \Psi}{\partial \beta} \end{aligned} \right\} \quad (41)$$

and

$$\left. \begin{aligned} \frac{\partial \Phi}{\partial \beta} &= \frac{\rho_a}{\rho} \sqrt{1 - M^2} \frac{\partial \Psi}{\partial q} \\ \frac{\partial \Phi}{\partial q} &= - \frac{\rho_a}{\rho} \sqrt{1 - M^2} \frac{\partial \Psi}{\partial \beta} \end{aligned} \right\} \quad (42)$$

Equations (42) can be simplified by the following considerations:

$$\frac{\rho_a}{\rho} \sqrt{1 - M^2} = \left(1 + \frac{\gamma - 1}{2} M^2\right)^{\frac{1}{\gamma - 1}} \sqrt{1 - M^2}$$

For $\gamma = -1$, $(\rho_a/\rho)\sqrt{1 - M^2} = 1$. Although $\gamma = -1$ does not correspond to any actual fluid, this value causes the adiabatic pressure-volume relation $p(1/\rho)^\gamma = \text{constant}$ to become linear in p and $1/\rho$. When a general linear relation between pressure and volume is assumed initially, the theory shows that $(\rho_a/\rho)\sqrt{1 - M^2} = 1$ in this case, also.

Thus, a straight line can be taken to represent the pressure-volume relation instead of the usual curve. Early workers in this field (e.g., ref. 47) allowed the approximating line to be tangent to the adiabatic curve at a point corresponding to the stagnation condition $p = p_a$. This is a poor choice for high-speed flows. Von Kármán and Tsien (refs. 48 and 49) took the point of tangency to correspond to free-stream conditions, which better approximated the true curve in the region of greatest interest. With this approximation, equations (42) become

$$\left. \begin{aligned} \frac{\partial \Phi}{\partial \beta} &= \frac{\partial \Psi}{\partial q} \\ \frac{\partial \Phi}{\partial q} &= - \frac{\partial \Psi}{\partial \beta} \end{aligned} \right\} \quad (43)$$

Comparing equations (43) with equations (41) shows that a solution of the incompressible-flow equations (41) will be a solution of the quasi-compressible-flow equations (43) when the velocities are related (from eq. (40)) by

$$\frac{dv}{v} = \sqrt{1 - M^2} \frac{dq}{q} \quad (44)$$

This relation integrates (with the help of the linear pressure-volume relation) to

$$q = \frac{4a_a^2 v}{4a_a^2 - v^2} \quad (45)$$

The density ratio becomes

$$\frac{\rho_a}{\rho} = \frac{4a_a^2 + v^2}{4a_a^2 - v^2} \quad (46)$$

The pressure coefficient for the incompressible flow is given by

$$C_{P,inc} = \frac{p - p_m}{(1/2)\rho_m v_m^2} = 1 - \frac{v^2}{v_m^2} \quad (47)$$

For compressible flow

$$C_{P,C} = \frac{p - p_m}{\frac{1}{2}\rho_m q_m^2} = 2 \frac{a_m^2}{q_m^2} \left(1 - \frac{\rho_m}{\rho} \right) \quad (48)$$

The pressure coefficients are related by the equation (called the Kármán-Tsien relation)

$$C_{P,C} = \frac{C_{P,inc}}{\sqrt{1 - M_m^2} + \frac{M_m^2}{\sqrt{1 - M_m^2} + 1} \frac{C_{P,inc}}{2}} \quad (49)$$

Hence, equations (45), (46), and (49) provide a compressible-flow solution when an incompressible-flow solution is known. It is evident, however, that the two solutions will not satisfy the same boundary conditions. Applying equations (45) and (46) will yield a solution for compressible flow about a cascade of somewhat different geometry. The correlation of the two flow fields is only approximately valid.

The relations presented herein as a simple means of approximating the effects of compressibility on a known incompressible-flow field are a byproduct of the hodograph theory. The aim of the theory in its complete form, to put the direct and inverse compressible-flow problems on a substantial theoretical foundation, has been realized to a certain extent. The inverse problem for cascades has been solved in its general form with the assumption of a linear pressure-volume relation by Costello (ref. 50); Costello, Cummings, and Sinnette (ref. 51); Clauser (ref. 52); and Lin

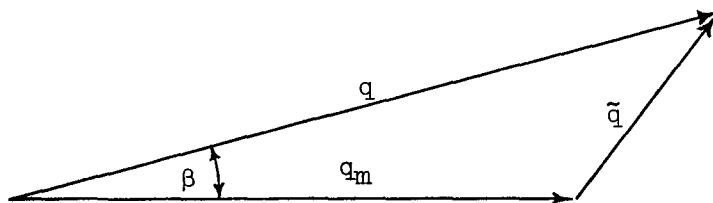
(ref. 53). These theories are based upon earlier work by von Kármán (ref. 48), Tsien (ref. 49), and Lin (ref. 54). Reference 51 offers a detailed computational procedure for the use of Costello's method.

The direct problem has not reached the same state of development. Even in the case of an incompressible-fluid flow, an iteration process is necessary. In the case of a compressible-fluid flow, a trial-and-error iteration is possible. However, no systematic process for converging to a solution in the case of compressible flow about a body of arbitrary shape has been given.

The method of appendix A for finding velocity distributions at angles of incidence other than the one of the original solution does not hold in the compressible-flow case. This fact makes the incompressible-flow solution more valuable for some investigations. For this reason, and because of the difficulty in presenting the material concisely, the compressible-flow solution for the inverse problem is not presented in detail in this chapter. The reader is referred again to references 50 and 51.

Small-perturbation method. - The equations governing the flow of a compressible fluid about a body can be linearized in the physical plane instead of the hodograph plane by making certain assumptions about the nature of the flow. These assumptions cause the equations to only approximate the actual flow. For slender bodies the approximation is generally good and the theory has proven to be useful.

Flows that differ only very little from the mean free-stream flow will be considered. The relations among the various velocity components can be seen in the following sketch. The assumption is made that second



and higher powers of \tilde{q} (disturbance velocity) or its components can be neglected and that derivatives of the disturbance-velocity components are approximately equal to the component over a characteristic length of the object in the flow field. These conditions are expressed

$$\tilde{q}^n \approx \tilde{q}_x^n \approx \tilde{q}_y^n \approx 0 \quad \text{for } n \geq 2 \quad (50)$$

$$\left. \begin{aligned} \frac{\partial \tilde{q}_x}{\partial x} &\approx \frac{\partial \tilde{q}_x}{\partial y} \approx \frac{\tilde{q}_x}{c^*} \\ \frac{\partial \tilde{q}_y}{\partial x} &\approx \frac{\partial \tilde{q}_y}{\partial y} \approx \frac{\tilde{q}_y}{c^*} \end{aligned} \right\} \quad (51)$$

where c^* is a characteristic length.

The actual velocities are related to the disturbance velocities by

$$\left. \begin{aligned} q_x &= q_m + \tilde{q}_x \\ q_y &= \tilde{q}_y \end{aligned} \right\} \quad (52)$$

Euler's equations of motion for a two-dimensional compressible steady flow with no external forces can be written

$$\left. \begin{aligned} q_x \frac{\partial q_x}{\partial x} + q_y \frac{\partial q_x}{\partial y} &= -\frac{1}{\rho} \frac{\partial p}{\partial x} = -\frac{a^2}{\rho} \frac{\partial \rho}{\partial x} \\ q_x \frac{\partial q_y}{\partial x} + q_y \frac{\partial q_y}{\partial y} &= -\frac{1}{\rho} \frac{\partial p}{\partial y} = -\frac{a^2}{\rho} \frac{\partial \rho}{\partial y} \end{aligned} \right\} \quad (53)$$

Combining equations (53), with the help of the continuity equation

$$\frac{\partial(\rho q_x)}{\partial x} + \frac{\partial(\rho q_y)}{\partial y} = 0$$

gives

$$q_x^2 \frac{\partial q_x}{\partial x} + q_x q_y \left(\frac{\partial q_x}{\partial y} + \frac{\partial q_y}{\partial x} \right) + q_y^2 \frac{\partial q_y}{\partial y} = a^2 \left(\frac{\partial q_x}{\partial x} + \frac{\partial q_y}{\partial y} \right) \quad (54)$$

By using the relations (52) and the hypotheses (50) and (51), equation (54) reduces to

$$\left(1 - \frac{q_m^2}{a^2} \right) \frac{\partial \tilde{q}_x}{\partial x} + \frac{\partial \tilde{q}_y}{\partial y} = 0 \quad (55)$$

It is shown in reference 55 that, within the hypotheses of this theory, equation (55) can be written as

$$\left(1 - M_m^2 \right) \frac{\partial \tilde{q}_x}{\partial x} + \frac{\partial \tilde{q}_y}{\partial y} = 0 \quad (56)$$

or, introducing the disturbance velocity potential,

$$(1 - M_m^2) \frac{\partial^2 \tilde{\Phi}}{\partial x^2} + \frac{\partial^2 \tilde{\Phi}}{\partial y^2} = 0 \quad (57)$$

Now consider the transformation

$$x_i = x, \quad y_i = y \sqrt{1 - M_m^2}, \quad \tilde{\Phi}_i = \Lambda \tilde{\Phi} \quad (58)$$

Applying transformation (58) to equation (57) gives

$$\frac{\partial^2 \tilde{\Phi}_i}{\partial x_i^2} + \frac{\partial^2 \tilde{\Phi}_i}{\partial y_i^2} = 0 \quad (59)$$

the Laplace equation for the disturbance potential in an incompressible flow. At affinely corresponding points (under transformation (58)) in the two planes, the following expressions relate the velocity vectors and their angles:

$$\left. \begin{aligned} \tilde{v}_{x_i} &= \frac{\partial \tilde{\Phi}_i}{\partial x_i} = \Lambda \frac{\partial \tilde{\Phi}}{\partial x} = \Lambda \tilde{q}_x \\ \tilde{v}_{y_i} &= \frac{\partial \tilde{\Phi}_i}{\partial y_i} = \Lambda \frac{\partial \tilde{\Phi}}{\partial y} \frac{\partial y}{\partial y_i} = \frac{\Lambda}{\sqrt{1 - M_m^2}} \tilde{q}_y \\ \beta_i &\approx \tan \beta_i = \frac{\tilde{v}_{y_i}}{\tilde{q}_m} = \frac{\Lambda}{\sqrt{1 - M_m^2}} \frac{\tilde{q}_y}{\tilde{q}_m} = \frac{\Lambda}{\sqrt{1 - M_m^2}} \beta \end{aligned} \right\} \quad (60)$$

From equation (60) it can be seen that, at affinely corresponding points of the flow fields, the ratio of β_i to β is constant and equal to $\Lambda / \sqrt{1 - M_m^2}$. Hence, for flow about geometrically similar boundaries, $\Lambda = \sqrt{1 - M_m^2}$ and

$$\tilde{q}_x = \frac{1}{\sqrt{1 - M_m^2}} \tilde{v}_{x_i} \quad (61)$$

It can be shown under the hypotheses of the small-perturbation theory that the pressure coefficient can be written

$$\left. \begin{aligned} C_{P,C} &= -2 \frac{\tilde{q}_x}{\tilde{q}_m} \\ C_{P,inc} &= -2 \frac{\tilde{v}_{x_i}}{\tilde{q}_m} \end{aligned} \right\} \quad (62)$$

Using equations (61) and (62) gives

$$C_{P,C} = \frac{1}{\sqrt{1 - M_m^2}} C_{P,inc} \quad (63)$$

Equation (63) is referred to as the Glauert-Prandtl compressibility correction and corresponds to equation (49) in the hodograph theory. When these equations are applied to cascades of blades, the corresponding cascades in the two flow fields will have the same blade shape but different chord angles and solidities. The relations between the cascades are given by Woolard in reference 56. Pressures predicted from equations (49) and (63) are compared with actual experimental data in reference 57.

The compressibility corrections of either the Glauert-Prandtl or Kármán-Tsien methods are quite simple in application and have yielded satisfactory results for cascades by using the local Mach number at points in the blade passage instead of the mean free-stream Mach number (ref. 58). The local Mach number is derived from a one-dimensional analysis.

HIGH-SOLIDITY CASCADES

In general, the mathematical techniques applied successfully to low-solidity-cascade problems become increasingly tedious to apply as solidities rise above 1.0. Although the methods are not out of the question for solidities greater than 1.0, difficulties may be expected for the range of solidity from 1.0 to 1.5, and above 1.5 these difficulties are apt to be excessive. The lines of demarcation are not clear but vary with individual methods and prescribed conditions other than solidity.

As was indicated previously, various mathematical techniques are available for handling the problems of closely spaced cascades. The decisive factor in the employment of the channel-flow techniques is the advance knowledge of the approximate streamline patterns, which results from the considerable guidance of the fluid by closely spaced blades. This factor is most clearly demonstrated in the stream-filament and power-series-expansion techniques.

Much of the work in the field of closely spaced blades has been done for quasi-three-dimensional flows. The formulation of the equations in a manner suitable for solution is often only slightly more difficult for flow on a general surface of revolution than for plane cascade flow. In addition to this advantage, it is generally possible to consider compressible flows.

The literature in the field has grown so quickly that priorities are not easily established. No attempt is made here to cover the many variations of method in common use for closely spaced blades. Only the fundamental approaches of a few authors have been selected as representative of the basic techniques involved.

The Direct Problem

Probably the most widely used channel-flow technique is the stream-filament method (e.g., ref. 59). A simplification by Huppert and MacGregor (ref. 60), based on an assumed linear variation of streamline curvature, is presented in some detail in this section. The method is simple in theory and application, and solutions are obtained quickly. The major drawback is the failure of the method to provide accurate results in the immediate regions of the leading and trailing edges. In reference 60 results are obtained for a solidity as low as 1.42.

A rapid approximate solution is given by Stanitz and Prian in reference 61. The method is based on the principle of zero absolute circulation, with linear variation of velocity and velocity angle assumed in the direction of the y-axis. Results are obtained only on the blade surfaces and not throughout the channel. Although this method has definite limitations, it has been used successfully at the NACA Lewis laboratory. A counterpart for treating the inverse problem is discussed in some detail later in this chapter.

Another approach to an approximate solution is with a power-series expansion, as illustrated by the work of Wu and Brown (ref. 62). The same difficulty exists in solving for the leading- and trailing-edge regions as exists in the stream-filament method. The results obtained in reference 62 compare satisfactorily in the region of applicability with results obtained by a more exact procedure.

The application of relaxation and matrix solution techniques is indicated in this section, based upon considerations from another work by Wu and Brown (ref. 63). A more exact solution is obtainable by these methods than by the stream-filament or series-expansion methods. However, more time is required to obtain the more exact answers, the time element varying considerably with the type of computing equipment available. Accurate time estimates are not readily available, since experience in this field is still not great. For use of high-speed digital computing machinery, the setup time may be prohibitive unless a number of solutions is desired.

Stream-filament method. - The stream-filament technique is a natural approach to the flow problem. Briefly, the procedure is as follows: (1)

Approximate the streamline positions using empirical data or intuition; (2) find a method of systematically improving the accuracy of the streamline arrangement. It will be shown that the velocities in the flow field can be computed, based on the assumed streamlines. This information can then be used to improve the streamline positions.

For two-dimensional irrotational flow, the rate of change of velocity in a direction normal to the streamlines is given by

$$\frac{dq}{dn} = - \frac{q}{r_c} = - q \mathcal{C} \quad (64)$$

where dn is an increment in a direction normal to the streamline, r_c is the radius of curvature, and \mathcal{C} is the curvature. This equation of motion and the continuity equation are the basic relations used in this stream-filament method.

The curvature is assumed to vary linearly with respect to n across the passage (ref. 60). Then,

$$\mathcal{C} = \mathcal{C}_s + \frac{\mathcal{C}_p - \mathcal{C}_s}{n_p} n = \mathcal{C}_s + \frac{\Delta \mathcal{C}}{n_p} n \quad (65)$$

On the suction surface, n is taken as zero. Differentiating equation (65) and substituting into equation (64) give

$$\frac{dq}{q} = - \frac{n_p}{\Delta \mathcal{C}} \mathcal{C} d\mathcal{C} \quad (66)$$

Integrating equation (66) gives

$$\frac{q}{q_l} = \exp \left[- \frac{n_p}{2\Delta \mathcal{C}} (\mathcal{C}^2 - \mathcal{C}_l^2) \right] \quad (67)$$

where the subscript l denotes an arbitrary position along the potential line. From equation (67) q is known at each point along the potential line if it is known at any point l . Noting that

$$\frac{\rho}{\rho_a} = \left(1 - \frac{q^2}{2c_p T_a}\right)^{\frac{1}{\gamma-1}} \quad (68)$$

the continuity equation can be written

$$d(\Delta w) = \rho q \, dn = \rho_a q \left(1 - \frac{q^2}{2c_p T_a}\right)^{\frac{1}{\gamma-1}} dn \quad (69)$$

where Δw is the mass flow per unit time. With the substitution

$$X = \frac{q^2}{2c_p T_a} \quad (70a)$$

equation (69) becomes

$$\frac{d(\Delta w)}{n_P \rho_a \sqrt{2c_p T_a}} = \sqrt{X} (1 - X)^{\frac{1}{\gamma-1}} \frac{dn}{n_P} \quad (71)$$

Now let

$$(1 - X)^{\frac{1}{\gamma-1}} = (1 - X_L)^{\frac{1}{\gamma-1}} \left(1 - \frac{X - X_L}{1 - X_L}\right)^{\frac{1}{\gamma-1}} \quad (72)$$

where

$$X_L = \frac{q_L^2}{2c_p T_a} \quad (70b)$$

Equation (71) is the fundamental equation to be solved. A convenient technique of solution is afforded by the binomial expansion. Expanding equation (72) by the binomial series and keeping only the first two terms give

$$(1 - X)^{\frac{1}{\gamma-1}} = (1 - X_L)^{\frac{2-\gamma}{\gamma-1}} \left[1 + X_L \left(\frac{2-\gamma}{\gamma-1}\right) - \frac{X}{\gamma-1}\right] \quad (73)$$

Now let

$$f = \sqrt{X_L} (1 - X_L)^{\frac{2-\gamma}{\gamma-1}} \left[1 + X_L \left(\frac{2-\gamma}{\gamma-1}\right)\right] \quad (74)$$

and

$$g = \frac{x_l^{3/2}}{\gamma-1} (1 - x_l)^{\frac{2-\gamma}{\gamma-1}} \quad (75)$$

Using (74) and (75) in equation (73) yields

$$(1 - x)^{\frac{1}{\gamma-1}} = \frac{f}{\sqrt{x_l}} - g \frac{x}{x_l^{3/2}} \quad (76)$$

Equation (71) becomes

$$\frac{d(\Delta w)}{n_P \rho_a \sqrt{2c_p T_a}} = \left[f \sqrt{\frac{x}{x_l}} - g \left(\frac{x}{x_l} \right)^{3/2} \right] \frac{dn}{n_P} \quad (77)$$

Let

$$\hat{\mu} = \frac{1}{\rho_a n_P \sqrt{2c_p T_a}} \int_0^{(\Delta w)_P} d(\Delta w) = \frac{(\Delta w)_P}{\rho_a n_P \sqrt{2c_p T_a}} \quad (78)$$

Integrating (77) and using (70a), (70b), and (78) yield

$$\hat{\mu} = \int_0^{n_P} f \frac{q}{q_l} \frac{dn}{n_P} - \int_0^{n_P} g \left(\frac{q}{q_l} \right)^3 \frac{dn}{n_P} \quad (79)$$

Let

$$\left. \begin{aligned} J &= \int_{\mathcal{C}_S}^{\mathcal{C}_P} \exp \left[- \frac{n_P}{2\Delta\mathcal{C}} (\mathcal{C}^2 - \mathcal{C}_l^2) \right] \frac{d\mathcal{C}}{\Delta\mathcal{C}} \\ K &= \int_{\mathcal{C}_S}^{\mathcal{C}_P} \exp \left[- \frac{3n_P}{2\Delta\mathcal{C}} (\mathcal{C}^2 - \mathcal{C}_l^2) \right] \frac{d\mathcal{C}}{\Delta\mathcal{C}} \end{aligned} \right\} \quad (80)$$

Using (67) and (80), equation (79) becomes

$$\hat{\mu} = fJ - gK \quad (81)$$

or

$$f = \frac{gK}{J} + \frac{\hat{\mu}}{J} \quad (82)$$

For $\mathcal{C}_s > \mathcal{C}_p$ the integrals in (80) can be simplified by a change of variables. Using

$$k^2 = \frac{-n_p \mathcal{C}^2}{2\Delta \mathcal{C}} \quad (83)$$

equations (80) become

$$\left. \begin{aligned} J &= \frac{\exp(-k_l^2)}{\sqrt{-\frac{\Delta \mathcal{C} n_p}{2}}} \int_{k_p}^{k_s} \exp(k^2) dk \\ K &= \frac{\exp(-3k_l^2)}{\sqrt{-\frac{3\Delta \mathcal{C} n_p}{2}}} \int_{\sqrt{3}k_p}^{\sqrt{3}k_s} \exp(3k^2) d\sqrt{3}k \end{aligned} \right\} \quad (84)$$

The values of k_s and k_p are fixed by the channel geometry, and $\int_0^x \exp(x^2) dx$ is available in standard tables.

It is clear at this point that the velocities at each location on a potential line are known when a reference velocity q_l is known (see eq. (67)). The value of q_l is conveniently taken at the point of average streamline curvature so that $X - X_l$ in the binomial expansion previously used is small. In equation (81) the quantities $\hat{\mu}$, J , and K are known from the mass-flow requirements and passage geometry, and f and g are functions of X_l alone for fixed values of γ . As shown in figure 8, f can be plotted against $\sqrt{X_l}$ and hence against g . In order to satisfy equation (82), f and g satisfy a straight-line relation with slope K/J and an f intercept of $\hat{\mu}/J$. This line is shown in figure 8. The intercept of this straight line with the curve for f against g yields the proper value of X_l , and hence q_l . All other velocities are now obtainable from equation (67).

An outline for the procedure to be used follows:

(1) Given a cascade as shown in figure 9, with upstream velocity prescribed, draw in upstream and downstream streamlines, continuing the blade channel. Draw in an orthogonal net of approximate streamlines and potential lines.

(2) Compute velocities at each node of the flow net. Since the streamlines AA', B'B, CC', and D'D are only approximate, good accuracy can be expected only in the region MNPQ of figure 9.

(3) Obtain the potential distribution along each streamline as a function of arc length l by integrating the velocity with respect to arc length. These values will be used in drawing new potential lines.

(4) New values of stream function are obtained by integrating pq along the potential lines. These values are used in drawing new streamlines.

(5) An adjusted grid of potential lines and streamlines is drawn and new velocities are computed. The iteration is continued until convergence is obtained.

A solution obtained by this method in reference 60 for a turbine cascade is illustrated in figure 10. The solidity is 1.4 in the computed example. It must be noted, however, that solidity is not the only consideration for determining the applicability of the method. Blade thickness and stagger angle combine with solidity to determine the effective channel formed by adjacent blades. To apply the method successfully, it is necessary that a significant portion of the blade surface form part of the effective channel. In compressor designs this is often not the case, and care must be used in determining the applicability of the method.

Techniques are available to increase the region of validity of the stream-filament results. A solution can be obtained for two adjacent channels formed by three blades. The stagnation streamline attached to the center blade must be congruent to the other stagnation streamlines in the final result. This serves as a check on the assumed stagnation streamlines outside the blade region. An alternate check can be made on the validity of these assumed streamlines by integrating the velocity about a closed path in the region exterior to the blades and setting it equal to zero. Either of these techniques might require more accuracy than is obtainable by assuming a linear variation of curvature. If the actual measured curvatures are used, the additional work involved may be prohibitive.

Relaxation and matrix solutions. - The technique presented herein is from reference 63. The basic differential equation is developed briefly, and the method of solving it is discussed in some detail.

The equation of continuity for a two-dimensional steady compressible flow is written

$$\frac{\partial(\rho q_x)}{\partial x} + \frac{\partial(\rho q_y)}{\partial y} = 0 \quad (85)$$

Equation (85) will be satisfied if a stream function exists such that

$$\left. \begin{aligned} \frac{\partial \Psi}{\partial x} &= -\rho q_y \\ \frac{\partial \Psi}{\partial y} &= \rho q_x \end{aligned} \right\} \quad (86)$$

The equation arising from the condition of irrotational motion is given by

$$\frac{\partial q_x}{\partial y} - \frac{\partial q_y}{\partial x} = 0 \quad (87)$$

Using equations (86) in equation (87) gives

$$\frac{\partial^2 \Psi}{\partial x^2} + \frac{\partial^2 \Psi}{\partial y^2} - \frac{1}{\rho} \left(\frac{\partial \rho}{\partial x} \frac{\partial \Psi}{\partial x} + \frac{\partial \rho}{\partial y} \frac{\partial \Psi}{\partial y} \right) = 0 \quad (88)$$

Then, letting

$$B = \frac{-1}{\rho} \left(\frac{\partial \rho}{\partial x} \frac{\partial \Psi}{\partial x} + \frac{\partial \rho}{\partial y} \frac{\partial \Psi}{\partial y} \right) \quad (89)$$

equation (88) becomes

$$\frac{\partial^2 \Psi}{\partial x^2} + \frac{\partial^2 \Psi}{\partial y^2} + B = 0 \quad (90)$$

Equation (90) is a nonlinear equation. If B were a known function of x and y , the equation would be linear. In the process of solution to be described herein, B will be treated as a known function of x and y in the first approximation. Then B will be adjusted from the results of the first approximate solution and will be held fixed while a second approximate solution is obtained, and so forth. That is, if a Ψ distribution is known, B can be computed at each point in the field from this distribution. Then B will be held fixed at this set of values while new values of Ψ are computed from equation (90). Then B will be recalculated on the basis of the new Ψ values.

Equation (90) is the basic equation of the present analysis. There are two steps to the solution of this equation: (1) to replace the differential equation with a finite-difference equation, and (2) to solve the finite-difference equation at a representative set of points in the flow field.

Suppose a function $y = f(x)$ is known at $n + 1$ values of x : x_0, x_1, \dots, x_n . It is assumed that $y = f(x)$ can be represented closely by a polynomial of degree n passing through the known points $(x_0, y_0), (x_1, y_1), \dots, (x_n, y_n)$. Such a polynomial P is given by (see ref. 64)

$$\begin{aligned}
 P_n(x) = & \frac{(x-x_1)(x-x_2) \dots (x-x_n)}{(x_0-x_1)(x_0-x_2) \dots (x_0-x_n)} y_0 + \\
 & \frac{(x-x_0)(x-x_2) \dots (x-x_n)}{(x_1-x_0)(x_1-x_2) \dots (x_1-x_n)} y_1 + \dots + \\
 & \frac{(x-x_0)(x-x_1) \dots (x-x_{n-1})}{(x_n-x_0)(x_n-x_1) \dots (x_n-x_{n-1})} y_n
 \end{aligned} \tag{91}$$

It is easily verified that this polynomial does pass through the required points. Furthermore, it is the only one that does, since $n + 1$ points define an n^{th} degree polynomial uniquely. The polynomial $P_n(x)$ can be differentiated successively, the m^{th} derivative being written

$$P_n^m(x) = A_0 y_0 + A_1 y_1 + \dots + A_n y_n \tag{92}$$

where the coefficients A_0, \dots, A_n are seen to be functions of the order of the derivative, the degree of the polynomial representing the function, and the point at which the derivative is evaluated. Equations (91) and (92) are considerably simplified when the derivative is evaluated at one of the points x_0, x_1, \dots, x_n . They are further simplified when the intervals $x_i - x_{i-1}$ are equal for $i = 1, \dots, n$. The coefficients A_i are available in a table in reference 65 for derivatives up to the fourth order and for spacings such that the last interval on either end differs in length from the other intervals. (The tables for unequal intervals are very useful for writing the difference equations at curved boundaries where such unequal spacings do occur.) Polynomial representations up to the fourth degree are included, and an error term is given.

If it is assumed that the function y can be represented by a polynomial over a small interval, equation (90) can be replaced by a finite-difference equation. In the nomenclature of reference 65, equation (90) can be written

$$\sum_{j=0}^n \frac{2}{n} B_j^i y^j + \sum_{k=0}^n \frac{2}{n} B_k^i y^k + B^i = 0 \tag{93}$$

where B is a coefficient of Ψ corresponding to the coefficients A_n in equation (92). The presubscript 2 of B represents the order of the derivative; the presubscript n is the degree of the polynomial representing Ψ . The postsubscript 1 denotes the point at which the equation is being applied; the postsubscripts j and k indicate that the values of Ψ are taken along the x - and y -directions, respectively. To clarify this notion, a set of grid points is drawn in figure 11 in the neighborhood of a point p somewhere in the flow field. Suppose, for simplicity, that a second-degree polynomial is adequate to represent Ψ in the neighborhood of the point p . Then $n = 2$ and, following the notation of figure 11, equation (93) can be written

$${}^2B_0^1 \Psi^{j=0} + {}^2B_1^1 \Psi^{j=k=1} + {}^2B_2^1 \Psi^{j=2} + {}^2B_0^1 \Psi^{k=0} + {}^2B_2^1 \Psi^{k=2} + B^1 = 0 \quad (94)$$

In this case the form of the coefficients ${}^2B_j^1$ and ${}^2B_k^1$ is quite simple over most of the flow region. At any point in the region that is surrounded by equally spaced points, equation (94) becomes

$$\Psi^{j=0} + \Psi^{j=2} + \Psi^{k=0} + \Psi^{k=2} - 4\Psi^{j=k=1} + B^1 = 0$$

Only at the boundaries of the region where unequal spacing of the flow net occurs do the coefficients of equation (94) take different values.

Higher degree polynomial representations could be used, resulting in more terms in equation (94). For example, a fourth-degree polynomial representation would involve additional terms containing $\Psi^{k=-1}$, $\Psi^{k=3}$, $\Psi^{j=-1}$, $\Psi^{j=3}$ (fig. 11). In general, higher degree polynomials substantially improve the approximation in regions of rapidly changing conditions. Increased accuracy can also be attained by decreasing the net size and hence increasing the number of points in the flow field at which a solution is found. Near the boundaries where unequally spaced grid points occur (e.g., where $\Psi = \Psi^{k=3}$ in fig. 11), the accuracy of the approximation often becomes critical and higher degree approximations or closer spacings are needed to achieve an accuracy comparable to that in other portions of the flow field. Additional points can be added in the course of solution if the accuracy of the results appears questionable.

Suppose the entire closed boundary ABFGCDHEA in figure 12 is fixed and the values of Ψ are known along this boundary. A network of equidistant points is placed on the flow field. The mesh size is taken sufficiently small that values of Ψ found at each point of the net will suffice to give a clear picture of the entire flow field. With the net size chosen, equation (94), or more generally equation (93), is used with the coefficients from reference 65 to determine a linear equation in the unknown values of Ψ at each nonboundary point of the net. It

is clear that there will be N unknown values of Ψ if the net has N inner points (i.e., points which are not on the boundary). At each of these points a linear equation can be written involving some of the unknown values of Ψ . Thus, there is a system of N equations in N unknowns for determining the values of Ψ at each point.

Unfortunately, conditions along the entire boundary ABFGCDHEA in figure 12 are not known at the outset for a given cascade of blades and a given upstream vector velocity. The boundaries AB and CD, parallel to the y -axis, are located far enough upstream and downstream, respectively, that uniform flow across these boundaries can be reasonably expected. If it is discovered subsequently that uniform flow does not exist at these stations, they must be adjusted to positions farther removed from the blades. Two to three chord lengths from the blade edges is usually a sufficient distance. The lines AE and BF are drawn parallel to the upstream velocity vector; the lines GC and HD are drawn parallel to the downstream velocity vector. Satisfaction of the trailing-edge condition (Kutta condition in the case of a sharp trailing edge) cannot be achieved at the outset of the problem. Initially, the downstream velocity vector is assumed. After a solution has been obtained, the downstream flow angle can be adjusted to satisfy the trailing-edge condition and a second solution can be obtained.

With the geometry of the boundaries now fixed, the values of Ψ along these boundaries are considered. The stream function Ψ is constant along the blade surfaces, since these boundaries are streamlines in the flow. The value on the suction surface can be taken as zero, and the value on the pressure surface can be found from the required mass flow

$$\Psi_P - \Psi_S = \int_{y_S}^{y_P} \frac{\partial \Psi}{\partial y} dy = \int_{y_S}^{y_P} \rho q_x dy = \text{mass flow}$$

Outside the blade channel the boundaries are not streamlines, and the values of Ψ on these boundaries are neither constant nor known. However, since the flow is periodic in the direction of the y -axis (with period equal to the spacing of the blades), the values of Ψ need not be known. For example, consider the point at which $\Psi = \Psi_a$ in figure 12. Normally the boundary value Ψ_b would enter into the finite-difference expression about Ψ_a , but in this case Ψ_b is not known. Instead, the finite-difference expression about Ψ_a is written in terms of Ψ_c . Furthermore, $\Psi_c = \Psi_1 + (\Psi_P - \Psi_S)$ because of the periodic nature of the flow. In this way the finite-difference expression about Ψ_a contains only values of Ψ at inner points. Thus, Ψ values have been determined everywhere except on the vertical boundaries.

To write the finite-difference expression about the point where $\Psi = \Psi_q$ in figure 12, the value of Ψ_t would normally be used. However,

~~CONFIDENTIAL~~

this value does not need to be known explicitly, since the following relation results from the linearity of Ψ :

$$\Psi_t = \Psi_r = \frac{2\delta_y - \delta_x \tan \beta_1}{2\delta_y} \Psi_q + \frac{\delta_x \tan \beta_1}{2\delta_y} \Psi_l$$

Since Ψ_q and Ψ_l are unknown values of Ψ at two inner points of the field, the finite-difference expression involving them is satisfactory for this solution. The same type of relation can be used at the downstream boundary.

A second method to satisfy these vertical boundary conditions is presented in reference 63. Although the second method is not as simple and accurate as the first, it has the advantage of not directly involving the inlet angle in the expressions for the boundary conditions. This characteristic is useful if the problem is being solved by matrices, for in that case other angles of inflow can be investigated with much less effort. This method will not be discussed further but can be found in detail in reference 63.

Suppose now that there are N inner grid points in the grid selected for the problem. Applying equation (90) to each point yields N simultaneous linear equations in N unknowns. (The B^i are not known and must be given an assumed value.) Now the problem is one of solving this set of simultaneous equations, by either a relaxation process (indirect) or a matrix process (direct). The latter process is too lengthy for hand computation when a reasonable number of grid points is used. Both methods are discussed in detail in references 65 and 66 and are indicated briefly in appendixes C and D, respectively.

When the values of Ψ have been obtained at each interior point by some process, the nonlinear term B in equation (90) must be recalculated on the basis of these Ψ values. A second solution is then carried out. With the relaxation technique, it may be advantageous to recalculate the B^i in the middle of a cycle if the changes in Ψ have been large. This is, of course, not possible in a matrix solution. In either case, the initial Ψ values estimated for relaxation and the B^i values estimated for matrices should be as close as possible to the final answer to obtain rapid convergence. The question of convergence has not been considered mathematically. In most examples that have been carried out so far, convergence has occurred.

Some difficulty has been encountered at the Lewis laboratory in obtaining convergence at high subsonic Mach numbers when equation (88) is used. From equation (89) it is seen that B contains first derivatives of ρ and, hence, second derivatives of Ψ . More rapid convergence could be expected if all second-derivative terms in equation (90) were to be included in the operative part of the equation rather than in the field function B . As in reference 55, equation (88) can be rewritten as

$$\frac{\partial^2 \Psi}{\partial x^2} \left[1 - \left(\frac{\rho_a}{\rho_a} \frac{\partial \Psi}{\partial y} \right)^2 \right] + \frac{\partial^2 \Psi}{\partial y^2} \left[1 - \left(\frac{\rho_a}{\rho_a} \frac{\partial \Psi}{\partial x} \right)^2 \right] + 2 \left(\frac{\rho_a}{\rho_a} \right)^2 \frac{\partial^2 \Psi}{\partial x \partial y} \frac{\partial \Psi}{\partial x} \frac{\partial \Psi}{\partial y} = 0 \quad (95)$$

where $(\rho_a/\rho_a)^2$ is a function of q and hence of $(\partial \Psi/\partial x)^2 + (\partial \Psi/\partial y)^2$. Equation (95) is linearized by writing

$$A \frac{\partial^2 \Psi}{\partial x^2} + B \frac{\partial^2 \Psi}{\partial y^2} + C \frac{\partial^2 \Psi}{\partial x \partial y} = 0 \quad (96)$$

where

$$A = 1 - \left(\frac{\rho_a}{\rho_a} \frac{\partial \Psi}{\partial y} \right)^2$$

$$B = 1 - \left(\frac{\rho_a}{\rho_a} \frac{\partial \Psi}{\partial x} \right)^2$$

$$C = 2 \frac{\partial \Psi}{\partial x} \frac{\partial \Psi}{\partial y} \left(\frac{\rho_a}{\rho_a} \right)^2$$

The coefficients A , B , and C are field functions (corresponding to B in eq. (90)) containing only first derivatives of Ψ . A complication is thus introduced into the coefficients of the finite-difference expressions, but convergence is expected to be more rapid.

The results of an example computed in reference 63 by the relaxation process and equation (89) for a turbine cascade are reproduced in figure 13. The method is easily adapted to a general surface of revolution (see ref. 63).

The Inverse Problem

Since the physical boundaries of the flow channel (i.e., the blade surfaces) are not known for the inverse problem, the relaxation and matrix solutions have not been used in the physical plane. A method has been developed, however, by Stanitz (ref. 67) and by Stanitz and Sheldrake (ref. 68) to solve the equations governing the fluid motion when the stream and potential functions replace the Cartesian coordinates as independent variables. Relaxation and matrix techniques can be employed in this $\Phi\Psi$ -plane.

Some simpler approximate techniques are available. Akeret (ref. 69) replaced the cascade of closely spaced blades by a continuous distribution of vortices and sources, periodic in the direction of the y-axis. This infinite strip of singularities yields an approximate velocity distribution and approximate thickness. A blade shape is then computed. The method is iterative in nature but does not require as much time as the exact solutions. Sawyer employed this method to design a cascade (ref. 70) for testing purposes. The time required for the complete theoretical solution was approximately 40 hours.

In reference 71, Alpert developed a method for designing a channel when the shape of one wall is known and a velocity distribution is prescribed on that wall. Although this appears to overprescribe the problem, the author necessarily uses only a finite number of points in actually obtaining a solution. A solution progresses from one streamline to the next, away from the known wall. The method is easily and rapidly carried out with the aid of tables the author has prepared. An example is worked by this method, but no comparison with an exact theoretical solution is made.

The method of expansion by power series is presented by Wu and Brown in reference 62 for the inverse problem as well as the direct problem. The same limitations to the method apply as those discussed previously for the direct problem.

A rapid approximate method is presented by Stanitz in reference 72. The assumptions made in the method are realized to a sufficient degree in a closely spaced cascade, but the nose and tail sections cannot be included in the design. A comparison of the results obtained by the author with stream-filament solutions showed good agreement. It should be pointed out, however, that the method is essentially limited to angles of incidence such that the mean streamlines enter the blade channel with curvatures close to the mean blade curvature. This approximate design method, which enables a practical and rapid solution, is presented in some detail in the following section. The exact solution by relaxation in the Φ -plane (refs. 67 and 68) is also presented.

Approximate method. - The design method to be presented (ref. 72) is not applicable in the immediate regions of the leading and trailing edges of the cascade blade, where the small radii of curvature of the blade sections invalidate the assumptions made in the method. When a pressure distribution is prescribed on the channel surfaces as a function of dimensionless distance \hat{x} along the x-axis¹, along with the upstream and downstream vector velocities, the solution will yield the channel shape in the region of validity.

¹All linear quantities are considered to be made dimensionless by division by \bar{x} , where \bar{x} is the axial length of the assumed region of validity of the solution.

Two important assumptions are made underlying the use of the method. At a given value of \hat{x} , it is assumed that (1) the mass-weight average flow direction is the same as the direction of the blade-element camber line, and (2) the mass-weight average velocity is equal to one-half the sum of the velocities prescribed on the suction and pressure surfaces.

The solidity σ can be defined as

$$\sigma = \frac{1}{\hat{s}} \quad (97)$$

Then the thickness ratio \hat{v} is defined as

$$\hat{v} = \frac{\hat{b}}{\hat{s}} \quad (98)$$

The blade-element profile is determined from σ and from \hat{v} and β as functions of \hat{x} . The method of this section is concerned with a determination of these quantities.

Consider an elemental strip of axial depth $d\hat{x}$. The tangential force on the strip of fluid can be equated to the rate of change in momentum in the tangential direction as follows:

$$\bar{x}(p_P - p_S)d\hat{x} = \Delta w dq_y \quad (99)$$

where Δw is the rate of mass flow in the channel formed by the two adjacent blades. Equation (99) can be written as

$$(p_P - p_S)d\hat{x} = \hat{s} \left(\frac{\Delta w}{\hat{x}\hat{s}} \right) dq_y \quad (100)$$

where $\Delta w/\hat{x}\hat{s}$ is the average rate of mass flow per unit area of the cascade channel. Then, from equations (97) and (100), it follows that

$$\sigma \int_{\hat{x}=0}^{\hat{x}=1} (p_P - p_S) d\hat{x} = \frac{\Delta w}{\hat{x}\hat{s}} (q_{y_2} - q_{y_1})$$

or

$$\sigma = \frac{\frac{\Delta w}{\hat{x}\hat{s}} (q_{y_2} - q_{y_1})}{\int_{\hat{x}=0}^{\hat{x}=1} (p_P - p_S) d\hat{x}} \quad (101)$$

The pressure p is determined from the prescribed velocity q and from given stagnation conditions by the equation

$$p = P \left(1 - \frac{\gamma-1}{2a_a^2} q^2 \right)^{\frac{\gamma}{\gamma-1}} \quad (102)$$

Since q_P and q_S are prescribed, p_P and p_S are calculable from equation (102), and σ is known from equation (101). With σ known, q_y can be calculated at any value of \hat{x} from

$$q_y = q_{y1} + \frac{\overline{\sigma x s}}{\Delta w} \int_{\hat{x}=0}^{\hat{x}} (p_P - p_S) d\hat{x} \quad (103)$$

The average flow angle β is given by

$$\beta = \sin^{-1} \left(\frac{q_y}{q} \right) \quad -\frac{\pi}{2} \leq \beta \leq \frac{\pi}{2} \quad (104)$$

where q is given by

$$q = \frac{q_S + q_P}{2} \quad (105)$$

Thus, from equations (101) to (105) the solidity and the β distribution are obtainable. The value \hat{v} will now be obtained from continuity considerations, whereby

$$\Delta w = \rho q (\hat{s} - \hat{b}) \bar{x} \cos \beta$$

Since $\hat{b} = \hat{v} \hat{s}$,

$$\frac{\Delta w}{\overline{x s}} = \rho q (1 - \hat{v}) \cos \beta$$

and

$$\hat{v} = 1 - \frac{\Delta w}{\rho q \overline{x s} \cos \beta} \quad (106)$$

where the density is given by

$$\rho = \rho_a \left(1 - \frac{\gamma-1}{2a_a^2} q^2 \right)^{\frac{1}{\gamma-1}} \quad (107)$$

Applying the continuity requirement upstream and downstream of the cascade gives

$$\frac{\Delta w}{\bar{x}s} = \rho_1 q_1 \cos \beta_1 = \rho_2 q_2 \cos \beta_2 \quad (108)$$

This condition must be satisfied by the prescribed quantities q_1 , q_2 , β_1 , and β_2 .

Following is a step-by-step procedure for solving a given problem:

(1) Prescribe the quantities q_1 , q_2 , β_1 , and β_2 so that equation (108) is satisfied.

(2) Prescribe q_s and q_p as functions of \hat{x} .

(3) Find $\Delta w / \bar{x}s$ from equation (108).

(4) Find p_p and p_s as functions of \hat{x} from equation (102).

(5) Find σ from equation (101).

(6) Find q_y from equation (103).

(7) Find q from equation (105).

(8) Find β from equation (104).

(9) Find \hat{v} from equation (106).

(10) Compute the equation of the blade mean camber line from

$$\hat{y} = \int_0^{\hat{x}} \frac{q_y}{q \cos \beta} d\hat{x} = \int_0^{\hat{x}} \tan \beta d\hat{x}$$

(11) Distribute the blade thickness \hat{b} symmetrically about the mean camber line.

(12) Fair in a leading- and trailing-edge section.

The preceding method is given in reference 72 in a form applicable to a general surface of revolution as well as to a plane cascade. Figure 14 shows the prescribed velocity distribution for a plane cascade computation (ref. 72) along with a stream-filament analysis of the final blade shape obtained.

Exact method. - As mentioned previously, the difficulty in applying the matrix and relaxation techniques for solving differential equations

to the design problem arises from the fact that the physical boundaries are not known. In a paper by Stanitz (ref. 67), the equations governing the motion of the fluid are written in terms of the $\Phi\Psi$ -coordinates, for in these coordinates the boundary location is known. The assumptions made in this solution are that the flow is nonviscous, two-dimensional, and irrotational. The problem of designing an infinite channel will be treated first, and this problem will then be adapted to cascade design.

At each point in the channel, the velocity has a magnitude q and a direction β with the positive x -axis.

From the condition of continuity, a stream function Ψ can be defined such that

$$d\Psi = \rho q \, dn \quad (109)$$

Similarly, from the condition of irrotationality, a potential function Φ can be defined such that

$$d\Phi = q \, dl \quad (110)$$

where dl is an increment taken along a streamline and dn is an increment in a direction normal to the streamline. It is clear from equations (109) and (110) that Ψ is constant along a streamline and Φ is constant along a line normal to the streamlines (potential line). The channel boundaries in the physical plane (xy -plane) are streamlines in the flow. Hence, these lines will become constant values of Ψ in the transformed $\Phi\Psi$ -plane (i.e., the curved channel in the xy -plane will become an infinite strip in the $\Phi\Psi$ -plane). Furthermore, the distribution of velocity as a function of Φ along the boundaries is known, since the velocity

$$q = q(l) \quad (111)$$

is prescribed as a function of arc length in the physical plane; therefore equation (110) integrates to give

$$\Phi = \Phi(l) \quad (112)$$

From equations (111) and (112),

$$q = f(\Phi) \quad (113)$$

Thus, the boundary conditions in the transformed plane are known, and only the equations governing the flow in the transformed plane are needed to complete the setup of the problem.

The continuity and irrotationality equations in the $\Phi\Psi$ -plane are developed in reference 67 and are, respectively,

$$\frac{1}{\rho} \left(\frac{\partial \log \rho}{\partial \Phi} + \frac{\partial \log q}{\partial \Phi} \right) + \frac{\partial \beta}{\partial \Psi} = 0 \quad (114)$$

$$\rho \frac{\partial \log q}{\partial \Psi} - \frac{\partial \beta}{\partial \Phi} = 0 \quad (115)$$

Differentiating equations (114) and (115) with respect to Φ and Ψ , respectively, and combining to eliminate $\partial^2 \beta / \partial \Phi \partial \Psi$ yield

$$\begin{aligned} \frac{\partial^2 \log \rho}{\partial \Phi^2} + \frac{\partial^2 \log q}{\partial \Phi^2} - \frac{\partial \log \rho}{\partial \Phi} \left(\frac{\partial \log \rho}{\partial \Phi} + \frac{\partial \log q}{\partial \Phi} \right) + \\ \rho^2 \frac{\partial \log q}{\partial \Psi} \frac{\partial \log \rho}{\partial \Psi} + \rho^2 \frac{\partial^2 \log q}{\partial \Psi^2} = 0 \end{aligned} \quad (116)$$

This equation, together with the relation (107) between velocity and density, determines the distribution of $\log q$ in the $\Phi\Psi$ -plane. Equation (116) can be solved by relaxation methods (appendix C) or matrix methods (appendix D). When the distribution of $\log q$ has been found throughout the channel for a given distribution of q along the boundaries, the distribution of β can be found along each streamline (constant Ψ) by integrating equation (115):

$$\beta = \int_{\Psi} \rho \frac{\partial \log q}{\partial \Psi} d\Phi \quad (117)$$

The distribution of β can be found along each potential line from equation (114):

$$\beta = - \int_{\Phi} \frac{1}{\rho} \left(\frac{\partial \log \rho}{\partial \Phi} + \frac{\partial \log q}{\partial \Phi} \right) d\Psi \quad (118)$$

At each point in the xy -plane,

$$\left. \begin{aligned} dx &= dl \cos \beta \\ dy &= dl \sin \beta \end{aligned} \right\} \quad (119)$$

Using equations (119) with equations (109) and (110) gives

$$\left. \begin{aligned} x &= \int_{\Psi} \frac{\cos \beta}{q} d\Phi \\ x &= - \int_{\Phi} \frac{\sin \beta}{\rho q} d\Psi \\ y &= \int_{\Psi} \frac{\sin \beta}{q} d\Phi \\ y &= \int_{\Phi} \frac{\cos \beta}{\rho q} d\Psi \end{aligned} \right\} \quad (120)$$

Equations (120) give the relation between a point (x,y) in the physical plane and a point (Φ, Ψ) in the transformed plane. In this fashion, the shape of the physical channel that produces the prescribed velocity distribution is found.

This method is adapted in reference 67 to a flow governed by a linear pressure-volume relation. Solutions of two problems, having the same prescribed boundary conditions, are compared for a compressible flow and a linearized compressible flow. The resulting channels are quite similar. Under the assumption of a linearized compressible flow, the following equation for the turning angle is given:

$$\Delta\beta = - \frac{1}{\Delta\Psi} \int_{-\infty}^{\infty} \Phi \left\{ \left[\frac{\partial \log_e \left(\frac{q}{1 + \sqrt{1+q^2}} \right)}{\partial \Phi} \right]_{\Delta\Psi} - \left[\frac{\partial \log_e \left(\frac{q}{1 + \sqrt{1+q^2}} \right)}{\partial \Phi} \right]_0 \right\} d\Phi \quad (121)$$

where the subscripts $\Delta\Psi$ and 0 refer to the channel boundaries. In the cascade design problem, equation (121) enables the designer to prescribe a velocity distribution that is consistent with the prescribed turning angle.

In figure 15 a cascade is shown with the stagnation streamline drawn in. The cascade can be formed by the "islands" between adjacent channels. The cascade design problem then becomes a problem in channel design. The channel design method considered in the preceding paragraphs does not allow zero velocities on the channel surfaces. This results in cusps on the leading and trailing edges of the islands, which must be rounded off to form a blade.

In applying the channel design method to a cascade design, it is necessary to determine the position of the leading and trailing edges on both suction and pressure surfaces in the $\Phi\Psi$ -plane. From figure 15 it is seen that

$$\Phi_C - \Phi_A = \Phi_D - \Phi_B$$

from which

$$\Phi_D - \Phi_C = \Phi_B - \Phi_A \quad (122)$$

But conditions are uniform far upstream, so that

$$\Phi_B - \Phi_A = \frac{\Delta\Psi \tan \beta_1}{\rho_1} = \Phi_D - \Phi_C \quad (123)$$

where $\Delta\Psi$ is the change in Ψ from one channel surface to the other. Similarly (see fig. 15),

$$\Phi_F - \Phi_E = \frac{\Delta\Psi \tan \beta_2}{\rho_2} = \Phi_H - \Phi_G \quad (124)$$

Equations (123) and (124) determine the relative positions on the boundaries in the $\Phi\Psi$ -plane that correspond to the leading and trailing edges of the blade, respectively.

The design procedure for a cascade of blades can now be formulated. A linear pressure-volume relation is assumed so that equation (121) can be used:

- (1) Prescribe a cascade turning angle.
- (2) Prescribe a velocity distribution.
- (3) Adjust the velocity distribution so that equations (121), (123), and (124) are satisfied.
- (4) Solve the resulting channel problem by the technique described in the preceding paragraphs.

An impulse cascade with 90° turning is investigated in reference 68. The prescribed velocity distribution on the suction surface and the final cascade obtained are presented in figure 16.

ANALOG TECHNIQUES

For many years attempts have been made to establish relations between the flow of compressible fluids and other physical problems that can be solved by nonanalytic techniques. Two physical problems have no mathematical individuality if the governing equations are the same (i.e., the same except for a possible change in nomenclature). This fact is utilized in the analogs considered in the present section.

As a result of the importance of experimental technique in most analog methods, such methods cannot be satisfactorily evaluated on the basis of theoretical correctness. In fact, the theory is generally of quite a simple nature, and the real problems involved are problems of operational technique. Because of this and because of the tremendous extent of the literature in this field, no attempt is made herein to evaluate individual contributions, some of which are discussed in references 73 to 84.

This section is concerned only with compressible flow. The incompressible-flow problem, resulting as it does in a Laplace equation, is the simpler to solve directly and to analogize. The basic theory is developed for several important types of analog that have been used successfully.

Hydraulic Analog

Consider the irrotational flow of water with a free surface over a horizontal plane. Bernoulli's equation for a stream filament of this flow can be written

$$p + \frac{\rho}{2} v^2 + \rho g z = p_0 + \frac{\rho}{2} v_0^2 + \rho g z_0 \quad (125)$$

The subscript 0 refers to conditions at a given point through which the filament passes, g is the acceleration due to gravity, and z is the coordinate in the vertical direction. If the flow emanates from a tank of sufficiently large volume, the velocity in the tank can be considered zero. Then, if the reference point is taken in the tank, equation (125) becomes

$$p + \frac{\rho}{2} v^2 + \rho g z = P + \rho g z_0$$

or

$$v^2 = \frac{2}{\rho} (P - p) + 2g(z_0 - z) \quad (126)$$

A simplifying assumption is now made that the acceleration in the vertical direction at any point is negligible when compared with the acceleration due to gravity. This assumption (not always sufficiently realized, see ref. 73) leads to the relations

$$\left. \begin{aligned} P &= \rho g(D_0 - z_0) \\ p &= \rho g(D - z) \end{aligned} \right\} \quad (127)$$

where D is the height of the water surface. Using equations (127) in equation (126) yields

$$v^2 = 2g(D_0 - D) \quad (128a)$$

The maximum attainable velocity is given by

$$v_{\max} = \sqrt{2gD_0} \quad (129a)$$

Combining equations (128a) and (129a) yields

$$\left(\frac{v}{v_{\max}}\right)^2 = \frac{D_0 - D}{D_0} \quad (130a)$$

The continuity equation for this flow is

$$\frac{\partial(Dv_x)}{\partial x} + \frac{\partial(Dv_y)}{\partial y} = 0 \quad (131a)$$

The irrotationality condition is utilized as follows: From equation (128a), since the flow is essentially two-dimensional,

$$\left. \begin{aligned} \frac{\partial D}{\partial x} &= -\frac{1}{2g} \frac{\partial(v^2)}{\partial x} = -\frac{1}{g} \left(v_x \frac{\partial v_x}{\partial x} + v_y \frac{\partial v_y}{\partial x} \right) \\ \frac{\partial D}{\partial y} &= -\frac{1}{2g} \frac{\partial(v^2)}{\partial y} = -\frac{1}{g} \left(v_x \frac{\partial v_x}{\partial y} + v_y \frac{\partial v_y}{\partial y} \right) \end{aligned} \right\} \quad (132)$$

Equation (131a) is rewritten as

$$D \left(\frac{\partial v_x}{\partial x} + \frac{\partial v_y}{\partial y} \right) + v_x \frac{\partial D}{\partial x} + v_y \frac{\partial D}{\partial y} = 0 \quad (133)$$

Then, substituting equation (132) into (133) yields

$$\frac{\partial v_x}{\partial x} \left(1 - \frac{v_x^2}{gD} \right) + \frac{\partial v_y}{\partial y} \left(1 - \frac{v_y^2}{gD} \right) - \frac{v_x v_y}{gD} \left(\frac{\partial v_x}{\partial y} + \frac{\partial v_y}{\partial x} \right) = 0 \quad (134)$$

If the flow is irrotational, $\frac{\partial v_x}{\partial y} - \frac{\partial v_y}{\partial x} = 0$ and a velocity potential $\Phi(x,y)$ exists such that

$$\left. \begin{aligned} v_x &= \frac{\partial \Phi}{\partial x} \\ v_y &= \frac{\partial \Phi}{\partial y} \end{aligned} \right\} \quad (135)$$

Using equations (135) in equation (134) yields

$$\frac{\partial^2 \Phi}{\partial x^2} \left[1 - \frac{\left(\frac{\partial \Phi}{\partial x} \right)^2}{gD} \right] + \frac{\partial^2 \Phi}{\partial y^2} \left[1 - \frac{\left(\frac{\partial \Phi}{\partial y} \right)^2}{gD} \right] - 2 \frac{\partial^2 \Phi}{\partial x \partial y} \frac{\frac{\partial \Phi}{\partial x} \frac{\partial \Phi}{\partial y}}{gD} = 0 \quad (136a)$$

These are the fundamental equations governing the flow of water under the conditions specified. They will now be compared with the fundamental equations governing the two-dimensional irrotational flow of a compressible fluid. The energy equation for the fluid flow can be written as

$$q^2 = 2gc_p(T - t) \quad (128b)$$

The maximum local velocity is given by

$$q_{\max} = \sqrt{2gc_p T} \quad (129b)$$

Then,

$$\left(\frac{q}{q_{\max}} \right)^2 = \frac{T - t}{T} \quad (130b)$$

Therefore, if the velocity ratio of the gas flow is equated to the velocity ratio of the water flow, equations (130a) and (130b) yield

$$\frac{D_0 - D}{D_0} = \frac{T - t}{T}$$

or

$$\frac{D}{D_0} = \frac{t}{T} \quad (137)$$

The continuity equation for the gas flow is written

$$\frac{\partial(\rho q_x)}{\partial x} + \frac{\partial(\rho q_y)}{\partial y} = 0 \quad (131b)$$

Comparing equations (131a) and (131b) yields the further condition for the analogy that

$$\frac{\rho}{\rho_a} = \frac{D}{D_0} \quad (138)$$

For adiabatic isentropic flow, the temperature and density of the gas are related by

$$\frac{\rho}{\rho_a} = \left(\frac{t}{T}\right)^{\frac{1}{\gamma-1}} \quad (139)$$

An examination of equations (137) and (138) indicates that $\frac{\rho}{\rho_a} = \frac{t}{T}$ in the analogy, so that $\gamma = 2$. Pressures are obtained from

$$\frac{p}{P} = \left(\frac{\rho}{\rho_a}\right)^{\gamma} = \left(\frac{\rho}{\rho_a}\right)^2 = \left(\frac{D}{D_0}\right)^2 \quad (140)$$

This value of γ is not valid for any real gas. However, since many relations are not significantly affected by using a value of γ slightly different from the true value, it should be possible to obtain at least qualitatively correct results.

The potential-flow equation for the gas is

$$\frac{\partial^2 \Phi}{\partial x^2} \left[1 - \frac{\left(\frac{\partial \Phi}{\partial x}\right)^2}{a^2} \right] + \frac{\partial^2 \Phi}{\partial y^2} \left[1 - \frac{\left(\frac{\partial \Phi}{\partial y}\right)^2}{a^2} \right] - 2 \frac{\partial^2 \Phi}{\partial x \partial y} \frac{\frac{\partial \Phi}{\partial x} \frac{\partial \Phi}{\partial y}}{a^2} = 0 \quad (136b)$$

Comparison of equations (136a) and (136b) shows that

$$\frac{gD}{2gD_0} = \frac{a^2}{2gc_p T} \quad (141)$$

Thus, \sqrt{gD} compares with the velocity of sound in the gas flow. It is known from the literature on hydraulics that \sqrt{gD} corresponds to the speed of propagation of long surface waves. The ratio v/\sqrt{gD} in liquid flow is seen to correspond to the Mach number q/a in gas flow. Liquid flows with $v/\sqrt{gD} < 1$ are called "streaming" and with $v/\sqrt{gD} > 1$ are called "shooting." The difference in the character of the equations governing subsonic and supersonic compressible flows exists also in the equations governing "streaming" and "shooting" incompressible flows.

It is seen that utilization of the hydraulic analogy reduces the problem of finding compressible-flow properties of a gas to measuring depth in a liquid flowing under certain conditions. The chief advantage of the analogy is that it provides a relatively inexpensive way to investigate high-speed flow of compressible fluids. A photograph of an apparatus used successfully in applying the hydraulic analogy (ref. 73) is shown in figure 17.

Mechanical Analogs

For a two-dimensional compressible isentropic flow, the following equations are valid:

$$\frac{d\Phi}{dl} = q \quad (142)$$

$$\frac{d\Psi}{dn} = \rho q \quad (143)$$

$$\frac{\rho}{\rho_a} = \left[1 - \frac{\gamma - 1}{2} \left(\frac{q}{a_a} \right)^2 \right]^{\frac{1}{\gamma - 1}} \quad (144)$$

where the derivatives in equations (142) and (143) are taken in the direction of a streamline and a potential line, respectively.

For purposes of mechanical representation, it is assumed that the total differentials $d\Phi$ and $d\Psi$ in (142) and (143) can be replaced by finite increments of a size sufficiently small in comparison with the cascade. Equations (142) and (143) become, respectively,

$$\left. \begin{aligned} \Delta\Phi &= q \Delta l \\ \Delta\Psi &= \rho q \Delta n \end{aligned} \right\} \quad (145)$$

Then, from equations (144) and (145),

$$a_a \rho_a \frac{\Delta n}{\Delta\Psi} = \frac{a_a}{q} \frac{\rho_a}{\rho} = \frac{a_a}{q} \frac{1}{\left[1 - \frac{\gamma - 1}{2} \left(\frac{q}{a_a} \right)^2 \right]^{\frac{1}{\gamma - 1}}} = a_a \frac{\Delta l}{\Delta\Phi} \frac{1}{\left[1 - \frac{\gamma - 1}{2} \left(\frac{\Delta\Phi}{a_a \Delta l} \right)^2 \right]^{\frac{1}{\gamma - 1}}} \quad (146)$$

giving the relation between $(a_a \rho_a \Delta n / \Delta\Psi)$ and $(a_a \Delta l / \Delta\Phi)$.

From equations (145),

$$\frac{a_a \rho_a \frac{\Delta n}{\Delta\Psi}}{a_a \frac{\Delta l}{\Delta\Phi}} = \frac{\frac{a_a \rho_a}{q \rho}}{\frac{a_a}{q}} = \frac{\rho_a}{\rho}$$

and it is clear that

$$a_a \rho_a \frac{\Delta n}{\Delta\Psi} = a_a \frac{\Delta l}{\Delta\Phi} \quad (147)$$

for stagnation conditions. Equation (146) is plotted for $\gamma = 1.4$ in figure 18. This equation is quite general in application and relates Δn to Δl for the meshes of a streamline - potential-line network in a compressible-flow field. From equation (144) the pressure at any point of the flow field is given by

$$\frac{p}{P} = \left[1 - \frac{\gamma-1}{2} \left(\frac{\Delta \Phi}{a_a \Delta l} \right)^2 \right]^{\frac{\gamma}{\gamma-1}} \quad (148)$$

Similarly, the local Mach number can be determined as

$$M^2 \left(a_a \frac{\Delta l}{\Delta \Phi} \right)^2 = 1 + \frac{\gamma-1}{2} M^2 \quad (149)$$

These equations may be used in several ways to determine the flow about a cascade of blades. A description of the graphical method (flux plot) will indicate the general theory and clarify the mechanical analogies arising from it. The blades to be investigated are first drawn to a convenient scale. Three blades (and hence two passages) are used to provide a clearer picture of the flow in the leading-edge region and a check on the accuracy of the assumed stagnation streamlines. That is, the stagnation streamline attached to the central airfoil must have the same shape in the final solution as the outside stagnation streamlines. As a first approximation, the stream and potential lines are drawn for an incompressible flow, which divides the field net into nearly square meshes. (Strict accuracy is not necessary, since this is only a first approximation to the compressible flow.) The meshes are then corrected to a rectangular shape by the application of equations (145) and (146).

A word must be said here about the use of these equations in a given problem. Generally, the upstream conditions q_1 and β_1 will be given as well as the cascade geometry. When a drawing of the cascade has been made to a convenient scale, the spacing s can be measured. The total mass flow through a single passage is given by

$$\Delta w = s \rho_1 q_1 \cos \beta_1 \quad (150)$$

and $\Delta \Psi$ is chosen as $\Delta \Psi = \Delta w / N$ where N is the desired number of incremental flow passages per cascade passage. The value of N should be chosen to represent the best compromise between time and accuracy. Then, if Δl is taken equal to Δn at stagnation conditions, equation (147) yields

$$\Delta \Phi = \frac{\Delta \Psi}{\rho_a} \quad (151)$$

Thus, from a given set of inlet conditions, a given cascade drawing, and a desired number of streamlines per passage, values of $\Delta\psi$ and $\Delta\phi$ are determined. These values are constant over the flow field, so that equation (146) yields a fixed relation between Δn and Δl . As a practical measure, it is often convenient to make a plot of Δl against Δn for the particular problem being considered. Such a plot follows at once from figure 18 when values of $\Delta\psi$ and $\Delta\phi$ have been chosen. The stream and potential lines can then be adjusted (generally by an iteration process) to satisfy the known relation between Δn and Δl .

The flux plot has the advantage of requiring no unusual equipment. However, the erasure and redrawing of the many lines in the flow net in the successive iterations is a time-consuming operation. Simple mechanical means of alleviating some of the difficulties are discussed in the following paragraphs.

The condition of orthogonality can be nearly satisfied by using a net of wires and pins. The stream and potential lines of the flow are represented by thin spring steel wires. The nodes of the net are steel pins with holes drilled at right angles through them (see fig. 19). When the wires have been threaded through the pins, the network, under distortion to satisfy boundary conditions, will maintain orthogonality to a certain degree. The friction present will prevent a complete self-alignment of the network. The diameter of the pins and tolerance of the holes will result in some deviation from orthogonality.

The boundary conditions are satisfied by using pins with sharply pointed ends to secure the bounding streamlines in their proper locations. Special pins are used for stagnation streamlines.

For the case of an incompressible fluid, the meshes of the network must be square. A second orthogonal network, forming diagonals of the small squares, can be superimposed to satisfy this condition. The pins must be drilled to receive this second network as well as the first. Use of the second network results in more accurate curvilinear squares than could be achieved by measuring distances between midpoints of opposite sides.

To facilitate the network adjustment in the case of compressible flow, a four-legged caliper has been devised by Sells (ref. 74). The spacing between one pair of legs is a function of the spacing between the other legs, and the functional relation is devised to maintain the width-to-length ratio of the small meshes of a compressible-flow net. This device was used successfully by the authors of reference 74.

Another mechanical method of adjustment (fig. 20) has been devised by Westphal and Dunavant (ref. 75). A few basic considerations must

be noted relating to its construction. If $\Delta l = \Delta n$ at stagnation conditions, then, as pointed out earlier, $\Delta\Phi = \Delta\Psi/\rho_a$. In this case,

$$a_a \rho_a \frac{\Delta n}{\Delta\Psi} = a_a \frac{\Delta n}{\Delta\Phi} \quad (152)$$

By choosing $\Delta\Phi = a_a/2$, equation (152) yields

$$a_a \rho_a \frac{\Delta n}{\Delta\Psi} = 2\Delta n \quad (153)$$

and also

$$a_a \frac{\Delta l}{\Delta\Phi} = 2\Delta l \quad (154)$$

Using equations (153) and (154) in equation (146) yields

$$\Delta n = \frac{\Delta l}{\left[1 - \frac{\gamma-1}{2(2\Delta l)^2}\right]^{\frac{1}{\gamma-1}}} \quad (155)$$

which is a universal relation between Δn and Δl for a fixed value of $\Delta\Phi$. To obtain this relation, it was necessary to give up the freedom of choosing $\Delta\Psi$, and hence $\Delta\Phi$, in each individual problem. In a given problem, equation (150) is used to determine $\Delta w/s$, and then s , from $\Delta\Psi$ and N . Then the cascade must be drawn to correspond to this value of s . Thus, in any given problem the scale of the drawing is uniquely determined by the inlet conditions, the desired number of streamlines per passage, and the fixed value of $\Delta\Phi$.

Figure 20 (from ref. 75) shows a slotted cam constructed to reproduce mechanically the functional relation given by equation (155). If the cams are placed over a network of pins and wires as shown in figure 21, the distance Δn will automatically require the distance Δl to be such that the proper relation, as expressed by equation (155), is preserved. In general procedure the wire net is fitted to the boundary conditions of a particular problem. Then the cams are placed over the pins beginning from a known portion of the flow field, usually far upstream. The alinement of the pins and wires is complete with the placement of the cams. Since additional measurements and corrections are not necessary, the procedure is fairly rapid.

The value $a_a/2$ was chosen for $\Delta\Phi$ to yield a reasonable cam size. Clearly, a value of $\Delta\Phi$ must be fixed in order to construct a cam of

fairly universal applicability. The cam reported in reference 75 is valid for a range of Mach number from 0.3 to 1.0 and for stream-tube widths of 0.864 to 1.760 inches.

The time required for obtaining a solution for turbine cascades and nozzles by use of the cams is estimated in reference 75 to be about 8 hours. However, some difficulty was encountered in reference 76 in applying the wire-mesh method to a compressor cascade. This difficulty was attributed to the more poorly defined passage of the compressor cascade investigated as compared with the cascade of turbines.

Electrical Analogs

The flow of an electric current through a nearly flat plate is governed by the following equations:

$$\left. \begin{aligned} \frac{\partial \hat{\Phi}}{\partial x} &= -I_x \Omega & \frac{\partial \hat{\Phi}}{\partial y} &= -I_y \Omega \\ \frac{\partial \hat{\Psi}}{\partial x} &= -I_y m & \frac{\partial \hat{\Psi}}{\partial y} &= I_x m \end{aligned} \right\} \quad (156)$$

where $\hat{\Phi}$ is the electric potential, $\hat{\Psi}$ is an electric-current function, Ω is the specific resistance of the plate, I is the current density, and m is the thickness of the plate. The following relations hold for the irrotational flow of a nonviscous compressible fluid:

$$\left. \begin{aligned} \frac{\partial \Phi}{\partial x} &= q_x & \frac{\partial \Phi}{\partial y} &= q_y \\ \frac{\partial \Psi}{\partial x} &= -\rho q_y & \frac{\partial \Psi}{\partial y} &= \rho q_x \end{aligned} \right\} \quad (157)$$

A comparison of equations (156) and (157) indicates that an analogy exists if

$$\left. \begin{aligned} \Phi &= -\hat{\Phi} & \Psi &= \hat{\Psi} \\ q_x &= \Omega I_x & q_y &= \Omega I_y \\ \rho q_y &= I_y m & \rho q_x &= I_x m \end{aligned} \right\} \quad (158)$$

Then, from equations (158) it follows that

$$\rho = \frac{m}{\Omega} \quad (159)$$

If the flow pattern is known in any field of fluid flow, the velocity, and hence the density, is known at each point. Then, if the ratio of plate thickness to plate specific resistance at each point is made equal to the density at the corresponding point of the flow field, the lines of flow of the electric current will correspond to streamlines of the compressible-fluid flow. Similarly, the lines of constant electric potential will correspond to potential lines of the flow field.

In the first approach to the use of this analogy, let $\Omega = \text{constant}$. That is, choose a conducting substance of constant specific resistance. Then m must be varied to satisfy relation (159). A convenient way to construct a conducting sheet of constant specific resistance and varying thickness is to use a tank containing an electrolyte. The electrolyte must be shallow, and the bottom of the tank must be made of a substance easily deformed into a desired shape (see ref. 77). The tank must be constructed of a nonconducting material, as must be the object about which the flow is to be determined. An arrangement must be made to enable a potential difference to be created between points far upstream and far downstream.

To solve a compressible-flow problem with such an apparatus, the bottom of the tank is left flat for the first approximation. This corresponds to obtaining an incompressible-flow solution. A potential difference is applied, and the current lines and electric potential lines are determined. Various apparatus have been developed for this operation (see refs. 77 and 78). The current lines are then interpreted as streamlines, and a velocity field is determined. From the velocities obtained in this first approximation, densities are computed at each point of the flow field, and corresponding thicknesses of the electrolyte are determined from equation (159). This varying thickness of the electrolyte is achieved by deformation of the tank bottom. With the shape of the tank bottom thus adjusted, new current lines are determined and the entire process is repeated. If the procedure is a convergent one, the result will be the desired compressible flow about the object considered.

To avoid the problems involved in varying the shape of the tank bottom, a method is desirable wherein the thickness is held constant and the resistance is varied. A conducting material in which the resistance varies in the proper manner with the local current density would make this type of analog realizable. Although no such material is known at the present time, a discrete-point type of analog can be used to achieve a properly varying resistance. The details of such a treatment using a direct-current board are given in reference 74.

Equations (156) are rewritten as

$$\left. \begin{aligned} \frac{\partial \hat{\Phi}}{\partial x} &= -E_x & \frac{\partial \hat{\Phi}}{\partial y} &= -E_y \\ I_x &= \frac{E_x}{\Omega} & I_y &= \frac{E_y}{\Omega} \\ \frac{\partial \hat{\Psi}}{\partial x} &= -I_y & \frac{\partial \hat{\Psi}}{\partial y} &= I_x \end{aligned} \right\} \quad (160)$$

where E_x , E_y are the electric-field components and I_x , I_y are now the electric-current components per unit thickness. The derivatives in equations (160) are now replaced by difference quotients of values of $\hat{\Phi}$ and $\hat{\Psi}$ at the nodes of a square lattice net with square mesh size δ . These difference equations then become the circuit equations for a network of resistances. The resistance R of each segment of the net is given by

$$\frac{R}{R_1} = \left[1 - \frac{\gamma-1}{2} \left(\frac{E}{E_1} \right)^2 \right]^{\frac{-1}{\gamma-1}} \quad (161)$$

The field strength E is given by

$$E = \left(\frac{1}{\delta} \right) \sqrt{(\Delta_x \hat{\Phi})^2 + (\Delta_y \hat{\Phi})^2} \quad (162)$$

where Δ_x and Δ_y denote differences in the x - and y -directions, respectively. The network has the same geometrical boundaries as the flow field to be investigated.

As a first approximation in the solution of a compressible-flow problem, the resistances in the net are all taken equal. The voltages are then read at all the lattice points, and E is found from equation (162). The resistances are determined from equation (161) and incorporated into the network. New readings are then taken and a second set of resistances calculated. These resistances are incorporated into the system, and so forth. If the method converges, the result will be a finite-difference approximation to the flow of a compressible fluid.

CONCLUDING REMARKS

A survey of the literature on plane potential flow about cascades has been presented. The theories are classified according to their application to high-solidity or low-solidity cascades and according to whether the method solves the direct or the inverse problem. Several

methods have been presented in considerable detail to illustrate acceptable solutions for the problems in the various classifications. These methods are considered to offer practical solutions, since they combine a reasonable amount of computing time with acceptable accuracy. The authors of these methods are Katzoff, Finn, and Laurence (ref. 21); Goldstein (unpublished lectures); Huppert and MacGregor (ref. 60); Wu and Brown (ref. 63); Stanitz (ref. 72); and Stanitz and Sheldrake (ref. 68).

APPENDIX A

VELOCITY DISTRIBUTION AT ARBITRARY ANGLE OF INCIDENCE

It is possible to map conformally an infinite cascade in the z -plane into a circle of radius 1 with center at the origin in the ζ -plane. The mapping can be chosen so that the points $\pm\infty$ in the z -plane map into the real points $\pm e^K$ in the circle plane (e.g., ref. 25). The complex potential function of the flow about the circle, which will have the desired singularities when mapped into the cascade plane, is given by

$$W_\zeta(\zeta) = \frac{v_m s}{2\pi} \left[e^{i\beta_m} \log_e \left(\frac{\zeta - e^K}{\zeta + e^K} \right) + e^{-i\beta_m} \log_e \left(\frac{\zeta - e^{-K}}{\zeta + e^{-K}} \right) \right] + \frac{\Gamma}{4\pi i} \log_e \left(\frac{\zeta^2 - e^{-2K}}{\zeta^2 - e^{+2K}} \right) + \text{constant} \quad (5)$$

The constants v_m , β_m , s , Γ , and K are determined from the cascade being investigated. Suppose now that a solution is known for the cascade at some angle of incidence. Then v_m , β_m , s , and Γ are known quantities. If K can also be found, equation (5) will give the flow in the circle plane which corresponds to the flow in the cascade plane. Then, a conformal mapping is determined between points of the z -plane and points of the ζ -plane by equating values of the respective potential functions. Actually, the value of K can be determined by requiring that the two flow fields be related conformally and utilizing the condition of correspondence of potential values. Note that, on the circle, $\zeta = e^{i\varphi}$ and equation (5) becomes

$$W_\zeta = \Phi_\zeta = \frac{v_m s}{2\pi} \left[\cos \beta_m \log_e \left(\frac{\cos \varphi - \cosh K}{\cos \varphi + \cosh K} \right) + 2 \sin \beta_m \tan^{-1} \left(\frac{\sin \varphi}{\sinh K} \right) + \frac{\Gamma}{v_m s} \tan^{-1} \left(\frac{\tan \varphi}{\tanh K} \right) \right] \quad (A1)$$

Let $\Delta\Phi_\zeta$ denote the change in potential from the leading-edge stagnation point φ_{le} to the trailing-edge stagnation point $\varphi_{te,s}$ along the upper portion of the circle (see fig. 6):

$$\Delta\Phi_{\zeta} = \frac{v_m s}{2\pi} \left\{ \cos \beta_m \log_e \left(\frac{\cos \phi_{te,s} - \cosh K}{\cos \phi_{te,s} + \cosh K} \frac{\cos \phi_{le} + \cosh K}{\cos \phi_{le} - \cosh K} \right) + \right. \\ \left. 2 \sin \beta_m \left[\tan^{-1} \left(\frac{\sin \phi_{te,s}}{\sinh K} \right) - \tan^{-1} \left(\frac{\sin \phi_{le}}{\sinh K} \right) \right] + \right. \\ \left. \frac{\Gamma}{v_m s} \left[\tan^{-1} \left(\frac{\tan \phi_{te,s}}{\tanh K} \right) - \tan^{-1} \left(\frac{\tan \phi_{le}}{\tanh K} \right) \right] \right\} \quad (A2)$$

where

$$-\frac{\pi}{2} < \tan^{-1} \left(\frac{\sin \phi_{te,s}}{\sinh K} \right) < \frac{\pi}{2}$$

$$-\frac{\pi}{2} < \tan^{-1} \left(\frac{\sin \phi_{le}}{\sinh K} \right) < \frac{\pi}{2}$$

and $\tan^{-1} \left(\frac{\tan \phi_{te,s}}{\tanh K} \right)$ and $\tan^{-1} \left(\frac{\tan \phi_{le}}{\tanh K} \right)$ are in the same quadrant as $\phi_{te,s}$ and ϕ_{le} , respectively.

The stagnation points are found by differentiating equation (A1) and equating to zero. This results in the following equation for $\phi_{te,s}$ and ϕ_{le} , which can be interpreted as a quadratic equation in $\sin \phi$:

$$\sin \phi \cos \beta_m + \cos \phi \sin \beta_m \tanh K + \frac{\Gamma}{2v_m s} \sinh K = 0 \quad (A3)$$

Since the two flow fields are to be related conformally, the potential difference $\Delta\Phi_z$ measured from the leading-edge stagnation point to the trailing edge of a cascade blade must equal the corresponding potential difference (as given by eq. (A2)) in the circle plane. The procedure for finding K is as follows:

- (1) Assume several values of K .
- (2) For each value of K , compute $\phi_{te,s}$ and ϕ_{le} from equation (A3).
- (3) Compute $\Delta\Phi_{\zeta}$ from equation (A2) for each value of K .
- (4) Plot $\Delta\Phi_{\zeta}$ against K , and select the value of K for which $\Delta\Phi_{\zeta} = \Delta\Phi_z$.

With this value of K , the flow function (5) is completely determined and velocity distributions at angles of incidence other than the one for the original solution can be considered.

If W_ζ and W_z denote the complex potential functions in the circle plane and the cascade plane, respectively, and $z = z(\zeta)$ is the desired mapping function, the following relations hold:

$$W_z(z) = W_\zeta(z(\zeta)) = W_\zeta(\zeta). \quad (17)$$

$$\frac{dW_\zeta}{d\zeta} = \frac{dW_z}{dz} \frac{dz}{d\zeta} \quad (A4)$$

or

$$w_z = w_\zeta \frac{d\zeta}{dz}$$

where w_z and w_ζ denote the complex velocity conjugates in the cascade and circle planes, respectively. If only the blade perimeters and the unit circle are considered, equation (A4) becomes

$$v_z = \left| \frac{d\zeta}{dz} \right|_{\text{boundary}} \frac{d\Phi_\zeta}{d\phi}$$

$$= \left| \frac{d\zeta}{dz} \right| \frac{v_{ms}}{\pi} \left[\frac{\cos \beta_m \cosh K (\sin \phi - \sin \phi_{te,s}) + \sin \beta_m \sinh K (\cos \phi - \cos \phi_{te,s})}{\cosh^2 K - \cos^2 \phi} \right] \quad (A5)$$

In order to satisfy the Kutta condition for a new value of β_m (corresponding to a new value of incidence angle), the flow must continue to leave the cascade blades at a point corresponding to $\phi = \phi_{te,s}$. Since the mapping function is unaltered, the velocity distribution for an arbitrary value of β_m (say β_m^*) is given by

$$(v_z)_{\beta_m^*}$$

$$= (v_z)_{\beta_m} \left[\frac{\cos \beta_m^* \cosh K (\sin \phi - \sin \phi_{te,s}) + \sin \beta_m^* \sinh K (\cos \phi - \cos \phi_{te,s})}{\cos \beta_m \cosh K (\sin \phi - \sin \phi_{te,s}) + \sin \beta_m \sinh K (\cos \phi - \cos \phi_{te,s})} \right] \quad (A6)$$

After K and $\phi_{te,s}$ have once been found for a given cascade, equation (A6) can be used to determine velocity distributions at any angles of incidence.

APPENDIX B

CASCADE MAPPING FUNCTION

The development of the cascade mapping function as presented herein is taken from unpublished lectures by Goldstein.

Consider an infinite cascade of blades in the $z = x + iy$ plane, oriented as in figure 1. If s is the blade spacing, the cascade can be mapped into a single closed curve by the function

$$z_1 = e^{\frac{2\pi z}{s}} \quad (B1)$$

By the mapping theorem of Riemann, the exterior of this closed curve can be mapped conformally onto the exterior of a unit circle in the z_2 -plane in such a way that

$$\lim_{z_2 \rightarrow \infty} z_1(z_2) = \infty \quad (B2a)$$

and

$$\lim_{z_2 \rightarrow \infty} \frac{dz_1}{dz_2} = A \quad (B2b)$$

where A is a real constant. Since the derivative of the function has no zeros outside the circle, the mapping function can be written

$$\frac{dz_1}{dz_2} = e^{f(z_2)} \quad (B3)$$

with conditions (B2a) and (B2b) satisfied.

The observation is now made that

$$\text{when } z \rightarrow -\infty, \text{ then } z_1 \rightarrow 0 \text{ and } z_2 \rightarrow \text{some point } a \quad (B4)$$

$$\text{when } z \rightarrow +\infty, \text{ then } z_1 \rightarrow +\infty \text{ and } z_2 \rightarrow +\infty \quad (B5)$$

The unit circle in the z_2 -plane can be mapped uniquely by a linear fractional transformation onto a unit circle in the ζ -plane with center

at the origin and such that $+\infty$ and a in the z_2 -plane map into e^K and $-e^K$, respectively (see ref. 85). This mapping can be written

$$z_2 - a = a \frac{\zeta + e^K}{\zeta - e^K} \tanh K \quad (B6)$$

If z_1 is considered as a function of ζ , certain conditions on $z_1(\zeta)$ must be fulfilled. From relations (B6) and (B5), $z_1(\zeta)$ has a pole of order 1 at $\zeta = e^K$. From relations (B6) and (B4), $z_1(\zeta)$ has a zero at $\zeta = -e^K$ of order 1. It is clear that the desired function has the form

$$z_1 = \frac{\zeta + e^K}{\zeta - e^K} g(\zeta) \quad (B7)$$

where $g(\zeta)$ is regular for $|\zeta| > 1$. Furthermore, $g(\zeta) \neq 0$ for $|\zeta| > 1$, because, if $g(\rho) = 0$ for some ρ such that $|\rho| > 1$, then $z_1 = 0$ would correspond to two points, $\zeta = -e^K$ and $\zeta = \rho$. But this is not possible, since z_1 is a regular one-to-one function of ζ . Hence, equation (B7) can be rewritten

$$z_1 = \frac{\zeta + e^K}{\zeta - e^K} e^{f(\zeta)} \quad (B8)$$

where $f(\zeta)$ is regular for $|\zeta| > 1$. Then

$$\frac{dz_1}{d\zeta} = \frac{e^{f(\zeta)}}{(\zeta - e^K)^2} \left[(\zeta^2 - e^{2K}) f'(\zeta) - 2e^K \right] \quad (B9)$$

From equations (B3) and (B6),

$$\frac{dz_1}{d\zeta} = \frac{dz_1}{dz_2} \frac{dz_2}{d\zeta} = \frac{-2e^{f(z_2)} a e^K \tanh K}{(\zeta - e^K)^2} \quad (B10)$$

Equating (B9) and (B10) yields

$$(\zeta^2 - e^{2K}) f'(\zeta) - 2e^K = -e^{(f-f)} 2ae^K \tanh K = -2e^K e^G(\zeta) \quad (B11)$$

where G is defined by the relation

$$e^{G(\zeta)} = a \tanh K e^{(f-f)}$$

Then,

$$f'(\zeta) = 2e^K \frac{1 - e^{G(\zeta)}}{(\zeta - e^K)(\zeta + e^K)} \quad (B12)$$

But $f(\zeta)$, and hence $f'(\zeta)$, is regular for $|\zeta| > 1$, so $1 - e^{G(\zeta)}$ must have zeros at $\zeta = e^K$ and $\zeta = -e^K$. It follows that $G(\zeta)$ has zeros at $\zeta = e^K$ and $\zeta = -e^K$. Then from equations (B1), (B9), and (B11),

$$\frac{dz}{d\zeta} = \frac{dz}{dz_1} \frac{dz_1}{d\zeta} = \frac{s}{2\pi z_1} \frac{-2e^K e^{G(\zeta)} e^{f(\zeta)}}{(\zeta - e^K)^2} = \frac{-se^K}{\pi} \frac{e^{G(\zeta)}}{(\zeta - e^K)(\zeta + e^K)} \quad (B13)$$

with the condition that $G(\zeta)$ is regular for $|\zeta| > 1$, and $G(\pm e^K) = 0$. Equation (B13) can be put into a more convenient form. Consider the function

$$h(\zeta) = F(\zeta) \left[G(\zeta) + \log_e \left(\frac{1 - \frac{e^{-2K}}{\zeta^2}}{1 - e^{-4K}} \right) \right] \quad (B14)$$

where

$$F(\zeta) = \frac{\zeta^2 (e^{2K} - e^{-2K})}{(e^{2K} - \zeta^2)(\zeta^2 - e^{-2K})} \quad (14)$$

Therefore, $h(\zeta)$ is regular for $|\zeta| > 1$ and has a zero of order two at $\zeta \rightarrow \infty$. Substituting equation (B14) into equation (B13) gives

$$\frac{dz}{d\zeta} = \frac{se^{-K}}{\pi} F(\zeta) e^{\frac{h(\zeta)}{F(\zeta)}} \quad (13)$$

and the condition on $h(\zeta)$ can be expressed as

$$\lim_{\zeta \rightarrow \infty} \zeta h(\zeta) = 0 \quad (16)$$

In a case where the cascade blade has a sharp trailing edge, the function $h(\zeta)$ will not be regular at the corresponding point on the mapping circle. As a result, the determination of h_2 from h_1 (where $h = h_1 + ih_2$) is unduly complicated in the preceding form. The singularity can

be factored out, however, and the computations simplified. The general mapping function (eq. (13)) then takes the following form:

$$\frac{dz}{d\zeta} = \frac{se^{-K}}{\pi} \left(1 - \frac{\zeta_{te}}{\zeta}\right)^{\frac{1-\epsilon}{\pi}} \left(1 - \frac{\zeta_{te}}{e^{\frac{K}{2}}}\right)^{-\frac{1}{2} + \frac{\epsilon}{2\pi}} F(\zeta) e^{\frac{h(\zeta)}{F(\zeta)}} \exp \left[\frac{e^{K\left(\frac{1}{2} - \frac{\epsilon}{2\pi}\right)}}{\zeta} \log \frac{e^K + \zeta_{te}}{e^K - \zeta_{te}} \right] \quad (B15)$$

where ϵ is the included trailing-edge angle and ζ_{te} is the point corresponding to the trailing edge. The function $h(\zeta)$ appearing in equation (B15) is regular on and outside the unit circle. For details of this computation see reference 40.

APPENDIX C

RELAXATION CONSIDERATIONS

Consider the set of five grid points 0, 1, 2, 3, and 4 shown in figure 12. The number 0 denotes the central point at which the finite-difference equation, under consideration in this discussion, is written. The subscripts 0, 1, 2, 3, and 4 refer to the five points 0, 1, 2, 3, and 4. The finite-difference equation is written at 0 as

$$A_0\Psi_0 + A_1\Psi_1 + A_2\Psi_2 + A_3\Psi_3 + A_4\Psi_4 + K_0 = 0 \quad (C1)$$

The coefficients A_i are known, and the nonlinear contribution K_0 is fixed from a previous approximate solution or from an assumed solution.

Equation (C1) is rewritten

$$A_0\Psi_0 + A_1\Psi_1 + A_2\Psi_2 + A_3\Psi_3 + A_4\Psi_4 + K_0 = R_0 \quad (C2)$$

where R_0 is called the residual at 0. When the correct values of Ψ_i are inserted in equation (C2), R_0 will be zero. If incorrect values of Ψ_i are used, R_0 will, in general, have a value different from zero.

When equation (C1) is applied to each of N points in the flow field, N simultaneous equations in N unknowns (Ψ_i) result. When values of Ψ_i ($i = 0, 1, \dots, N$) are assumed, equation (C2) yields N residual values R_i ($i = 0, 1, \dots, N$). The purpose of the relaxation process is to reduce these residuals to small values. From equation (C2) it is seen that R_0 can be reduced to zero by a new choice of Ψ_0 , say Ψ'_0 , such that

$$\Psi'_0 = \Psi_0 - \frac{R_0}{A_0} \quad (C3)$$

This choice of a new Ψ'_0 has an influence on other residuals. In this case, the residuals at points 1, 2, 3, and 4 in figure 12 are immediately affected. The finite-difference equations written at these four points each contain Ψ'_0 multiplied by a coefficient that has been determined at the outset. Thus, it is seen that R_1 , for example, is a function of Ψ_0 and subsequently of Ψ'_0 . A change in Ψ_0 then must cause a corresponding change in R_1 .

A simple way to carry out this process is to list the initial values of Ψ_i and R_i at each point on an oversized drawing of the flow field. Then a change in Ψ_i of $\Delta\Psi_i$ is recorded under Ψ_i at the point in question. Resulting changes ΔR_i are recorded at the respective points affected.

In this illustration second-order polynomial representation (resulting in five values appearing in each difference equation) was used. The principal is the same for higher order representations where more points are involved in each equation. Unequal spacing of points near the boundaries does not affect the general procedure. Residuals are systematically reduced over the entire flow field, usually beginning with the larger ones. As there is considerable interaction of effects, the residual at a given point may undergo many changes in the course of a solution.

There are many devices for obtaining rapid convergence that can be used to great advantage when employing relaxation methods (see ref. 44).

APPENDIX D

MATRIX CONSIDERATIONS

Applying equation (90) to each grid point in the flow field results in a collection of N linear equations in N unknowns. In a flow problem of this nature, so many points are required in the solution that matrices can be used to solve the equations only if high-speed computing equipment is available. Various matrix techniques are available in the literature. A brief outline of a method that has been used successfully in references 65 and 66 is presented herein.

The finite-difference equations are written in matrix form as follows:

$$[A] \{Y\} = \{J\} \quad (D1)$$

where

$[A]$ square matrix of order N

$\{Y\}$, $\{J\}$ column matrices having N elements

The square matrix $[A]$ can be written as

$$[A] = [l][d][u] \quad (D2)$$

where

$[l]$ lower triangular matrix with unity in the diagonal

$[u]$ upper triangular matrix with unity in the diagonal

$[d]$ diagonal matrix

The matrices $[l]$ and $[d]$ can be combined into a lower triangular matrix $[L]$, and (D2) is then written

$$[A] = [L][u] \quad (D3)$$

If i denotes row and j denotes column, the elements of $[L]$ and $[u]$ can be written

$$L_j^i = A_j^i - \sum_{k=1}^{j-1} L_k^i u_j^k \quad i \geq j \quad (D4)$$

$$L_1^i = A_1^i$$

$$u_j^i = \frac{A_j^i - \sum_{k=1}^{i-1} L_k^i u_j^k}{L_1^i} \quad j > i \quad (D5)$$

$$u_i^i = 1$$

$$u_j^1 = \frac{A_j^1}{L_1^1}$$

It is seen from equations (D4) and (D5) that L_1^i can be found first from a knowledge of A_1^i . Then u_j^1 can be found from (D5) since $u_j^1 = \frac{A_j^1}{L_1^1}$. Next, the second column of $[L]$ can be found and then the second row of $[u]$. In this manner, all elements of both matrices are known.

Now define a column matrix $\{Q\}$ such that

$$[L] \{Q\} = \{J\} \quad (D6)$$

It can be shown that

$$Q_i = \frac{J^i - \sum_{k=1}^{i-1} L_k^i Q^k}{L_1^i} \quad (D7)$$

$$Q_1 = \frac{J^1}{L_1^1}$$

Hence, $[Q]$ can be found by finding Q^1, Q^2, \dots in successive order.

From (D3) and (D1),

$$[L] [u] \{Y\} = \{J\} \quad (D8)$$

From (D6) and (D8),

$$[u] \{Y\} = \{Q\} \quad (D9)$$

Since $[u]$ is a known upper diagonal matrix and $\{Q\}$ is a known column matrix, $\{\Psi\}$ can be determined from $\Psi_n, \Psi_{n-1}, \dots$ in successive order. In general,

$$\Psi^i = Q^i - \sum_{k=n}^{i+1} u_k^i \Psi^k \quad (D10)$$

$$\Psi^n = Q^n$$

In this manner, the Ψ^i are found and the problem is solved. Suggestions for a computational layout designed for minimum time expenditures are made in reference 66.

REFERENCES

1. Compressor and Turbine Research Division: Aerodynamic Design of Axial-Flow Compressors. Vol. II. NACA RM E56B03a, 1956.
2. Giacomelli, R., and Pistolesi, E.: Historical Sketch. Vol. I of Aerodynamic Theory, Div. D, ch. III, W. F. Durand, ed., Durand Reprinting Comm. (C.I.T.), 1943, pp. 336-394.
3. Munk, Max M.: General Theory of Thin Wing Sections. NACA Rep. 142, 1922.
4. Glauert, H.: A Theory of Thin Aerofoils. R. & M. No. 910, British A.R.C., Feb. 1924.
5. Birnbaum, W.: Die tragende Wirbelfläche als Hilfsmittel zur Behandlung des ebenen Problems der Tragflügeltheorie. Z.a.M.M., Bd. 3, Heft 4, 1923, pp. 290-297.
6. Glauert, H.: The Elements of Aerofoil and Airscrew Theory. University Press (Cambridge), 1926.
7. Allen, H. Julian: General Theory of Airfoil Sections Having Arbitrary Shape or Pressure Distribution. NACA Rep. 833, 1945. (Supersedes NACA ACR 3G29.)
8. Theodorsen, Theodore: Theory of Wing Sections of Arbitrary Shape. NACA Rep. 411, 1931.
9. Theodorsen, T., and Garrick, I. E.: General Potential Theory of Arbitrary Wing Sections. NACA Rep. 452, 1933.

10. Naiman, Irven: Numerical Evaluation of the ϵ -Integral Occurring in the Theodorsen Arbitrary Airfoil Potential Theory. NACA WR L-136, 1944. (Supersedes NACA ARR L4D27a.)
11. Naiman, Irven: Numerical Evaluation by Harmonic Analysis of the ϵ -Function of the Theodorsen Arbitrary-Airfoil Potential Theory. NACA WR L-153, 1945. (Supersedes NACA ARR L5H18.)
12. Warschawski, S. E.: On Theodorsen's Method of Conformal Mapping of Nearly Circular Regions. Quart. Appl. Math., vol. III, no. 1, Apr. 1945, pp. 12-28.
13. Collar, A. R.: The Flow of a Perfect Fluid through Cascades of Aerofoils. Rep. No. 4589, British A.R.C., July 4, 1940.
14. Merchant, W., and Collar, A. R.: Flow of an Ideal Fluid Past a Cascade of Blades, Pt. II. R. & M. No. 1893, British A.R.C., May 26, 1941.
15. Weinig, F.: Die Strömung um die Schaufeln von Turbomaschinen. Johann Ambrosius Barth (Leipzig), 1935.
16. Pistolesi, E.: On the Calculation of Flow Past an Infinite Screen of Thin Airfoils. NACA TM 968, 1941.
17. Lieblein, V. (Wilhelm Bente, trans.): The Calculation of the Lift Characteristics of an Aerofoil Section in a Cascade. Rep. and Trans. No. 442, M.O.S. Völkenrode, Feb. 1947.
18. Erwin, John R., and Yacobi, Laura A.: Method of Estimating the Incompressible-Flow Pressure Distribution of Compressor Blade Sections at Design Angle of Attack. NACA RM L53F17, 1953.
19. Woolard, Henry W.: The Incompressible Flow about a Cascade of Airfoils. Rep. No. AF-734-A-1, Cornell Aero. Lab., Inc., Nov. 1950.
20. Scholz, N.: On an Extension of Glauert's Theory of Thin Airfoils to Profiles in Cascade. Jour. Aero. Sci., vol. 18, no. 9, Sept. 1951, pp. 637-638.
21. Katzoff, S., Finn, Robert S., and Laurence, James C.: Interference Method for Obtaining the Potential Flow Past an Arbitrary Cascade of Airfoils. NACA Rep. 879, 1947. (Supersedes NACA TN 1252.)
22. Howell, A. R.: A Theory of Arbitrary Airfoils in Cascade. Phil. Mag., vol. 39, no. 299, Dec. 1948, pp. 913-927.
23. Carter, A. D. S., and Hughes, Hazel P.: A Theoretical Investigation into the Effect of Profile Shape on the Performance of Aerofoils in Cascade. Power Jets Rep. No. R.1192, Res. and Dev., Power Jets, Ltd., Mar. 1946.

24. Vazsonyi, Andrew: On the Aerodynamic Design of Axial-Flow Compressors and Turbines. Jour. Appl. Mech., vol. 15, no. 1, Mar. 1948, pp. 53-64.
25. Garrick, I. E.: On the Plane Potential Flow Past a Lattice of Arbitrary Airfoils. NACA Rep. 788, 1944. (Supersedes NACA ARR 4A07.)
26. Kawada, S.: A Contribution to the Theory of Latticed Wings. Proc. Third Int. Cong. Appl. Mech., vol. I, pt. I, Aug. 24-29, 1930.
27. von Kármán, Th., and Bergers, J. M.: Flow through a Lattice Composed of Airfoils. Vol. II of Aerodynamic Theory, div. E, ch. II, pt. B, sec. 23, W. F. Durand, ed., Julius Springer (Berlin) 1935, pp. 91-96.
28. Traupel, W.: Die Berechnung der Potentialströmung durch Schaufelgitter. Schweizer Archiv f. Angewandte Wiss. und Tech., Bd. 10, Heft 12, 1944.
29. Calderwood, James: Some Researches on Internal Combustion Prime Movers. Trans. North East Coast Inst. Eng. and Shipbuilders, vol. 62, 1945-1946, pp. 283-310; Appendix by W. Traupel, pp. 311-328.
30. Mütterperl, William: The Conformal Transformation of an Airfoil into a Straight Line and Its Application to the Inverse Problem of Airfoil Theory. NACA WR L-113, 1944. (Supersedes NACA ARR L4K22a.)
31. Mütterperl, William: A Solution of the Direct and Inverse Potential Problems for Arbitrary Cascades of Airfoils. NACA WR L-81, 1944. (Supersedes NACA ARR L4K22b.)
32. Resnick, Robert, and Green, L. J.: Velocity Distributions and Design Data for Ideal Incompressible Flow through Cascades of Airfoils. Jour. Appl. Mech., vol. 18, no. 3, Sept. 1951, pp. 253-259.
33. Katzoff, S., and Hannah, Margery E.: Further Comparisons of Theoretical and Experimental Lift and Pressure Distributions on Airfoils in Cascade at Low-Subsonic Speed. NACA TN 2391, 1951.
34. Betz, Albert: Diagrams for Calculation of Airfoil Lattices. NACA TM 1022, 1942.
35. Goldstein, Arthur W., and Jerison, Meyer: Isolated and Cascade Airfoils with Prescribed Velocity Distribution. NACA Rep. 869, 1947. (Supersedes NACA TN 1308.)

36. Betz, A.: Modification of Wing-Section Shape to Assure a Predetermined Change in Pressure Distribution. NACA TM 767, 1935.
37. Theodorsen, Theodore: Airfoil-Contour Modifications Based on ϵ -Curve Method of Calculating Pressure Distribution. NACA WR L-135, 1944. (Supersedes NACA ARR L4G05.)
38. Gebelein, H.: Theory of Two-Dimensional Potential Flow about Arbitrary Wing Sections. NACA TM 886, 1939.
39. Peebles, Glenn H.: A Method for Calculating Airfoil Sections from Specifications on the Pressure Distributions. Jour. Aero. Sci., vol. 14, no. 8, Aug. 1947, pp. 451-456.
40. Hansen, Arthur G., and Yohner, Peggy L.: A Numerical Procedure for Designing Cascade Blades with Prescribed Velocity Distributions in Incompressible Potential Flow. NACA TN 2101, 1950.
41. Lighthill, M. J.: A Mathematical Method of Cascade Design. R. & M. No. 2104, British A.R.C., June 1945.
42. Southwell, R. V.: Relaxation Methods in Theoretical Physics. Clarendon Press (Oxford), 1946.
43. Emmons, Howard W.: The Numerical Solution of Partial Differential Equations. Quart. Appl. Math., vol. II, no. 3, Oct. 1944, pp. 173-195.
44. Shaw, F. S.: Introduction to Relaxation Methods. Dover Pub., 1953.
45. Chaplygin, S.: Gas Jets. NACA TM 1063, 1944.
46. Garrick, I. E., and Kaplan, Carl: On the Flow of a Compressible Fluid by the Hodograph Method. I - Unification and Extension of Present-Day Results. NACA Rep. 789, 1944. (Supersedes NACA ACR L4C24.)
47. Demtchenko, B.: Quelques problèmes d'hydrodynamique bidimensionnelle des fluides compressibles. Pub. Scientifiques et Techniques du Ministère de l'Air (France), No. 144, 1939.
48. von Kármán, Th.: Compressibility Effects in Aerodynamics. Jour. Aero. Sci., vol. 8, no. 9, July 1941, pp. 337-356.
49. Tsien, Hsue-Shen: Two-Dimensional Subsonic Flow of Compressible Fluids. Jour. Aero. Sci., vol. 6, no. 10, Aug. 1939, pp. 399-407.

50. Costello, George R.: Method of Designing Cascade Blades with Prescribed Velocity Distributions in Compressible Potential Flows. NACA Rep. 978, 1950. (Supersedes NACA TN's 1913 and 1970.)
51. Costello, George R., Cummings, Robert L., and Sinnette, John T., Jr.: Detailed Computational Procedure for Design of Cascade Blades with Prescribed Velocity Distributions in Compressible Potential Flows. NACA Rep. 1060, 1952. (Supersedes NACA TN 2281.)
52. Clauser, Francis H.: Two-Dimensional Compressible Flows Having Arbitrarily Specified Pressure Distributions for Gases with Gamma Equal to Minus One. Rep. NOLR 1132, Symposium on Theoretical Compressible Flow, U. S. Naval Ord. Lab., June 28, 1949, pp. 1-33.
53. Lin, C. C.: On the Subsonic Flow through Circular and Straight Lattices of Airfoils. Jour. Math. and Phys., vol. XXXVIII, no. 2, July 1949, pp. 117-130.
54. Lin, C. C.: On an Extension of the von Kármán-Tsien Method to Two-Dimensional Subsonic Flows with Circulation around Closed Profiles. Quart. Appl. Math., vol. IV, no. 3, Oct. 1946, pp. 291-297.
55. Sauer, Robert: Introduction to Theoretical Gas Dynamics. J. W. Edwards (Ann Arbor), 1947.
56. Woolard, Henry W.: A Note on the Subsonic Compressible Flow about Airfoils in a Cascade. Jour. Aero. Sci., vol. 17, no. 6, June 1950, pp. 379-381.
57. Briggs, William B.: Effect of Mach Number on the Flow and Application of Compressibility Corrections in a Two-Dimensional Subsonic-Transonic Compressor Cascade Having Varied Porous-Wall Suction at the Blade Tips. NACA TN 2649, 1952.
58. Erwin, John R., Savage, Melvyn, and Emery, James C.: Two-Dimensional Low-Speed Cascade Investigation of NACA Compressor Blade Sections Having a Systematic Variation in Mean-Line Loading. NACA RM L53I30b, 1953.
59. Stodola, A.: Steam and Gas Turbines. Vol. II. McGraw-Hill Book Co., Inc., 1927, p. 992. (Reprinted, Peter Smith (New York), 1945.)
60. Huppert, M. C., and MacGregor, Charles: Comparison between Predicted and Observed Performance of Gas-Turbine Stator Blade Designed for Free-Vortex Flow. NACA TN 1810, 1949.
61. Stanitz, John D., and Prian, Vasily D.: A Rapid Approximate Method for Determining Velocity Distribution on Impeller Blades of Centrifugal Compressors. NACA TN 2421, 1951.

62. Wu, Chung-Hua, and Brown, Curtis A.: A Theory of the Direct and Inverse Problems of Compressible Flow Past Cascades of Arbitrary Airfoils. Jour. Aero. Sci., vol. 19, no. 3, Mar. 1952, pp. 183-196.
63. Wu, Chung-Hua, and Brown, Curtis A.: Method of Analysis for Compressible Flow Past Arbitrary Turbomachine Blades on General Surface of Revolution. NACA TN 2407, 1951.
64. Milne, William Edmund: Numerical Calculus. Princeton Univ. Press, 1949.
65. Wu, Chung-Hua: Formulas and Tables of Coefficients for Numerical Differentiation with Function Values Given at Unequally Spaced Points and Application to Solution of Partial Differential Equations. NACA TN 2214, 1950.
66. Wu, Chung-Hua: Matrix and Relaxation Solutions That Determine Subsonic Through Flow in an Axial-Flow Gas Turbine. NACA TN 2750, 1952.
67. Stanitz, John D.: Design of Two-Dimensional Channels with Prescribed Velocity Distributions along the Channel Walls. NACA Rep. 1115, 1953. (Supersedes NACA TN's 2593 and 2595.)
68. Stanitz, John D., and Sheldrake, Leonard J.: Application of a Channel Design Method to High-Solidity Cascades and Tests of an Impulse Cascade with 90° of Turning. NACA Rep. 1116, 1953. (Supersedes NACA TN 2652.)
69. Ackeret, J. (V. P. Akimoff, trans.): The Design of Closely Spaced Blade Grids. R.T.P. Trans. No. 2007, British M.A.P.
70. Sawyer, William T.: Experimental Investigation of a Stationary Cascade of Aerodynamic Profiles. Mitt. aus d. Inst. f. Aero., Heft 17, Zurich, 1949.
71. Alpert, Sumner: Design Method for Two-Dimensional Channels for Compressible Flow with Application to High-Solidity Cascades. NACA TN 1931, 1949.
72. Stanitz, John D.: Approximate Design Method for High-Solidity Blade Elements in Compressors and Turbines. NACA TN 2408, 1951.
73. Orlin, W. James, Lindner, Norman J., and Bitterly, Jack G.: Application of the Analogy between Water Flow with a Free Surface and Two-Dimensional Compressible Gas Flow. NACA Rep. 875, 1947. (Supersedes NACA TN 1185.)

74. Poritsky, H., Sells, B. E., and Danforth, C. E.: Graphical, Mechanical, and Electrical Aids for Compressible Fluid Flow. Jour. Appl. Mech., vol. 17, no. 1, Mar. 1950, pp. 37-46.
75. Westphal, Willard R., and Dunavant, James C.: A Compressible-Flow Plotting Device and Its Application to Cascade Flows. NACA TN 2681, 1952.
76. Westphal, Willard R., and Dunavant, James C.: Application of the Wire-Mesh Plotting Device to Incompressible Cascade Flow. NACA TN 2095, 1950.
77. Taylor, G. I., and Sharman, C. F.: A Mechanical Method for Solving Problems of Flow in Compressible Fluids. R. & M. No. 1195, British A.R.C., Aug. 1928.
78. Malavard, L.: Use of Rheoelectrical Analogies. Jour. Roy. Aero. Soc., vol. 51, no. 441, 1947.
79. Peres, J.: Les Methodes D'Analogie en Mecanique Appliquee. Proc. Fifth Int. Cong. Appl. Mech., 1938, pp. 9-19.
80. Preiswerk, Ernst: Application of the Methods of Gas Dynamics to Water Flows with Free Surface. I - Flows with No Energy Dissipation. NACA TM 934, 1940.
81. Hargest, T. J.: The Theoretical Pressure Distributions around Some Related Aerofoils in Cascade. Memo. No. M.68, British N.G.T.E., Nov. 1949.
82. Hargest, T. J.: The Theoretical Pressure Distributions around Some Conventional Turbine Blades in Cascade. Rep. No. R.67, British N.G.T.E., Mar. 1950.
83. deHaller, P.: Application of Electrical Analogy to the Investigation of Cascades. Sulzer Tech. Rev., No. 3/4, 1947, pp. 11-17.
84. Vandrey, F.: Investigations of Plane Subsonic Flow with the Help of an Electrical Analogy. LFA Völkenrode Trans. No. 34, British M.O.S.
85. Bieberbach, L.: Conformal Mapping. Chelsea Pub. Co. (New York), 1953.

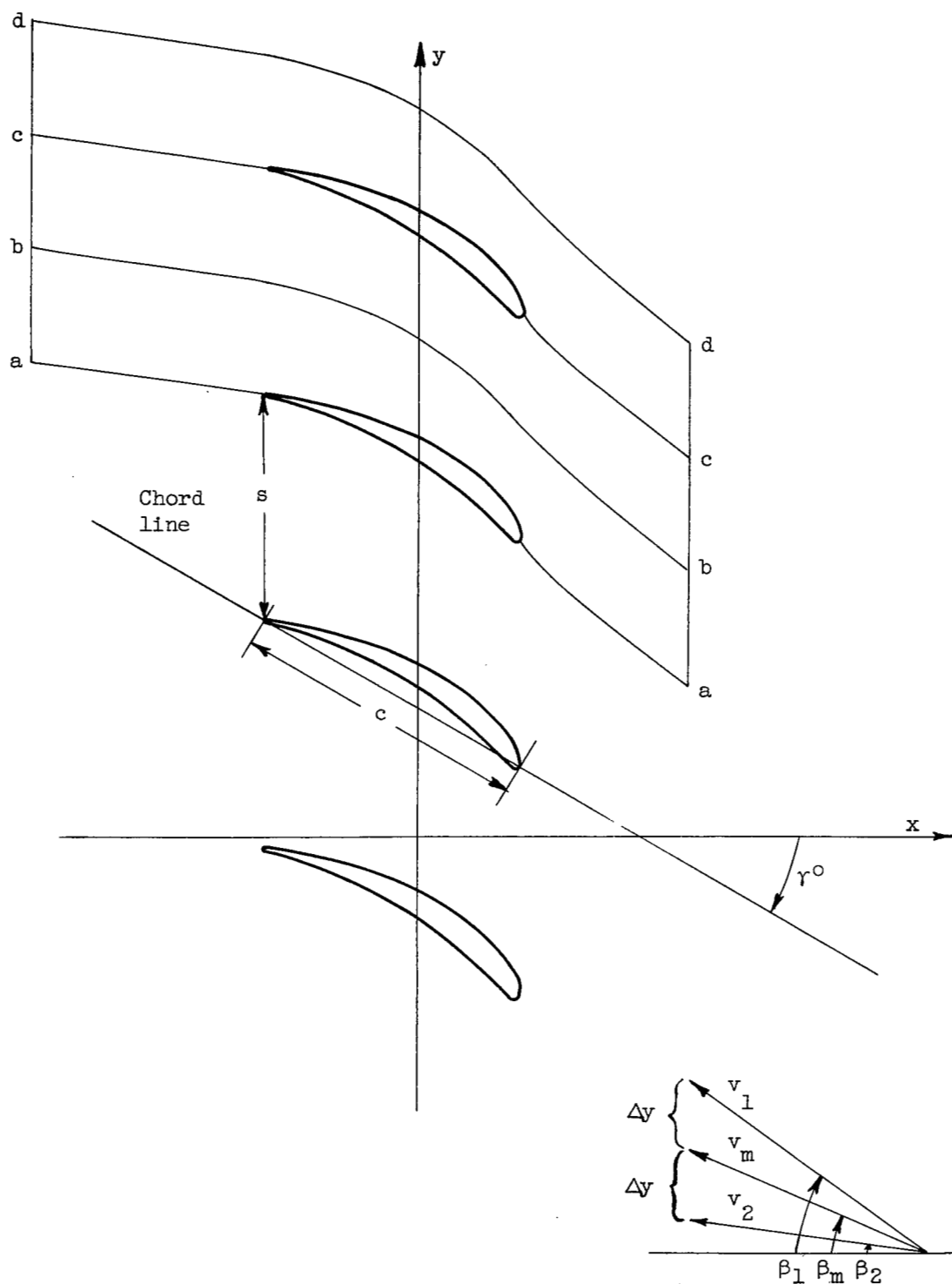


Figure 1. - Two-dimensional cascade.

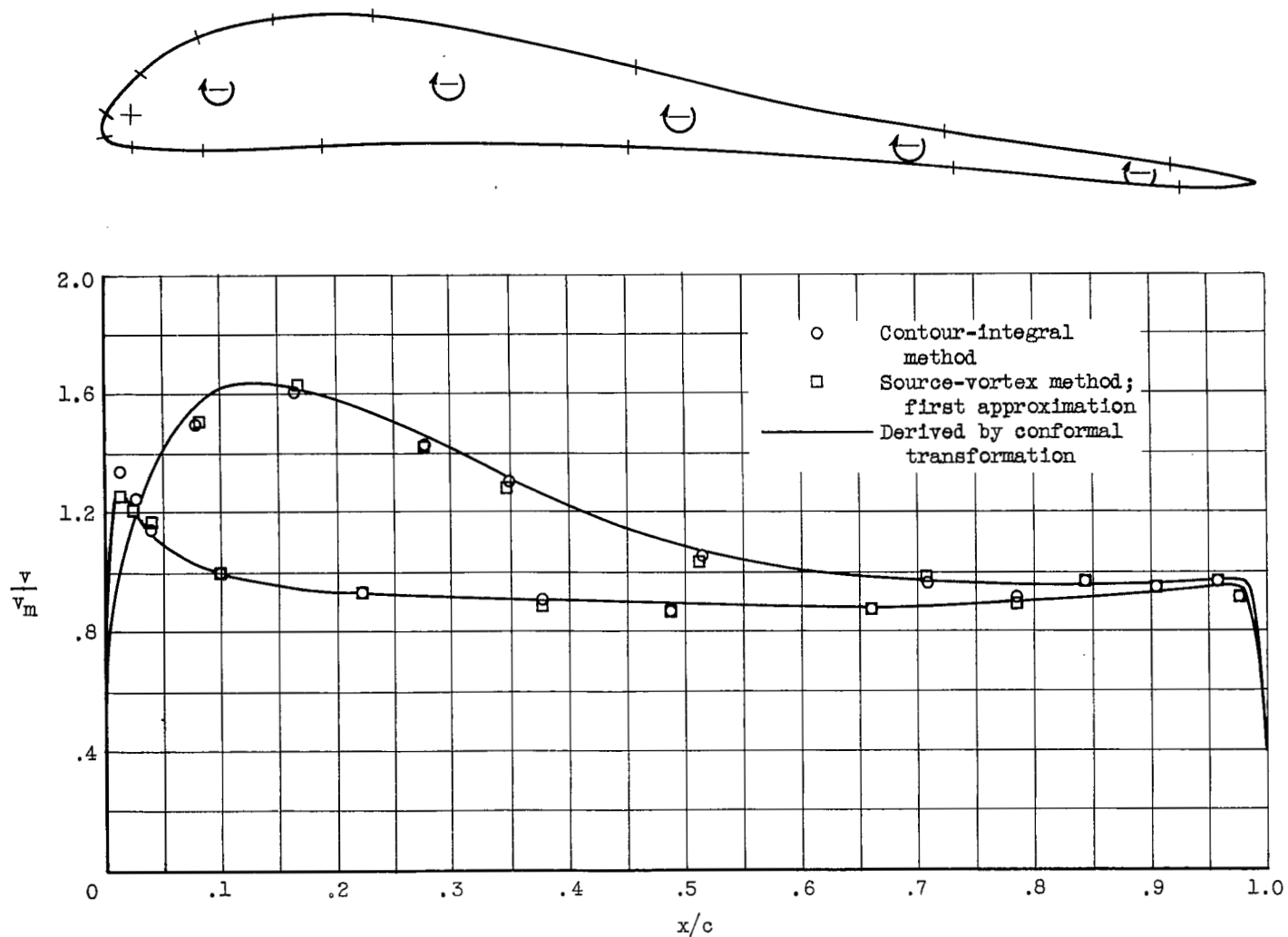


Figure 2. - Comparison of velocity distribution for blade shown, computed by methods of reference 21, with exact solution known from actual conformal-mapping function.

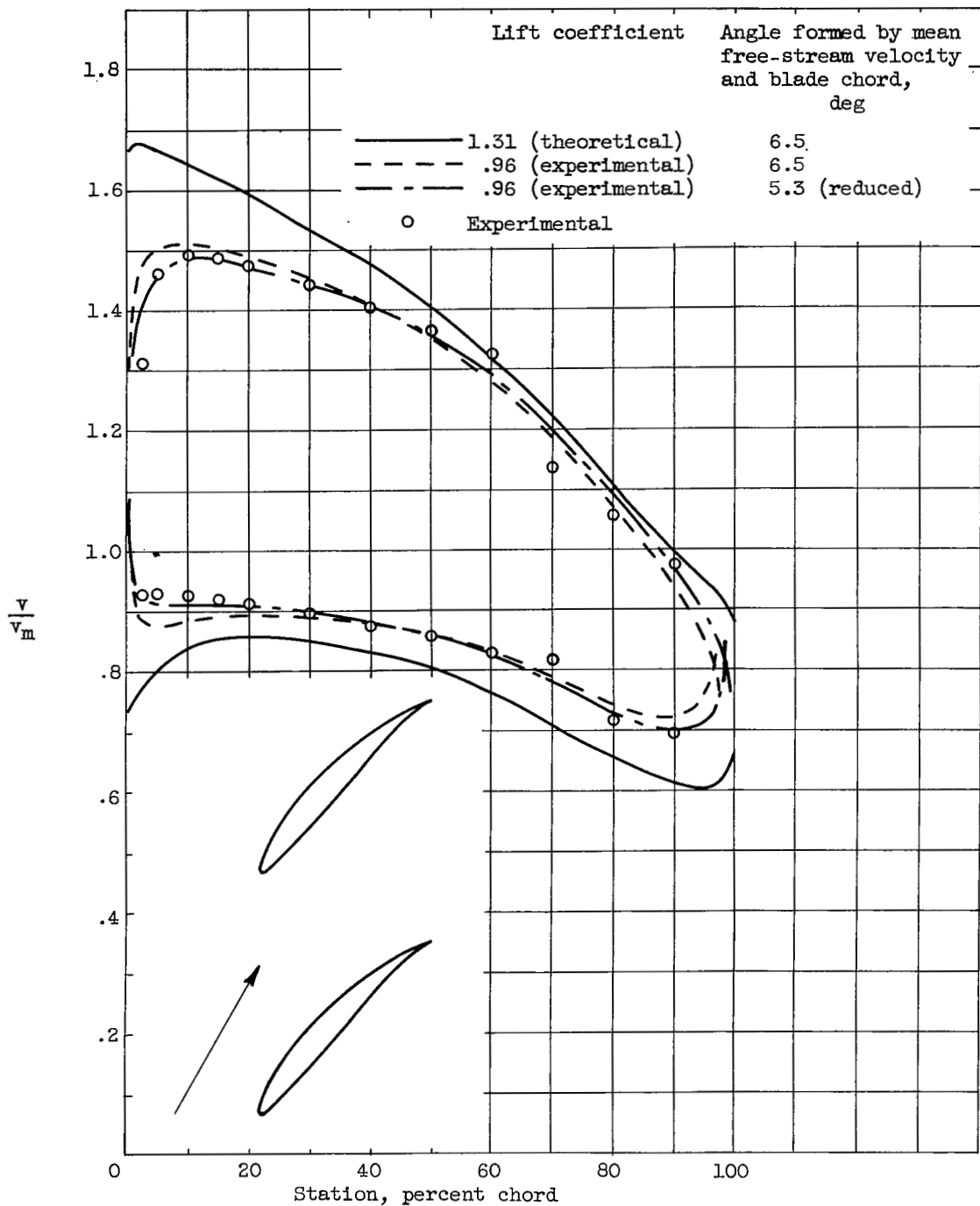


Figure 3. - Comparison of experimental and theoretical velocity distribution on airfoil in cascade. Airfoil, NACA 65-(12)10; inlet-air angle, 60° ; blade-chord angle, 45.9° ; solidity, 1.0 (ref. 33).

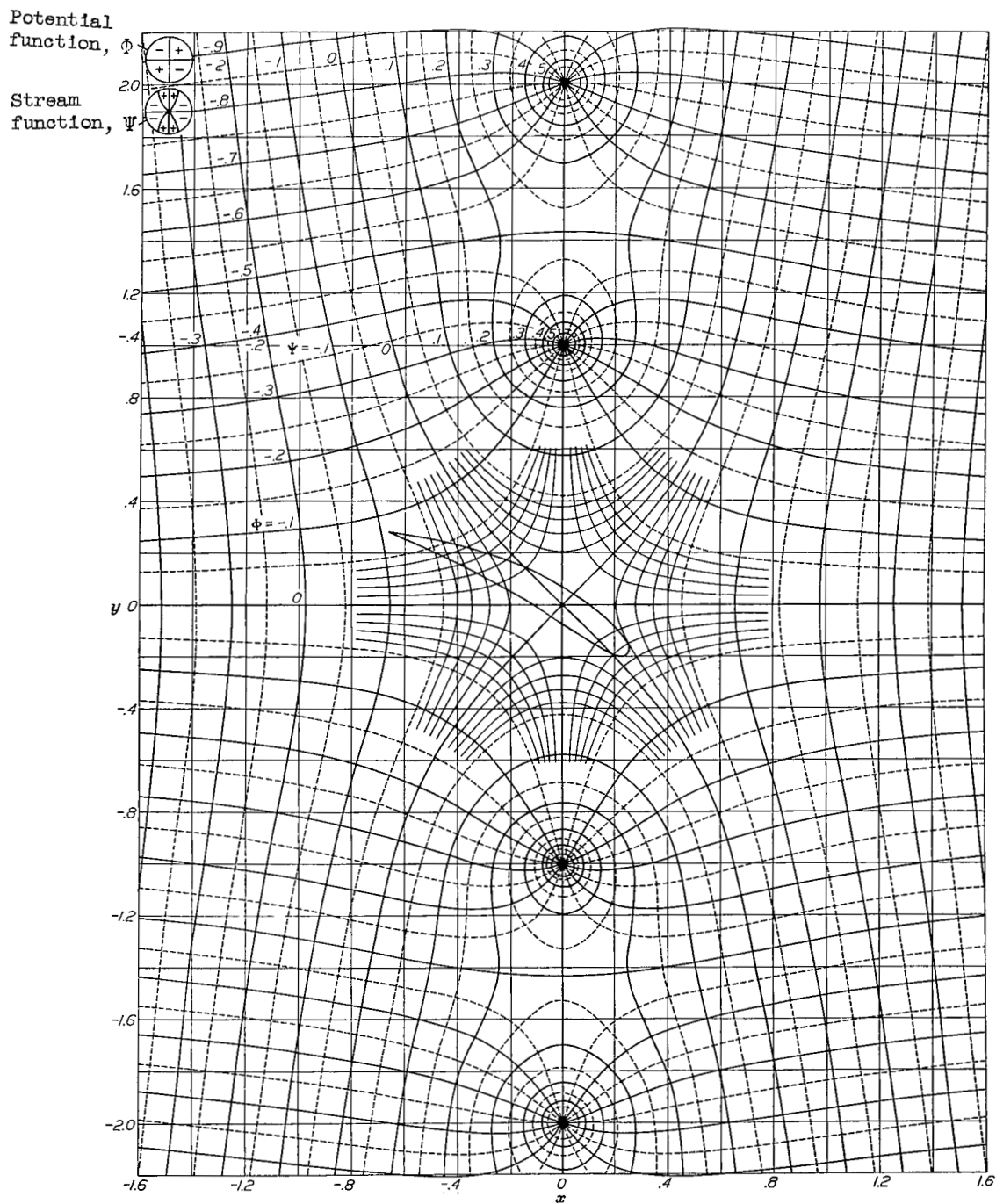


Figure 4. - Velocity potential and stream function for row of vortices of unit strength spaced at unit distance along the y-axis with central vortex omitted (ref. 34).

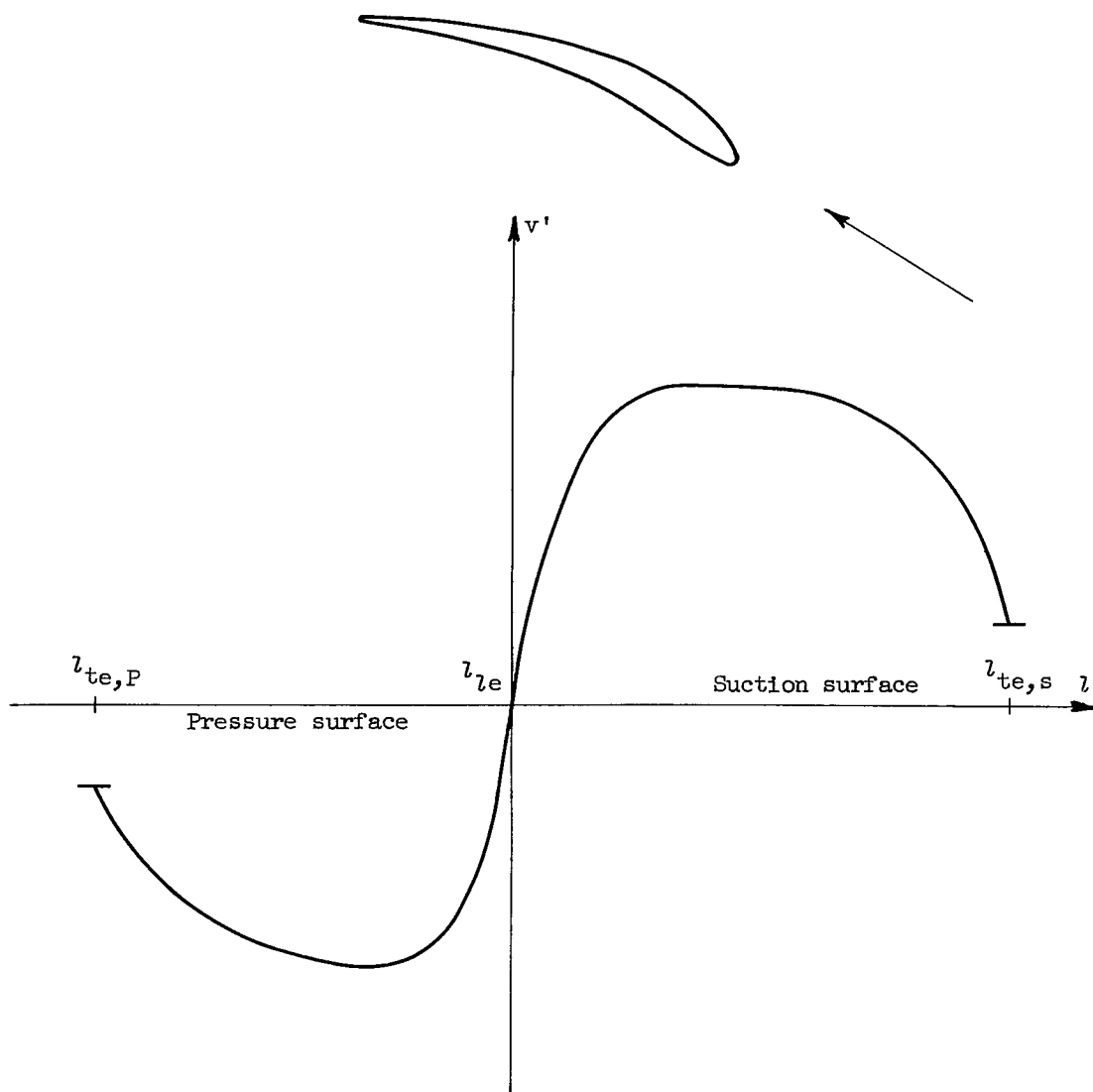


Figure 5. - Velocity distribution prescribed as function of arc length, with velocity taken as positive when velocity vector is in direction of increasing arc length.

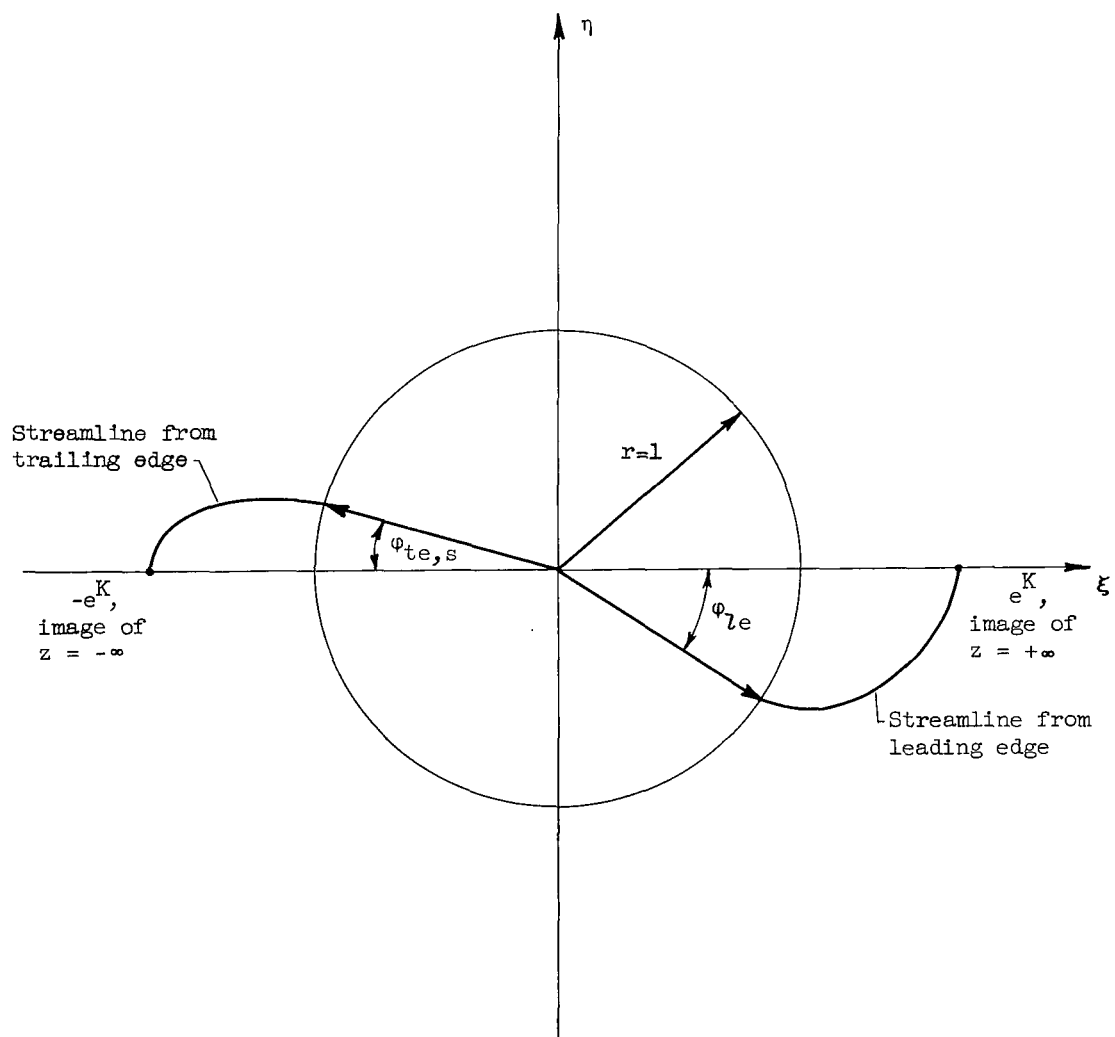
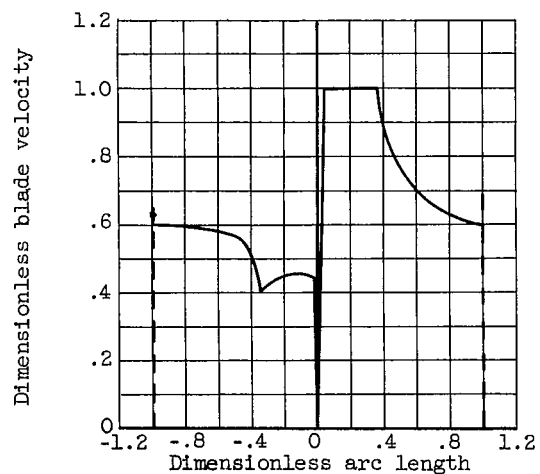
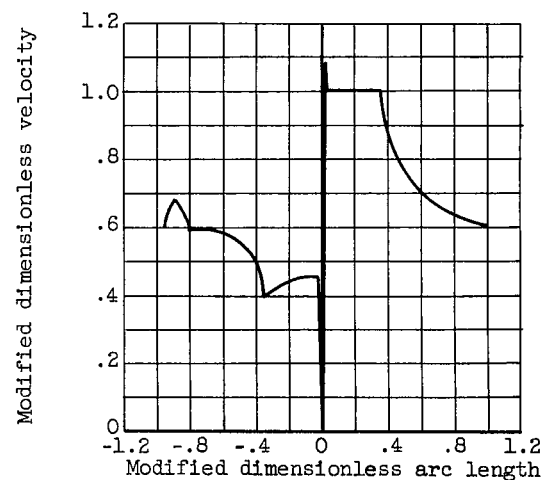


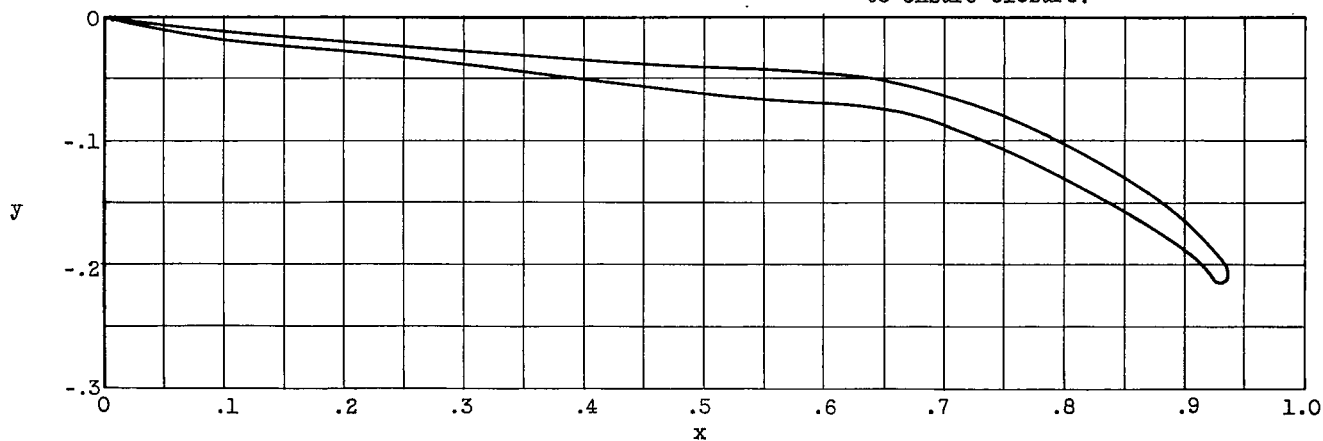
Figure 6. - Image of cascade in circle plane.



(a) Prescribed velocity distribution.



(b) Modified velocity distribution to ensure closure.



(c) Resulting blade shape.

Figure 7. - Prescribed velocity distribution used in blade design with velocity distribution modified for closure and resulting blade shape (obtained in ref. 40).

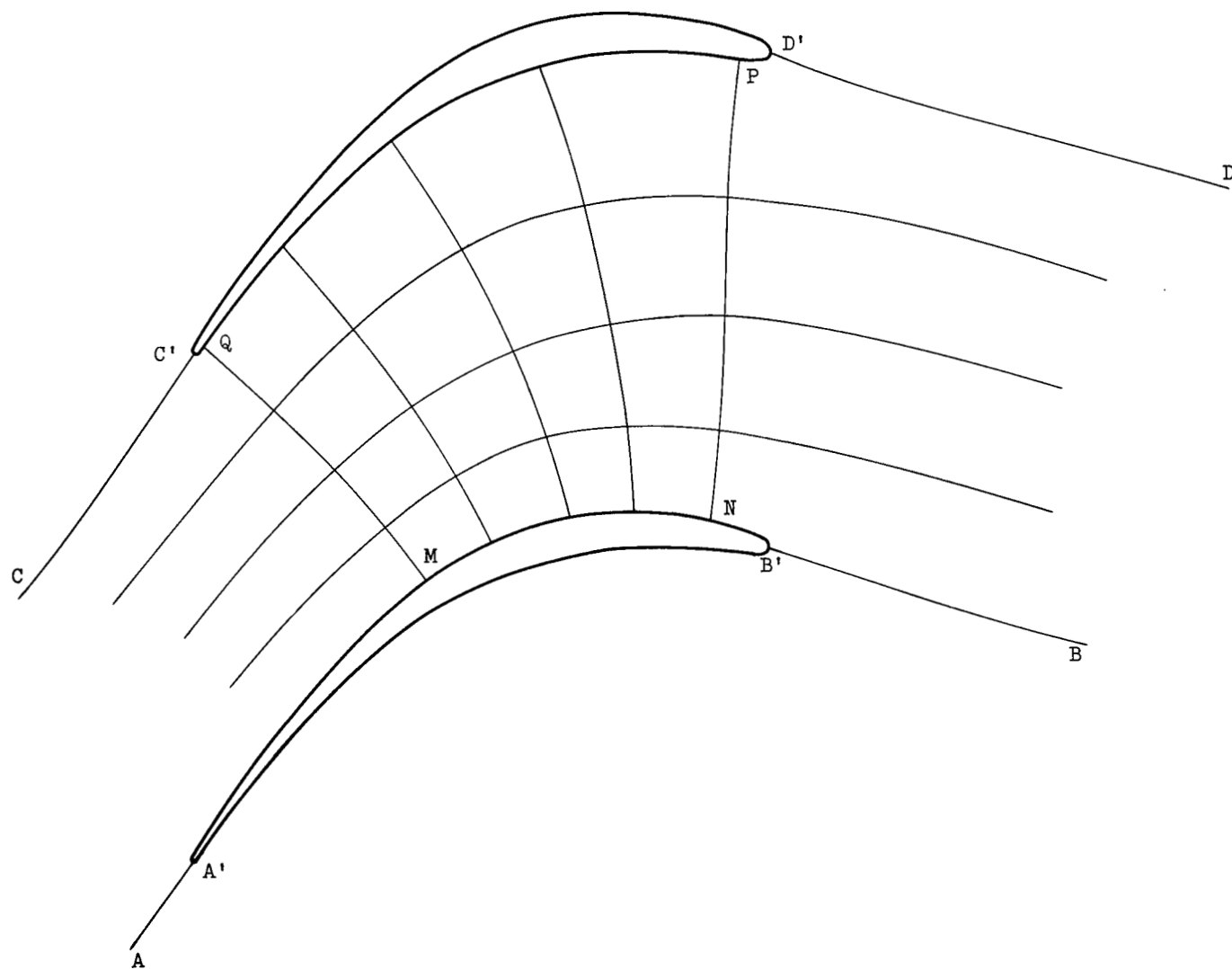


Figure 9. - High-solidity cascade showing streamlines and potential lines.

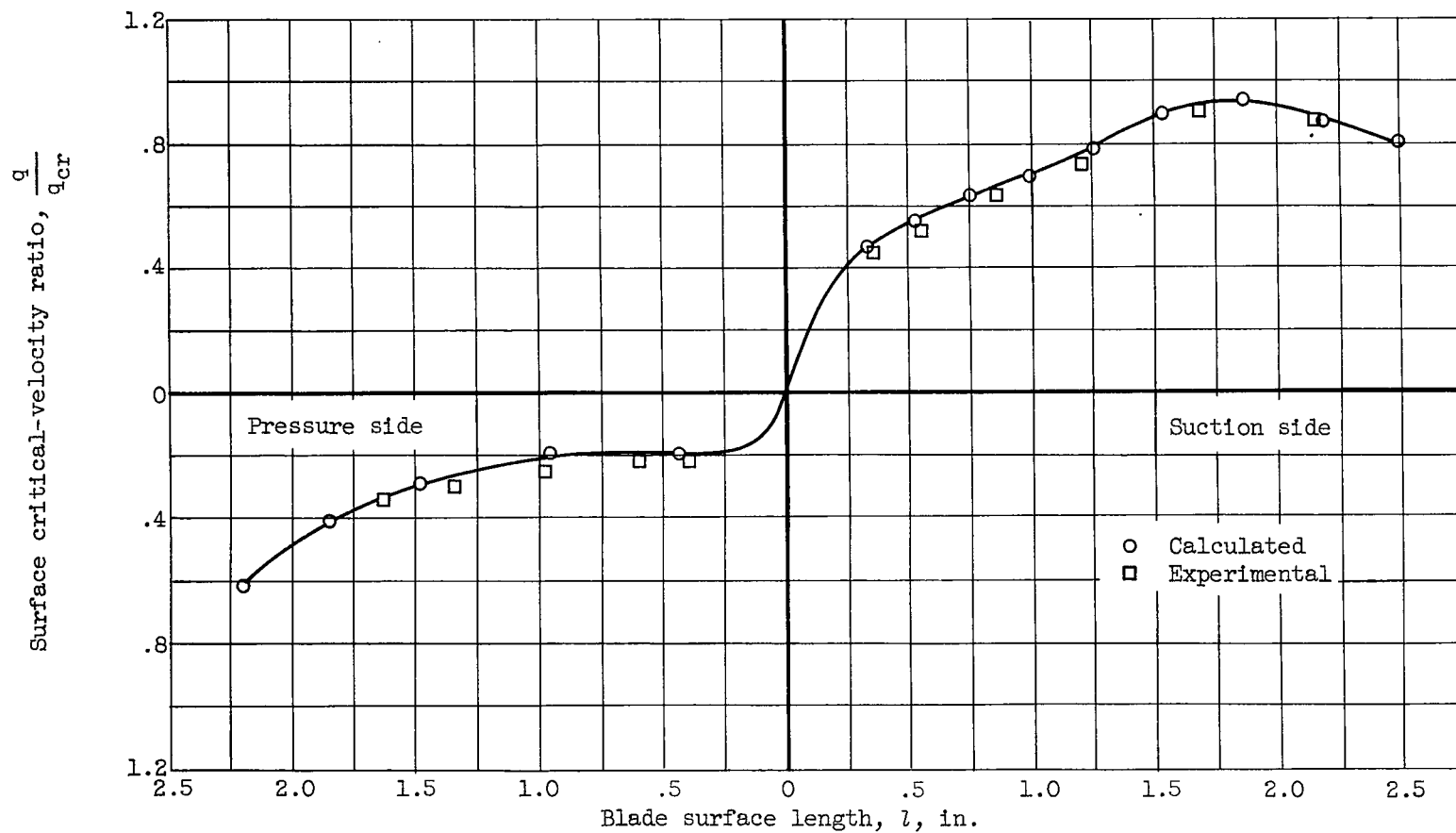


Figure 10. - Blade surface velocities at design conditions (ref. 60).

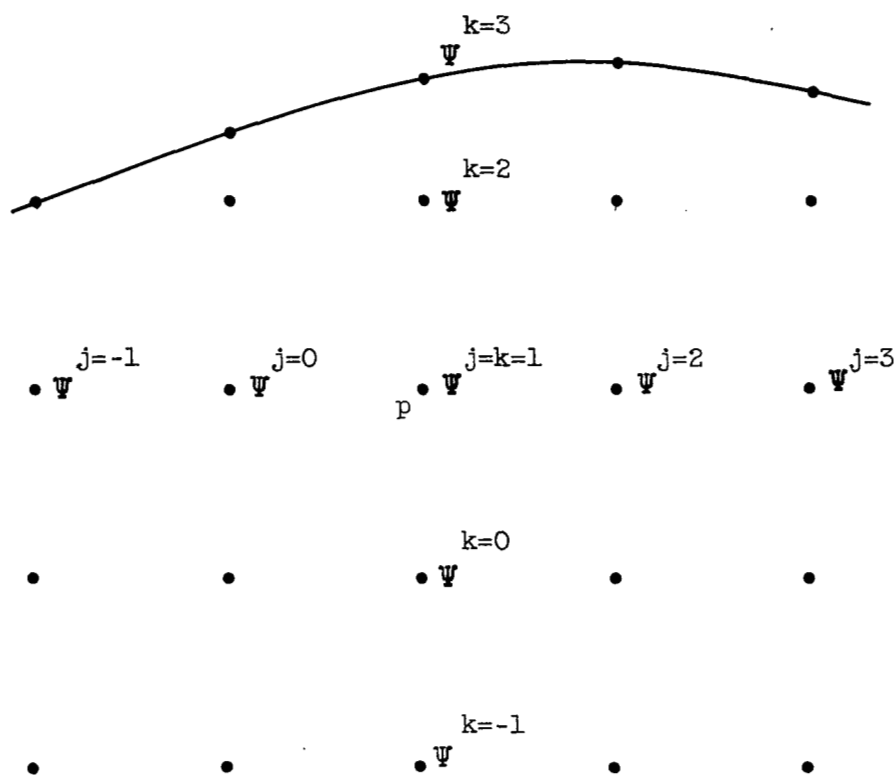


Figure 11. - A portion of grid used for finite-difference solution.

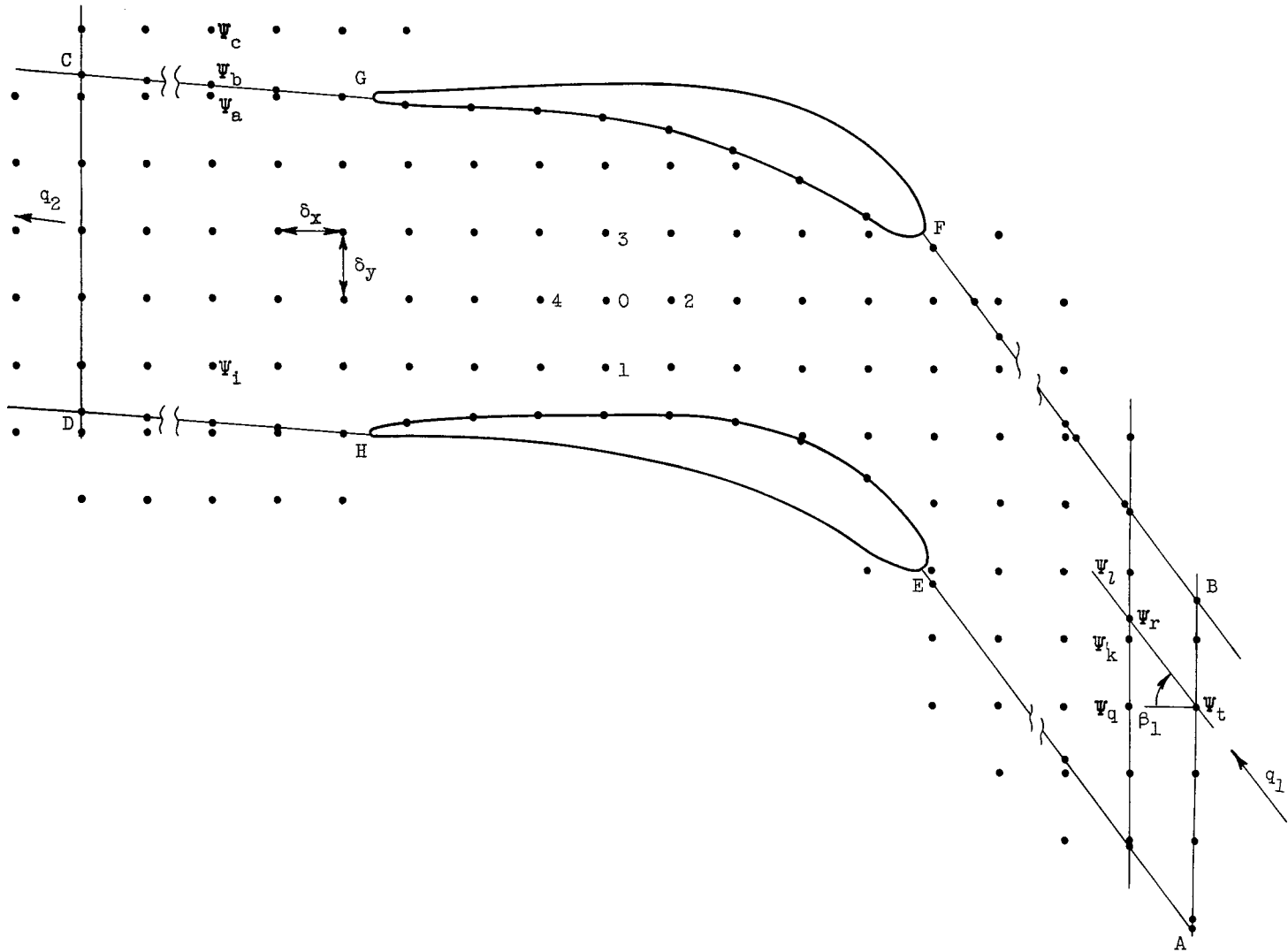


Figure 12. - Cascade channel showing grid points and boundary of solution.

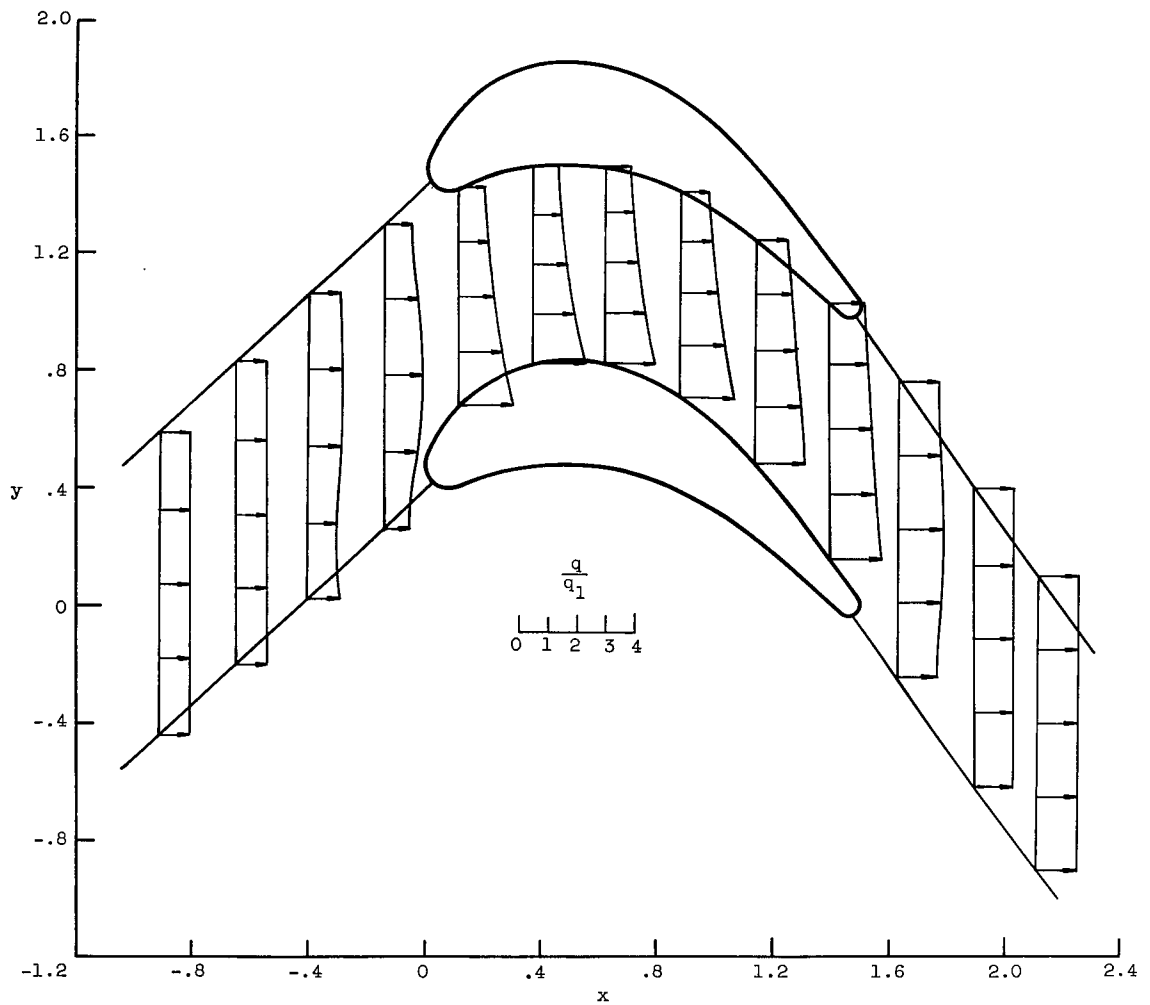


Figure 13. - Variation of magnitude of resultant velocity across channel for compressible-flow solution. Inlet Mach number, 0.42 (ref. 63).

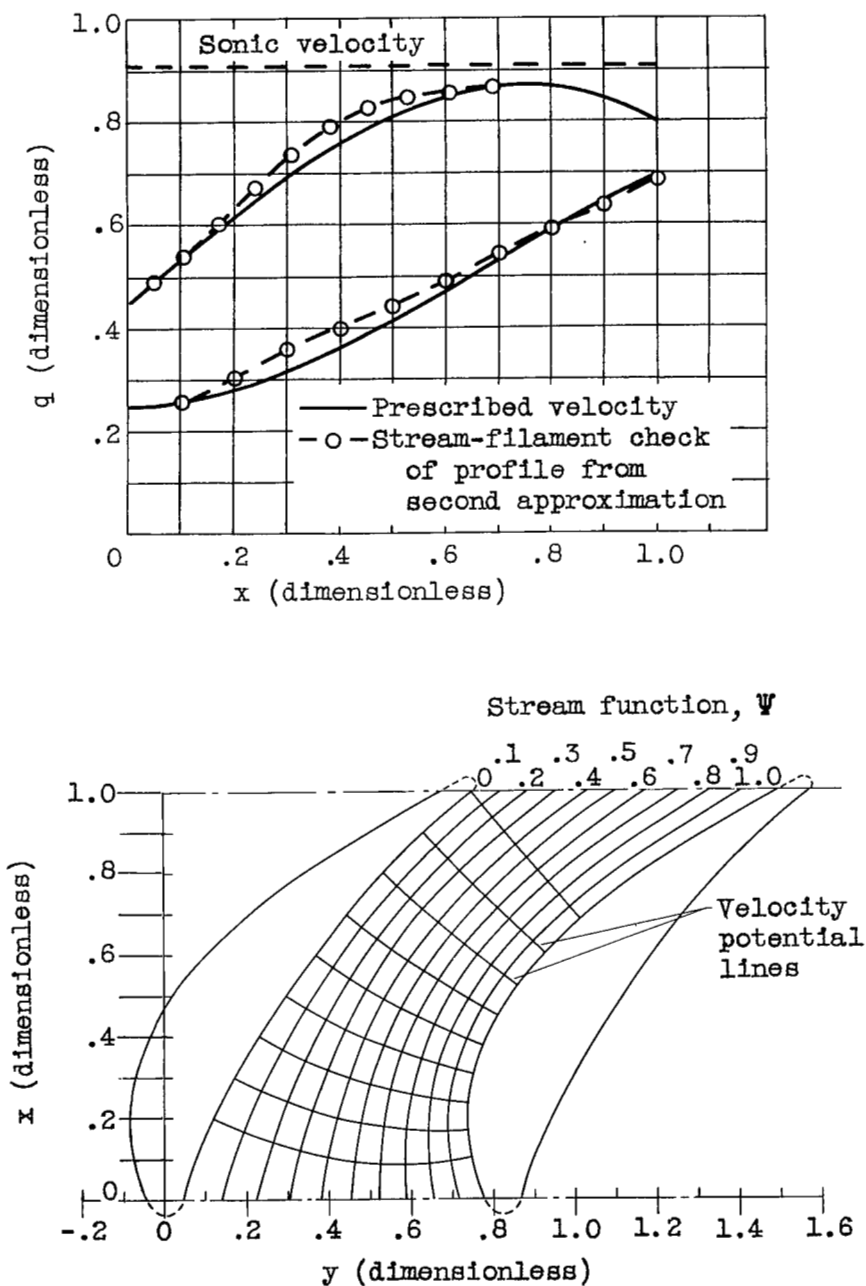


Figure 14. - Prescribed velocity distribution and resulting blade shape obtained by method of reference 72.

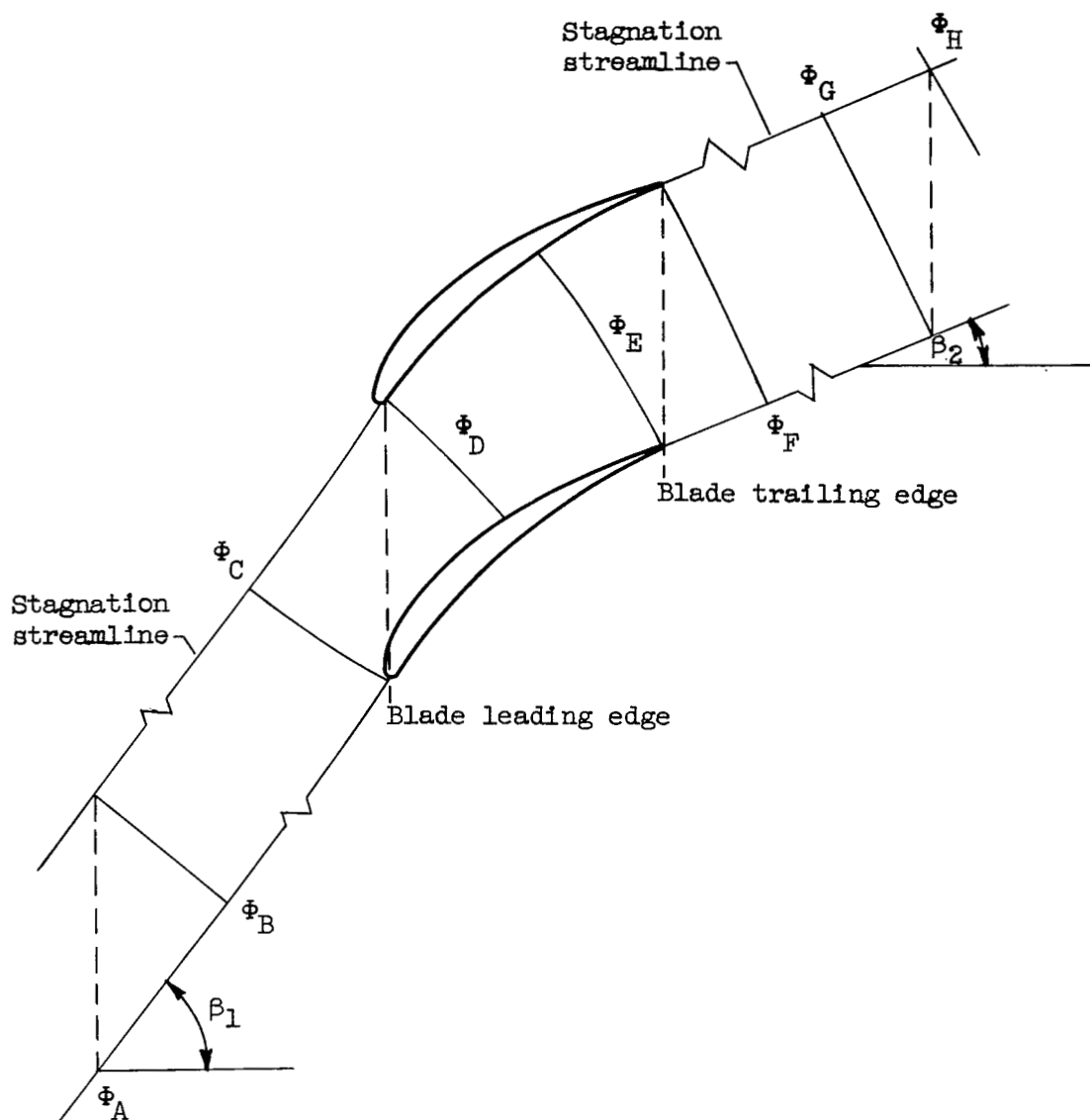


Figure 15. - Related potentials on cascade.

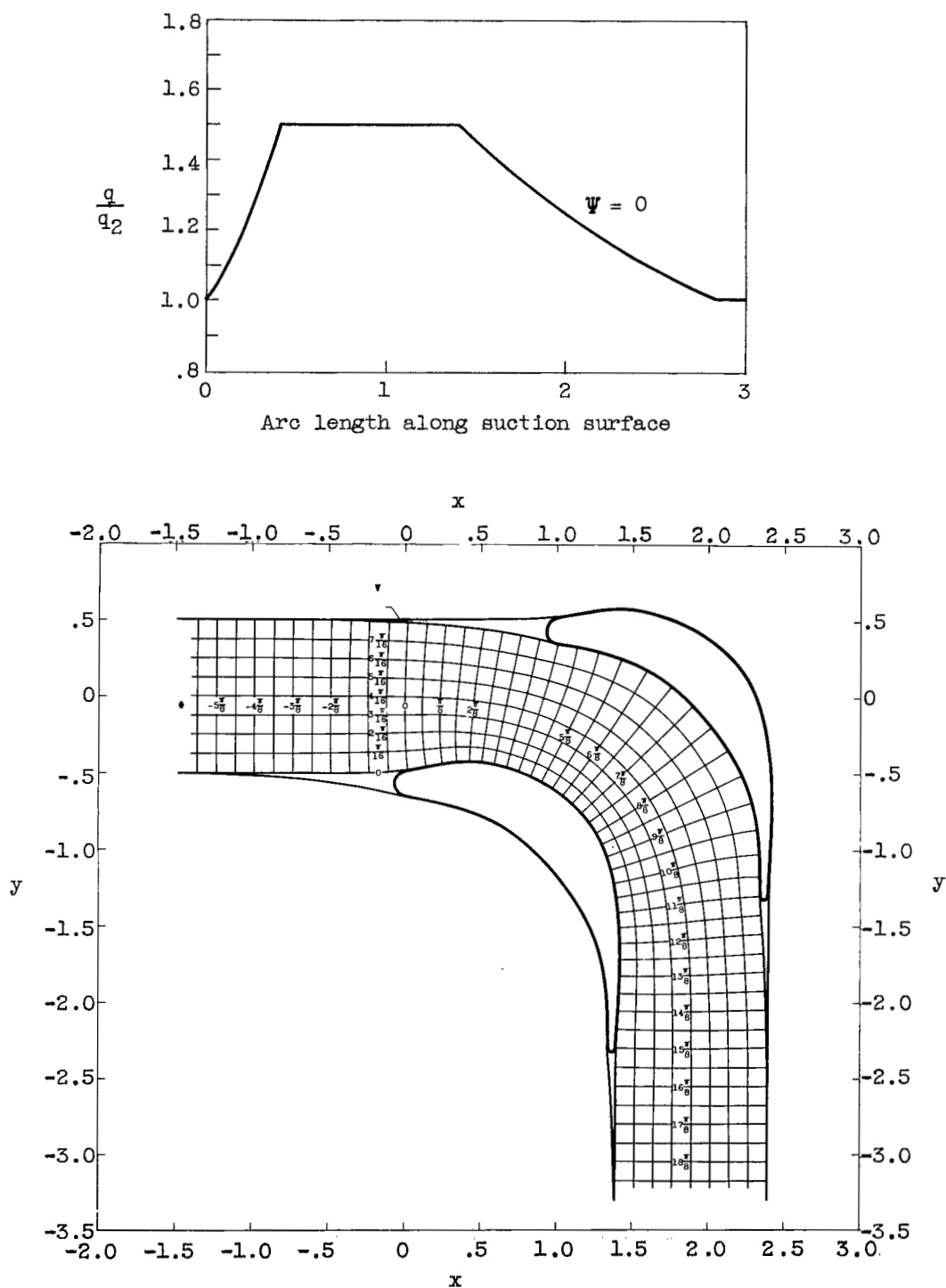
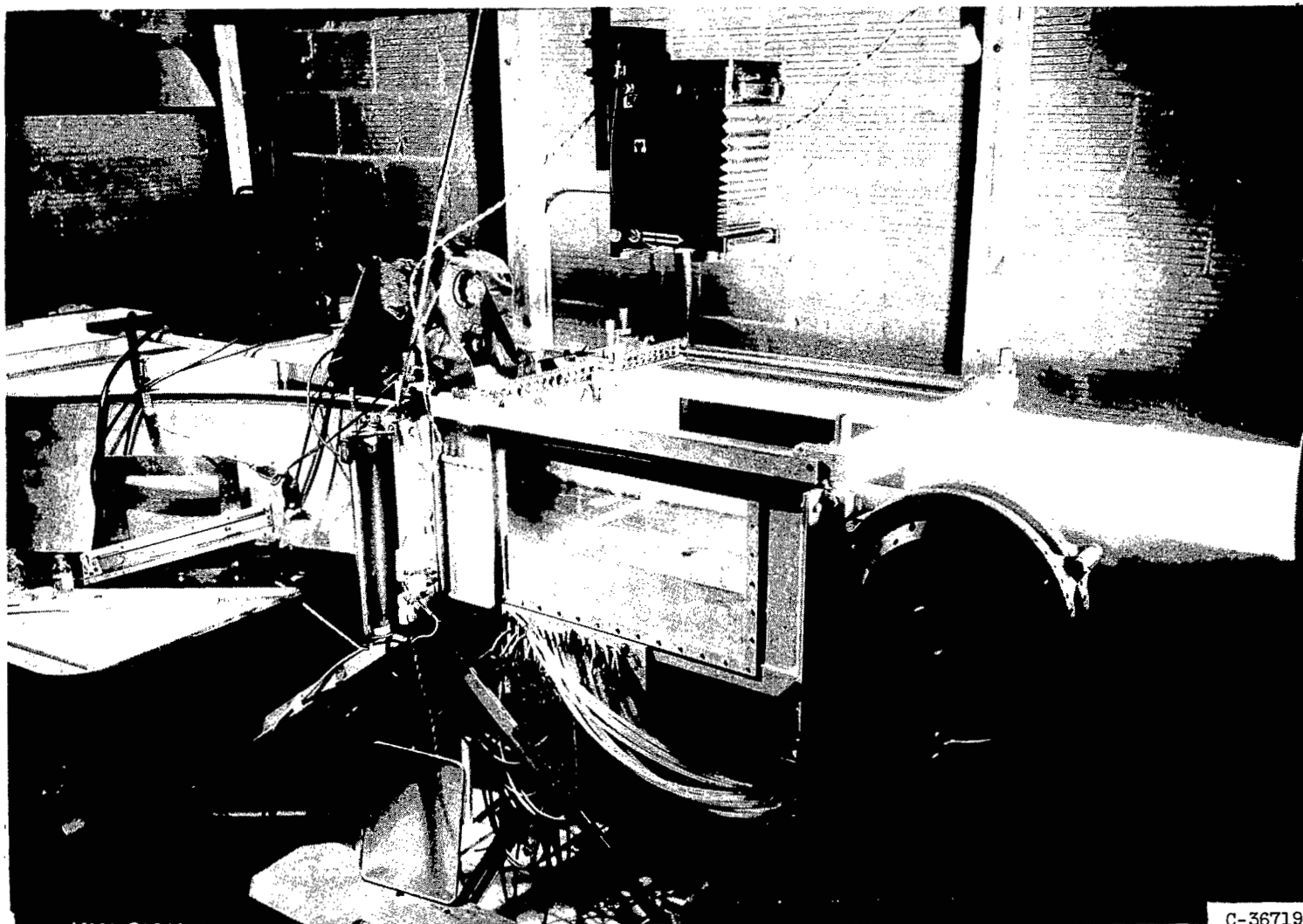


Figure 16. - Prescribed suction-surface velocity with resulting blade shape for impulse cascade with 90° turning. (Obtained by method of ref. 68.)



C-36719

Figure 17. - Equipment used in water analogy (from ref. 73).

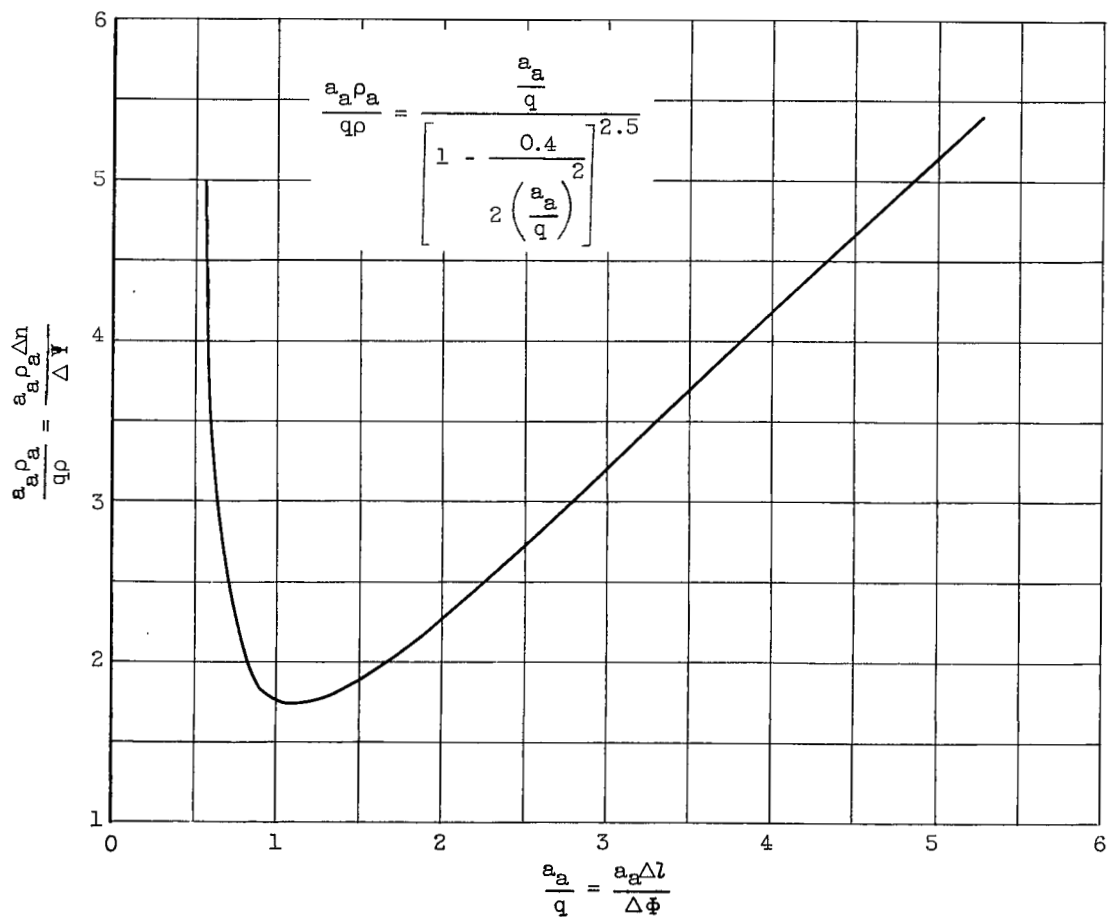


Figure 18. - Velocity - mass-flux reciprocal relation for $\gamma = 1.4$.

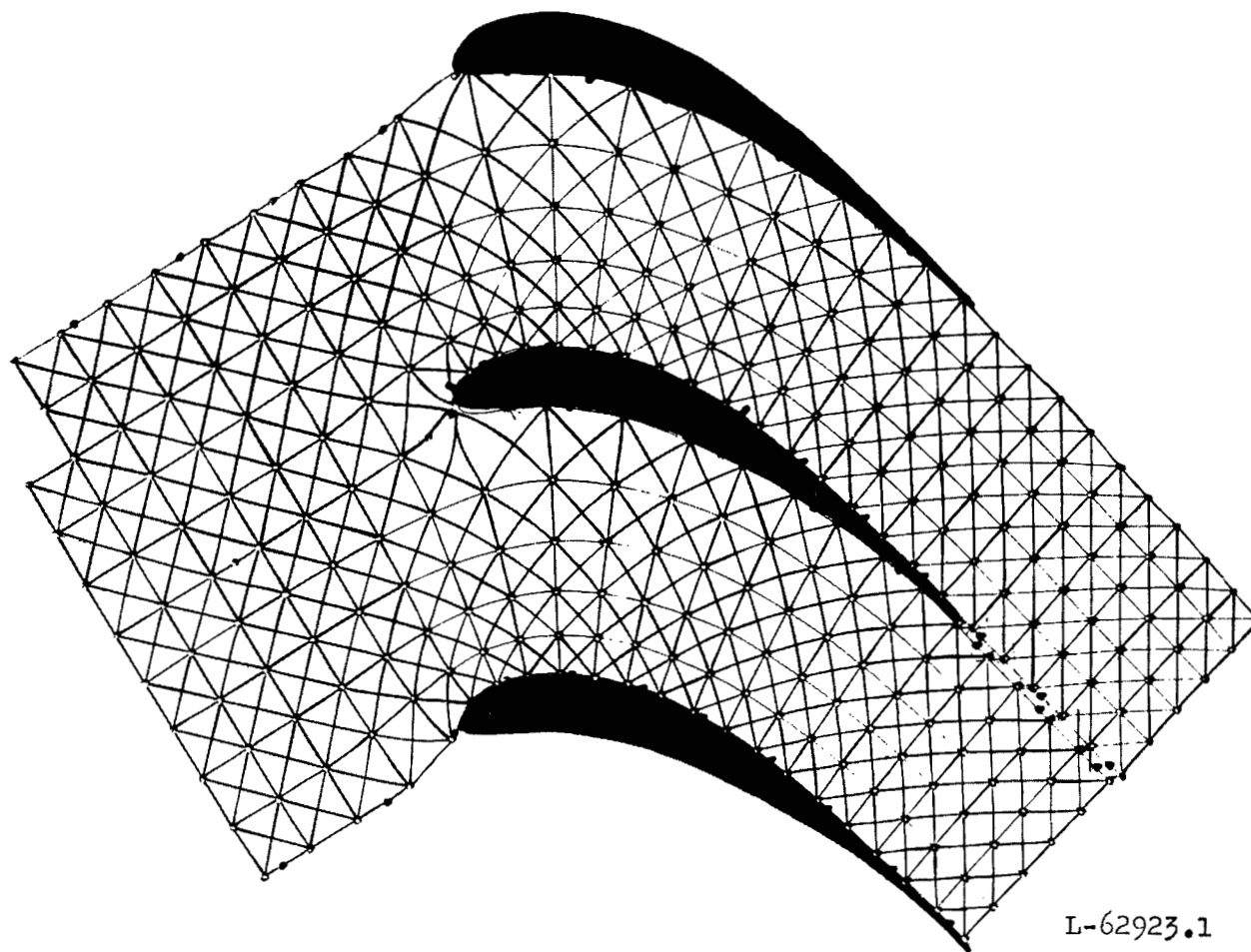
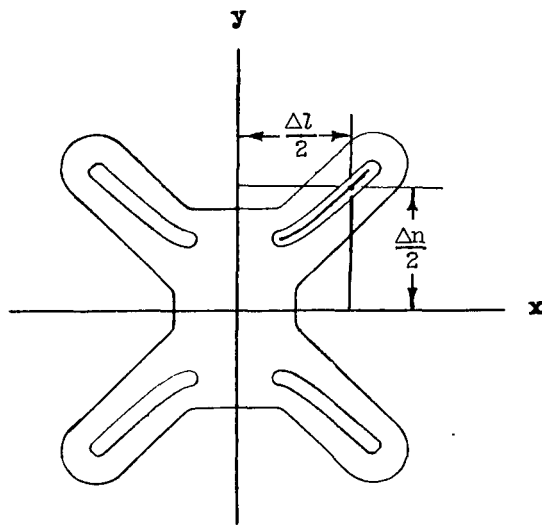


Figure 19. - Flow through adjacent channels by wire-mesh plotting (from ref. 76).



Cam ordinates	
$\frac{\Delta l}{2}$	$\frac{\Delta n}{2}$
0.2740	0.4318
.2750	.4322
.3000	.4360
.3250	.4435
.3500	.4580
.3750	.4730
.4000	.4905
.4250	.5083
.4500	.5370
.5000	.5683
.5500	.6108
.6000	.6555
.6500	.7008
.7000	.7465
.7500	.7932
.8000	.8408
.8405	.8795

Figure 20. - Mechanical device used to determine compressible flows (ref. 75).

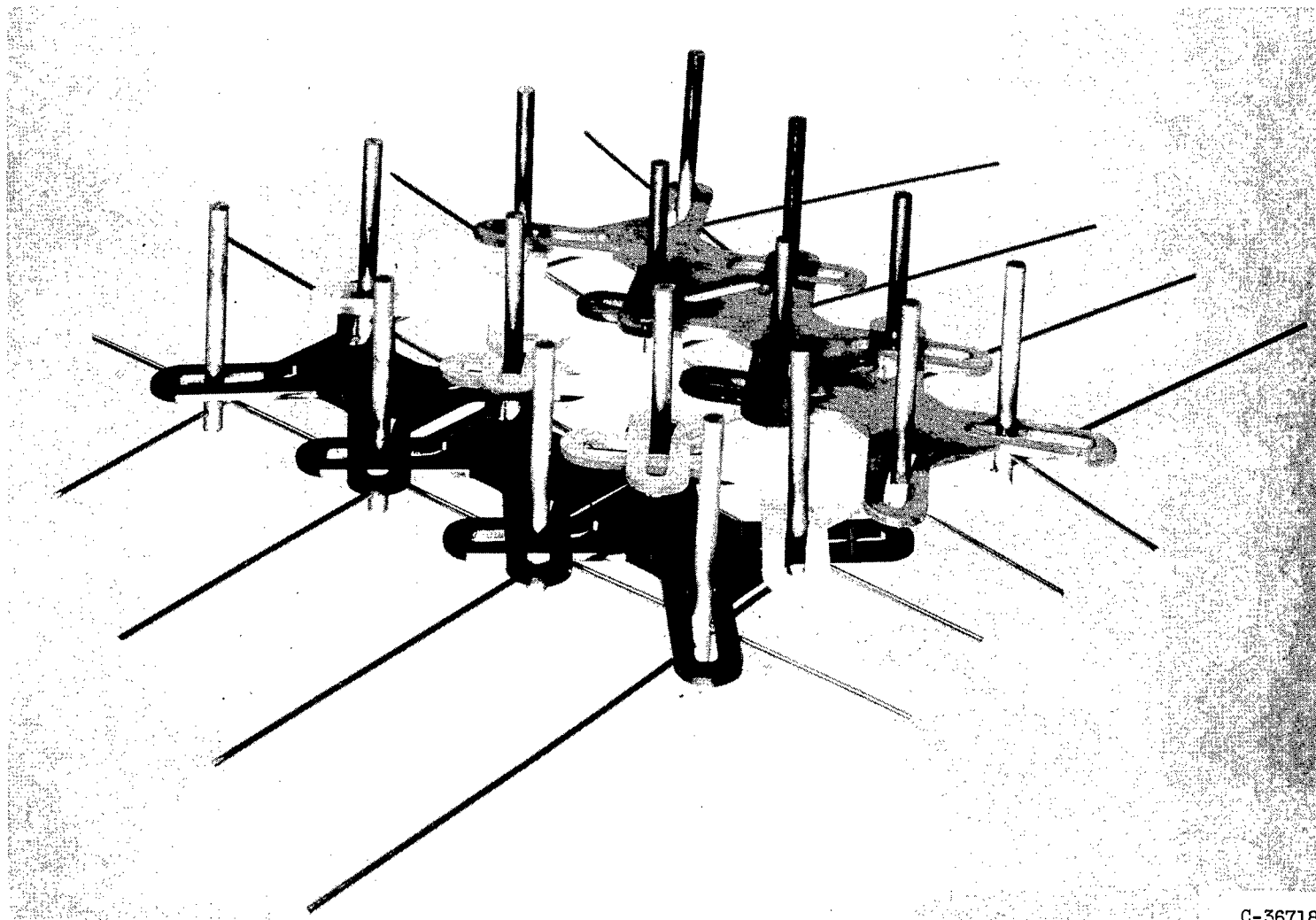


Figure 21. - Cams and pins used to determine compressible flow (ref.75).

CHAPTER V

VISCOUS FLOW IN TWO-DIMENSIONAL CASCADES

By William H. Roudebush and Seymour Lieblein

SUMMARY

Boundary-layer behavior on two-dimensional compressor blade sections is described, based on a review of available theory and experiment. The material is divided into two main sections, one presenting a qualitative discussion of boundary-layer behavior, and the other treating the quantitative aspects of boundary-layer theory as applied to cascade blades.

In the qualitative analysis, the general characteristics of laminar and turbulent boundary layers are reviewed. Instability and transition and their influence on boundary-layer behavior are discussed. An attempt is then made to construct a qualitative picture of blade losses determined over a wide range of Reynolds number, surface pressure gradient, and free-stream turbulence.

The section on quantitative boundary-layer theory discusses some approximate methods for computing the growth and separation of laminar and turbulent boundary layers. The loss in total pressure and defect in circulation resulting from blade boundary-layer growth are also considered.

INTRODUCTION

Considerable effort in the past several decades has been devoted to the determination of the two-dimensional potential or inviscid flow about airfoil and cascade sections. Comprehensive surveys of the state of potential-flow theory for two-dimensional cascades are presented in chapter IV and reference 1. These surveys indicate that the theory available for analysis of ideal two-dimensional flow, although not simple, is usable and has provided a firm understanding of the ideal flow on and around two-dimensional-cascade blade sections. A real fluid, however, is viscous, and it is well-known that the presence of viscosity exerts a considerable influence on the behavior of the flow.

The determination of the viscous flow about two-dimensional-cascade sections is considered important in the development of compressor flow theory for two reasons. First, it will aid in obtaining a basic understanding of the general nature of viscous-flow effects. Second, it will provide a background for the interpretation and correlation of experimental and theoretical cascade data. This is essential for the successful application of blade-element theory to compressor design (ch. III).

In fluid-flow theory, a complete representation of the two-dimensional viscous flow is given by the Navier-Stokes equations (ref. 2). General exact solutions of these equations have not as yet appeared. The principal advances in viscous-flow solutions have come as a result of various approximations to the basic relations. The viscous-flow literature is covered extensively in reference 3, published in 1938. More recent literature is reviewed in reference 4. Compressible boundary-layer flow is surveyed in reference 5.

Concurrently with the development of boundary-layer theory, considerable experimental research on boundary-layer behavior has been conducted. These experiments not only provide empirical data necessary for obtaining approximate solutions to the boundary-layer equations, but contribute to the establishment of a valuable qualitative picture of the behavior of boundary layers.

This chapter reviews the problem of determining viscous effects on the two-dimensional incompressible flow about compressor blade profiles in cascade. The material is divided into two major parts, entitled QUALITATIVE BOUNDARY-LAYER THEORY and QUANTITATIVE BOUNDARY-LAYER THEORY. In the first part, some of the more important terminology is presented, and general trends to be anticipated in real fluid flows are indicated. Laminar and turbulent boundary layers, instability, transition, and separation are discussed. The general effects of Reynolds number on total-pressure loss for several levels of blade loading are evaluated qualitatively. In the second part, selected methods are presented for actually calculating laminar- and turbulent-boundary-layer growth and predicting separation. In addition, some consideration is given to the computation of the defect in circulation and the total-pressure loss caused by the growth of the blade surface boundary layers. The analysis indicates the extent to which current viscous-flow theory can predict the important phenomena involved in the flow of a real fluid about a two-dimensional cascade.

SYMBOLS

The following symbols are used in this chapter:

C_D drag coefficient

C_{fr}	local friction coefficient
C_L	lift coefficient
c	chord length
H	boundary-layer form factor, δ^*/θ^*
I	turbulence intensity
i	incidence angle, angle between inlet-air direction and tangent to blade mean camber line at leading edge, deg
L	scale of turbulence
l^*	characteristic length
n	coordinate normal to blade surface
P	total or stagnation pressure
$\Delta \bar{P}$	mass-averaged loss in total pressure
p	static or stream pressure
q	arbitrary constant
Re_c	Reynolds number based on chord length, V_{1c}/ν
Re_δ	Reynolds number based on boundary-layer thickness, $V_0\delta/\nu$
Re_θ	Reynolds number based on boundary-layer momentum thickness, $V_0\theta^*/\nu$
s	coordinate along direction of blade surface
s'	distance along blade surface from leading to trailing edge
u	s -component of velocity in boundary layer
V	air velocity
v	n -component of velocity in boundary layer
x	abscissa in cascade plane (fig. 2)
y	ordinate in cascade plane (fig. 2)

α	angle of attack, angle between inlet-air direction and blade chord, deg
β	air angle, angle between air velocity and x-axis, deg
Γ	turbulent-boundary-layer parameter, $(\theta/V_0)(dV_0/ds)$
δ	boundary-layer thickness
δ^*	boundary-layer displacement thickness
ζ	turbulent-boundary-layer parameter, $(C_{fr}/2)Re_\theta^q$
θ	turbulent-boundary-layer parameter, $\theta^*Re_\theta^q$
θ^*	boundary-layer momentum thickness
λ	Pohlhausen parameter, $(\delta^2/\nu)(dV_0/ds)$
μ	viscosity
ν	kinematic viscosity
ρ	density
σ	solidity, ratio of chord to spacing
τ	time
$\hat{\tau}$	shear stress
$\hat{\tau}_w$	shear stress at wall
$\bar{\omega}$	total-pressure-loss coefficient

Subscripts:

cr	critical
f.p.	flat plate
m	mean of upstream and downstream conditions
n	n-direction
ref	reference

s	s-direction
te	trailing edge
tr	transition
0	outer edge of boundary layer
1	upstream at infinity
2	downstream at infinity

QUALITATIVE BOUNDARY-LAYER THEORY

General Considerations

For an ideal fluid, the velocity tangent to a fixed surface is generally nonzero at the surface and (for small surface curvature) is nearly equal to the velocity at points near the surface, as shown in figure 1(a). A viscous fluid, however, adheres to the surface over which it is flowing, so that the velocity tangent to the surface is zero at the surface. The velocity near the surface rapidly increases and attains the value of the free-stream velocity at a short distance from the surface, as shown in figure 1(b). The region of flow in which the local velocity is retarded is referred to as the boundary layer. The static pressure across the boundary layer is nearly constant.

In two-dimensional-cascade flow, boundary layers develop on both the suction and pressure surfaces of the blade. These surface boundary layers then come together at the blade trailing edge and form the blade wake, as shown in figure 2. As the wake moves downstream, a mixing takes place between the wake and free stream and, through viscous action, the flow becomes uniform at some distance behind the blade trailing edge.

Although, in many practical problems, the blade surface boundary layer constitutes a small portion of the flow field, it plays a decisive part in the determination of the actual flow characteristics of the cascade. The effect of blade boundary-layer development on cascade losses is obvious, since the resulting wake formation contains a defect in total pressure. The surface boundary layers can also exert a strong influence on the surface pressure distribution and outlet-angle characteristics of the blade. If the boundary layer is very thin, the pressure distribution obtained from potential-flow calculations over the original body will be a good approximation to the actual distribution. As the boundary layer thickens, however, the actual pressure distribution will depart from the potential-flow determination. Under certain conditions, the boundary layer actually separates from the surface of the blade

somewhere in advance of the trailing edge. In this event, the entire flow pattern about the cascade is altered by the displacement of fluid accompanying such separation, and the potential-flow solution about the original profile loses its significance almost completely.

It is evident, therefore, that a knowledge of general boundary-layer behavior is vital to the accurate prediction and interpretation of cascade flow characteristics. In the present section, the discussion is presented in the following order:

- (1) Preliminary boundary-layer definitions and concepts
- (2) Description of laminar boundary layer in some detail with particular emphasis on effects of Reynolds number
- (3) Description of turbulent boundary layer and comparison with laminar layer
- (4) Discussion of instability and transition with regard to their importance in cascade operation and data interpretation
- (5) Combination of considerations (1) to (4) to form a qualitative picture of the loss spectrum as influenced by pressure gradient and Reynolds number variation

Boundary-Layer Concepts

Types of boundary layers. - The two general types of boundary layer occurring on blade surfaces are designated laminar and turbulent. The boundary layer is initially laminar and usually becomes turbulent somewhere along the blade surface. The boundary layer is said to be in a laminar state if the flow, at any instant, can be represented as a sequence of layers, each layer tracing a path essentially tangent to the surface of the cascade blade. In this case, the velocity varies uniformly through the boundary layer from a value zero at the blade surface to a value almost equal to the free-stream velocity at a short distance from the surface. The boundary layer in a turbulent state is characterized by a rapid random fluctuation with time of the velocity at any point and a large interchange of momentum. The velocity is again zero at the blade surface, and the mean velocity averaged with respect to time varies continuously through the boundary layer and attains a value approaching the free-stream velocity a short distance from the surface.

Typical velocity distributions through the boundary layer for the laminar and turbulent cases are illustrated in figure 3. The turbulent-flow velocities remain higher closer to the boundary because of the turbulent infiltration of high-energy particles into the boundary layer.

In the laminar flow, the interchange of momentum is due only to the shear stress exerted between two neighboring layers of fluid. This difference between the two types is manifest when an adverse pressure gradient is impressed on the boundary layer by a deceleration of the main stream. A turbulent boundary layer often receives sufficient momentum influx to advance some distance against an adverse pressure gradient before separation occurs. The laminar boundary layer, on the other hand, with very little momentum influx, is unable to advance far into the face of a rising pressure. Eventually, in either case, the particles near the wall are slowed down to a stop and finally actually reverse their direction and begin to flow upstream (fig. 4). This results in separation of the through-flow from the blade surface.

In the range of Reynolds number and turbulence of conventional cascades and compressors, the boundary layer is laminar over the forward portion and turbulent over the rearward portion of the blade. Since the loss characteristics of these two boundary-layer regions are markedly different, the location and nature of the transition between the regions are significant in determining the magnitude of the resulting wake.

Boundary-layer parameters. - A definition of certain basic terms is prerequisite to any further discussion of boundary layers. The more important of these terms are defined in this section.

There are several boundary-layer thickness parameters that occur throughout the literature. The actual full physical thickness δ is taken to be the distance normal to a fixed surface wherein the velocity in the boundary layer attains some fixed percentage, say 99 percent, of the free-stream velocity. The boundary-layer velocity theoretically equals the free-stream velocity only at an infinite distance normal to the surface. However, for practical considerations, the two can usually be considered equal at a short distance δ from the surface (fig. 1(b)).

Since the velocity in the boundary layer goes to zero at the wall, the weight flow in the boundary-layer region is decreased. This decrease in weight flow can be expressed in terms of a length δ^* , called the displacement thickness, obtained by dividing the integrated defect in weight flow within the boundary layer by the free-stream velocity $V_{0,s}$ at the outer edge of the layer. For incompressible flow, this gives

$$\delta^* = \int_0^{\delta} \left(1 - \frac{u}{V_{0,s}} \right) dn$$

in which the coordinate n is taken in a direction normal to the surface (similarly, the coordinate s represents distance in the direction of the surface, fig. 1(a)); u is the local velocity in the s -direction within the boundary layer; and $V_{0,s}$ is the velocity in the s -direction at the outer edge of the boundary layer.

In a similar manner, a momentum thickness θ^* is obtained to represent the corresponding decrease in momentum in the boundary layer. The momentum thickness is obtained by dividing the integrated defect in momentum by $V_{0,s}^2$ to give

$$\theta^* = \int_0^\delta \frac{u}{V_{0,s}} \left(1 - \frac{u}{V_{0,s}} \right) dn$$

The momentum thickness in the wake is directly related (as shown in a later section) to the loss in total pressure across a cascade.

Another parameter frequently encountered is the boundary-layer form factor H , defined as the ratio of displacement thickness to momentum thickness:

$$H = \frac{\delta^*}{\theta^*}$$

The form factor appears as a parameter in approximate boundary-layer theory in the determination of the magnitude of the momentum thickness. It also gives a rough indication of the state of the boundary layer with regard to possible separation.

One of the most significant parameters characterizing boundary-layer behavior is the Reynolds number, a dimensionless parameter proportional to the ratio of inertial force to viscous force, given by

$$Re = \frac{V_i l^*}{\nu}$$

where V_i is a characteristic velocity of the flow, l^* is a characteristic length, and ν is the kinematic viscosity. In particular, V_i can be taken as the upstream velocity V_1 and l^* as the blade chord c to give what is called the body Reynolds number, or blade-chord Reynolds number, $Re_c = V_1 c / \nu$. In another formulation, the velocity can be taken to be the velocity V_0 at the outer edge of the boundary layer and the characteristic length as the momentum thickness θ^* to give the boundary-layer Reynolds number $Re_\theta = V_0 \theta^* / \nu$, where Re_θ is a function of the particular location at which V_0 and θ^* are computed. As will be indicated later, Reynolds number exercises a considerable influence on the boundary-layer growth, instability, and transition.

Loss parameters. - In the flow about airfoil sections, friction exerts a tangential force that opposes the forward motion of the airfoil.

The retarding component arising from the friction force is called the friction drag. In addition to friction, a retarding force component is also obtained from the normal pressure forces of the real flow. This force component is called the form drag. The total drag of the section, which is the sum of the friction and form drags, is called the profile drag. Ordinarily, the profile drag force is expressed as a drag coefficient C_D , defined as the drag force per unit span divided by a reference kinetic head and the chord length.

For the isolated airfoil, at a distance sufficiently far downstream that static pressure is uniform normal to the flow direction, the drag coefficient can be related to the momentum-thickness ratio θ^*/c by the following equation (ref. 6):

$$C_D = 2 \left(\frac{\theta^*}{c} \right)$$

The downstream wake momentum thickness appearing in this relation is directly related to the momentum thickness of the surface boundary layers at the blade trailing edge. An analogous approximate equation

$$C_D \approx 2 \left(\frac{\theta^*}{c} \right)_{te} \frac{\cos \beta_m}{\cos \beta_{te}} \left[1 + \frac{1}{2} \left(\frac{\theta^*}{c} \right)_{te} \frac{\sigma H_{te}^2}{\cos \beta_{te}} \right]$$

exists between the drag coefficient based on dynamic pressure in the free stream at the trailing edge and on the trailing-edge wake momentum-thickness ratio of the cascade airfoil. Thus, the drag coefficient can be considered as a measure of the momentum-thickness ratio of the surface boundary layers for both isolated and cascade airfoils.

In compressor design and analysis, it has been found convenient to use a loss parameter based on the defect in total pressure across a blade element. A general compressor total-pressure-loss coefficient $\bar{\omega}$ has been defined (ref. 7) as

$$\bar{\omega} = \frac{\Delta \bar{P}}{\frac{1}{2} \rho V_{ref}^2}$$

where $\Delta \bar{P}$ represents the mass-averaged decrease in relative total pressure across the blade element, and $\frac{1}{2} \rho V_{ref}^2$ represents the dynamic pressure at some reference location. It is desirable, therefore, in the discussion of real cascade flow, to consider the effects of viscosity on the defect in total pressure. Since $\bar{\omega}$ depends on $\Delta \bar{P}$, the value changes with distance downstream of the trailing edge (because of turbulent mixing) and therefore depends, to some extent, on the location of the measuring station. The complete loss in total pressure is obtained at a

station sufficiently far downstream that the flow has become uniform. This is contrary to the case of drag coefficient, which is theoretically the same at any axial location downstream of the blade trailing edge.

For the two-dimensional cascade with incompressible flow, reference 7 shows that, if the static pressure is uniform across the blade spacing at the trailing edge, the total-pressure-loss coefficient for complete mixing (based on $\frac{1}{2} \rho V_{0,te}^2$) is given approximately by

$$\bar{\omega} \approx 2 \left(\frac{\theta^*}{c} \right)_{te} \frac{\sigma}{\cos \beta_{te}} \left[1 + \frac{1}{2} \left(\frac{\theta^*}{c} \right)_{te} \frac{\sigma H_{te}^2}{\cos \beta_{te}} \right]$$

Thus, the trailing-edge momentum thickness should be an indication of the complete loss in total pressure.

In view of the preceding discussions, the boundary-layer momentum thickness at the blade trailing edge is considered herein as the basic parameter reflecting qualitatively the total-pressure loss or the profile drag for an airfoil section.

Laminar Boundary Layer

A laminar boundary layer is always present on the forward portion of a cascade blade. The growth of the laminar layer (expressed as boundary-layer thickness δ) in the absence of a longitudinal pressure gradient (flat-plate flow) proceeds essentially according to the proportionality relation

$$\delta \propto \sqrt{\frac{\nu s}{V_1}} \quad (1)$$

where ν is kinematic viscosity, s is distance along the surface, and V_1 is the velocity far upstream. In the presence of a negative pressure gradient the boundary-layer thickness is somewhat less, and for a positive pressure gradient somewhat greater than for the constant-pressure case of equation (1).

To relate equation (1) to a body in the flow field, let Re_c be the Reynolds number based on blade chord length (the length of the plate in the case of a flat plate). Then, equation (1) can be rewritten as

$$\frac{\delta}{c} \propto \frac{\sqrt{\frac{s}{c}}}{\sqrt{Re_c}} \quad (2)$$

where $Re_c = V_1 c / \nu$. Therefore, δ/c varies inversely with the square root of the body Reynolds number for a given value of s/c .

The drag due to friction in the laminar flow depends on the integral of the local surface shear stress $\hat{\tau}_w$ and, therefore, on the velocity gradient at the wall (i.e., $\hat{\tau}_w = \mu \left(\frac{\partial u}{\partial n} \right)_{n=0}$). For flat-plate flow, the drag coefficient varies with the body Reynolds number as

$$C_D \propto \frac{1}{\sqrt{Re_c}} \quad (3)$$

For accelerating flow the friction coefficient is greater (larger $\partial u / \partial n$ at wall, see fig. 5), and for decelerating flow the friction coefficient is smaller (smaller $\partial u / \partial n$) than for the flat plate, but in all cases a decreasing trend with body Reynolds number is observed.

In the presence of a positive pressure gradient, the boundary-layer momentum is often insufficient to overcome the increase in pressure, and separation will occur. Specifically, separation occurs when the surface shear stress is zero (i.e., when $(\partial u / \partial n)_{n=0} = 0$). According to simplified theory, the separation condition depends on the value of a flow parameter of the form

$$\lambda = \frac{\delta^2}{\nu} \frac{dV_0}{ds} \quad (4)$$

as in the Pohlhausen theory (ref. 8), or

$$m = \frac{-\theta^*2}{\nu} \frac{dV_0}{ds} \quad (5)$$

as in the Thwaites theory (to be discussed later). According to the Pohlhausen theory, separation occurs when $\lambda = -12$. As will be seen later, this is not entirely reliable, since the theory is least applicable in regions of rising pressure. Thwaites gives a value of $m = 0.082$ for separation to occur. This criterion appears to be more valid than that of Pohlhausen. In any event, the location of the point of laminar separation is primarily characterized by a boundary-layer

thickness and the local gradient of free-stream velocity. The location is unaffected by changes in blade-chord Reynolds number.

Now consider the laminar flow over a blade section at fixed angle of attack (fig. 6). The velocity distributions on the pressure and suction surfaces are indicated in the lower part of the figure. The laminar boundary layer grows along the surface until some point after the maximum velocity is reached. The laminar boundary layer then separates if a sufficiently severe pressure gradient occurs. The location of the separation point behind the point of peak velocity varies with the magnitude of the positive pressure gradient and is independent of the body Reynolds number (if the Reynolds number is low enough that transition to turbulent flow does not occur). With a separation of the laminar boundary layer, the free-stream velocity distribution is altered as indicated by the dashed line in figure 6, and an increase in form drag results. The magnitude of the form drag depends on the thickness of the profile at the point of separation and the camber of the airfoil. For a cascade airfoil, the variation of the free-stream velocity after the separation may be slightly different from that for the isolated airfoil because of the channel effect of adjacent blades.

The pronounced effect of the surface velocity gradient on the calculated location of the point of laminar separation is illustrated in figure 7 (obtained from ref. 2) for a Joukowski profile. As the pressure gradient increases, the point of separation moves closer to the point of peak velocity. The different velocity gradients in the figure were achieved by varying the angle of attack of the airfoil.

Turbulent Boundary Layer

In the range of turbulence and Reynolds number usually encountered in cascade blade rows, the laminar boundary layer generally becomes turbulent somewhere along the blade surface. It is chiefly because of this transition that practical compressors are realizable. The turbulent interchange of momentum between the free stream and the turbulent boundary layer increases the energy level in the boundary layer so that it can advance farther, without separating, in the face of a pressure rise than could a laminar boundary layer.

The turbulent-boundary-layer thickness develops (e.g., ref. 3), in the absence of a pressure gradient, as

$$\delta \propto \sqrt[5]{\frac{v s^4}{V_1}} \quad \text{or} \quad \frac{\delta}{c} \propto \frac{\sqrt[5]{\frac{s^4}{c^4}}}{\sqrt[5]{Re_c}} \quad (6)$$

The turbulent δ is generally larger than the laminar δ for the same Re_c . This increased thickness contributes to a slightly larger form drag for the turbulent boundary layer than for an equivalent un-separated laminar layer (at the same Reynolds number).

In a laminar boundary layer the local shear stress is given throughout by $\hat{\tau} = \mu(\partial u / \partial n)$. This simple equation does not hold for the turbulent boundary layer because of the turbulent shear stresses present. The wall shear stress is given by $\hat{\tau}_w = \mu(\partial u / \partial n)_{n=0}$ in both cases, since a very thin laminar boundary layer, called a laminar sublayer, is always present between the turbulent layer and the wall. However, not enough is known of the velocity distribution in the laminar sublayer to enable the utilization of this expression to compute wall shear stress for the turbulent layer. As a result, the problem must be approached empirically.

From velocity profiles observed in pipe flow, the drag coefficient for a flat plate is found to vary inversely with the fifth root of Re_c :

$$C_D \propto \frac{1}{\sqrt[5]{Re_c}} \quad (7)$$

Experience shows that many factors such as boundary-layer form factor, Reynolds number, and pressure gradient (ref. 9) influence the magnitude of the shear stress. To date, many empirical relations have been established between local shearing stress and boundary-layer characteristics. One of the most recent is due to Ludwig and Tillmann (ref. 10):

$$\frac{\hat{\tau}_w}{\frac{1}{2} \rho V_0^2} = 0.246 e^{-1.561H} Re_\theta^{-0.268} \quad (8)$$

where Reynolds number $Re_\theta = V_0 \theta^* / \nu$, and H is the form factor. The empirical skin-friction formulas lead to the general conclusion that the turbulent skin-friction coefficient is greater than the laminar skin-friction coefficient for the same Reynolds number.

The condition that $\hat{\tau}_w = 0$ defines the point of separation in both laminar- and turbulent-boundary-layer flows. In the case of the turbulent boundary layer, the point at which $\hat{\tau}_w = 0$ is determined from an empirical equation such as equation (8). In reference 11 this equation is used in conjunction with experimentally determined values of H and Re_θ to predict separation. It is clear that $\hat{\tau}_w$, in equation (8), never

actually becomes zero. However, the decreasing trend is sufficiently pronounced as the separation point is approached that extrapolation to $\dot{t}_w = 0$ is possible. Figure 8 shows the results of such a calculation from reference 11.

For conventional two-dimensional compressor sections, several gross parameters have been developed to indicate whether separation is likely in certain areas of blade design (refs. 12 and 13). These parameters, based on the diffusion in velocity on the blade suction surface, involve consideration of only the peak and outlet suction-surface velocities or approximations to these velocities in terms of over-all (inlet and outlet) velocities and flow angles. Implicit in the work is the consideration that the boundary-layer history at the start of the diffusion and the velocity distributions along the surface are generally the same for conventional blade sections. Location of the point of separation, however, cannot be determined from these parameters.

Transition

For conventional airfoil shapes, the initial laminar boundary layer, if it remains laminar, will separate at some point downstream of the pressure minimum. Depending on certain flow characteristics to be considered in this section, a transition to turbulent flow may occur at a point prior to the laminar separation point. In this event, the turbulent flow will remain attached for some distance farther along the blade surface. Such a transition will normally occur under ordinary cascade flow conditions. The region in which the transition to turbulent flow takes place is small and is conveniently thought of as a point, called the transition point.

The exact location and conditions under which the transition from a laminar to a turbulent boundary layer will occur are not currently predictable, and the question of transition constitutes a major problem in present-day boundary-layer research. Transition can result either from disturbances of finite magnitude such as free-stream turbulence, or from an instability of the laminar steady flow in which infinitesimal disturbances, under proper conditions, grow exponentially with respect to time. The length of travel or time before transition occurs depends on the rate of amplification of the disturbances and therefore on the particular flow conditions in and about the boundary layer.

Experiment shows (ref. 14) that transition occurs because of infinitesimal disturbance instability when the free-stream turbulence intensity is less than about 0.2 percent and when no other external disturbances are present. For free-stream turbulence greater than about 0.2 percent, which is generally the situation in cascade and compressor

flow, the characteristics of the free-stream turbulence (scale and intensity) play a decisive role in affecting the transition. In any event, the transition phenomena can generally be related in terms of the Reynolds number and another parameter or parameters describing the characteristics of the disturbance (i.e., free-stream turbulence, surface roughness, etc.).

Infinitesimal-disturbance theory. - The first significant theoretical work on transition was concerned with the instability of the laminar boundary layer with respect to infinitesimal oscillations within the layer (e.g., ref. 15). In a stable laminar boundary layer the disturbances are damped, while in an unstable boundary layer the disturbances are amplified. The point of division, called the neutral or instability point, depends on the origin of the disturbance. The existence of instability in a laminar boundary layer indicates that transition is possible but not necessarily present after the neutral point. The actual transition to a fully developed turbulent motion will occur some distance downstream of the instability point, since a finite time is required for the oscillations to build to full strength and permeate the boundary-layer region.

According to this theory, an instability of the laminar boundary layer (i.e., an amplification of oscillations) results from (1) the presence of viscosity and (2) an inflection in the boundary-layer velocity profile normal to the surface. The theory further indicates that the instability point is a function of the boundary-layer Reynolds number; that is, below some value of Reynolds number infinitesimal oscillations are damped, while above this value oscillations are amplified. The instability value of the boundary-layer Reynolds number depends largely on the form of the velocity profile of the basic boundary-layer flow. This profile is determined primarily by the longitudinal pressure gradient of the flow. The greater the positive pressure gradient, the lower the boundary-layer Reynolds number at instability. In translating these results into terms of the blade-chord Reynolds number, the boundary-layer Reynolds number Re_δ can be expressed as

$$Re_\delta = \frac{V_0 \delta}{\nu} \frac{V_1}{V_1} \frac{c}{c} = Re_c \frac{V_0}{V_1} \left(\frac{\delta}{c} \right) \quad (9)$$

Thus, in general, the closer the point in question to the blade leading edge (the smaller the value of δ/c), the larger the blade-chord Reynolds number necessary for the attainment of the instability value of the boundary-layer Reynolds number at that point. That is, the higher the blade-chord Reynolds number, the sooner will the instability condition occur. These considerations are illustrated graphically in figure 9, which shows the results of the calculation of the instability point for various blade-chord Reynolds numbers on the suction surface

of a Joukowski airfoil at several angles of attack (from ref. 16). The effect of the increased surface pressure gradient and Reynolds number on the location of the instability point as angle of attack is increased is clearly indicated.

Finite-disturbance theory. - In a second general theory of transition (ref. 17), disturbances of finite magnitude are considered to be imposed on the laminar boundary layer from outside sources. In this case, the transition of the laminar boundary layer depends on the characteristics of the imposed disturbance. The principal source of external disturbance is a function of the intensity and scale of free-stream turbulence according to the parameter $\mathcal{J}(\lambda^*/L)^{1/5}$, where \mathcal{J} is the intensity of the turbulence, L is the scale of the turbulence, and λ^* is some characteristic dimension of the body such as chord length or diameter. The greater the free-stream turbulence parameter, the lower the magnitude of the critical Reynolds number. Intensity of turbulence is defined as the ratio of the root mean square of the disturbance velocity to the mean flow velocity. Scale of turbulence is a measure of the effective size of the turbulent eddies and has an inverse effect on the turbulence parameter. Experimental confirmation of this theory has been obtained by several investigators (refs. 18 and 19) in the study of the drag characteristics of spheres.

Flow about spheres. - In the development of the boundary layer on cascade blade sections, a primary consideration is whether the transition occurs before or after the point of laminar separation. The effect of transition location on the loss characteristics of submerged bodies is graphically illustrated by the well-known flow around a sphere at a fixed turbulence level as represented in figures 10 and 11. At low Reynolds numbers, when no transition occurs, the laminar boundary layer separates and high profile drag results. When transition occurs before the point of laminar separation at high Reynolds numbers, the resulting turbulent boundary layer can tolerate a greater pressure gradient; separation of the turbulent layer is delayed, and a lower profile drag is observed. The Reynolds number at which the rather sudden change of drag characteristic occurs, called the critical Reynolds number of the sphere, corresponds to the point where the transition and separation coincide.

The drag characteristics of spheres have provided a means for evaluating the effects of free-stream turbulence on transition. As previously discussed, theory indicates that the critical Reynolds number will be a function of the turbulence parameter $\mathcal{J}(\lambda^*/L)^{1/5}$. Experimental verification of this effect (ref. 18) is represented by figure 12, which illustrates the earlier transition associated with increasing free-stream turbulence. The turbulence correlation of figure 12 provides a means for identifying the free-stream turbulence

level from the measured drag characteristics of spheres. The turbulence in a cascade tunnel is frequently expressed in terms of a turbulence factor, defined as the ratio of the critical Reynolds number at zero turbulence to the measured critical Reynolds number of the sphere (ref. 19).

The effective Reynolds number for a blade section, defined as blade-chord Reynolds number times turbulence factor of the tunnel, has been used to represent a transition parameter that includes the effects of free-stream turbulence. Blade sections at the same effective Reynolds number, although of different blade-chord Reynolds numbers and turbulence levels, are expected to exhibit approximately the same transition (and therefore the same drag) characteristics. The subject of turbulence-level measurements is treated more fully in references 18 and 19.

Boundary-layer reattachment. - Under certain conditions it is possible for a laminar boundary layer that has separated to reattach to the blade surface. In most instances the reattached layer is turbulent, transition having occurred in the separated region. In these turbulent reattachments the location of the transition point is the principal determinant.

Generally speaking, the boundary-layer behavior is fairly well understood as long as the transition occurs either before the separation point or at a large distance downstream of the separation. In the former case a thickening of the boundary layer occurs in the region of transition as the flow passes to the turbulent state. In the latter case, the laminar boundary layer remains separated, and the flow break-away and high form drag are observed. When transition occurs close behind the point of laminar separation, however, under certain conditions, the separated laminar boundary layer may reattach to the surface as a turbulent layer, forming a sort of bubble of locally separated flow. The reattached turbulent boundary layer is considerably thicker than if transition had occurred at that point without a previous laminar separation. The turbulent reattachment has been observed for both isolated and cascade airfoil sections. Detailed discussions of the nature of the separation bubble and the various factors influencing its characteristics are presented in references 20 to 22. Various experimental methods of determining the extent and location of the laminar separation are discussed in references 20, 22, and 23.

Experimental variations of the boundary-layer momentum thickness, boundary-layer form factor, and pressure distribution observed in the region of the laminar bubble for an isolated airfoil section (ref. 20) are illustrated in figure 13. A similar illustration of the pressure distribution on the suction surface of a cascade section with laminar separation bubble (ref. 21) is shown in figure 14(a). The most detrimental effect of the laminar separation bubble is the rather sharp increase in momentum thickness associated with the turbulent reattachment.

The effect of a suction-surface laminar separation bubble on the loss characteristics of a blade section is illustrated in figure 14(b), which presents the variation of drag coefficient C_D with angle of attack α for a typical cascade blade section (from ref. 21). The solid line represents the measured drag coefficient, and the dotted line is a hypothetical variation for the case of no laminar separation. A noticeable increase in the drag coefficient occurs in the low-loss range of operation.

Obviously, the occurrence of laminar separation bubbles will make the correlation of cascade data difficult. The effects of turbulence level and Reynolds number further increase the problem. Although the theory governing these effects is not complete, some qualitative ideas can be drawn from the foregoing descriptive material.

Composite Loss Variations

In the previous sections, a qualitative picture was presented of the characteristics of the three general regimes of boundary-layer development, the laminar region, the fully turbulent region, and the transition region. On the basis of available theory and experimental evidence, the manner in which each type of flow influenced the resulting thickness of the boundary layer was indicated. On conventional cascade blade surfaces, all three boundary-layer regimes are known to exist. The momentum thickness of the boundary layer at the blade trailing edge depends on the extent of each flow regime. The momentum thickness at the blade trailing edge is a principal factor in the determination of the loss in total pressure of the cascade system. The prediction of the loss characteristics of a given cascade geometry thus involves an analysis of the composite effects of the boundary-layer regimes.

From the previous discussions, it is known that the principal factors affecting the boundary layer are the local surface pressure distribution, the blade-chord Reynolds number, and the free-stream turbulence level. It is desirable to construct a qualitative picture of the anticipated variation of boundary-layer momentum thickness on a blade surface over a wide range of Reynolds number, pressure distribution, and turbulence level. Such a composite plot will not only constitute an effective summary of the preceding theory as applied to blade sections, but may also be of interest in identifying desirable or undesirable areas of cascade operation.

The comparative variation of trailing-edge boundary-layer momentum thickness (actually the ratio θ^*/c) with blade-chord Reynolds number is presented qualitatively for several levels of pressure gradient in figure 15. Pressure distributions are considered ranging from zero pressure rise (no blade loading) to a severe pressure gradient (very high loading) resulting in a separation of the turbulent layer. The

analysis is made for the flow along the convex (suction) surface of conventional compressor blade sections. The pressure distributions considered, therefore, contain a decreasing pressure over the forward portion of the blade and a rising pressure over the rearward portion.

The variation of trailing-edge momentum-thickness ratio is presented in figure 15 for a fixed low turbulence level (as normally encountered in low-turbulence cascade tunnels). It must be emphasized that the trends established are only qualitative and that no sufficient substantiating data are available. The values of Reynolds number at which the transition phenomena are indicated in figure 15 are not to be interpreted as accurate definitions of these regions. These values are largely unpredictable at this time.

Zero loading. - The limiting case of no blade surface pressure gradient can be represented by the boundary-layer flow along a flat plate. For flat-plate flow, no separation occurs, and the two regimes of laminar and turbulent flow are described by the drag variations of equations (3) and (7), respectively. Curve a-a in figure 15 represents the momentum-thickness variation for laminar flow, and curve a'-a' represents the variation for turbulent flow for the flat plate.

At low values of Re_c the boundary layer is entirely laminar, and θ^*/c decreases with increasing Re_c as shown by curve a-a. At some value of Re_c , indicated by A in the figure, Re_c becomes sufficiently large that transition from a laminar to a turbulent layer occurs at the trailing edge. This Reynolds number appears to yield the minimum boundary-layer thickness. With a further increase in Re_c , the transition moves forward from the trailing edge, and the boundary-layer thickness falls somewhere between the laminar and turbulent curves (dashed portion). Finally, as the transition point approaches the leading edge, the boundary layer will essentially assume the characteristics of the fully turbulent flow. [Strictly speaking, since the boundary-layer transition point actually arrives at the leading edge only at an infinite Reynolds number (in the absence of outside disturbance), the dashed transition curve will asymptotically approach the turbulent curve as Re_c approaches infinity.]

Increased turbulence will cause the boundary-layer transition phenomena to occur at lower values of Reynolds number and will therefore have the effect of shifting point A farther to the left on curve a-a. For zero pressure gradient, therefore, increased turbulence may increase the minimum boundary-layer momentum thickness.

Low loading. - The curve b-b in figure 15 represents the case of a very lightly loaded blade whose surface pressure gradient is such that laminar separation will not occur. In this case, the picture is much the same as for the flat plate, except that the boundary-layer thicknesses will generally be somewhat greater. It is also quite possible that both the presence of a pressure gradient and the location of the minimum pressure will have some influence on the location of point A. However, it is not believed that these effects will be marked for the lightly loaded surface.

Moderate loading. - The boundary-layer thickness variations for a moderately loaded blade surface are illustrated by curve c-c in figure 15. The moderately loaded blade probably represents the major portion of current design experience. The blade loading in this case can be achieved by a blade with moderate camber operated at its best (minimum-loss) angle of attack, or by a section of smaller camber operated at a relatively high angle of attack.

At low Reynolds number, the adverse pressure gradient is sufficient to cause a separation of the laminar boundary layer somewhere downstream of the point of minimum pressure. A marked rise in the momentum loss compared with the low-loading case will therefore be obtained in the low Reynolds number range. The precise magnitude of the separated boundary-layer thickness depends on the shape and angle of attack of the blade. A separation point close to the leading edge would tend to produce a relatively large separated wake (form drag). Inasmuch as the point of laminar separation is independent of Reynolds number, the laminar layer remains separated, and the high values of θ^*/c continue as Reynolds number is increased to point A. A slight decrease in θ^*/c in this high-loss region is to be expected, however, because of the thinning of the boundary layer upstream of the point of separation.

At a Reynolds number corresponding to the point A, the transition to turbulent flow would take place at the trailing edge if the laminar layer were still attached. Since the laminar layer has separated, there is no transition and the thickness continues high from A to C. With increasing Re_c , the transition point moves closer to the point of laminar breakaway. When the two points are sufficiently close together, the separated laminar layer may be infused with sufficient turbulence to reattach itself a short distance beyond the point of separation, resulting in a separation bubble. After reattachment starts at point C, the θ^*/c curve drops rather sharply with Reynolds number increase in the region from C to D as the extent of the separation bubble decreases. Finally, the transition occurs right at the point of separation indicated by point D. Thereafter, the curve of θ^*/c tends to approach the variation of the fully turbulent flow (curve c'-c). The rate at which the fully turbulent curve is approached will probably depend to

a large extent on the chordwise location of the point of minimum pressure. (Since the blade is moderately loaded, the separation point is probably not far beyond the minimum-pressure point and any further movement of the transition point will be slow.) An experimental illustration of the type of loss against Reynolds number curve represented by curve c-c in figure 15 is shown in figure 16 for a conventional cascade blade section at several angles of incidence.

In view of the many factors influencing the formation and extent of the separation bubble, it would appear possible to obtain a wide range of possible transition paths between laminar breakaway (below point C, fig. 15) and turbulent attachment (beyond point D). Also, if for some reason, a separation bubble does not occur and attachment does not take place until the transition point and the laminar separation point essentially coincide (as in the case of the flow about a sphere or cylinder), then the laminar breakaway region will extend farther out along the line A-C and a very sharp drop in boundary-layer thickness will be observed to D (as in the case of the sphere). Furthermore, the chordwise location of the minimum-pressure point will probably affect the location of the transition region. For example, if the minimum-pressure point occurs far back on the blade, the reattachment of the laminar layer will probably begin very shortly after the transition point first occurs on the blade. This would tend to reduce the flat portion of the curve between A and C, and probably also give a steeper drop-off in θ^*/c . (The magnitude of the loss of the separated laminar boundary layer would not, however, be as large as in the case of a forward pressure minimum.)

The preceding picture will be further complicated by considerations of varying turbulence levels. In general, however, it is probable that increased free-stream turbulence will cause an earlier boundary-layer transition and therefore tend to move the transition region of the curve to lower values of Reynolds number (c-D'-c). An experimental illustration of such an effect is presented in figure 17 in terms of the loss parameter ω . A further extension of the turbulent layer into the lower range of Reynolds number (extension along curve c'-c) may also be obtained by employing artificial means for tripping the boundary layer at the leading edge. Such measures, however, although extending the range of low loss to lower Reynolds numbers, probably result in an increase in the magnitude of the loss at higher Reynolds numbers.

High loading. - Curve d-d in figure 15 represents a highly loaded blade. As in the previous case, the laminar boundary layer separates at low values of Reynolds number. As Re_c increases, the transition point moves forward (starting at A) until it approaches the separation point. The laminar layer may then reattach (point C) and proceed as a turbulent layer. The momentum-thickness ratio then decreases as the extent of the laminar separation is reduced, as indicated by the dashed

curve after point C. (The establishment of turbulent flow in the high-loading case may require actual coincidence of the transition and separation points, in which case the drop in θ^*/c after point C will be much steeper.)

The surface pressure distribution is such, however, that the established turbulent layer will now separate at some point downstream of the transition. The resulting momentum-thickness ratio when the local laminar separation has disappeared (transition moves forward of the laminar separation) will then be greater, as indicated by point D, than for the corresponding condition in the moderately loaded blade. Then, as Reynolds number is increased and the boundary-layer characteristics upstream of the separation are improved, the turbulent boundary layer will be able to proceed farther into the adverse pressure gradient. Thus, with a resulting downstream movement of the turbulent separation, the trailing-edge boundary-layer thickness will decrease with increasing Reynolds number from point D on.

The actual magnitude of the loss in the presence of turbulent separation depends to a large extent on the chordwise location of the point of turbulent separation. For separation close to the blade trailing edge, as represented by curve d-d, the increase of boundary-layer thickness will not be very great (level of curve D-d). If the separation occurs forward on the blade close behind the transition, as represented by curve e-e, the increase in thickness will be much greater (level of curve D-e).

Summary. - The previous considerations indicate that a considerable range of trailing-edge boundary-layer momentum thickness can be obtained from blade sections, depending on the surface pressure distribution, Reynolds number, and turbulence level. In two-dimensional-cascade research, therefore, it appears highly desirable to identify the range of operation of the blade sections in the general loss against Reynolds number spectrum. Actually, some effective Reynolds number should be considered, so that turbulence level can also be included. Such identification can aid in determining the best regions of cascade operation and also be of use in correlating data from different tunnels. Furthermore, in view of the possible pronounced effect of the laminar breakaway at low Reynolds number, the question of Reynolds number effects might be a significant consideration in compressor design. Reduced Reynolds number in compressor design may arise for small-scale units and for operation at high altitude.

It must be repeated that the curves presented in figure 15 are only qualitative. The magnitude of loss and the values of Reynolds number indicated for the ranges of different loss characteristics are not to be interpreted as quantitatively correct. The precise wake momentum-thickness variations of a specific cascade geometry can currently be determined only by experiment.

QUANTITATIVE BOUNDARY-LAYER THEORY

General Considerations

Unfortunately, current ability to determine cascade boundary-layer behavior quantitatively falls below the ability to establish a qualitative picture. The principal difficulty in this respect lies in obtaining satisfactory solutions of the viscous-flow equations.

The complete viscous flow about cascade sections is generally considered to be described by the equations of Navier-Stokes and the continuity equation. For two-dimensional incompressible flow, neglecting body forces, these equations are written as follows (ref. 2):

$$\left. \begin{aligned} \frac{\partial u}{\partial \tau} + u \frac{\partial u}{\partial s} + v \frac{\partial u}{\partial n} &= -\frac{1}{\rho} \frac{\partial p}{\partial s} + \nu \left(\frac{\partial^2 u}{\partial s^2} + \frac{\partial^2 u}{\partial n^2} \right) \\ \frac{\partial v}{\partial \tau} + u \frac{\partial v}{\partial s} + v \frac{\partial v}{\partial n} &= -\frac{1}{\rho} \frac{\partial p}{\partial n} + \nu \left(\frac{\partial^2 v}{\partial s^2} + \frac{\partial^2 v}{\partial n^2} \right) \\ \frac{\partial u}{\partial s} + \frac{\partial v}{\partial n} &= 0 \end{aligned} \right\} \quad (10)$$

The last equation represents the condition of continuity. The Euler equations for nonviscous fluids can be obtained by setting the kinematic viscosity ν equal to zero. As long as the viscosity term is retained, however, no matter how small ν is taken to be, equations (10) remain of the second-order and are fundamentally different from the first-order equations governing the ideal fluid. This difference is reflected in the boundary conditions allowable in the two problems. For viscous flow, the resultant velocity is required to be zero at solid boundaries in the flow field. For nonviscous flow, only the component normal to the boundary is required to be zero.

The solution of equations (10) has not been found in any but the simple cases of laminar flow. A solution for the flow through an arbitrary cascade is not feasible at the present time. However, when the predominant viscous effects are confined to the boundary region, a simplifying approximation is possible. By considering the relative magnitudes (within the boundary layer) of the terms appearing in equations (10), that system of equations can be reduced (ref. 2) to the following:

$$\left. \begin{aligned} \frac{\partial u}{\partial \tau} + u \frac{\partial u}{\partial s} + v \frac{\partial u}{\partial n} &= -\frac{1}{\rho} \frac{\partial p}{\partial s} + \nu \frac{\partial^2 u}{\partial n^2} \\ \frac{\partial u}{\partial s} + \frac{\partial v}{\partial n} &= 0 \end{aligned} \right\} \quad (11)$$

where s is the coordinate along the blade surface, and n is the coordinate normal to the surface. The boundary layer is assumed sufficiently thin and the curvature of the surface sufficiently small that the pressure gradient normal to the surface is negligible within the boundary layer; $\partial p / \partial s$ can then be determined from the potential flow outside the boundary layer. Equations (11) represent a significant simplification of equations (10) and have proved reliable in many flow problems. Unfortunately, these equations, also, are very difficult to solve in most cases of practical interest.

A decisive simplification in approach was made by von Kármán (ref. 24), who integrated the first of equations (11) with respect to n and thus replaced the boundary-layer equation with an integral condition that can be written in the following form:

$$\frac{\hat{\tau}_w}{\rho V_0^2} = \frac{d\theta^*}{ds} + \frac{\theta^*}{V_0} (2 + H) \frac{dV_0}{ds} \quad (12)$$

where V_0 is the velocity at the outer edge of the boundary layer and $\hat{\tau}_w$ is the surface shear stress. In this manner, the boundary-layer equations are required to be satisfied only in the mean instead of at each point along a normal to the surface in the boundary-layer region. Equation (12) has provided the basic equation for most of the general boundary-layer investigations.

Many theories have been developed from equation (12) for approximately solving the boundary-layer problem with pressure gradient for both laminar and turbulent flows. These theories, although not completely successful, provide some orderly means of attacking the problem for either the laminar or the turbulent boundary layer. The question of transition, however, remains relatively unanswered and constitutes a serious defect in current quantitative theory.

The present approach to the viscous-flow cascade problem requires that the potential flow about the cascade be determined first. The surface pressure distributions thus obtained are used to determine the boundary-layer characteristics from equation (12). The defect in total pressure resulting from the formation of the boundary layer can then be established. Potential-flow pressure distributions can serve as an initial basis for the boundary-layer calculation, since, as indicated previously, the viscous effects are generally restricted to the boundary layer and exert a negligible influence on the potential flow outside the layer. Under certain conditions, however (as in the case of a very thick boundary layer), the original blade potential flow may need to be adjusted for the effects of the boundary-layer development.

The subject of potential-flow calculation is covered in chapter IV. The present analysis is concerned with the computation of the boundary-layer characteristics. In the succeeding sections, two simple approximate methods, one for the computation of laminar boundary layers and the other for turbulent layers, are presented. The resulting defects in total pressure and circulation are also considered.

Laminar Boundary Layer

The approximate methods of solution available for laminar-boundary-layer flows are generally satisfactory for engineering use. The more recent methods (e.g., refs. 25 and 26) are so simple and accurate that little further work is being done on the problem. The technique presented here in some detail is due to Thwaites (ref. 26). It was developed from a comprehensive analysis of previously obtained solutions of laminar-boundary-layer flows. From the method, the distributions of θ^* and H can be accurately obtained and the point of laminar separation located.

The methods of Thwaites (ref. 26) and Loitsianskii (ref. 25) are both based initially on the simplified system of equations given by equation (11). For steady incompressible flow, since the static pressure is constant through the boundary layer, the first of equations (11) can be put in the form

$$u \frac{\partial u}{\partial s} + v \frac{\partial u}{\partial n} = V_0 V_0' + \nu \frac{\partial^2 u}{\partial n^2} \quad (13)$$

where $V_0' = dV_0/ds$ denotes the derivative with respect to s of the velocity V_0 at the outer edge of the boundary layer. With the help of the continuity equation (second of eqs. (11)), equation (13) can be written

$$\frac{\partial}{\partial s} [u(V_0 - u)] + \frac{\partial}{\partial n} [v(V_0 - u)] + V_0'(V_0 - u) - \nu \frac{\partial^2 (V_0 - u)}{\partial n^2} = 0 \quad (14)$$

The developments in the two methods then differ in the subsequent handling of equation (14).

Thwaites' method. - In the method of reference 26, equation (14) is integrated through the boundary layer from the wall ($n=0$) to the outer edge ($n=\delta$) to give ultimately

$$\frac{d\theta^*}{ds} + \frac{V_0' \theta^*}{V_0} (2 + H) = \frac{\nu}{V_0^2} \left(\frac{\partial u}{\partial n} \right)_{n=0} \quad (15)$$

Equation (15) is the same as (12) with $\hat{\tau}_w = \mu(\partial u/\partial n)_{n=0}$.

Equation (15) is used by Thwaites in conjunction with the equation obtained from (13) by setting n equal to zero, namely

$$0 = V_0 V_0' + \nu \left(\frac{\partial^2 u}{\partial n^2} \right)_{n=0} \quad (16)$$

The quantities $(\partial u / \partial n)_{n=0}$, $(\partial^2 u / \partial n^2)_{n=0}$, and H appearing in equations (15) and (16) characterize the velocity distribution in the boundary layer. The first two terms indicate the behavior of the velocity in the significant region of the boundary layer at the wall, and $H = \delta^* / \theta^*$ indicates the over-all form of the distribution. The term $(\partial^2 u / \partial n^2)_{n=0}$ is given explicitly by equation (16) as equal to $-V_0 V_0' / \nu$ and hence as a known function of s . If the relation between $(\partial u / \partial n)_{n=0}$ and $(\partial^2 u / \partial n^2)_{n=0}$ for a given flow is known, then $(\partial u / \partial n)_{n=0}$ is also known as a function of s through $-V_0 V_0' / \nu$. If, furthermore, the relation between H and $(\partial^2 u / \partial n^2)_{n=0}$ is known for the given flow, H is also known as a function of s . Then, the momentum equation (15) can be integrated to obtain the distribution of θ^* . Such relations among $(\partial u / \partial n)_{n=0}$, $(\partial^2 u / \partial n^2)_{n=0}$, and H are obtained now by examining velocity distributions from known solutions.

The quantities l and m are defined as follows:

$$\left. \begin{aligned} l &= \frac{\theta^*}{V_0} \left(\frac{\partial u}{\partial n} \right)_{n=0} \\ m &= \frac{\theta^{*2}}{V_0} \left(\frac{\partial^2 u}{\partial n^2} \right)_{n=0} \end{aligned} \right\} \quad (17)$$

The definitions are constructed in this way to eliminate the effect of θ^* and V_0 on the partial derivatives. This allows l and m to depend only on the form of the velocity distribution. According to this preliminary analysis, the terms l and H are regarded as functions of m and are plotted as such for all theoretical laminar-boundary-layer velocity distributions available to Thwaites at the time of his work.

The solutions used are identified in figures 18 and 19, where the derived functional relations are plotted. The values of l , H , and m are computed from the actual velocity distributions obtained in these solutions. The figures are divided into positive and negative values

of m , corresponding respectively to decelerating and accelerating flow ($m = -V_0 \theta^{*2}/\nu$ from eqs. (16) and (17)). Figures 18(a) and 19(a) reveal a remarkable similarity for $m < 0$ (accelerating flow) in the $l(m)$ and $H(m)$ curves for the variety of velocity distributions appearing in the wide range of solutions used.

On the other hand, figures 18(b) and 19(b) show that the agreement for $m \geq 0$ (decelerating flow) is not nearly as good. The curve corresponding to the solution of the problem $f''' + \frac{1}{2}ff'' = 0$ is dis-

missed on the grounds that the problem it defines in this region is of no interest (i.e., blowing out through the boundary layer). The three exact solutions, Schubauer's ellipse (Hartree), $V_0 = A - Bs$ (Howarth), and $V_0 = V_1 (s/c)^k$, are in reasonable agreement. Pohlhausen's approximate method gives values of $l(m)$, and, hence, values of skin friction, that are far too large. This explains the failure of the Pohlhausen method in regions of rising pressure.

As previously pointed out, the momentum equation can be integrated if the relations $l(m)$ and $H(m)$ are known for the problem at hand. The present method uses figures 18 and 19 to obtain universal curves that best fit the whole family of particular solutions. The curves thus obtained are tabulated in table I. Note that separation is taken to occur at $m = 0.082$. This value is chosen arbitrarily to agree with the value for the ellipse, since the flow about an ellipse is similar to the flow about conventional airfoils.

With these functions tabulated, the analysis can proceed as follows. Substituting equations (17) into (15) and (16) gives

$$\frac{d\theta^*}{ds} = - (H + 2) \frac{V_0' \theta^*}{V_0} + \frac{\nu l(m)}{V_0 \theta^{*2}} \quad (18)$$

$$0 = V_0 V_0' + \frac{\nu V_0 m}{\theta^{*2}} \quad (19)$$

Substituting (19) into (18) gives

$$\frac{1}{\nu} \frac{V_0}{2} \frac{d\theta^{*2}}{ds} = m[H(m) + 2] + l(m) \quad (20)$$

Then, defining $\mathcal{L}(m)$ to be

$$\mathcal{L}(m) = 2 \left\{ m[H(m) + 2] + l(m) \right\} \quad (21)$$

and substituting equation (21) into equation (20) give

$$\frac{V_0}{v} \frac{d\theta^2}{ds} = \mathcal{L}(m) \quad (22)$$

The function $\mathcal{L}(m)$ is tabulated in table I.

The solution proceeds now by a direct integration of equation (22) to obtain the distribution of θ^* . Thereafter, the other properties of the boundary layer are obtained by using $l(m)$ and $H(m)$.

A very simple solution can also be obtained in a slightly different manner. The function $\mathcal{L}(m)$ is plotted against m in figure 20. It is found that $\mathcal{L}(m)$ can be approximated by a linear function of the form

$$\mathcal{L}(m) = 0.45 + 6m \quad (23)$$

Equation (23) is then substituted into equation (22), which is integrated to give

$$\theta^2 = \frac{0.45v}{V_0^6} \int_0^s V_0^5 ds \quad (24)$$

Therefore, with the potential-flow velocity distribution known, θ^2 can be obtained directly from equation (24). The distribution of m , and hence of $l(m)$ and $H(m)$, follows from θ^2 . In this way, all the significant boundary-layer parameters are obtained with very little effort.

To demonstrate the accuracy of the simple solution, Thwaites solved by the approximate method the flow given by $V_0 = A - Bs$ and compared the results with the exact solution as given by Howarth. The results of these comparative calculations are given in figure 21. The parameters of principal interest, δ^* , θ^* , and $(\partial u / \partial n)_{n=0}$, are presented in a nondimensional form. The agreement between the approximate and exact solutions is satisfactory for all parameters. A similar comparison is made in reference 26 for the problem of Schubauer's ellipse. Both comparisons are discussed extensively in that reference.

Comparisons between experimental and calculated predictions of the point of laminar separation based on Thwaites' method are demonstrated for the isolated airfoil and cascade airfoil, respectively, in references 27 and 28. The fact that close agreement was obtained in the references between calculated and experimentally observed locations of the separation point indicates that the method may be satisfactory for prediction of the other boundary-layer characteristics.

Loitsianskii's method. - In reference 25 Loitsianskii presents a final equation similar to equation (24) but developed from a quite different approach. Equation (14) is multiplied by n^k and integrated through the boundary layer. The second and third integrals (i.e., $k = 1$ and $k = 2$) are also used. The three equations are solved simultaneously for three parameters characterizing the boundary-layer velocity distribution. In order to do this, a simple assumed velocity form in the boundary layer is used to evaluate certain of the integrals involved in the three equations. The final equations are (in the terminology of Thwaites)

$$\theta^{*2} = \frac{0.44\nu}{V_0^{5.5}} \int_0^s V_0^{4.5} ds$$

$$l(m) = 0.22 - 1.85m - 7.55m^2$$

$$H(m) = 2.59 + 7.55m$$

These equations show that the method in application differs very little from that of Thwaites. Analytical expressions for $l(m)$ and $H(m)$ are used instead of the tabulated values used by Thwaites. In general, the values of Thwaites correspond more nearly to the values of $l(m)$ and $H(m)$ obtained from exact solutions. The differences, however, may not be significant.

Turbulent Boundary Layer

The turbulent boundary layer is more difficult to treat theoretically than the laminar layer. The use of characteristic velocity forms, as in many approximate methods for the laminar layer, has not proved satisfactory in the turbulent case. Furthermore, the shear stress is not given as a simple function $\mu(\partial u / \partial n)$ of the velocity distribution, except in the laminar sublayer. An additional difficulty is the determination of the proper value of H or δ^* at the point of transition. As a result of these difficulties, the best methods available for calculating the characteristics of a turbulent boundary layer are more tedious and less accurate than the method given for the laminar problem.

Since the turbulent boundary layer is preceded, on a blade, by a laminar layer, it is necessary first to determine the values of θ^* and H immediately after transition. These values, as well as the location of the transition point, are determined with the help of the computation of the preceding laminar boundary layer. Once these values are known, certain differential equations for θ^* and H can be solved to obtain the entire distribution.

In the technique of Maskell (ref. 11) presented here, the momentum thickness can be obtained simply and with acceptable accuracy. The determination of the distribution of the form factor H is more difficult. When θ^* and H have been obtained, the point of turbulent separation can be obtained accurately by the use of a skin-friction formula for turbulent flow given by Ludwig and Tillmann (ref. 10).

Approach. - From the conservation of momentum in the boundary layer, the momentum equation can be developed for the turbulent case as

$$\frac{d\theta^*}{ds} = \frac{C_{fr}}{2} - (H + 2) \frac{\theta^*}{V_0} \frac{dV_0}{ds} \quad (25)$$

where

$$C_{fr} = \frac{\hat{\tau}_w}{\frac{1}{2} \rho V_0^2} \quad (26)$$

and $\hat{\tau}_w$ is the friction stress for a turbulent boundary layer. It has always been observed that the distribution of θ^* calculated from equation (25) is not greatly affected by the way H varies with s . In fact, H can be taken as constant and reasonably accurate values of θ^* obtained in some cases. For this reason, Maskell proposes a simplification of equation (25) (based on the insensitivity to H) which enables that equation to be directly integrated for θ^* . Then, he uses the derived values of θ^* , in conjunction with an empirical differential equation in H , for obtaining values of H accurately. This approach is simpler than the well-known method of von Doenhoff and Tetervin (ref. 29), in which an empirical differential equation in H is constructed and solved simultaneously with equation (25). The results obtained for θ^* and H in the two methods are comparable. The method of Maskell recommends itself not only because of its simplicity, but also because of its ability to predict separation with acceptable accuracy.

Momentum thickness. - The first part of the boundary-layer problem is to determine the momentum thickness. To do so, equation (25) is first written in the following form:

$$\frac{d\theta}{ds} = (1 + q) \left[\xi - \left(H + \frac{2 + q}{1 + q} \right) r \right] \quad (27)$$

where

$$\left. \begin{aligned} \Theta &= \theta^* \text{Re}_\theta^q \\ \Gamma &= \frac{\Theta}{V_0} \frac{dV_0}{ds} \\ \zeta &= \frac{C_{fr}}{2} \text{Re}_\theta^q \end{aligned} \right\} \quad (28)$$

and q is an arbitrary constant that will be determined later. The friction coefficient C_{fr} is given by the formula

$$C_{fr} = 0.246e^{-1.561H} \text{Re}_\theta^{-0.268} \quad (29)$$

which is developed in reference 10. This formula, which Maskell adopts for his method, is probably superior to previously used formulas for C_{fr} .

Equation (27) can be integrated directly if the right side can be approximated in the linear form $A + B\Gamma$. For flat-plate flow, dV_0/ds (and hence Γ) equals zero, and equation (27) becomes

$$\left(\frac{d\Theta}{ds}\right)_{f.p.} = (1 + q)\zeta = A \quad (30)$$

Therefore, an approximation of equation (27) in the form $A + B\Gamma$ requires that $(1 + q)\zeta$ be constant if the approximation is to agree in the simple case of flat-plate flow. The value of q required to make the ζ term constant in equation (30) is determined as indicated in the following paragraph.

The experimental variation of H with $\log \text{Re}_\theta$ for a flat plate is illustrated in figure 22, along with two simple analytic approximations to the experimental data. The simplest approximation,

$$H = 1.630 - 0.0775 \log_{10} \text{Re}_\theta \quad (31)$$

is used in this part of the analysis. Substitution of equations (31) and (29) in the definition of ζ (eq. (28)) gives

$$\zeta = 0.00965 \text{Re}_\theta^{q-0.2155} \quad (32)$$

Therefore, taking $q = 0.2155$ in equation (32) gives a constant value of ξ as desired. With this value of q , equation (27) becomes

$$\frac{d\Theta}{ds} = 1.2155[\xi - (H + 1.823)\Gamma] \quad (33)$$

The right side of equation (33) is now evaluated from experimental data and plotted against Γ to see whether an approximation of the form $A + B\Gamma$ will be satisfactory. These results, shown in figure 23, indicate that such a linear approximation should be adequate. The best approximation to the data is given by $A = 0.01173$, $B = 4.200$; and equation (33) becomes

$$\frac{d\Theta}{ds} = 0.01173 - 4.200\Gamma$$

which can be written as (from eq. (28))

$$\frac{d\Theta}{ds} + 4.200 \frac{\Theta}{V_0} \frac{dV_0}{ds} = 0.01173 \quad (34)$$

The solution of (34) is then given by

$$(\Theta V_0^{4.200})_s - (\Theta V_0^{4.200})_{s_{tr}} = 0.01173 \int_{s_{tr}}^s V_0^{4.200} ds \quad (35)$$

where s_{tr} is the starting point of the turbulent boundary layer.

Equation (35) thus requires a simple integration for the calculation of the momentum thickness once the initial value of θ^* is known.

Form factor. - With the momentum thickness known, it becomes necessary to determine H accurately in order to ascertain δ^* and C_{fr} . In order to determine H , Maskell develops an empirical differential equation. A considerable amount of data is used in the development, including zero and negative pressure-gradient data. The resulting equation must be divided into three parts to fit the available data accurately. The division is made in terms of the Γ range by $\Gamma = 0$ and $\Gamma = \Gamma_i$, where Γ_i is itself a function of H . The following relation is obtained in reference 11:

$$\left. \begin{aligned} H &= 1.754 - 0.149 \log_{10} Re_\theta + 0.01015 (\log_{10} Re_\theta)^2 \quad \text{for } \Gamma > 0 \\ \frac{dH}{ds} &= \frac{1}{\theta^* Re_\theta^{0.268}} [\phi - \Gamma(0.30H - 0.32)] \quad \text{for } 0 > \Gamma > \Gamma_i \\ \frac{dH}{ds} &= \frac{1}{\theta^* Re_\theta^{0.268}} [-0.15(H - 1.2) - \Gamma(0.30H - 0.15)] \quad \text{for } \Gamma_i > \Gamma \end{aligned} \right\} \quad (36)$$

where

$$\Gamma_i = \frac{-0.15(H - 1.2) - \phi}{0.17} \quad (37)$$

and ϕ is given in figure 24. The portion of the curve for $H < 1.4$ is given by $\phi = -10^{-0.678H} (0.01399H - 0.01485)$; for $H > 1.6$, by $\phi = -0.054H + 0.0796$; and for $1.4 < H < 1.6$ the curve is faired.

Assuming the distribution of θ^* is now known, and also the value of H at transition, equations (36) and (37) can be solved step-by-step for the complete distribution of H . With H and θ^* known, C_{fr} can be found from equation (29).

The point of turbulent separation is determined in the method from the variation of the friction coefficient ($C_{fr} = 0$ at separation). It is clear from its form that equation (29) cannot lead directly to a value of $C_{fr} = 0$. However, the calculated C_{fr} curve falls off toward zero in such a way that an extrapolation to zero is easily made. Examples of the separation-point extrapolation are shown in figure 8.

Initial conditions. - The problem yet remaining is the proper determination of H and θ^* at the onset of turbulent flow. The velocity profile undergoes an abrupt change from laminar type to turbulent type. The initial value of θ^* is taken from the value occurring in the laminar computation at the point of transition. This is equivalent to assuming that the momentum thickness is continuous through the point of transition. Requiring continuity of the momentum thickness results in a discontinuity (i.e., rapid change) in displacement thickness and, hence, in H (ref. 30). The experimental data now available do not point clearly to a suitable means of determining the initial value of H . Maskell does recognize some systematic trend and presents an analysis leading to highly qualified relations for predicting the value of H at transition. For details of his development, see reference 11.

As an indication of the sensitivity of the calculation to the initial value of H , Maskell tried two widely different initial values and obtained the results shown in figure 25. In spite of the large difference in initial value, the computed curves of H are in fair agreement. The computed values of C_{fr} are in even better agreement. These results, although not susceptible to the general interpretation that the calculations are insensitive to the value of H at transition, are encouraging.

Evaluation. - The accuracy of the method, given the location of the transition point, is demonstrated in several examples in reference 11.

Figure 26, taken from reference 11, illustrates the computed boundary-layer characteristics for an NACA airfoil and compares the results with actual experimental data and with the results of the method of von Doenhoff and Tetervin. The agreement is generally satisfactory for the entire range of θ^* , H , and C_{fr} . The agreement of the calculated separation point with the experimentally obtained separation point is also quite good.

Transition

A major difficulty yet remaining in the computation of blade boundary layers is the successful prediction of the location of the transition point. This problem is in a very difficult realm of viscous-flow theory because of the close relation of the transition point to the Reynolds number and free-stream turbulence of the flow. The problem has been discussed qualitatively in a previous section. An indication of the errors that may result from mislocation of the transition point in the calculation of the drag coefficient of an isolated airfoil is given in figure 27. The figure presents a plot of the variation of calculated profile drag coefficient against distance of the transition point from the leading edge.

Although reliable criteria for transition-point location for general airfoil flow are not currently available, some work has been done along these lines. A low-turbulence investigation of an NACA 65(215)-114 airfoil in reference 31, for example, revealed that, for blade-chord Reynolds numbers ranging from 26×10^6 to 49×10^6 , a criterion for transition based on boundary-layer Reynolds number can be satisfactorily established as $Re_\delta = 8000$. ($Re_\delta = V_0 \delta / \nu$, where δ is the normal distance from the airfoil surface to a point within the boundary layer where the velocity is equal to 0.707 of the velocity at the outer edge of the boundary layer.) These results were obtained for values of Reynolds number that are considerably higher than those encountered in conventional low-speed-cascade practice.

Much more work will have to be done on this problem before reliable criteria are determined for very general conditions of Reynolds number, turbulence, and pressure distribution. Until such criteria are available, theoretical boundary-layer calculations will probably have to concern themselves with a range of possible transition-point locations.

Circulation Defect

Potential-flow calculations provide a tool for determining the surface velocity distribution and hence the circulation and air outlet angle

of cascade blades. For a viscous fluid, the potential flow is altered because of the development of the boundary layer. For many practical blade shapes, the error in the velocity distribution obtained from potential-flow calculations about the original blade may be large. Figure 28, taken from reference 32, indicates the error in a typical cascade calculation. The theoretical potential-flow circulation is always greater than the actual circulation.

References 32 and 33 found that, if the actual (real-flow) circulation of a given blade section could be predicted, the use of this actual value of circulation in the potential-flow calculation for the section would yield theoretical velocity distributions that agreed much better with the measured values. Two mechanisms of incorporating the actual circulation in the velocity-distribution calculation were discussed in reference 33. The first method neglects the Kutta condition and directly reduces the theoretical circulation to the actual value obtained from measurements. By neglecting the Kutta condition an exact potential flow about the original airfoil is obtained, wherein the rear stagnation point occurs on the upper surface. The second method is to distort the airfoil by curving up the trailing edge until the theoretical lift, with the stagnation point at the trailing edge, equals the experimental lift.

The investigation also found that a small reduction in the angle of attack of the section in the theoretical calculation improved the agreement between calculated and observed velocities. An illustration of the effectiveness of the reduced circulation, with and without change in angle of attack, in providing a close comparison between theoretical and measured cascade velocity distributions is shown in figure 29. These results are interesting in that a simple procedure is established for satisfactorily incorporating the circulation decrement into the potential-flow velocity-distribution calculation, once that decrement is known.

The principal problem now is the determination of the actual circulation in the presence of boundary-layer growth. To date, no analytical or empirical data have appeared to permit the general estimation of actual circulation (or lift) for conventional cascade sections. An investigation of an analytical determination of the actual lift of isolated airfoil sections is presented in reference 34. A brief discussion of the method is included herein, since the concepts and procedures involved should be significant also for the cascade airfoil.

The analysis of reference 34 postulates that the presence of surface boundary layers will affect the potential flow about the airfoil in two principal ways. First, since the boundary layers tend to displace the main flow away from the surfaces of the airfoil, the effective shape of

the airfoil will be altered according to the variation of the displacement thicknesses of the surface boundary layers. In general, with the boundary layer thicker on the upper than on the lower surface, an effective reduction in blade camber will result. In addition, a reduced angle of attack will result from altering the effective camber line.

The altering of the effective angle of attack possibly accounts for the general improvement in velocity-distribution comparisons (as in fig. 29) obtained when a slight reduction in angle of attack is included in the theoretical calculation.

The second effect on circulation is the destruction of the Kutta condition at the trailing edge. Reference 34 replaces the Kutta condition with the theorem that, for steady motion, the rates of discharge of positive and negative vorticity into the wake at the trailing edge are equal. Methods of computing the reduction in circulation resulting from the change in profile shape and trailing-edge condition are presented in the reference. Results of calculations for two airfoil shapes show that a considerable portion of the difference between theoretical and actual lift can be predicted on the basis of these considerations. The results further show that the effective altering of the profile shape contributed most to the lift defect.

The theoretical calculation of the lift defect resulting from an effective profile change will generally be more difficult for a cascade airfoil than for the isolated airfoil. Accordingly, the consideration of an empirical correlation between actual lift ratio and some significant boundary-layer thickness parameter may offer more immediate promise for cascade sections.

In view of the preceding discussion, it appears that an iteration process may prove necessary for some boundary-layer computation on airfoils in cascade. The procedure would be as follows:

- (1) Compute potential velocity distribution.
- (2) Compute boundary-layer development from (1).
- (3) Compute circulation defect from boundary-layer characteristics (2).
- (4) Recompute potential velocity distribution on the basis of corrected circulation (3).
- (5) Continue iteration until process converges.

Calculation of Total-Pressure Loss

In compressor design and performance analysis, it is desirable to determine the loss in total pressure incurred across a blade row. In the present section, a method is discussed for relating the total-pressure loss of a cascade section to the boundary-layer characteristics at the blade trailing edge. This makes possible, within the limits of the assumptions involved, the complete theoretical calculation of the cascade loss once the blade boundary-layer conditions have been established. The loss so determined represents the basic two-dimensional profile loss of the section.

If separation has not occurred, the flow field in the plane of the blade trailing edge will appear essentially as a core of potential (or free-stream) flow bounded by viscous layers adjoining the blade surfaces. A considerable portion of the complete loss in total pressure across a cascade is already realized in the viscous layers at the blade trailing edge. However, owing to the lack of uniformity of the velocity distribution in the wake (and also in the free stream), a turbulent mixing of the fluid takes place resulting in an additional loss in total pressure downstream of the blade trailing edge. The complete loss attributable to the cascade can only be measured at an axial position sufficiently far downstream to assure that uniformity has been achieved. Since the rate of dissipation of the wake depends on many factors, experimental loss data obtained at a fixed location for various cascade configurations will not be completely comparable unless properly interpreted in relation to the complete loss involved.

A notable achievement was made in the calculation of the complete loss for isolated airfoils by Squire and Young (ref. 6), who succeeded in relating the total drag to the boundary-layer state at the airfoil trailing edge. The cascade case was treated by Loitsianskii in references 35 and 36. With the assumption that conditions are nearly uniform in the plane of coalescence of the wakes from neighboring blades, the conditions far downstream are related to conditions at the plane of coalescence. Then, the conditions at the plane of coalescence, and consequently at the far-downstream position, are related to the trailing-edge boundary-layer characteristics.

More recently, simplified analyses have been presented in references 7 and 37. In these theories, losses far downstream again are related to the trailing-edge boundary-layer characteristics. This relation is easily and directly established by assuming free-stream conditions to be uniform tangentially in the plane of the trailing edge.

Although this restriction is severe, it is likely that the theory can provide a simple guide to better understanding and estimating cascade loss data.

The assumptions and results of reference 7 are now presented briefly. Only the incompressible-flow case is considered. For purposes of this analysis, the velocity distributions in the tangential direction at various axial locations are assumed to occur as shown in figure 30. Far downstream of the blade row, the wake is ultimately dissipated and the flow is completely uniform in the tangential direction. The mass-averaged loss in total pressure is then (since free-stream total pressure in the plane of the trailing edge is taken equal to the inlet total pressure)

$$\Delta \bar{P} = P_1 - P_2 = P_{0,te} - P_2 \quad (38)$$

where subscripts 1 and 2 denote positions far upstream and far downstream of the blade row (fig. 30), and $P_{0,te}$ is the total pressure in the potential-flow region at the trailing-edge position.

From consideration of the Bernoulli equation, conservation of mass flow and of axial and tangential momentum over the control surface bounded by the dotted streamlines in figure 30, and the conventional definitions of displacement and momentum thickness, the loss coefficient is given by

$$\bar{\omega} = \frac{\Delta \bar{P}}{\frac{1}{2} \rho V_{0,te}^2} = 2 \left(\frac{\theta^*}{c} \right)_{te} \frac{\sigma}{\cos \beta_{te}} \left(1 + \frac{1}{2} \left(\frac{\theta^*}{c} \right)_{te} \frac{\sigma}{\cos \beta_{te}} \left\{ H_{te}^2 - \sin^2 \beta_{te} \left[H_{te} - \frac{1}{1 - \left(\frac{\theta^*}{c} \right)_{te} \frac{\sigma H_{te}}{\cos \beta_{te}}} \right]^2 \right\} \right) \quad (39)$$

where, if desired, $V_{0,te}$ can be related to the inlet velocity V_1 through the expression

$$\frac{V_1}{V_{0,te}} = \frac{\cos \beta_{te}}{\cos \beta_1} \left[1 - \left(\frac{\theta^*}{c} \right)_{te} \frac{\sigma H_{te}}{\cos \beta_{te}} \right]$$

In this manner, the loss involved in the flow from an upstream position to a position of complete dissipation of the wake is related to the boundary-layer characteristics at the trailing edge of the blade and to the cascade geometry. For a more detailed presentation of the development and some calculated results, see reference 7.

CONCLUDING REMARKS

It is apparent from the preceding analysis that the boundary-layer theory currently available is incapable of completely predicting the viscous flow about a two-dimensional cascade. However, the qualitative information provided by the theory can serve as a useful guide in obtaining and interpreting cascade data. Furthermore, some quantitative results can be obtained from the theory in its present state for a limited range of flow conditions and assumptions.

The principal conclusion reached from the qualitative evaluation of cascade boundary-layer behavior is the large sensitivity of the losses to blade-chord Reynolds number and free-stream turbulence. Apparently, a wide range of boundary-layer loss can be obtained for a conventional cascade geometry, depending upon Reynolds number and turbulence. The importance of the identification and evaluation of Reynolds number effects in cascade operation and data analysis is thereby indicated.

The primary shortcoming of quantitative evaluations is the inability of theory to predict the location and characteristics of the transition from laminar to turbulent flow. The computation for a completely laminar or completely turbulent boundary layer is acceptably simple and accurate. Widespread use of the quantitative calculations will follow the ability to successfully locate the transition point. This problem is so difficult theoretically that an attempt should be made to determine an empirical correlation valid for the limited variety of blade shapes currently in use.

The question of possible serious Reynolds number effects in compressor operation is raised in view of the large increases in loss that may be obtained at reduced Reynolds number because of laminar separation in the cascade flow. Reduced Reynolds numbers are encountered in compressors for small-size units and high-altitude operations. However, it is recognized that the viscous-flow phenomena in the compressor configuration are far more complex than in the cascade. First, the development of the boundary layers along the blade elements is complicated by the various spanwise boundary-layer motions and three-dimensional effects existing in compressor blade rows. Secondly, the turbulence picture differs because of blade wakes and inlet flow distortions. Finally, there are other sources of Reynolds number effects in the development of the casing boundary layers and of the other three-dimensional effects. The observed loss characteristics in the compressor result from the various compressor viscous phenomena. Therefore, the extent to which cascade viscous-flow characteristics will be reflected in the compressor is questionable. The answers to these questions must be supplied by continued comparative research.

REFERENCES

1. Schilhansl, Max J.: Survey of Information on Two-Dimensional Cascades. Tech. Rep. 54-322, Wright Air Dev. Center, Air Res. and Dev. Command, USAF, Wright-Patterson Air Force Base, Mar. 1955. (Aero. Res. Lab. Contract AF 33(616)-16, Proj. 3066.)
2. Schlichting, H.: Lecture Series "Boundary Layer Theory." Pt. I - Laminar Flows. NACA TM 1217, 1949.
3. Goldstein, Sydney, ed.: Modern Developments in Fluid Dynamics. Vols. I and II. Clarendon Press (Oxford), 1938.
4. Dryden, Hugh L.: Recent Advances in the Mechanics of Boundary Layer Flow. Advances in Appl. Mech., vol. 1, 1948.
5. Howarth, L., ed.: Modern Developments in Fluid Dynamics; High Speed Flow. Vols. I and II. Clarendon Press (Oxford), 1953.
6. Squire, H. B., and Young, A. D.: The Calculation of the Profile Drag of Aerofoils. R. & M. No. 1838, British A.R.C., Nov. 1937.
7. Lieblein, Seymour, and Roudebush, William H.: Theoretical Loss Relations for Low-Speed Two-Dimensional-Cascade Flow. NACA TN 3662, 1956.
8. Pohlhausen, K.: Zur näherungsweise Integration der Differentialgleichung der laminaren Grenzschicht. Z.a.M.M., Bd. 1, Heft 4, Aug. 1921, pp. 252-268.
9. Clauser, Francis H.: Turbulent Boundary Layers in Adverse Pressure Gradients. Jour. Aero. Sci., vol. 21, no. 2, Feb. 1954, pp. 91-108.
10. Ludwig, H., and Tillmann, W.: Investigations of the Wall-Shearing Stress in Turbulent Boundary Layers. NACA TM 1285, 1950.
11. Maskell, E. C.: Approximate Calculation of the Turbulent Boundary Layer in Two-Dimensional Incompressible Flow. Rep. No. AERO 2443, British R.A.E., Nov. 1951.
12. Lieblein, Seymour, Schwenk, Francis C., and Broderick, Robert L.: Diffusion Factor for Estimating Losses and Limiting Blade Loadings in Axial-Flow-Compressor Blade Elements. NACA RM E53D01, 1953.
13. Savage, Melvyn: Analysis of Aerodynamic Blade-Loading-Limit Parameters for NACA 65-(C₇A₁₀)10 Compressor-Blade Sections at Low Speeds. NACA RM L54L02a, 1955.

14. Schubauer, G. B., and Skramstad, H. K.: Laminar-Boundary-Layer Oscillations and Transition on a Flat Plate. NACA Rep. 909, 1948. (Supersedes NACA WR W-8.)
15. Schlichting, H.: Lecture series "Boundary Layer Theory." Pt. II - Turbulent Flows. NACA TM 1218, 1949.
16. Bussmann, K., and Ulrich, A.: Systematic Investigations of the Influence of the Shape of the Profile upon the Position of the Transition Point. NACA TM 1185, 1947.
17. Taylor, G. I.: Some Recent Developments in the Study of Turbulence. Proc. Fifth Int. Cong. Appl. Mech., 1938, pp. 294-310.
18. Dryden, Hugh L., Schubauer, G. B., Mock, W. C., Jr., and Skramstad, H. K.: Measurements of Intensity and Scale of Wind-Tunnel Turbulence and Their Relation to the Critical Reynolds Number of Spheres. NACA Rep. 581, 1937.
19. Seiferth, R., ed.: D_1 - Model Testing Technique. I - Test Installations. Measurement of the Tunnel Turbulence by Means of a Sphere and Its Relation to the Hot-Wire Measurement. Rep. and Trans. No. 994, M.A.P. Völkenrode, June 15, 1947.
20. Bursnall, William J., and Loftin, Laurence K., Jr.: Experimental Investigation of Localized Regions of Laminar-Boundary-Layer Separation. NACA TN 2338, 1951.
21. Herrig, L. Joseph, Emery, James C., and Erwin, John R.: Systematic Two-Dimensional Cascade Tests of NACA 65-Series Compressor Blades at Low Speeds. NACA RM L51G31, 1951.
22. Blight, F. G., and Howard W.: Tests on Four Airfoil Cascades. Pt. II. Boundary Layer Characteristics. Rep. E.75, Dept. Supply, Aero. Res. Labs., Melbourne (Australia), July 1952.
23. Carter, A. D. S., Andrews, S. J., and Shaw, H.: Some Fluid Dynamic Research Techniques. Proc. Inst. Mech Eng., (London), vol. 163, 1950, pp. 249-263.
24. von Kármán, Th.: Über laminare und turbulente Reibung. Z.a.M.M., Bd. 1, Heft 4, Aug. 1921, pp. 233-252.
25. Loitsianskii, L. G.: Approximate Method of Integration of Laminar Boundary Layer in Incompressible Fluid. NACA TM 1293, 1951.
26. Thwaites, B.: Approximate Calculation of the Laminar Boundary Layer. The Aero. Quarterly, vol. 1, Nov. 1949, pp. 245-280.

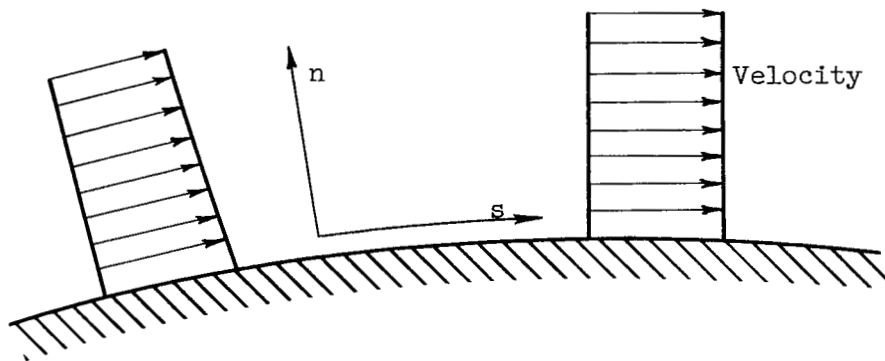
27. Owen, P. R., and Klanfer, L.: On the Laminar Boundary Layer Separation from the Leading Edge of a Thin Aerofoil. Rep. No. AERO 2508, British R.A.E., Oct. 1953.
28. Crooks, P. V., and Howard W.: Low Speed Tests on Three Aerofoil Cascades Designed for Prescribed Surface Velocity Distributions. Res. & Dev. Branch, Aero. Res. Labs., Melbourne (Australia), Rep. ME.76, June 1954.
29. von Doenhoff, Albert E., and Tetervin, Neal: Determination of General Relations for the Behavior of Turbulent Boundary Layers. NACA Rep. 772, 1943. (Supersedes NACA WR L-382.)
30. Persh, Jerome: The Behavior of the Boundary Layer in the Region of Transition from Laminar to Turbulent Flow. Jour. Aero. Sci., vol. 22, no. 6, June 1955, pp. 443-444.
31. Braslow, Albert L., and Visconti, Fioravante: Investigation of Boundary-Layer Reynolds Number for Transition on an NACA 65(215)-114 Airfoil in the Langley Two-Dimensional Low-Turbulence Pressure Tunnel. NACA TN 1704, 1948.
32. Katzoff, S., and Hannah, Margery E.: Further Comparisons of Theoretical and Experimental Lift and Pressure Distributions on Airfoils in Cascade at Low-Subsonic Speed. NACA TN 2391, 1951.
33. Katzoff, S., Bogdonoff, Harriet E., and Boyet, Howard: Comparisons of Theoretical and Experimental Lift and Pressure Distributions on Airfoils in Cascade. NACA TN 1376, 1947.
34. Preston, J. H.: The Calculation of the Lift Taking Account of the Boundary Layer. R. & M. No. 2725, British A.R.C., 1949.
35. Loitsianskii, L. G.: Soprotivlenie Reshetki Profilei Obtekaemoi Viazkoi Neszhimaemoi Zhidkost'iu. Prikladnaya Matematika i Mekhanika, vol. XI, no. 4, 1947. (Resistance of Cascade of Airfoils in Viscous Incompressible Fluid.) (Trans. available from NACA headquarters.)
36. Loitsianskii, L. G.: Resistance of Cascade of Airfoils in Gas Stream at Subsonic Velocity. NACA TM 1303, 1951.
37. Schlichting, H., und Scholz, N.: Über die theoretische Berechnung der Strömungsverluste eines ebenen Schaufelgitters. Ing.-Archiv, Bd. XIX, Heft 1, 1951, pp. 42-65.

38. Platt, Robert C.: Turbulence Factors of NACA Wind Tunnels as Determined by Sphere Tests. NACA Rep. 558, 1936.
39. Lawson, T. V.: An Investigation into the Effect of Reynolds Number on a Cascade of Blades with Parabolic Arc Camber Line. Memo. No. M.195, British N.G.T.E., Nov. 1953.
40. Blight, F. G., and Howard W.: Tests on Four Airfoil Cascades. Pt. I - Deflection, Drag, and Velocity Distribution. Rep. E.74, Dept. Supply, Aero. Res. Labs., Melbourne (Australia), July 1952.

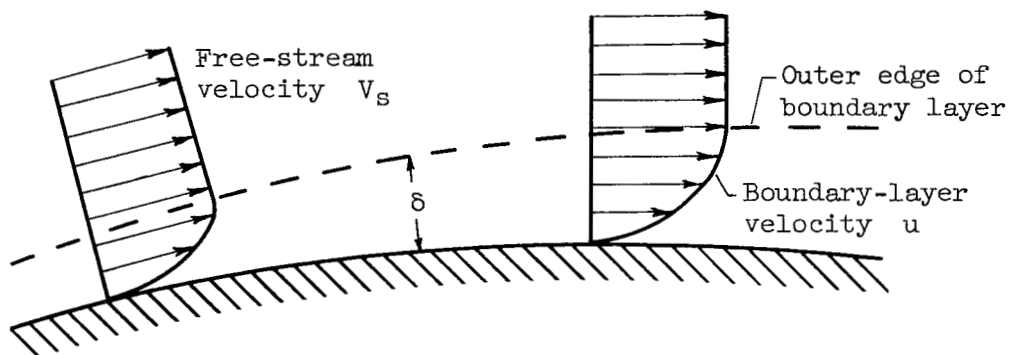
TABLE I. - FUNCTIONS FOR THWAITES SOLUTION OF
LAMINAR BOUNDARY LAYER (REF. 26)

m	$l(m)$	H(m)	$\mathcal{L}(m)$
0.082	0	3.70	0.938
.0818	.011	3.69	.953
.0816	.016	3.66	.956
.0812	.024	3.63	.962
.0808	.030	3.61	.967
.0804	.035	3.59	.969
.080	.039	3.58	.971
.079	.049	3.52	.970
.078	.055	3.47	.963
.076	.067	3.38	.952
.074	.076	3.30	.936
.072	.083	3.23	.919
.070	.089	3.17	.902
.068	.094	3.13	.886
.064	.104	3.05	.854
.060	.113	2.99	.825
.056	.122	2.94	.797
.052	.130	2.90	.770
.048	.138	2.87	.744
.040	.153	2.81	.691
.032	.168	2.75	.640
.024	.182	2.71	.590
.016	.195	2.67	.539
.008	.208	2.64	.490
0	.220	2.61	.440
-.016	.244	2.55	.342
-.032	.268	2.49	.249
-.048	.291	2.44	.156
-.064	.313	2.39	.064
-.080	.333	2.34	-.028
-.10	.359	2.28	-.138
-.12	.382	2.23	-.251
-.14	.404	2.18	-.362
-.20	.463	2.07	-.702
-.25	.500	2.00	-1.000

~~CONFIDENTIAL~~



(a) Nonviscous flow.



(b) Viscous flow.

Figure 1. - Velocity profiles near a fixed boundary.

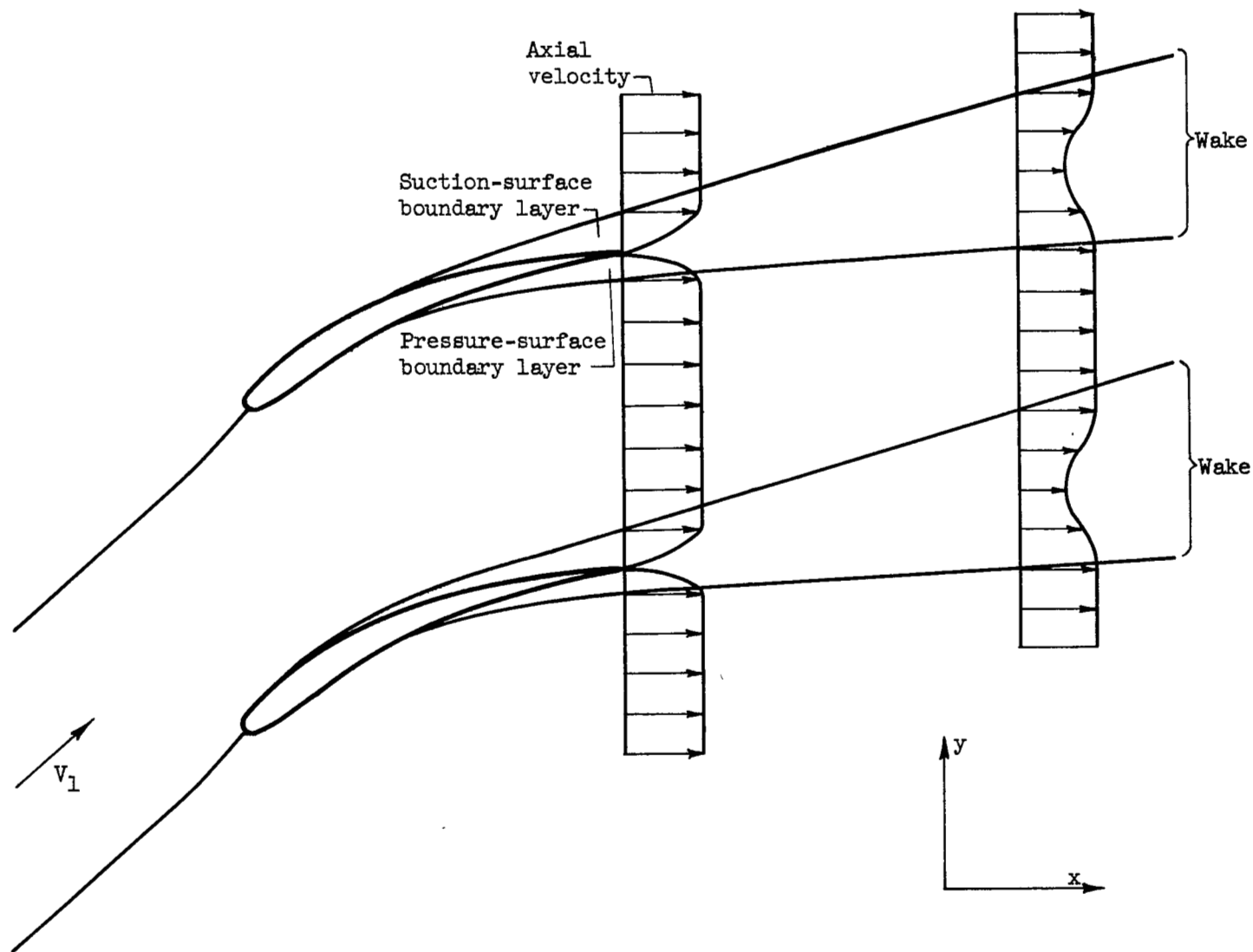


Figure 2. - Boundary layers and blade wake in two-dimensional-cascade flow.

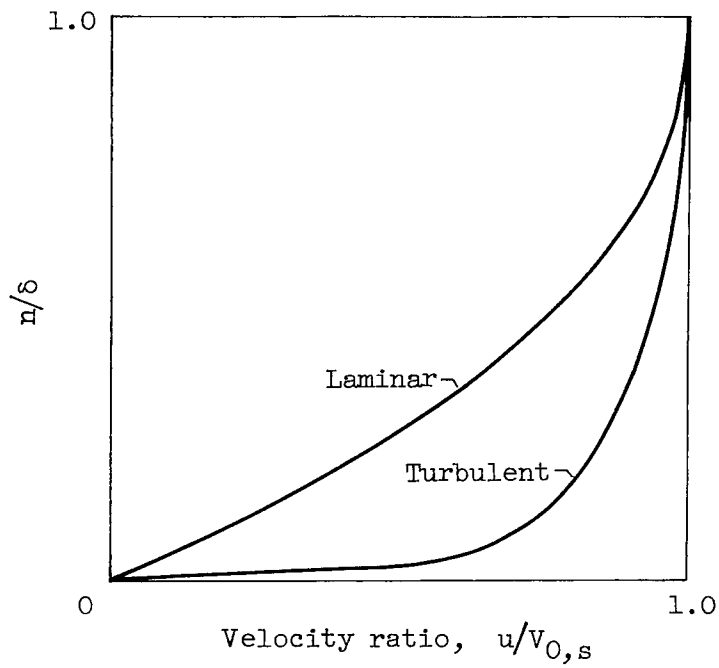


Figure 3. - Typical velocity profiles for laminar and turbulent boundary layers.

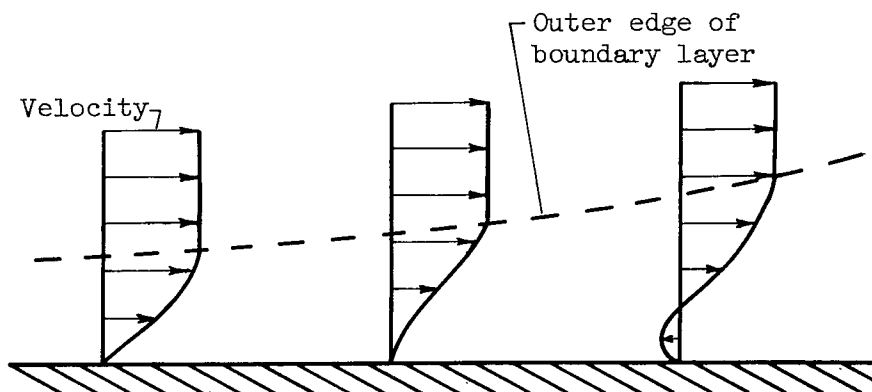


Figure 4. - Boundary-layer flow reversal in presence of adverse pressure gradient.

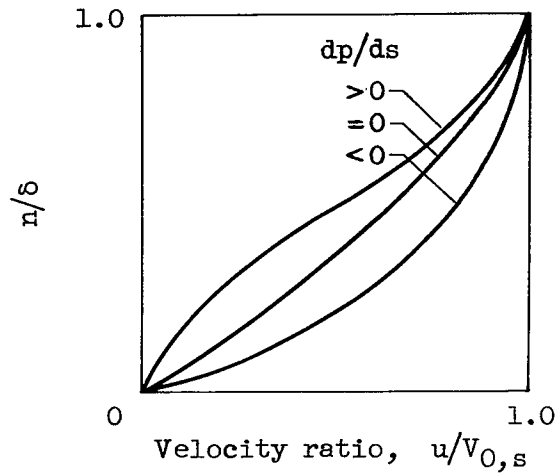


Figure 5. - Laminar-boundary-layer velocity distributions for different surface pressure gradients.

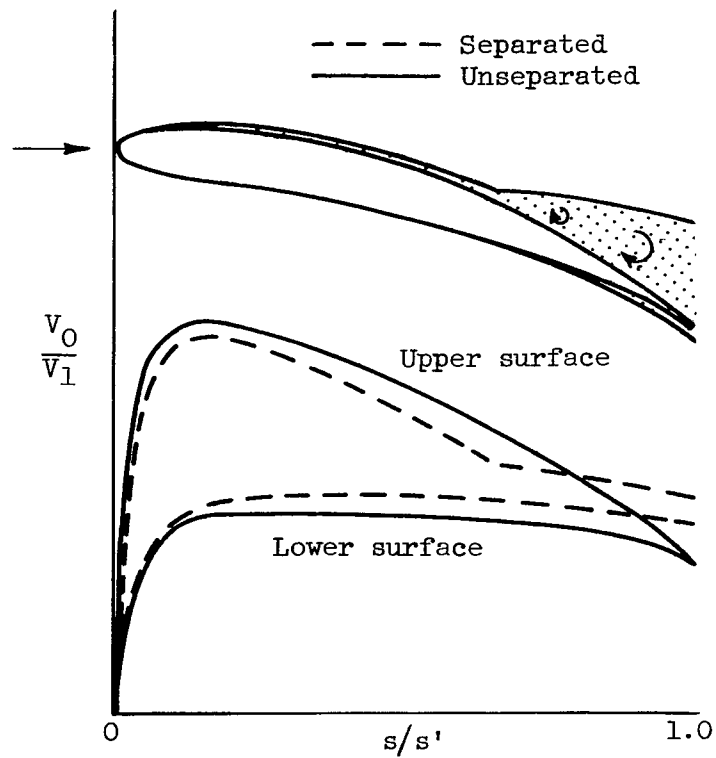


Figure 6. - Effect of separation on velocity distribution about an airfoil.

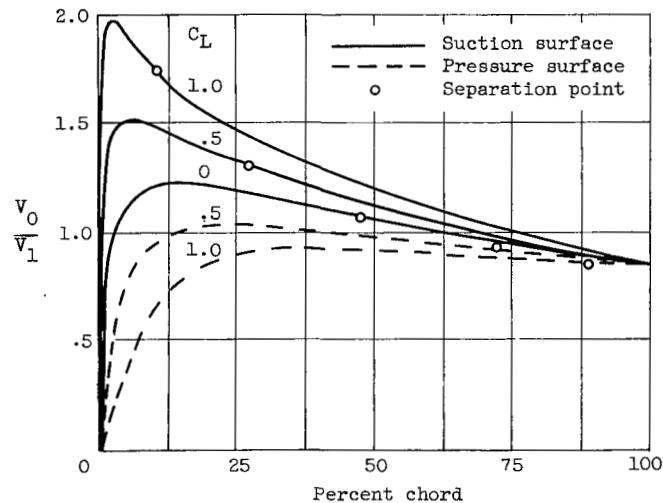


Figure 7. - Potential-theoretical velocity distribution showing calculated point of laminar separation for Joukowski profile J 015 for lift coefficients of 0, 0.5, and 1.0 (ref. 2).

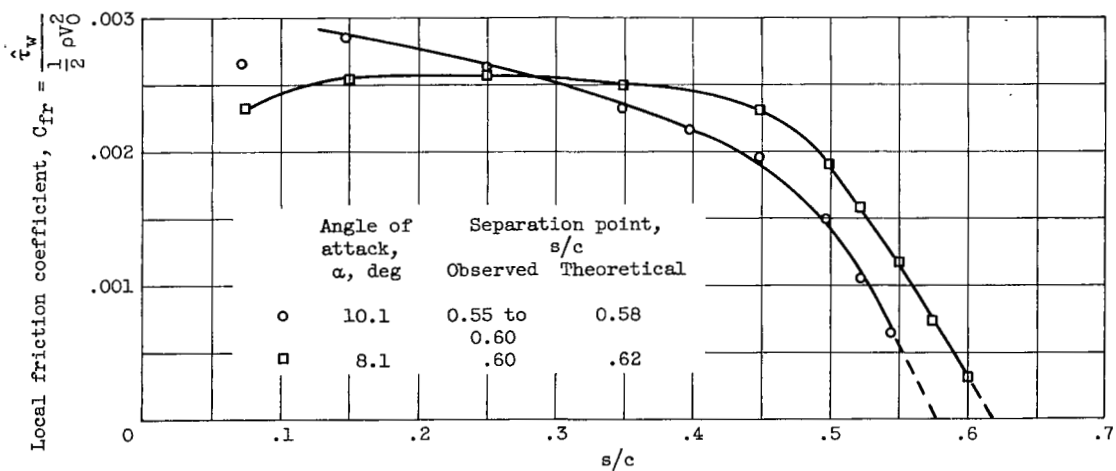


Figure 8. - Comparison of experimentally observed separation points with those obtained by extrapolating values of C_{fr} obtained from Ludwig-Tillmann formula using experimental data of reference 29 for NACA airfoil section 65(216)-222 (approx.) (ref. 11).

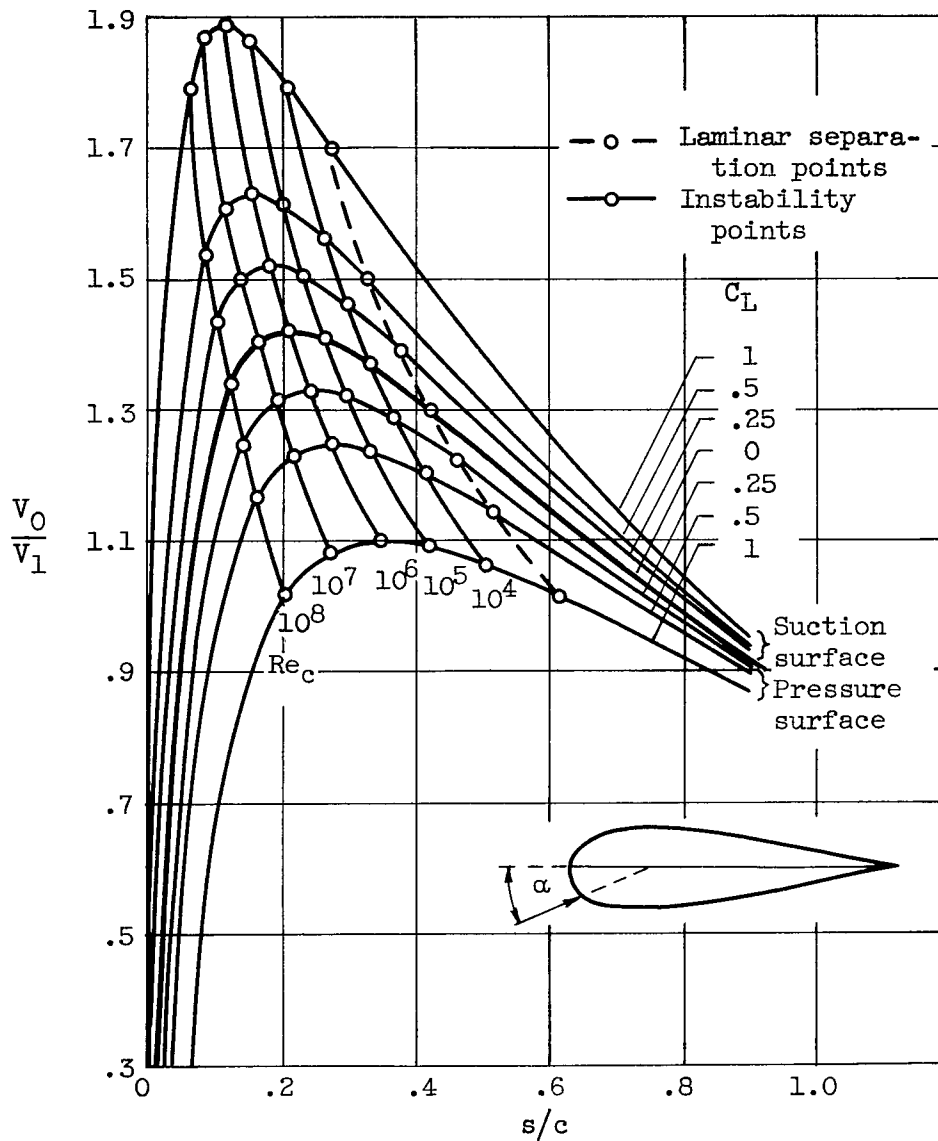


Figure 9. - Theoretical velocity distributions for J O25 airfoil at various values of lift coefficient (obtained by varying angle of attack) with instability and separation points calculated for various values of blade-chord Reynolds number (ref. 16).

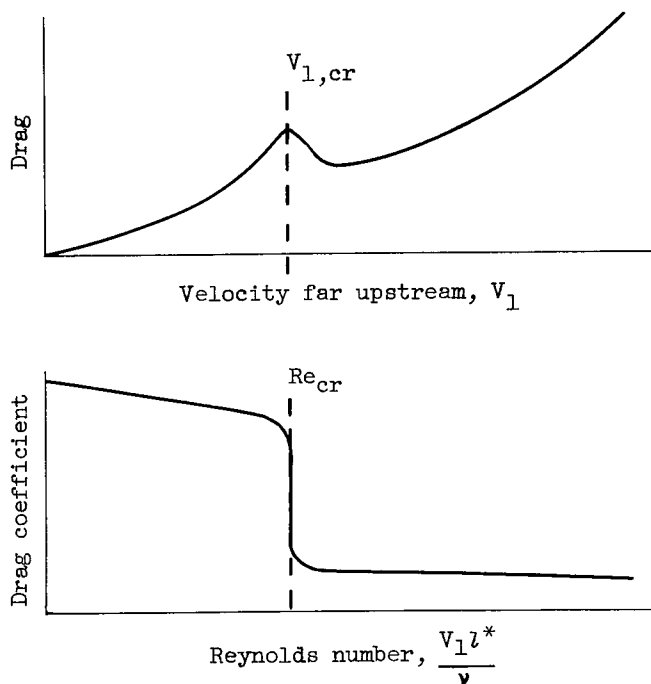


Figure 10. - Drag and drag coefficient of sphere in region of critical Reynolds number.

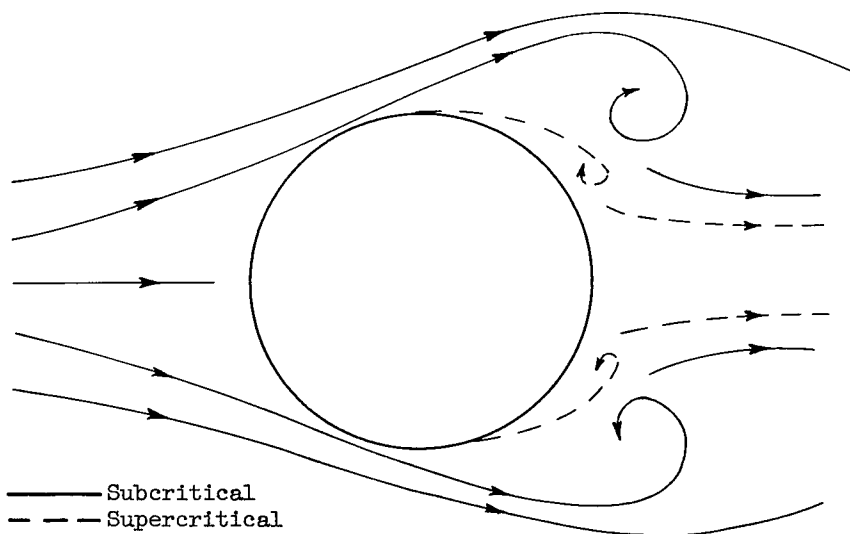


Figure 11. - Subcritical and supercritical flow around sphere (schematic, after ref. 15).

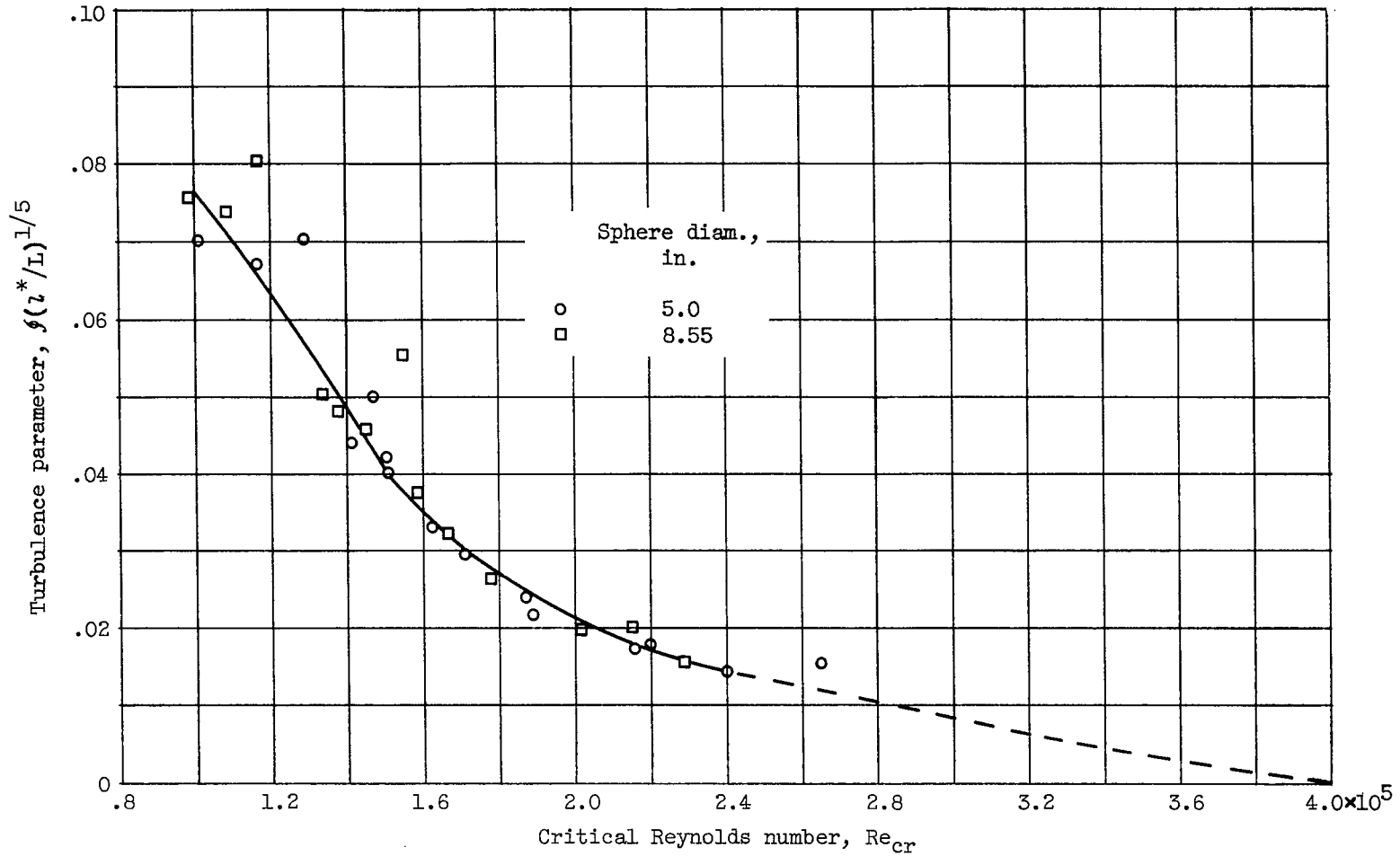
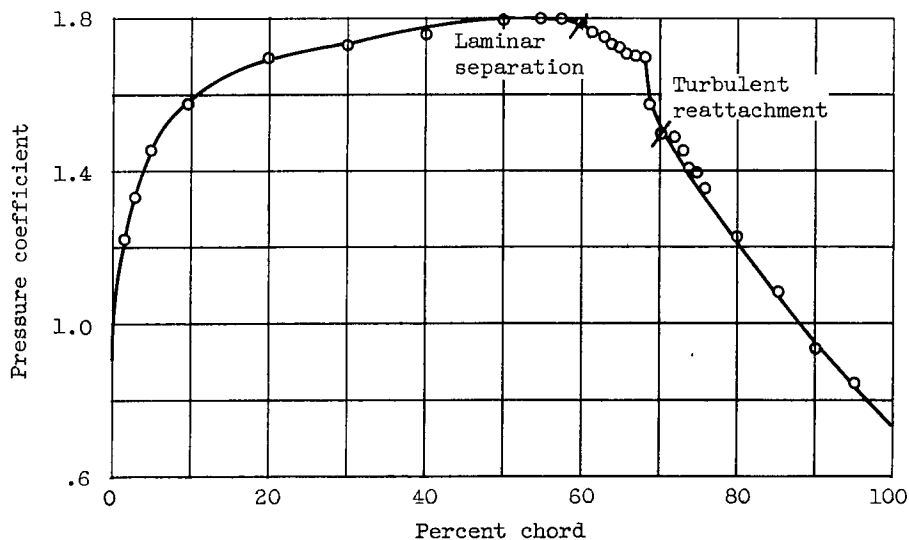
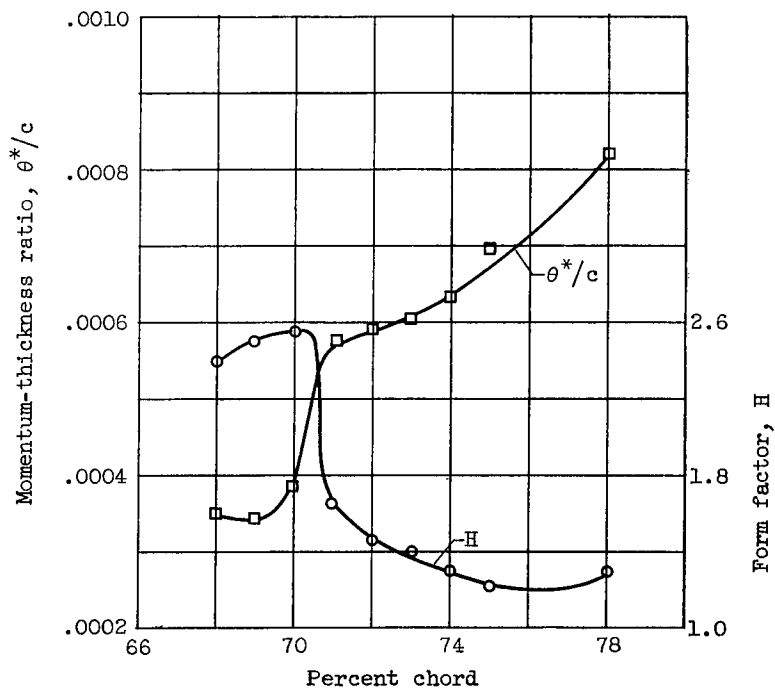


Figure 12. - Experimental variation of critical Reynolds number of spheres with turbulence factor; extrapolated to zero turbulence (data of ref. 18). Value of Re_{cr} for zero turbulence indicated to be between 3.85×10^5 (ref. 38) and 4.11×10^5 (ref. 19).

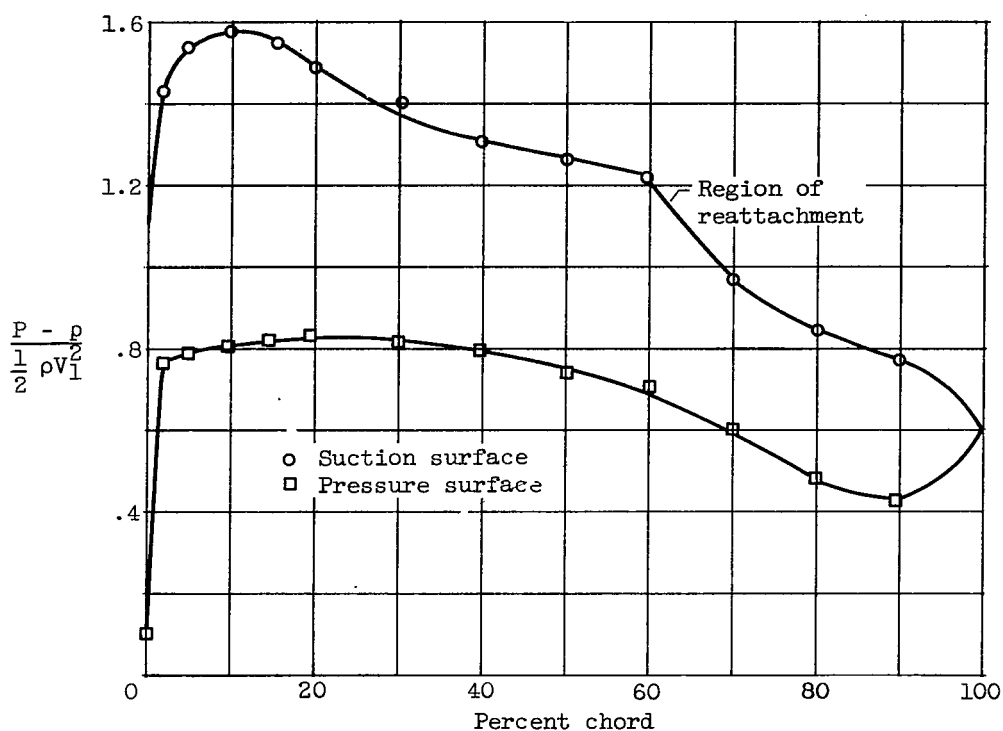


(a) Pressure distribution.

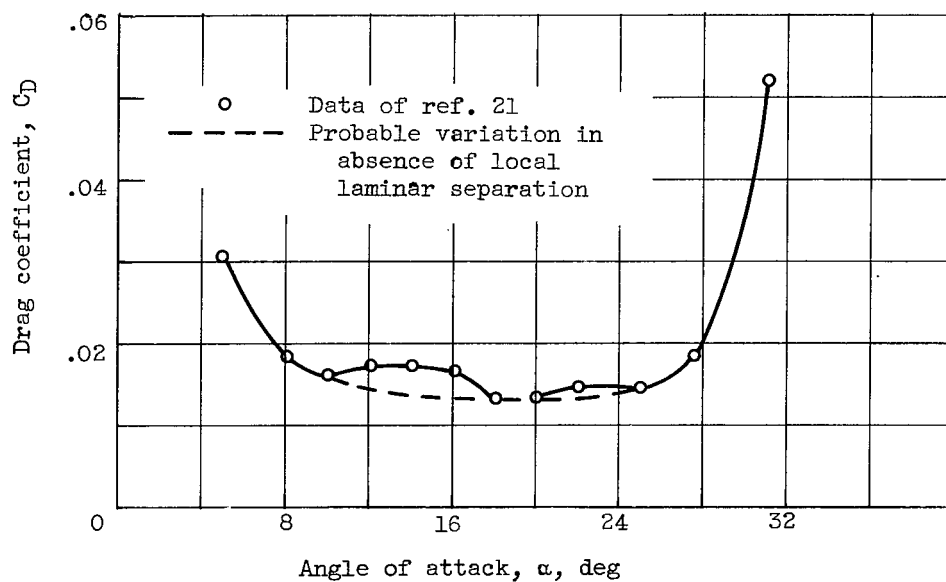


(b) Momentum thickness and form factor.

Figure 13. - Pressure distribution on NACA 663-018 airfoil at zero angle of attack and blade-chord Reynolds number of 2.4×10^6 , and variation of momentum-thickness ratio and form factor in region of reattachment of locally separated flow (ref. 20).



(a) Pressure distribution at 16.1° angle of attack.



(b) Variation of drag coefficient with angle of attack.

Figure 14. - Illustration of effect of local laminar separation on pressure distribution and drag characteristics for NACA 65-(12)10 airfoil in cascade. Inlet-air angle, 45°; solidity, 1.5.

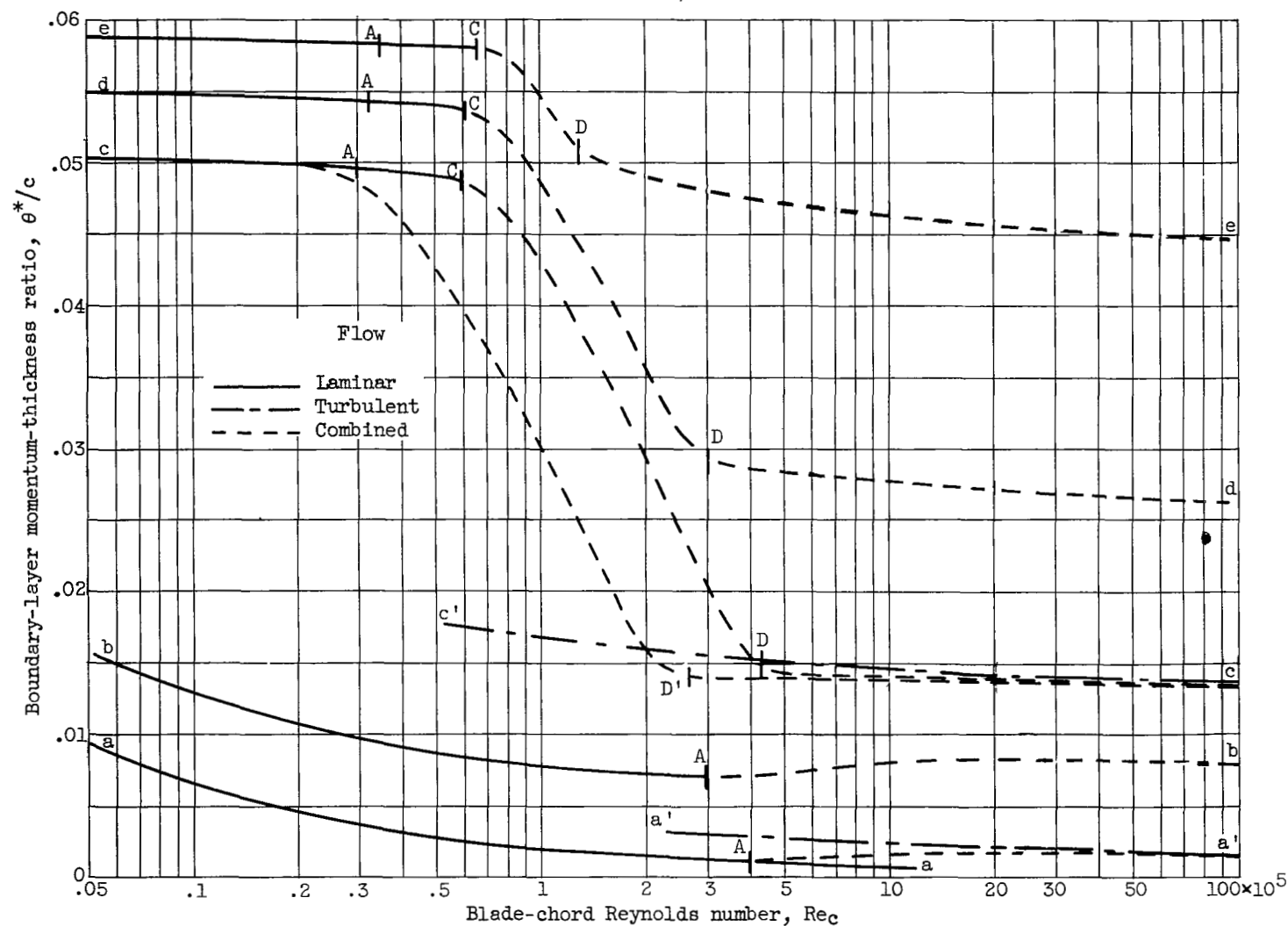


Figure 15. - Qualitative variation of trailing-edge momentum-thickness ratio with blade-chord Reynolds number for several levels of blade loading on conventional airfoils in cascade. (Not to be considered quantitatively correct.)

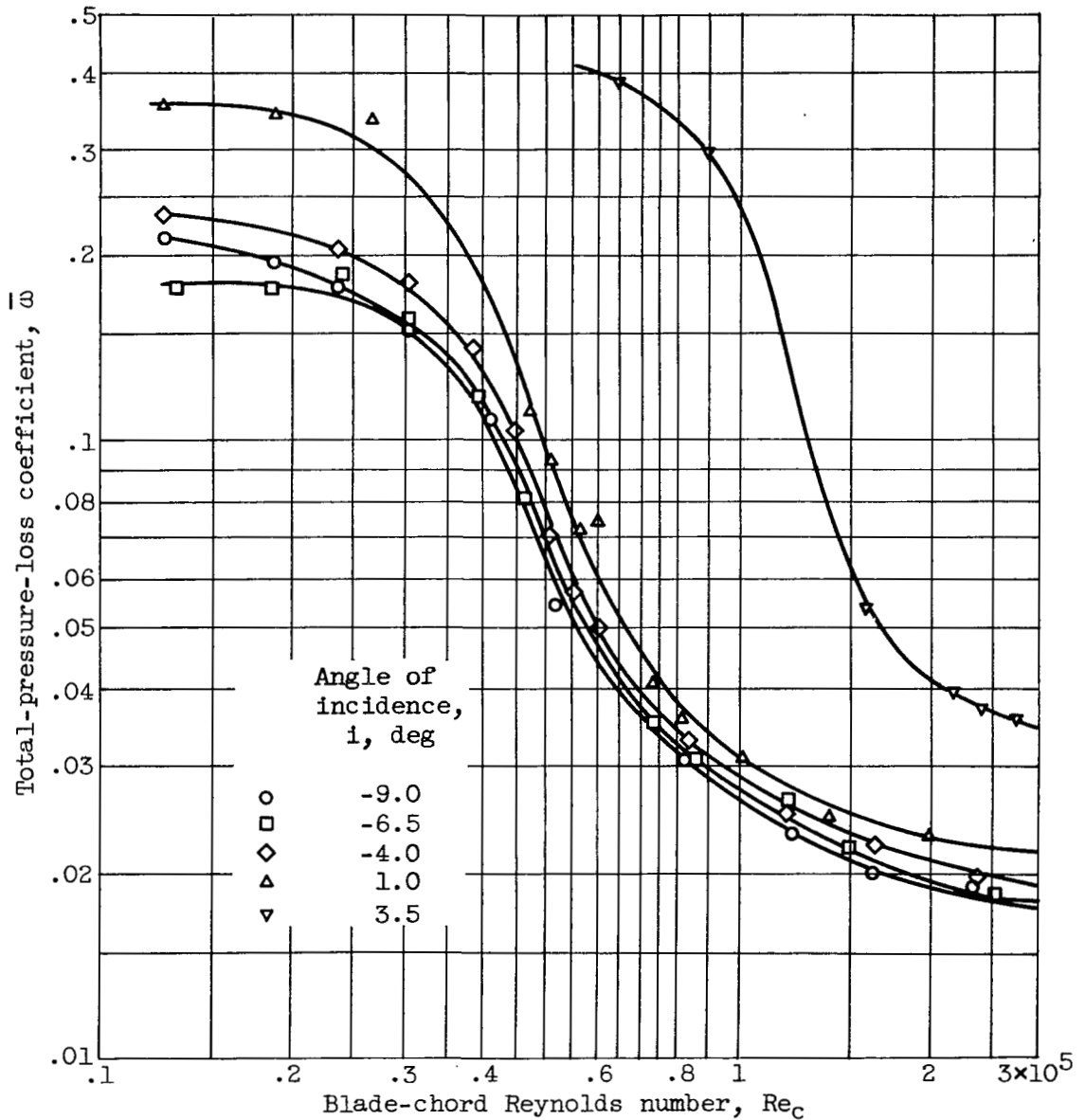
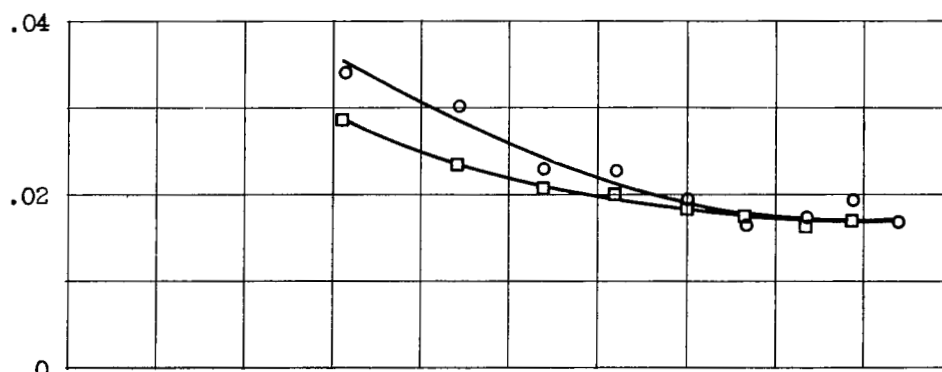
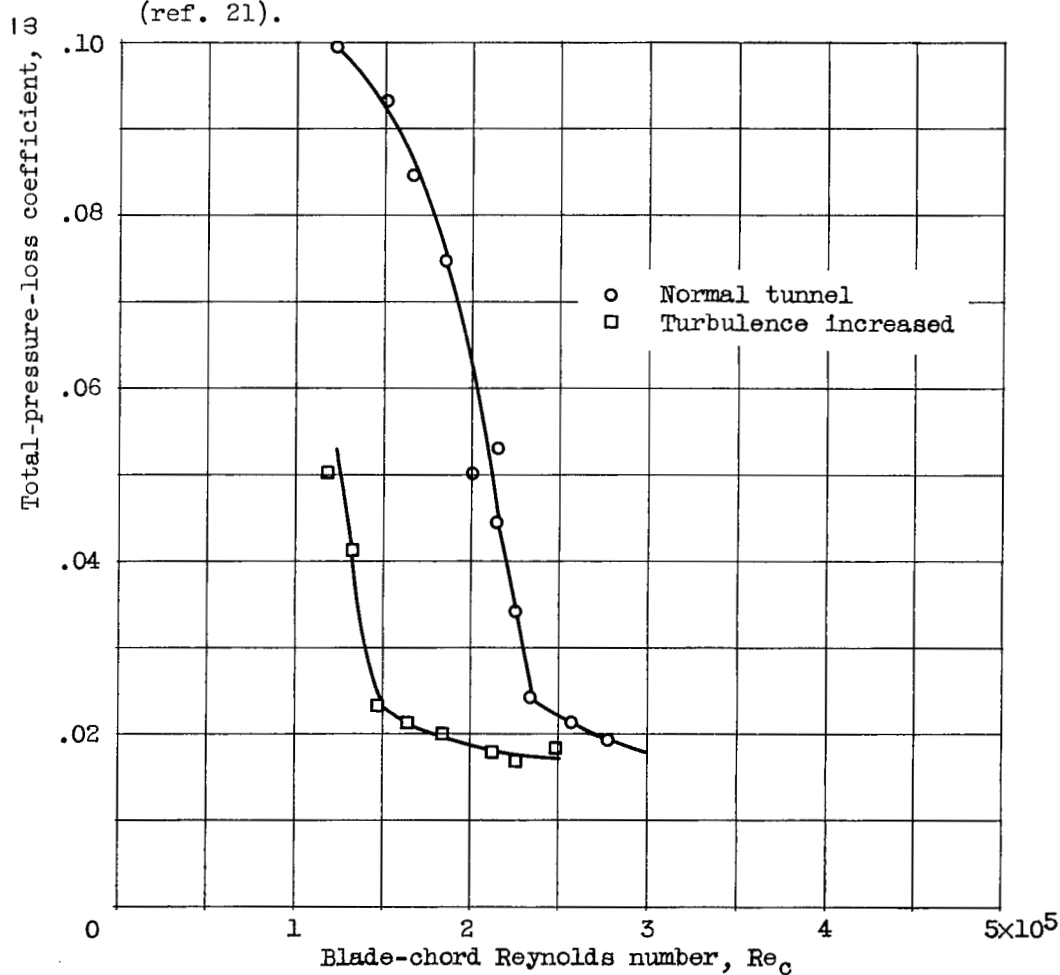


Figure 16. - Variation of total-pressure-loss coefficient with blade-chord Reynolds number for parabolic-arc blade 10C4/40 P40. Inlet-air angle, 28° to 40° ; solidity, 1.333 (ref. 39).



(a) NACA 65-(12)10 blade. Inlet-air angle, 45° ; solidity, 1.5 (ref. 21).



(b) Lighthill blade, 50 percent laminar flow. Inlet-air angle, 45.5° ; solidity, 1.0 (ref. 40).

Figure 17. - Effect of blade-chord Reynolds number and free-stream turbulence on minimum-loss coefficient of cascade blade section in two-dimensional tunnel.

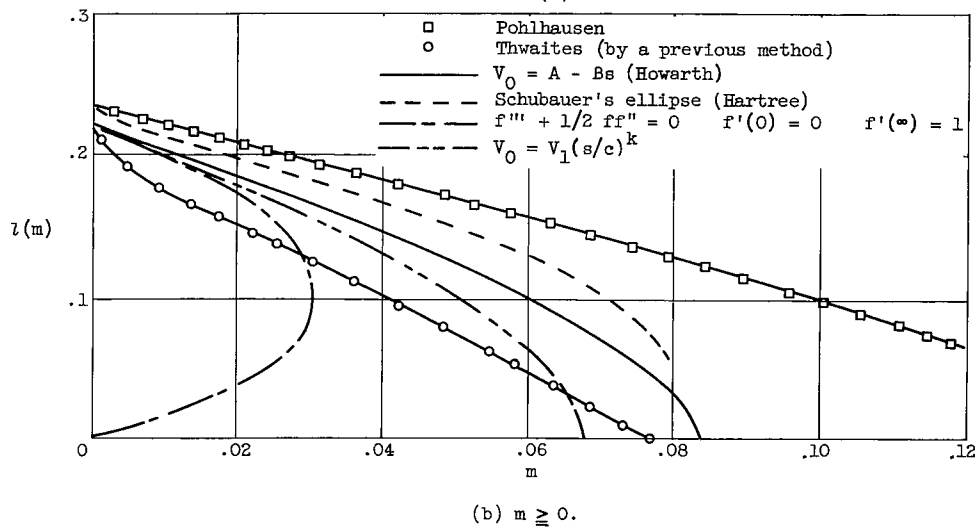
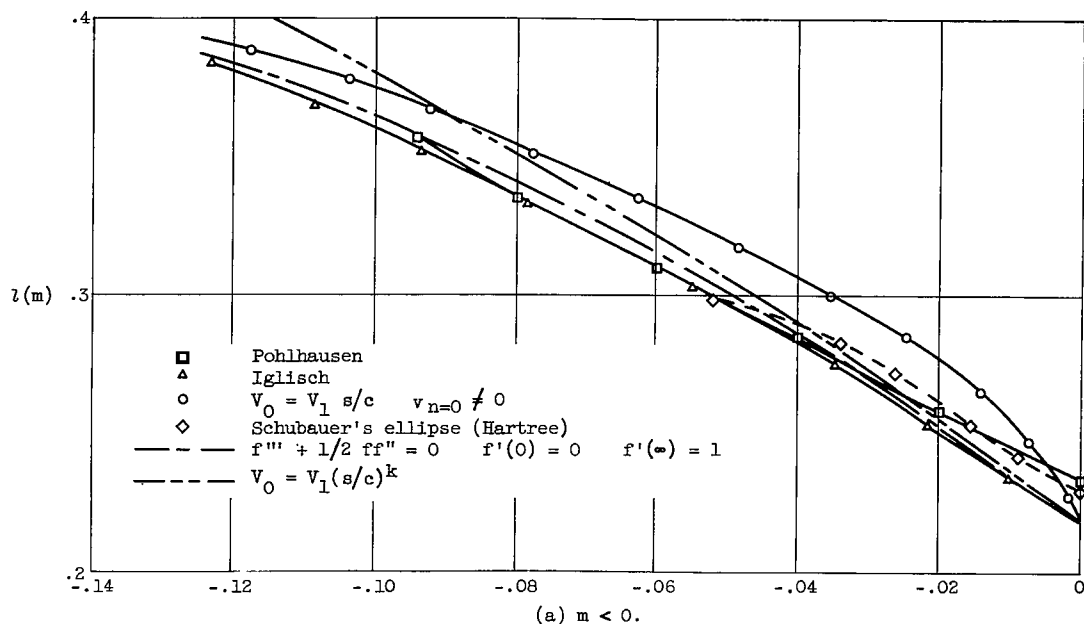
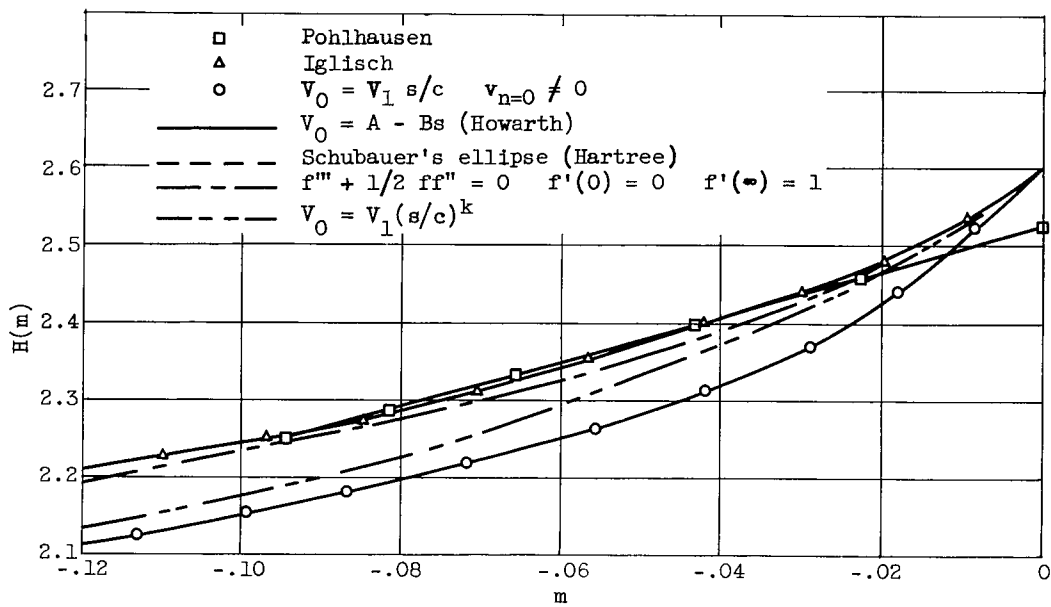
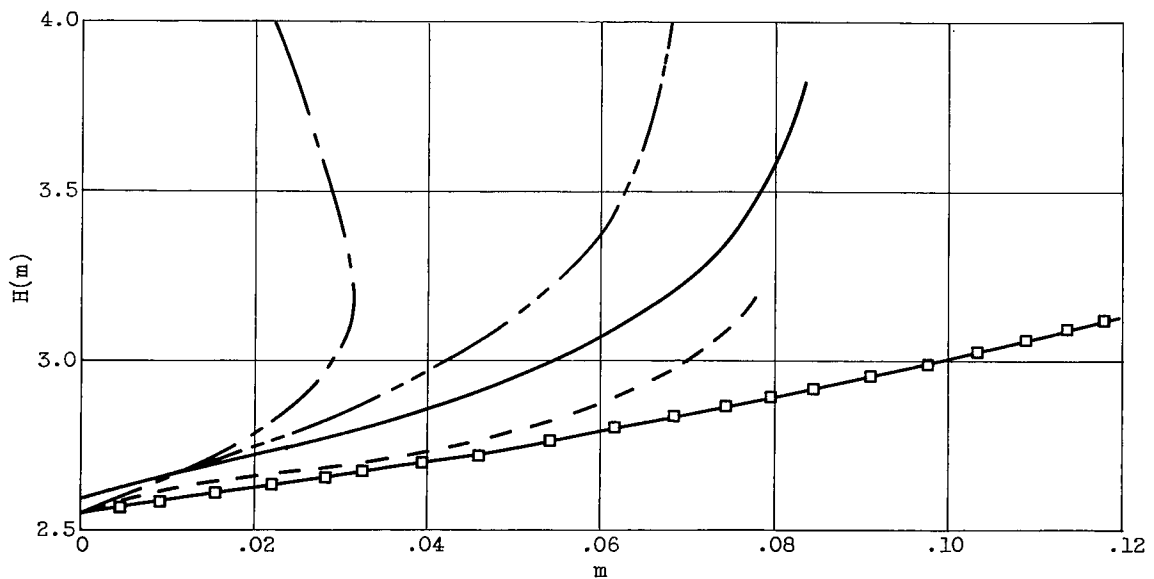


Figure 18. - Variation of $l(m)$ with m for theoretical velocity distributions (ref. 26).

(a) $m < 0$.(b) $m \geq 0$.Figure 19. - Variation of $H(m)$ with m for theoretical velocity distributions (ref. 26).

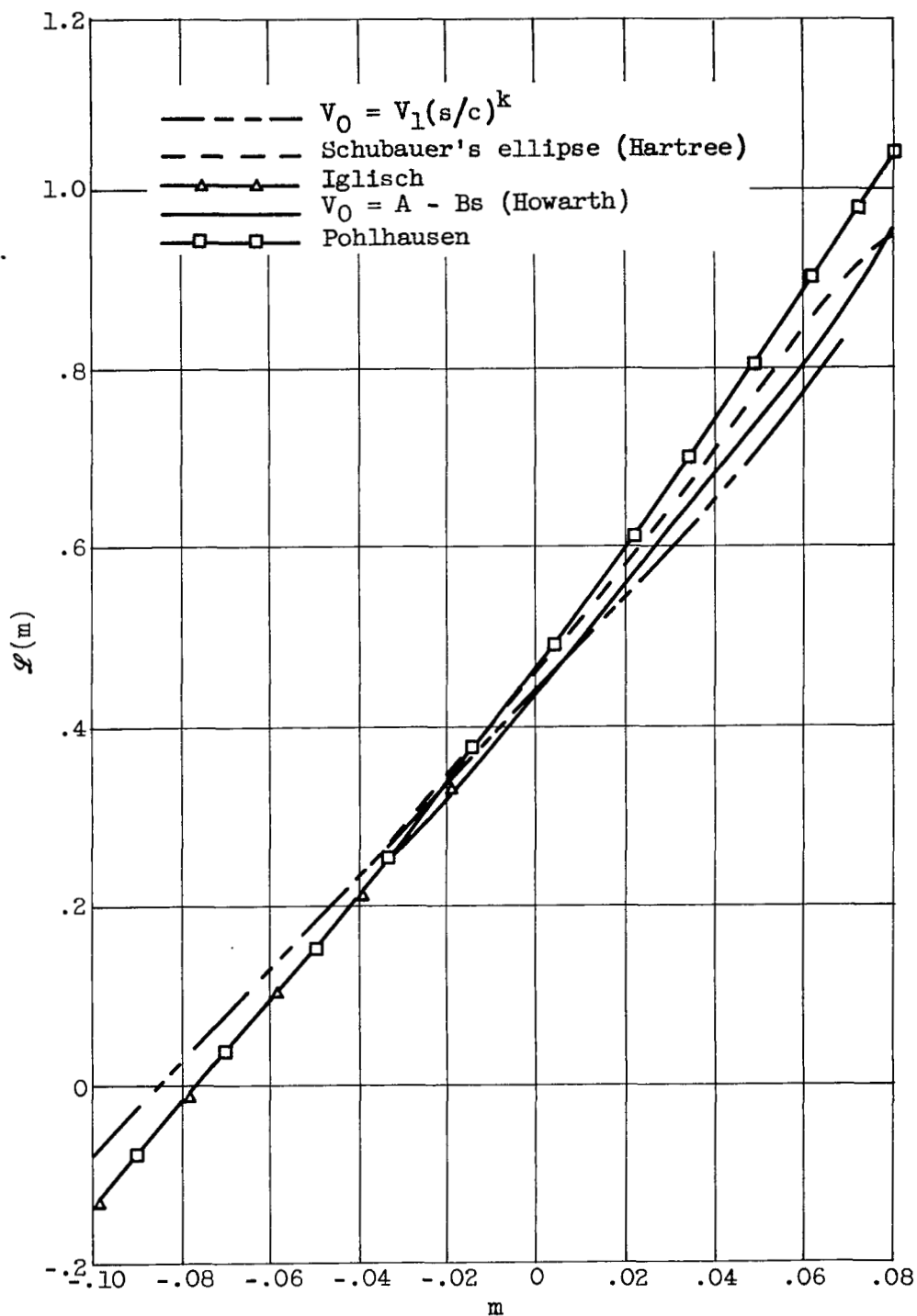


Figure 20. - Variation of $L(m)$ with m for theoretical velocity distributions (ref. 26).

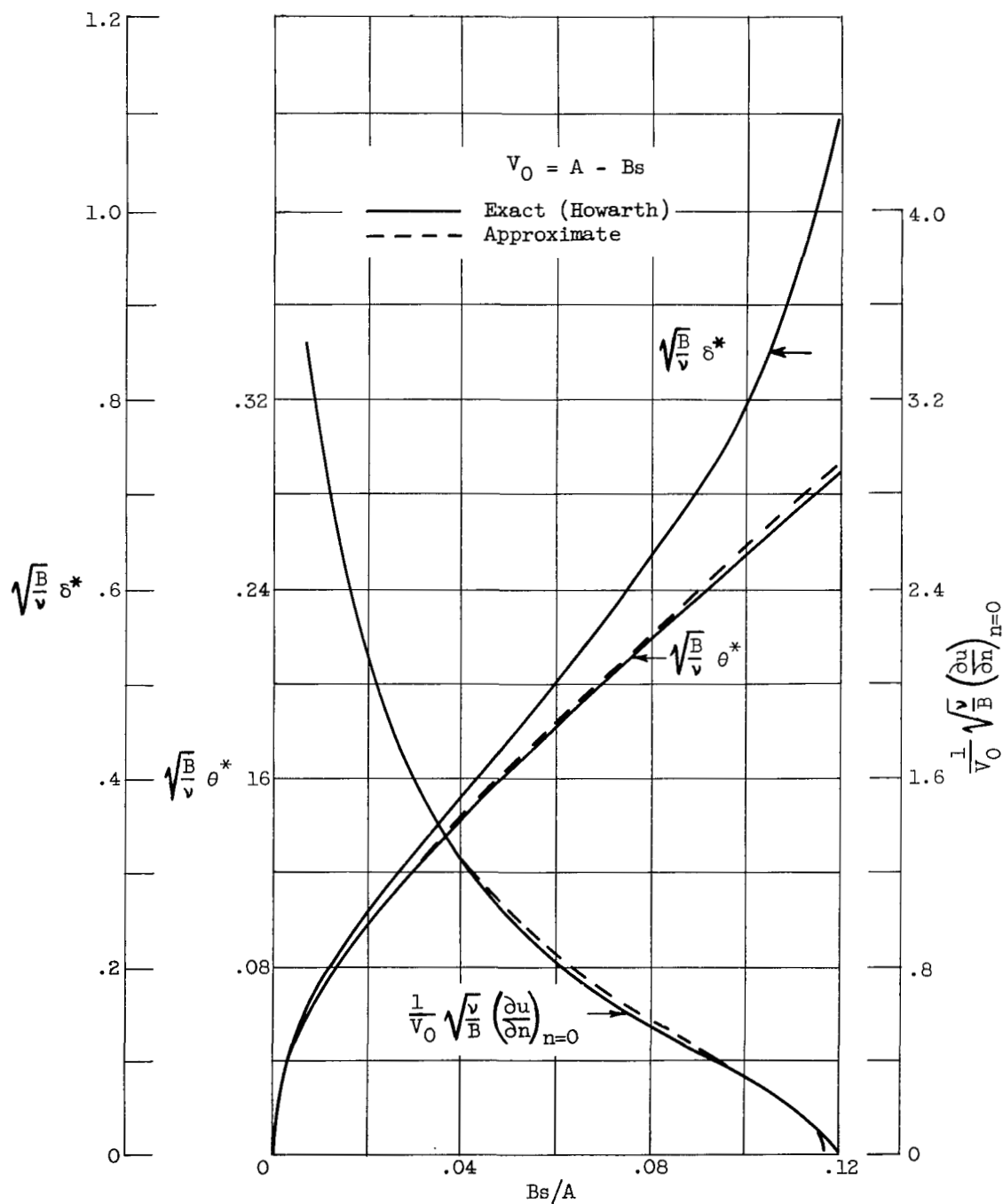


Figure 21. - Comparison of solutions obtained by approximate method of Thwaites with exact solutions (ref. 26).

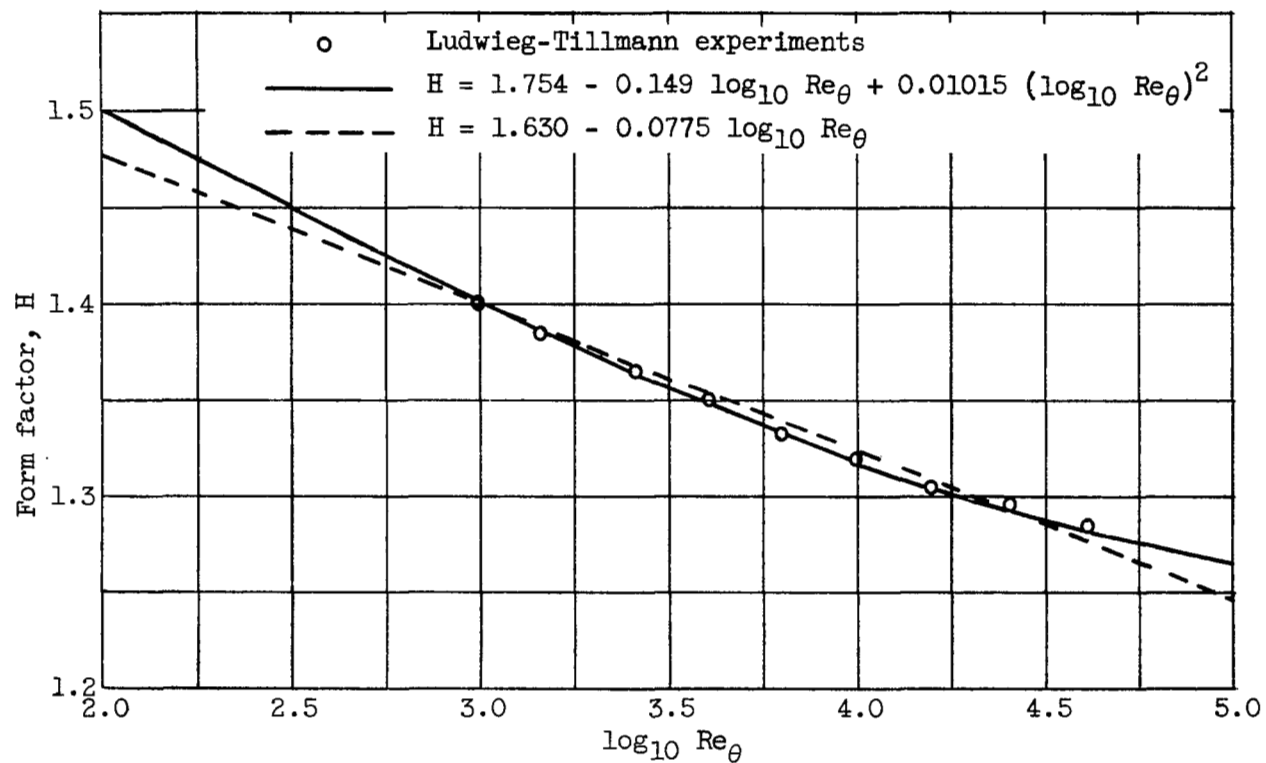
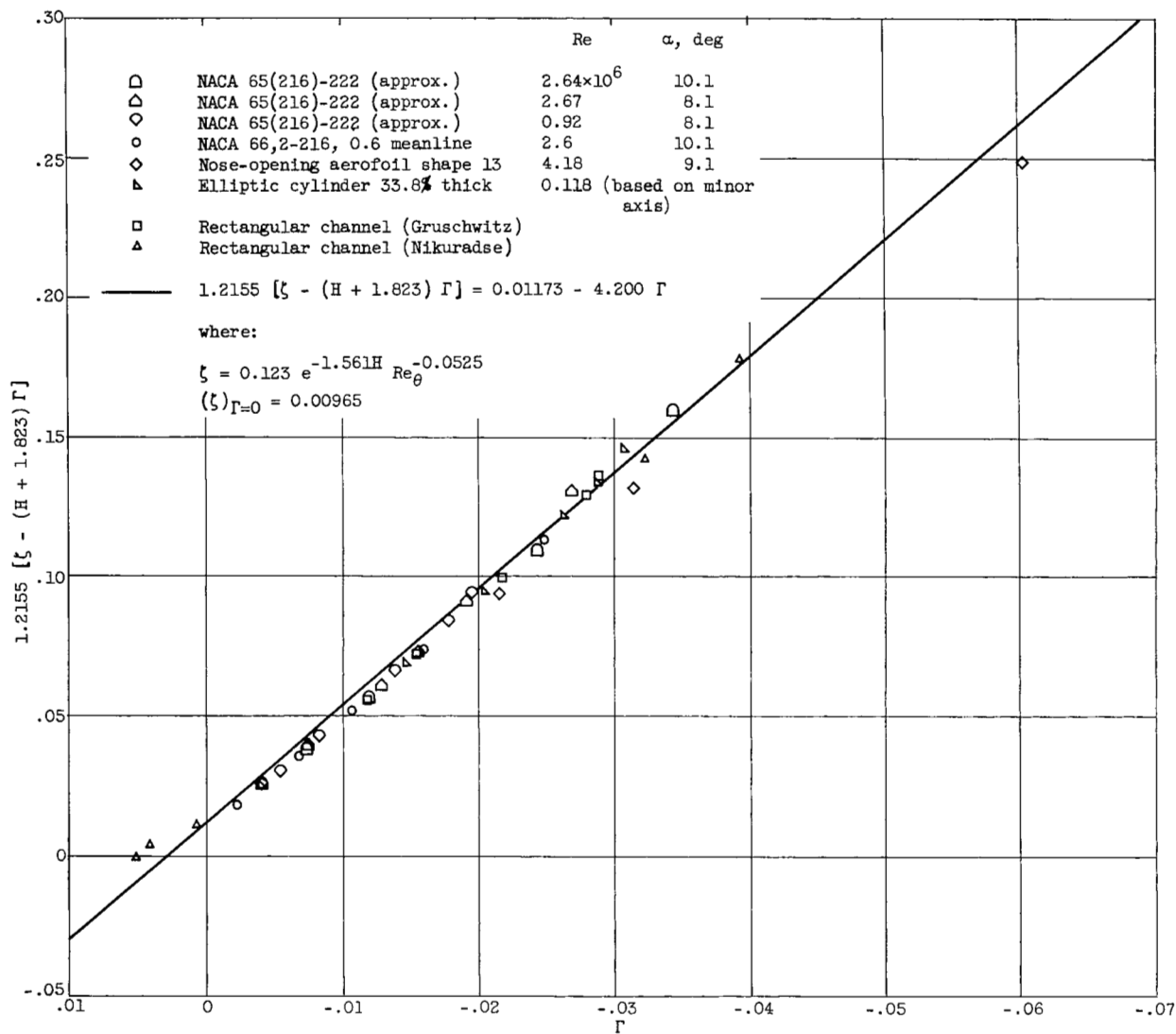


Figure 22. - Profile parameter H for flat-plate flow (ref. 11).

Figure 23. - Experimental values of function $1.2155 [\zeta - (H + 1.823) \Gamma]$ (ref. 11).

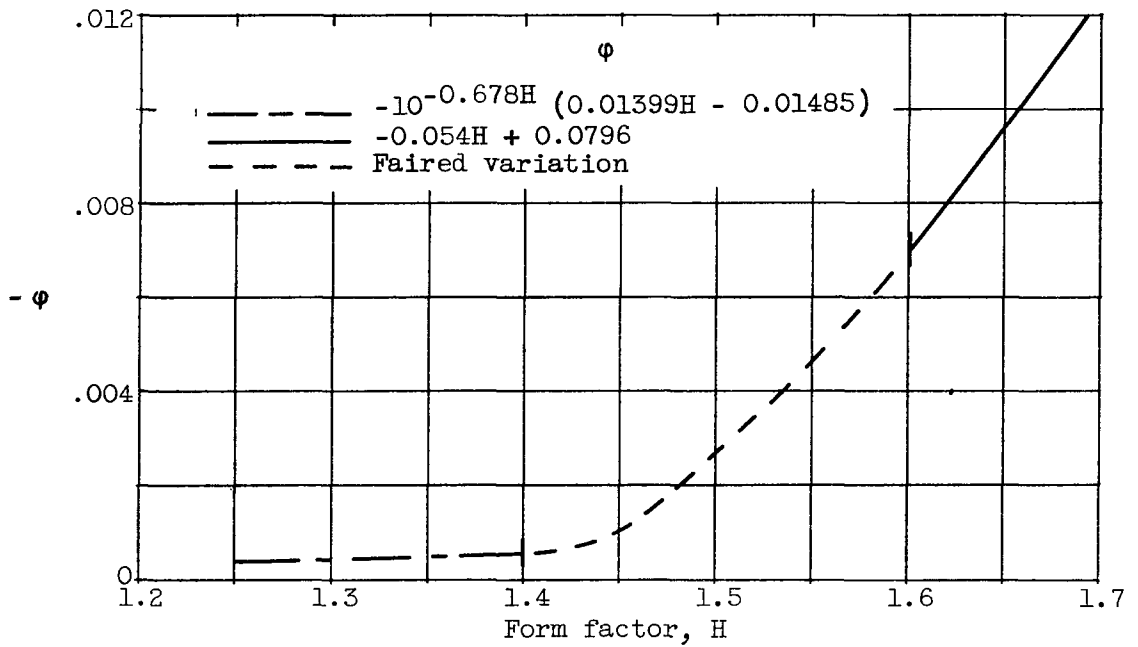


Figure 24. - Definition of ϕ as function of H (ref. 11).

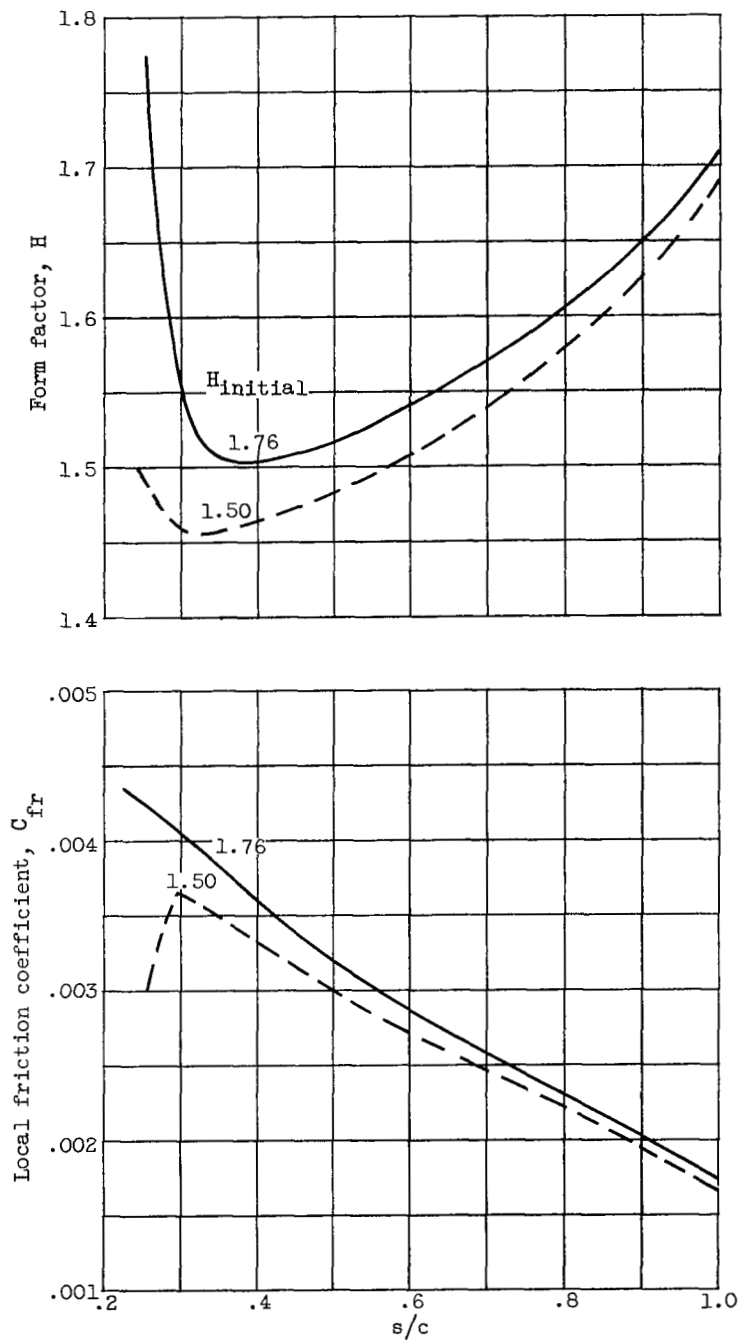


Figure 25. - Effect of initial value of H on calculated values of form factor and skin-friction coefficient in turbulent boundary layer on upper surface of airfoil section RAE 101. Blade-chord Reynolds number, 1.7×10^6 ; lift coefficient, 0.4 (ref. 11).

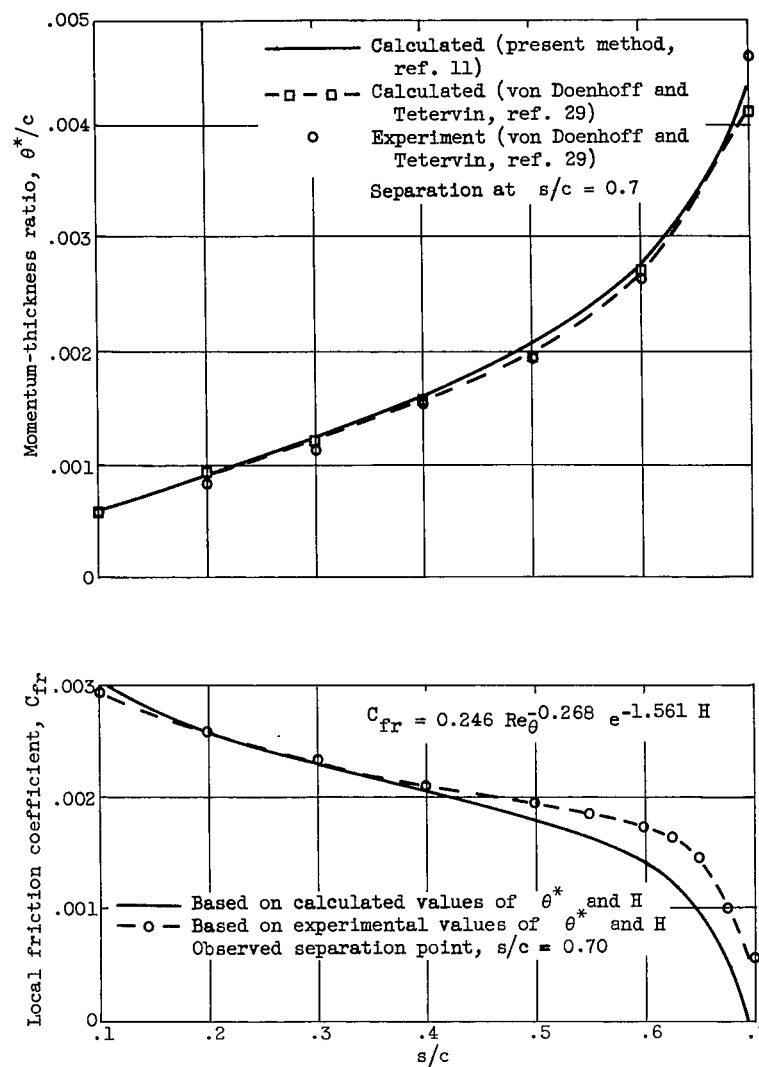
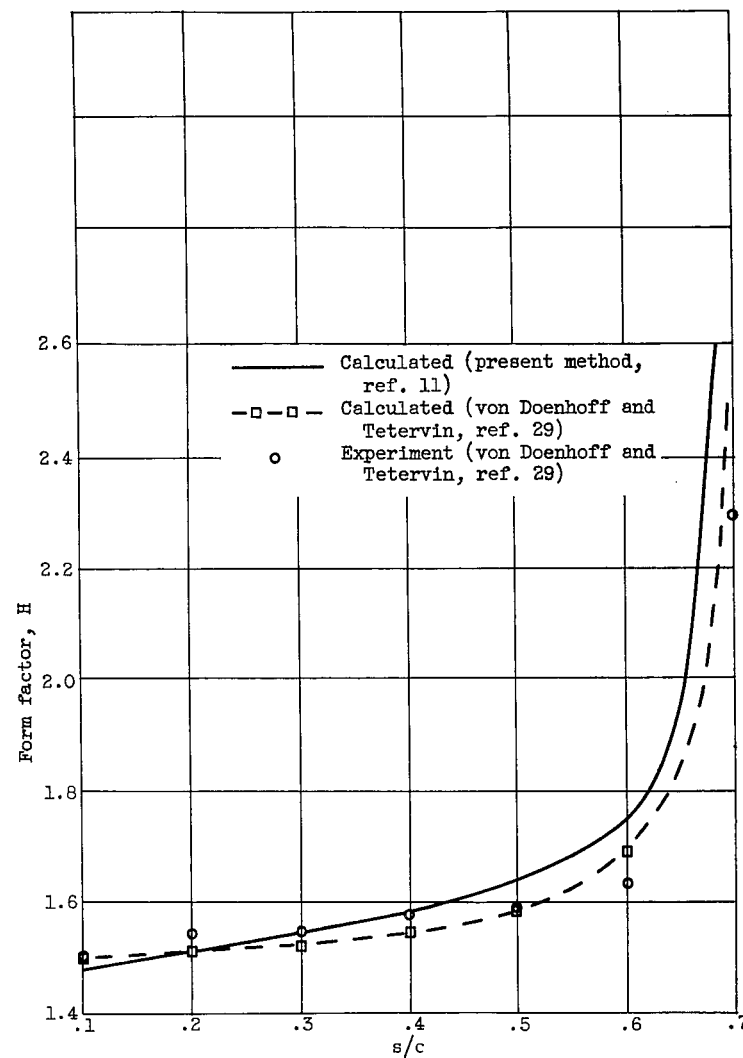


Figure 26. - Comparison of experimental and calculated distributions of boundary-layer parameters for NACA airfoil section 66,2-216. Blade-chord Reynolds number, 2.64×10^6 ; angle of attack, 10.1° (ref. 11).



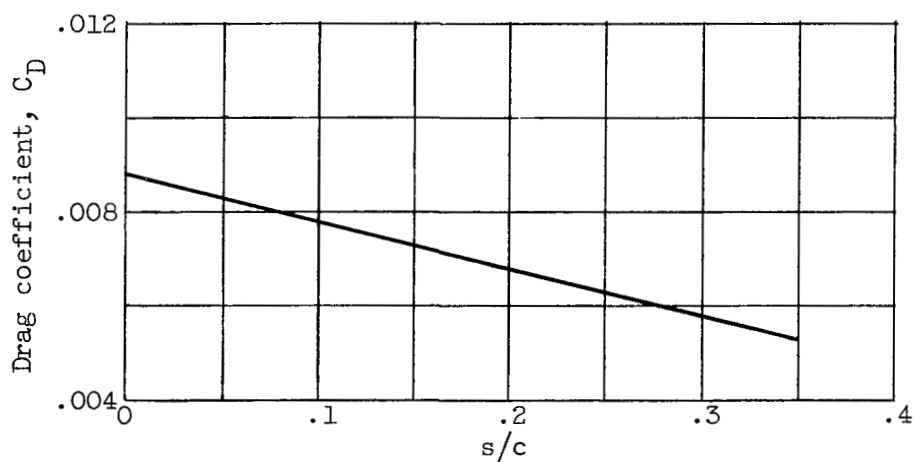


Figure 27. - Variation of profile drag with location of transition point for 14-percent-thick wing at blade-chord Reynolds number of 10^7 (ref. 6).

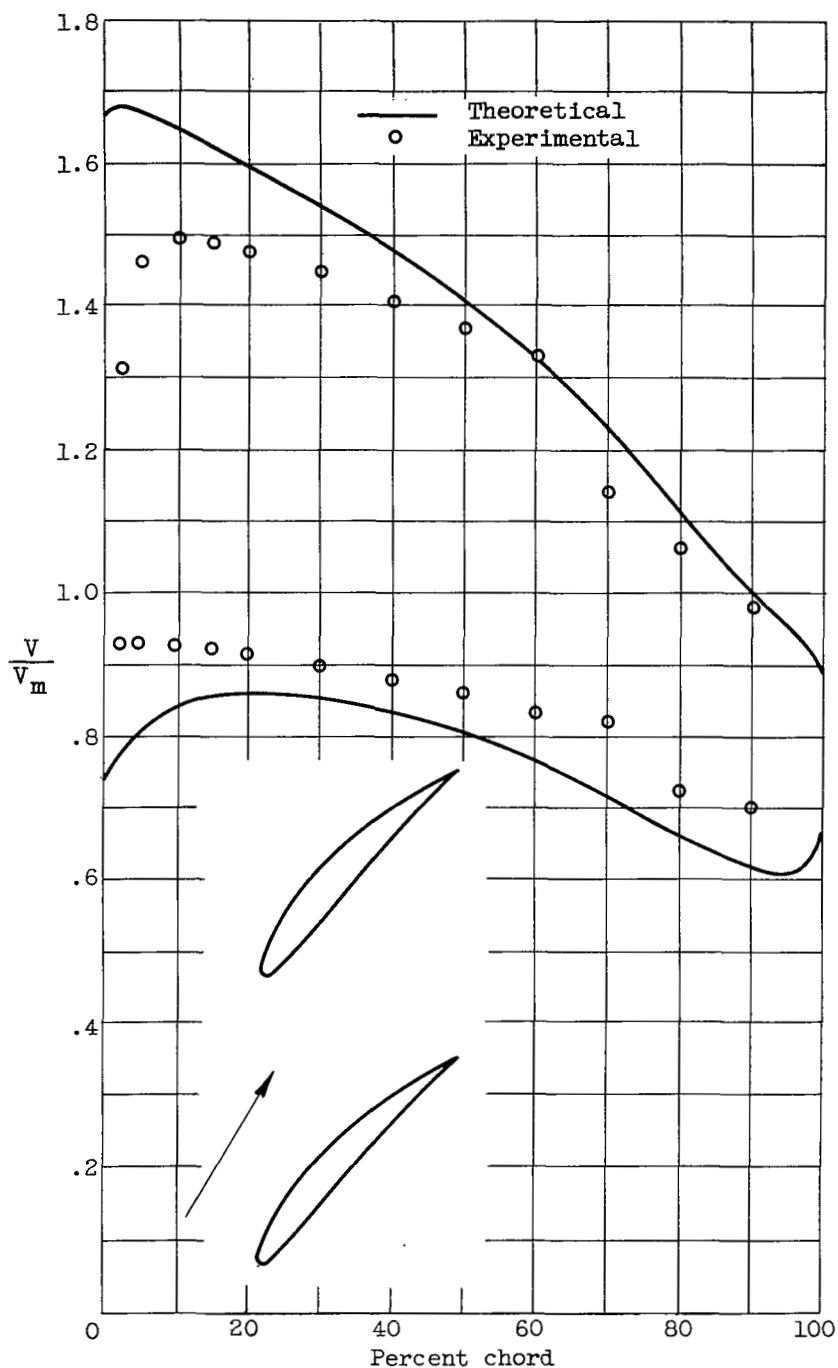


Figure 28. - Comparison of experimental and theoretical velocity distribution on airfoil in cascade. Airfoil, NACA 65-(12)10; inlet-air angle, 60° ; angle of attack, 14.1° ; angle of attack of mean vector velocity, 6.5° ; turning angle, 18.6° ; solidity, 1.0 (ref. 32).

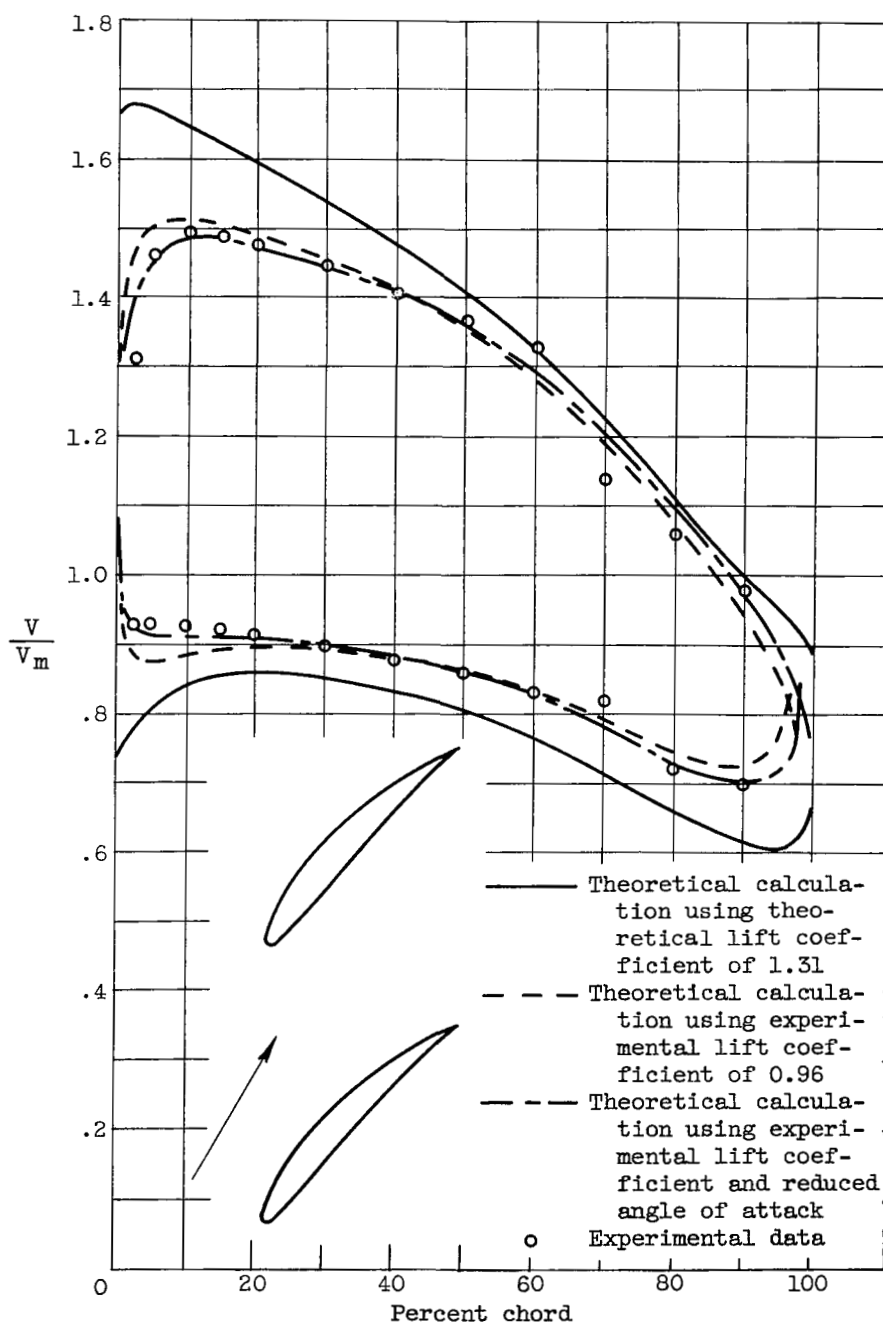


Figure 29. - Comparison of experimental velocity distribution with theoretical velocity distribution corrected for circulation and angle of attack on airfoil in cascade. Airfoil, NACA 65-(12)10; inlet-air angle, 60° ; angle of attack, 14.1° ; angle of attack of mean vector velocity, 6.5° ; turning angle, 18.6° ; solidity, 1.0 (ref. 32).

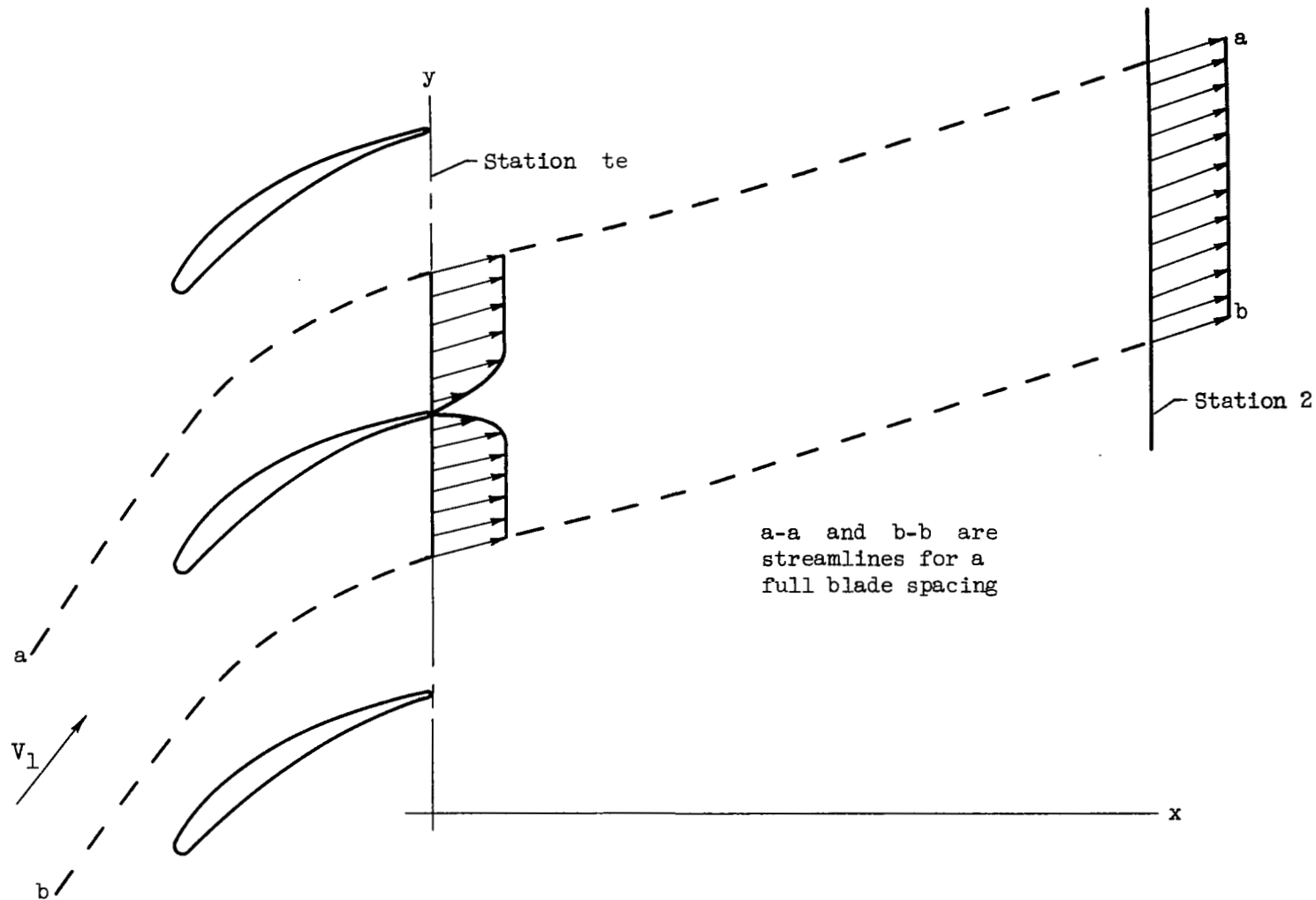


Figure 30. - Cascade flow indicating velocity distribution at trailing edge and after complete mixing has occurred.



3 1176 01438 6628

~~CONFIDENTIAL~~